BEILSTEIN JOURNAL OF ORGANIC CHEMISTRY

π-Conjugated molecules and materials

Edited by Chunyan Chi and Aurelio Mateo-Alonso

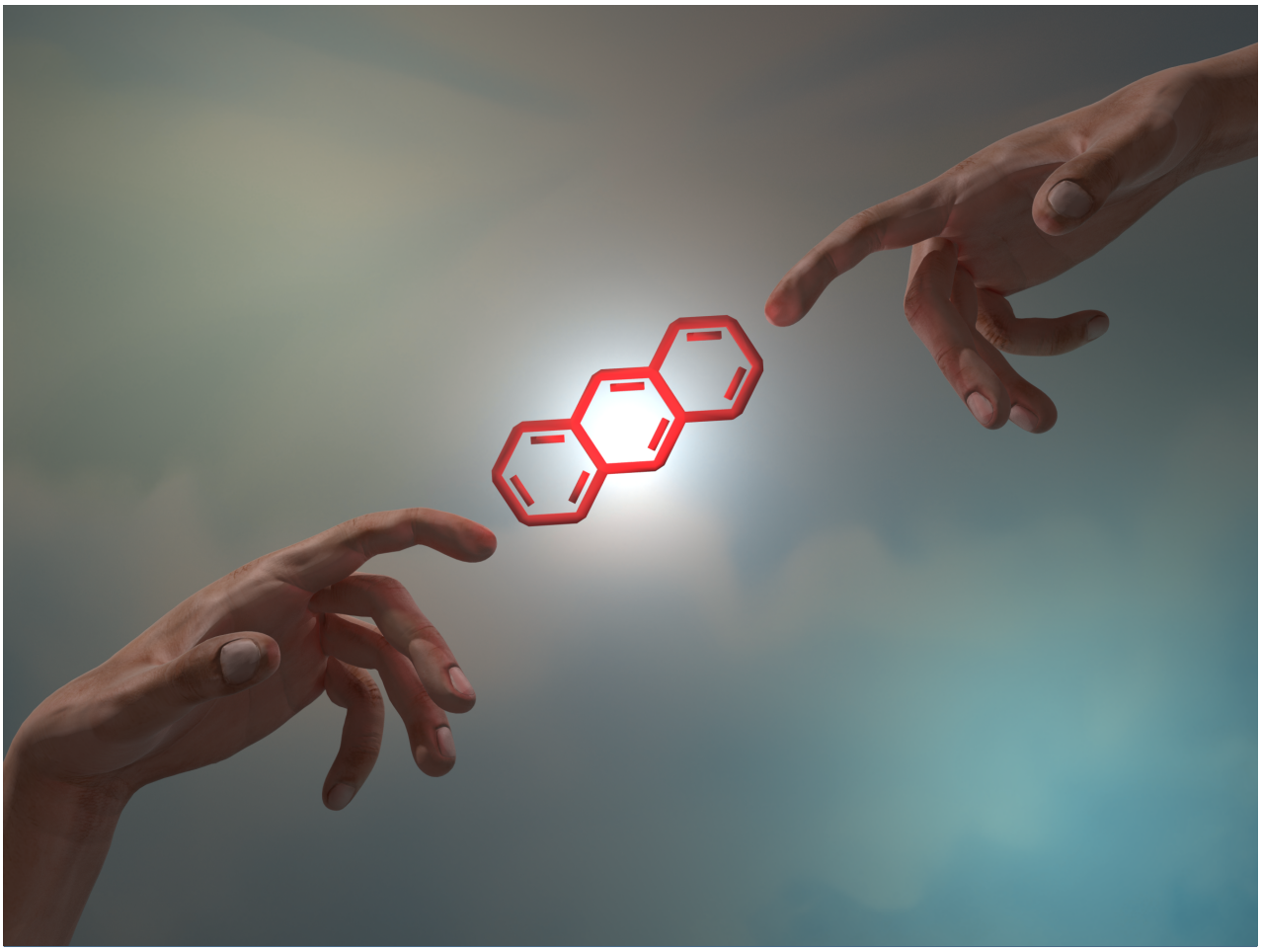

Imprint

Beilstein Journal of Organic Chemistry
www.bjoc.org
ISSN 1860-5397
Email: journals-support@beilstein-institut.de

The *Beilstein Journal of Organic Chemistry* is published by the Beilstein-Institut zur Förderung der Chemischen Wissenschaften.

Beilstein-Institut zur Förderung der Chemischen Wissenschaften
Trakehner Straße 7–9
60487 Frankfurt am Main
Germany
www.beilstein-institut.de

BEILSTEIN JOURNAL OF ORGANIC CHEMISTRY

Kinetically stabilized 1,3-diarylisobenzofurans and the possibility of preparing large, persistent isoacenofurans with unusually small HOMO–LUMO gaps

Qian Liu and Glen P. Miller*

Full Research Paper

Open Access

Address:
Department of Chemistry, University of New Hampshire, 23 Academic Way, Durham, New Hampshire 03864-3598, USA

Email:
Glen P. Miller* - glen.miller@unh.edu

* Corresponding author

Keywords:
acene; DFT calculation; highly delocalized π-system; isoacenofuran; isobenzofuran; kinetically stabilized; organic semiconductor; small HOMO–LUMO gap; synthesis

Beilstein J. Org. Chem. **2024,** *20,* 1099–1110.
https://doi.org/10.3762/bjoc.20.97

Received: 04 December 2023
Accepted: 24 April 2024
Published: 17 May 2024

This article is part of the thematic issue "π-Conjugated molecules and materials".

Guest Editor: A. Mateo-Alonso

Abstract

DFT calculations demonstrate that an isoacenofuran of any size possesses a smaller HOMO–LUMO gap than the corresponding acene bearing an isoelectronic π-system (i.e., the same total number of rings). Isoacenofurans show limited stability due in part to the highly reactive 1,3-carbons of the furan ring. Both 1,3-dimesitylisobenzofuran and 1,3-di(2',4',6'-triethylphenyl)isobenzofuran, each bearing sterically congesting *ortho*-alkyl groups on their phenyl substituents, have been synthesized and shown to adopt non-planar conformations with the *ortho*-alkyl groups located above and below the most reactive 1,3-carbons of the furan ring. These bulky substituents provide a strong measure of kinetic stabilization. Thus, 1,3-dimesitylisobenzofuran and 1,3-di(2',4',6'-triethylphenyl)isobenzofuran are significantly less reactive than 1,3-diphenylisobenzofuran toward the strong dienophiles DMAD and acrylonitrile. The insights gained here suggest that the synthesis of large, persistent, kinetically stabilized isoacenofurans with unusually small HOMO–LUMO gaps is achievable. As such, these molecules deserve increased attention as potential p-type organic semiconductors.

Introduction

Acenes are composed of linearly annellated benzene rings. Compared to their non-linearly annellated isomers, acenes possess smaller HOMO–LUMO gaps. This is attributed to their novel electronic structures which manifest that no more than one benzene ring can be drawn with a full aromatic sextet in any neutral, closed-shell resonance form (Figure 1) [1]. One can view an aromatic sextet in any one resonance form as a set of six π-electrons that are localized to one ring whereas other π-electrons are delocalized over the remaining π-system. We associate larger, more highly delocalized π-systems with smaller HOMO–LUMO gaps.

Isoacenofurans are composed of linearly annellated benzene rings that terminate with a furan ring. Isoacenofurans and

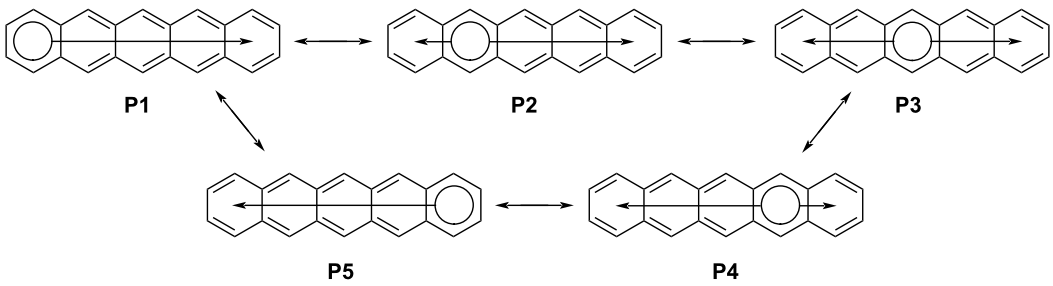

Figure 1: Neutral, closed-shell resonance forms for pentacene highlighting Clar aromatic sextets (see [1]) and the degree to which the remaining π-electrons are extensively delocalized, or not.

acenes possess isoelectronic π-systems when the total number of rings is the same. Unlike acenes, none of the 6-membered rings in an isoacenofuran possess an aromatic sextet in any neutral, closed-shell resonance form (Figure 2). Thus, compared to the corresponding acene, an isoacenofuran could possess a more highly delocalized π-system and an even smaller HOMO–LUMO gap. For example, consider pentacene and isotetracenofuran. Pentacene can be drawn in several neutral, closed-shell resonance forms (Figure 1) in which any one of the five 6-membered rings possess an aromatic sextet. If the aromatic sextet is located in a terminal ring of the molecule, as in resonance forms **P1** and **P5** of Figure 1, then the remaining π-electrons are delocalized over four rings. However, calculations indicate that the center ring of pentacene and other acenes is the most aromatic [2] and therefore resonance form **P3** of Figure 1 is most significant.

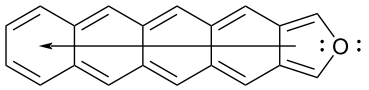

Figure 2: The only neutral, closed-shell resonance form for 5-ring isotetracenofuran with its highly delocalized π-system.

By contrast, isotetracenofuran and other isoacenofurans can only be drawn in one neutral, closed-shell resonance form in which only the furan ring possesses an aromatic sextet (Figure 2). The remaining π-electrons of isotetracenofuran are fully delocalized over the remaining four rings. This analysis suggests that all isoacenofurans should possess a more highly delocalized π-system than their acene counterparts, and potentially with smaller HOMO–LUMO gaps. However, a systematic study of HOMO–LUMO gaps for isoelectronic acene–isoacenofuran pairs has not been published. Should such a study reveal unusually small HOMO–LUMO gaps for isoacenofurans, we would consider persistent versions of these molecules to be a highly interesting class of organic semiconductors.

Hamura and co-workers pioneered the synthesis of large isoacenofurans. They prepared a pair of 1,3-diarylisoanthracenofurans [3] and a pair of 1,3-diphenethynylisoanthracenofurans [4], and impressively utilized the latter as intermediates for the synthesis of stabilized hexacenes. Their beautiful work documented the lack of stability associated with isoanthracenofurans. Thus, their 1,3-diarylisoanthracenofurans rapidly oxidized in solution to form endoperoxides [3]. These compounds persisted longer in the solid state, but clearly the lack of stability and persistence associated with isoacenofurans is of great concern if these molecules are to be utilized as organic semiconductors. Likewise, Hamura and co-workers' 1,3-diphenethynylisobenzofurans were fleeting intermediates that could not be isolated, but were instead trapped in situ by a suitable dienophile [4].

Large acenes are prone to photooxidation, especially when dissolved in solution while exposed to ambient light and air. They sensitize singlet oxygen formation, and the same is expected from large isoacenofurans. Indeed, the endoperoxides observed by Hamura and co-workers [3] confirm this expectation. We previously studied substituent effects in acenes and reported that several substituents promote photooxidative resistance in pentacenes [5] and larger acenes including heptacene [6] and nonacene [7]. One or more substituents that promote photooxidative resistance by quenching singlet oxygen could be utilized on isoacenofurans, too. Additionally, the 1,3-carbons of the furan ring in isoacenofurans are highly reactive towards dienophiles, including singlet oxygen. Thus, we believe that the design of large, persistent isoaceneofurans should include multiple substituents that provide photooxidative resistance, especially along the acene-like segment, plus a strong measure of kinetic stabilization at the 1,3-carbons of the furan ring.

As described here, there are compelling reasons to contemplate the synthesis of large, persistent isoacenofurans with unusually small HOMO–LUMO gaps. In this work, we probe several

aspects of this challenge. First, we utilize a DFT method to calculate HOMO–LUMO gaps associated with several isoacenofurans and compare them to the calculated HOMO–LUMO gaps of their isoelectronic acenes. Second, we synthesized two 1,3-diarylisobenzofurans that provide steric resistance to the most reactive 1,3-carbons of the furan ring. A combination of experimental and computational studies clarifies the impacts of these sterically congesting substituents on each molecule's electronic structure. We further studied the reaction rates of 1,3-diarylisobenzofurans with the strong dienophiles dimethyl acetelyenedicarboxylate (DMAD) and acrylonitrile. We conclude that the synthesis of large, persistent, kinetically stabilized isoacenofurans with unusually small HOMO–LUMO gaps is an achievable goal.

Results and Discussion

Computational HOMO–LUMO gaps for isoacenofurans and comparable acenes

We studied the HOMO–LUMO gaps associated with acenes and isoacenofurans (Figure 3) using a DFT method that has proven reliable for large acenes both in terms of absolute values and trends. In all cases, isoacenofurans possess a smaller HOMO–LUMO gap than the corresponding acene with an isoelectronic π-system. For example, naphthalene and isobenzofuran (**1**) both possess 10 π-electrons and are calculated to have HOMO–LUMO gaps of 4.73 and 4.05 eV, respectively. The incorporation of 1,3-diphenyl substituents (compound **2**) or 1,3-diphenylthio substituents (compound **4**) lowers the HOMO–LUMO gaps of the corresponding isobenzofurans to 3.05 and 3.65 eV, respectively. These groups provide for expanded delocalization of π-electron density outside the isobenzofuran core. Phenylthio substituents have also been shown to impart considerable photooxidative resistance to pentacene [5]. The incorporation of 1,3-dimesityl substituents (compound **3**) also provides for modest lowering of the HOMO–LUMO gap despite the non-planar geometry that these groups must adopt (Figure 4). We are keenly interested in preparing isoacenofurans with small HOMO–LUMO gaps. The non-planar geometry of mesityl and similar groups additionally provides for enhanced steric congestion at the most reactive 1,3-carbons of the furan ring (vide infra), and this could prove to be

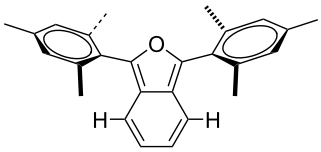

Figure 4: A structural rendering of 1,3-dimesitylisobenzofuran showing the requirement for non-planar mesityl groups in order to avoid steric repulsion between *ortho*-methyl groups and the nearest benzo hydrogen atoms.

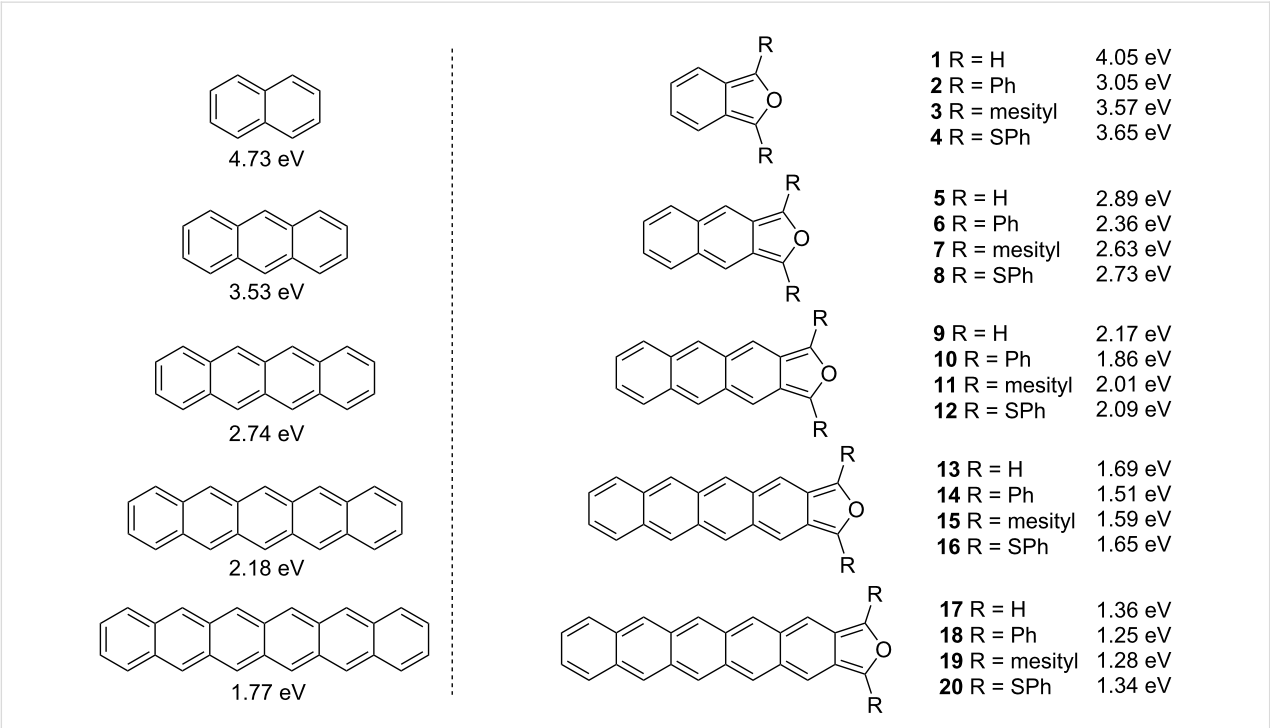

Figure 3: DFT calculated HOMO–LUMO gaps of acenes and isoacenofurans performed at the B3LYP/6-311+G(d,p)//B3LYP/6-31G(d) level of theory using Spartan '20 [8].

an important design strategy for large, persistent isoacenofurans.

The trend continues for the entire acene series calculated, from anthracene to hexacene (Figure 3). Thus, pentacene, a benchmark organic semiconductor, has a calculated HOMO–LUMO gap of 2.18 eV, nearly 0.5 eV greater than that of isotetracenofuran (**13**) with an isoelectronic π-system (22 π-electrons each). The incorporation of phenylthio groups (compound **16**) further lowers the HOMO–LUMO gap to 1.65 eV. Even in the presence of sterically congesting, non-planar 1,3-dimesityl groups, the corresponding isotetracenofuran (**15**) possesses an unusually small HOMO–LUMO gap of 1.59 eV.

Among the isoacenofurans studied here, the smallest calculated HOMO–LUMO gaps are observed in the isopentacenofuran series (compounds **17**–**20**). They possess HOMO–LUMO gaps between 1.25 and 1.36 eV, well below the 1.77 eV value calculated for hexacene. These Spartan '20 [8] calculations confirm our expectation of a more highly delocalized π-system in any isoacenofuran (Figure 2) compared to the corresponding acene with isoelectronic π-system (Figure 1). As such, isoacenofurans represent a highly interesting class of molecules that, although largely ignored in the literature, deserve increased attention as organic semiconductors with unusually small HOMO–LUMO gaps.

Synthesis of two 1,3-diarylisobenzofurans with sterically congesting substituents

In order to study the impacts of sterically congesting substituents at the 1,3-carbons of the furan ring, we synthesized two 1,3-diarylisobenzofurans (compounds **3** and **23**, Scheme 1). Combined with commercially available **2**, these compounds provide varying degrees of steric congestion to the highly reactive 1,3-carbons on the furan ring. Thus, phthaloyl chloride was reacted with mesitylene or 1,3,5-triethylbenzene to produce the corresponding diketones **21** and **22**. Each diketone was in turn reacted with zinc metal in glacial acetic acid [9] to afford the corresponding 1,3-diarylisobenzofurans **3** and **23**. The latter reductions in the presence of zinc likely proceed through the corresponding ketols which are known to undergo ring closure in acidic solution [10,11]. These syntheses utilizing mesitylene or 1,3,5-triethylbenzene are considerably simpler than other approaches that would place sterically congesting groups only at the *ortho* positions of the 1,3-diaryl substituents. Compounds **3** and **23** contain an additional *para* substituent that serves no particular purpose but is innocuous.

The syntheses of compounds **24** and **25** with 2',4',6'-triisopropylphenyl and 2',4',6'-tri-*tert*-butylphenyl substituents, respectively, were also attempted but without success. In these cases, the sterically congesting *ortho* isopropyl and *tert*-butyl groups stymie the Friedel–Crafts acylation step leading to diketone (Scheme 1).

Experimental and computational studies of 1,3-diarylisoacenofurans

Purified isobenzofurans **2**, **3** and **23** were studied by UV–vis and fluorescence spectroscopies (Figure 5). Compound **2** is devoid of *ortho* groups on its 1,3-diphenyl substituents and shows the longest wavelengths of absorption (λ_{max} = 415 nm) and emission (emission λ_{max} = 484 nm) in this series, consistent with a more highly conjugated π-system in which the 1,3-diphenyl substituents lie flat or nearly flat relative to the isobenzofuran backbone. Likewise, compound **2** is yellow while compounds **3** and **23** are colorless. Compounds **3** and **23** show similar absorption (λ_{max} = 364 and 360 nm for **3** and **23**, respectively) and emission (λ_{max} = 442 and 436 nm for **3** and **23**, respec-

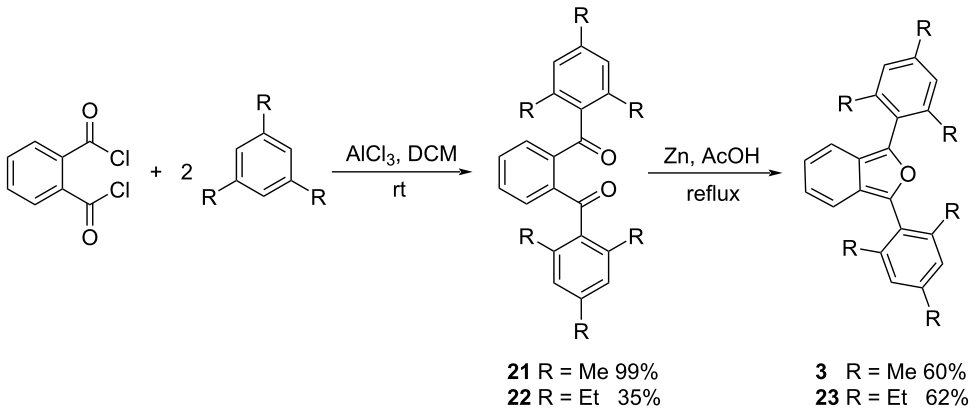

Scheme 1: Synthesis of 1,3-diarylisobenzofurans **3** and **23**.

tively) spectra, both consistent with a less conjugated π-system compared to **2**. This is due entirely to out-of-plane rotation of the sterically congesting 1,3-diaryl groups (Figure 4).

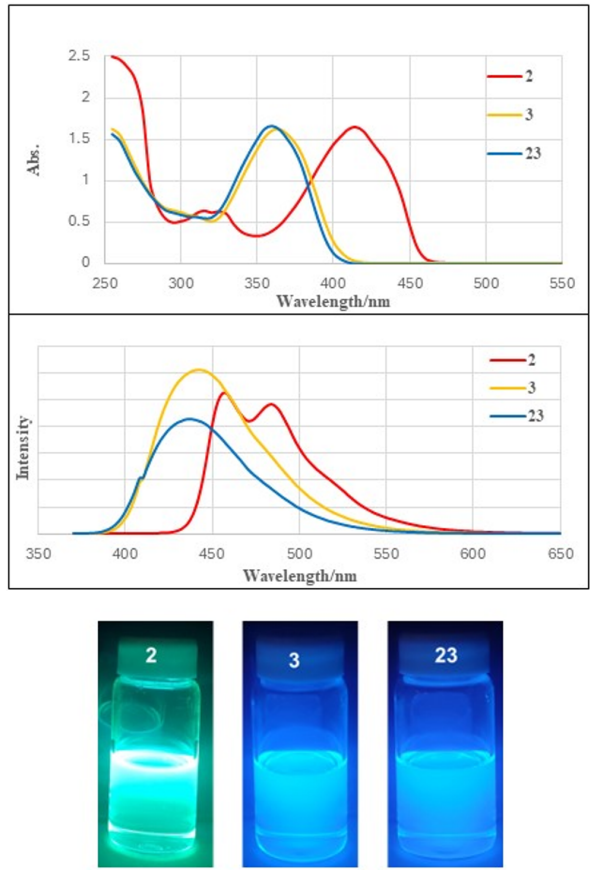

Figure 5: UV–vis (top) and fluorescence (middle) spectra for 10^{-6} M solutions of 1,3-diarylisobenzofurans **2**, **3** and **23** in CH_2Cl_2 solvent. The vials of **2**, **3** and **23** showing fluorescence emission (bottom) were excited at 365 nm.

In order to further probe the impact of sterically congesting 1,3-diaryl substituents in 1,3-diarylisobenzofurans, we studied compounds **1**, **2**, **3**, **23**, **24** and **25** (Figure 6) using a DFT method. The calculated HOMO and LUMO orbitals are shown in Figure 6. Here, the impacts of 1,3-diaryl substituents are illuminated. Thus, both HOMO and LUMO orbital densities for **2** are spread throughout the molecule's entire π-system including the 1,3-diphenyl substituents. This extensive delocalization of orbital density significantly raises the HOMO energy level and lowers the LUMO energy level compared to parent isobenzofuran (**1**). Conversely, both the HOMO and LUMO orbitals for compound **3** with 1,3-dimesityl substituents show reduced orbital density on the mesityl substituents compared to the phenyl substituents of **2**. Likewise, **3** possesses a lower energy HOMO orbital and a higher energy LUMO orbital compared to **2**. The π-systems for compounds **23**, **24** and **25** with 2',4',6'-triethylphenyl, 2',4',6'-triisopropylphenyl and 2',4',6'-tri-*tert*-butylphenyl substituents are quite similar to each other. Each shows little or no HOMO or LUMO orbital densities on their respective 1,3-diaryl groups indicating greater out-of-plane rotation compared to **3** and modestly larger HOMO–LUMO gaps.

The calculated UV–vis spectra for this series are shown in Figure 7. Compounds **23**, **24** and **25** show nearly identical spectra indicating that each hindered 1,3-diaryl ring is similarly rotated out of plane leading to π-systems with similar HOMO–LUMO gaps. These findings inform any design strategy leading to large, persistent isoacenofurans. Thus, unless there is a need for improved kinetic stabilization of the most reactive 1,3-carbons on the furan ring, there appears little benefit of utilizing highly hindered 2',4',6'-triisopropyl- (compound **24**) or 2',4',6'-tri-*tert*-butyl (compound **25**) substituents, especially as these compounds are considerably more difficult to synthesize compared to **3** and **23**.

Relative rates for the reactions between 1,3-diarylisobenzofurans **2**, **3** and **23** with the strong dienophiles dimethyl acetelyene-dicarboxylate (DMAD) and acrylonitrile

We studied the reactions of **2**, **3** and **23** under pseudo-1st order kinetic conditions by utilizing a 7000-fold excess of dimethyl acetylenedicarboxylate (DMAD) at room temperature. The reactions were monitored by UV–vis spectroscopy. Compound **2** undergoes rapid reaction with DMAD under these conditions and is more than 90% consumed after 2.5 hours (Figure 8, top). Conversely, compounds **3** (Figure 8, bottom) and **23** are unreactive under these conditions, even after extended periods of time. The absorptions for **3** and **23** actually increased slowly over extended time due to the gradual evaporation of CH_2Cl_2 solvent in the capped UV–vis cuvette. Similar results were obtained upon switching the dienophile from DMAD to acrylonitrile. Once again, compounds **3** and **23** were unreactive, even after 184 hours of reaction time with a 13,500-fold excess of acrylonitrile.

The reaction between **3** and a large excess of DMAD (116 equivalents) in boiling toluene (111 °C) was also studied by ^{1}H NMR spectroscopy. After 51 hours of reaction in boiling CH_2Cl_2, Diels–Alder adduct **27** was observed in 22% yield. Compound **27** was identified by ^{1}H NMR and ^{13}C NMR spectroscopies as well as high-resolution ESI mass spectrometry.

Although the lack of reactivity observed for **3** and **23** limited our kinetic analysis, we can nonetheless conclude that the rates of reactions between either **3** or **23** and either of the strong

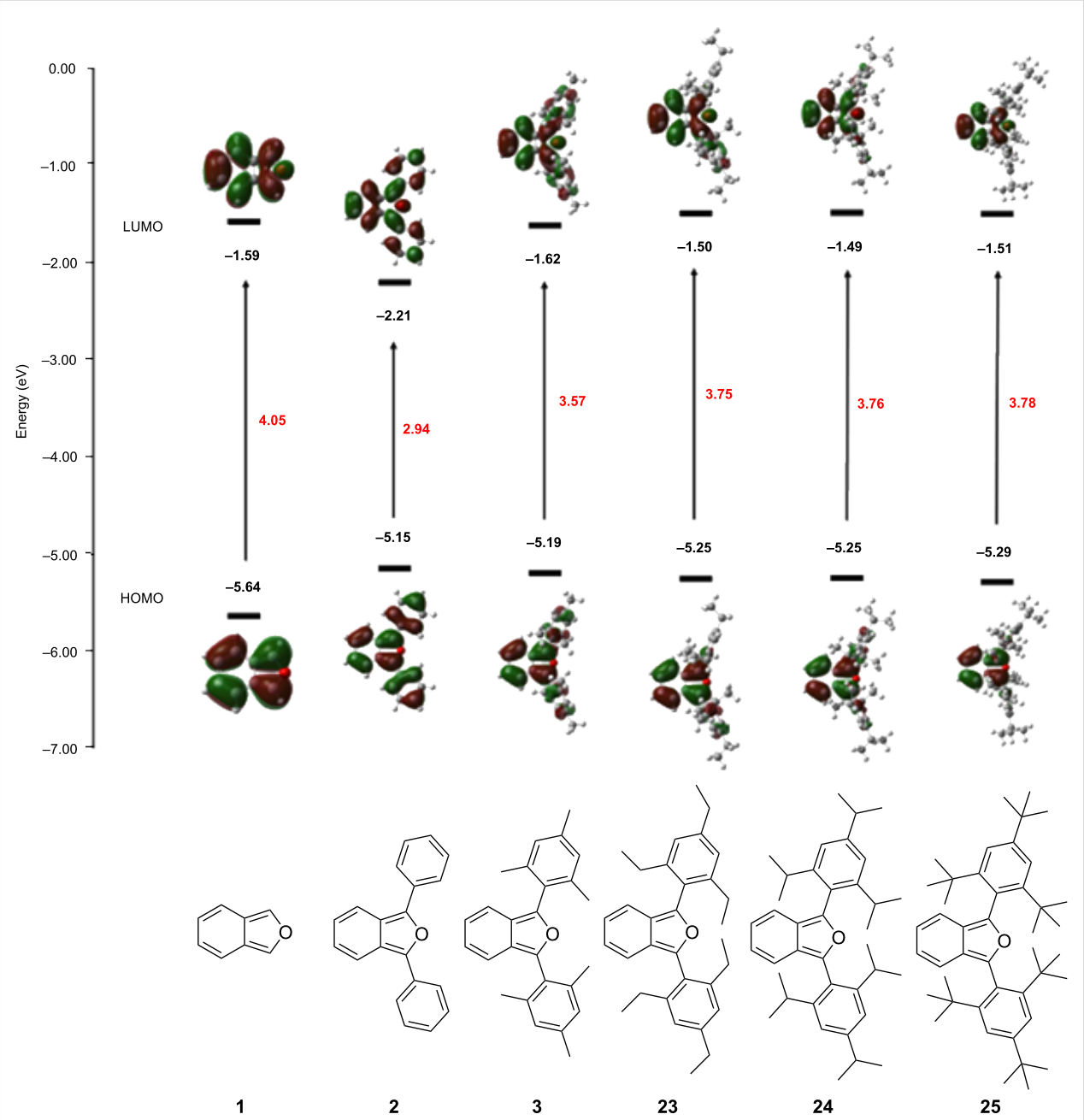

Figure 6: Calculated HOMO and LUMO orbitals for parent isobenzofuran (**1**) and 1,3-diarylisobenzofuran derivatives **2**, **3**, **23**, **24** and **25** using a DFT method performed at the B3YLP/6-311+G(d,p)//B3YLP/6-31G(d) level using Gaussian 09 [12].

dienophiles, DMAD or acrylonitrile, are at least two orders of magnitude slower than the corresponding reactions involving **2** (Scheme 2). Clearly, the non-planar geometry of the mesityl (Figure 4) and 2',4',6'-triethylphenyl substituents in compounds **3** and **23**, respectively, provides for enhanced steric congestion at the most reactive 1,3-carbons of the furan ring. Likewise, **3** and **23** are stable indefinitely in the solid state and persist for days in solution phase without significant decomposition (see Supporting Information File 1). The mesityl and 2',4',6'-triethylphenyl substituents both provide a strong measure of kinetic stabilization. Solution phase stability is particularly important if isoacenofurans are to be utilized as thin-film organic semiconductors cast from solution.

Conclusion

We utilized DFT calculations to demonstrate that isoacenofurans of any size possess smaller HOMO–LUMO gaps than the corresponding acene bearing an isoelectronic π-system. This

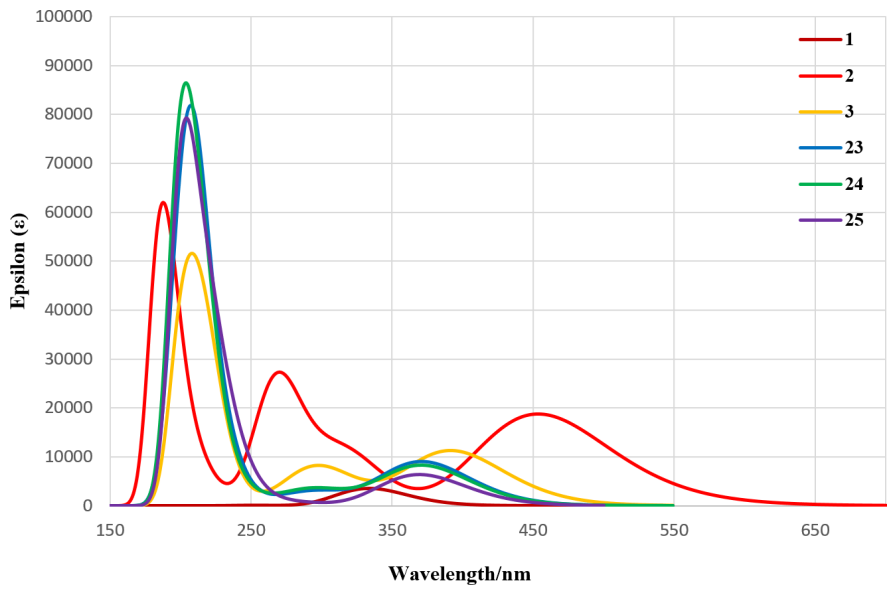

Figure 7: UV–vis spectra calculated for 1,3-diarylisobenzofuran derivatives **1**, **2**, **3**, **23**, **24** and **25** using a DFT method performed at the B3YLP/6-311+G(d,p)//B3YLP/6-31G(d) level using Gaussian 09 [12].

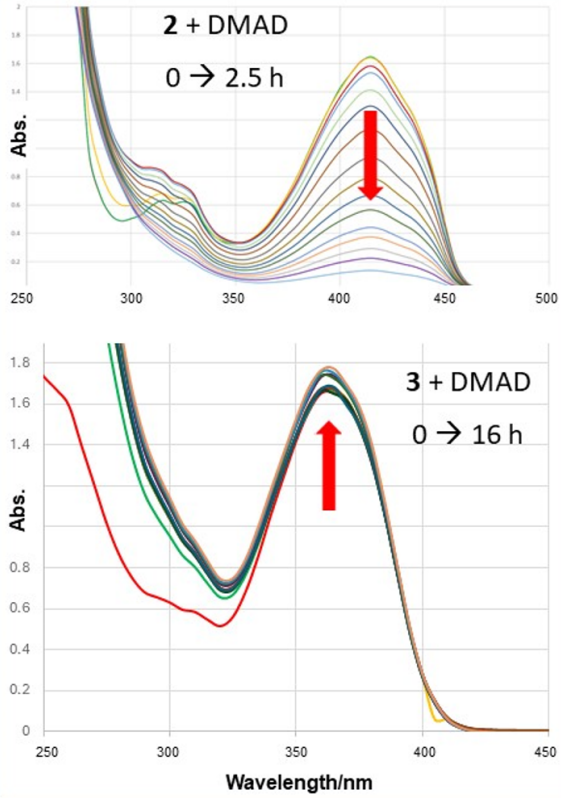

Figure 8: UV–vis spectra for the reactions of **2** (top) and **3** (bottom) with a 7000-fold excess of DMAD in CH_2Cl_2 solvent at room temperature.

finding alone provides compelling reasons to attempt the synthesis of large, persistent isoacenofurans for use as organic semiconductors. However, such syntheses must account for the projected lack of stability associated with isoacenofurans. We demonstrated that sterically congesting *ortho* groups on 1,3-diarylisobenzofurans like **3** and **23** force the molecules to adopt non-planar conformations in which the aryl groups rotate out-of-plane. The out-of-plane rotations provide for enhanced steric congestion both above and below the most reactive 1,3-carbons of the furan ring, dramatically reducing their reactivity with dienophiles including DMAD, acrylonitrile and singlet oxygen. Due to these non-planar conformations, the HOMO and LUMO orbitals for **3** and **23** and related compounds show reduced orbital densities on their aryl substituents, effectively reducing π-conjugation and raising HOMO–LUMO gaps. There appears little benefit to utilizing highly hindered 2',4',6'-triisopropylphenyl groups as in **24** or 2',4',6'-tri-*tert*-butylphenyl groups as in **25**, especially as (i) isoacenofurans with these substituents are considerably more difficult to synthesize, and (ii) compounds **3** and **23** already provide excellent kinetic stabilization to the most reactive 1,3-carbons of the furan ring. Like acenes, large isoacenofurans will be prone to photooxidation along their acene-like backbones, necessitating additional, strategically placed substituents that are known to slow photooxidation. The insights gained here suggest that the synthesis of large, persistent, kinetically stabilized isoacenofurans with unusually small HOMO–LUMO gaps is achievable. As such, these molecules deserve increased attention as a new class of organic semiconductors.

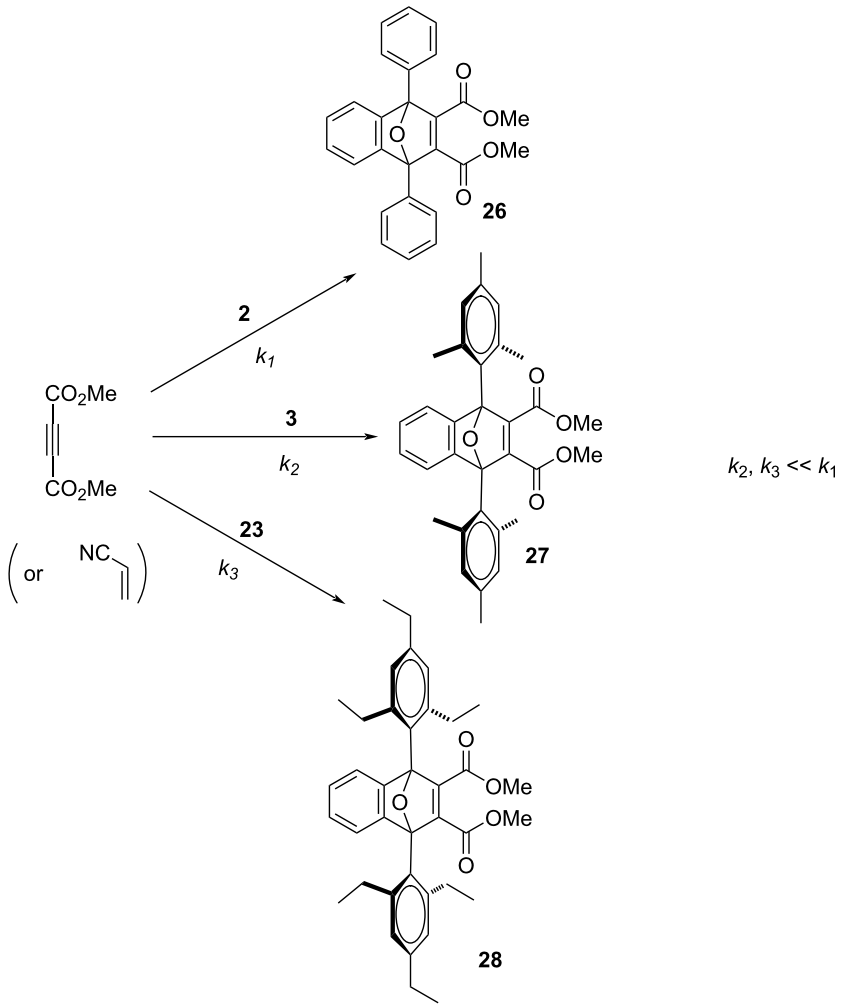

Scheme 2: Reactions between 1,3-diarylisobenzofurans **2**, **3** and **23** and DMAD to produce Diels–Alder adducts **26**, **27** and **28**.

Experimental

Materials and methods

Commercial reagents and solvents were purchased from Sigma-Aldrich, Alfa Aesar, TCI America or Thermo Fisher Scientific, and used as received. Dry solvents were obtained using a solvent purification system (Innovative Technologies, Inc.) and handled under a nitrogen atmosphere, unless otherwise noted. Flash chromatography was performed using SiliaFlash® F60 40–63 μm (230–400 mesh) 60 Å silica from Silicycle Inc. and RediSep® Rf Silica Flash Columns (12 g, 24 g or 40 g) on a CombiFlash® Rf 200 instrument (Teledyne Isco, Inc.). Evaporation of solvents was accomplished using an IKA® RV 10 digital rotary evaporator. Baker-flex® silica gel IB2-F thin-layer chromatography (TLC) plates were purchased from J.T. Baker. A 4 watt 254 nm lamp (Analtytik Jena Co.) and a modified cardboard box were utilized for detection of TLC spots. Melting points were determined in open capillary tubes using a Mel-Temp apparatus, and are uncorrected. Proton nuclear magnetic resonance (^{1}H NMR) spectra and carbon nuclear magnetic resonance (^{13}C NMR) spectra were recorded on either a Bruker 500 MHz or Bruker 700 MHz nuclear magnetic resonance spectrometer using 5 mm NMR tubes with plastic caps. High-resolution mass spectra (HRMS) were obtained on a Thermo Scientific Vanquish UHPLC and Exploris 120 Mass Spectrometer at the University of New Hampshire's University Instrumentation Center using a peak-matching protocol to determine the mass and error range of the molecular ion, and employing electrospray as the ionization technique. UV–vis absorption spectra were measured with a Varian Cary 50 Scan UV–visible spectrophotometer and corrected for background signal with a solvent-filled cuvette. Fluorescence spectra were measured on a FS5 spectrofluorometer (150 W CW Ozone-free xenon arc lamp) from Edinburgh Instruments.

1,3-Dimesitylisobenzofuran (**3**)

To a round bottom flask was added 1,2-phenylenebis(mesitylmethanone) (**21**, 0.10 g, 0.27 mmol), zinc dust (0.70 g, 11 mmol) and 10 mL glacial acetic acid. After attaching a reflux condenser, the mixture was heated to reflux for 12 hours with stirring. The hot reaction solution was filtered. To the hot filtrate was added 5 mL of cold water leading to the precipitation of crude product. The crude product was vacuum filtered, washed with 5 mL water, and then air dried to give **3** as a white solid (57 mg, 60%, Scheme 3). Mp 169–170 °C (from [13], 188–189 °C); ^{1}H NMR (500 MHz, $CDCl_3$) δ 7.15–7.08 (m, 2H), 6.98 (s, 4H), 6.86–6.79 (m, 2H), 2.35 (s, 6H), 2.12 (s, 12H); ^{13}C NMR (126 MHz, $CDCl_3$) δ 143.54, 139.17, 138.71, 128.23, 127.43, 123.39, 121.93, 119.78, 21.22, 20.49; UV–vis λ_{max} (7×10^{-5} M in CH_2Cl_2): 364.3 nm; HRESIMS: calcd for $[M + H]^+$, 355.2062; found, 355.2042. For an alternative synthesis, see [13].

1,2-Phenylenebis(mesitylmethanone) (**21**)

To a 100 mL round bottom flask equipped with a stir bar was added anhydrous aluminum chloride (0.26 g, 2.0 mmol) and 10 mL of CH_2Cl_2 solvent. An addition funnel was attached and to this was added phthaloyl dichloride (0.20 g, 0.99 mmol) and 5 mL CH_2Cl_2. The content of the addition funnel was added dropwise into the round bottom flask over 5 minutes with stirring. The addition funnel was reloaded with mesitylene (0.215 g, 1.79 mmol) and an additional 5 mL CH_2Cl_2. The content of the addition funnel was once again added dropwise into the round bottom flask over 5 minutes with stirring. The light-yellow solution turned to dark brown. After 15 min, 10 mL of a saturated aqueous solution of NaCl was added to quench the reaction. The content of the flask was transferred to a 125 mL separatory funnel and extracted twice with 20 mL of CH_2Cl_2. The organic extracts were combined, dried over anhydrous Na_2SO_4 and gravity filtered. The solvent was evaporated at reduced pressure leaving a yellow solid as crude product. The crude product was recrystallized using 10 mL of hexane to obtain **21** as a crystalline white solid (0.33 g, 99%, Scheme 4). Mp 234–235 °C (from [14], 237–238 °C); ^{1}H NMR (500 MHz, $CDCl_3$) δ 7.48–7.36 (m, 4H), 6.86 (s, 4H), 2.30 (s, 6H), 2.19 (s, 12H); ^{13}C NMR (126 MHz, $CDCl_3$) δ 199.60, 141.23, 139.54, 136.54, 136.07, 131.22, 130.38, 129.00, 21.17, 20.29. For an alternative synthesis, see [14].

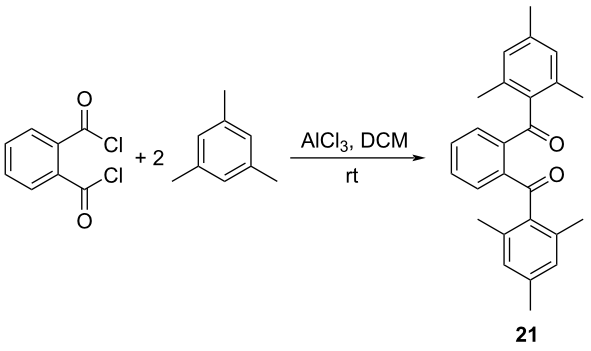

Scheme 4: Synthesis of 1,2-phenylenebis(mesitylmethanone) (**21**).

1,2-Phenylenebis((2,4,6-triethylphenyl)methanone) (**22**)

To a 100 mL round bottom flask equipped with a stir bar was added anhydrous aluminum chloride (0.66 g, 4.9 mmol) and 10 mL of CH_2Cl_2 solvent. An addition funnel was attached and to this was added phthaloyl dichloride (0.56 g, 2.8 mmol) and 5 mL CH_2Cl_2. The content of the addition funnel was added dropwise into the round bottom flask over 5 minutes with stirring. The addition funnel was reloaded with 1,3,5-triethylbenzene (0.90 g, 5.5 mmol) and an additional 5 mL CH_2Cl_2. The content of the addition funnel was once again added dropwise into the round bottom flask over 5 minutes with stirring. The light-yellow solution turned to dark brown. After 30 min, 10 mL of a saturated aqueous solution of NaCl was added to quench the reaction. The contents of the flask were transferred to a 125 mL separatory funnel and extracted twice with 20 mL of CH_2Cl_2. The organic extracts were combined, dried over anhydrous Na_2SO_4 and gravity filtered. The solvent was evaporated at reduced pressure leaving a yellow oil. The oil was purified by silica gel CombiFlash chromatography (hexane/EtOAc 9:1) to obtain **22** as a yellow solid (0.44 g, 35%, Scheme 5). Mp 59–60 °C; ^{1}H NMR (500 MHz, $CDCl_3$) δ 7.43 (s, 4H), 6.93 (s, 4H), 2.64 (q, J = 7.6 Hz, 4H), 2.53 (q, J = 7.5 Hz, 8H), 1.25 (t, J = 7.6 Hz, 6H), 1.08 (t, J = 7.5 Hz, 12H); ^{13}C NMR (126 MHz,

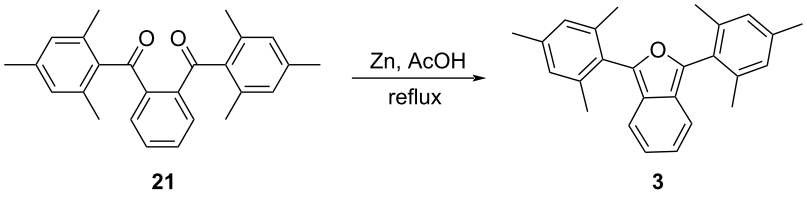

Scheme 3: Synthesis of 1,3-dimesitylisobenzofuran (**3**).

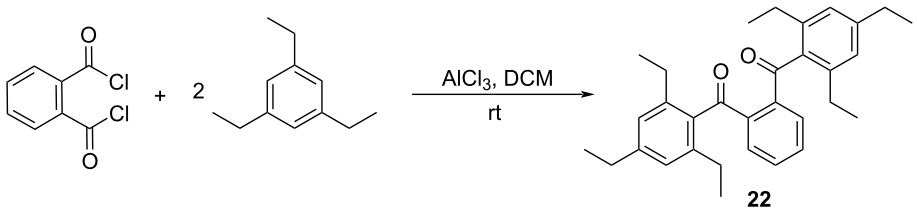

Scheme 5: Synthesis of 1,2-phenylenebis((2,4,6-triethylphenyl)methanone) (**22**).

$CDCl_3$) δ 199.43, 145.73, 142.40, 141.03, 135.73, 131.19, 131.05, 125.93, 28.78, 26.50, 15.81, 15.34; HRESIMS: calcd for $[M + H]^+$, 455.2950; found, 455.2938.

1,3-Bis(2,4,6-triethylphenyl)isobenzofuran (**23**)

To a round bottom flask was added 1,2-phenylenebis((2,4,6-triethylphenyl)methanone) (**22**, 0.20 g, 0.44 mmol), zinc dust (1.15 g, 17.6 mmol) and 13 mL glacial acetic acid. After attaching a reflux condenser, the mixture was heated to reflux for 12 hours with stirring. The hot reaction solution was filtered. To the hot filtrate was added 5 mL of cold water leading to precipitation of crude product. The crude product was vacuum filtered, washed with 5 mL water, and then air dried to give **23** as a white solid (0.12 g, 62%, Scheme 6). Mp 83–84 °C; ^{1}H NMR (500 MHz, $CDCl_3$) δ 7.15–7.08 (m, 2H), 7.02 (s, 4H), 6.84–6.77 (m, 2H), 2.69 (q, J = 7.6 Hz, 4H), 2.44 (m, 8H), 1.30 (t, J = 7.6 Hz, 6H), 1.01 (t, J = 7.5 Hz, 12H); ^{13}C NMR (126 MHz, $CDCl_3$) δ 145.90, 145.48, 143.28, 126.29, 125.50, 123.32, 122.18, 119.64, 28.85, 27.14, 15.82, 15.37; UV–vis λ_{max} (7×10^{-5} M in CH_2Cl_2): 360.2 nm; HRESIMS: calcd for $[M + H]^+$, 439.3001; found, 439.2987.

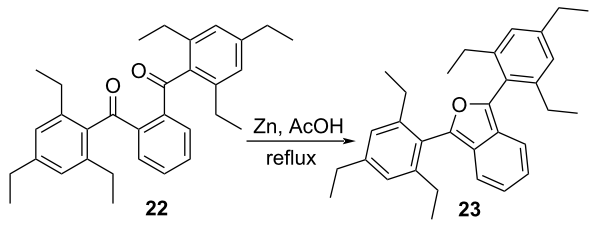

Scheme 6: Synthesis of 1,3-bis(2,4,6-triethylphenyl)isobenzofuran (**23**).

Dimethyl 1,4-diphenyl-1,4-dihydro-1,4-epoxynaphthalene-2,3-dicarboxylate (**26**)

In a similar manner to [15], 1,3-diphenylisobenozfuran (**2**, 0.10 g, 0.37 mmol), 5 mL CH_2Cl_2 and dimethyl acetylenedicarboxylate (DMAD, 0.116 g, 0.814 mmol) were added to a round bottom flask. The reaction mixture was stirred at room temperature for 2 hours. The solvent was removed by rotary evaporation at reduced pressure to give a light-yellow solid as crude product. The crude product was recrystallized using 5 mL of a hexane/ethanol mixture (10:1) and then air dried to give **26** as a white solid (0.11 g, 72%, Scheme 7). Mp 153.5–154.0 °C (from [15], 181–183 °C); ^{1}H NMR (500 MHz, $CDCl_3$) δ 7.76–7.70 (m, 4H), 7.53 (m, 2H), 7.50–7.40 (m, 6H), 7.15 (m, 2H), 3.68 (s, 6H); ^{13}C NMR (126 MHz, $CDCl_3$) δ 164.14, 153.90, 149.13, 133.16, 129.08, 128.58, 128.00, 125.99, 122.20, 94.05, 52.29; UV–vis λ_{max} (1×10^{-4} M in CH_2Cl_2): 230 nm; HRESIMS: calcd for $[M - OCH_3]^+$, 381.1127; found, 381.1115.

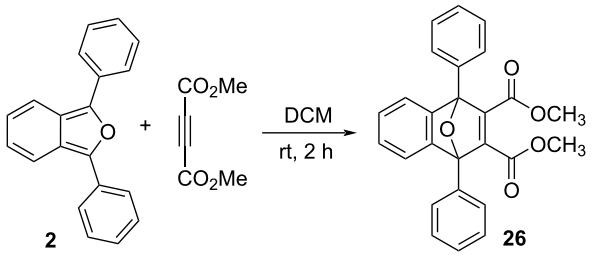

Scheme 7: Synthesis of dimethyl 1,4-diphenyl-1,4-dihydro-1,4-epoxynaphthalene-2,3-dicarboxylate (**26**).

Dimethyl 1,4-dimesityl-1,4-dihydro-1,4-epoxynaphthalene-2,3-dicarboxylate (**27**)

To a round bottom flask was added 1,3-dimesitylisobenozfuran (**3**, 0.05 g, 0.14 mmol), 5 mL CH_2Cl_2 and dimethyl acetylenedicarboxylate (DMAD, 2.31 g, 16.3 mmol). The reaction mixture was stirred at room temperature for 4 hours. The solvent was removed by rotary evaporation at reduced pressure to give a light-yellow solid. TLC (hexane/EtOAc 3:1) indicated no reaction. Additional DMAD was added to the unreacted mixture in the round bottom flask (2.31 g, 16.3 mmol) along with 2 mL toluene. After attaching a reflux condenser, the mixture was heated to reflux for 51 hours. The mixture was cooled to room temperature and toluene was removed by rotary evaporation at reduced pressure to give a sticky, dark brown solid. The solid was pre-purified by silica gel CombiFlash chromatography (hexane/EtOAc 9:1) to obtain a yellow oil as crude product (23 mg). Finally, the crude product was purified by preparative

TLC (petroleum ether/EtOAc 3:1) to give **27** as a yellow powdery solid (15 mg, 22%, 35% based on reacted **3**, Scheme 8). Mp 180 °C (dec.); ^{1}H NMR (700 MHz, $CDCl_3$) δ 7.29 (m, 2H), 6.98 (m, 2H), 6.88 (s, 4H), 3.64 (s, 6H), 2.30 (s, 12H), 2.28 (s, 6H); ^{13}C NMR (176 MHz, $CDCl_3$) δ 164.38, 155.13, 151.10, 139.03, 137.93, 130.68, 128.02, 124.72, 124.49, 95.54, 51.98, 23.71, 20.75; HRESIMS: calcd for $[M + H]^+$, 497.2328; found, 497.2316.

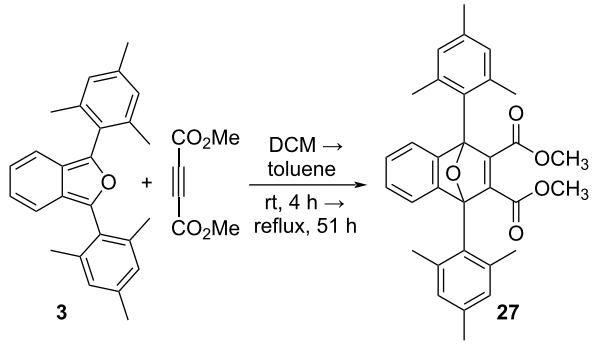

Scheme 8: Synthesis of dimethyl 1,4-dimesityl-1,4-dihydro-1,4-epoxynaphthalene-2,3-dicarboxylate (**27**).

Supporting Information

Supporting Information File 1

^{1}H NMR stability studies for compounds **3** and **23**, ^{1}H and ^{13}C NMR spectra for key compounds and ESI high-resolution mass spectra.
[https://www.beilstein-journals.org/bjoc/content/supplementary/1860-5397-20-97-S1.pdf]

Funding

The authors gratefully acknowledge financial support from the University of New Hampshire.

ORCID® iDs

Qian Liu - https://orcid.org/0009-0000-1479-1657
Glen P. Miller - https://orcid.org/0009-0004-7751-3573

Data Availability Statement

All data that supports the findings of this study is available in the published article and/or the supporting information to this article.

Preprint

A non-peer-reviewed version of this article has been previously published as a preprint: https://doi.org/10.3762/bxiv.2023.55.v1

References

1. Clar, E. *The Aromatic Sextet;* John Wiley & Sons: London, UK, 1972; pp 12–16.
2. Schleyer, P. v. R.; Manoharan, M.; Jiao, H.; Stahl, F. *Org. Lett.* **2001,** *3,* 3643–3646. doi:10.1021/ol016553b
3. Matsuoka, S.; Jung, S.; Miyakawa, K.; Chuda, Y.; Sugimoto, R.; Hamura, T. *Chem. – Eur. J.* **2018,** *24,* 18886–18889. doi:10.1002/chem.201804655
4. Kitamura, K.; Kudo, R.; Sugiyama, H.; Uekusa, H.; Hamura, T. *Chem. Commun.* **2020,** *56,* 14988–14991. doi:10.1039/d0cc06620f
5. Kaur, I.; Jia, W.; Kopreski, R. P.; Selvarasah, S.; Dokmeci, M. R.; Pramanik, C.; McGruer, N. E.; Miller, G. P. *J. Am. Chem. Soc.* **2008,** *130,* 16274–16286. doi:10.1021/ja804515y
6. Kaur, I.; Stein, N. N.; Kopreski, R. P.; Miller, G. P. *J. Am. Chem. Soc.* **2009,** *131,* 3424–3425. doi:10.1021/ja808881x
7. Kaur, I.; Jazdzyk, M.; Stein, N. N.; Prusevich, P.; Miller, G. P. *J. Am. Chem. Soc.* **2010,** *132,* 1261–1263. doi:10.1021/ja9095472
8. Shao, Y.; Gan, Z.; Epifanovsky, E.; Gilbert, A. T. B.; Wormit, M.; Kussmann, J.; Lange, A. W.; Behn, A.; Deng, J.; Feng, X.; Ghosh, D.; Goldey, M.; Horn, P. R.; Jacobson, L. D.; Kaliman, I.; Khaliullin, R. Z.; Kuś, T.; Landau, A.; Liu, J.; Proynov, E. I.; Rhee, Y. M.; Richard, R. M.; Rohrdanz, M. A.; Steele, R. P.; Sundstrom, E. J.; Woodcock, H. L., III; Zimmerman, P. M.; Zuev, D.; Albrecht, B.; Alguire, E.; Austin, B.; Beran, G. J. O.; Bernard, Y. A.; Berquist, E.; Brandhorst, K.; Bravaya, K. B.; Brown, S. T.; Casanova, D.; Chang, C.-M.; Chen, Y.; Chien, S. H.; Closser, K. D.; Crittenden, D. L.; Diedenhofen, M.; DiStasio, R. A., Jr.; Do, H.; Dutoi, A. D.; Edgar, R. G.; Fatehi, S.; Fusti-Molnar, L.; Ghysels, A.; Golubeva-Zadorozhnaya, A.; Gomes, J.; Hanson-Heine, M. W. D.; Harbach, P. H. P.; Hauser, A. W.; Hohenstein, E. G.; Holden, Z. C.; Jagau, T.-C.; Ji, H.; Kaduk, B.; Khistyaev, K.; Kim, J.; Kim, J.; King, R. A.; Klunzinger, P.; Kosenkov, D.; Kowalczyk, T.; Krauter, C. M.; Lao, K. U.; Laurent, A. D.; Lawler, K. V.; Levchenko, S. V.; Lin, C. Y.; Liu, F.; Livshits, E.; Lochan, R. C.; Luenser, A.; Manohar, P.; Manzer, S. F.; Mao, S.-P.; Mardirossian, N.; Marenich, A. V.; Maurer, S. A.; Mayhall, N. J.; Neuscamman, E.; Oana, C. M.; Olivares-Amaya, R.; O'Neill, D. P.; Parkhill, J. A.; Perrine, T. M.; Peverati, R.; Prociuk, A.; Rehn, D. R.; Rosta, E.; Russ, N. J.; Sharada, S. M.; Sharma, S.; Small, D. W.; Sodt, A.; Stein, T.; Stück, D.; Su, Y.-C.; Thom, A. J. W.; Tsuchimochi, T.; Vanovschi, V.; Vogt, L.; Vydrov, O.; Wang, T.; Watson, M. A.; Wenzel, J.; White, A.; Williams, C. F.; Yang, J.; Yeganeh, S.; Yost, S. R.; You, Z.-Q.; Zhang, I. Y.; Zhang, X.; Zhao, Y.; Brooks, B. R.; Chan, G. K. L.; Chipman, D. M.; Cramer, C. J.; Goddard, W. A., III; Gordon, M. S.; Hehre, W. J.; Klamt, A.; Schaefer, H. F., III; Schmidt, M. W.; Sherrill, C. D.; Truhlar, D. G.; Warshel, A.; Xu, X.; Aspuru-Guzik, A.; Baer, R.; Bell, A. T.; Besley, N. A.; Chai, J.-D.; Dreuw, A.; Dunietz, B. D.; Furlani, T. R.; Gwaltney, S. R.; Hsu, C.-P.; Jung, Y.; Kong, J.; Lambrecht, D. S.; Liang, W.; Ochsenfeld, C.; Rassolov, V. A.; Slipchenko, L. V.; Subotnik, J. E.; Van Voorhis, T.; Herbert, J. M.; Krylov, A. I.; Gill, P. M. W.; Head-Gordon, M. *Mol. Phys.* **2015,** *113,* 184–215. doi:10.1080/00268976.2014.952696
9. Blicke, F. F.; Patelski, R. A. *J. Am. Chem. Soc.* **1936,** *58,* 273–276. doi:10.1021/ja01293a023
10. Cava, M. P.; Mitchell, M. J.; Deana, A. A. *J. Org. Chem.* **1960,** *25,* 1481–1484. doi:10.1021/jo01079a005
11. Nishina, Y.; Kida, T.; Ureshino, T. *Org. Lett.* **2011,** *13,* 3960–3963. doi:10.1021/ol201479p
12. *Gaussian 09,* Revision E.01; Gaussian, Inc.: Wallingford, CT, 2013.

13. Franco, M. L. T. M. B.; Lazana, M. C. R. L. R.; Herold, B. J. *J. Chem. Soc., Faraday Trans.* **1991,** *87,* 1837–1842. doi:10.1039/ft9918701837
14. Volz, W.; Voß, J. *Synthesis* **1990,** 670–674. doi:10.1055/s-1990-26976
15. Karunakaran, J.; Nandakumar, M.; Senthil Kumar, N.; Mohanakrishnan, A. K. *Org. Biomol. Chem.* **2016,** *14,* 4247–4259. doi:10.1039/c6ob00628k

License and Terms

BEILSTEIN JOURNAL OF ORGANIC CHEMISTRY

Synthesis and characterization of 1,2,3,4-naphthalene and anthracene diimides

Adam D. Bass, Daniela Castellanos, Xavier A. Calicdan and Dennis D. Cao*

Full Research Paper

Open Access

Address:
Chemistry Department, Macalester College, 1600 Grand Avenue, Saint Paul, Minnesota 55105, United States

Email:
Dennis D. Cao* - dcao@macalester.edu

* Corresponding author

Keywords:
electron acceptors; organic materials; polycyclic aromatic hydrocarbons

Beilstein J. Org. Chem. **2024,** *20,* 1767–1772.
https://doi.org/10.3762/bjoc.20.155

Received: 18 March 2024
Accepted: 11 July 2024
Published: 25 July 2024

This article is part of the thematic issue "π-Conjugated molecules and materials".

Guest Editor: A. Mateo-Alonso

Abstract

We report the synthesis and characterization of naphthalene and anthracene scaffolds end-capped by cyclic imides. The solid-state structures of the *N*-phenyl derivatives, determined by X-ray crystallography, reveal changes in packing preference based on the number of aromatic rings in the core. The optical and electronic properties of the title compounds compare favorably with other previously described isomers and expand the toolbox of electron-deficient aromatic compounds available to organic materials chemists.

Introduction

Aromatic diimides are ubiquitous molecular scaffolds that have served as the basis for robust polymers, supramolecular assemblies, and (opto)electronic materials. The vast majority of this research has focused on 1,2,4,5-benzene (pyromellitic), 1,4,5,8-naphthalene, and 3,4,9,10-perylene diimides. Beyond these, researchers have demonstrated that translocating the cyclic imides around the periphery of the aromatic core to yield different structural isomers is effective for producing interesting new materials. Ourselves and others have investigated 1,2,3,4-benzene diimide, also known as mellophanic diimide [1], as a building block for heteroacenes [2-5] and polyimides [6-8]. The 1,2,5,6- [9,10] and 2,3,6,7-naphthalene diimides (NDIs) have been produced and utilized in electronically active polymers (Figure 1). The linear extension of 1,4,5,8-naphthalene diimide to produce tetracene [11] and hexacene [12] diimides, some with interesting properties such as near-IR absorption, has been achieved as well. Other efforts have demonstrated that anthracene diimides (ADIs) can be tuned to achieve decent electron mobilities in electronic settings [13,14]. Although there have been calculations conducted that suggest 6-membered cyclic imides are more compelling than 5-membered cyclic imides in organic electronic materials [15], the experimental ob-

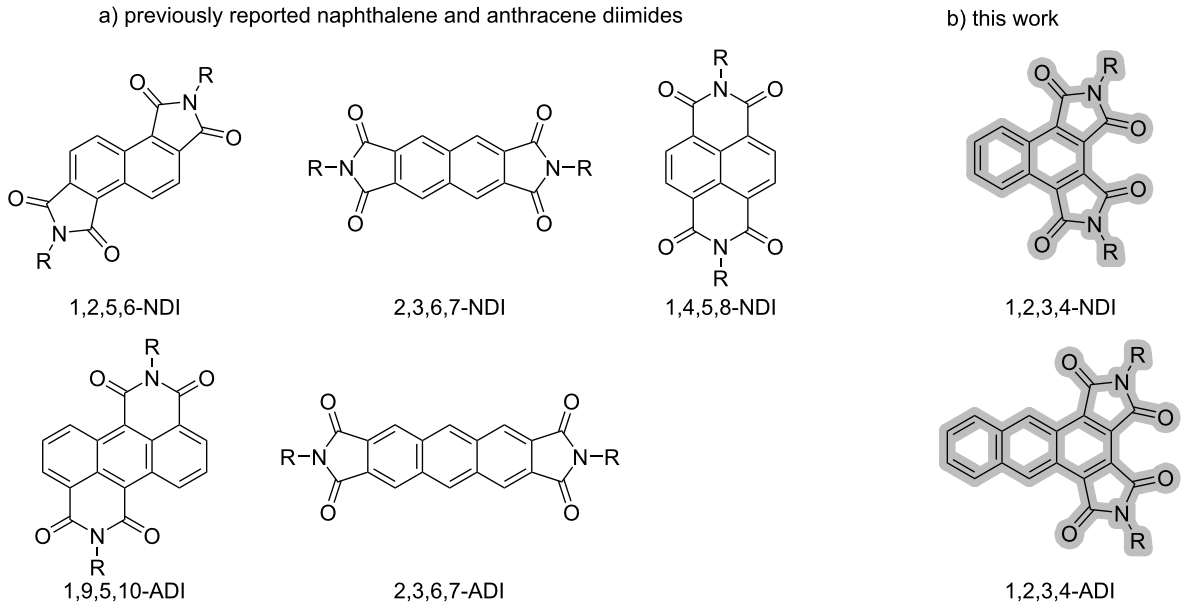

Figure 1: a) Structures of previously reported naphthalene and anthracene diimide isomers. b) The novel 1,2,3,4-naphthalene and -anthracene diimides reported here.

servation of similar electron mobilities across different structural isomers of naphthalene and anthracene diimide [16] confirms the need to experimentally evaluate the unstudied isomers.

We became interested in the *cata*- (i.e. 1,2,3,4-) derivatization of aromatic scaffolds because it can be exploited to stabilize the longer (hetero)acenes. In contrast to *cata*-benzannulation, *cata*-imide-annulation does not perturb aromaticity patterns and further introduces inductive stabilization of frontier MO levels, which has enabled the production of n-type organic thin-film transistors from heteroacenes. Inspired by these results, we sought to demonstrate the preparation of all-carbon scaffolds, i.e., acenes, that are *cata*-annulated with cyclic imides. Here, we communicate the successful synthesis of 1,2,3,4-NDIs and -ADIs and the characterization of their physical properties.

Results and Discussion

Synthesis

The synthesis of the title compounds is shown in Scheme 1. To obtain a naphthalene core with the requisite 1,2,3,4-tetracarbonyl derivatization pattern, we leveraged the cycloaddition of 1 equiv of aryne percursor **1** with 2 equiv of dimethyl acetylenedicarboxylate (DMAD). Although this [2 + 2 + 2] cycloaddition reactivity strategy has been reported under a variety of aryne generation conditions [17-19], in our hands we were only able to generate practical amounts of tetraesters **3** using the method reported by Peña et al. [18]. Hydrolysis of **3** with sodium hydroxide, followed by acidification with HCl, yielded a mixture of carboxylic acids and anhydrides **5**, as evidenced by ^{1}H NMR spectroscopy (Figure S13 in Supporting Information File 1). Gratifyingly, purification of these mixtures was not necessary as they could be used directly for imidization. Heating **5** with hexylamine or aniline in refluxing acetic acid successfully led to the formation of the targeted aromatic diimides bearing either *N*-hexyl (**7-Hex**) or *N*-phenyl (**7-Ph**) substitutions in good yields. The same strategy was employed to create the imide-capped anthracenes **8-Hex** and **8-Ph**.

Crystallography

Despite exhaustive efforts, we were unable to obtain single crystals of **7-Hex** and **8-Hex**; these compounds formed polycrystalline bundles that are fragile and insufficient for obtaining diffraction data. Fortunately, single crystals of the *N*-phenyl compounds were successfully grown by slow evaporation of CH_2Cl_2/MeOH solutions and characterized by X-ray crystallography. **7-Ph** crystallizes in the *Pbcn* space group into a solvent superstructure of π-stacked columns of **7-Ph**. The imide groups are pointed in alternating directions within a stack. While this may occur in part as a consequence of the steric demands of the *N*-phenyl groups, there are also C–H···π interactions between phenyl groups of adjacent π stacks, with the closest Ph centroid to H distance being 2.613 Å (Figure 2a). Additionally, the middle carbonyl oxygens are in short contact (2.376 Å) with the 7- and 8-H atoms of the naphthalene in the adjacent molecule (Figure 2a).

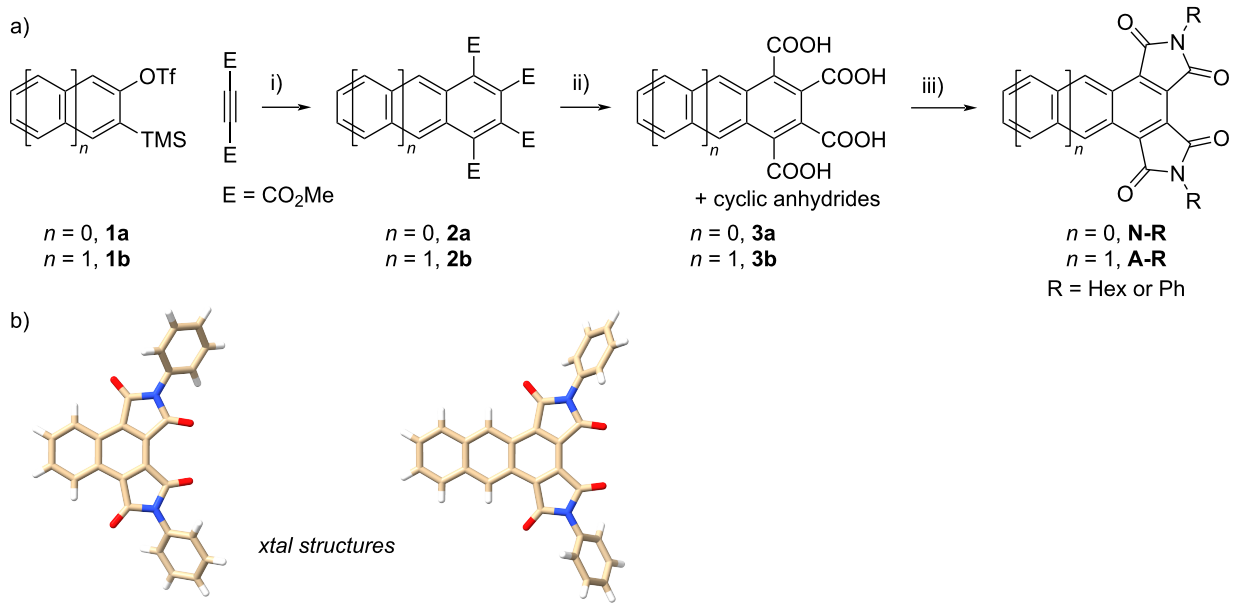

Scheme 1: a) Synthesis of the 1,2,3,4-naphthalene and -anthracene diimides. Conditions: i) CsF/$Pd_2(dba)_3$/MeCN; ii) NaOH/H_2O/THF, then HCl; iii) R-NH_2/AcOH. b) X-ray crystal structures of **7-Ph** and **8-Ph**.

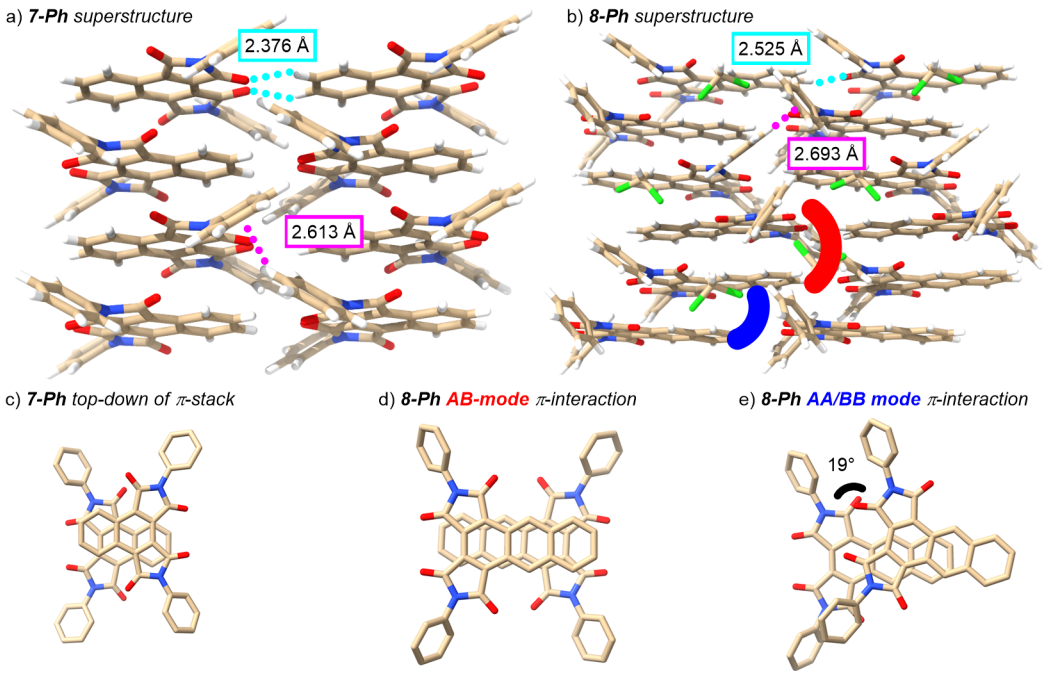

Figure 2: Superstructures for a) **7-Ph** and b) **8-Ph** as determined by X-ray crystallography. Representative C=O···H–C and C–H···π interactions are indicated in teal and magenta, respectively. Top-down views of π-stacking modes in c) **7-Ph** and d, e) **8-Ph**. Hydrogen atoms have been removed for clarity in c–e. Atom color code: C = tan, H = white, Cl = green, N = blue, and O = red.

On the other hand, **8-Ph** crystallizes in the *Pbca* space group with two molecules of interest along with one molecule of CH_2Cl_2. Pairs of **8-Ph** molecules are π-stacked together with their imide groups oriented in opposing directions (Figure 2d) in a fashion analogous to that observed for **7-Ph** (Figure 2c). These pairs, however, are then infinitely packed such that adjacent **8-Ph** molecules are aligned in the same direction to create an AA–BB stacking pattern, unlike the more common

A–B–A–B stacking pattern found for **7-Ph**. Additionally, it is worth observing that the π-interaction involving two **8-Ph** molecules pointed in the same nominal direction is not linearly aligned, but is instead twisted by 19°. This angle, likely enforced by the sterics of the phenyl groups, may be an interesting approach to inducing helical turns in supramolecular assemblies derived from the title compounds.

Despite this different packing mode within the stack, the interstack interactions exhibited by **8-Ph** are similar to those found in **7-Ph**. Although there are still observable C–H···π interactions and C=O···H–C interactions between stacks, they appear to be weaker, as evidenced by the longer interaction distances and interceding incorporation of CH_2Cl_2 (Figure 2b). Furthermore, in **8-Ph** the interstack C=O···H–C interaction is skewed such as to involve only one C=O, compared to the symmetric dual-contact that is seen for **7-Ph**.

Optical and electronic characterization

The absorption spectra of the diimides dissolved in CH_2Cl_2 are depicted in Figure 3a. All of these compounds exhibit broad absorption bands. **7-Hex** has more well-defined features with λ_{max} = 391 nm while **7-Ph** has a slightly longer wavelength absorption with λ_{max} = 398 nm. A similar trend is observed for **8-Hex** and **8-Ph**, with λ_{max} = 489 and 499 nm, respectively. These absorption features are roughly comparable to other naphthalene and anthracene diimides that have been reported in the literature. The emission profiles of all four compounds are shown in Figure 3b. While *N*,*N*'-dibutyl-1,4,5,8-naphthalene diimide has low fluorescence intensity (Φ = 0.006) [20], **7-Hex** emits more efficiently with Φ = 0.41. Interestingly, **7-Ph** has nearly no emission intensity, as evidenced by the low signal-to-noise ratio in the data and a near-zero quantum yield when excited at 400 nm. This fluorescence quenching is likely related to non-radiative emission that is observed for *N*-phenyl-substituted imides [21]. It is possible this effect is more significant for **7-Ph** than **8-Ph** because the naphthalene core is less conformationally locked than the anthracene scaffold.

As is expected for aromatic diimides, the title compounds undergo reversible chemical reduction processes, as determined by cyclic voltammetry in CH_2Cl_2 solvent (Figure 4). There are two factors at play. The imide substitution is impactful as the *N*-phenyl derivatives are roughly by 100 mV easier to reduce than the *N*-hexyl analogs. The anthracene scaffold also lends itself to a more facile reduction process, with an approximately 150 mV shift of the event toward more positive potentials for **8-R** vs **7-R**. When compared to other structural isomers, aromatic diimides with 5-membered cyclic imides tend to be slightly harder to reduce than those with 6-membered cyclic imides (Table 1). Overall, however, the *cata*-annulation does not lead to substantially different electrochemical behavior, which is encouraging because we had anticipated that the deflection away from planarity caused by adjacent placement of cyclic imides might adversely affect extent of π-delocalization.

As part of our previous work constructing heteroacenes bearing *cata*-imide groups, we investigated the 9,10-diaza analog of compound **8-Hex** (**9**, Figure 5). It is interesting to note that the all-carbon scaffold in **8-Hex** results in a narrower bandgap than that of **9**, with $\Delta\lambda_{max}$ = 85 nm. This difference can be attributed to a significantly higher HOMO level in **8-Hex** arising from having fewer electronegative atoms in the aromatic backbone. For the same reasons, compound **9** is a superior electron acceptor by 0.36 V. These trends confirm the value of backbone atom substitution for fine-tuning molecular properties.

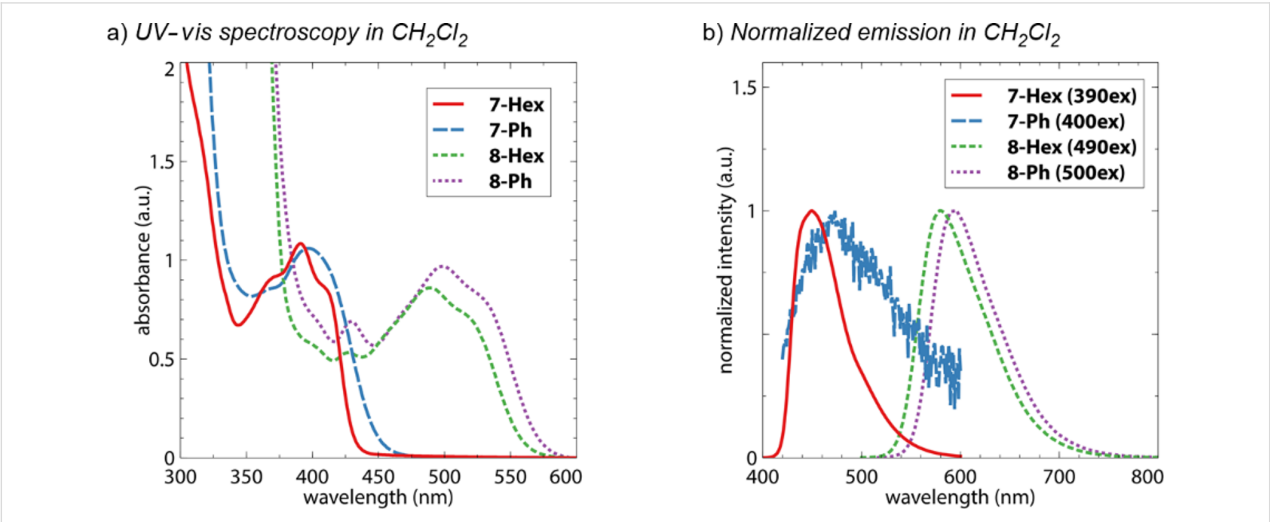

Figure 3: a) Absorption and b) emission spectra of the compounds dissolved in CH_2Cl_2.

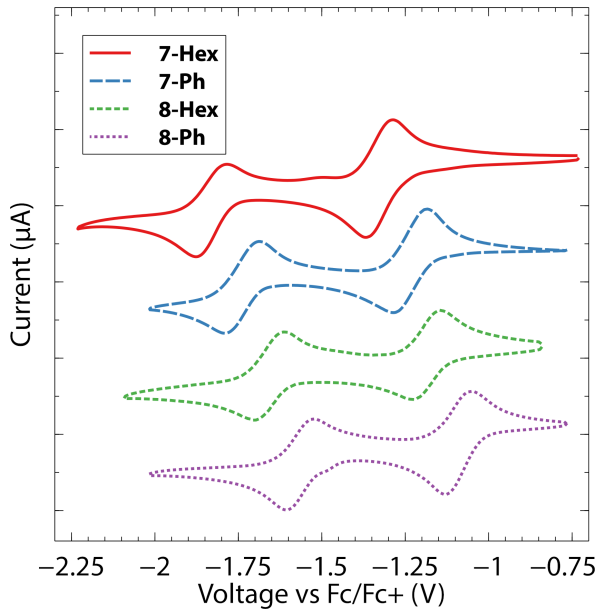

Figure 4: Cyclic voltammograms of the compounds collected on ca. 1 mM solutions of the analyte in CH_2Cl_2 with 0.1 M Bu_4NPF_6 as electrolyte. The major *y*-axis tick mark spacing corresponds to 5 μA.

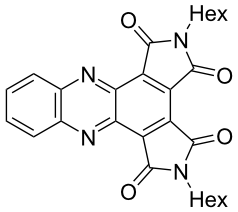

9

Figure 5: Structural formula of **9**, the diaza-analog of compound **8-Hex** that was reported previously [2].

Conclusion

In conclusion, we have demonstrated the facile construction of two new aromatic diimide scaffolds: 1,2,3,4-naphthalene and -anthracene diimides through a cycloaddition approach to construct the aromatic backbone prior to imide formation. The physical characterization of the title compounds indicates that they are optically and electronically similar to previously reported naphthalene and anthracene diimides, absorbing/emitting light in the visible region and readily undergoing one-electron-reduction processes. As such, this work opens the possibility of incorporating the 1,2,3,4-naphthalene and -anthracene diimide motifs as productive building blocks in imide-based organic materials.

Supporting Information

Supporting Information File 1

Experimental procedures, synthetic protocols, and X-ray crystallographic data.
[https://www.beilstein-journals.org/bjoc/content/supplementary/1860-5397-20-155-S1.pdf]

Supporting Information File 2

Crystallographic information file for compound **7-Ph**.
[https://www.beilstein-journals.org/bjoc/content/supplementary/1860-5397-20-155-S2.cif]

Supporting Information File 3

Crystallographic information file for compound **8-Ph**.
[https://www.beilstein-journals.org/bjoc/content/supplementary/1860-5397-20-155-S3.cif]

Table 1: Summary and comparison of optical and electronic properties.

	$E_{½}$ (V vs Fc/Fc$^+$)[a]							
	E_{2r} (V)	E_{1r} (V)	λ_{max}[b] (nm)	λ_{em} (nm)	E_g[c] (eV)	LUMO[d] (eV)	HOMO[e] (eV)	Φ
7-Hex	−1.83	−1.33	391	450	2.82	−3.5	−6.3	0.41
7-Ph	−1.74	−1.23	398	519[f]	2.64	−3.6	−6.2	<0.01
1,2,5,6-NDI [9]		−1.20[g]				−3.6		
1,4,5,8-NDI [22]	−1.51	−1.10	370		3.18	−3.7	−6.9	0.006 [20]
8-Hex	−1.66	−1.19	489	575	2.15	−3.6	−5.7	0.20
8-Ph	−1.56	−1.09	498	595	2.07	−3.5	−5.6	0.04
1,9,5,10-ADI[h] [14]	−1.40[g]	−1.10[g]	480	525	2.2	−3.8	−6.0	
2,3,6,7-ADI [13]		−1.69						
9 [2]	−1.30	−0.76	404		2.56	−4.2	−6.8	

[a]Unless otherwise noted, ca. 1 mM analyte in CH_2Cl_2, 0.1 M Bu_4NPF_6. [b]Unless otherwise noted, longest wavelength absorption maxima of analyte in CH_2Cl_2 solution. [c]Optical bandgap estimated from absorption onset. [d]LUMO estimated from reduction onset. [e]HOMO = LUMO – E_g. [f]Low intensity emission. [g]Estimated from graphical data. [h]PhCl solvent.

Acknowledgements

We thank Victor G. Young, Jr. of the University of Minnesota X-Ray Crystallographic Laboratory for acquiring X-ray diffraction data and solving crystal structures.

Funding

The Bruker-AXS D8 Venture diffractometer was purchased through a grant from NSF/MRI (#1229400) and the University of Minnesota. This work was additionally supported by the National Science Foundation under Grant No. NSF 1954975 and the Beckman Foundation Beckman Scholars Program.

ORCID® iDs

Adam D. Bass - https://orcid.org/0000-0003-2899-0686
Dennis D. Cao - https://orcid.org/0000-0002-0315-1619

Data Availability Statement

All data that supports the findings of this study is available in the published article and/or the supporting information to this article.

References

1. Zou, B.; Stellmach, K. A.; Luo, S. M.; Gebresilassie, F. L.; Jung, H.; Zhang, C. K.; Bass, A. D.; Janzen, D. E.; Cao, D. D. *J. Org. Chem.* **2022,** *87,* 13605–13614. doi:10.1021/acs.joc.2c01241
2. Luo, S. M.; Stellmach, K. A.; Ikuzwe, S. M.; Cao, D. D. *J. Org. Chem.* **2019,** *84,* 10362–10370. doi:10.1021/acs.joc.9b01502
3. Elter, M.; Ahrens, L.; Luo, S. M.; Rominger, F.; Freudenberg, J.; Cao, D. D.; Bunz, U. H. F. *Chem. – Eur. J.* **2021,** *27,* 12284–12288. doi:10.1002/chem.202101573
4. Hippchen, N.; Heinzel, E.; Zhang, C. K.; Jäger, P.; Elter, M.; Ludwig, P.; Rominger, F.; Freudenberg, J.; Cao, D. D.; Bunz, U. H. F. *ChemPlusChem* **2023,** *88,* e202300158. doi:10.1002/cplu.202300158
5. Yi, X.; Gao, J.; Qin, H.; Zheng, L.; Zeng, W.; Chen, H. *Org. Lett.* **2023,** *25,* 972–976. doi:10.1021/acs.orglett.3c00001
6. Fang, X.; Yang, Z.; Zhang, S.; Gao, L.; Ding, M. *Macromolecules* **2002,** *35,* 8708–8717. doi:10.1021/ma0204610
7. Hasegawa, M.; Nomura, R. *React. Funct. Polym.* **2011,** *71,* 109–120. doi:10.1016/j.reactfunctpolym.2010.11.021
8. Zhao, L.; Li, W.; Qin, H.; Yi, X.; Zeng, W.; Zhao, Y.; Chen, H. *Macromolecules* **2023,** *56,* 2990–3003. doi:10.1021/acs.macromol.3c00252
9. Chen, S.-c.; Zhang, Q.; Zheng, Q.; Tang, C.; Lu, C.-Z. *Chem. Commun.* **2012,** *48,* 1254–1256. doi:10.1039/c2cc15733k
10. Zhao, Z.; Zhang, F.; Zhang, X.; Yang, X.; Li, H.; Gao, X.; Di, C.-a.; Zhu, D. *Macromolecules* **2013,** *46,* 7705–7714. doi:10.1021/ma4013994
11. Yue, W.; Gao, J.; Li, Y.; Jiang, W.; Di Motta, S.; Negri, F.; Wang, Z. *J. Am. Chem. Soc.* **2011,** *133,* 18054–18057. doi:10.1021/ja207630a
12. Cui, X.; Xiao, C.; Winands, T.; Koch, T.; Li, Y.; Zhang, L.; Doltsinis, N. L.; Wang, Z. *J. Am. Chem. Soc.* **2018,** *140,* 12175–12180. doi:10.1021/jacs.8b07305
13. Wang, Z.; Kim, C.; Facchetti, A.; Marks, T. J. *J. Am. Chem. Soc.* **2007,** *129,* 13362–13363. doi:10.1021/ja073306f
14. Mohebbi, A. R.; Munoz, C.; Wudl, F. *Org. Lett.* **2011,** *13,* 2560–2563. doi:10.1021/ol200659c
15. Chen, X.-K.; Zou, L.-Y.; Guo, J.-F.; Ren, A.-M. *J. Mater. Chem.* **2012,** *22,* 6471–6484. doi:10.1039/c2jm15935j
16. Zhan, X.; Facchetti, A.; Barlow, S.; Marks, T. J.; Ratner, M. A.; Wasielewski, M. R.; Marder, S. R. *Adv. Mater. (Weinheim, Ger.)* **2011,** *23,* 268–284. doi:10.1002/adma.201001402
17. Hsieh, J.-C.; Cheng, C.-H. *Chem. Commun.* **2008,** 2992–2994. doi:10.1039/b801870g
18. Peña, D.; Pérez, D.; Guitián, E.; Castedo, L. *J. Org. Chem.* **2000,** *65,* 6944–6950. doi:10.1021/jo000535a
19. Jafarpour, F.; Hazrati, H.; Nouraldinmousa, S. *Org. Lett.* **2013,** *15,* 3816–3819. doi:10.1021/ol401318v
20. Maniam, S.; Higginbotham, H. F.; Bell, T. D. M.; Langford, S. J. *Chem. – Eur. J.* **2019,** *25,* 7044–7057. doi:10.1002/chem.201806008
21. Demeter, A.; Bérces, T.; Biczók, L.; Wintgens, V.; Valat, P.; Kossanyi, J. *J. Phys. Chem.* **1996,** *100,* 2001–2011. doi:10.1021/jp951133n
22. Thalacker, C.; Röger, C.; Würthner, F. *J. Org. Chem.* **2006,** *71,* 8098–8105. doi:10.1021/jo0612269

BEILSTEIN JOURNAL OF ORGANIC CHEMISTRY

Hetero-polycyclic aromatic systems: A data-driven investigation of structure–property relationships

Sabyasachi Chakraborty‡, Eduardo Mayo Yanes‡ and Renana Gershoni-Poranne*

Full Research Paper

Open Access

Address:
Schulich Faculty of Chemistry and the Resnick Sustainability Center for Catalysis, Technion – Israel Institute of Technology, Haifa 32000, Israel

Email:
Renana Gershoni-Poranne* - rporanne@technion.ac.il

* Corresponding author ‡ Equal contributors

Keywords:
computational chemistry; database; dataset; π-conjugated; polycyclic aromatic hydrocarbons; polycyclic aromatic systems

Beilstein J. Org. Chem. **2024,** *20,* 1817–1830.
https://doi.org/10.3762/bjoc.20.160

Received: 02 May 2024
Accepted: 16 July 2024
Published: 31 July 2024

This article is part of the thematic issue "π-Conjugated molecules and materials".

Guest Editor: A. Mateo-Alonso

Abstract

Polycyclic aromatic systems (PASs) are pervasive compounds that have a substantial impact in chemistry and materials science. Although their specific structure–property relationships hold the key to the design of new functional molecules, a detailed understanding of these relationships remains elusive. To elucidate these relationships, we performed a data-driven investigation of the newly generated COMPAS-2 dataset, which contains ~500k molecules consisting of 11 types of aromatic and antiaromatic rings and ranging in size from one to ten rings. Our analysis explores the effects of electron count, geometry, atomic composition, and heterocyclic composition on a range of electronic molecular properties of PASs.

Introduction

Polycyclic aromatic systems (PASs) – molecules made up of fused aromatic rings – are among the most prevalent classes of molecules known to humankind; indeed, it is estimated that two-thirds of known molecules contain (or are themselves) an aromatic moiety [1]. In addition to their presence in naturally occurring molecules, such as DNA and proteins, they have also been harnessed for various uses, ranging from ligands for catalysts [2], through pharmaceuticals [3], to organic semiconductors [4,5]. Despite their fundamental and applicative importance to many fields, the vast chemical space of PASs has remained largely unexplored. As a result, the relationships between the arrangement and composition of a PAS's rings and its various molecular properties remain elusive. Revealing these relationships can deepen our understanding of these systems, as well as pave the way toward efficient and effective design of new functional PASs.

Given its breadth and complexity, a natural approach to exploring the PAS chemical space is with data-driven methods, which have proven in the last few years to be extremely suc-

cessful at uncovering underlying structure–property relationships. To enable such exploration, we initiated the COMPAS Project (COMputational database of PASs), the first database dedicated to PASs and their molecular properties. The first installment, COMPAS-1 [6], contains ~35k *cata*-condensed polybenzenoid hydrocarbons (cc-PBHs) and has already enabled various directions of investigation, including by training of both interpretable machine [7] and deep learning methods [8], which led to new insights into these molecules. [Note: *cata*-condensed refers to fused PASs in which each atom participates in no more than two rings].

The second installment, COMPAS-2 [9], houses ~500k *cata*-condensed heterocyclic-PASs (cc-hPASs) comprising 11 types of aromatic and antiaromatic rings containing the heteroatoms boron, nitrogen, oxygen, and sulfur and ranging in size from four-membered to six-membered rings. Compared to the parent polycyclic aromatic hydrocarbons (PAHs), PASs containing heterocycles offer greater structural diversity as well as a much broader range of optoelectronic properties. Such molecules have been used in diverse settings, functioning as organic field effect transistors [10-12], light-emitting diodes [13-15], organic semiconductors [16,17], organic photovoltaics [1,18-22], photocatalysts [23], and biological agents for tracking or inhibition [24,25], and have also been incorporated into larger structures such as nano-hoops, in order to tune and expand their functionality [26].

Herein, we perform an in-depth analysis of the data contained within COMPAS-2, aiming to elucidate the effects of electron count, geometry, atomic composition, and aromatic nature on the molecular properties of PASs. Our goal is to delineate specific structure–property relationships that may shed light on these prevalent, yet still mysterious, compounds and serve as design principles for future PASs.

Data

The molecules in COMPAS-2 contain 11 cyclic building blocks varying in size, composition, and aromatic character: benzene, pyridine, pyrazine, borinine, 1,4-diborinine, 1,4-dihydro-1,4-diborinine, borole, pyrrole, furan, thiophene, and cyclobutadiene (Figure 1A). These building blocks encompass 6-, 5-, and 4-membered rings with aromatic and antiaromatic character, and contain nitrogen, boron, oxygen, and sulfur atoms. Using these building blocks, we generated a chemical library of *cata*-condensed hetero-PASs (cc-hPASs) ranging in size from 3- to 10-ring systems, by combining the rings according to the annulation types shown in Figure 1B. The number, type, and position of the individual building blocks were determined randomly to avoid biasing the data and to increase the likelihood of sampling previously unstudied cc-hPAS structures. Further details on the structure enumeration and data generation are reported elsewhere [9].

It is important to note that in constructing the COMPAS-2 dataset, we opted to maintain equal percentages of the different types of heterocycles (~10% of each type). This was done to avoid biasing the construction of molecules towards specific motifs. However, because there are multiple types of B-containing and N-containing heterocycles, and because some of them contain more than one heteroatom, this resulted in an unequal distribution of the heteroatoms themselves. Thus, due to the design of the dataset construction, the relative prevalence is approximately 6:4:1:1 for B:N:O:S.

COMPAS-2 comprises two datasets – COMPAS-2x and COMPAS-2D. The former contains geometries and molecular properties obtained at the GFN1-xTB [27] level for 524,392 unique cc-hPASs. The latter is a representative subset of the former, containing 52,000 cc-hPASs with geometries optimized and properties obtained at the CAM-B3LYP/def2-SVP

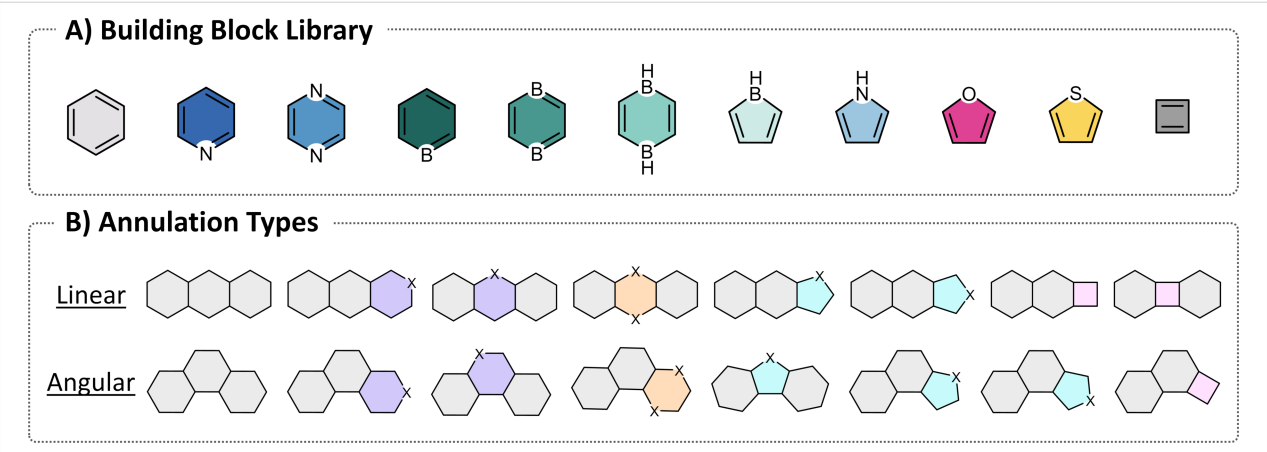

Figure 1: A) The building blocks used in the COMPAS-2 datasets. B) Possible annulation types formed when combining the different types of rings.

[28-33] level, including the D3 dispersion correction [29] by Grimme with Becke-Johnson damping [30]. We used the DFT-calculated dataset to generate fitting functions, such that all xTB-generated data was corrected to near DFT-level accuracy [9]. It is these corrected data that we use in this report to analyze the structure–property relationships of the cc-hPASs.

Results and Discussion

At first glance, the chemical space of PASs may appear to be quite homogenous. After all, the molecules share certain structural features, such as their multi-ring structures, rigidity, and π-conjugation. Nevertheless, simply by changing the combination of the individual building blocks (i.e., rings), we obtain molecules with varying sizes, geometries, atomic compositions, and aromatic character. In such multi-faceted data, it can be difficult to ascertain which structural features determine the different molecular properties. Therefore, we designed the current study with an aim to chart a clear path through this chemical space, and we present our findings along these same lines (as illustrated in Figure 2). In the first section, we provide context, giving a short comparison between the data contained within COMPAS-2 [9] and COMPAS-1 [6]. The second, third, and fourth sections then present analyses of the data, each focused on different structural aspects: global electronic and geometric features, atomic composition, and heterocyclic composition. A roadmap of the article structure is shown in Figure 2.

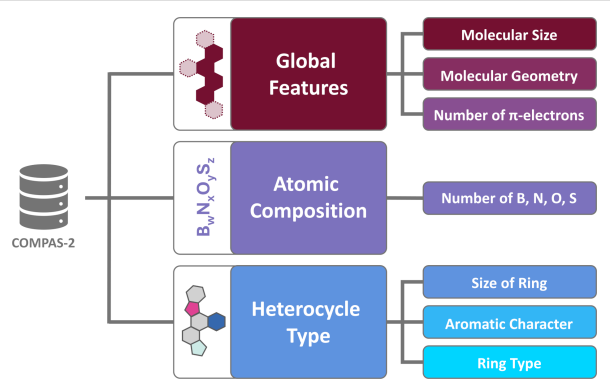

Figure 2: Roadmap of the work described in this article. Three main criteria are defined in increasing structural information content. For each criterion, we note the specific features that are studied in this work. For each of these, we investigate the effect of the feature on the set of molecular properties.

Comparison between COMPAS-1 and COMPAS-2

To obtain a better overview of the COMPAS-2 chemical space and to study the effects of including these new components, we first compare the cc-PBHs in COMPAS-1 to the cc-hPASs in COMPAS-2, in terms of their shape diversity and molecular properties. As mentioned above, COMPAS-1 houses PBHs, molecules comprising only one type of ring – the aromatic, six-membered, carbon-based benzene.

The principal moments of inertia (PMI) plots in Figure 3A show that the two datasets have similar tendencies to form "rod" and "disc"-like structures (i.e., 1D or 2D, respectively). Because some of the building blocks contained in the COMPAS-2 library can only annulate linearly (specifically, cyclobutadiene, pyrazine, 1,4-diborinine, 1,4-dihydro-1,4-diborinine), this dataset shows a greater density of structures close to the "rod" vertex and along the "rod/disc" edge of the PMI plot.

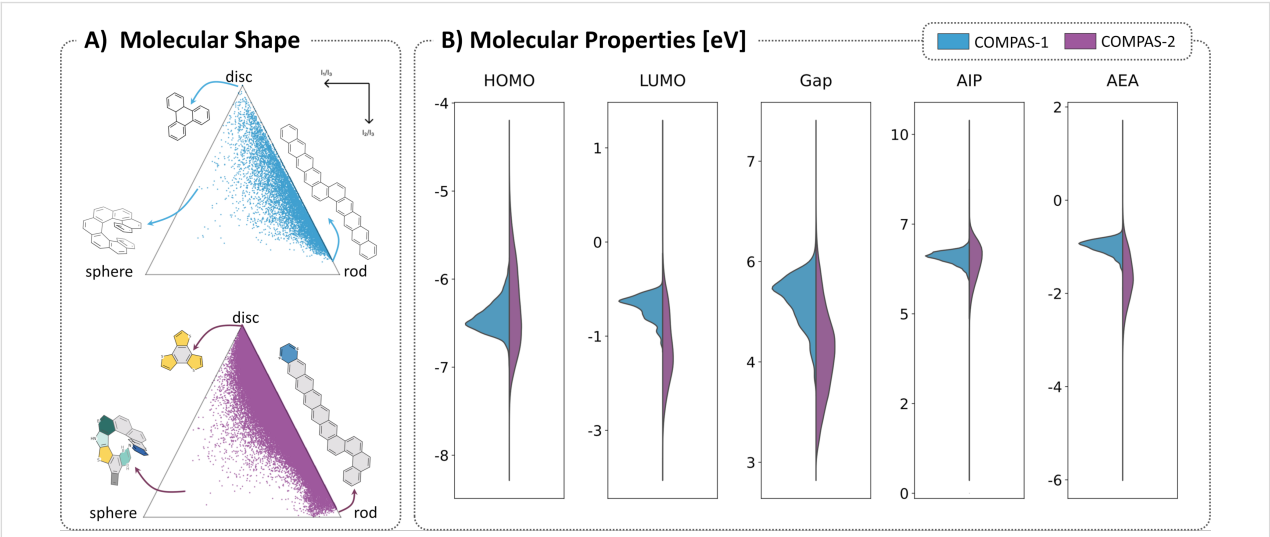

Figure 3: Comparison between COMPAS-1 (blue) and COMPAS-2 (purple). A) Principal Moments of Inertia shape distribution, all molecules sorted according to their normalized principal moments of inertia (I_n, n = 1–3), with $I_1 < I_2 < I_3$. B) Molecular properties (all reported in eV): HOMO, LUMO, AIP, and AEA.

COMPAS-1 molecules have a higher tendency to form angular annulations and branching points and therefore we observe the increased density closer to the "disc" corner. Both datasets have very few structures close to the "sphere"-like vertex, which represents 3D geometries, i.e., non-planar molecules. For PASs, it is unlikely to find actual "sphere"-like molecules, as the individual building blocks have rigid and planar geometries and fusing such components together in a *cata*-condensed fashion is unlikely to generate molecules with a spherical structure. Rather, for our dataset, the 3D-type molecules are expected to be those with helical structure. Indeed, as we highlight in Figure 3A, the polycyclic molecules that inhabit the spherical corner of the plot are those that have helical structures, and this is common to both data sets. In other words, the comparison between the two datasets demonstrates that increasing the diversity of conjugated cyclic building blocks does not have a notable impact on the relative distribution of molecular shapes.

In contrast to their relatively high geometric similarity, the molecular properties of the two datasets vary substantially. We compared the distributions of five molecular properties: highest occupied molecular orbital (HOMO) energy, lowest unoccupied molecular orbital (LUMO) energy, HOMO–LUMO gap (Gap), adiabatic ionization potential (AIP), and adiabatic electron affinity (AEA). As shown in the violin plots in Figure 3B, for all properties, the distribution of the COMPAS-1 molecules (light blue) is contained within the distribution of the COMPAS-2 molecules (purple). In other words, the expansion of the building block library widens the property distributions towards both higher and lower energies, providing access to functional molecules with different (opto)electronic properties. For example, while the HOMO energies of the COMPAS-1 PBHs range between −7 and −6 eV, the HOMO energies for the COMPAS-2 cc-hPAS cover the range from −8 to −4.5 eV, a widening of 3.5 eV. Similarly, the range of LUMO energies expands substantially, from −0.8 to −1.8 eV in the cc-PBHs to +0.2 to −3.5 eV in the cc-hPASs, with a larger tendency towards lower-lying LUMOs than in the PBHs. The remaining properties show similar expansions of property ranges.

Overall, the comparison between the two datasets demonstrates that the cc-hPASs are structurally similar to cc-PBHs, notwithstanding the higher tendency of the COMPAS-2 molecules towards linear annulations (due to the types of building blocks used). In contrast, their electronic properties cover much broader ranges, which is what makes them so promising as functional compounds. However, to what extent each type of building block affects the properties, and whether these effects are due solely to the presence of the heteroatoms or to the aromatic nature of heterocycles are among the questions we aim to answer in the subsequent sections.

Influence of global structural features

In this section, we investigate the effect of global structural features on the set of electronic properties detailed above (HOMO, LUMO, Gap, AIP, AEA). At this lowest resolution analysis, we aim to ascertain to what extent the overall molecular size and geometry determines molecular properties.

Molecular size

The molecular size of cc-hPASs may be evaluated in various ways – e.g., by the total number of atoms, total number of rings, total number of electrons (or specifically π-electrons). In our view, the number of rings is the simplest and most intuitive metric; it has the added benefit of revealing trends while still rendering a manageable number of groups. Therefore, we chose this descriptor and plotted the kernel-density estimates (KDEs) of the distributions of the five properties described above, colored according to the number of rings in the molecule (Figure 4). In all cases we observe "drifts": for the HOMO, the values become less negative as the molecules increase in size; for the LUMO, Gap, AIP and AEA, the values become smaller or more negative as the molecules increase in size. These trends align with the commonly known effect in polyenes and annulenes, whereby increasing conjugation causes the HOMO to be raised, the LUMO to be lowered, and the Gap to be reduced. The differences between consecutive groups become smaller as the molecules grow in size, which is consistent with the $1/n$ relationship reported for other polycyclic systems [34].

Molecular geometry

In our previous work on cc-PBHs, we observed a similar correlation to size, however, our data-driven analysis revealed that the underlying source of the correlation is not just the molecular size, *per se*, but rather the formation of linear stretches (substructures that are linearly annulated) [6]. Accordingly, the longer the linear stretch, the higher the HOMO, the lower the LUMO, etc., and the apparent size dependency arises simply because larger molecules have more opportunities to create longer linear stretches.

The scatter plot of the HOMO/LUMO space showed that a similar trend does exist for COMPAS-2, albeit weaker than the COMPAS-1 case (see section 1.1 in Supporting Information File 1 for further details). To investigate this further, and to avoid the size-dependency issue, we focused only on the 9-ring systems in the dataset. In this collection of 152,121 molecules, all molecules have the same number of rings but differ in their annulations and composition and therefore have varying numbers of atoms and π-electrons. We plotted the KDE distributions of the HOMO, LUMO, and Gap for this subset of data, colored according to the longest linear stretch in the molecules (Figure 5A). Note that, for cc-hPASs, a linear annulation is

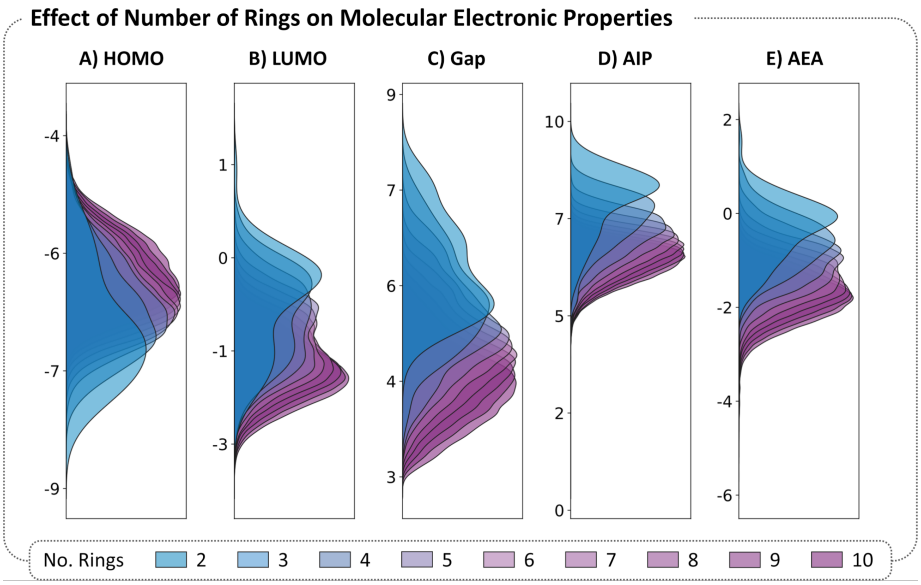

Figure 4: Distributions of electronic properties of the dataset. KDE plots of HOMO, LUMO, Gap, AIP, and AEA colored according to the number of rings in the molecule. The KDEs are normalized such that the area under the curve is equal to 1 for each family.

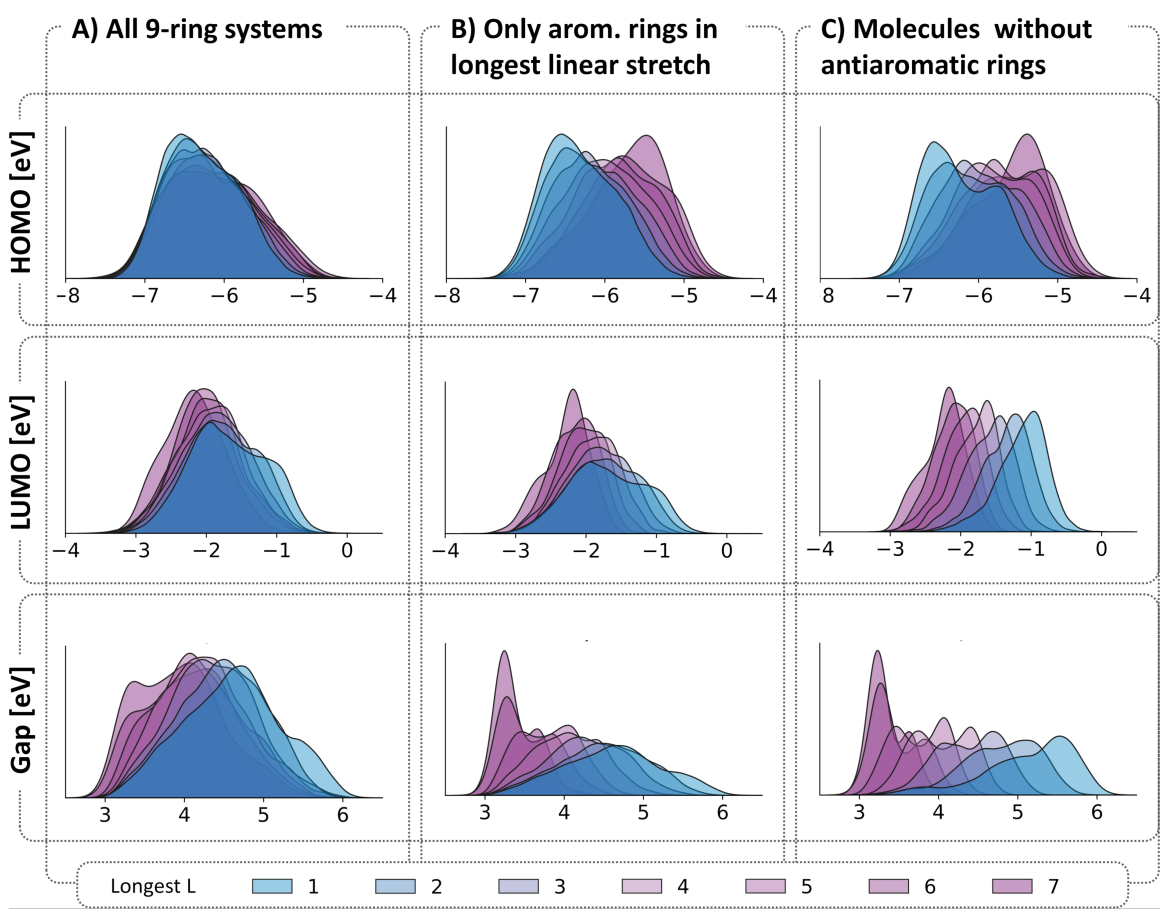

Figure 5: KDE distributions of the HOMO, LUMO, and Gap separated and colored by the longest L for: A) all 9-ring molecules; B) all 9-ring molecules that do not have an antiaromatic moiety in the longest linear stretch; C) all 9-ring molecules that do not contain any antiaromatic moiety. The KDEs are normalized such that the area under each curve is 1.

defined as three consecutive rings having an angle of 180° between the ring centroids; any angle that is not 180° is considered to be an angular annulation (see Figure 1B). Indeed, although a trend may be observed, it is not nearly as pronounced as the trend we observed for the cc-PBHs in COMPAS-1 [6]. This led us to hypothesize that the presence of antiaromatic moieties in the linear stretch (cyclobutadiene and/or 1,4-dihydro-1,4-diborinine) may be distorting the results. In other words, perhaps the effect is only relevant to linear stretches of aromatic rings. To verify this, we identified within the same molecules the longest linear stretch comprising only aromatic rings. These distributions (shown in Figure 5B) do indeed show a clearer trend, but it is still weaker than the cc-PBHs. Therefore, in the next step, we plotted the distributions of all 9-ring molecules containing only aromatic building blocks (i.e., have no cyclobutadiene, borole, or 1,4-dihydro-1,4-diborinine moieties; a collection of 127,019 molecules). In this case (Figure 5C), the stratification of the data did become more pronounced, indicating that antiaromatic rings mask the longest linear stretch effect. Overall, these results show that the longest linear stretch effect does generalize from cc-PBHs to cc-hPASs, but it is most significant for cc-hPASs that comprise only aromatic rings. This observation aligns with previous experimental work from the groups of Vollhardt. Miao, and Xia, who studied diareno-fused cyclobutadienes and found similar trends [35-38].

In addition to this structural feature, we also examined the effects of the number of branching points and deviation from planarity. Neither of these structural features showed any meaningful trend (further details are provided in sections 1.2 and 1.3 of Supporting Information File 1).

π-Electron count

In contrast to COMPAS-1, COMPAS-2 contains both molecules with a $(4n + 2)$ π-electron count and molecules with a $4n$ π-electron count, allowing us to study the difference between formally Hückel aromatic and formally Hückel antiaromatic PASs. We note in this regard that the 'Hückel Rule' (a term that was actually introduced by Doering) [39] was originally developed solely for monocyclic systems, but was later extended by Vol'pin to *cata*-condensed polycyclic systems [40].

It is generally assumed that aromatic molecules are characterized by excess stability and a large Gap, while antiaromatic molecules are less stable and have smaller Gaps. To investigate whether this assumption holds true for cc-hPASs, we plotted the distributions of several properties for the two subsets of molecules, separated by size. As seen in Figure 6A, the distributions of the HOMO and LUMO values are both higher for the $(4n + 2)$ systems than for the $(4n)$. However, these differences diminish at different rates: for the HOMOs, the two distributions become essentially indistinguishable at 4-ring systems, whereas for the LUMOs it is only at 10-ring systems that the values attain parity. Unsurprisingly, the $(4n + 2)$ systems show higher Gap values (Figure 6B), however, the difference consistently diminishes until it is negligible for 10-ring systems. (For further analysis based on this criterion, including molecular stability, see section 1.4 of Supporting Information File 1.)

Influence of atomic composition

The incorporation of different atoms is a well-known strategy for modulating the frontier molecular orbitals of π-conjugated

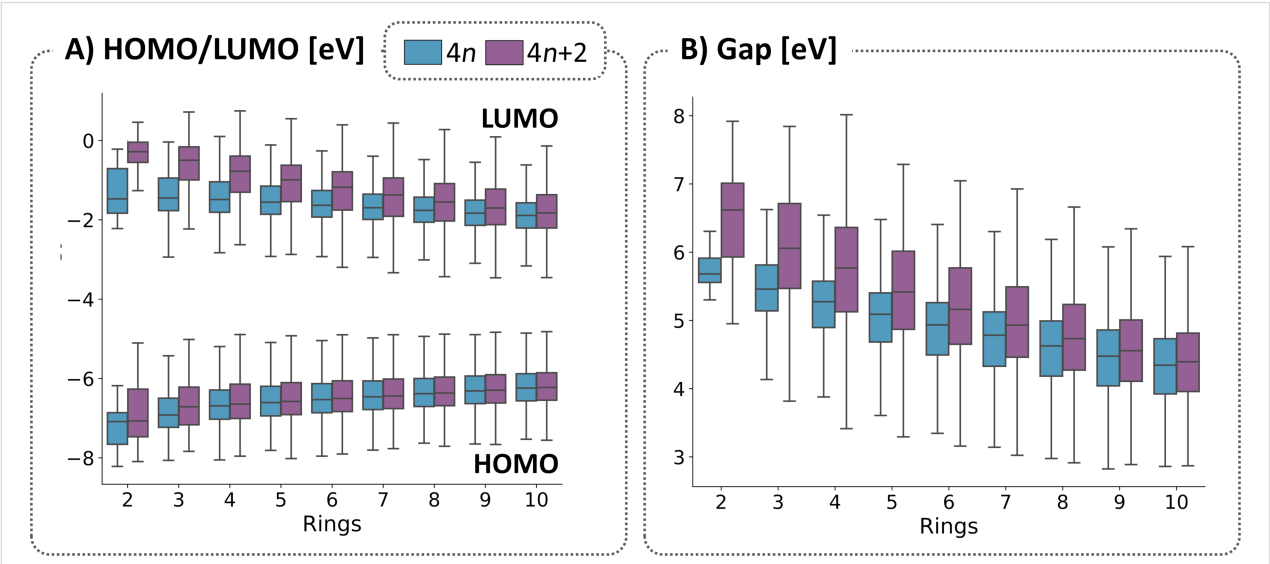

Figure 6: Distributions of molecular properties for $4n$ and $(4n + 2)$ π-electron count systems, divided by the number of rings for: A) HOMO and LUMO energies and B) Gaps.

systems. For example, it has been empirically observed, and can also be rationalized with molecular orbitals-based considerations, that lone-pair bearing heteroatoms such as oxygen raise the HOMO level [41,42], while boron lowers the LUMO level [43]. COMPAS-2 provides, for the first time, the possibility to substantiate these observations in a data-driven manner and, perhaps, to extract quantitative assessments of these effects. In this section, we study the effects of the presence and number of different heteroatoms on the electronic properties of the molecules in COMPAS-2.

We first visualized the distribution of the various types of heteroatoms across the property space by generating a series of scatter plots (HOMO versus LUMO) and coloring each plot according to the number of heteroatoms of a certain type (section 2 of Supporting Information File 1). These plots (Figure S6 in Supporting Information File 1) made it readily apparent that the B atoms unsurprisingly accumulate in the regions of lower LUMO value and, to a lesser extent, higher HOMO values. The N, O, and S atoms appear to be more evenly distributed over the property space, however, certain areas can be identified with slightly higher populations of heteroatom-rich PASs.

To explore this further, we divided each property into ten evenly spaced sections and binned all the molecules in each respective section (as before, this analysis focused on the 9-ring systems, to avoid any size-dependency artifacts). For each bin, we plotted the relative prevalence of the various heteroatoms as a stacked histogram (Figure 7), where the different colored blocks represent the different heteroatoms and the sum of all blocks in each bin is equal to 1. The size of each block represents the likelihood of a heteroatom from this bin being a certain type. As we noted in the Data section, the total numbers of heteroatoms are not equal (the ratios of B:N:O:S atoms are approximately 6:4:1:1). Therefore, each block was normalized according to the relative prevalence of the heteroatom in the dataset, which allows for a more straightforward comparison between different heteroatoms, as well as for the same heteroatom across the property range.

Figure 7 shows that the likelihood of finding O and S atoms is relatively uniform across the HOMO range, while it decreases for N and increases for B as the HOMO values rise. The trends are more pronounced for the LUMO: the B atoms are clearly most prevalent at the lower LUMO levels and steadily decrease towards the higher LUMO levels, concurrent with a steady rise in the likelihood of O and S atoms, while the N likelihood remains rather uniform. The trends become even more pronounced in the plot of the Gap, as it is a sum of the HOMO and LUMO complementary effects. For the Gap and AIP, an increase in N towards higher values can be noted. For the AEA, the B clearly dominates the lower values, while again N, S, and especially O show an increase towards the higher values. We note that the relative uniformity of the N prevalence across the various property ranges could be due to contradicting effects of the different types of N-containing rings and does not necessarily imply that N does not have a strong impact on the properties. Conversely, the prevalence of B at certain property values does not mean that all B-containing systems have similar effects; it could be that one or more B-containing systems have stronger effects that dominate. These questions are addressed in subsequent sections.

Influence of heterocycle type

In this section, we focus on the character and type of the rings comprising the cc-hPASs, going from the broader perspective

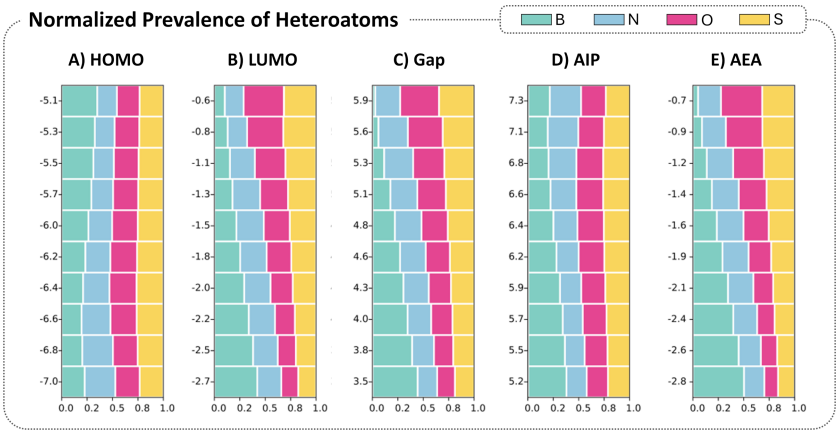

Figure 7: Stacked histograms showing the prevalence of the different heteroatoms across different areas of the property space, for A) HOMO, B) LUMO, C) Gap, D) AIP, and E) AEA. The colors of each block correspond to the color-coded heteroatoms shown at the top. The size of each block represents the fraction of that heteroatom out of the overall number of heteroatoms in that respective bin. The sum of all heteroatoms is 1 for each bin. Molecules below and above the 0.01 and 0.99 percentiles, respectively, were discarded as not statistically meaningful.

(size) to a more detailed view (aromatic/antiaromatic) and finally to the specific type of ring.

Size of ring

In the broadest sense, without analyzing their specific composition or character, the individual building blocks in our library may be categorized according to their sizes. To study the effect on the molecular properties, we plotted the KDE distributions of the various properties, separated by the number of 4-, 5-, and 6-membered rings, respectively. We observed that the sizes of the individual rings do not have an inherent effect on the electronic properties (see Supporting Information File 1, section 3.1 for further details).

Aromatic character of the rings

The rings can be further classified as Hückel aromatic [$(4n + 2)$ π-electrons] or antiaromatic [$(4n)$ π-electrons)]. To study the relationship between the number of rings of each type and the molecular properties, we plotted the distributions of the five molecular properties, separated by the number of antiaromatic rings (Figure 8). Once again, to circumvent the size-dependency issue (see section "Molecular size" above), we analyzed only the molecules containing 9 rings (a subset of 152,121 molecules). All the properties showed a definite trend, although it appears to be strongest for the LUMO and Gap and smallest for the AIP. Overall, molecules with a higher number of antiaromatic moieties show lower HOMOs, lower LUMOs, lower Gaps, and stronger electron affinity – regardless of the specific type of rings that are contained in the molecule. However, we note that two of the three antiaromatic rings in our library are B-containing heterocycles. As shown above, boron also has a strong effect on the molecular properties. Thus, it is unclear whether the apparent trends here stem from the boron atom or from the antiaromatic character of the building blocks. This will be addressed in the subsequent section. (Additional analysis based on this descriptor is provided in Supporting Information File 1, section 3.2.).

Specific identity of heterocycle

The previous analyses revealed two relationships: lower LUMO values were shown to correspond to both the presence of boron-containing rings and to the presence of antiaromatic rings. However, two-thirds of our antiaromatic building blocks *are* boron-containing rings (borole, 1,4-dihydro-1,4-diborinine). Thus, it is not clear whether these trends are due to the identity of the heteroatom or to the nature of the ring. To answer this question, we investigated the influence of each individual building block.

Figure 9A shows scatter plots of the HOMO versus LUMO, each colored according to the presence of a specific type of heterocycle. To avoid ambiguity, only molecules that contain benzene and the heterocycle highlighted in the respective plot are colored (i.e., molecules that contain mixtures of heterocycles are not colored). This is to ensure that our focus is on the effect of one specific heterocycle at a time.

Several observations can be made based on Figure 9, which are best demonstrated in comparison to the cc-PBH data (i.e., using

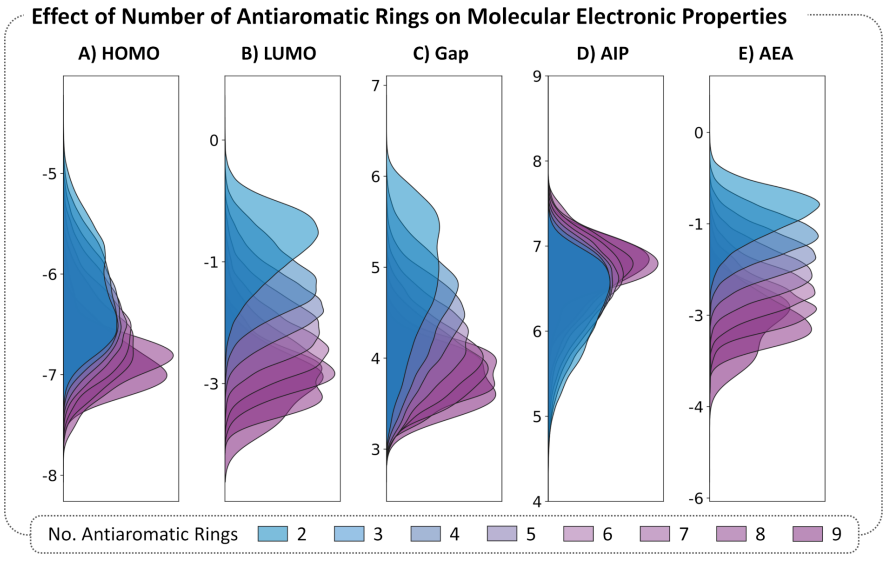

Figure 8: Distributions of electronic properties of the dataset. KDE plots of A) HOMO, B) LUMO, C) Gap, D) AIP, and E) AEA colored according to the number of antiaromatic rings in the molecule. The KDEs are normalized such that the area under the curve is equal to 1 for each family.

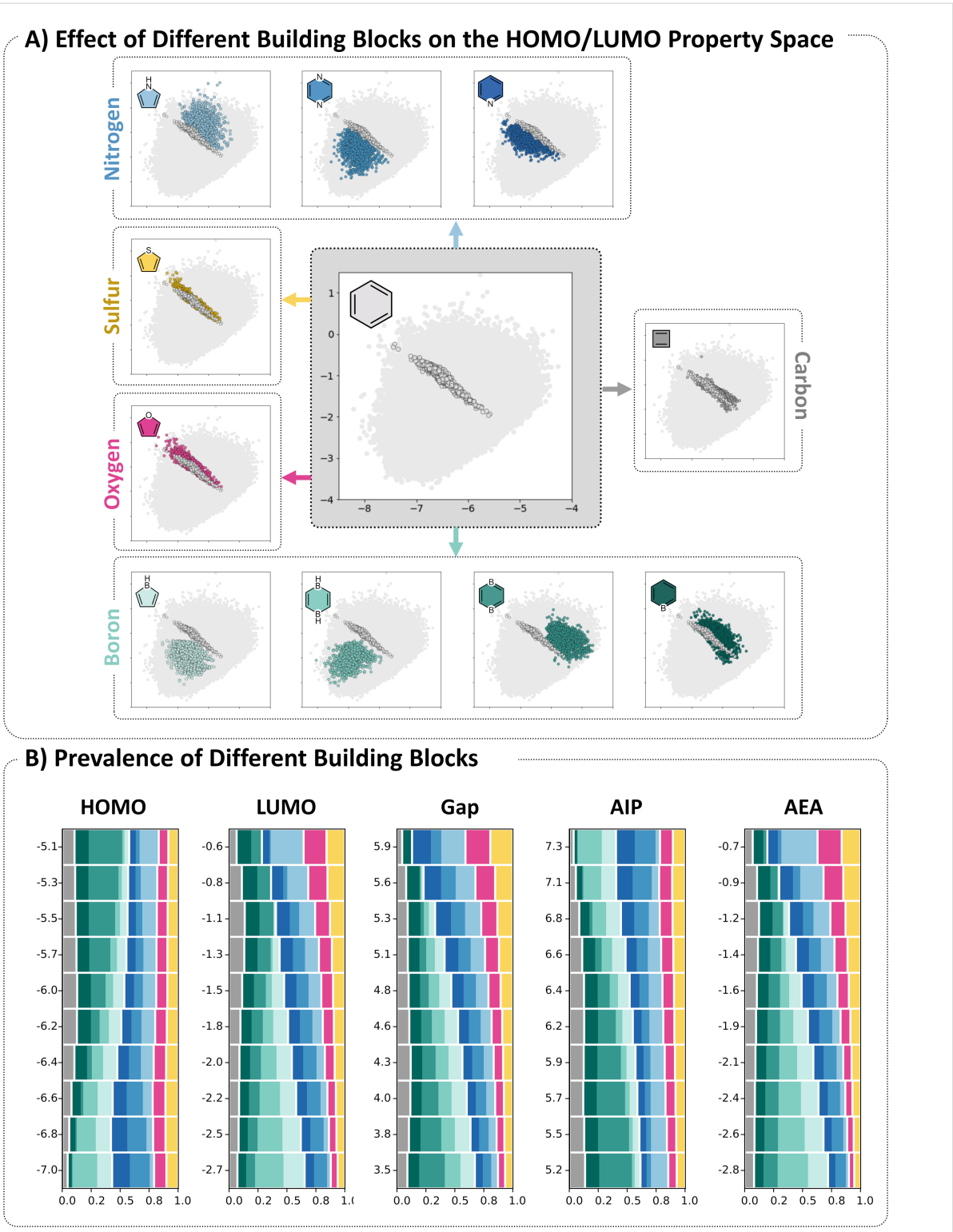

Figure 9: A) Scatter plot of the HOMO (*x*-axis) and LUMO (*y*-axis) values of the molecules in COMPAS-2. In each plot, the molecules containing only benzene are colored in gray and the molecules containing only benzene and a single other type of building block are colored according to the color-coded library. B) Stacked histograms showing the prevalence of the different building blocks for HOMO, LUMO, Gap, AIP, and AEA. The colors of each block correspond to the color-coded molecules. The size of each block represents the fraction of that building block out of the overall building blocks (excluding benzene). The sum of all building blocks is 1 for each bin. Molecules below and above the 0.01 and 0.99 percentiles, respectively, were discarded as not statistically meaningful. Note: for the plot of borinine, 5 outlier data points were removed following visual inspection, which determined that these molecules did not optimize correctly.

this data as a "baseline"). Thus, each different types of building block are plotted together with the cc-PBHs contained in COMPAS-2 (light gray circles). First and foremost, we note that molecules containing the same heterocycle tend to cluster in the same region of the HOMO/LUMO space, rather than be dispersed over the entire space. Secondly, we note that the shape and breadth of the property space covered differs noticeably. Furan, thiophene, and cyclobutadiene all cover a similar region of the property space as the baseline PBHs, which is a relatively small swath that shows a linear relationship – meaning, molecules with higher HOMOs have lower LUMOs and vice versa. In contrast, for all the B- and N-containing heterocycles, the respective regions are quite broad and without a well-defined shape, meaning that it is possible to find molecules with different combinations of low/high/mid-range HOMO and LUMO values within the region. Overall, it is apparent that the significant increase in property space over the COMPAS-1 baseline (Figure 3) is due mostly to the B- and N-containing heterocycles, or to heterogeneous mixing of different types of heterocycles, which suggests a cumulative effect of incorporating different types of building blocks (for additional details on the coverage of property space, see section 4 of Supporting Information File 1).

Having several types of N-containing and B-containing heterocycles enables us to further explore the behavior of these systems. For the B-containing heterocycles, we observe that the two aromatic rings (borinine and 1,4-diborinine) both shift the distribution to the right of the PBH baseline, towards higher HOMO values, while remaining in a similar range of LUMO values. In contrast, the two antiaromatic rings (borole and 1,4-dihydrodibornine) both shift the distribution to the left and downwards, towards lower HOMO and lower LUMO values. This sheds new light on our previous observations and the question we posed at the beginning of this section, regarding the "boron-effect" and the effect of antiaromatic rings. Namely, these plots elucidate that the LUMO-lowering effect of the boron atoms is not a general rule for boron, nor is it a general rule for antiaromatic components (cyclobutadiene, another antiaromatic building block, does not exhibit the same effect). Rather, it stems from the presence of boron atoms in antiaromatic rings. Further substantiation of this conclusion is provided in section 5 of Supporting Information File 1.

For the N-containing heterocycles, we observe a similar dichotomy, although in this case all systems are aromatic. The two six-membered rings (pyridine and pyrazine) shift the distribution to the left and downwards of the baseline, towards lower HOMO and LUMO values (the effect is more pronounced for pyrazine than pyridine). Conversely, the five-membered ring (pyrrole) shifts it to the right and upwards, maintaining a similar HOMO range to COMPAS-1, but extending into much higher LUMO values. The behavior of the various N-containing rings is well documented in the literature [17,44-49], although to the best of our knowledge, these three systems have never been compared directly before in a data-driven manner.

These findings are summarized in a more quantitative manner in Figure 9B. In this set of stacked histogram plots, the colored rectangles represent the relative prevalence of the various building blocks (in this case, we also included cyclobutadiene as a non-benzene building block). These plots reiterate the findings described above for the HOMO and LUMO properties and provide further information regarding the change in prevalence for each building block across the other property spaces, as well. In the interest of conciseness, we provide a detailed MO-based rationalization for all of the trends in section 6 of Supporting Information File 1.

Having studied the property space covered by the individual heterocycles, we performed a final analysis to investigate the effects of having multiple building blocks of a certain type in a single cc-hPAS (regardless of the presence and number of the other building blocks). To circumvent the size dependency, we once again focused only on the 9-ring systems. For this subset of molecules, we plotted the various molecular properties as a function of the number of building blocks of each type (from 1–4; the number of examples containing more than 4 building blocks of a single type are too few to be statistically meaningful).

Not surprisingly, the trends shown in Figure 10 reiterate and further substantiate some of the previous findings, however they also reveal additional information. Primarily, these plots demonstrate the cumulative effect of incorporating multiple rings. Furthermore, the slopes of the lines indicate the strength of the effects – e.g., it can be seen clearly that pyrrole has a much stronger effect on the HOMO values than either furan or thiophene, and that 1,4-diborinine has the strongest LUMO-lowering effect of all building blocks in our library. In addition, these plots can provide further insight into the three building blocks that showed similar coverage as the cc-PBHs, namely, furan, thiophene, and cyclobutadiene. Although the distribution plot itself indicated a weak or negligible effect of these building blocks, Figure 10 reveals that indeed they do influence the molecular properties. Cyclobutadiene appears to have very little effect on the LUMO but does contribute to raising the HOMO and therefore decreasing the Gap. Furan and thiophene display very similar behaviors, as can be seen from the slopes of their plots for all three properties. An additional version of this figure that includes the benzene trend in provided in section 3.3 of Supporting Information File 1.

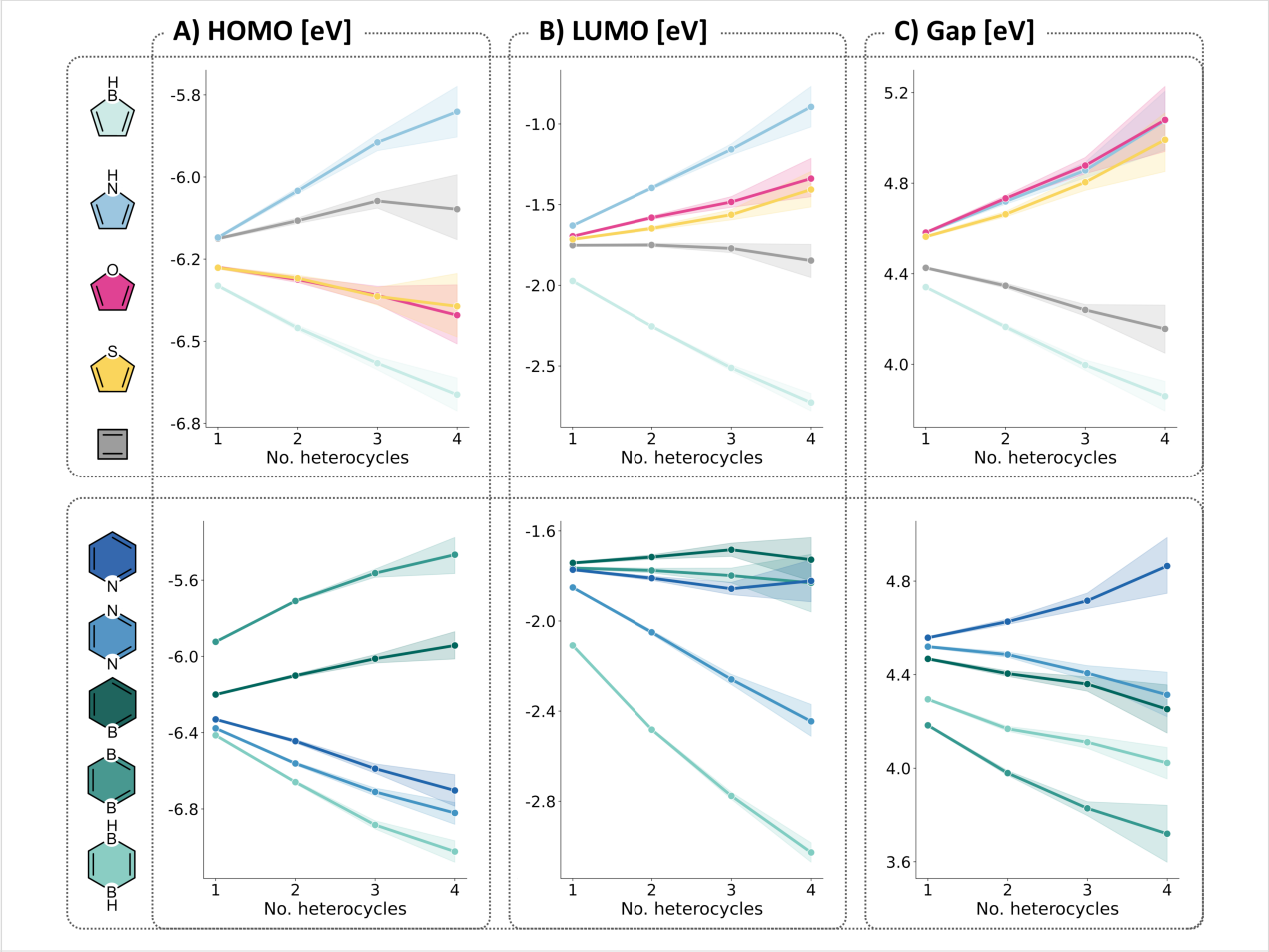

Figure 10: The effect of multiple heterocycles of a certain type on the A) HOMO, B) LUMO, and C) Gap. For all 9-ring systems in the dataset, we calculated the average property value of the rings containing 1, 2, 3, and 4 building blocks of a certain type, respectively. The data corresponding to each building block and each number of repeating units is represented by points corresponding to the color-coding shown on the left. For clarity, we have separated the 4- and 5-membered rings (top row) from the 6-membered rings (bottom row) and connected the points in each series by lines to assist in visual identification. The shading represents the 95% confidence interval of the value.

Conclusion

We have performed a comprehensive data-driven analysis of the new dataset of *cata*-condensed hetero-polycyclic aromatic systems, COMPAS-2, which contains over 500,000 molecules. Following a comparison to cc-PBHs to establish a baseline for our study, our analysis was divided into three main levels, proceeding from low to high structural resolution: a) global properties, b) atomic composition, and c) building block composition. At each of these levels, we analyzed the data according to various structural features, to elucidate the underlying structure–property relationships and delineate clear principles that can aid in rational design of new cc-hPASs.

The main findings of our analysis are as follows:

1. Global features: this analysis revealed that molecular size affects electronic properties, but that the sensitivity to size becomes less apparent in larger molecules. Similarly, the overall electron count [(4n) or (4n + 2)] has a noticeable effect in smaller molecules but becomes unimportant in medium-sized and larger PASs. Finally, no specific trends were found between geometric features and molecular properties, except for the longest linear stretch. However, this effect is only clearly apparent in PASs that contain no antiaromatic rings.

2. Atomic composition: the analysis in this section revealed a clear "boron effect" (the presence of boron corresponds to high HOMO, low LUMO, small Gap). However, it could not be ascertained whether the boron effect stems solely from the presence of the atom, or from the fact that the boron atoms are often found in antiaromatic rings (borole, 1,4-dihydrodiborinine). Similarly, the N, O, and S atoms appeared more prevalent in molecules with high LUMOs and high HOMO–LUMO gaps, but it remained unclear whether this is due to the electronegativity of these atoms or their presence in aromatic building blocks.

3. Building block composition: the investigation in this section uncovered several findings. We observed that the molecular properties of cc-hPASs are dictated to some extent by the aromatic character of the building blocks contained in the molecule – the more antiaromatic rings there are, the lower the HOMO, LUMO, and Gap become. Further analysis revealed that, in fact, cyclobutadiene has a relatively small effect on the frontier molecule orbitals, thus the majority of observed trend stems from the B-containing antiaromatic rings. Indeed, we found that boron atoms have a strong impact on the molecular properties, however, the direction of this impact is in opposite directions, depending on whether the specific heterocycle is aromatic or antiaromatic. Furthermore, we observed an interesting divergence between pyrrole and the other five-membered aromatic rings. Although all three rings lead to an increase in the Gap, the pyrrole raises the HOMO and LUMO while furan and thiophene lower the HOMO and raise the LUMO. In addition, thiophene and furan show similar behavior both in the magnitudes of their effects and in the size of the property space they cover, whereas pyrrole displays a much stronger impact on the property values and a much more broadly distributed property space. This suggests that the properties of the pyrrole-containing cc-hPASs are much more sensitive to variations in structure than their furan- and thiophene-containing counterparts. The other N-containing building blocks, pyridine and pyrazine, lower both frontier molecular orbitals, with the pyrazine having a stronger effect, due to the fact that it contains two nitrogens. Indeed, we demonstrated that for all building blocks there is a cumulative effect on the properties, whereby incorporation of multiple building blocks continuously impacts the molecular properties.

To the best of our knowledge, this is the first data-driven investigation of this kind. It provides for the first time a clear overview of the property space that is achievable with these molecules, as well as detailed information on how to access different parts of this property space through structural design. The insight gleaned from this analysis not only deepens our understanding of the chemical properties of these important molecules, but also provides us with important tools for designing new molecules with desired properties. We emphasize that there is still much more to be learned from this rich database, including the reciprocal effects of adjacent building blocks, the importance of multi-ring substructures, and the interplay of different building blocks. Combining different types of heterocycles has been found to endow cc-hPASs with promising properties (e.g., pyrrole and thiophene [50], pyrrole and furan [51], borinine and thiophene [52]). Our data now shines new light on the interplay of these building blocks, but the exact relationships governing the resulting properties are unknown. Such complex relationships require more advanced data-analysis tools, and we are currently leveraging different machine learning and deep learning techniques to tap the full potential of the COMPAS-2 dataset.

Supporting Information

The COMPAS-2 dataset is freely available online at the Poranne Group repository: https://gitlab.com/porannegroup/compas.

Supporting Information File 1

Further discussion and additional visualizations, an MO-based explanation of the chemical trends detailed in this analysis.
[https://www.beilstein-journals.org/bjoc/content/supplementary/1860-5397-20-160-S1.pdf]

Acknowledgements

The authors express their deep appreciation to Prof. Dr. Peter Chen for his ongoing support, to Dr. Alexandra Tsybizova for helpful comments on the draft version of this manuscript, to Dr. Alexandra Wahab for her assistance with data handling and visualization, and to Mr. Itay Almog for fruitful discussions.

Funding

This study was financially supported by a Branco Weiss Fellowship – Society in Science grant and by an ISF Personal Research Grant (Grant Number 1745/23), both awarded to R. G. P.

Author Contributions

Sabyasachi Chakraborty: data curation; formal analysis; investigation; validation; visualization; writing – original draft; writing – review & editing. Eduardo Mayo Yanes: data curation; formal analysis; investigation; methodology; visualization; writing – original draft. Renana Gershoni-Poranne: conceptualization; formal analysis; funding acquisition; project administration; resources; supervision; validation; visualization; writing – original draft; writing – review & editing.

ORCID® iDs

Sabyasachi Chakraborty - https://orcid.org/0000-0003-4183-811X
Eduardo Mayo Yanes - https://orcid.org/0000-0002-6488-7734
Renana Gershoni-Poranne - https://orcid.org/0000-0002-2233-6854

Data Availability Statement

The data used for/in this study is openly available in Figshare at https://doi.org/10.6084/m9.figshare.24347152 and on Gitlab at https://gitlab.com/porannegroup/compas. The data was derived from sources available in the public domain [COMPAS-2, 1/2024].

Preprint

A non-peer-reviewed version of this article has been previously published as a preprint:
https://chemrxiv.org/engage/chemrxiv/article-details/6633d87691aefa6ce1ff32fb

References

1. Anthony, J. E. *Chem. Rev.* **2006,** *106,* 5028–5048. doi:10.1021/cr050966z
2. Lindhorst, A. C.; Haslinger, S.; Kühn, F. E. *Chem. Commun.* **2015,** *51,* 17193–17212. doi:10.1039/c5cc07146a
3. Becker, F. F.; Banik, B. K. *Front. Chem. (Lausanne, Switz.)* **2014,** *2,* 55. doi:10.3389/fchem.2014.00055
4. Bulumulla, C.; Gunawardhana, R.; Gamage, P. L.; Miller, J. T.; Kularatne, R. N.; Biewer, M. C.; Stefan, M. C. *ACS Appl. Mater. Interfaces* **2020,** *12,* 32209–32232. doi:10.1021/acsami.0c07161
5. Gidron, O.; Bendikov, M. *Angew. Chem., Int. Ed.* **2014,** *53,* 2546–2555. doi:10.1002/anie.201308216
6. Wahab, A.; Pfuderer, L.; Paenurk, E.; Gershoni-Poranne, R. *J. Chem. Inf. Model.* **2022,** *62,* 3704–3713. doi:10.1021/acs.jcim.2c00503
7. Fite, S.; Wahab, A.; Paenurk, E.; Gross, Z.; Gershoni-Poranne, R. *J. Phys. Org. Chem.* **2023,** *36,* e4458. doi:10.1002/poc.4458
8. Weiss, T.; Wahab, A.; Bronstein, A. M.; Gershoni-Poranne, R. *J. Org. Chem.* **2023,** *88,* 9645–9656. doi:10.1021/acs.joc.2c02381
9. Mayo Yanes, E.; Chakraborty, S.; Gershoni-Poranne, R. *Sci. Data* **2024,** *11,* 97. doi:10.1038/s41597-024-02927-8
10. Jiang, H.; Zhu, S.; Cui, Z.; Li, Z.; Liang, Y.; Zhu, J.; Hu, P.; Zhang, H.-L.; Hu, W. *Chem. Soc. Rev.* **2022,** *51,* 3071–3122. doi:10.1039/d1cs01136g
11. Dong, H.; Wang, C.; Hu, W. *Chem. Commun.* **2010,** *46,* 5211–5222. doi:10.1039/c0cc00947d
12. Kilaru, S.; Gade, R.; bhongiri, Y.; Tripathi, A.; Chetti, P.; Pola, S. *Mater. Sci. Semicond. Process.* **2022,** *147,* 106730. doi:10.1016/j.mssp.2022.106730
13. Tsuji, H.; Nakamura, E. *Acc. Chem. Res.* **2017,** *50,* 396–406. doi:10.1021/acs.accounts.6b00595
14. Gidron, O.; Dadvand, A.; Sheynin, Y.; Bendikov, M.; Perepichka, D. F. *Chem. Commun.* **2011,** *47,* 1976–1978. doi:10.1039/c0cc04699j
15. Li, M.; Xie, W.; Cai, X.; Peng, X.; Liu, K.; Gu, Q.; Zhou, J.; Qiu, W.; Chen, Z.; Gan, Y.; Su, S.-J. *Angew. Chem., Int. Ed.* **2022,** *61,* e202209343. doi:10.1002/anie.202209343
16. Fan, J.-X.; Ji, L.-F.; Zhang, N.-X.; Lin, P.-P.; Qin, G.-Y.; Zhang, S.-F.; Ren, A.-M. *New J. Chem.* **2019,** *43,* 3583–3600. doi:10.1039/c8nj04714f
17. Chen, X.-K.; Guo, J.-F.; Zou, L.-Y.; Ren, A.-M.; Fan, J.-X. *J. Phys. Chem. C* **2011,** *115,* 21416–21428. doi:10.1021/jp206617e
18. Lin, Y.; Li, Y.; Zhan, X. *Chem. Soc. Rev.* **2012,** *41,* 4245–4272. doi:10.1039/c2cs15313k
19. Sirringhaus, H. *Adv. Mater. (Weinheim, Ger.)* **2014,** *26,* 1319–1335. doi:10.1002/adma.201304346
20. Marques, G.; Leswing, K.; Robertson, T.; Giesen, D.; Halls, M. D.; Goldberg, A.; Marshall, K.; Staker, J.; Morisato, T.; Maeshima, H.; Arai, H.; Sasago, M.; Fujii, E.; Matsuzawa, N. N. *J. Phys. Chem. A* **2021,** *125,* 7331–7343. doi:10.1021/acs.jpca.1c04587
21. Staker, J.; Marshall, K.; Leswing, K.; Robertson, T.; Halls, M. D.; Goldberg, A.; Morisato, T.; Maeshima, H.; Ando, T.; Arai, H.; Sasago, M.; Fujii, E.; Matsuzawa, N. N. *J. Phys. Chem. A* **2022,** *126,* 5837–5852. doi:10.1021/acs.jpca.2c04221
22. Wang, C.; Zhang, X.; Hu, W. *Chem. Soc. Rev.* **2020,** *49,* 653–670. doi:10.1039/c9cs00431a
23. Tanaka, K.; Iwama, Y.; Kishimoto, M.; Ohtsuka, N.; Hoshino, Y.; Honda, K. *Org. Lett.* **2020,** *22,* 5207–5211. doi:10.1021/acs.orglett.0c01852
24. Yamaguchi, A. D.; Chepiga, K. M.; Yamaguchi, J.; Itami, K.; Davies, H. M. L. *J. Am. Chem. Soc.* **2015,** *137,* 644–647. doi:10.1021/ja512059d
25. Chen, X.; Yan, L.; Liu, Y.; Yang, Y.; You, J. *Chem. Commun.* **2020,** *56,* 15080–15083. doi:10.1039/d0cc06997c
26. Hermann, M.; Wassy, D.; Esser, B. *Angew. Chem., Int. Ed.* **2021,** *60,* 15743–15766. doi:10.1002/anie.202007024
27. Grimme, S.; Bannwarth, C.; Shushkov, P. *J. Chem. Theory Comput.* **2017,** *13,* 1989–2009. doi:10.1021/acs.jctc.7b00118
28. Yanai, T.; Tew, D. P.; Handy, N. C. *Chem. Phys. Lett.* **2004,** *393,* 51–57. doi:10.1016/j.cplett.2004.06.011
29. Grimme, S.; Antony, J.; Ehrlich, S.; Krieg, H. *J. Chem. Phys.* **2010,** *132,* 154104. doi:10.1063/1.3382344
30. Grimme, S.; Ehrlich, S.; Goerigk, L. *J. Comput. Chem.* **2011,** *32,* 1456–1465. doi:10.1002/jcc.21759
31. Johnson, E. R.; Becke, A. D. *J. Chem. Phys.* **2006,** *124,* 174104. doi:10.1063/1.2190220
32. Weigend, F. *Phys. Chem. Chem. Phys.* **2006,** *8,* 1057–1065. doi:10.1039/b515623h
33. Weigend, F.; Ahlrichs, R. *Phys. Chem. Chem. Phys.* **2005,** *7,* 3297–3305. doi:10.1039/b508541a
34. Gershoni-Poranne, R.; Rahalkar, A. P.; Stanger, A. *Phys. Chem. Chem. Phys.* **2018,** *20,* 14808–14817. doi:10.1039/c8cp02162g
35. Berris, B. C.; Hovakeemian, G. H.; Lai, Y. H.; Mestdagh, H.; Vollhardt, K. P. C. *J. Am. Chem. Soc.* **1985,** *107,* 5670–5687. doi:10.1021/ja00306a013
36. Gao, M.; Chen, H.; Miao, Q. *Eur. J. Org. Chem.* **2022,** e202101315. doi:10.1002/ejoc.202101315
37. Jin, Z.; Teo, Y. C.; Zulaybar, N. G.; Smith, M. D.; Xia, Y. *J. Am. Chem. Soc.* **2017,** *139,* 1806–1809. doi:10.1021/jacs.6b12888
38. Jin, Z.; Teo, Y. C.; Teat, S. J.; Xia, Y. *J. Am. Chem. Soc.* **2017,** *139,* 15933–15939. doi:10.1021/jacs.7b09222
39. von E. Doering, W.; Detert, F. L. *J. Am. Chem. Soc.* **1951,** *73,* 876–877. doi:10.1021/ja01146a537
40. Vol'pin, M. E. *Russ. Chem. Rev.* **1960,** *29,* 129–160. doi:10.1070/rc1960v029n03abeh001224
41. Kobayashi, N.; Sasaki, M.; Nomoto, K. *Chem. Mater.* **2009,** *21,* 552–556. doi:10.1021/cm802826m
42. Luo, T.; Wang, Y.; Hao, J.; Chen, P.-A.; Hu, Y.; Chen, B.; Zhang, J.; Yang, K.; Zeng, Z. *Angew. Chem.* **2023,** *135,* e202214653. doi:10.1002/ange.202214653
43. von Grotthuss, E.; John, A.; Kaese, T.; Wagner, M. *Asian J. Org. Chem.* **2018,** *7,* 37–53. doi:10.1002/ajoc.201700495
44. Zhang, S.-F.; Chen, X.-K.; Fan, J.-X.; Guo, J.-F.; Ren, A.-M.; Li, Y.-W. *J. Mol. Model.* **2014,** *20,* 2502. doi:10.1007/s00894-014-2502-3
45. Winkler, M.; Houk, K. N. *J. Am. Chem. Soc.* **2007,** *129,* 1805–1815. doi:10.1021/ja067087u
46. Bunz, U. H. F.; Engelhart, J. U.; Lindner, B. D.; Schaffroth, M. *Angew. Chem., Int. Ed.* **2013,** *52,* 3810–3821. doi:10.1002/anie.201209479

47. Chen, Y.; Shen, L.; Li, X. *J. Phys. Chem. A* **2014,** *118,* 5700–5708. doi:10.1021/jp503114b
48. Momicchioli, F.; Rastelli, A. *J. Mol. Spectrosc.* **1967,** *22,* 310–324. doi:10.1016/0022-2852(67)90178-6
49. Delaere, D.; Nguyen, M. T.; Vanquickenborne, L. G. *Phys. Chem. Chem. Phys.* **2002,** *4,* 1522–1530. doi:10.1039/b109008a
50. Gao, P.; Cho, D.; Yang, X.; Enkelmann, V.; Baumgarten, M.; Müllen, K. *Chem. – Eur. J.* **2010,** *16,* 5119–5128. doi:10.1002/chem.200903562
51. Sun, W.; Wang, C.-H.; Lv, S.-F.; Jiang, J.-X.; Guo, X.; Zhang, F.-B. *Org. Electron.* **2020,** *77,* 105548. doi:10.1016/j.orgel.2019.105548
52. Saito, S.; Matsuo, K.; Yamaguchi, S. *J. Am. Chem. Soc.* **2012,** *134,* 9130–9133. doi:10.1021/ja3036042

License and Terms

BEILSTEIN JOURNAL OF ORGANIC CHEMISTRY

Radical reactivity of antiaromatic Ni(II) norcorroles with azo radical initiators

Siham Asyiqin Shafie[‡1], Ryo Nozawa[‡1], Hideaki Takano[1,2] and Hiroshi Shinokubo[*1]

Letter

Open Access

Address:
[1]Department of Molecular and Macromolecular Chemistry, Graduate School of Engineering and Integrated Research Consortium Chemical Sciences (IRCCS), Nagoya University, Furo-cho, Chikusa-ku, Nagoya, Aichi 464-8603, Japan and [2]Institute for Advanced Research, Nagoya University, Furo-cho, Chikusa-ku, Nagoya, Aichi 464-8601, Japan

Email:
Hiroshi Shinokubo[*] - hshino@chembio.nagoya-u.ac.jp

* Corresponding author ‡ Equal contributors

Keywords:
16π; antiaromatic; norcorrole; porphyrinoid; radical

Beilstein J. Org. Chem. **2024,** *20,* 1967–1972.
https://doi.org/10.3762/bjoc.20.172

Received: 21 May 2024
Accepted: 01 August 2024
Published: 12 August 2024

This article is part of the thematic issue "π-Conjugated molecules and materials".

Guest Editor: A. Mateo-Alonso

Abstract

Norcorrole is a stable 16π-antiaromatic porphyrinoid that exhibits characteristic reactivities and physical properties. Here, we disclose the reaction of Ni(II) norcorroles with alkyl radicals derived from azo radical initiators. The radical selectively attacked the distal α-position relative to the *meso*-position to construct a nonaromatic bowl-shaped structure. The photophysical and electrochemical properties of the obtained radical adducts were compared to those of the parent Ni(II) norcorrole. The radical reactivity of Ni(II) norcorroles was investigated by density functional theory (DFT) calculations.

Introduction

Considerable attention has been directed toward antiaromatic norcorroles [1-3] due to the fascinating physical properties, such as reversible redox properties [4,5] and stacked-ring aromaticity [6-10]. While Ni(II) norcorroles are stable under ambient conditions despite the distinct 16π-antiaromaticity, they show unique reactivities with various reagents due to the high-lying HOMO and low-lying LUMO (Figure 1) [11]. Reactions with nucleophiles (Nu) proceed with perfect regioselectivity at the distal β-position relative to the *meso*-position [12-15]. On the other hand, reactions with electrophiles (El) also occur preferentially at the β-positions, but the regioselectivity depends on the electrophile [16-18]. In addition, C–C double bonds of the norcorrole skeleton outside the π-delocalization pathway exhibit a reactivity similar to an alkene to afford hydrogenated norcorroles by hydrogenation [19] or reduction with hydrazine [20] and [3 + 2]-cycloadducts with 1,3-dipoles [21]. Moreover, the ring-expansion or ring-opening reactions of Ni(II) norcorroles are induced by an activated zwitterionic intermediate [22], oxidants [23,24], and carbenes [25,26].

During the last decade, the various reactivities of Ni(II) norcorroles have been elucidated. However, the reaction with radical species has remained unexplored. Here, we disclose the radical functionalization of Ni(II) norcorroles with simple and

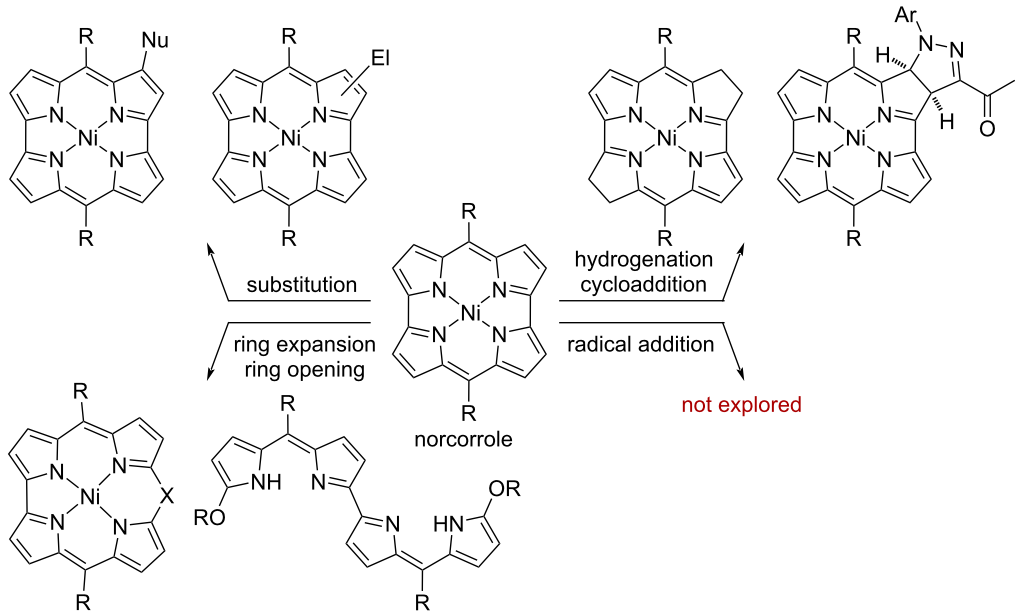

Figure 1: Reactivities of norcorroles with various reagents.

frequently used azo radical initiators to furnish nonconjugated macrocycles with bowl-shaped structures [27]. The photophysical and electronic properties of the obtained products are also presented. We also discuss the selectivity of the radical addition to Ni(II) norcorroles using DFT calculations.

Results and Discussion

Reactivity with azo radical initiators

We selected 2,2'-azobis(isobutyronitrile) (AIBN) as a radical source. Ni(II) dimesitylnorcorrole **1** was treated with AIBN in refluxing toluene (Scheme 1). The reaction smoothly proceeded to afford dialkylated macrocycle **2a** in 92% yield. In addition to **2a**, monoalkylated product **3a** and dipyrrin dimer **4a** were obtained as minor products in 4% and 3% yield, respectively.

The structure of **2a** was unambiguously confirmed by single-crystal X-ray analysis, which revealed that two alkyl substituents were located on the same side of the molecule (Figure 2a). Compared to the planar structure of **1** (Figure 2b) [2], **2a** displays a nonplanar structure due to the sp^3 carbon atoms adjacent to the nitrogen atoms. The ^{1}H NMR spectrum of **2a** confirmed that the antiaromatic character of the macrocycle

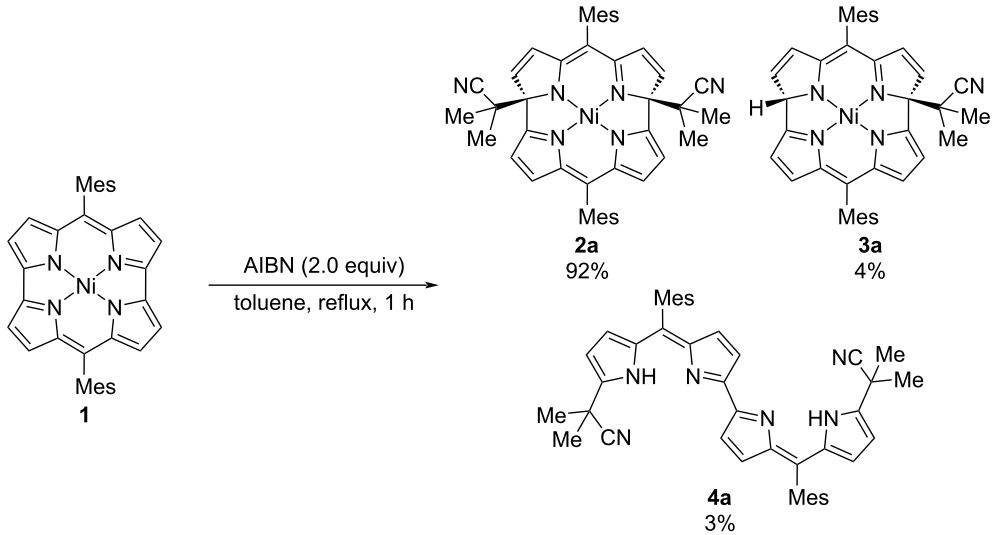

Scheme 1: Reaction of norcorrole **1** with AIBN.

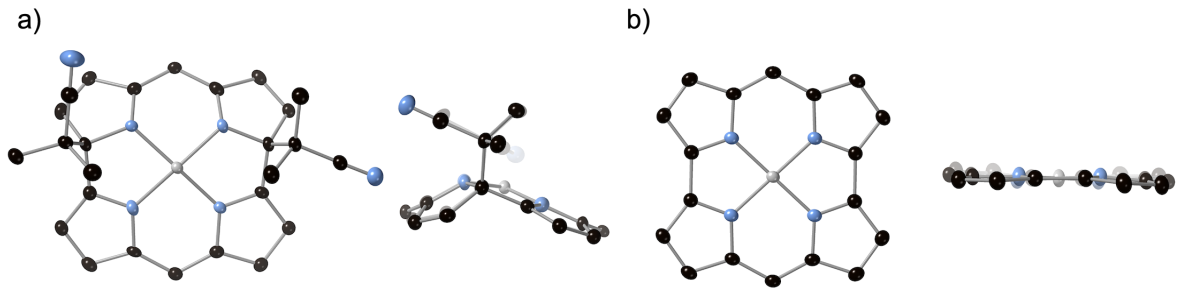

Figure 2: Top and side views of the X-ray structures of a) **2a** and b) **1** [2]. Mesityl groups and hydrogen atoms were omitted for clarity. Thermal ellipsoids are drawn at 50% probability.

changed to nonaromatic upon radical addition (see Supporting Information File 1).

1,1'-Azobis(cyclohexane-1-carbonitrile) (V-40) was also examined as a radical source. The reaction afforded **2b** in 87% yield (Scheme 2). Unfortunately, other radical sources, such as benzoyl peroxide, TEMPO, and the combination of alkyl halides with BEt_3, were not applicable to this reaction.

Physical properties

The electronic absorption spectra of norcorrole **1** and adduct **2a** are shown in Figure 3. While norcorrole **1** exhibited a weak absorption band from 600 nm to the NIR region, due to the characteristic forbidden HOMO–LUMO transition of the antiaromatic compound, nonconjugated macrocycle **2a** did not possess such an absorption band, indicating the loss of antiaromaticity in **2a**. Macrocycle **2a** possessed new absorption bands

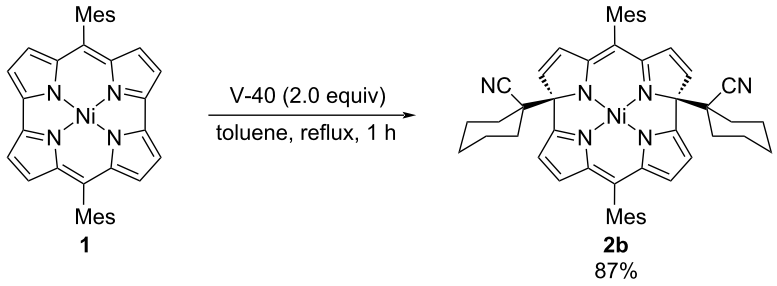

Scheme 2: Reaction of norcorrole **1** with V-40.

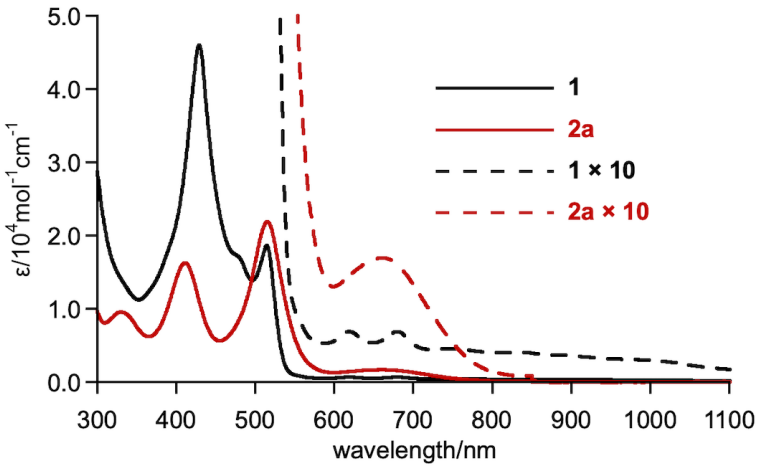

Figure 3: UV–vis–NIR absorption spectra of **1** and **2a** in CH_2Cl_2.

from 600 to 800 nm. The simulated absorption spectrum of **2a** obtained by TD DFT calculations at the M06/6-31G(d)+SDD//B3LYP-D3/6-31G(d)+SDD level of theory was consistent with the experimental results. Therein, the absorption band at 670 nm (f = 0.0026) was attributed to the transition from HOMO to LUMO+1.

Next, the electrochemical properties of **2a** in CH_2Cl_2 were examined using cyclic voltammetry (Figure 4). Macrocycle **2a** exhibited one reversible oxidation wave at 0.44 V and two reversible reduction waves at −0.85 V and −1.14 V. The electrochemical HOMO–LUMO gap of **2a** is 1.29 V, which is larger than that of **1a** (1.08 V) [2].

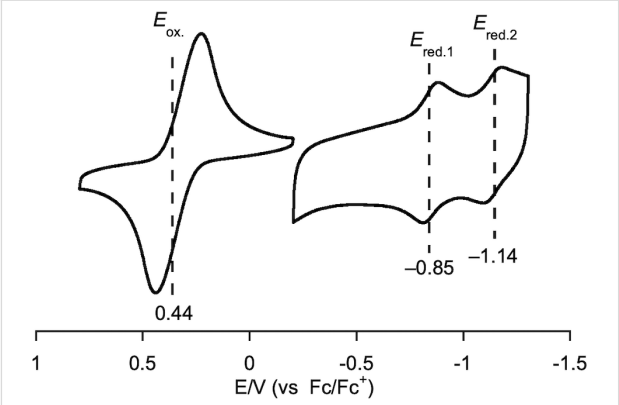

Figure 4: Cyclic voltammogram of **2a** in CH_2Cl_2. Supporting electrolyte: 0.1 M Bu_4NPF_6; working electrode: glassy carbon; counter electrode: Pt; reference electrode: $Ag/AgNO_3$; scan rate: 50 mV·s^{-1}.

DFT calculations

We next conducted DFT calculations using Gaussian 16 [28] to elucidate the reactivity of Ni(II) norcorroles with radical species (Scheme 3). All calculations for the ground state were performed at the (U)B3LYP-D3/6-31G(d)+SDD level of theory. The SOMO of an isobutyronitrile radical (−5.98 eV), which was generated through denitrogenation of AIBN, is closer to the HOMO level of Ni(II) norcorrole **1** (−4.68 eV) rather than its LUMO (−3.16 eV). This result explains the selective addition of the electrophilic isobutyronitrile radical to the distal α-position of the pyrrole unit. The calculated molecular orbital coefficient of the HOMO indicates that two α-carbon atoms of the pyrrole

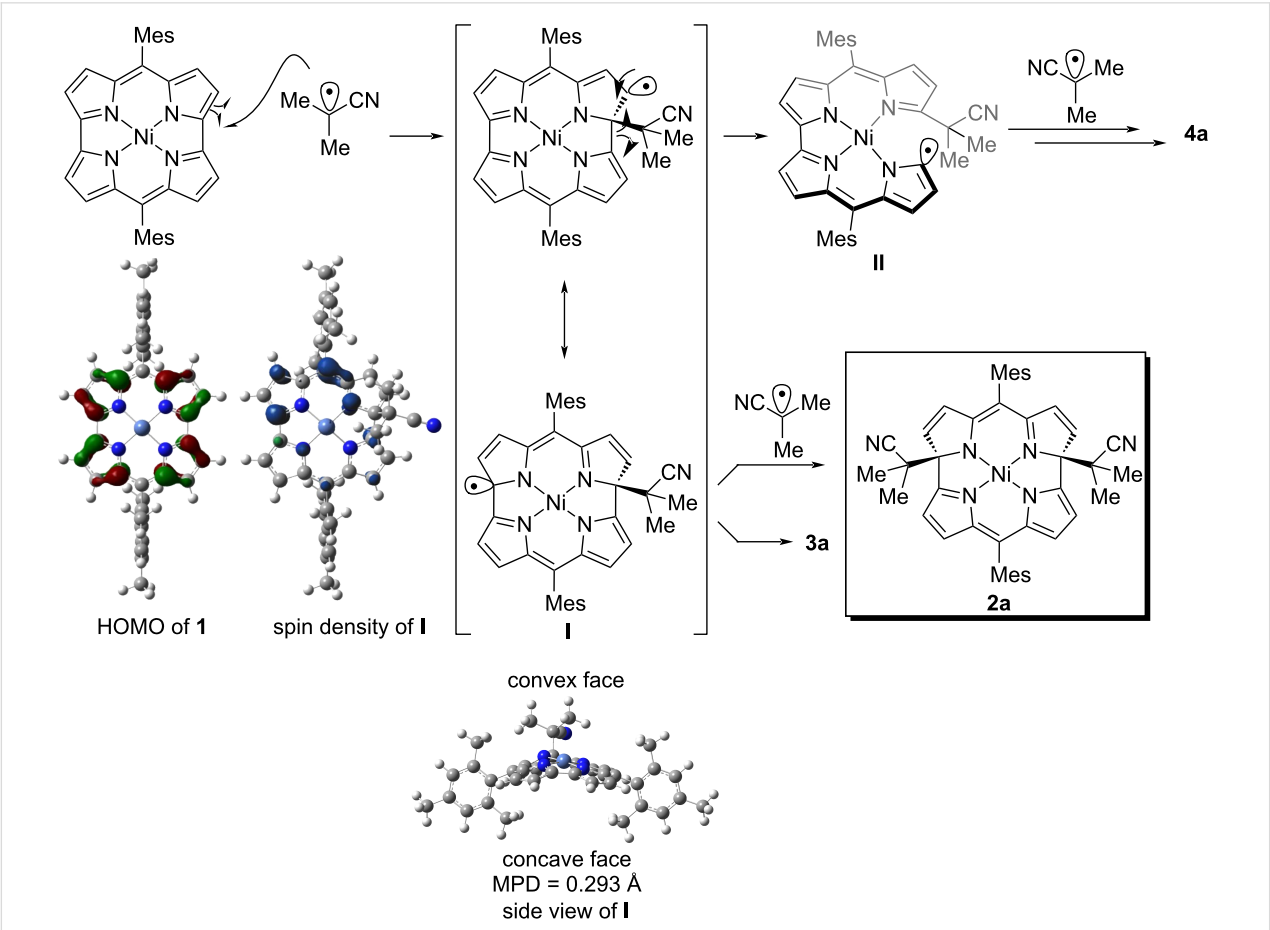

Scheme 3: Plausible reaction mechanism.

subunits are the most reactive positions for electrophilic species. In addition, the distal α-carbon atom relative to the *meso*-position could be more reactive than the proximal α-carbon atom due to the steric hindrance of bulky mesityl groups. Consequently, the isobutyronitrile radical predominantly attacks the distal α-carbon atom relative to the *meso*-position to afford the corresponding radical intermediate **I**. The calculated spin density of radical **I** revealed a substantial radical character at the α-position of the pyrrole skeleton. Finally, another isobutyronitrile radical reacts with **I** at the convex face to form the major product **2a,** with two alkyl substituents on the same side of the molecule. The mean-plane deviation (MPD) of **I** was 0.293 Å, where the mean plane was defined by carbon, nitrogen, and nickel atoms of the norcorrole core. For the byproducts, **3a** would be generated through the quenching of radical **I** with a hydrogen atom source. Bisdipyrrin **4a** could be formed through the ring-opening reaction of **I** by the homolytic cleavage of the $C(sp^2)$–$C(sp^2)$ bond to radical **II**, the addition of the isobutyronitrile radical, and subsequent demetallation.

Conclusion

In conclusion, we have investigated the addition reaction of electrophilic alkyl radicals derived from azo radical initiators to antiaromatic Ni(II) norcorroles. The reaction smoothly proceeded to afford bowl-shaped nonconjugated macrocycles **2a** in excellent yield, which exhibited markedly different photophysical and electrochemical properties with norcorrole **1**. The intrinsic reactivities of Ni(II) norcorroles with neutral radical species were revealed by DFT calculations, where populations of the HOMO of the norcorrole unit and the spin density of the radical intermediate governed the regioselectivity.

Supporting Information

Supporting Information File 1

Experimental procedures, compound characterization data including NMR and MS spectra, additional crystal data and details from DFT calculations.
[https://www.beilstein-journals.org/bjoc/content/supplementary/1860-5397-20-172-S1.pdf]

Funding

This work was supported by Japan Society for the Promotion of Science (JSPS) KAKENHI grants JP20H05863, JP22H04974, and JP22K19025. H. T. is grateful to the Ministry of Education, Culture, Sports, Science and Technology (MEXT) Leading Initiative for Excellent Young Researchers (Grant JPMXS0320220200) and the Foundation of Public Interest Tatematsu.

Author Contributions

Siham Asyiqin Shafie: investigation; writing – original draft. Ryo Nozawa: investigation. Hideaki Takano: investigation; writing – original draft; writing – review & editing. Hiroshi Shinokubo: funding acquisition; resources; supervision; writing – review & editing.

ORCID® iDs

Hideaki Takano - https://orcid.org/0000-0003-0744-9292
Hiroshi Shinokubo - https://orcid.org/0000-0002-5321-2205

Data Availability Statement

All data that supports the findings of this study is available in the published article and/or the supporting information to this article.

Preprint

A non-peer-reviewed version of this article has been previously published as a preprint: https://doi.org/10.3762/bxiv.2024.32.v1

References

1. Bröring, M.; Köhler, S.; Kleeberg, C. *Angew. Chem., Int. Ed.* **2008,** *47,* 5658–5660. doi:10.1002/anie.200801196
2. Ito, T.; Hayashi, Y.; Shimizu, S.; Shin, J.-Y.; Kobayashi, N.; Shinokubo, H. *Angew. Chem., Int. Ed.* **2012,** *51,* 8542–8545. doi:10.1002/anie.201204395
3. Yonezawa, T.; Shafie, S. A.; Hiroto, S.; Shinokubo, H. *Angew. Chem., Int. Ed.* **2017,** *56,* 11822–11825. doi:10.1002/anie.201706134
4. Shin, J.-Y.; Yamada, T.; Yoshikawa, H.; Awaga, K.; Shinokubo, H. *Angew. Chem., Int. Ed.* **2014,** *53,* 3096–3101. doi:10.1002/anie.201310374
5. Ukai, S.; Fukui, N.; Ikeue, T.; Shinokubo, H. *Chem. Lett.* **2022,** *51,* 182–184. doi:10.1246/cl.210715
6. Nozawa, R.; Tanaka, H.; Cha, W.-Y.; Hong, Y.; Hisaki, I.; Shimizu, S.; Shin, J.-Y.; Kowalczyk, T.; Irle, S.; Kim, D.; Shinokubo, H. *Nat. Commun.* **2016,** *7,* 13620. doi:10.1038/ncomms13620
7. Kawashima, H.; Ukai, S.; Nozawa, R.; Fukui, N.; Fitzsimmons, G.; Kowalczyk, T.; Fliegl, H.; Shinokubo, H. *J. Am. Chem. Soc.* **2021,** *143,* 10676–10685. doi:10.1021/jacs.1c04348
8. Kawashima, H.; Fukui, N.; Phung, Q. M.; Yanai, T.; Shinokubo, H. *Cell Rep. Phys. Sci.* **2022,** *3,* 101045. doi:10.1016/j.xcrp.2022.101045
9. Ishikawa, S.; Yamasumi, K.; Sugiura, S.; Sato, S.; Watanabe, G.; Koo, Y. H.; Seki, S.; Bando, Y.; Haketa, Y.; Shinokubo, H.; Maeda, H. *Chem. Sci.* **2024,** *15,* 7603–7609. doi:10.1039/d4sc01633e
10. Kino, S.; Ukai, S.; Fukui, N.; Haruki, R.; Kumai, R.; Wang, Q.; Horike, S.; Phung, Q. M.; Sundholm, D.; Shinokubo, H. *J. Am. Chem. Soc.* **2024,** *146,* 9311–9317. doi:10.1021/jacs.4c01142
11. Li, S.; Sun, Y.; Meng, Y.; Li, X.; Zhang, S. *Chin. J. Org. Chem.* **2022,** *42,* 2390. doi:10.6023/cjoc202202039
12. Nozawa, R.; Yamamoto, K.; Shin, J.-Y.; Hiroto, S.; Shinokubo, H. *Angew. Chem., Int. Ed.* **2015,** *54,* 8454–8457. doi:10.1002/anie.201502666
13. Liu, B.; Yoshida, T.; Li, X.; Stępień, M.; Shinokubo, H.; Chmielewski, P. J. *Angew. Chem., Int. Ed.* **2016,** *55,* 13142–13146. doi:10.1002/anie.201607237

14. Yoshida, T.; Shinokubo, H. *Mater. Chem. Front.* **2017,** *1,* 1853–1857. doi:10.1039/c7qm00176b
15. Ren, D.; Fu, X.; Li, X.; Koniarz, S.; Chmielewski, P. J. *Org. Chem. Front.* **2019,** *6,* 2924–2933. doi:10.1039/c9qo00679f
16. Deng, Z.; Li, X.; Stępień, M.; Chmielewski, P. J. *Chem. – Eur. J.* **2016,** *22,* 4231–4246. doi:10.1002/chem.201504584
17. Kawashima, H.; Hiroto, S.; Shinokubo, H. *J. Org. Chem.* **2017,** *82,* 10425–10432. doi:10.1021/acs.joc.7b01899
18. Li, S.; Smaga, O.; Sun, Y.; Li, X.; Pawlicki, M.; Sukniewicz, M.; Chmielewski, P. J. *Org. Chem. Front.* **2021,** *8,* 3639–3652. doi:10.1039/d1qo00621e
19. Liu, B.; Li, X.; Stępień, M.; Chmielewski, P. J. *Chem. – Eur. J.* **2015,** *21,* 7790–7797. doi:10.1002/chem.201500736
20. Nozawa, R.; Yamamoto, K.; Hisaki, I.; Shin, J.-Y.; Shinokubo, H. *Chem. Commun.* **2016,** *52,* 7106–7109. doi:10.1039/c6cc02918c
21. Fu, X.; Meng, Y.; Li, X.; Stępień, M.; Chmielewski, P. J. *Chem. Commun.* **2018,** *54,* 2510–2513. doi:10.1039/c8cc00447a
22. Ren, D.; Smaga, O.; Fu, X.; Li, X.; Pawlicki, M.; Koniarz, S.; Chmielewski, P. J. *Org. Lett.* **2021,** *23,* 1032–1037. doi:10.1021/acs.orglett.0c04227
23. Liu, S.-Y.; Tanaka, H.; Nozawa, R.; Fukui, N.; Shinokubo, H. *Chem. – Eur. J.* **2019,** *25,* 7618–7622. doi:10.1002/chem.201901292
24. Shafie, S. A.; Kawashima, H.; Miyake, Y.; Shinokubo, H. *ChemPlusChem* **2019,** *84,* 623–626. doi:10.1002/cplu.201900068
25. Fukuoka, T.; Uchida, K.; Sung, Y. M.; Shin, J.-Y.; Ishida, S.; Lim, J. M.; Hiroto, S.; Furukawa, K.; Kim, D.; Iwamoto, T.; Shinokubo, H. *Angew. Chem., Int. Ed.* **2014,** *53,* 1506–1509. doi:10.1002/anie.201309921
26. Liu, S.-Y.; Fukuoka, T.; Fukui, N.; Shin, J.-Y.; Shinokubo, H. *Org. Lett.* **2020,** *22,* 4400–4403. doi:10.1021/acs.orglett.0c01402
27. Tabata, N.; Uchino, T.; Kitamura, C.; Yoshizawa, K.; Shiota, Y.; Kato, S.-i. *Chem. Sci.* **2023,** *14,* 5974–5982. doi:10.1039/d3sc00381g
28. *Gaussian 16,* Revision C.01; Gaussian, Inc.: Wallingford, CT, 2016.

License and Terms

BEILSTEIN JOURNAL OF ORGANIC CHEMISTRY

Synthesis and reactivity of the di(9-anthryl)methyl radical

Tomohiko Nishiuchi[*1,2], Kazuma Takahashi[1], Yuta Makihara[1] and Takashi Kubo[*1,2,3]

Letter

Open Access

Address:
[1]Department of Chemistry, Graduate School of Science, Osaka University, 1-1 Machikaneyama, Toyonaka, Osaka 560-0043, Japan, [2]Innovative Catalysis Science Division, Institute for Open and Transdisciplinary Research Initiatives (ISC-OTRI), Osaka University, Osaka, Japan and [3]Spintronics Research Network Division, Institute for Open and Transdisciplinary Research Initiatives (SRN-OTRI), Osaka University, Osaka, Japan

Email:
Tomohiko Nishiuchi[*] - nishiuchit13@chem.sci.osaka-u.ac.jp;
Takashi Kubo[*] - kubo@chem.sci.osaka-u.ac.jp

* Corresponding author

Keywords:
anthracene; cation; dimerization; radical; reactivity

Beilstein J. Org. Chem. **2024,** *20,* 2254–2260.
https://doi.org/10.3762/bjoc.20.193

Received: 30 May 2024
Accepted: 26 August 2024
Published: 05 September 2024

This article is part of the thematic issue "π-Conjugated molecules and materials" and is dedicated to the memory of Prof. Masahiko Iyoda.

Guest Editor: A. Mateo-Alonso

Abstract

The di(9-anthryl)methyl (DAntM) radical was synthesized and investigated to elucidate its optical, electrical properties, and reactivity. The generation of the DAntM radical was confirmed by its ESR spectrum, which showed two broad signals. The unpaired electron is primarily localized on the central sp^2 carbon and slightly delocalized over the two anthryl moieties. Although the DAntM radical undergoes dimerization in solution, the radical still remains even at 190 K due to the bulky nature of the two anthryl groups. Interestingly, upon exposure to air, the purple color of the radical solution quickly fades to orange, resulting in decomposition to give 9-anthryl aldehyde and anthroxyl radical derivatives.

Introduction

Organic radicals have garnered significant attention in various research fields, including catalysis [1-4], chromophores [5-8], and as agents in dynamic nuclear polarization [9-12]. Recently, highly stable aromatic hydrocarbon radicals, which can persist in air-saturated solutions for several days to months, have been synthesized by employing bulky substituents around the spin-localized carbon center [13-15]. These stable radicals have paved the way to elucidate the nature of radical species, advancing the field of radical chemistry. However, reducing the reactivity of radical species can mean losing one of their most attractive properties. Therefore, it is very important to explore aromatic hydrocarbon radicals that are sufficiently stable for handling, yet reactive under specific conditions.

Previously, we reported aromatic hydrocarbon radicals with 9-anthryl (Ant) units at the spin-center carbon, exhibiting high stability (Figure 1a) [16-21]. Although bulky phenyl substitutions at the spin-center carbon can also provide high stability [13-15], the introduction of an Ant unit allows for spin localization at the 10-position of anthracene through C–C bond rotation,

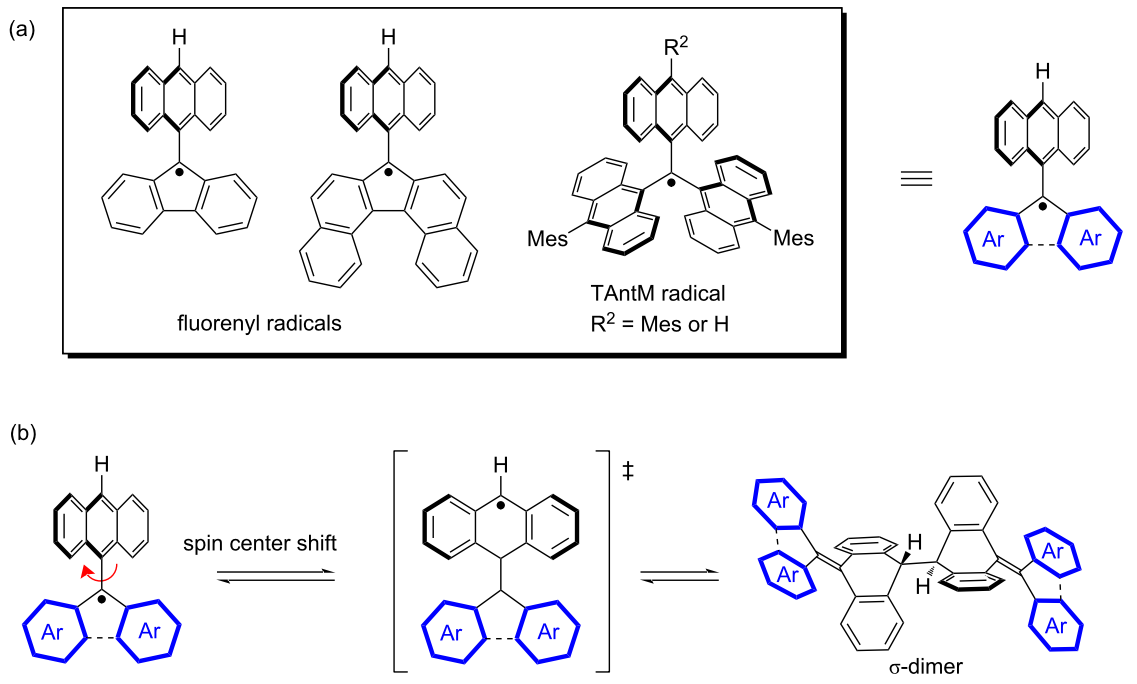

Figure 1: (a) Typical example of stable aromatic hydrocarbon radicals with 9-anthryl units. (b) Tail-to-tail σ-dimer formation by rotating anthryl group and spin center shift.

resulting in a tail-to-tail σ-dimer (Figure 1b). The σ-dimer exhibits an equilibrium state between the monomer radical and the σ-dimer in solution, and mechano-stimulus-induced C–C bond fission in the solid state yields the monomer radical [16-18]. Therefore, aromatic hydrocarbon radicals with Ant units possess both stability and reactivity depending on the conditions, giving them high potential for use as reactive catalysts [22,23] and stimuli-responsive sensors [24,25].

To further investigate this system, we designed the di(9-anthryl)methyl (DAntM) radical, which lacks one Ant unit compared to the tri(9-anthryl)methyl (TAntM) radical (Figure 2) [17]. By reducing the number of Ant units, we anticipated that the DAntM radical would exhibit spin delocalization between the two Ant units, differing from the basic skeleton of the highly reactive diphenylmethyl radical [26-28]. This spin delocalization is similar to that of the galvinoxyl radical, which

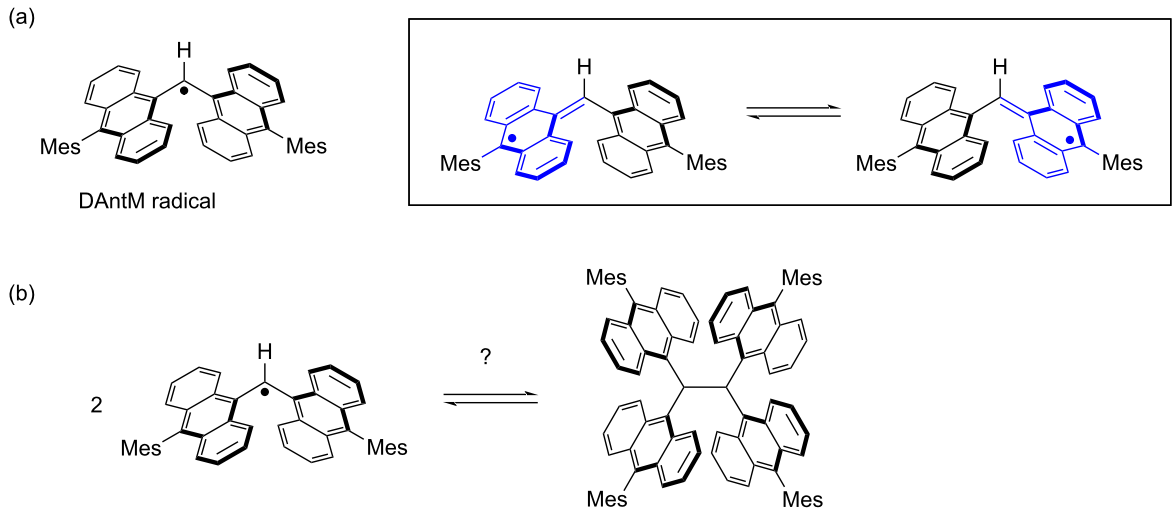

Figure 2: (a) The structure of DAntM radical (left) and its spin delocalization on two anthryl units. (b) Plausible head-to-head σ-dimerization of the DAntM radical.

shows high stability in air [29]. Thus, the DAntM radical would be a stable radical with a reactive site. Additionally, utilizing the reactive site, head-to-head σ-dimerization of the DAntM radical could yield 1,1,2,2-tetra(9-anthryl)ethane, which is a new anthracene embedded ethane [30] and would be a good candidate for the synthesis of overcrowded ethylene [31-36].

Herein, we report the synthesis and properties of the DAntM radical. The unpaired electron is primarily located at the central sp^2 carbon, a highly reactive site. The DAntM radical readily reacts with oxygen, leading to 1,2-dioxetane intermediate and decomposition to give anthryl aldehyde and a stable anthroxyl radical.

Results and Discussion

The synthetic route to the DAntM radical is shown in Scheme 1. The alcohol precursor **3** was prepared via addition reaction of lithium reagent **2** to 10-mesitylanthracene-9-carbaldehyde (**1**) in moderate yield (59%). The generation of the DAntM radical was performed using stannous chloride dihydrate with hydrogen chloride in THF. Upon adding hydrogen chloride to the solution, the solution color changed from orange to deep purple. The presence of the DAntM radical under this reaction conditions was confirmed by ESR measurement.

For the ESR measurement, a sample was prepared by taking an aliquot from the reaction solvent to ESR tube, evaporating it, and then dissolving it in degassed toluene. The ESR spectrum of the DAntM radical displayed two broad signals with g = 2.0028 (Figure 3a). The simulated spectrum indicated that the unpaired electron mainly locates at the central sp^2 carbon but is slightly delocalized over the two anthryl moieties (Figure 3b, Supporting Information File 1, Figure S1). DFT calculations for structural optimization revealed that the energy difference between two DAntM radical structures with different spin positions, spin localization at the central sp^2 carbon and on the anthryl group, is small about 1.18 kcal mol^{-1} (Supporting Information File 1, Figure S2). To investigate the activation barrier of this equilibrium, potential energy curve by changing the dihedral angle θ of one anthryl group was calculated. The transition state was calculated with the dihedral angle θ = 30.6° and the activation barrier is only 2.94 kcal mol^{-1} (Supporting

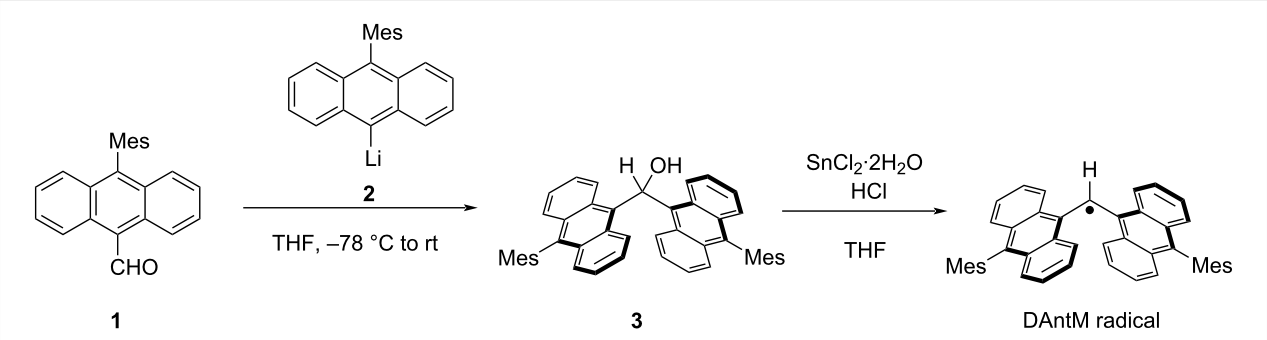

Scheme 1: Synthetic route to the DAntM radical.

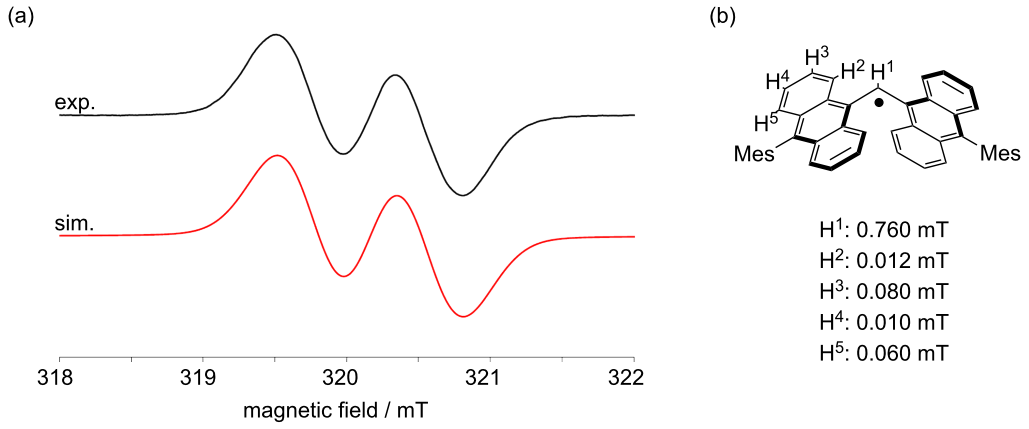

Figure 3: (a) ESR spectrum of the DAntM radical (black line, Exp.) and its simulated pattern (red line, Sim.). (b) Hyperfine coupling constant of the DAntM radical.

Information File 1, Figure S3). Thus, these two structures are likely in equilibrium and rapidly exchange with each other in solution. The energy difference between DAntM dimer (head-to-head σ-dimer) and DAntM radical monomer was also evaluated, showing that the dimer form is energetically preferable by about 3.97 kcal mol^{-1} (Supporting Information File 1, Figure S2). In VT-ESR measurements at low temperatures, the ESR signal integral decreased with cooling (Supporting Information File 1, Figure S4). However, even at 190 K, the relative signal integral compared to that at 295 K remained 0.56. Thus, the σ-dimer formation occurs but the σ-dimer readily dissociates, probably due to the steric bulkiness of the two Ant units [37].

It is noteworthy that the purple colored solution of the DAntM radical immediately fade to orange when exposed to air, indicating that the high reactivity of the central sp^2 carbon. To evaluate the decomposition pathway, the decomposed materials were characterized. Surprisingly, the major compound detected by ^{1}H NMR measurement of the crude material was compound **1**, along with di(10-mesityl-9-anthryl)methane (**4**) as a minor product. After silica gel column purification, the isolated yield of these compounds were 64% and 13%, respectively. Additionally, a radical species, showing an ESR peak pattern distinct from that of the DAntM radical and mainly splitting into five peaks with g = 2.0037, was confirmed (Figure 4, Figure S7, Supporting Information File 1). ESR and MS measurements as well as X-ray crystallography revealed that the radical species was assigned 10-mesityl-9-anthroyxyl radical (**5**), obtained in 47% yield (Figure 4c, Figure S8, Supporting Information File 1). Thus, two decomposition pathways were considered: a minor pathway involving hydrogen abstraction from water yielding **4**, and a major pathway involving oxygen addition to the central carbon to afford 1,2-dioxetane (DOT) intermediate. Usually, DOT derivatives are known to readily decompose [38], and this DOT intermediate is also considered to decompose upon C–C and O–O bond cleavage to give compounds **1** and **5** (Scheme 2).

Owing to the high reactivity of the DAntM radical, cyclic voltammogram (CV) was measured by using the stable DAntM cation, prepared from compound **3** oxidized by antimony(V) chloride, which can be characterized by ^{1}H, ^{13}C NMR, and UV–vis spectroscopy under ambient conditions. The CV of DAntM species showed a reversible wave at $E_{1/2}$ = −0.20 V

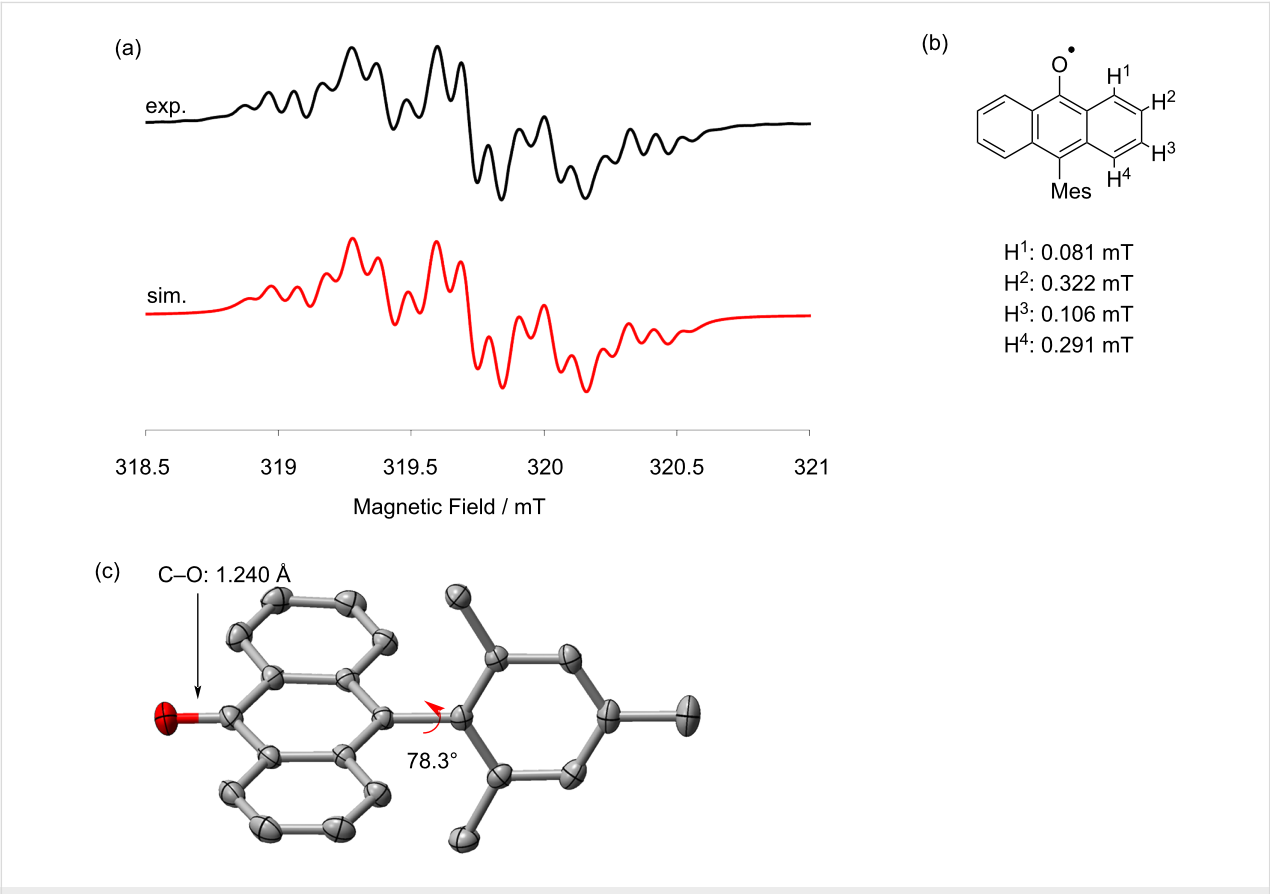

Figure 4: (a) ESR spectrum of anthroxyl radical **5** (black line, Exp.) and its simulated pattern (red line, Sim.). (b) Hyperfine coupling constant of **5**. (c) X-ray structure of **5**. Hydrogen atoms are omitted for clarity.

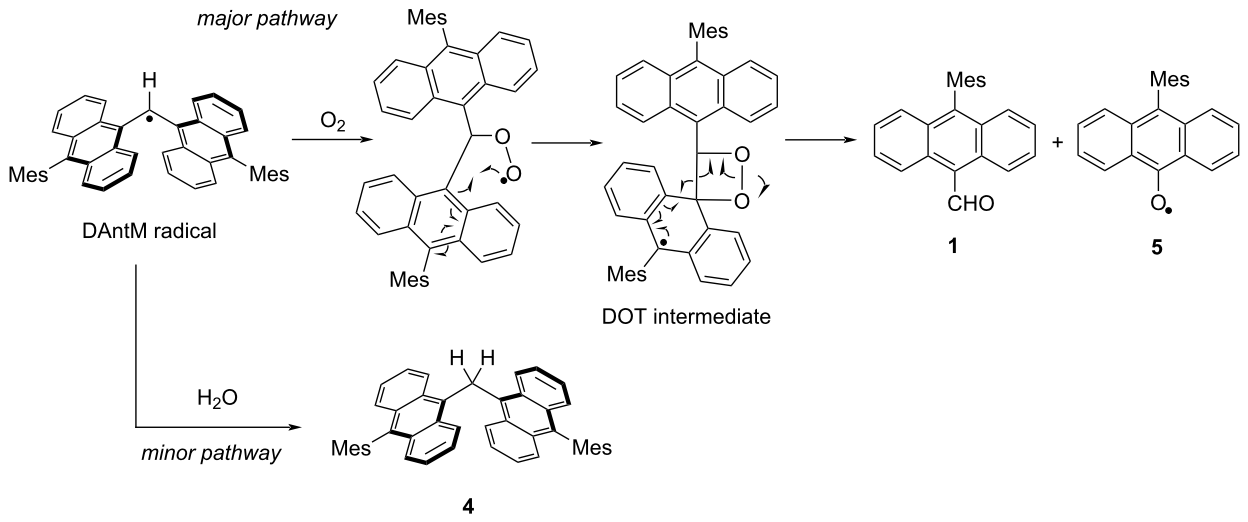

Scheme 2: Decomposition pathway of the DAntM radical under air conditions.

(V vs Fc/Fc^+) (Figure 5a) [39]. This redox potential is close to that of TAntM radical and cation [17]. Additionally, at a scan rate of 0.1 V s^{-1}, the current peak intensity on the anodic side (from radical to cation) was significantly lower than that on the cathodic side (from cation to radical), resulting in an irreversible redox wave. However, by increasing the scan rate, the current peak intensity on the anodic side gradually increased, and the difference in current intensity between the anodic and cathodic sides became smaller, resulting in a reversible redox wave (Figure 5b). This indicates that the generated DAntM radical rapidly decomposes during the CV measurement, leading to the irreversible redox wave at slow scan rate.

The UV–vis spectra of the DAntM radical and cation were shown in Figure 6a and 6b, respectively. The DAntM radical exhibited a forbidden near-IR (NIR) band centered at 900 nm and relatively intense bands at 580 and 540 nm, whose spectral pattern is similar to the spectrum pattern of the TAntM radical [17]. The result of TD-DFT calculations could reproduce the obtained spectrum shape (Supporting Information File 1, Figure S10). On the other hand, the UV–vis spectrum of the DAntM cation, generated from **3** in TFA solution, showed an intense absorption band at 890 nm, which is the opposite trend compared to the DAntM radical.

Conclusion

The synthesis and characterization of the DAntM radical were successfully conducted. Although the DAntM radical exhibits σ-dimerization in solution, it readily dissociates into a monomeric radical due to the presence of two bulky 9-anthryl

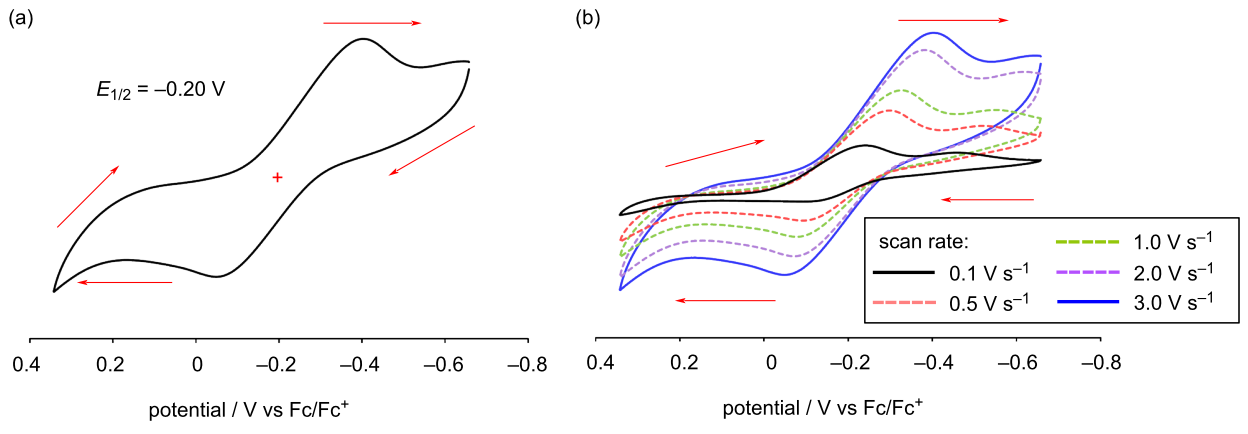

Figure 5: Cyclic voltammogram (CV) of DAntM cation. (a) CV measured with scan rate at 3.0 V s^{-1}. (b) Scan rate dependency (0.1, 0.5, 1.0, 2.0, and 3.0 V s^{-1}) of the redox wave. Measurement conditions: 100 mM *n*-Bu_4NPF_6 and 1 mM DAntM cation in CH_2Cl_2. Red arrows indicate the sweep direction.

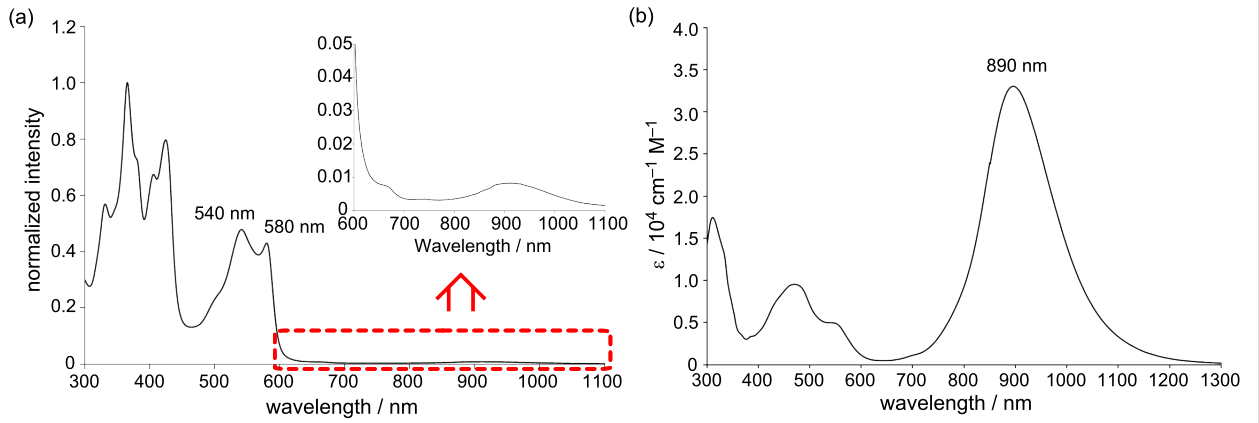

Figure 6: UV–vis–NIR spectra of (a) DAntM radical in toluene, (b) DAntM cation in TFA.

groups. However, the DAntM radical retains a highly reactive nature with oxygen, resulting in the formation of a 1,2-dioxetane (DOT) intermediate and decomposition to aldehyde **1** and anthroxyl radical **5** via C–C and O–O bond cleavage. This reactivity is attributed to the predominant localization of an unpaired electron at the central sp^2 carbon of the DAntM radical. These findings provide variable insights for the molecular design of readily handled aromatic hydrocarbon radicals that possess both stability and reactivity.

Supporting Information

Supporting Information File 1

Synthetic procedure and compound characterization data (^{1}H, ^{13}C NMR, MS, melting point, X-ray crystallography) of new compounds. DFT calculation results and optimized structural Cartesian coordinates.
[https://www.beilstein-journals.org/bjoc/content/supplementary/1860-5397-20-193-S1.pdf]

Supporting Information File 2

Crystallographic information file for compound **5**.
[https://www.beilstein-journals.org/bjoc/content/supplementary/1860-5397-20-193-S2.cif]

Funding

This study was supported by Grant-in-Aid for Scientific Research (C) (JSPS KAKENHI Grant Number JP20K05475, T. N.), Scientific Research (B) (JSPS KAKENHI Grant Number JP24K01454, T. N.), Transformative Research Areas (A) (Grant Number JP20H05865, T. K.), and by research grant from The Murata Science Foundation (T. N.). Quantum chemical calculations were performed at the Research Center for Computational Science, Okazaki, Japan (Project: 23-IMS-C212 and 24-IMS-C214). This work was the result of using research equipment shared in the MEXT Project for promoting public utilization of advanced research infrastructure (Program for supporting construction of core facilities. Grant Number JPMXS0441200024.).

Author Contributions

Tomohiko Nishiuchi: conceptualization; data curation; funding acquisition; investigation; project administration; supervision; visualization; writing – original draft; writing – review & editing. Kazuma Takahashi: formal analysis; investigation. Yuta Makihara: formal analysis; investigation. Takashi Kubo: funding acquisition; writing – review & editing.

ORCID® iDs

Tomohiko Nishiuchi - https://orcid.org/0000-0002-2113-0731
Takashi Kubo - https://orcid.org/0000-0001-6809-7396

Data Availability Statement

All data that supports the findings of this study is available in the published article and/or the supporting information to this article.

Preprint

A non-peer-reviewed version of this article has been previously published as a preprint:
https://chemrxiv.org/engage/chemrxiv/article-details/6659448521291e5d1db5d909

References

1. Braunecker, W. A.; Matyjaszewski, K. *Prog. Polym. Sci.* **2007,** *32,* 93–146. doi:10.1016/j.progpolymsci.2006.11.002
2. Studer, A.; Curran, D. P. *Angew. Chem., Int. Ed.* **2016,** *55,* 58–102. doi:10.1002/anie.201505090
3. Volger, T.; Studer, A. *Synthesis* **2008,** 1979–1993. doi:10.1055/s-2008-1078445

4. Ahmed, J.; P, S.; Vijaykumar, G.; Jose, A.; Raj, M.; Mandal, S. K. *Chem. Sci.* **2017,** *8,* 7798–7806. doi:10.1039/c7sc02661g
5. Hattori, Y.; Kusamoto, T.; Nishihara, H. *Angew. Chem., Int. Ed.* **2014,** *53,* 11845–11848. doi:10.1002/anie.201407362
6. Ai, X.; Evans, E. W.; Dong, S.; Gillett, A. J.; Guo, H.; Chen, Y.; Hele, T. J. H.; Friend, R. H.; Li, F. *Nature* **2018,** *563,* 536–540. doi:10.1038/s41586-018-0695-9
7. Gao, S.; Cui, Z.; Li, F. *Chem. Soc. Rev.* **2023,** *52,* 2875–2885. doi:10.1039/d2cs00772j
8. Arikawa, S.; Shimizu, A.; Shiomi, D.; Sato, K.; Takui, T.; Sotome, H.; Miyasaka, H.; Murai, M.; Yamaguchi, S.; Shintani, R. *Angew. Chem., Int. Ed.* **2023,** *62,* e202302714. doi:10.1002/anie.202302714
9. Haze, O.; Corzilius, B.; Smith, A. A.; Griffin, R. G.; Swager, T. M. *J. Am. Chem. Soc.* **2012,** *134,* 14287–14290. doi:10.1021/ja304918g
10. Ardenkjær-Larsen, J. H.; Laursen, I.; Leunbach, I.; Ehnholm, G.; Wistrand, L.-G.; Petersson, J. S.; Golman, K. *J. Magn. Reson.* **1998,** *133,* 1–12. doi:10.1006/jmre.1998.1438
11. Reddy, T. J.; Iwama, T.; Halpern, H. J.; Rawal, V. H. *J. Org. Chem.* **2002,** *67,* 4635–4639. doi:10.1021/jo011068f
12. Lurie, D. J.; Li, H.; Petryakov, S.; Zweier, J. L. *Magn. Reson. Med.* **2002,** *47,* 181–186. doi:10.1002/mrm.10029
13. Zeng, Z.; Sung, Y. M.; Bao, N.; Tan, D.; Lee, R.; Zafra, J. L.; Lee, B. S.; Ishida, M.; Ding, J.; López Navarrete, J. T.; Li, Y.; Zeng, W.; Kim, D.; Huang, K.-W.; Webster, R. D.; Casado, J.; Wu, J. *J. Am. Chem. Soc.* **2012,** *134,* 14513–14525. doi:10.1021/ja3050579
14. Li, Y.; Huang, K.-W.; Sun, Z.; Webster, R. D.; Zeng, Z.; Zeng, W.; Chi, C.; Furukawa, K.; Wu, J. *Chem. Sci.* **2014,** *5,* 1908–1914. doi:10.1039/c3sc53015a
15. Zeng, W.; Gopalakrishna, T. Y.; Phan, H.; Tanaka, T.; Herng, T. S.; Ding, J.; Osuka, A.; Wu, J. *J. Am. Chem. Soc.* **2018,** *140,* 14054–14058. doi:10.1021/jacs.8b09075
16. Tian, Y.; Uchida, K.; Kurata, H.; Hirao, Y.; Nishiuchi, T.; Kubo, T. *J. Am. Chem. Soc.* **2014,** *136,* 12784–12793. doi:10.1021/ja507005c
17. Nishiuchi, T.; Aibara, S.; Kubo, T. *Angew. Chem., Int. Ed.* **2018,** *57,* 16516–16519. doi:10.1002/anie.201811314
18. Nishiuchi, T.; Ito, R.; Takada, A.; Yasuda, Y.; Nagata, T.; Stratmann, E.; Kubo, T. *Chem. – Asian J.* **2019,** *14,* 1830–1836. doi:10.1002/asia.201801806
19. Nishiuchi, T.; Ito, R.; Stratmann, E.; Kubo, T. *J. Org. Chem.* **2020,** *85,* 179–186. doi:10.1021/acs.joc.9b02432
20. Nishiuchi, T.; Ishii, D.; Aibara, S.; Sato, H.; Kubo, T. *Chem. Commun.* **2022,** *58,* 3306–3309. doi:10.1039/d2cc00548d
21. Nishiuchi, T.; Uchida, K.; Kubo, T. *Chem. Commun.* **2023,** *59,* 7379–7382. doi:10.1039/d3cc02157b
22. Huang, P.; Baldenhofer, R.; Martinho, R. P.; Lefferts, L.; Faria Albanese, J. A. *ACS Catal.* **2023,** *13,* 6590–6602. doi:10.1021/acscatal.3c00276
23. Thaggard, G. C.; Haimerl, J.; Fischer, R. A.; Park, K. C.; Shustova, N. B. *Angew. Chem., Int. Ed.* **2023,** *62,* e202302859. doi:10.1002/anie.202302859
24. Beyer, M. K.; Clausen-Schaumann, H. *Chem. Rev.* **2005,** *105,* 2921–2948. doi:10.1021/cr030697h
25. Caruso, M. M.; Davis, D. A.; Shen, Q.; Odom, S. A.; Sottos, N. R.; White, S. R.; Moore, J. S. *Chem. Rev.* **2009,** *109,* 5755–5798. doi:10.1021/cr9001353
26. Quinkert, G.; Opitz, K.; Wiersdorff, W. W.; Weinlich, J. *Tetrahedron Lett.* **1963,** *4,* 1863–1868. doi:10.1016/s0040-4039(01)90931-1
27. Gould, I. R.; Zimmt, M. B.; Turro, N. J.; Baretz, B. H.; Lehr, G. F. *J. Am. Chem. Soc.* **1985,** *107,* 4607–4612. doi:10.1021/ja00302a001
28. Hirano, T.; Li, W.; Abrams, L.; Krusic, P. J.; Ottaviani, M. F.; Turro, N. J. *J. Am. Chem. Soc.* **1999,** *121,* 7170–7171. doi:10.1021/ja9912628
29. Coppinger, G. M. *J. Am. Chem. Soc.* **1957,** *79,* 501–502. doi:10.1021/ja01559a073
30. Aoki, S.; Tsurumaki, E.; Yamashina, M.; Wakamatsu, K.; Toyota, S. *ChemPlusChem* **2022,** *87,* e202100447. doi:10.1002/cplu.202100447
31. Agranat, I.; Suissa, M. R. *Struct. Chem.* **1993,** *4,* 59–66. doi:10.1007/bf00672100
32. Suzuki, T.; Fukushima, T.; Miyashi, T.; Tsuji, T. *Angew. Chem., Int. Ed. Engl.* **1997,** *36,* 2495–2497. doi:10.1002/anie.199724951
33. Ishigaki, Y.; Hayashi, Y.; Suzuki, T. *J. Am. Chem. Soc.* **2019,** *141,* 18293–18300. doi:10.1021/jacs.9b09646
34. Ishigaki, Y.; Hashimoto, T.; Sugawara, K.; Suzuki, S.; Suzuki, T. *Angew. Chem., Int. Ed.* **2020,** *59,* 6581–6584. doi:10.1002/anie.201916089
35. Nishiuchi, T.; Aibara, S.; Yamakado, T.; Kimura, R.; Saito, S.; Sato, H.; Kubo, T. *Chem. – Eur. J.* **2022,** *28,* e202200286. doi:10.1002/chem.202200286
36. Nishiuchi, T.; Aibara, S.; Sato, H.; Kubo, T. *J. Am. Chem. Soc.* **2022,** *144,* 7479–7488. doi:10.1021/jacs.2c02318
37. Although VT-^{1}H NMR measurements were performed to detect the ^{1}H NMR signals of dimer structure, it was difficult to observe even at 173 K probably due to the equilibrium between monomer and dimer. See Supporting Information File 1, Figure S5.
38. Vacher, M.; Fdez. Galván, I.; Ding, B.-W.; Schramm, S.; Berraud-Pache, R.; Naumov, P.; Ferré, N.; Liu, Y.-J.; Navizet, I.; Roca-Sanjuán, D.; Baader, W. J.; Lindh, R. *Chem. Rev.* **2018,** *118,* 6927–6974. doi:10.1021/acs.chemrev.7b00649
39. Due to the high reactivity, only irreversible redox wave corresponding to DAntM radical and anion at negative potential field was observed. See Supporting Information File 1, Figure S9.

License and Terms

BEILSTEIN JOURNAL OF ORGANIC CHEMISTRY

C–C Coupling in sterically demanding porphyrin environments

Liam Cribbin[1], Brendan Twamley[2], Nicolae Buga[1], John E. O' Brien[2], Raphael Bühler[3], Roland A. Fischer[3] and Mathias O. Senge[*1,4]

Full Research Paper

Open Access

Address:
[1]School of Chemistry, Chair of Organic Chemistry, Trinity Biomedical Sciences Institute, 152-160 Pearse Street, Trinity College Dublin, The University of Dublin, Dublin, D02 R590, Ireland, [2]School of Chemistry, Trinity College Dublin, The University of Dublin, Dublin 2, Ireland, [3]TUM School of Natural Sciences, Technical University of Munich, Lichtenbergstr. 4, 85748 Garching, Germany and [4]Institute for Advanced Study (TUM-IAS), Technical University of Munich, Lichtenberg, Str. 2a, 85748 Garching, Germany

Email:
Mathias O. Senge[*] - sengem@tcd.ie

* Corresponding author

Keywords:
C–C coupling; conformational analysis; nonplanar porphyrin; Pd-catalysis; porphyrin

Beilstein J. Org. Chem. **2024,** *20,* 2784–2798.
https://doi.org/10.3762/bjoc.20.234

Received: 17 August 2024
Accepted: 17 October 2024
Published: 04 November 2024

This article is part of the thematic issue "π-Conjugated molecules and materials".

Guest Editor: A. Mateo-Alonso

Abstract

Unlike their planar counterparts, classic synthetic protocols for C–C bond forming reactions on nonplanar porphyrins are underdeveloped. The development of C–C bond forming reactions on nonplanar porphyrins is critical in advancing this field of study for more complex porphyrin architectures, which could be used in supramolecular assemblies, catalysis, or sensing. In this work a library of arm-extended dodecasubstituted porphyrins was synthesized through the optimization of the classic Suzuki–Miyaura coupling of peripheral haloaryl substituents with a range of boronic acids. We report on palladium-catalyzed coupling attempts on the *ortho*-, *meta*-, and *para*-meso-phenyl position of sterically demanding dodecasubstituted saddle-shaped porphyrins. While *para*- and *meta*-substitutions could be achieved, *ortho*-functionalization in these systems remains elusive. Furthermore, borylation of a dodecasubstituted porphyrin's meso-phenyl position was explored and a subsequent C–C coupling showed the polarity of the reaction can be reversed resulting in higher yields. X-ray analysis of the target compounds revealed the formation of supramolecular assemblies, capable of accommodating substrates in their void.

Introduction

Porphyrins are tetrapyrrolic macrocycles that perform essential processes in nature, such as oxygen transport in hemoglobin and photosynthesis [1]. Porphyrins are often described as planar 18π aromatic macrocycles; however, molecular structure analysis frequently reveals nonplanar ring distortion [2,3]. In fact, porphyrins with nonplanar ring distortions are vital for many natural processes to occur, e.g., nonplanarity can alter oxygen affinity of the metal iron core [4,5]. Nonplanar porphyrins offer a marked difference in chemical and physical properties when compared to their planar compatriots [6], with relatively smaller

HOMO–LUMO gaps resulting in an observed bathochromic shift in the UV–vis absorption spectrum [7]. The phenomenon of nonplanarity results from the porphyrin ring deforming from the mean porphyrin plane either by steric repulsion in the core of the macrocycle or by bulky substituents at the porphyrin periphery [3]. This affords four principle distortion modes, saddle, dome, ruffle or wave [8], which can be quantified by the normal-coordinate structural decomposition (NSD) method developed by Shelnutt and co-workers [9] and further implemented and visualized by us [8,10]. Of the four main quantifiable distortion modes, saddle-shaped porphyrins can be afforded by *peri*-interactions between β-substituents and the meso-substituents [3,11], or alternatively by core protonation, whereby all four-core nitrogen atoms are protonated to produce the diacid [12,13]; these diacids can tilt the pyrrole rings 20–40° [14] from the mean-porphyrin plane. Norvaiša et al. showed that a saddle-shaped porphyrin as a dodecasubstituted diacid can bind anions via two independent faces and trap anions such as pyrophosphate [15]. Saddle-shaped porphyrins have also been exploited by researchers for the use in organocatalysis as bifunctional system [16,17]. Dodecasubstitution of porphyrin, as seen in Figure 1, often results in saddle-shaped distortion; however, ruffled [18] and almost planar [19] dodecasubstituted porphyrins have been reported.

Despite the increasing interest in the chemical and physical properties of nonplanar porphyrins only limited synthetic methods are available for the functionalization of these macrocycles [6]. An attractive approach to accomplish further substitution directly on the meso- or a meso-phenyl *ortho/meta/para* positions of a porphyrin, is the introduction of C–C bond forming chemistry. This is typically achieved using palladium and/or another transition-metal catalyst [20]. Sonagashira [21], Suzuki–Miyaura [22], Heck [23], Stille [24,25], Negishi [26], and Kumada [27] coupling reactions, as well as modern iridium and rhodium-based coupling techniques [28], are just some examples of the C–C bond formations that have been implemented to achieve complex substitution patterns and functional arrangements on porphyrins.

Of these named coupling reactions, Suzuki–Miyaura couplings are known to be a robust tool when functionalizing porphyrins [29,30]. Many complex porphyrinoid architectures have been synthesized in this manner, from functional porphyrin arrays

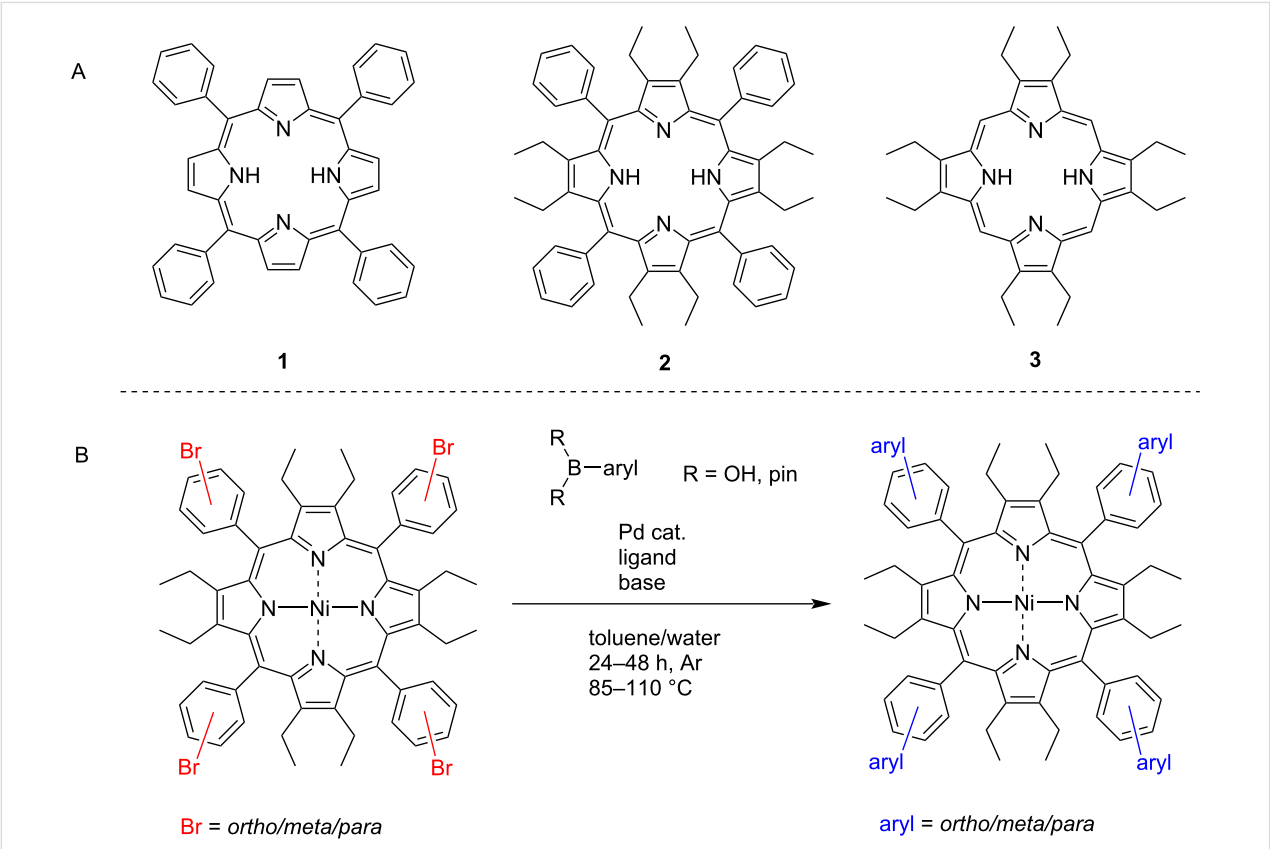

Figure 1: (A) Structures of tetrasubstituted 5,10,15,20-tetraphenylporphyrin (TPP, **1**), dodecasubstituted 2,3,7,8,12,13,17,18-octaethyl-5,10,15,20-tetraphenylporphyrin (OETPP, **2**), and octasubstituted 2,3,7,8,12,13,17,18-octaethylporphyrin (OEP, **3**). (B) Aim of this work, the arm extension of the meso-phenyl position of dodecasubstituted porphyrins.

[31-33] to sterically challenging meso-substituted aryl bis-pocket porphyrins [34] and tetrabromoanthracenyl porphyrins [35]. In general, the halogen atom needed for the Suzuki coupling reaction resides on the porphyrin; however, Suzuki–Miyaura reactivity has also been shown to be reversed whereby the synthesis of borolanylporphyrins leads to a different approach to reactivity [36]. Borolanylporphyrins can be synthesized by Miyaura-borylation of the halogenated porphyrin [24,37]. There are also reported instances of borolanylporphyrins being synthesized under condensation conditions [36,38]. Despite the many synthetic advancements for the decoration of porphyrins, many of these strategies are utilized only with planar porphyrins. Apart from the arylation of the β-position of 2,3,5,7,8,10,12,13,15,17,18,20-dodecaarylporphyrins, developed by Smith and co-workers [39] few reports on synthetic techniques for dodecasubstituted nonplanar porphyrins can be found in literature. In light of the promise of appropriately designed nonplanar porphyrins as receptors and catalysts we report here on our efforts to use the Suzuki–Miyaura reaction for the modification of the *o,m,p*-phenyl positions in 5,10,15,20-tetraryl-2,3,7,8,12,13,17,18-octaethylporphyrins.

Results and Discussion

Investigation of the Suzuki coupling reaction at the meso-phenyl position of dodecasubstituted porphyrins

Synthesis of porphyrin precursors

To investigate the Suzuki coupling at the *ortho*-, *meta*- and *para*-position of a dodecasubstituted saddle-shaped porphyrin, first the precursor porphyrins **11**, **12**, and **13** had to be synthesized (Scheme 1). The synthetic route to achieve OET-xBrPPs (2,3,7,8,12,13,17,18-octaethyl-5,10,15,20-tetra(x-bromo)phenylporphyrin, where x = *ortho/meta/para*) pyrrole **7** was synthesized through literature procedures [40,41]. Pyrrole **7** was then subjected to condensation with aldehydes **8**, **9**, and **10** under Lindsey conditions [42] utilizing $BF_3{\cdot}OEt_2$ and DDQ [43] to achieve porphyrins **4**, **5**, and **6**, which were not isolated and instead reacted immediately.

Ni(II)porphyrins **11**, **12**, and **13** were prepared by reacting porphyrins **4**, **5**, and **6** in toluene for 18 hours using Ni(II)(acac)$_2$ under an inert atmosphere [43] attaining a 18%, 28%, and 29% yield for porphyrins **11**, **12**, and **13**, respectively, over two steps. Porphyrins **6** and **13** had previously been described in literature [43].

Coupling at the meso-*para*-phenyl position

The exploration of aryl substitution of OET-xBrPPs using the Suzuki coupling began with investigating first the Suzuki reaction compatibility of boronic acid **14** with porphyrin **13**. Porphyrin **13** and phenylboronic acid (**14**) were subjected to coupling at 85 °C for 48 hours using Pd_2dba_3/SPhos as a catalyst/ligand giving porphyrin **26** in a 32% yield, based on a literature procedure [35]. With initial success in the synthesis porphyrin **26**, this Suzuki coupling reaction was performed on **13**, for a range of boronic acids/esters as shown in Figure 2 and Scheme 2. Boronic acids/esters were chosen based on their electronic properties (activating/deactivating) as well as their steric bulk (e.g., 9-anthracenylboronic acid (**15**)). Table 1 lists all attempts at the meso-*para*-phenyl position.

When attempting the synthesis of tetra(*p*-phenylanthracene)porphyrin (**27**) the conditions used before (Table 1, entry 1)

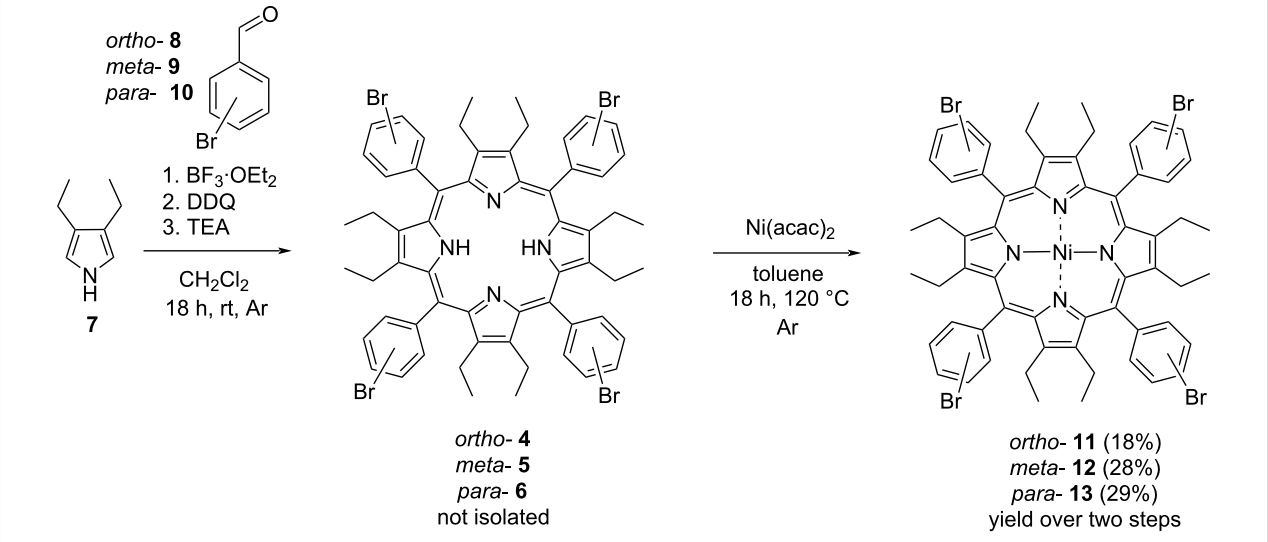

Scheme 1: Reaction scheme for the synthesis of OET-xBrPPs and subsequent Ni(II) metalation.

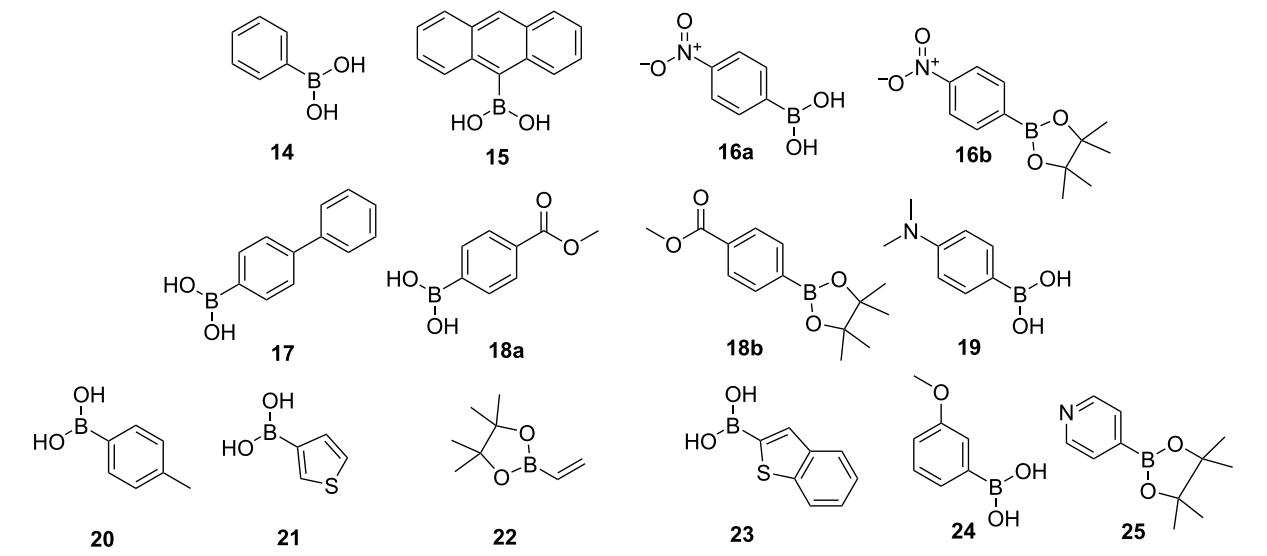

Figure 2: Substrates used for the investigations for the Suzuki–Miyaura coupling reactions.

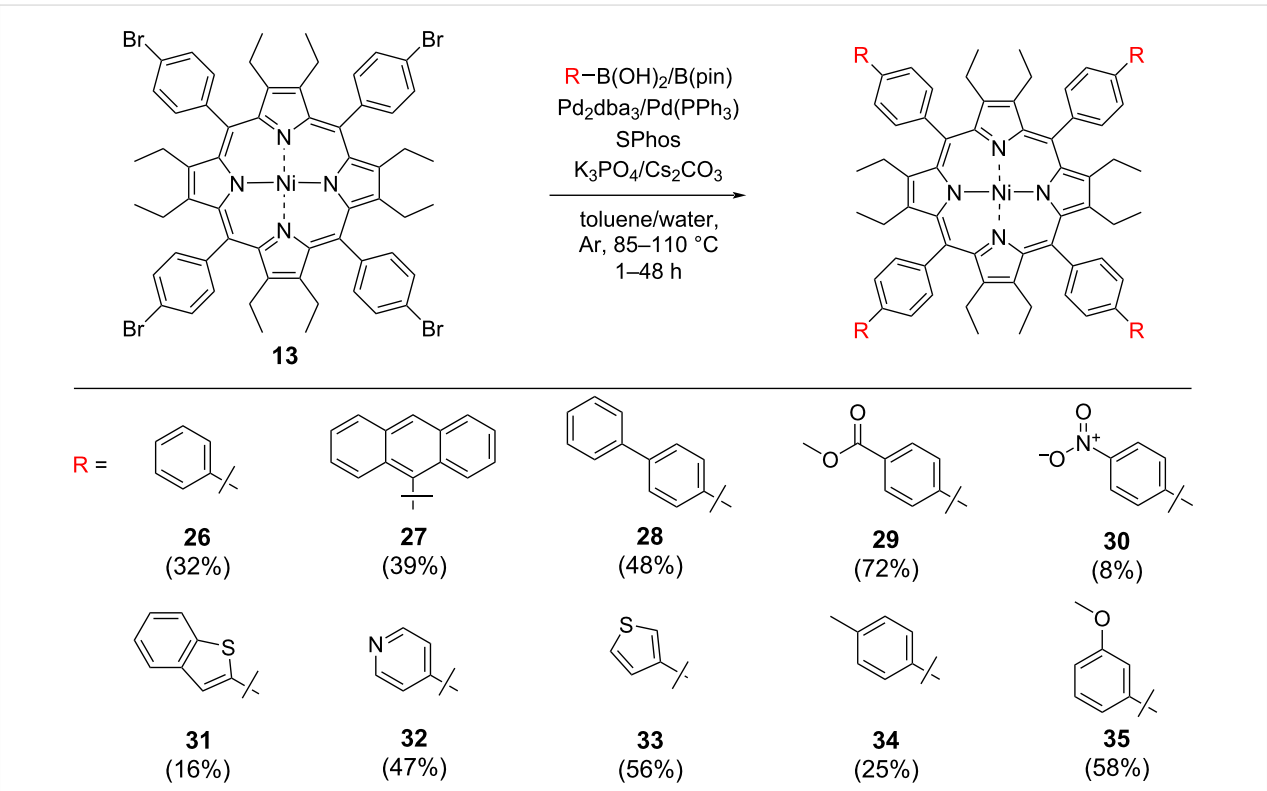

Scheme 2: Scope of arm-extended dodecasubstituted porphyrins synthesized via modification of the meso-*para*-phenyl position of porphyrin **13**.

resulted only in trace amounts of porphyrin **27** (Table 1, entry 2).

The reaction temperature was increased to 110 °C, affording the desired porphyrin **27** in a 39% yield (Table 1, entry 3). A temperature of 110 °C was also used for the synthesis of terphenylporphyrin **28** using boronic acid **17**, affording terphenylporphyrin **28** in 48% yield (Table 1, entry 7).

Boronic acids with heteroatoms and activating/deactivating electronic properties were investigated next. Attempts to introduce electron-withdrawing groups at the *para*-position with

Table 1: Optimization table for the Suzuki–Miyaura coupling reactions with porphyrin **13**.

Entry	Catalyst/ligand SPhos (1 equiv)	Cat. mol % per C–Br	Base (24 equiv)	Temperature	Time	Boronic acid/ester (3 equiv per C–Br)	Yield % (porphyrin)
1	Pd_2dba_3/Sphos	6.25%	K_3PO_4	85 °C	48 h	**14**	32% (**26**)
2	Pd_2dba_3/Sphos	6.25%	K_3PO_4	85 °C	48 h	**15**	trace
3	Pd_2dba_3/SPhos	6.25%	K_3PO_4	110 °C	48 h	**15**	39% (**27**)
4	Pd_2dba_3/Sphos	6.25%	K_3PO_4	85 °C	48 h	**16a**	0
5	Pd_2dba_3/Sphos	6.25%	Cs_2CO_3	85 °C	48 h	**16a**	0
6	Pd_2dba_3/SPhos	6.25%	Cs_2CO_3	85 °C	48 h	**16b**	8% (**30**)
7	Pd_2dba_3/SPhos	6.25%	K_3PO_4	110 °C	48 h	**17**	48% (**28**)
8	Pd_2dba_3/SPhos	12.5%	K_3PO_4	110 °C	48 h	**18a**	0
9	Pd_2dba_3/SPhos	6.25%	Cs_2CO_3	85 °C	48 h	**18b**	72% (**29**)
10	Pd_2dba_3/Sphos	6.25%	K_3PO_4	85 °C	48 h	**19**	0
11	Pd_2dba_3/SPhos	6.25%	K_3PO_4	110 °C	48 h	**19**[a]	trace
12	Pd_2dba_3/SPhos	12.5%	K_3PO_4	110 °C	24 h	**20**	25% (**34**)
13	Pd_2dba_3/SPhos	6.25%	Cs_2CO_3	110 °C	24 h	**21**	56% (**33**)
14	Pd_2dba_3/SPhos	6.25%	K_3PO_4	110 °C	48 h	**23**	trace
15	Pd_2dba_3/SPhos	6.25%	Cs_2CO_3	85 °C	48 h	**23**	trace
16	$Pd(PPh_3)_4$	10%	Na_2CO_3	100 °C	1 h	**23**[b]	0
17	Pd_2dba_3/SPhos	6.25%	Cs_2CO_3	85 °C	24 h	**23**	trace
18	Pd_2dba_3/SPhos	6.25%	Cs_2CO_3	110 °C	24 h	**23**	trace
19	Pd_2dba_3/SPhos	25%	Cs_2CO_3	110 °C	24 h	**23**	16% (**31**)
20	Pd_2dba_3/SPhos	12.5%	Cs_2CO_3	110 °C	24 h	**24**	58% (**35**)
21	Pd_2dba_3/SPhos	6.25%	Cs_2CO_3	85 °C	24 h	**25**	47% (**32**)

[a]5 equiv of boronic acid used in this reaction per C–Br. [b]Microwave irradiation instead of conventional heating was used.

substrate boronic acid **16a** (Table 1, entries 4 and 5) yielded no tetracoupled product. Similarly, coupling with **18a** resulted in most of the starting material porphyrin **13** being left unreacted. On switching the substrate from boronic acid to the boronic acid ester and opting for the weaker base Cs_2CO_3 instead of K_3PO_4, a significant difference in reactivity was observed with a 72% yield accomplished in the synthesis of porphyrin **29** (Table 1, entry 9), bearing a methoxycarbonyl electron-withdrawing group utilizing boronic acid pinacol ester **18b**. Following on from these results porphyrin **30** was synthesized in an 8% yield, when switching to weaker base Cs_2CO_3 using pinacol ester **16b** (Table 1, entry 6). Switching the base to a weaker one, may have slowed down the protodeboronation process, as substrates with electron-withdrawing groups are postulated to increase the Lewis acidity of the boronic acid, which may allow an increased incidence of protodeboronation to occur. It is also known that aryl–B(Pin) complexes have a greater stability than boronic acids and other employed esters as the four methyl groups protect the boron center from attack of water [44,45], preventing protodeboronation from the hydrolysis route. However, protodeboronation can be complex when it comes to pK_a considerations, for example, 3,5-dinitrophenylboronic acid has a marginally lower pK_a than pentafluorophenyl boronic acid [46]; however, it undergoes protodeboronation, several orders of magnitude slower [47].

The synthesis of porphyrin **31** with a benzothiophene moiety, proved challenging (Table 1, entries 14–19). Use of a microwave-assisted procedure [48], switching catalyst to $Pd(PPh)_3$, and base to Na_2CO_3 (Table 1, entry 16) gave no product.

Ultimately, an increased catalyst loading of 25 mol % per C–Br bond gave the desired porphyrin in a 16% yield when using Cs_2CO_3 as base. The synthesis of other heterocycle-appended dodecasubstituted porphyrins, achieved porphyrins **32** and **33** in a 47% and 56% yield, respectively (Table 1, entries 13 and 21), using Cs_2CO_3 as the base. Electron-withdrawing sulfur-containing heterocyclic substrates **21** and **23** do not readily undergo protodeboronation even at high pH [44,47] making the yields of porphyrins **31** and **33** higher than expected considering the electronic similarities between substrates 4-nitrophenylboronic acid and 3-thiaphenylboronic acid (**16a** and **21**) and the yields obtained when coupling. The weakly electron-withdrawing boronic acid **24** when coupled with porphyrin **13**, resulted in porphyrin **35** in a 58% yield (Table 1, entry 20). Reactivity with the electron-donating 4-methylphenylboronic acid (**34**) was

established using K_3PO_4 at 110 °C (Table 1, entry 12). No product was obtained in the coupling of electron-donating (4-(dimethylamino)phenyl)boronic acid (**19**), even upon increasing the number of equivalents of boronic acid (Table 1, entries 10 and 11).

Coupling at the meso-*meta*-phenyl position

Optimization of conditions for OET-*meta*-BrPPs **12** (Scheme 3) were investigated next. Table 2 summarizes the reaction conditions used to synthesize a library of OET-*meta*-arylPPs as shown in Scheme 3. As a starting point initial conditions used in the synthesis for porphyrin **26** were used (Table 1, entry 1). This gave biphenylporphyrin **36** in a 16% yield (Table 2, entry 1). The lower yield is expected due to the increased steric demand at the *meta*-positions. Coupling of sterically bulky 9-anthracenylboronic acid (**15**) and porphyrin **12** gave no conversion when the base was switched from K_3PO_4 to Cs_2CO_3 (Table 2, entry 2). K_3PO_4 was reimplemented in the reaction and trace reactivity was observed by TLC (Table 2, entry 3). Next, the catalyst loading was increased to 12.5 mol % (Table 2, entry 4). Formation of palladium black was observed but product formation was also indicated by TLC and ^{1}H NMR. For a final attempt at establishing reactivity with boronic acid **15** the temperature was increased to 110 °C and gave the desired anthracenylporphyrin **37** in a 32% yield. In the case of boronic acids with larger π-systems, e.g., **15**, K_3PO_4 was required to achieve the tetra-coupled product. This trend is consistent in reactivity observed with porphyrins **12** and **13.** Similarly, no terphenyl product was formed in the coupling reaction between **12** and **17** (Table 2, entry 6) when using Cs_2CO_3. Similar to the reactivity observed with 9-anthracenylboronic acid (**15**), no conversion to the desired product was established. Increasing the temperature and catalyst loading (Table 2, entry 5) gave the terphenylporphyrin **38** in a 7% yield (Table 2, entry 7).

The use of Cs_2CO_3 is still required for boronic acids bearing electron-withdrawing functionalities at the *meta*-phenyl position (Table 2, entries 9 and 10). However, an increase in catalyst loading to 12.5% was required per C–Br bond when coupling at the meso-*meta*-phenyl position in **12** compared to the corresponding *para*- position in **13** (Table 2**,** entry 8). Porphyrins **39** and initially **40** were synthesized in a 23% and 4% yield, respectively. This is significantly lower than for the corresponding *para*-products. Porphyrin **45** was synthesized in a 31% yield (Table 2, entry 15), with a 3-methoxy electron-withdrawing group, again a lower yield compared to the *para*-analogue porphyrin **35**. Use of the electron-donating *p*-tolylboronic acid (**20**), resulted in a 30% yield (Table 2, entry 12) again requiring

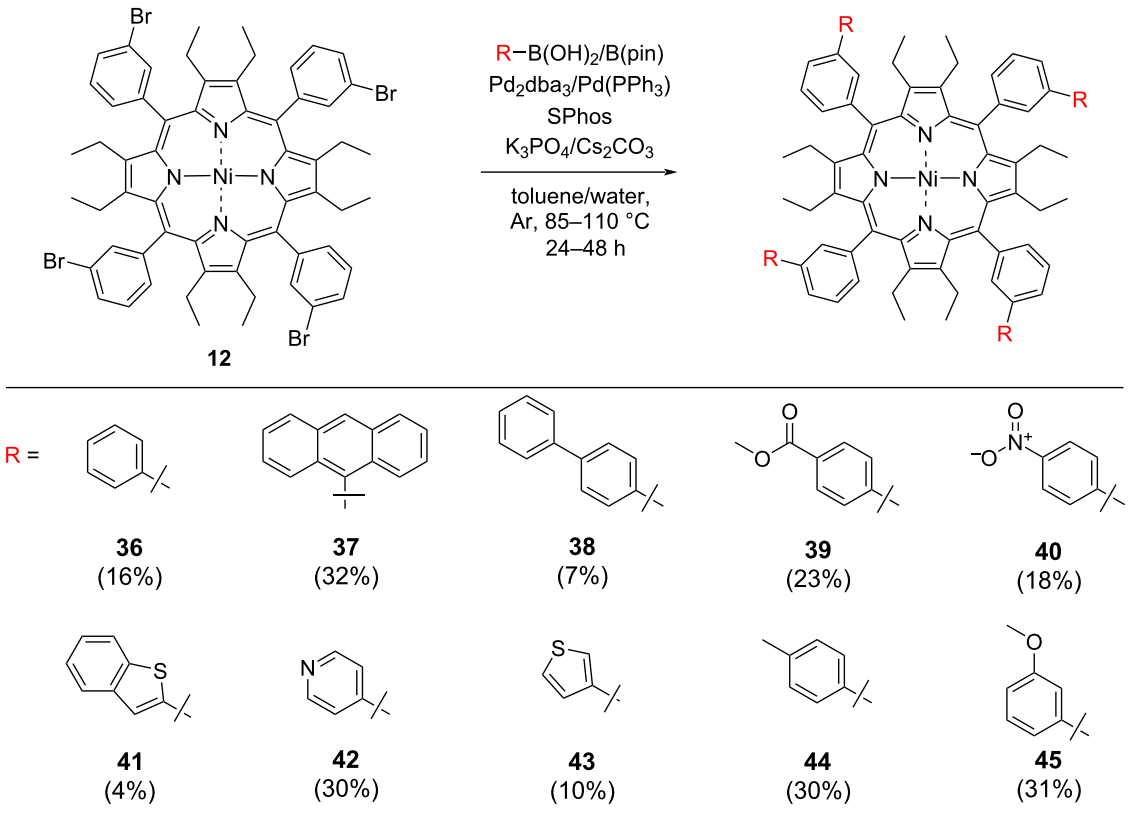

Scheme 3: Scope of arm-extended dodecasubstituted porphyrins synthesized via reaction at the meso-*meta*-phenyl position of porphyrin **12**.

Table 2: Optimization table for the Suzuki-coupling reaction on porphyrin **12**.

Entry	Catalyst/ligand SPhos (1 equiv)	Cat. mol % per C–Br	Base (24 equiv)	Temp.	Time	Boronic acid/ester (3 equiv per C–Br)	Yield % (porphyrin)
1	Pd_2dba_3/SPhos	6.25%	K_3PO_4	85 °C	48 h	**14**	16% (**36**)
2	Pd_2dba_3/SPhos	6.25%	Cs_2CO_3	85 °C	48 h	**15**	0
3	Pd_2dba_3/SPhos	6.25%	K_3PO_4	85 °C	48 h	**15**	trace
4	Pd_2dba_3/SPhos	12.5%	K_3PO_4	85 °C	48 h	**15**	trace
5	Pd_2dba_3/SPhos	12.5%	K_3PO_4	110 °C	48 h	**15**	32% (**37**)
6	Pd_2dba_3/SPhos	6.25%	Cs_2CO_3	85 °C	48 h	**17**	0
7	Pd_2dba_3/SPhos	12.5%	K_3PO_4	110 °C	24 h	**17**	7% (**38**)
8	Pd_2dba_3/SPhos	6.25%	Cs_2CO_3	85 °C	48 h	**18b**	0
9	Pd_2dba_3/SPhos	12.5%	Cs_2CO_3	85 °C	48 h	**18b**	23% (**39**)
10	Pd_2dba_3/SPhos	12.5%	Cs_2CO_3	85 °C	24 h	**16b**	4% (**40**)
11	Pd_2dba_3/SPhos	6.25%	Cs_2CO_3	85 °C	48 h	**20**	0
12	Pd_2dba_3/SPhos	12.5%	K_3PO_4	110 °C	24 h	**20**	30% (**44**)
13	Pd_2dba_3/SPhos	12.5%	Cs_2CO_3	110 °C	24 h	**21**	10% (**43**)
14	Pd_2dba_3/SPhos	25%	Cs_2CO_3	110 °C	24 h	**23**	4% (**41**)
15	Pd_2dba_3/SPhos	12.5%	Cs_2CO_3	110 °C	24 h	**24**	31% (**45**)
16	Pd_2dba_3/SPhos	12.5%	Cs_2CO_3	110 °C	24 h	**25**	30% (**42**)
17	Pd_2dba_3/SPhos	12.5%	NaOAc	110 °C	24 h	**16a**	18% (**40**)

an increase of catalyst loading and a change of base to K_3PO_4. Heterocyclic boronic acids/esters were again investigated for coupling reactivity with a consistent trend of lower yields experienced for porphyrins **41**, **42**, and **43** of 4%, 30%, and 10%, respectively. Overall, a general trend of decreased yield moving from the *para*- to *meta*-position was observed, also a general increased catalyst concentration was needed for reactivity to occur at the *meta*-position.

Lastly, decreasing the basicity of the solution further by switching to sodium acetate as a basic source increased the yield of porphyrin **40** from 4% with Cs_2CO_3 to 18% using sodium acetate (Table 2, entry 17). This indicates that a further decrease in basicity may improve yields.

Coupling at the meso-*ortho*-phenyl position

Unlike the success achieved in the synthesis of OET-*meta/para*-arylPPs, the *ortho*-position on the meso-phenyl proved much more intractable (Scheme 4). Table 3 provides a summary of the attempts made to achieve Suzuki-coupling reactivity in OET-*ortho*-BrPPs.

Increasing the reaction temperature compared to the 85 °C used in the synthesis of the *para*-equivalent **26** gave no conversion and was accompanied by the formation of palladium black [49]. No reactivity was observed by either TLC or mass spectrometry when switching back to $Pd_2(dba)_3$ with three different ligands SPhos, XantPhos, and *Rac*-Binap (Table 3, entries 3–5). Increasing the time of reaction, catalyst loading, and equiva-

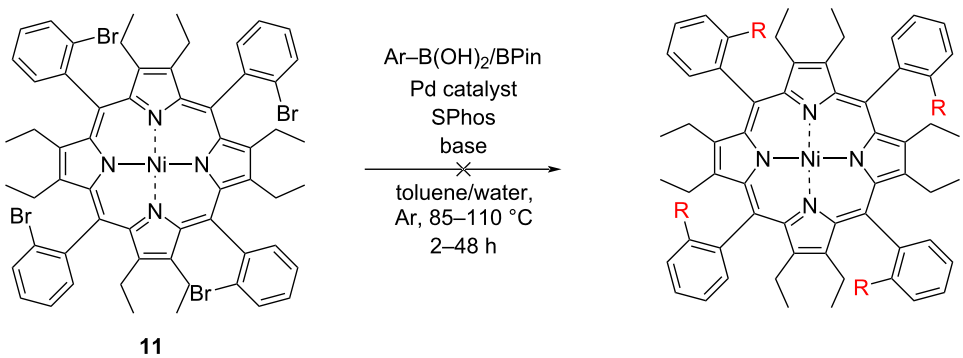

Scheme 4: Attempts of arm-extension of dodecasubstituted porphyrins at the meso-*ortho*-phenyl position.

Table 3: Optimization table for the Suzuki-coupling reaction on porphyrin **11**.

Entry	Catalyst/ligand	Cat. mol % per C–Br	Base (24 equiv)	Temp. (ºC)	Time	Boronic acid/ester (3 equiv per C–Br)	Product detected by HRMS
1	Pd_2dba_3/SPhos	6.25%	K_3PO_4	110 °C	48 h	**14**	no
2	Pd_2dba_3/SPhos	6.25%	K_3PO_4	130 ºC	48 h	**14**	no
3	Pd_2dba_3/SPhos	12.5%	Cs_2CO_3	110 °C	48 h	**14**	no
4	Pd_2dba_3/Xantphos	12.5%	Cs_2CO_3	110 °C	48 h	**14**	no
5	Pd_2dba_3/Rac BINAP	12.5%	Cs_2CO_3	110 °C	48 h	**14**	no
6	Pd_2dba_3/SPhos	100%	Cs_2CO_3	85 °C	7 days	**14**[a]	no
7	Pd(dppf)Cl_2	2%	Cs_2CO_3	100 °C	20 h	**20**[b]	no
8	$Pd(PPh_3)_4$	5%	Cs_2CO_3	100 °C	20 h	**20**[b]	no
9	$Pd(PPh_3)_4$	12.5%	Na_2CO_3	120 °C	2 h	**21**[c]	no
10	$Pd(PPh_3)_4$	12.5%	Cs_2CO_3	100 °C	48 h	**21**	no
11	Pd_2dba_3/SPhos	12.5%	Cs_2CO_3	85 °C	48 h	**22**	no
12	Pd_2dba_3/SPhos	6.25%	Cs_2CO_3	85 °C	24 h	**25**	no

[a]12 equiv of boronic acid used in this reaction per C–Br. [b]Alternative procedure for Suzuki–Miyaura coupling [34]. [c]Microwave irradiation instead of conventional heating was used [48].

lents of boronic acid significantly also resulted in no product formation (Table 3, entry 6).

Next, a change in the catalyst was investigated, based on a literature procedure which was developed by Johnstone and co-workers for the synthesis of meso-substituted aryl bis-pocket porphyrins [34]. Therein catalysts Pd(dppf)Cl_2 and $Pd(PPh_3)_3$ were identified to be the most effective for accomplishing the Suzuki–Miyaura coupling at the *ortho*-position of the meso-phenyl position in sterically hindered planar porphyrins (Table 3, entries 7 and 8). The same success could not be replicated for OET-*o*-BrPPs with no reactivity being observed by TLC or by mass spectrometry. Likewise, a microwave-assisted coupling [48], resulted in no product formation (Table 3, entry 9). Thiophene-3-ylboronic acid (**21**) was also chosen for this reaction due to the smaller size compared to the phenyl- and *p*-tolylboronic acids **14** and **20**. Using **21** as the starting material and the procedure by Droege et al. [34] it was anticipated the less steric substrate size would possibly allow conversion to occur; however, no product formation was observed (Table 3, entries 9 and 10). 4-Pyridylboronic acid pinacol ester (**25**) was also attempted; however, no product was formed. Vinylboronic acid ester **22**, was also explored as a substrate, with multiple porphyrin products being observed by TLC and by ^{1}H NMR. Desymmetrization of the porphyrin was also observed with the β-ethyl CH_3 resonances splitting into two separate chemical environments; however, the identity of the product synthesized was not fully characterized. In future, if reactivity for OET-*o*-BrPPs were to be further explored a larger library of ligands whether biphenyl-based or other could be explored, or further changes in the pH of the solution. Enrichment to the αβαβ-atropisomer may also be favorable [50], as to alleviate the steric hindrance caused by the short distances (4.3–4.4 Å) between bromines in the $\alpha_2\beta_2$-atropisomers (cf., Figure 5).

Borylation and further coupling of dodecasubstituted porphyrins

A Miyaura borylation was performed on porphyrin **13**, using bis(pinacolato)diboron (B_2Pin_2), adapting a procedure from the literature [51]. This procedure was further optimized (Table 4) by utilizing conditions in the synthesis of **29** (Table 1, entry 9). Next, a reversed polarity Suzuki reaction was performed on the

Table 4: Optimization of the borylation of porphyrin **13** to yield **46**.

Entry	Catalyst mol % per C–Br bond	Catalyst	Equiv of B_2Pin_2 per C–Br bond	Temp.	Time	Product
1	20%	Pd(dppf)Cl_2	1	80 °C	48 h	0
2	20%	Pd(dppf)Cl_2	10	80 °C	48 h	0
3	20%	Pd(dppf)Cl_2	10	80 °C	48 h	trace
4	40%	Pd(dppf)Cl_2	20	100 °C	48 h	30%

borolanyl porphyrin **46** (Scheme 5). This reaction yielded porphyrin **26** in a 53% yield and tetrapyrenylporphyrin **47** in a 36% yield, respectively. Compared to the synthesis of **26** by Suzuki coupling of *para*-bromo-phenylporphyrin **13** a significant increase in yield was observed. Furthermore, pyrene was installed on the *para*-phenyl position, showing large aromatic systems can also be installed through this route. Failure of the similar anthracenylboronic acid **15** to react in the presence of Cs_2CO_3 at 85 °C (Table 2, entry 2) shows reversing the polarity of the reaction can induce reactivity, where not previously possible.

X-ray crystal structure analysis

Despite the many examples in literature of the crystal structure and packing of nonplanar porphyrins [3,6,8,13,52,53], few examples of crystal structure and packing analysis exist for arm-extended porphyrins. One of the few examples are azide-porphyrin derivatives reported by Flanagan et al. [43]. Here, five crystal structures were obtained of meso-*para*-phenyl arm-extended porphyrins (**26**, **27**, **28**, **29**, **33**) and two crystal structures for meso-*meta*-phenyl derivatives **36** and **37**. In addition, single crystal structures of **11** and **46** were determined. All structures were investigated using the NSD method [8,9], which allows a quantification and visualization of distortion modes.

It can be observed from the crystal structures that the porphyrins' rings all exhibit the typical saddle-shaped conformation. Interestingly, substitution at the *para*- or *meta*-position can also induce partial ruffling of the porphyrin core (Table 5). Of all *para*-functionalized structures, porphyrin **33** bears the most similarity to that of compound **26**, with minimal ruffling observed and the overall magnitudes of out-of-plane and in-plane distortions are comparable.

With compound **26**, no ruffling of the porphyrin ring is observed; however, with anthracene residues (**27**) a ruffling distortion of almost 1 Å is observed. This is not obvious at first, but differences in molecular symmetry [55] can be easily visualized using the neoplastic NSD plot [10] shown in Figure 3. Furthermore, the mean pyrrole ring tilt increases by 3–5° in the case of compounds **28** and **29** compared to that of compound **26**. Saddle-shape distortion is reduced compared to that of biphenyl **26**; this may be due to the proximity of the anthracene moiety to the β-ethyl positions, with C_{23}–C_{14B} within 3.63 Å

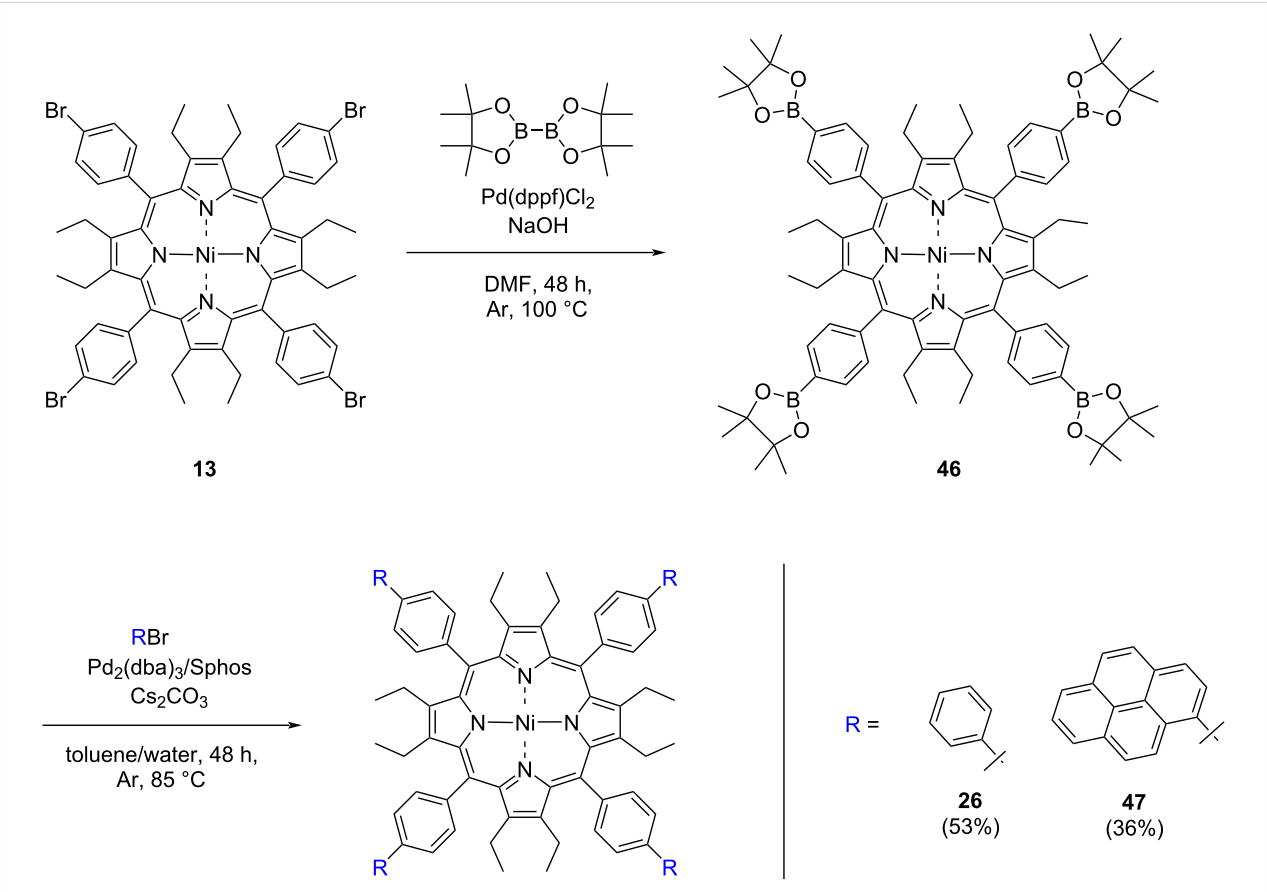

Scheme 5: Borylation and subsequent Suzuki–Miyaura coupling of porphyrin **13**.

Table 5: Mean geometrical parameters of OET-*meta*/*para*-ArylPP and out-of-plane and in-plane distortion magnitudes.

Compound	**26**	**27**	**28**	**29**	**33**	**36**	**37**	Units
pyrrole tilt	28.0	28.4	31.2	32.9	29.0	29.0	31.1	º
N–N dist. (adj)	2.70	2.71	2.71	2.72	2.73	2.71	2.71	Å
N–N dist. (opp)	3.77	3.80	3.80	3.81	3.83	3.78	3.79	Å
ΔC_{meso}[a]	0.03	0.32	0.13	0.15	0.03	0.22	0.22	Å
ΔC_{alpha}[b]	0.5	0.47	0.51	0.53	0.5	0.5	0.5	Å
ΔC_{beta}[c]	1.21	1.13	1.28	1.32	1.21	1.21	1.26	Å
Δip[d]	1.06	1.03	1.22	1.28	1.09	1.14	1.24	Å
B_{1g}	0.07	0.05	0.02	0.00	0.06	0.12	0.04	Å
$E_u(x)$	0.08	0.00	0.07	0.00	0.05	0.00	0.05	Å
A_{1g}	1.06	0.99	1.21	1.27	1.08	1.11	1.21	Å
A_{2g}	0.00	0.27	0.11	0.17	0.04	0.21	0.22	Å
Δoop[e]	3.73	3.58	3.93	4.06	3.72	3.78	3.91	Å
B_{2U} (sad)	3.73	3.46	3.91	4.04	3.72	3.72	3.86	Å
B_{1u} (ruf)	0.00	0.92	0.35	0.45	0.1	0.66	0.61	Å
A_{2U} (dom)	0.11	0.06	0.01	0.00	0.04	0.14	0.04	Å

[a]Average displacement of meso-carbon atoms from the *xy* plane, (C5, C10, C15, and C20) relative to the 24-atom mean porphyrin plane (mean plane defined as $\Delta z = 0$). [b]Average displacement of α-carbon atoms from the *xy* plane (C1, C4, C6, C9, C11, C14, C16, C19) relative to the 24-atom mean porphyrin plane ($\Delta z = 0$). [c]Average displacement of β-carbon atoms from the *xy* plane (C2, C3, C7, C8, C12, C13, C17, C18) relative to the mean porphyrin plane ($\Delta z = 0$). [d]Average deviation of the 24-atom macrocycle (*x*,*y* coordinates) from the mean porphyrin plane, based on the least-squares method (mean plane defined as Δx and $\Delta y = 0$). [e]Average deviation of the 24-atom macrocycle (*z* coordinates) with respect to the least-squares plane (mean plane defined as $\Delta z = 0$) [54].

and their respective hydrogen atoms 1.97 Å away from each other. However, this does not account for the increased ruffling observed in porphyrins **28** and **29**, with similar distances to the β-ethyl groups as in porphyrin **26**, and despite this there is almost 0.5 Å magnitude of ruffle distortion. This may also be due to crystal packing effects or the Ni(II) metal center [56,57], as well as the crystallization solvent [43]. It is not possible to ascertain whether steric effects of the β-ethyl and the anthracenyl carbons are causing the ruffling observed, and a full statistical model of a large library of dodecasubstituted porphyrins is needed to understand these observed effects.

When comparing *meta*-substituted porphyrins **36** and **37**, ruffle distortion of the porphyrin ring is also observed. Interestingly in the case of the *meta*-anthracenyl derivative, the *para*-anthracenylporphyrin **27** experiences a magnitude of ≈0.3 Å less ruffling when compared to that of the *meta*-substituted porphyrin **37**. In terms of *meta*-phenyl-substituted porphyrin **36** a contribution of ruffling is observed, but no ruffling is observed in the planar analogue.

Crystal packing analysis of arm-extended *para*-substituted porphyrins

Nonplanar porphyrins are known to form supramolecular assemblies [6], either through hydrogen-bonding networks or through π–π interactions. Examples of this can be seen in the trapping of Keggin-type heteropolyoxometalate (POM) through nonplanar Mo(V)–porphyrin complexes [58], or porphyrin nanotubes/nanochannels by intermolecular π–π interactions of the peripheral phenyl groups [59]. Additionally nonplanar supramolecular assemblies have found use in anion capture [12,15], and sensing [60], making the synthesis of these structures desirable from a supramolecular standpoint.

Two especially interesting crystal packing features were that observed in the structures of compound **27** and borylated porphyrin **46**. In the case of porphyrin **27**, when crystallized by slow evaporation from $CDCl_3$, a crystal structure with a void diameter of approximately 5.8 Å was obtained (Figure 4). The void was measured from the Ni(II)···Ni(II) vector approximately perpendicular to the metals through the *c*-axis.

Upon co-crystallization of borylated porphyrin **46** and bis(pinacolato)diboron, the accommodation of bis(pinacolato)diboron in the void of the lattice was observed (Figure 4). The crystal packing of this structure is quite similar to the supramolecular assembly of borylated porphyrin 5,10,15,20-tetrakis(5,5-dimethyl-1,3,2-dioxaborinan-2-yl)porphyrin, where nitrobenzene accommodated tunnels of width of 7–8 Å [61]. The assembly of compound **46** also presents channel-type voids,

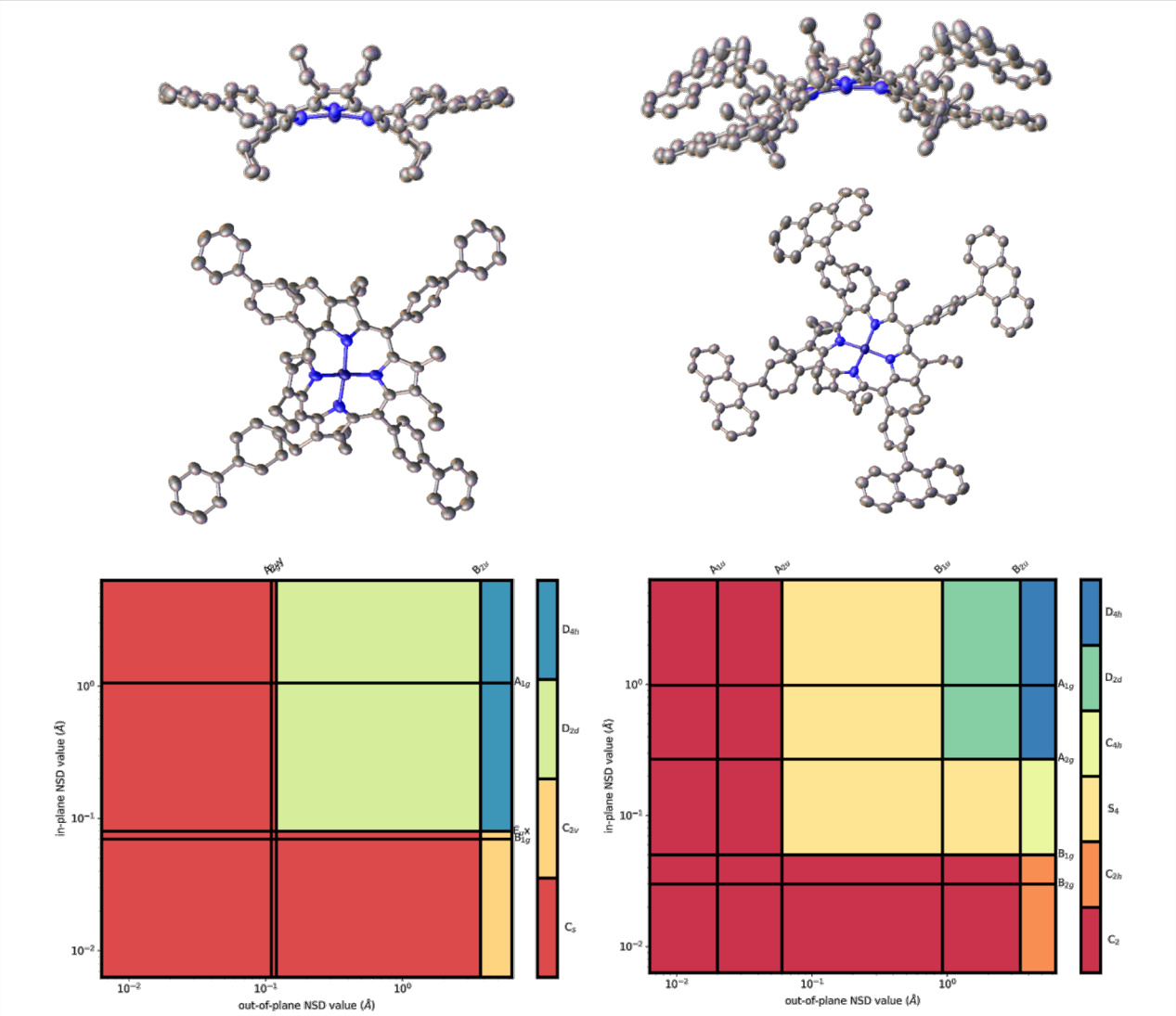

Figure 3: View of the molecular structure of compounds **26** (top left) and **27** (top right) with atomic displacements at 50% probability and hydrogen atoms omitted for clarity. Bottom left: Neoplastic representation of the molecular symmetry of compound **26**. Bottom right: Neoplastic representation of the molecular symmetry of compound **27**.

making it part of only a few porphyrins appended with boronic ester groups to be structurally disseminated by X-ray crystallography [62,63]. Compound **46** was found to crystallize in a 1:1 ratio with bis(pinacolato)diboron, with a void size of 8–9 Å. The formation of channel-type lattice structures is thermodynamically unfavorable, when compared to tightly packed arrangements, similar to nitrobenzene, bis(pinacolato)diboron may be templating the formation of these channels [61]. However, more research is needed to understand the formation of these supramolecular assemblies.

X-ray crystal structure analysis of compound **11**

As observed in the single crystal X-ray structure of **11** (Figure 5), the environment around the *ortho*-bromo-position is extremely sterically hindered.

Figure 5, shows the Br···Br separations in the $\alpha_2\beta_2$-atropsiomer of compound **11** to be 4.3–4.4 Å. While only an illustration of the situation in the solid phase this illustrates that coupling phenyl, thiophene or other aryl moieties at this position would be extremely difficult. Furthermore, the distance between the *o*-bromine atoms and the nearest carbon neighbor of the β-ethyl groups is 3.7 Å, further complicates the success of coupling at this position. As discussed previously, enrichment to the αβαβ, isomer may be necessary to remove the impact of opposing bromine atoms on the coupling reaction. Separation of the four individual atropisomers (αβαβ, $\alpha_2\beta_2$, $\alpha_3\beta$, α_4) has been accomplished before in dodecasubstituted porphyrins through Ni(II) metalation [15]. The core metalation effect prevents inner core N–H tautomerism [64] and thus increases the structural symmetry of the macrocycle [65,66], leading to more facile

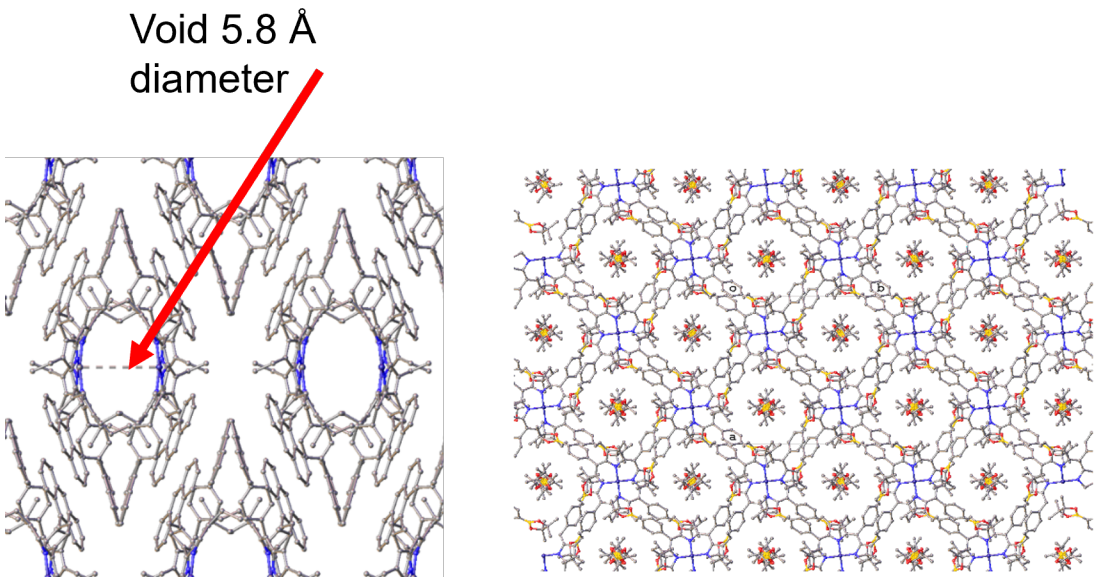

Figure 4: Left: packing diagram of **27** viewed normal to the *c*-axis showing the channels in the lattice with the solvent molecule density removed using masking in OLEX2. Hydrogen atoms omitted for clarity. Right: packing diagram of **46**, viewed normal to the *c*-axis, with bis(pinacolato)diboron occupying the cavities of the major **46**. Hydrogen atoms omitted for clarity.

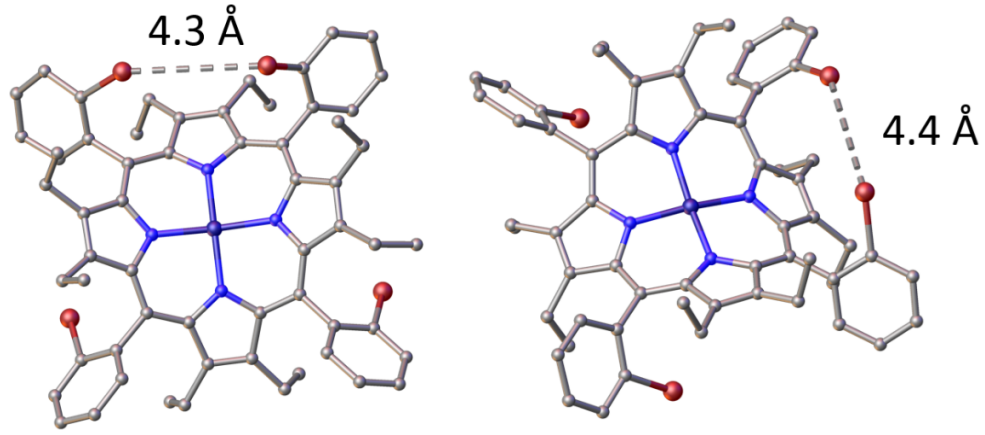

Figure 5: Left: view of part 0 2 in the molecular structure of the $\alpha_2\beta_2$-atropisomer, **11** in the crystal, hydrogen atoms omitted for clarity. Displacement parameters shown at 50% probability and heteroatoms labelled only. Right: view of part 0 1 of the molecular structure of the $\alpha_2\beta_2$-atropisomer, **11** in the crystal. Displacement parameters shown at 50% probability and heteroatoms labelled only.

atropisomeric separation. However, in the case of compound **11** the atropisomers could not be separated due to low rotational barriers and similar polarities, even with Ni(II) metalation. There are many other methods available to achieve different desired atropisomeric ratios. These include thermal enrichment [67,68], photoracemization [69,70], axial-ligand coordination [71], precise separation techniques [50] or a combination of the procedures mentioned [72]. Many more examples of atropisomeric enrichment methods can be found in a 2024 review on atropisomerism by Maguire et al. [73] and could be further explored to isolate the αβαβ-atropisomer of porphyrin **11**.

X-ray crystal structure analysis of compound **37**

Interestingly the anthracenyl arm-extension on the meso-*meta*-phenyl position revealed a doubly sandwiched, intercalated dimeric structure, wherein by two anthracenyl units is sandwiched a single anthracenylphenyl arm whilst a anthracenylphenyl arm is sandwiched on the opposing side of the molecules in the same fashion (Figure 6). Support of the existence of this structure in solution was obtained from VT-NMR studies (Figure S51 and Figure S52 in Supporting Information File 1), with asymmetry observed in the β-ethyl CH_3 resonances δ_H = 0.58 and 0.73 ppm and peak broadening in both the aromatic

region and the $\{^1H\}^{13}C$ NMR spectra. Coalescence of the β-ethyl resonances was observed when heating the sample to 70 °C and the same ^1H NMR spectrum was observed after subsequent cooling of the sample as before heating. This indicates the thermodynamically favored dimeric structure to reassemble when cooling, reverting to the previous NMR trace.

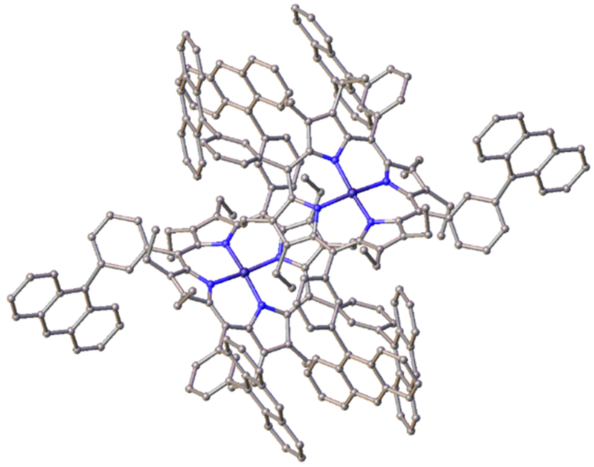

Figure 6: Schematic representation of porphyrin **37** showing a doubly intercalated structure.

Conclusion

When considering sterically demanding systems with haloaryl and boronic acids as substrates for the Suzuki–Miyaura coupling, many may consider 2,6-alkyl-disubstituted phenyl rings as a model sterically demanding system to test the robust nature of both metal catalyst and ligand, for example, much work has been done on the synthesis of *ortho*-substituted biaryls, by the groups of Buchwald [74], Snieckus [75], Ackermann [76], and Tang [77] among others. Many of these examples have steric hindrance 'adjacent' to that of the reactive halogen/boronic site as opposed to the 'adjacent' and 'opposite' steric demand as seen with compound **11** with opposing bromines, coupled with the added complication of being a rotameric mixture, as well as adjacent hindrance of the nearby β-ethyl groups. Examples of palladium coupling on 'opposing' halogen atoms can be seen in the annulation of *vic*-bis(pinacolatoboryl)alkenes and -phenanthrenes [78]; yet, adjacent hindrance is not a problem in this case. Clearly, more work is required on the Suzuki–Miyaura coupling of molecules with sterically demanding 'pockets' with opposing and adjacent hindrance.

In conclusion, a library of arm-extended dodecasubstituted porphyrins was synthesized through classic C–C coupling reactions at the meso-phenyl position. It was found varying temperature and the pH of the solution are effective mitigations to overcome unfavorable reaction electronics or demanding sterics presented at the meso-phenyls' *meta*- or *para*-position. Functionalization at the meso-phenyls' *ortho*- position was not manageable and more research is needed to optimize conditions. Comparing the yields in coupling of borylated porphyrins and the halogenated analogues revealed a greater yield, when the polarity of the reaction was reversed; however, due to tedious synthesis and a lower yield over two steps, this synthetic approach is disadvantageous.

X-ray crystal structures were reported for almost half of these compounds. Crystal packing arrangements revealed this new library of arm-extended porphyrins as interesting candidates for the formation of supramolecular assemblies possibly capable of carrying out sensing and or capturing molecules of interest, as well as a dimeric intercalated structure.

Supporting Information

Supporting Information File 1

Experimental methods, synthetic procedures, ^1H, ^{11}B and ^{13}C NMR, VT-NMR, UV–vis, IR, HRMS (*m*/*z*)-APCI and HRMS (*m*/*z*)-LIFDI spectra and X-ray crystallographic data.
[https://www.beilstein-journals.org/bjoc/content/supplementary/1860-5397-20-234-S1.pdf]

Supporting Information File 2

Crystallographic information files for porphyrins **11** (tcd2100), **28** (tcd2038), **27** (tcd2036), **36** (tcd2056), **26** (tcd2017), **29** (tcd2127), **37** (tcd2277), **46** (tcd2153) and **33** (tcd2288).
[https://www.beilstein-journals.org/bjoc/content/supplementary/1860-5397-20-234-S2.zip]

Acknowledgements

We would like to thank Dr. Gary Hessman from the Mass Spectrometry Unit in Trinity College Dublin for acquiring APCI data used in this manuscript.

Funding

This project has received funding from Science Foundation Ireland (SFI award 21/FFP-A/9469, PORPHYSHAPE) and was supported by the Technical University of Munich – Institute for Advanced Study through a Hans Fischer Senior Fellowship.

Author Contributions

Liam Cribbin: investigation; methodology; writing – original draft. Brendan Twamley: data curation; formal analysis; investigation. Nicolae Buga: investigation. John E. O' Brien: investi-

gation; methodology. Raphael Bühler: data curation; investigation; methodology. Roland A. Fischer: investigation; methodology; supervision. Mathias O. Senge: conceptualization; funding acquisition; methodology; project administration; supervision; validation; writing – original draft; writing – review & editing.

ORCID® iDs

Liam Cribbin - https://orcid.org/0009-0003-2997-4140
Nicolae Buga - https://orcid.org/0009-0007-2553-0445
Raphael Bühler - https://orcid.org/0009-0005-9277-8809
Mathias O. Senge - https://orcid.org/0000-0002-7467-1654

Data Availability Statement

All data that supports the findings of this study is available in the published article and/or the supporting information of this article.

References

1. Brothers, P. J.; Senge, M. O., Eds. *Fundamentals of Porphyrin Chemistry: A 21st Century Approach;* John Wiley & Sons: Hoboken, NJ, USA, 2022. doi:10.1002/9781119129301
2. Fleischer, E. B. *J. Am. Chem. Soc.* **1963,** *85,* 146–148. doi:10.1021/ja00885a007
3. Senge, M. O. *Chem. Commun.* **2006,** 243–256. doi:10.1039/b511389j
4. Olea, C., Jr.; Boon, E. M.; Pellicena, P.; Kuriyan, J.; Marletta, M. A. *ACS Chem. Biol.* **2008,** *3,* 703–710. doi:10.1021/cb800185h
5. Senge, M. O.; MacGowan, S. A.; O'Brien, J. M. *Chem. Commun.* **2015,** *51,* 17031–17063. doi:10.1039/c5cc06254c
6. Ishizuka, T.; Grover, N.; Kingsbury, C. J.; Kotani, H.; Senge, M. O.; Kojima, T. *Chem. Soc. Rev.* **2022,** *51,* 7560–7630. doi:10.1039/d2cs00391k
7. Haddad, R. E.; Gazeau, S.; Pécaut, J.; Marchon, J.-C.; Medforth, C. J.; Shelnutt, J. A. *J. Am. Chem. Soc.* **2003,** *125,* 1253–1268. doi:10.1021/ja0280933
8. Kingsbury, C. J.; Senge, M. O. *Coord. Chem. Rev.* **2021,** *431,* 213760. doi:10.1016/j.ccr.2020.213760
9. Shelnutt, J. A. *J. Porphyrins Phthalocyanines* **2001,** *5,* 300–311. doi:10.1002/jpp.320
10. Kingsbury, C. J.; Senge, M. O. *Angew. Chem., Int. Ed.* **2024,** *63,* e202403754. doi:10.1002/anie.202403754
11. Norvaiša, K.; Yeow, K.; Twamley, B.; Roucan, M.; Senge, M. O. *Eur. J. Org. Chem.* **2021,** 1871–1882. doi:10.1002/ejoc.202100154
12. Stone, A.; Fleischer, E. B. *J. Am. Chem. Soc.* **1968,** *90,* 2735–2748. doi:10.1021/ja01013a001
13. Senge, M. O.; Forsyth, T. P.; Nguyen, L. T.; Smith, K. M. *Angew. Chem., Int. Ed. Engl.* **1995,** *33,* 2485–2487. doi:10.1002/anie.199424851
14. Cheng, B.; Munro, O. Q.; Marques, H. M.; Scheidt, W. R. *J. Am. Chem. Soc.* **1997,** *119,* 10732–10742. doi:10.1021/ja9716214
15. Norvaiša, K.; Flanagan, K. J.; Gibbons, D.; Senge, M. O. *Angew. Chem., Int. Ed.* **2019,** *58,* 16553–16557. doi:10.1002/anie.201907929
16. Roucan, M.; Kielmann, M.; Connon, S. J.; Bernhard, S. S. R.; Senge, M. O. *Chem. Commun.* **2018,** *54,* 26–29. doi:10.1039/c7cc08099a
17. Cavalleri, M.; Damiano, C.; Manca, G.; Gallo, E. *Chem. – Eur. J.* **2023,** *29,* e202202729. doi:10.1002/chem.202202729
18. Senge, M. O.; Renner, M. W.; Kalisch, W. W.; Fajer, J. *J. Chem. Soc., Dalton Trans.* **2000,** 381–385. doi:10.1039/a905927j
19. Senge, M. O.; Medforth, C. J.; Sparks, L. D.; Shelnutt, J. A.; Smith, K. M. *Inorg. Chem.* **1993,** *32,* 1716–1723. doi:10.1021/ic00061a030
20. Hiroto, S.; Miyake, Y.; Shinokubo, H. *Chem. Rev.* **2017,** *117,* 2910–3043. doi:10.1021/acs.chemrev.6b00427
21. Godlewski, B.; Baran, D.; de Robichon, M.; Ferry, A.; Ostrowski, S.; Malinowski, M. *Org. Chem. Front.* **2022,** *9,* 2396–2404. doi:10.1039/d1qo01909k
22. Bakar, M. A.; Sergeeva, N. N.; Juillard, T.; Senge, M. O. *Organometallics* **2011,** *30,* 3225–3228. doi:10.1021/om200137p
23. Locos, O. B.; Arnold, D. P. *Org. Biomol. Chem.* **2006,** *4,* 902–916. doi:10.1039/b516989e
24. Shinokubo, H.; Osuka, A. *Chem. Commun.* **2009,** 1011–1021. doi:10.1039/b817941g
25. Sergeeva, N. N.; Scala, A.; Bakar, M. A.; O'Riordan, G.; O'Brien, J.; Grassi, G.; Senge, M. O. *J. Org. Chem.* **2009,** *74,* 7140–7147. doi:10.1021/jo901535c
26. Kato, K.; Kim, J. O.; Yorimitsu, H.; Kim, D.; Osuka, A. *Chem. – Asian J.* **2016,** *11,* 1738–1746. doi:10.1002/asia.201600424
27. Sugita, N.; Hayashi, S.; Hino, F.; Takanami, T. *J. Org. Chem.* **2012,** *77,* 10488–10497. doi:10.1021/jo302122f
28. Chen, J.; Aratani, N.; Shinokubo, H.; Osuka, A. *Chem. – Asian J.* **2009,** *4,* 1126–1133. doi:10.1002/asia.200900053
29. Miyaura, N.; Yanagi, T.; Suzuki, A. *Synth. Commun.* **1981,** *11,* 513–519. doi:10.1080/00397918108063618
30. Wang, K.; Osuka, A.; Song, J. *ACS Cent. Sci.* **2020,** *6,* 2159–2178. doi:10.1021/acscentsci.0c01300
31. Peng, X.; Aratani, N.; Takagi, A.; Matsumoto, T.; Kawai, T.; Hwang, I.-W.; Ahn, T. K.; Kim, D.; Osuka, A. *J. Am. Chem. Soc.* **2004,** *126,* 4468–4469. doi:10.1021/ja0392972
32. Aratani, N.; Osuka, A. *Org. Lett.* **2001,** *3,* 4213–4216. doi:10.1021/ol0168770
33. Götz, D. C. G.; Bruhn, T.; Senge, M. O.; Bringmann, G. *J. Org. Chem.* **2009,** *74,* 8005–8020. doi:10.1021/jo901483q
34. Droege, D. G.; Parker, A. L.; Milligan, G. M.; Jenkins, R.; Johnstone, T. C. *J. Org. Chem.* **2022,** *87,* 11783–11795. doi:10.1021/acs.joc.2c01538
35. Pijeat, J.; Dappe, Y. J.; Thuéry, P.; Campidelli, S. *Org. Biomol. Chem.* **2018,** *16,* 8106–8114. doi:10.1039/c8ob02150c
36. Ferrero, S.; Barbero, H.; Miguel, D.; García-Rodríguez, R.; Álvarez, C. M. *RSC Adv.* **2020,** *10,* 36164–36173. doi:10.1039/d0ra07407a
37. Miyaura, N.; Suzuki, A. *Chem. Rev.* **1995,** *95,* 2457–2483. doi:10.1021/cr00039a007
38. Wan, S.; Gándara, F.; Asano, A.; Furukawa, H.; Saeki, A.; Dey, S. K.; Liao, L.; Ambrogio, M. W.; Botros, Y. Y.; Duan, X.; Seki, S.; Stoddart, J. F.; Yaghi, O. M. *Chem. Mater.* **2011,** *23,* 4094–4097. doi:10.1021/cm201140r
39. Muzzi, C. M.; Medforth, C. J.; Voss, L.; Cancilla, M.; Lebrilla, C.; Ma, J.-G.; Shelnutt, J. A.; Smith, K. M. *Tetrahedron Lett.* **1999,** *40,* 6159–6162. doi:10.1016/s0040-4039(99)01105-3
40. Barton, D. H. R.; Zard, S. Z. *J. Chem. Soc., Chem. Commun.* **1985,** 1098–1100. doi:10.1039/c39850001098
41. Roth, S. D.; Shkindel, T.; Lightner, D. A. *Tetrahedron* **2007,** *63,* 11030–11039. doi:10.1016/j.tet.2007.08.041
42. Lindsey, J. S.; Schreiman, I. C.; Hsu, H. C.; Kearney, P. C.; Marguerettaz, A. M. *J. Org. Chem.* **1987,** *52,* 827–836. doi:10.1021/jo00381a022

43. Flanagan, K. J.; Twamley, B.; Senge, M. O. *Inorg. Chem.* **2019,** *58,* 15769–15787. doi:10.1021/acs.inorgchem.9b01963
44. Hayes, H. L. D.; Wei, R.; Assante, M.; Geogheghan, K. J.; Jin, N.; Tomasi, S.; Noonan, G.; Leach, A. G.; Lloyd-Jones, G. C. *J. Am. Chem. Soc.* **2021,** *143,* 14814–14826. doi:10.1021/jacs.1c06863
45. Fasano, V.; McFord, A. W.; Butts, C. P.; Collins, B. S. L.; Fey, N.; Alder, R. W.; Aggarwal, V. K. *Angew. Chem., Int. Ed.* **2020,** *59,* 22403–22407. doi:10.1002/anie.202007776
46. Yamamoto, Y.; Matsumura, T.; Takao, N.; Yamagishi, H.; Takahashi, M.; Iwatsuki, S.; Ishihara, K. *Inorg. Chim. Acta* **2005,** *358,* 3355–3361. doi:10.1016/j.ica.2005.05.026
47. Cox, P. A.; Reid, M.; Leach, A. G.; Campbell, A. D.; King, E. J.; Lloyd-Jones, G. C. *J. Am. Chem. Soc.* **2017,** *139,* 13156–13165. doi:10.1021/jacs.7b07444
48. Garai, S.; Schaffer, P. C.; Laprairie, R. B.; Janero, D. R.; Pertwee, R. G.; Straiker, A.; Thakur, G. A. *Bioorg. Med. Chem.* **2021,** *50,* 116421. doi:10.1016/j.bmc.2021.116421
49. Alimardanov, A.; Schmieder-van de Vondervoort, L.; de Vries, A. H. M.; de Vries, J. G. *Adv. Synth. Catal.* **2004,** *346,* 1812–1817. doi:10.1002/adsc.200404210
50. Lindsey, J. *J. Org. Chem.* **1980,** *45,* 5215. doi:10.1021/jo01313a042
51. Tang, X.-f.; Feng, S.-h.; Wang, Y.-k.; Yang, F.; Zheng, Z.-h.; Zhao, J.-n.; Wu, Y.-f.; Yin, H.; Liu, G.-z.; Meng, Q.-w. *Tetrahedron* **2018,** *74,* 3624–3633. doi:10.1016/j.tet.2018.05.023
52. Senge, M. O.; Medforth, C. J.; Forsyth, T. P.; Lee, D. A.; Olmstead, M. M.; Jentzen, W.; Pandey, R. K.; Shelnutt, J. A.; Smith, K. M. *Inorg. Chem.* **1997,** *36,* 1149–1163. doi:10.1021/ic961156w
53. Kingsbury, C. J.; Kielmann, M.; Twamley, B.; Senge, M. O. *Molecules* **2022,** *27,* 7060. doi:10.3390/molecules27207060
54. Jentzen, W.; Song, X.-Z.; Shelnutt, J. A. *J. Phys. Chem. B* **1997,** *101,* 1684–1699. doi:10.1021/jp963142h
55. Kingsbury, C. J.; Senge, M. O. *Chem. Sci.* **2024,** *15,* 13638–13649. doi:10.1039/d4sc01670j
56. Brennan, T. D.; Scheidt, W. R.; Shelnutt, J. A. *J. Am. Chem. Soc.* **1988,** *110,* 3919–3924. doi:10.1021/ja00220a033
57. Kozlowski, P. M.; Rush, T. S.; Jarzecki, A. A.; Zgierski, M. Z.; Chase, B.; Piffat, C.; Ye, B.-H.; Li, X.-Y.; Pulay, P.; Spiro, T. G. *J. Phys. Chem. A* **1999,** *103,* 1357–1366. doi:10.1021/jp9819700
58. Yokoyama, A.; Kojima, T.; Fukuzumi, S. *Dalton Trans.* **2011,** *40,* 6445–6450. doi:10.1039/c0dt01708f
59. Kojima, T.; Harada, R.; Nakanishi, T.; Kaneko, K.; Fukuzumi, S. *Chem. Mater.* **2007,** *19,* 51–58. doi:10.1021/cm062031k
60. Norvaiša, K.; Kielmann, M.; Senge, M. O. *ChemBioChem* **2020,** *21,* 1793–1807. doi:10.1002/cbic.202000067
61. Muniappan, S.; Lipstman, S.; Goldberg, I. *Acta Crystallogr., Sect. C: Cryst. Struct. Commun.* **2008,** *64,* 177–179. doi:10.1107/s010827010800468x
62. Hata, H.; Shinokubo, H.; Osuka, A. *J. Am. Chem. Soc.* **2005,** *127,* 8264–8265. doi:10.1021/ja051073r
63. Hyslop, A. G.; Kellett, M. A.; Iovine, P. M.; Therien, M. J. *J. Am. Chem. Soc.* **1998,** *120,* 12676–12677. doi:10.1021/ja982410h
64. Urbani, M.; Torres, T. *Chem. – Eur. J.* **2014,** *20,* 16337–16349. doi:10.1002/chem.201403881
65. Gouterman, M.; Wagnière, G. H.; Snyder, L. C. *J. Mol. Spectrosc.* **1963,** *11,* 108–127. doi:10.1016/0022-2852(63)90011-0
66. Senge, M. O.; Ryan, A. A.; Letchford, K. A.; MacGowan, S. A.; Mielke, T. *Symmetry* **2014,** *6,* 781–843. doi:10.3390/sym6030781
67. Hatano, K.; Anzai, K.; Kubo, T.; Tamai, S. *Bull. Chem. Soc. Jpn.* **1981,** *54,* 3518–3521. doi:10.1246/bcsj.54.3518
68. Nishino, N.; Kobata, K.; Mihara, H.; Fujimoto, T. *Chem. Lett.* **1992,** *21,* 1991–1994. doi:10.1246/cl.1992.1991
69. Freitag, R. A.; Mercer-Smith, J. A.; Whitten, D. G. *J. Am. Chem. Soc.* **1981,** *103,* 1226–1228. doi:10.1021/ja00395a045
70. Freitag, R. A.; Whitten, D. G. *J. Phys. Chem.* **1983,** *87,* 3918–3925. doi:10.1021/j100243a026
71. Mansour, A.; Belghith, Y.; Belkhiria, M. S.; Bujacz, A.; Guérineau, V.; Nasri, H. *J. Porphyrins Phthalocyanines* **2013,** *17,* 1094–1103. doi:10.1142/s1088424613500843
72. Zimmer, B.; Bulach, V.; Drexler, C.; Erhardt, S.; Hosseini, M. W.; De Cian, A. *New J. Chem.* **2002,** *26,* 43–57. doi:10.1039/b104084g
73. Maguire, S.; Strachan, G.; Norvaiša, K.; Donohoe, C.; Gomes-da-Silva, L. C.; Senge, M. O. *Chem. – Eur. J.* **2024,** *30,* e202401559. doi:10.1002/chem.202401559
74. Yin, J.; Rainka, M. P.; Zhang, X.-X.; Buchwald, S. L. *J. Am. Chem. Soc.* **2002,** *124,* 1162–1163. doi:10.1021/ja017082r
75. Demchuk, O. M.; Yoruk, B.; Blackburn, T.; Snieckus, V. *Synlett* **2006,** 2908–2913. doi:10.1055/s-2006-951538
76. Ackermann, L.; Potukuchi, H. K.; Althammer, A.; Born, R.; Mayer, P. *Org. Lett.* **2010,** *12,* 1004–1007. doi:10.1021/ol1000186
77. Zhao, Q.; Li, C.; Senanayake, C. H.; Tang, W. *Chem. – Eur. J.* **2013,** *19,* 2261–2265. doi:10.1002/chem.201203898
78. Shimizu, M.; Nagao, I.; Tomioka, Y.; Hiyama, T. *Angew. Chem., Int. Ed.* **2008,** *47,* 8096–8099. doi:10.1002/anie.200803213

License and Terms

BEILSTEIN JOURNAL OF ORGANIC CHEMISTRY

The charge transport properties of dicyanomethylene-functionalised violanthrone derivatives

Sondos A. J. Almahmoud[1], Joseph Cameron[2], Dylan Wilkinson[2], Michele Cariello[2], Claire Wilson[2], Alan A. Wiles[2], Peter J. Skabara[*2] and Graeme Cooke[*2]

Full Research Paper

Open Access

Address:
[1]Department of Chemistry, College of Science, Imam Mohammad Ibn Saud Islamic University (IMSIU), Riyadh 11623, Saudi Arabia and [2]School of Chemistry, University of Glasgow, Glasgow, G12 8QQ, UK

Email:
Peter J. Skabara[*] - Peter.Skabara@glasgow.ac.uk; Graeme Cooke[*] - Graeme.Cooke@glasgow.ac.uk

* Corresponding author

Keywords:
Knoevenagel condensation; organic field-effect transistor; organic semiconductor; violanthrone

Beilstein J. Org. Chem. **2024,** *20,* 2921–2930.
https://doi.org/10.3762/bjoc.20.244

Received: 19 July 2024
Accepted: 29 October 2024
Published: 13 November 2024

This article is part of the thematic issue "π-Conjugated molecules and materials".

Guest Editor: A. Mateo-Alonso

Abstract

The study of organic small molecule semiconductor materials as active components of organic electronic devices continues to attract considerable attention due to the range of advantages these molecules can offer. Here, we report the synthesis of three dicyanomethylene-functionalised violanthrone derivatives (**3a**, **3b** and **3c**) featuring different alkyl substituents. It is found that the introduction of the electron-deficient dicyanomethylene groups significantly improves the optical absorption compared to their previously reported precursors **2a**–**c**. All compounds are p-type semiconductors with low HOMO–LUMO gaps (≈1.25 eV). The hole mobilities, measured from fabricated organic field-effect transistors, range from 3.6×10^{-6} to 1.0×10^{-2} cm^2 V^{-1} s^{-1}. We found that the compounds featuring linear alkyl chains (**3b** and **3c**) displayed a higher mobility compared to the one with branched alkyl chains, **3a**. This could be the result of the more highly disordered packing arrangement of this molecule in the solid state, induced by the branched side chains that hinder the formation of π–π stacking interactions. The influence of dicyanomethylene groups on the charge transport properties was most clearly observed in compound **3b** which has a 60-fold improvement in mobility compared to **2b**. This study demonstrates that the choice of the solubilising group has a profound effect on the hole mobility on these organic semiconductors.

Introduction

Recently, organic semiconductors have received considerable attention due to their potential technological applications in semiconductor devices, such as organic field-effect transistors (OFETs) [1,2], organic light-emitting diodes (OLEDs) [3], and organic photovoltaic devices (OPVs)[4-6]. The charge transporting properties of organic semiconductors are key to the

success of the devices and research focusing upon increasing this remains an important goal to enhance the commercial viability of the technologies. Typically, organic semiconductor molecules with large fused conjugated systems have achieved high charge carrier mobility. Such molecular structures improve the intermolecular interactions (such as π–π stacking) that are required to facilitate the hopping of charge carriers between adjacent molecules [7-9].

Among many intensively investigated organic semiconductors [10-12], are perylene diimide (PDI) derivatives which feature a rigid, planar, fused π-skeleton. These molecules have been widely utilised as n-type materials, due to their exceptional charge mobility ($\mu_e \approx 0.1–2.1$ cm^2 V^{-1} s^{-1}) [13-17], high electron affinity, excellent self-assembling properties [18-20], and thermal and photochemical stabilities [21]. The excellent charge carrier mobility of PDIs has been explained by the intermolecular π–π interactions with an interplanar distance (3.3–3.5 Å) [22-25] that leads to the formation of large crystalline domains which influence charge transport. However, the microscale domains reduce the donor–acceptor interface which ultimately impacts on efficient exciton dissociation in OPV devices [12]. Therefore, it is important to further investigate other fused π systems to determine if this drawback can be overcome while maintaining the favourable properties of PDIs.

Violanthrones are a class of materials featuring a large π-conjugated system composed of nine fused benzene rings with two carbonyl groups, in the 5 and 10 positions (Figure 1). The related structural features of violanthrones suggest that these materials may possess similar charge transport, optical and electrochemical properties to those of PDIs. However, the larger π-conjugated system of violanthrone, along with the two carbonyl groups, increases the possibility of stronger π–π intermolecular interactions which might result in a narrower HOMO–LUMO gap than that of PDI, and an absorption band extending to the near-infrared (NIR) region [26]. This makes violanthrone and its derivatives potential candidates for NIR optoelectronic applications. In fact, the intrinsic semiconducting properties of violanthrone is traced back to 1950, when Akamatu and Inokuchi measured its electrical conductivity (σ), which was found to be 3.4×10^{-4} Ω^{-1} cm^{-1} [27,28]. The chemical structure of violanthrone allows for its modification and hence the synthesis of materials with interesting spectral properties. Due to the low solubility of violanthrone in the majority of organic solvents, special attention has been drawn to its dihydroxy derivative (Figure 1), which allows further modification to the materials via etherification or esterification [29,30].

There has been a report on the structural modification of dihydroxyviolanthrone where the effect of three alkoxy substituents on the 16,17-*bis*(2-ethylhexyloxy)anthra[9,1,2-*cde*]benzo[*rst*]pentaphene-5,10-dione, on aggregation and photovoltaic properties was studied [30]. It was found that derivatives with the shortest linear alkyl chain (*n*-hexyl) exhibit the strongest π–π interactions since the distance between two adjacent molecules is shorter and less steric repulsion is observed. This was reflected by the highest hole mobility of the derivatives with *n*-hexyl chains (3.15×10^{-4} cm^2 V^{-1} s^{-1}), compared to derivatives with *n*-octyl chains (1.76×10^{-4} cm^2 V^{-1} s^{-1}) and 2-ethylhexyl chains (4.93×10^{-5} cm^2 V^{-1} s^{-1}). The stronger π–π interactions led to a higher power conversion efficiency (PCE) as a result of the higher short-circuit current density (J_{sc}), due to films with higher crystallinity providing a smoother pathway to charge carriers to pass through the device [30].

The π–π intermolecular interactions, the molecular stacking and mobility of a solution-processable violanthrone derivative has been studied. It was shown that π–π stacking can be enhanced in solution and in the solid state by adding a non-solvent (*n*-hexane) to chloroform. Therefore, the resulting film of the compound obtained from a solvent mixture of chloroform/*n*-hexane showed a hole mobility of an order of magnitude higher (4.44×10^{-4} cm^2 V^{-1} s^{-1}) than that of the film obtained from pure chloroform (4.93×10^{-5} cm^2 V^{-1} s^{-1}) [26]. Another study reported the capability of violanthrone **2b** to act as an electron acceptor in OPVs when blended with PDI as a co-acceptor, which showed an enhanced light harvesting and photocurrent generation compared to the device without violanthrone being incorporated (Figure 2) [31].

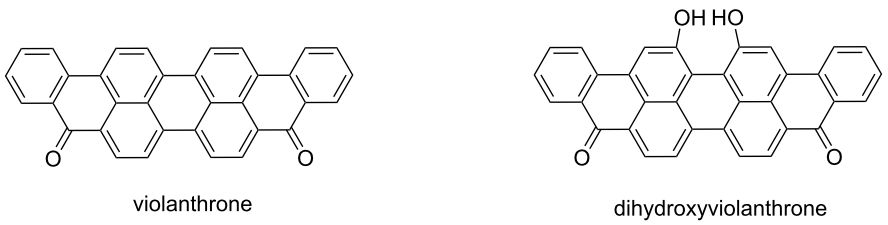

Figure 1: Chemical structures of violanthrone and dihydroxyviolanthrone.

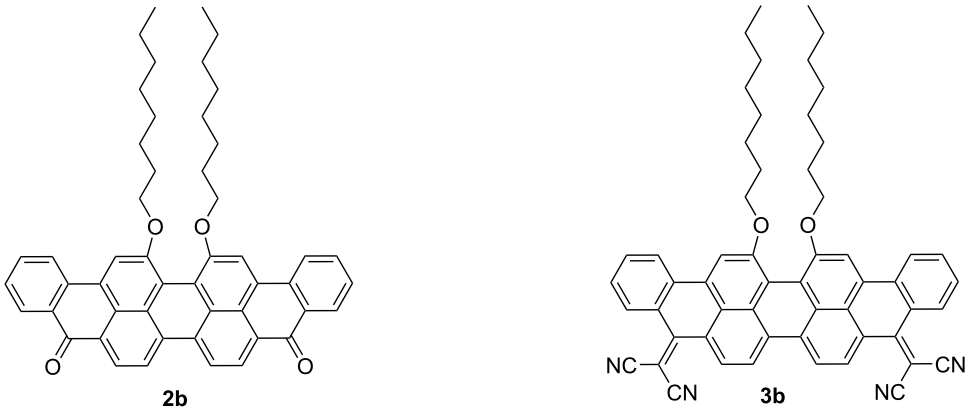

Figure 2: Chemical structures of **2b** and **3b**.

Liu et al. [32] reported a novel violanthrone derivative **3b** via the incorporation of the strong electron-withdrawing dicyanomethylene unit. The study suggested that **3b** could be a potential n-type material for OPVs. The incorporation of two dicyanomethylene groups resulted in a material with strong electron affinity and low reduction potential of −0.56 V vs NHE, and a λ_{max} at 701 nm with ε of 4.69×10^4 L mol^{-1} cm^{-1} which might lead to the contribution of **3b** to the photocurrent.

All previous studies suggested that violanthrone and its derivatives display electronic functionality and could be potentially used in organic electronics. Nevertheless, to the best of our knowledge, neither OPV device fabrication nor the charge mobility of **3b** has been reported. Therefore, in this work, the synthesis of compound **3b** and other new analagous solution-processable derivatives are reported. The performance of these materials as the semiconductor layer in OFETs was studied to determine the effect of the different side chains.

Results and Discussion

Synthesis

The synthesis of compounds **2a**–**c** and **3a**–**c** is shown in Scheme 1. Compounds **2a**–**c** were synthesised through a well-established etherification protocol [30] via the reaction of the

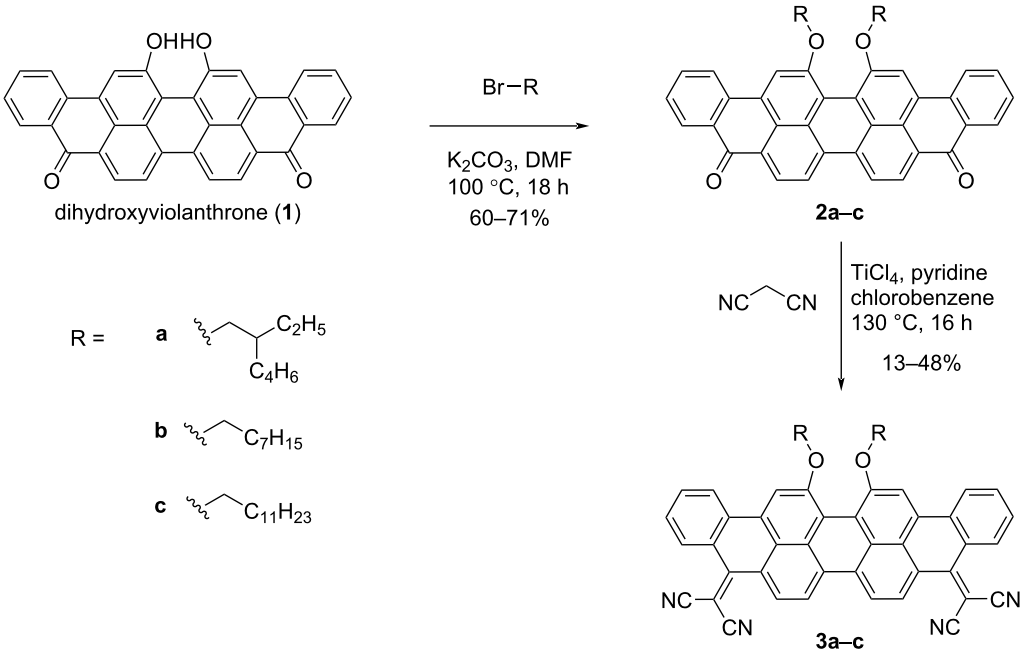

Scheme 1: Synthesis of compounds **2a**–**c** and **3a**–**c**.

commercially available compound 16,17-dihydroxyviolanthrone with 2-ethylhexyl bromide (**a**), 1-bromooctane (**b**), and 1-bromododecane (**c**) resulting in compounds, **2a**, **2b** and **2c**, respectively. The final target compounds **3a**–**c** were synthesised in 13%, 48% and 36% yield, respectively, following the reported procedure for anthraquinone, where the Knoevenagel condensation with malononitrile was successfully reported [33].

Theoretical studies

Density functional theory (DFT) calculations of two derivatives of compounds **2** and **3**, having methoxy groups instead of the longer alkyl chains have been reported in the literature [32], providing information on the molecular structure and packing of these materials. However, no significant information about the electronic and orbital distributions was provided, therefore further investigation was needed, using a more suitable basis set. The molecules were geometrically optimised at the ground state using the B3LYP functional with the 6-311G (d,p) basis set. The geometry of the two molecules was found to be nearly identical to the ones previously reported, with the nine fused rings of compound **2** almost planar, compared to the more twisted geometry of compound **3**. This could possibly result in weak π–π interactions with the potential to form nanoscale pure and mixed domains in the bulk heterojunction on the length scale of the exciton diffusion length (5–15 nm), leading to an efficient exciton dissociation and charge generation [12].

Figure 3 gives an insight into the spatial distribution and the energies of the frontier molecular orbitals of molecules **2** and **3**. In both cases, the highest occupied molecular orbital (HOMO) and the lowest unoccupied molecular orbital (LUMO) are uniformly delocalised throughout the nine fused rings, indicating that the two molecules could benefit from a potentially efficient and isotropic charge transport [12]. It is also evident that the presence of the two dicyanomethylene groups in compound **3** are responsible for lowering the energy of the two frontier molecular orbitals and for narrowing the energy gap between HOMO and LUMO. This is likely due to an enhanced push–pull effect in this molecule due to the presence of a stronger acceptor. Furthermore, the energy of the LUMO of compound **3** is comparable to reported PDI-based acceptors which have been used in OPVs with PCE > 7% [34].

Crystallographic study

Needle-shape crystals of compound **3b** suitable for single-crystal X-ray analysis were obtained by slow evaporation of a dichloromethane/isopropanol solution of **3b**. The crystal structure of **3b**, displayed in Figure 4, shows a very similar twisted conformation of the core of the molecule to that of the related methoxy-substituted structure obtained from theoretical studies [32] (Table S1 in Supporting Information File 1).

Molecules of **3b** form stacks along the *b*-axis linked by π–π interactions with centroid–centroid distances of 3.65 and

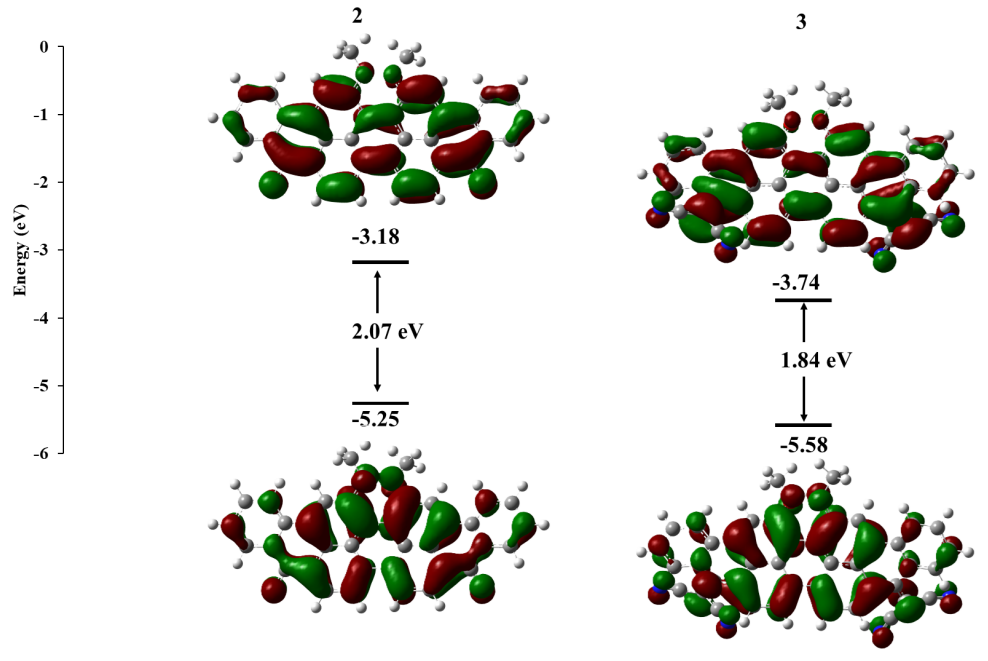

Figure 3: Optimised ground state geometries of compounds **2** and **3** calculated using B3LYP/6-311G(d,p) in the gas phase.

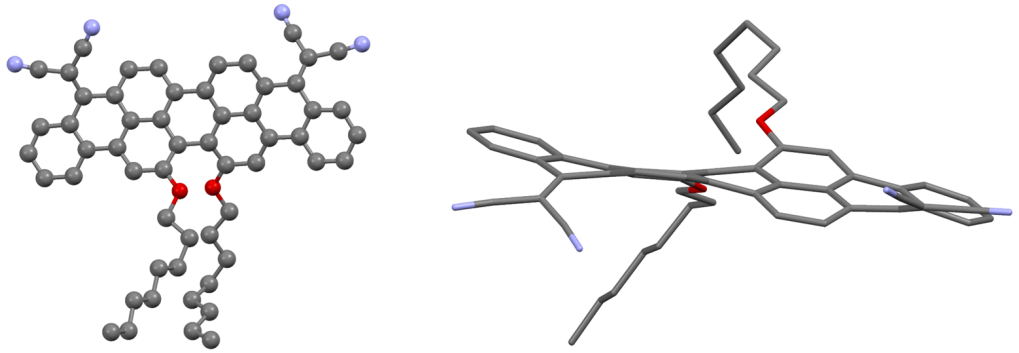

Figure 4: Views of the crystal structure of **3b** (left, shows displacement ellipsoids drawn at 50% probability level, right showing the twisted conformation).

3.98 Å. These stacks lie in sheets with alternating aromatic–aliphatic layers (Figure S3 in Supporting Information File 1).

Optical studies

The UV–vis absorption spectra of **3a**, **3b**, and **3c** are presented in Figure 5, and were carried out in dichloromethane solution (1×10^{-5} mol L^{-1}). The absorption properties are summarised in Table 1. The UV–vis absorption spectra of the materials show a wide absorption band from 530 nm to 860 nm for all compounds. Compound **3a** shows a slight hypsochromic shift (λ_{max} = 741 nm) in comparison with **3b** (λ_{max} = 745 nm) and **3c** (λ_{max} = 746 nm). All compounds displayed very similar extinction coefficients between 45000 and 48000 L mol^{-1} cm^{-1}. The optical gaps (E_{opt}) were estimated from the onset values of absorption (λ_{onset}), and little difference was found with values of 1.47 eV for **3b** and 1.46 eV for **3a** and **3c**. It is noted that the optical properties did not show a significant change upon altering the alkyl chains which indicates that different alkyl substituents have a minimal effect on the frontier orbitals.

Electrochemical studies

The electrochemical properties of the dyes were investigated by square wave voltammetry (SWV) and cyclic voltammetry (CV) and the data are summarised in Table 1, with the plots shown in

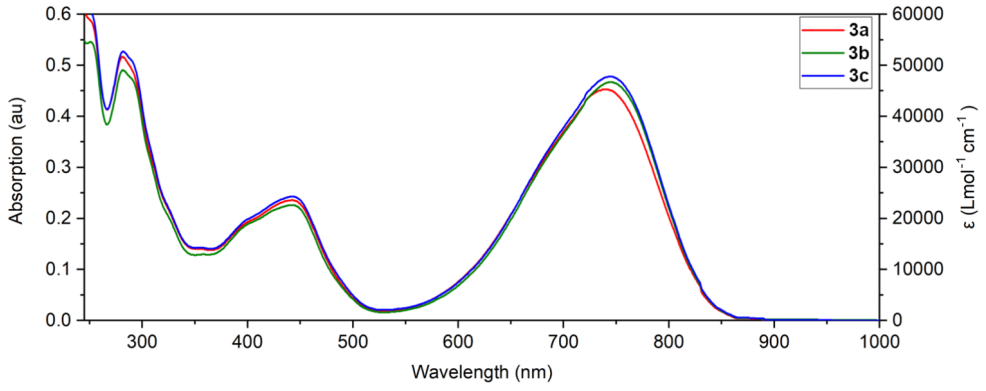

Figure 5: Absorption spectra of **3a–c** measured in dichloromethane solution (1×10^{-5} M).

Table 1: The optical and the electrochemical data of compounds **3a–c**.

	optical properties				electrochemical properties		
	λ_{max} (nm)	λ_{onset} (nm)	E_{opt} (eV)	ε (L mol^{-1} cm^{-1})	IE (eV)	EA (eV)	E_{fund} (eV)
3a	741	851	1.46	45300	−5.38	−4.11	1.27
3b	745	845	1.47	46700	−5.34	−4.09	1.25
3c	746	851	1.46	47800	−5.40	−4.15	1.25

Figure 6. All the materials exhibit at least one reversible reduction and two reversible oxidation waves as shown from the CV data (Figure 6 and Table 1). This reversibility is crucial for the regeneration of dyes following redox processes. The compounds display ionisation energies (IEs) of −5.38 eV, −5.34 eV, and −5.40 eV for **3a**, **3b**, and **3c**, respectively, with electron affinities (EAs) of −4.11 eV, −4.09 eV, and −4.15 eV. Consequently, the estimated E_{fund} are 1.27, 1.25 and 1.25 eV for **3a**, **3b**, and **3c**, respectively. The EA value is in a similar range (from −3.70 to −4.30 eV) of some of the most widely used fullerene-based acceptors such as $PC_{60}BM$ and $PC_{70}BM$ [35], which suggests that the three materials might function effectively as electron acceptors.

OFET device studies

The electrical characteristics were confirmed by the fabrication of OFETs. Compounds **3a–c** were deposited by spin-coating onto n-doped Si/SiO_2/Au substrates. The device performance parameters are summarised in Table 2, and their representative output and transfer curves are shown in Figure S5 (Supporting Information File 1). The charge mobility was determined in the saturation regime. The OFET devices based on **3a–c** showed only p-type charge transport, with the highest hole mobility obtained by **3b**. The hole mobilities (μ_h) of **3b** and **3c** are calculated as 1.07×10^{-2} and 1.21×10^{-3} cm^2 $V^{-1}s^{-1}$, respectively. However, the hole mobility of **3a** is only 3.62×10^{-6} cm^2 V^{-1} s^{-1}.

Table 2: Summary of OFET characteristics with **3a–c** materials.

	ON/OFF ratio	V_{th} (V)	μ_h (cm^2 V^{-1} s^{-1})[a]
3a	10^2	−3	3.62×10^{-6} ($\pm 0.64 \times 10^{-7}$)
3b	10^3	−14	1.07×10^{-2} ($\pm 0.44 \times 10^{-2}$)
3c	10^4	−19	1.21×10^{-3} ($\pm 0.30 \times 10^{-3}$)

[a]Calculated from an average of 8 devices. Standard deviation is listed in parentheses.

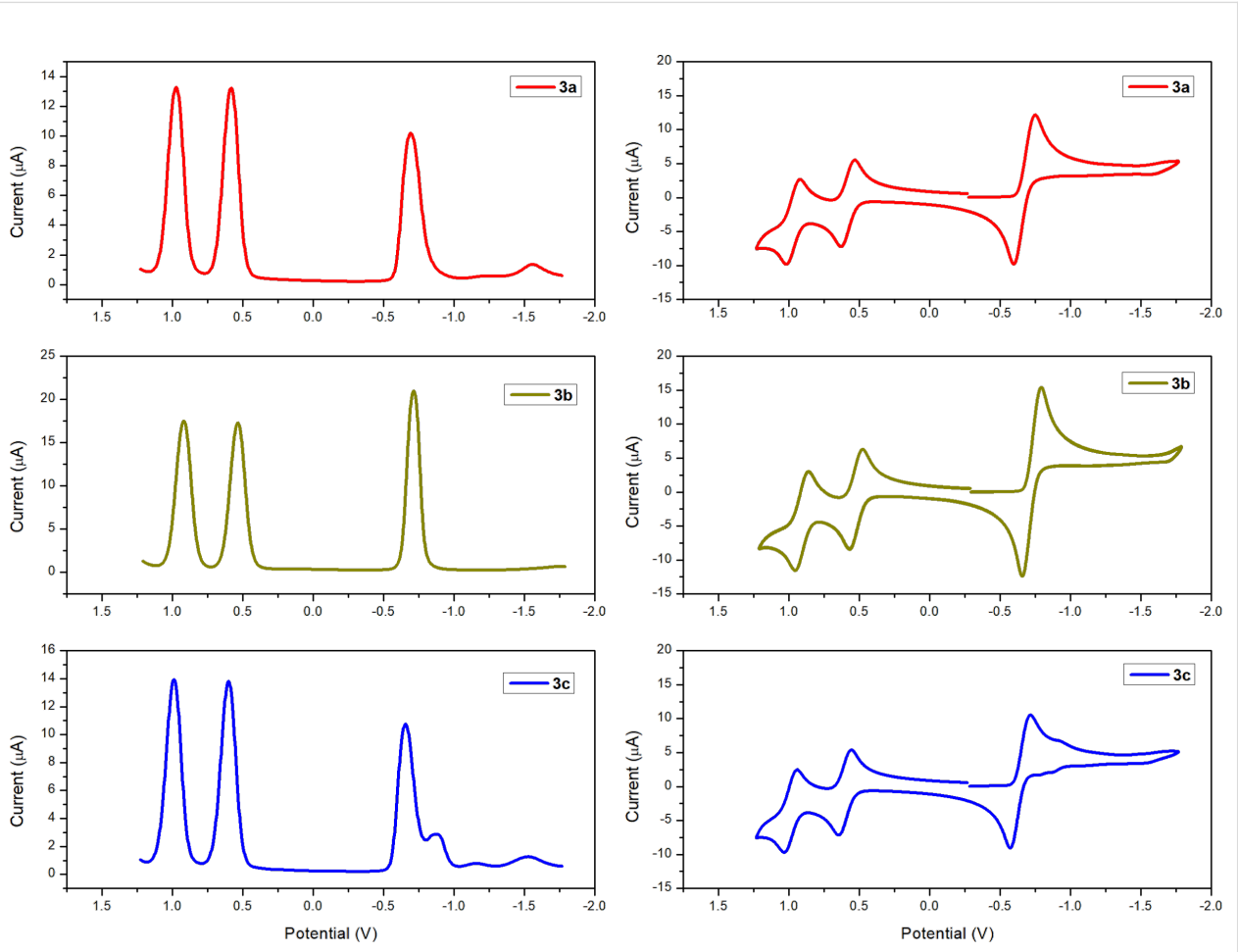

Figure 6: SWV (left) and CV (right) of compound **3a–c** (in dichloromethane 1×10^{-3} M) (V vs Fc/Fc^+).

Side chain engineering is crucial for OFET performance since it plays an important role in determining solubility, molecular packing, polarity, and film-forming properties. Molecular packing, in particular, is greatly affected by alkyl chain length and branching point position [36]. Here, the difference in hole mobility among the three compounds can rationally be attributed to their distinguishing aggregate structures. Compared to **3a**, the linear side chains in compounds **3b** and **3c**, might favour intermolecular π–π interactions and crystallinity in the solid state, therefore providing an easier pathway for charge carriers to hop from one molecule to nearby molecules. The introduction of the bulky dicyanomethylene groups in **3b** resulted in a dramatic increase in μ_h (1.07×10^{-2} cm^2 $V^{-1}s^{-1}$) compared to the previously reported **2b** (1.76×10^{-4} cm^2 $V^{-1}s^{-1}$) [30]. On the other hand, the twisted configuration of the material's backbone upon the introduction of dicyanomethylene groups, along with branched alkyl side chains in **3a**, might have contributed to a lower intermolecular π–π interaction and, therefore, lower μ_h (3.62×10^{-6} cm^2 V^{-1} s^{-1}) compared to the previously reported **2a** (4.93×10^{-5} cm^2 V^{-1} s^{-1}) [30].

Conclusion

Violanthrone derivatives represent a promising group of semiconductor materials for organic electronics. It has been shown that molecular tailoring of violanthrone is simple and feasible. We have synthesised three soluble violanthrone derivatives with different side chains and found that due to the introduction of the electron-deficient dicyanomethylene groups, along with the extended π-conjugated framework, all compounds exhibit a narrow HOMO–LUMO gap (1.46–1.47 eV), with a wide absorption range exceeding 800 nm compared to their previously reported precursors [30]. The electrochemical studies of the three materials show reversible oxidation and reduction waves with EA values that are in a similar range (from −3.70 to −4.30 eV) of some of the most widely used fullerene-based acceptors such as $PC_{60}BM$ and $PC_{70}BM$ [35], which suggests that the three materials might function well as components in OPVs. Among the three materials the introduction of dicyanomethylene groups to compound **2b** significantly improved the μ_h by 60-fold. It is also notable that **3a** bearing branched 2-ethylhexyl side chains showed inferior performance compared to the isomeric **3b** with linear *n*-octyl chains. The poor device performance is most likely caused by branched side chains that might induce a stronger disorder in the film, which results in hindered charge transport.

Experimental

Computational

Density functional theory (DFT) calculations were performed using Gaussian 09 software. Molecular geometries were initially optimised semi-empirically (AM1) and then reoptimised by DFT using the B3LYP method with the 6-311G(d,p) basis set unless stated otherwise. The absence of transition states was confirmed by the absence of imaginary frequencies in vibrational frequency calculations. The long side chains were replaced by methyl units to aid the convergence of the geometry optimisations.

Crystallography

Single crystal X-ray diffraction data for **3b** were collected by the EPSRC National Crystallography Service using a ROD, Synergy Custom system, HyPix diffractometer with Cu Kα radiation, λ = 1.54178 Å. Data were collected and processed using CrysAlis PRO 1.171.39.30d (Rigaku OD, 2015). The structure was solved using SHELXT 2018/2 [37] and refined using SHELXL 2018/3 [38] within Olex2 1.3 [39]. Non-H atoms were refined with anisotropic atomic displacement parameters (ADPs) and H-atoms were placed in geometrically calculated positions and included as part of a riding model except the Me H-atoms which were included as a rigid rotor.

Organic field-effect transistors (OFETs) fabrication and measurement

Bottom-gate, bottom-contact organic field-effect transistors were made using prefabricated substrates (Fraunhofer IPMS, product code 1301). The substrates consisted of an n-doped Si gate electrode, SiO_2 (230 nm) dielectric layer and Au (30 nm + 10 nm ITO adhesion layer) interdigitated source and drain electrodes, 1 cm in width. The substrate contained source-drain electrodes at channel lengths of 20, 10, 5, and 2.5 μm. For all compounds, four devices of 20 μm channel length and four devices with 10 μm channel length were tested, with the exception of **2b** where some devices failed due to high resistance and testing was carried out using 5 μm channel length due to the low currents measured at higher channel lengths. Testing was carried out using a Keithley 4200 Semiconductor Characterisation System. Charge mobility was calculated in the saturation regime.

The substrates were washed using deionised H_2O, acetone, and isopropanol before being dried over a stream of compressed air. Octadecyltrichlorosilane (30 μM) was dropcast onto the substrate for 5 minutes before the substrate was washed with toluene. The substrate was then dried over compressed air. A solution (10 mg mL^{-1} in $CHCl_3$) of the semiconductor material was deposited by spin-coating at 1000 rpm for 60 seconds.

Synthesis

Compound **2a**

16,17-Dihydroxyviolanthrone (500 mg, 1.02 mmol) and 2-ethylhexyl bromide (550 μL, 3.06 mmol) were dissolved in *N*,*N*-dimethylformamide (30 mL). Then, potassium carbonate

was added (300 mg, 2.04 mmol), and the reaction mixture was stirred at 100 °C overnight. After cooling the reaction mixture to room temperature, it was poured into methanol (200 mL), and the resulting precipitate was filtered, then washed with water (150 mL) to give the title compound as a dark solid (440 mg, 60%). ^{1}H NMR (400 MHz, $CDCl_3$) δ 8.79 (d, J = 8.0 Hz, 2H), 8.65 (d, J = 8.1 Hz, 2H), 8.56 (d, J = 7.6 Hz, 2H), 8.40 (d, J = 7.8 Hz, 2H), 8.30 (s, 2H), 7.82 (t, J = 7.6 Hz, 2H), 7.62 (t, J = 7.4 Hz, 2H), 4.05 (m, 4H), 1.77 (m, 2H), 1.38 (m, 16H), 0.93–0.51 (m, 12H); ^{13}C NMR (100 MHz, $CDCl_3$) δ 183.4, 157.1, 135.7, 134.7, 133.3, 131.1, 129.6, 128.6, 128.3, 127.9, 127.7, 127.3, 123.9, 123.3, 122.9, 117.6, 114.6, 65.5, 42.1, 40.1, 30.2, 29.2, 23.5, 23.2, 14.2, 11.2; ASAP–HRMS (m/z): $[M + H]^+$ calcd for $C_{50}H_{49}O_4$, 713.3646; found 713.3631.

Compound **2b**

16,17-Dihydroxyviolanthrone (2.00 g, 4.09 mmol) and 1-bromooctane (2.12 mL, 12.28 mmol) were dissolved in *N*,*N*-dimethylformamide (60 mL). Then, potassium carbonate was added (1.13 g, 8.19 mmol), and the reaction mixture was stirred at 100 °C overnight. After cooling the reaction mixture to room temperature, it was poured into methanol (400 mL), and the resulting precipitate was filtered, then washed with water (300 mL) to give the title compound as a dark solid (1.90 g, 65%). ^{1}H NMR (400 MHz, $CDCl_3$) δ 8.72 (d, J = 8.0 Hz, 2H), 8.60–8.47 (m, 4H), 8.37 (d, J = 8.2 Hz, 2H), 8.27 (s, 2H), 7.80 (t, J = 7.2 Hz, 2H), 7.60 (t, J = 7.3 Hz, 2H), 4.25 (br, 4H), 1.94–1.80 (m, 4H), 1.34 (d, J = 90.2 Hz, 20H), 0.82 (d, J = 6.9 Hz, 6H); ^{13}C NMR (100 MHz, $CDCl_3$) δ 183.2, 156.3, 135.6, 134.5, 133.2, 131.0, 129.4, 128.6, 128.3, 127.7, 127.5, 127.1, 123.6, 123.2, 122.7, 117.2, 113.5, 69.8, 31.9, 29.9, 29.6, 29.5, 26.2, 22.8, 14.2; HRESIMS (m/z): $[M + Na]^+$ calcd for $C_{50}H_{48}NaO_4$, 753.3409; found, 735.3445.

Compound **2c**

16,17-Dihydroxyviolanthrone (500 mg, 1.02 mmol) and 1-bromododecane (800 µL, 3.06 mmol) were dissolved in *N*,*N*-dimethylformamide (30 mL). Then, potassium carbonate was added (300 mg, 2.04 mmol), and the reaction mixture was stirred at 100 °C overnight. After cooling the reaction mixture to room temperature, it was poured into methanol (200 mL), and the resulting precipitate was filtered, then washed with water (150 mL) to give the title compound as a dark solid (600 mg, 71%). ^{1}H NMR (400 MHz, $CDCl_3$) δ 8.78 (d, J = 8.0 Hz, 2H), 8.63 (d, J = 8.3 Hz, 2H), 8.57 (d, J = 7.7 Hz, 2H), 8.39 (d, J = 8.0 Hz, 2H), 8.30 (s, 2H), 7.81 (t, J = 7.4 Hz, 2H), 7.62 (t, J = 7.6 Hz, 2H), 4.26 (s, 4H), 1.92–1.72 (m, 4H), 1.55–1.02 (m, 36H), 0.86 (t, J = 6.8 Hz, 6H); ^{13}C NMR (100 MHz, $CDCl_3$) δ 183.2, 156.4, 135.6, 134.5, 133.2, 131.1, 129.5, 128.6, 128.3, 127.8, 127.5, 127.2, 123.7, 123.2, 122.8, 117.3, 113.6, 69.8, 63.2, 32.9, 32.0, 29.7, 29.6, 29.5, 29.4, 26.2, 25.8 , 22.8, 14.2; ASAP–HRMS (m/z): $[M + H]^+$ calcd for $C_{58}H_{64}O_4$, 825.4875; found, 825.4883.

Compound **3a**

Compound **2a** (200 mg, 0.280 mmol) and malononitrile (100 mg, 0.840 mmol) were dissolved in anhydrous chlorobenzene (6 mL). To the dark blue mixture titanium tetrachloride (100 µL, 0.840 mmol) and pyridine (130 µL, 1.68 mmol) were added and the mixture was stirred under reflux overnight. After cooling the reaction mixture to room temperature, it was poured into ice-water (50 mL) and extracted with dichloromethane (3 × 20 mL). The combined organic extract was dried over $MgSO_4$, filtered and concentrated under reduced pressure. The crude product was purified by silica column chromatography (SiO_2, CH_2Cl_2/diethyl ether 98:2) to give the title compound as a dark solid (30.0 mg, 13%). Mp 295–296 °C; ^{1}H NMR (400 MHz, $CDCl_3$) δ 8.75 (d, J = 8.2 Hz, 2H), 8.55 (dd, J = 12.5, 8.2 Hz, 4H), 8.35 (d, J = 8.1 Hz, 2H), 8.25 (s, 2H), 7.80 (t, J = 7.4 Hz, 2H,), 7.63 (t, J = 7.7 Hz, 2H), 4.24–3.96 (m, 4H), 1.79 (br, 2H), 1.54–1.21 (m, 16H), 0.84 (m, 12H); ^{13}C NMR (100 MHz, $CDCl_3$) δ 183.4, 157.1, 135.7, 134.7, 133.3, 131.1, 129.6, 128.6, 128.3, 127.9, 127.7, 127.3, 123.9, 123.3, 122.9, 117.6, 114.6, 65.5, 42.1, 40.1, 30.2, 29.2, 23.2 (C, 14.2, 11.2; ASAP–HRMS (m/z): $[M + H]^+$ calcd for $C_{56}H_{49}N_4O_2$, 809.3841; found, 809.3856 .

Compound **3b**

Compound **2b** (200 mg, 0.28 mmol) and malononitrile (60.0 mg, 0.840 mmol) were dissolved in anhydrous chlorobenzene (6 mL). To the dark blue mixture, titanium tetrachloride (50.0 µL, 0.420 mmol) and pyridine (70.0 µL, 0.84 mmol) were added and the mixture was stirred under reflux overnight. After cooling the reaction mixture to room temperature, it was poured into ice-water (50 mL) and extracted with dichloromethane (3 × 20 mL). The combined organic extract was dried over $MgSO_4$, filtered and concentrated under reduced pressure. The crude product was purified by column chromatography (SiO_2, petroleum ether/CH_2Cl_2 1:9) to give the title compound as a dark solid (110 mg, 48%). Analysis is in agreement with previously reported data [32]. Mp 294–295 °C; ^{1}H NMR (400 MHz, $CDCl_3$) δ 8.75 (d, J = 8.2 Hz, 2H), 8.56 (dd, J = 8.1, 1.0 Hz, 2H), 8.51 (d, J = 8.4 Hz, 2H), 8.35 (d, J = 7.9 Hz, 2H), 8.26 (s, 2H), 7.82–7.75 (m, 2H), 7.65–7.58 (m, 2H), 4.31 (s, 4H), 1.94–1.84 (m, 4H), 1.54–1.07 (m, 20H), 0.89–0.78 (m, 6H); ^{13}C NMR (100 MHz, $CDCl_3$) δ 161.0, 157.1, 133.8, 132.9, 132.6, 129.1, 129.0, 128.5, 128.3, 127.9, 127.2, 127.1, 124.2, 122.5, 120.9, 117.6, 116.3, 112.5, 76.8, 70.0, 31.9, 29.8, 29.5, 29.4, 26.1, 22.7, 14.2; FAB^+–HRMS (m/z): $[M + H]^+$ calcd for $C_{56}H_{49}N_4O_2$, 809.3856; found, 809.3879 .

Details of the crystal structure of **3b** are given in the CIF which can be obtained from the CCDC free of charge CCDC 2128169 from the Cambridge Crystallographic Data Centre [40].

Compound **3c**

Compound **2c** (300 mg, 0.360 mmol) and malononitrile (100 mg, 1.08 mmol) were dissolved in anhydrous chlorobenzene (6 mL). To the dark blue mixture titanium tetrachloride (120 µL, 1.08 mmol) and pyridine (170 µL, 2.16 mmol) were added and the mixture was stirred under reflux overnight. After cooling the reaction mixture to room temperature, it was poured into ice-water (50 mL) and extracted with dichloromethane (3 × 20 mL). The combined organic extracts were dried over $MgSO_4$, filtered and concentrated under reduced pressure. The crude product was purified by silica column chromatography (SiO_2, CH_2Cl_2/diethyl ether 98:2) to give the title compound as a dark solid (120 mg, 36%). Mp 241–242 °C; ^{1}H NMR (400 MHz, $CDCl_3$) δ 8.60 (d, J = 8.2 Hz, 2H), 8.48 (d, J = 8.1 Hz, 2H), 8.35 (d, J = 8.0 Hz, 2H), 8.30 (d, J = 8.3 Hz, 2H), 8.24 (s, 2H), 7.78 (t, J = 7.3 Hz, 2H), 7.57 (t, J = 7.7 Hz, 2H), 4.34 (s, 4H), 1.98–1.86 (m, 4H), 1.49–1.18 (m, 36H), 0.87 (t, J = 6.9 Hz, 6H); ^{13}C NMR (100 MHz, $CDCl_3$) δ 183.2, 156.4, 135.6, 134.5, 133.2, 131.1, 129.5, 128.6, 128.3, 127.8, 127.5, 127.2, 123.7, 123.2, 122.8, 117.3, 113.6, 69.8, 63.2, 32.9, 32.0, 29.9, 29.7, 29.5, 29.4, 26.2, 25.8, 22.8, 14.2; ASAP–HRMS (m/z): $[M + H]^+$ calcd for $C_{64}H_{65}N_4O_2$, 921.5107; found, 921.5108.

Supporting Information

Supporting Information File 1

NMR spectra of compounds, crystallographic informnation and OFET plots.
[https://www.beilstein-journals.org/bjoc/content/supplementary/1860-5397-20-244-S1.pdf]

Acknowledgements

We acknowledge EPSRC UK National Mass Spectrometry Facility at Swansea University and EPSRC UK National Crystallography Service.

Funding

Sondos Abdullah J. Almahmoud acknowledges the Ministry of Education and Imam Mohammad Ibn Saud Islamic University (IMSIU) in Saudi Arabia for the funding and support. Graeme Cooke thanks the Leverhulme Trust for a Research Fellowship. Joseph Cameron and Peter J. Skabara thank the Engineering and Physical Sciences Research Council (EPSRC) for funding (EP/R03480X/1).

ORCID® iDs

Sondos A. J. Almahmoud - https://orcid.org/0000-0003-4941-7192
Joseph Cameron - https://orcid.org/0000-0001-8622-8353
Dylan Wilkinson - https://orcid.org/0009-0001-4690-6938
Claire Wilson - https://orcid.org/0000-0002-0090-5374
Peter J. Skabara - https://orcid.org/0000-0001-7319-0464
Graeme Cooke - https://orcid.org/0000-0003-0890-5720

Data Availability Statement

Data generated and analysed during this study is available from the corresponding author upon reasonable request.

References

1. Sun, Y.; Liu, Y.; Zhu, D. *J. Mater. Chem.* **2005,** *15,* 53–65. doi:10.1039/b411245h
2. Wakayama, Y.; Hayakawa, R.; Seo, H.-S. *Sci. Technol. Adv. Mater.* **2014,** *15,* 024202. doi:10.1088/1468-6996/15/2/024202
3. Zou, S.-J.; Shen, Y.; Xie, F.-M.; Chen, J.-D.; Li, Y.-Q.; Tang, J.-X. *Mater. Chem. Front.* **2020,** *4,* 788–820. doi:10.1039/c9qm00716d
4. Spanggaard, H.; Krebs, F. C. *Sol. Energy Mater. Sol. Cells* **2004,** *83,* 125–146. doi:10.1016/j.solmat.2004.02.021
5. Liu, S.; Yuan, J.; Deng, W.; Luo, M.; Xie, Y.; Liang, Q.; Zou, Y.; He, Z.; Wu, H.; Cao, Y. *Nat. Photonics* **2020,** *14,* 300–305. doi:10.1038/s41566-019-0573-5
6. Hong, L.; Yao, H.; Cui, Y.; Ge, Z.; Hou, J. *APL Mater.* **2020,** *8,* 120901. doi:10.1063/5.0027948
7. Bashir, A.; Heck, A.; Narita, A.; Feng, X.; Nefedov, A.; Rohwerder, M.; Müllen, K.; Elstner, M.; Wöll, C. *Phys. Chem. Chem. Phys.* **2015,** *17,* 21988–21996. doi:10.1039/c5cp03171k
8. Bronstein, H.; Nielsen, C. B.; Schroeder, B. C.; McCulloch, I. *Nat. Rev. Chem.* **2020,** *4,* 66–77. doi:10.1038/s41570-019-0152-9
9. Dalton, L. R.; Sun, S. S. *Introduction to Organic Electronic and Optoelectronic Materials and Devices,* 2nd ed.; CRC Press: Boca Raton, FL, USA, 2016. doi:10.1201/9781315374185
10. Wu, J.-L.; Lee, Y.-T.; Chen, C.-T.; Chen, C.-T. *J. Chin. Chem. Soc.* **2018,** *65,* 87–106. doi:10.1002/jccs.201700244
11. Cui, Y.; Yao, H.; Hong, L.; Zhang, T.; Tang, Y.; Lin, B.; Xian, K.; Gao, B.; An, C.; Bi, P.; Ma, W.; Hou, J. *Natl. Sci. Rev.* **2020,** *7,* 1239–1246. doi:10.1093/nsr/nwz200
12. Wadsworth, A.; Moser, M.; Marks, A.; Little, M. S.; Gasparini, N.; Brabec, C. J.; Baran, D.; McCulloch, I. *Chem. Soc. Rev.* **2019,** *48,* 1596–1625. doi:10.1039/c7cs00892a
13. Tatemichi, S.; Ichikawa, M.; Koyama, T.; Taniguchi, Y. *Appl. Phys. Lett.* **2006,** *89,* 112108. doi:10.1063/1.2349290
14. Briseno, A. L.; Mannsfeld, S. C. B.; Reese, C.; Hancock, J. M.; Xiong, Y.; Jenekhe, S. A.; Bao, Z.; Xia, Y. *Nano Lett.* **2007,** *7,* 2847–2853. doi:10.1021/nl071495u
15. Chesterfield, R. J.; McKeen, J. C.; Newman, C. R.; Frisbie, C. D.; Ewbank, P. C.; Mann, K. R.; Miller, L. L. *J. Appl. Phys.* **2004,** *95,* 6396–6405. doi:10.1063/1.1710729
16. Struijk, C. W.; Sieval, A. B.; Dakhorst, J. E. J.; van Dijk, M.; Kimkes, P.; Koehorst, R. B. M.; Donker, H.; Schaafsma, T. J.; Picken, S. J.; van de Craats, A. M.; Warman, J. M.; Zuilhof, H.; Sudhölter, E. J. R. *J. Am. Chem. Soc.* **2000,** *122,* 11057–11066. doi:10.1021/ja000991g
17. Malenfant, P. R. L.; Dimitrakopoulos, C. D.; Gelorme, J. D.; Kosbar, L. L.; Graham, T. O.; Curioni, A.; Andreoni, W. *Appl. Phys. Lett.* **2002,** *80,* 2517–2519. doi:10.1063/1.1467706

18. May, F.; Marcon, V.; Hansen, M. R.; Grozema, F.; Andrienko, D. *J. Mater. Chem.* **2011,** *21,* 9538–9545. doi:10.1039/c1jm10500k
19. Kim, Y.-J.; Lee, Y.; Park, K.; Ahn, C. W.; Jung, H.-T.; Jeon, H.-J. *J. Phys. Chem. Lett.* **2020,** *11,* 3934–3940. doi:10.1021/acs.jpclett.0c01226
20. You, C.-C.; Würthner, F. *J. Am. Chem. Soc.* **2003,** *125,* 9716–9725. doi:10.1021/ja029648x
21. Tahir, M.; Sayyad, M. H.; Wahab, F.; Aziz, F.; Shahid, M.; Munawar, M. A. *Phys. B (Amsterdam, Neth.)* **2013,** *426,* 6–12. doi:10.1016/j.physb.2013.05.009
22. Che, Y.; Datar, A.; Balakrishnan, K.; Zang, L. *J. Am. Chem. Soc.* **2007,** *129,* 7234–7235. doi:10.1021/ja071903w
23. Nolde, F.; Pisula, W.; Müller, S.; Kohl, C.; Müllen, K. *Chem. Mater.* **2006,** *18,* 3715–3725. doi:10.1021/cm060742c
24. Chen, Z.; Stepanenko, V.; Dehm, V.; Prins, P.; Siebbeles, L. D. A.; Seibt, J.; Marquetand, P.; Engel, V.; Würthner, F. *Chem. – Eur. J.* **2007,** *13,* 436–449. doi:10.1002/chem.200600889
25. Würthner, F. *Chem. Commun.* **2004,** 1564–1579. doi:10.1039/b401630k
26. Shi, M.-M.; Chen, Y.; Nan, Y.-X.; Ling, J.; Zuo, L.-J.; Qiu, W.-M.; Wang, M.; Chen, H.-Z. *J. Phys. Chem. B* **2011,** *115,* 618–623. doi:10.1021/jp109683h
27. Akamatu, H.; Inokuchi, H. *J. Chem. Phys.* **1950,** *18,* 810–811. doi:10.1063/1.1747780
28. Inokuchi, H. *Bull. Chem. Soc. Jpn.* **1955,** *28,* 570–572. doi:10.1246/bcsj.28.570
29. Kakuichi, M.; Kasatani, K.; Morita, Y. *Trans. Mater. Res. Soc. Jpn.* **2012,** *37,* 471–474. doi:10.14723/tmrsj.37.471
30. Shi, M.; Hao, F.; Zuo, L.; Chen, Y.; Nan, Y.; Chen, H. *Dyes Pigm.* **2012,** *95,* 377–383. doi:10.1016/j.dyepig.2012.05.003
31. Vivo, P.; Vuorinen, T.; Chukharev, V.; Tolkki, A.; Kaunisto, K.; Ihalainen, P.; Peltonen, J.; Lemmetyinen, H. *J. Phys. Chem. C* **2010,** *114,* 8559–8567. doi:10.1021/jp1009862
32. Liu, B.; Fan, D.; Zhang, Q.; Chen, Y.; Zhu, W. *Front. Chem. China* **2010,** *5,* 200–207. doi:10.1007/s11458-010-0115-7
33. Bureš, F.; Schweizer, W. B.; Boudon, C.; Gisselbrecht, J.-P.; Gross, M.; Diederich, F. *Eur. J. Org. Chem.* **2008,** 994–1004. doi:10.1002/ejoc.200700970
34. Patil, Y.; Misra, R. *Chem. Rec.* **2018,** *18,* 1350–1364. doi:10.1002/tcr.201800037
35. He, Y.; Li, Y. *Phys. Chem. Chem. Phys.* **2011,** *13,* 1970–1983. doi:10.1039/c0cp01178a
36. Lei, T.; Dou, J.-H.; Pei, J. *Adv. Mater. (Weinheim, Ger.)* **2012,** *24,* 6457–6461. doi:10.1002/adma.201202689
37. Sheldrick, G. M. *Acta Crystallogr., Sect. A: Found. Adv.* **2015,** *71,* 3–8. doi:10.1107/s2053273314026370
38. Sheldrick, G. M. *Acta Crystallogr., Sect. C: Struct. Chem.* **2015,** *71,* 3–8. doi:10.1107/s2053229614024218
39. Dolomanov, O. V.; Bourhis, L. J.; Gildea, R. J.; Howard, J. A. K.; Puschmann, H. *J. Appl. Crystallogr.* **2009,** *42,* 339–341. doi:10.1107/s0021889808042726
40. The Cambridge crystallographic data centre webpage. https://www.ccdc.cam.ac.uk (accessed Oct 18, 2024).

License and Terms

BEILSTEIN JOURNAL OF ORGANIC CHEMISTRY

Tunable full-color dual-state (solution and solid) emission of push–pull molecules containing the 1-pyrindane moiety

Anastasia I. Ershova, Sergey V. Fedoseev, Konstantin V. Lipin, Mikhail Yu. Ievlev, Oleg E. Nasakin and Oleg V. Ershov*

Full Research Paper

Open Access

Address:
Chuvash State University named after I.N. Ulyanov, Moskovsky pr., 15, Cheboksary, Russia

Email:
Oleg V. Ershov* - oleg.ershov@mail.ru

* Corresponding author

Keywords:
dual-state emission; full-color emission; nitriles; push–pull molecules; pyrindane; stilbazole

Beilstein J. Org. Chem. **2024,** *20,* 3016–3025.
https://doi.org/10.3762/bjoc.20.251

Received: 08 August 2024
Accepted: 04 November 2024
Published: 19 November 2024

This article is part of the thematic issue "π-Conjugated molecules and materials".

Guest Editor: A. Mateo-Alonso

Abstract

A facile method for the synthesis of arylidene derivatives of pyrindane – (*E*)-7-arylmethylene-2-chloro-6,7-dihydro-5*H*-cyclopenta[*b*]pyridine-3,4-dicarbonitriles – was developed. Tunable full-color emission was achieved for the synthesized push–pull molecules, solely by changing donor groups while keeping both the conjugated system and acceptor part of the molecule unchanged. This represents a rare approach for the design of such fluorophores. Arylidene derivatives of pyrindane were found to be efficient fluorescent dyes showing a moderate to high emission quantum yield. The push–pull molecules were also characterized by a dual-state emission (in solution and in the solid state). Emission maxima ranged from 469 to 721 nm in solution depending on the solvent and type of donor substituent, and from 493 to 767 nm in the solid state. For the arylidene derivative of pyrindane with a dimethylamino group, it was shown that fluorescence can be changed by the action of an acid both in solution and in the solid state.

Introduction

Over the past decades, heteroaromatic push–pull molecules have attracted great attention due to their widespread use in materials chemistry. This type of chromophores is of particular interest in the fields of organic electronics, photonics, and optoelectronics due to their unique optical and electronic properties [1-13]. Among heteroaromatic push–pull molecules, stilbazole derivatives (pyridostilbenes, azastilbenes, styrylpyridines or azinylarylethenes) are an important class. Uniquely, stilbazole provides a universal framework (exclusive matrix) for the design of donor–π–acceptor (D–π–A) molecules [14,15]. It has a branched π-conjugated system, in which the aromatic ring acts as a donor and pyridine as an acceptor. The introduction of additional substituents to stilbazole makes it possible to change the optical properties of this molecular framework within a

wide range [16-19]. This approach has found many applications in the synthesis of compounds that are used in various optical materials [14,20-33]. For example, organic π-systems whose main structural unit is stilbazole are used as active compounds in organic light-emitting diodes (OLEDs) [20], dye-sensitized solar cells (DSSCs) [21], nonlinear optics (NLO) materials [22,23], positron emission tomography (PET) imaging [24], fluorescent probes and labels [25-27] detecting H_2S in foodstuff, water, and living cells [28], Fe^{3+} ions [29], Hg^{2+} ions [30], and cyanide anions [31], for acid–base vapor sensing [32], and as candidate material for photonics devices, optical switches, and optical power limiting applications [33].

Materials with tunable full-color emission based on small organic molecules have attracted attention due to their great potential for applications [34-44]. These compounds provide unique benefits due to their flexibility, high efficiency, and versatility, making them essential for modern high-tech applications. Despite the wide variety of known push–pull molecules, the number of fluorescent cores with synthetic potential for tuning the emission wavelength to achieve a full-emission spectrum is limited. Typically, full-color fluorescence of organic molecules is achieved by extending π-conjugated systems or by introducing combinations of donor and acceptor groups, which changes the electronic properties and consequently the emission spectra [35-44]. This approach is synthetically challenging since it requires optimization of the reaction conditions for each modification step of the conjugated system. In this work, full-color fluorescence has been achieved solely by changing the donor groups, while the conjugated system and the multiacceptor part of the molecule were left unchanged, which is a rare approach for such fluorophores.

Another rare phenomenon for push–pull molecules is dual-state emission (DSE) [45-47]. At the same time, the scope of applications of fluorophores exhibiting DSE is much wider. This is due to the fact that DSE molecules, after absorbing energy, are able to emit in two different states (solution and solid state). This makes them more versatile and allows them to be used for the creation of fluorescent materials with different characteristics. Molecules exhibiting DSE are required to have certain structural features. First, they often contain donor and acceptor groups arranged in a specific sequence, such as in D–π–A chromophores. This creates the conditions for efficient intramolecular charge transfer (ICT), which plays a key role in the DSE phenomenon. Also, additional substituents can affect the geometry and conformation of the molecule, which may be important for the manifestation of the DSE phenomenon [45,46].

Previously, we have reported the synthesis of stilbazoles **A** (Figure 1) [17]. In the present work, we developed a method for the synthesis of a rare class of compounds: arylidene derivatives of pyrindane **1** with conformational rigidity along the C–C bond between the heterocycle and ethene bridge due to the fused cyclic fragment. As a consequence of the additional ring, the fluorescence efficiency increased. At the same time, solid-state emission was observed due to the steric hindrance, which prevented intermolecular interactions in the nonplanar pyrindanes **1**. The obtained compounds **1**, having a 2-chloropyridine-3,4-dicarbonitrile moiety, contained easily modifiable functional groups [48-55]. This qualified compounds **1** as promising building blocks for diversity-oriented synthesis [56,57] and for the facile preparation of molecular libraries with an emphasis on skeletal diversity for the development of new push–pull molecules.

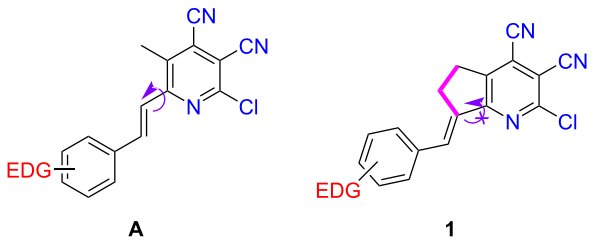

Figure 1: Structure of previously synthesized stilbazoles **A** and arylidene derivatives of pyrindane **1** reported herein.

Results and Discussion

Synthesis and structure determination

A two-step procedure was used to obtain the target compounds (Scheme 1). Cyclopenta[*b*]pyridine derivative **2** [58] was prepared in the first step via three-component reaction between tetracyanoethylene, cyclopentanone, and hydrogen chloride. Then, multiacceptor compound **2** was involved in the condensation with aromatic aldehydes bearing electron-donor groups. As a result, a series of new push–pull molecules containing various numbers of substituents at the donor site, which differed in their electron-donating strength, was obtained.

It was found that the reaction of pyridine **2** with aromatic aldehydes occurred with complete stereoselectivity – only the *E*-isomer was obtained as the reaction product. The configuration of the double bond was confirmed using ^{1}H,^{1}H-NOESY spectroscopy. As shown in Figure 2, a correlation between protons of the allyl moiety and the aryl substituent evidenced their spatial proximity in molecule **1c**. The absence of a correlation between allyl and vinyl protons additionally supported the *E*-configuration.

Spectral–luminescence properties

Compounds **1** form colored crystals, from pale-yellow (i.e., **1a**) to almost black (i.e., **1h**). They are soluble and luminescent in

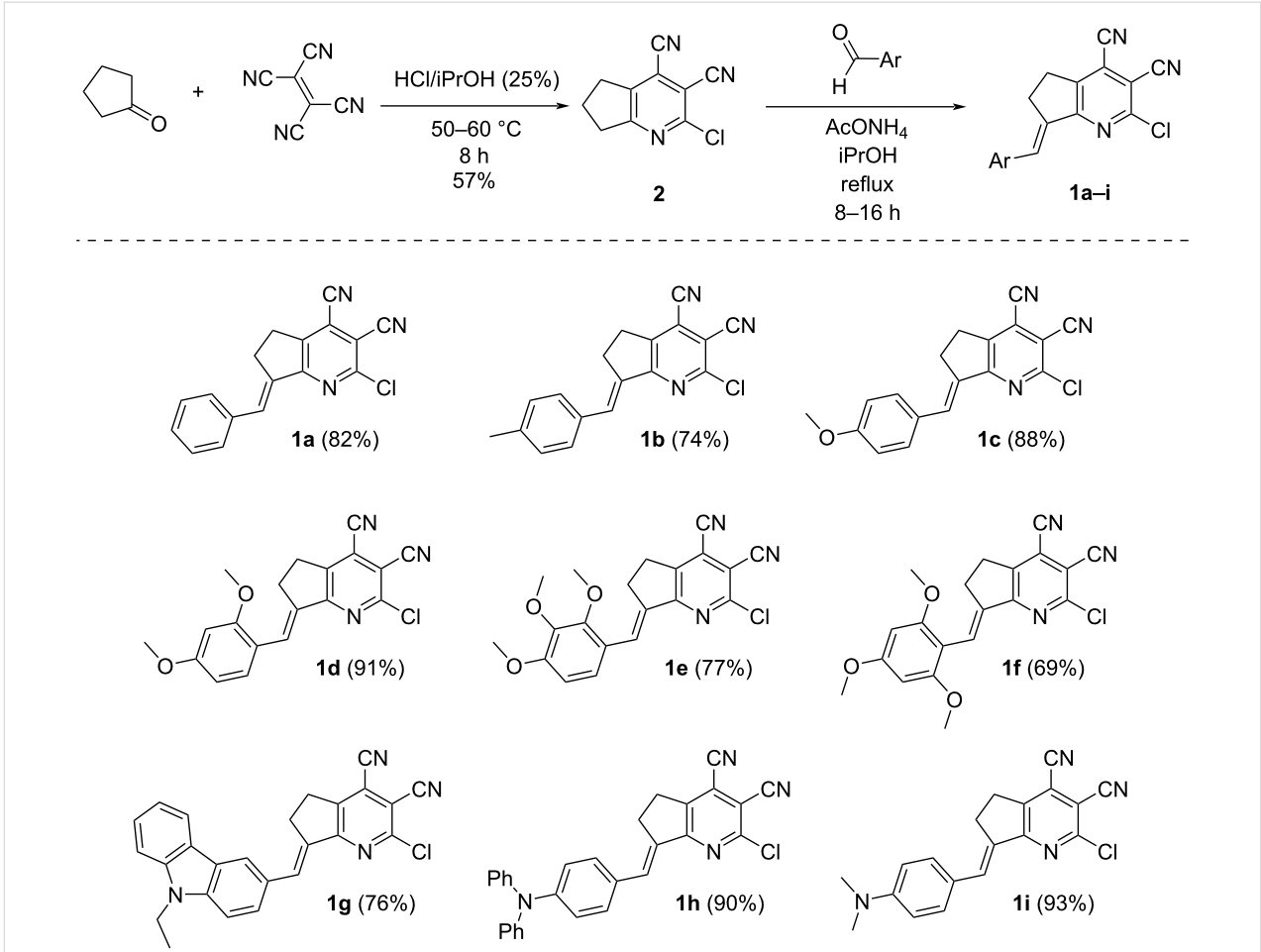

Scheme 1: Synthesis of donor–acceptor 1-pyrindane derivatives **1**.

most common organic solvents. Solvatochromism of stilbazole **1c**, containing a *para*-methoxy group, was studied first (see Table S1 and Figure S1, Supporting Information File 1). The electronic absorption spectra were characterized by a pronounced maximum in the visible region centered at 431–448 nm. Emission maxima of compound **1c** were more significantly affected by the change of polarity and ranged from 475 nm (blue-green) in tetrachloromethane (CTC) to 588 nm (orange) in formic acid. Therefore, it was found that compound **1c** was characterized by a large Stokes shift upon increasing the solvent polarity, which reached 150 nm (5824 cm^{-1}) in formic acid. This was associated with the bathochromic shift of the emission band, indicating that the more polar singlet excited state (S_1) was much better stabilized by polar solvents than the ground state (S_0). The highest fluorescence quantum yield of about 87% was observed in toluene.

Then, the solvatochromic properties of stilbazole **1i**, bearing a stronger electron-donating dimethylamino group, were studied (Table 1 and Figure 3). It was found that in most solvents, compound **1i** was characterized by a single pronounced absorption maximum in the range of 503–525 nm that red-shifted upon increasing the solvent polarity. In formic acid, due to the protonation of the dimethylamino group, a strong blue shift occurred down to 394 nm. The only exception was a solution of **1i** in acetic acid, where two peaks were observed. Apparently, the weaker acetic acid caused just a partial protonation of the amino group, and the equilibrium shown in Scheme 2 was observed. This was evidenced by two observed absorption maxima: the first almost coincided with the corresponding maximum of the solution in formic acid, and the second one was in the same region as with other aprotic solvents.

The emission maxima of stilbazole **1i** were within a very wide range of 264 nm and covered almost the entire visible region of the spectrum (from blue to red, Figure 3B and Figure 4). Acidic solutions were the most blue-shifted due to the formation of the protonated form **1i**H^+ (Scheme 2). Two emission maxima were observed in acetic acid and associated with the corresponding absorption maxima. The first, located at 467 nm (excitation at

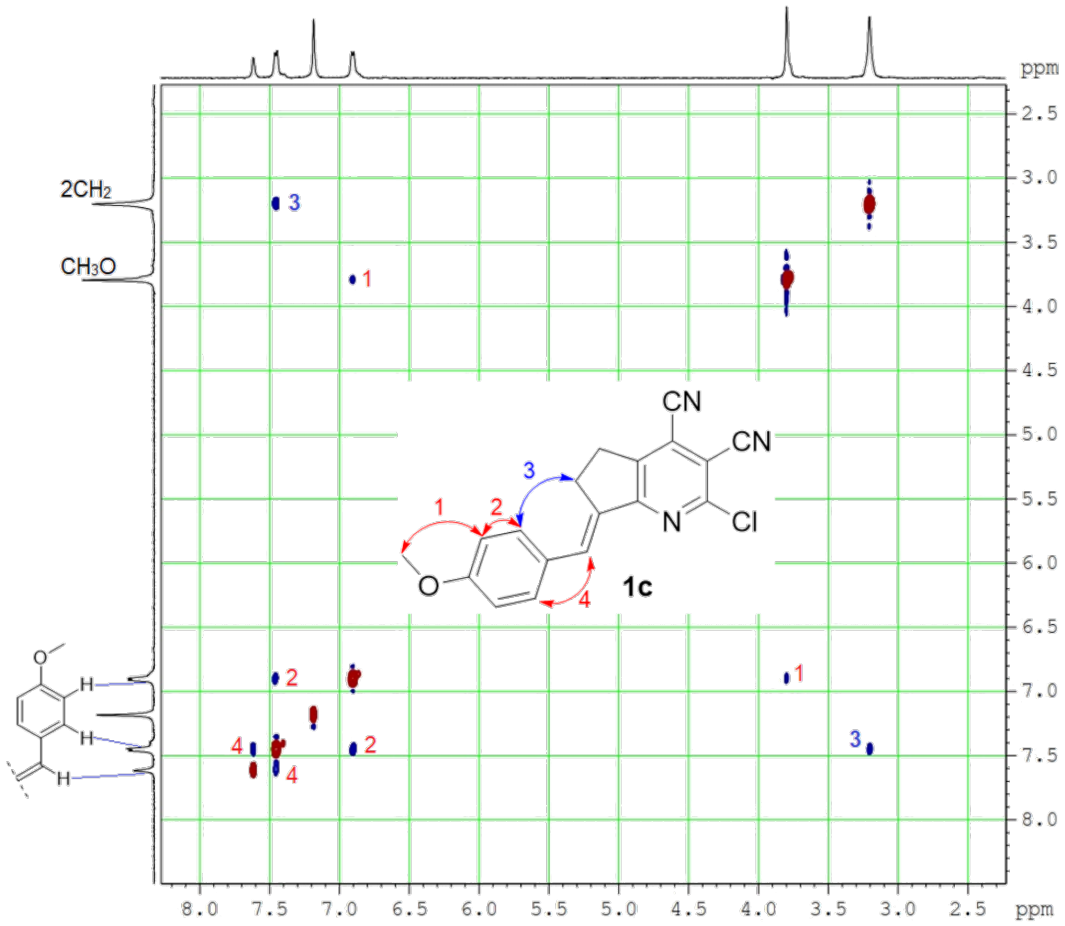

Figure 2: ^{1}H,^{1}H-NOESY spectrum of compound **1c** in DMSO-d_6.

Table 1: Solvatochromic properties of compound **1i**.

solvent	λ_{abs}, nm[a]	ε, $M^{-1}\cdot cm^{-1}$	λ_{em}, nm[b]	Stokes shift		Φ_{em}, %[c]
				nm	cm^{-1}	
CCl_4 (CTC)	515	31000	554	39	1367	73.9
PhMe	510	36700	598	88	2885	49.5
1,4-dioxane	503	39400	614	111	3594	27.4
DCM	526	44400	656	130	3768	4.9
AcOEt	505	39900	651	146	4441	3.0
MeCN	510	40200	710	200	5523	0.7
DMSO	525	34900	721	196	5178	0.9
AcOH	389	19700	467	78	4294	24.6[d]
	511	10100	662	151	4464	1.8
HCOOH	394	28200	486	92	4805	30.9[d]
MeOH	510	—[e]	691	181	5136	0.1

[a]Absorption maxima were recorded in solution ($c = 10^{-5}$ M). [b]Emission maxima were recorded in solution ($c = 10^{-5}$ M, absorption maxima were used for excitation. [c]Relative emission quantum yield was estimated using a solution of rhodamine 6G in ethanol (Φ_{em} = 0.95 at 450 nm). [d]Relative emission quantum yield was estimated using a solution of 7-hydroxy-4-methylcoumarin in phosphate buffer at pH 10 (Φ_{em} = 0.7 at 330 nm). [e]Poorly soluble sample.

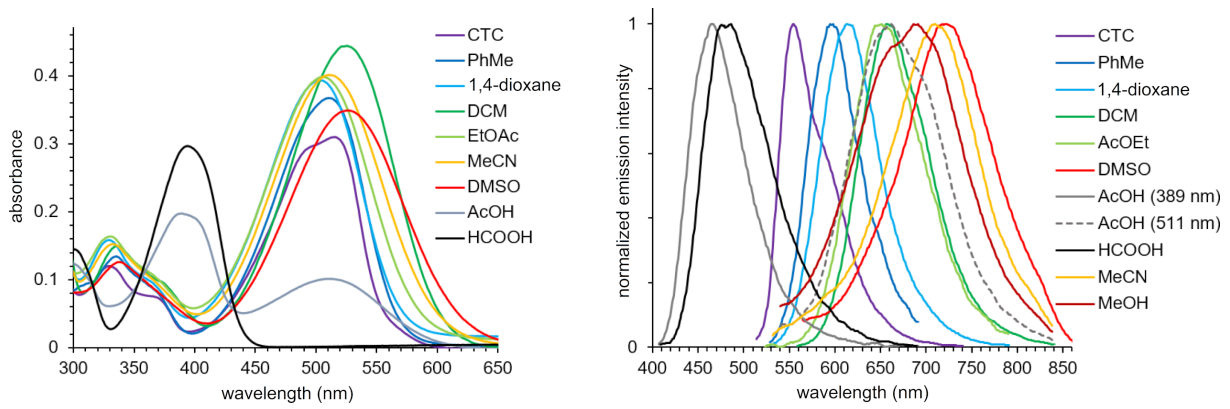

Figure 3: Absorption (left) and normalized emission spectra (right) of compound **1i** in various solvents (c = 10^{-5} M).

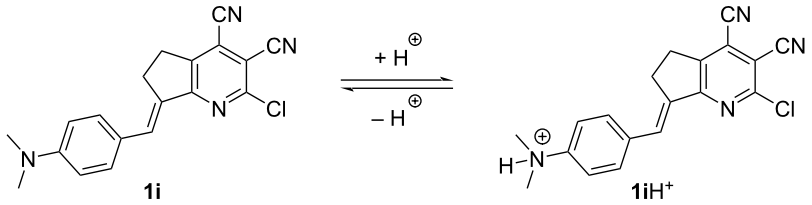

Scheme 2: Plausible equilibrium of compounds **1i** and **1i**H$^+$ in acidic solution.

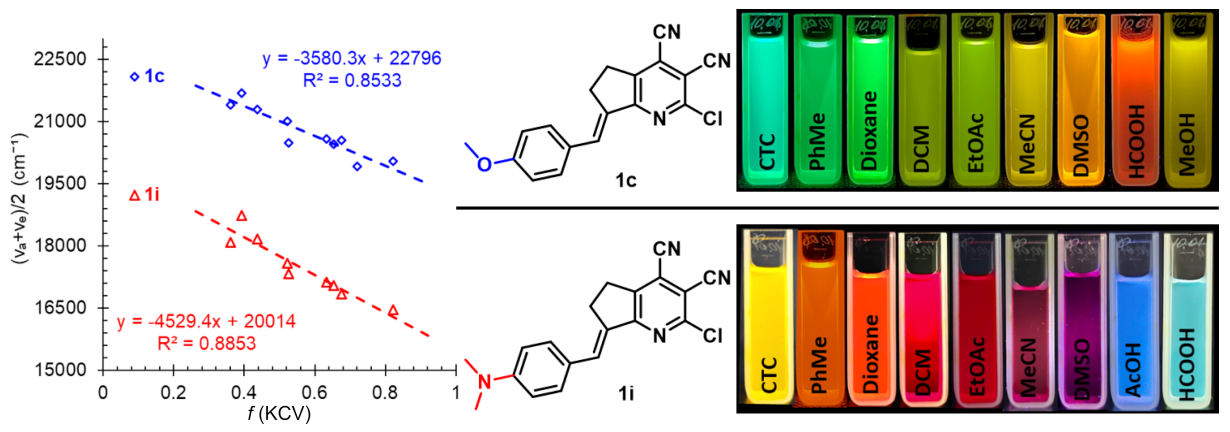

Figure 4: Solvatochromic behavior of compounds **1c** and **1i**: plots of arithmetic mean of emission/absorption wavenumbers vs Kawsk–Chamma–Viallet polarity function (left) and photos of fluorescent solutions in various solvents taken under a 365 nm UV lamp (right).

389 nm) was assigned to the formed **1i**H$^+$ cation. This band showed a blue shift of 19 nm relative to formic acid due to the lower polarity of acetic acid. At the same time, the second band was assigned to the molecular form **1i** (Scheme 2) and observed at 662 nm (excitation at 511 nm), in the region of solvents with medium polarity. Protonation of the dimethylamino group was additionally confirmed by titration of pyrindane **1i** in toluene using trifluoroacetic acid (see Figure S2, Supporting Information File 1). According to the data obtained, an increasing amount of acid caused a blue shift of the maximum at 511 nm, and a new maximum in the region of 380–400 nm appeared in the absorption spectra. The intensity of the short-wavelength band also increased upon addition of trifluoroacetic acid. At the same time, a second band centered at 440 nm also appeared in the emission spectra. Additional evidence for protonation of the dimethylamino group in **1i**H$^+$ (Scheme 2), rather

than the pyridine fragment, was the solvatochromic behavior of compound **1c** (see Table S1, Supporting Information File 1). The solutions in AcOH and HCOOH did not show a strong blue shift since protonation did not occur. In these solvents, a classical pattern for the bathochromic emission shift was observed upon increasing the solvent polarity.

Generally, both stilbazoles **1c** and **1i** were characterized by solvatochromic behavior typical for molecules showing an ICT. A significant long-wavelength shift of the emission band was observed upon increasing the solvent polarity from carbon tetrachloride to DMSO, and the strongest fluorescence was registered in nonpolar medium (Φ_{em} = 87.5 % for compound **1c** in toluene and Φ_{em} = 73.9% for compound **1i** in CCl_4). Slopes of the Lippert–Mataga plots (Figures S3 and S4, Supporting Information File 1) and the Kawski–Chamma–Viallet plots [59,60] (Figure 4, see Supporting Information File 1 for details) showed good linearity. This also indicated that the excited-state dipole moment of the molecules was much higher than that in the ground state. This phenomenon was even more pronounced for compound **1i** than for **1c** due to presence of the stronger electron-donating group.

Then, the substituent effects on the spectral properties of stilbazoles **1a**–**i** were studied in two different solvents: nonpolar toluene (Table 2) and highly polar DMSO (Table 3). The absorption maxima of compounds **1a**–**i** were in the range of 402–510 nm (Figure 5, left). The most blue-shifted absorbance was observed for stilbazole **1a**, bearing no conjugated donor groups. Depending on their number and donor strength, the

Table 2: Photophysical properties of stilbazoles **1** in toluene.

compound	λ_{abs}, nm[a]	ε, $M^{-1}\cdot cm^{-1}$	λ_{em}, nm[b]	Stokes shift		Φ_{em}, %[c]
				nm	cm^{-1}	
1a	402	13100	459	57	3089	32.9[d]
1b	411	23500	470	59	3054	12.2[d]
1c	443	22900	500	57	2573	87.5
1d	454	13600	520	66	2796	35.8
1e	444	26300	511	68	2953	43.2
1f	444	11800	531	87	3690	7.7
1g	485	18300	544	59	2236	53.1
1h	509	29400	582	73	2464	55.2
1i	510	36700	598	88	2885	49.5

[a]Absorption maxima were recorded in solution ($c = 10^{-5}$ M). [b]Emission maxima were recorded in solution ($c = 10^{-5}$ M, absorption maxima were used for excitation). [c]Relative emission quantum yield was estimated using a solution of rhodamine 6G in ethanol (Φ_{em} = 0.95 at 450 nm). [d]Relative emission quantum yield was estimated using a solution of fluorescein in a 0.01 M KOH solution in ethanol (Φ_{em} = 0.97 at 425 nm).

Table 3: Photophysical properties of stilbazoles **1** in DMSO.

compound	λ_{abs}, nm[a]	ε, $M^{-1}\cdot cm^{-1}$	λ_{em}, nm[b]	Stokes shift		Φ_{em}, %[c]
				nm	cm^{-1}	
1a	409	25600	506	97	4687	12.3[d]
1b	419	26300	528	109	4927	53.4[d]
1c	439	26400	578	139	5478	48.4
1d	460	22100	602	142	5128	20.5
1e	442	28800	596	154	5846	2.0
1f	453	17100	609	156	5655	5.1
1g	483	33000	649	166	5296	1.5
1h	505	31000	712	207	5757	0.2
1i	525	34900	721	196	5178	0.6

[a]Absorption maxima were recorded in solution ($c = 10^{-5}$ M). [b]Emission maxima were recorded in solution ($c = 10^{-5}$ M, absorption maxima were used for excitation. [c]Relative emission quantum yield was estimated using a solution of rhodamine 6G in ethanol (Φ_{em} = 0.95 at 450 nm). [d]Relative emission quantum yield was estimated using a solution of fluorescein in a 0.01 M KOH solution in ethanol (Φ_{em} = 0.97 at 425 nm).

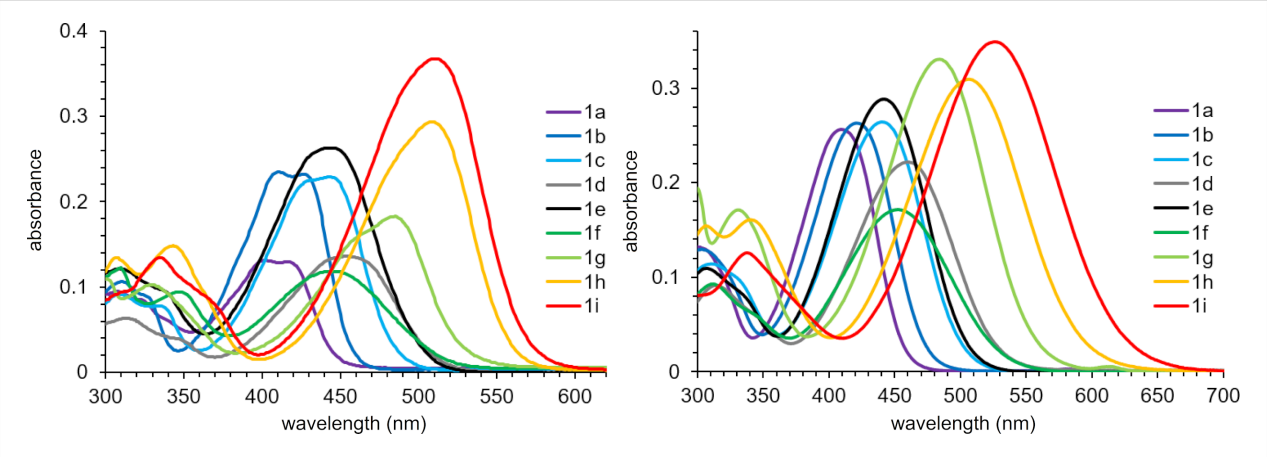

Figure 5: Absorption spectra of compounds **1a–i** in toluene (left) and DMSO (right, $c = 10^{-5}$ M).

introduction of electron-donating substituents led to a bathochromic shift. The only exceptions were compounds **1e** and **1f**, containing three methoxy groups. In these cases, a blue shift of the absorption band in comparison to the disubstituted derivative **1d** was observed, which was apparently caused by a partial planarity violation due to steric hindrance. In DMSO, the absorption maxima of compounds **1a–i** were bathochromically shifted to 409–525 nm (Figure 5, right) and showed similar behavior to that described above.

The photoluminescence spectra of stilbazoles **1a–i** in toluene were characterized by a maximum in the range of 459–598 nm (Figure 6, left), associated with an emission color from blue to orange (Figure 7, top). The most blue-shifted emission was observed for stilbazole **1a** without additional substituents. The introduction of an electron-donating group led to a red shift of the emission in accordance with increasing donor strength and number of substituents. Stilbazoles **1** in toluene were characterized by a high fluorescence quantum yield, reaching 87.5% for the *para*-methoxy-substituted derivative **1c**. Emission maxima in DMSO were found to be in the range of 506–721 nm (Figure 6, right), associated with a fluorescence color from green to red (Figure 7, bottom). The highest fluorescence efficiency of 53.4% was observed for the *para*-methyl derivative **1b**. Solutions of stilbazoles **1** in DMSO were also characterized by large Stokes shift values, reaching 207 nm (5846 cm^{-1}) and showing nonradiative loss of excitation energy.

It should be noted that stilbazoles **1**, in contrast to related compounds **A** (Figure 1), were characterized by solid-state emission (Table 4 and Figure 8). This was apparently caused by the presence of the dimethylene bridge, preventing intermolecular interactions. Emission maxima of compounds **1** ranged from 540–767 nm, namely from the green to the near-infrared region of the spectrum. The highest intensity was observed for stilbazole **1a**, bearing no donor groups. The emission intensity de-

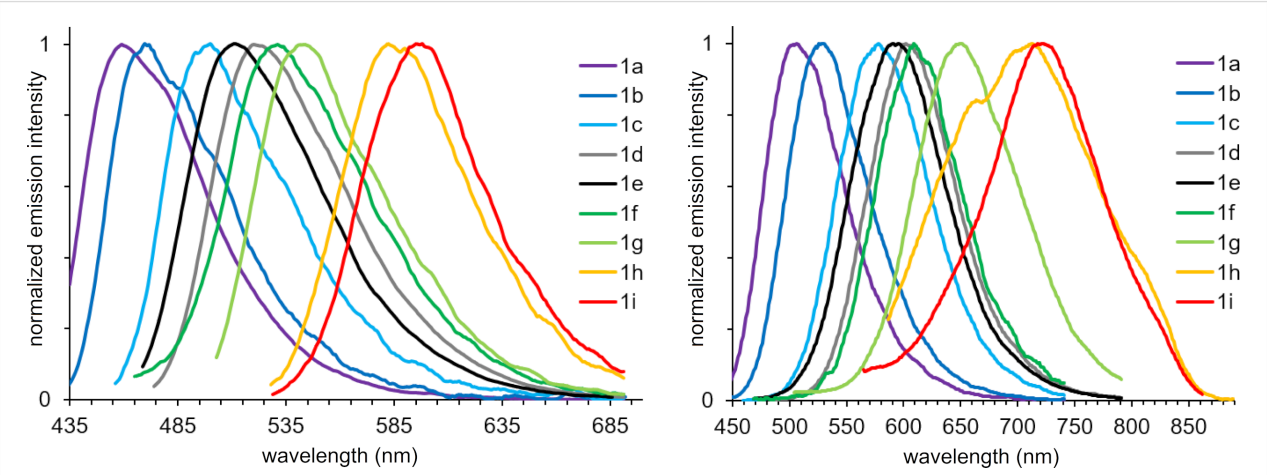

Figure 6: Normalized emission spectra of compounds **1a–i** in toluene (left) and DMSO (right, $c = 10^{-5}$ M).

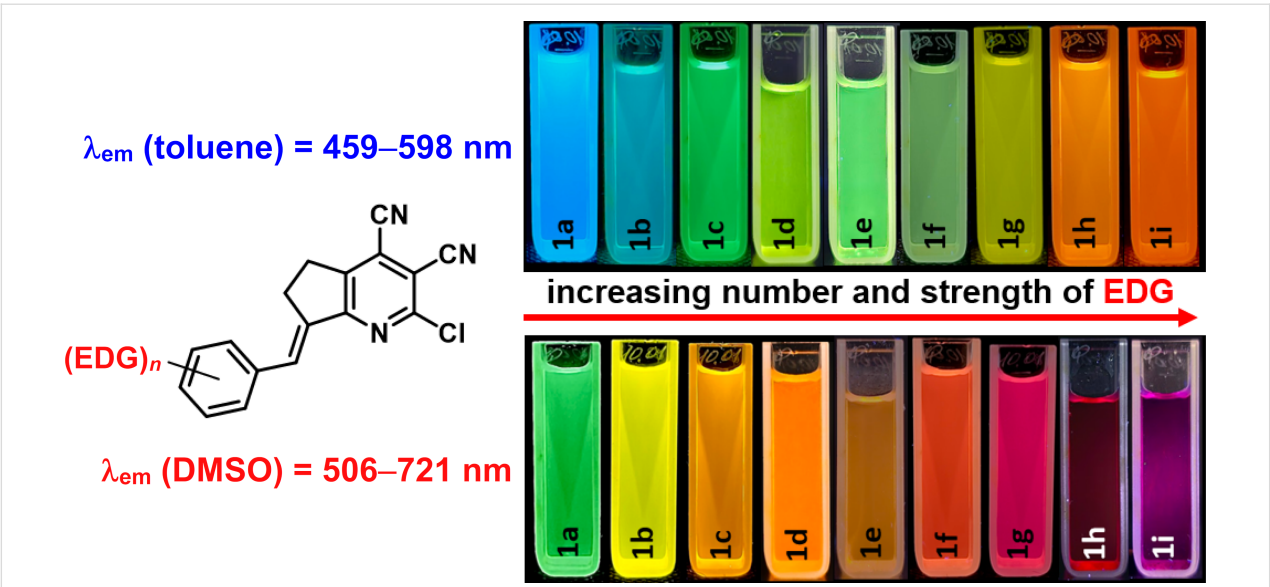

Figure 7: Photos of fluorescent solutions of compounds **1a–i** in toluene (top) and DMSO (bottom) taken under a 365 nm UV lamp.

Table 4: Solid-state photoluminescence of stilbazoles **1**.

compound	λ_{em}, nm	emission intensity, a.u.[a]
1a	540	798
1b	573	391
1c	641	139
1d	629	127
1e	596	202
1f	596	142
1g	631	77
1h	795	31
1i	762	12
1iH^+	493	322

[a]Emission intensity is given in arbitrary units (a.u.) of the Cary Eclipse fluorescence spectrometer, see Supporting Information File 1 for details.

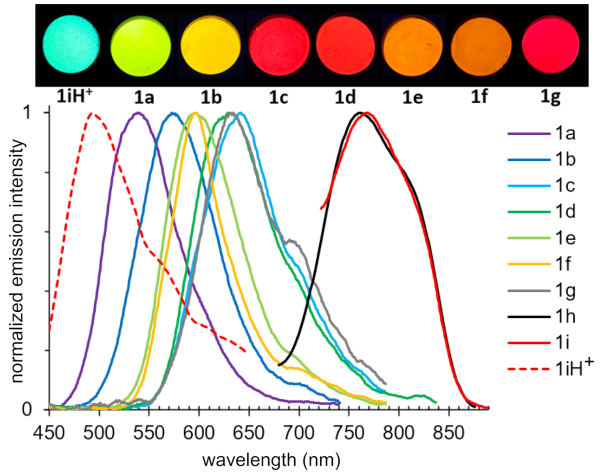

Figure 8: Normalized solid-state emission spectra of compounds **1a–i** (bottom) and photos of powders taken under a 365 nm UV lamp (top).

creased upon increasing the donor strength of the substituent. As shown in Scheme 2 and according to the fluorescence spectra recorded in acidic solutions, compound **1i** could form the salt **1i**H^+. Therefore, the effect of acid vapors on the solid-state emission was studied. It was found that pyrindane **1i** was sensitive to formic and trifluoroacetic acid vapors. As a result of protonation, a significant blue shift of the emission maximum from 762 nm down to 493 nm was observed.

Conclusion

A method for the synthesis of new push–pull stilbazoles of the type D–π–A was developed. The obtained compounds represent a rare class of benzylidene derivatives of 1-pyrindane. They were characterized by an unusual type of photoluminescence in two states (dual-state emission), namely in solution and in the solid state. Emission in solution was in the range of 469–721 nm, depending on the solvent, number, and type of substituent and covered almost the entire visible spectrum. In the solid state, the emission ranged from 493–767 nm. It was found that the presence of a dimethylene bridge in arylidene derivatives of pyrindane **1** led to an increase in the emission quantum yield and caused an appearance of solid-state photoluminescence, in contrast to the previously synthesized analogues (stilbazoles **A**, Figure 1) without such a bridge (Tables S3 and S4, Supporting Information File 1). Moreover, it was found that the emission band could be adjusted by about 200 nm in solu-

tion and by 270 nm in the solid state through directed protonation of the dimethylamino group.

Supporting Information

Supporting Information File 1

Synthetic procedure and compound characterization data, solvatochromic studies for compound **1c**, titration data, and ^{1}H and ^{13}C NMR spectra for compounds **1a**–**i**.
[https://www.beilstein-journals.org/bjoc/content/supplementary/1860-5397-20-251-S1.pdf]

Funding

This work was performed within the framework of the state task of the Ministry of Science and Higher Education of the Russian Federation (project no. FEGR-2023-0004).

Author Contributions

Anastasia I. Ershova: investigation; methodology. Sergey V. Fedoseev: data curation; validation. Konstantin V. Lipin: formal analysis; visualization. Mikhail Yu. Ievlev: software; writing – original draft. Oleg E. Nasakin: project administration; resources. Oleg V. Ershov: conceptualization; funding acquisition; writing – review & editing.

ORCID® iDs

Anastasia I. Ershova - https://orcid.org/0000-0003-4095-6122
Mikhail Yu. Ievlev - https://orcid.org/0000-0003-0741-2254
Oleg V. Ershov - https://orcid.org/0000-0002-0938-4659

Data Availability Statement

All data that supports the findings of this study is available in the published article and/or the supporting information of this article.

References

1. Bureš, F. *RSC Adv.* **2014,** *4,* 58826–58851. doi:10.1039/c4ra11264d
2. Klikar, M.; Solanke, P.; Tydlitát, J.; Bureš, F. *Chem. Rec.* **2016,** *16,* 1886–1905. doi:10.1002/tcr.201600032
3. Wang, J.; Gadenne, V.; Patrone, L.; Raimundo, J.-M. *Molecules* **2024,** *29,* 559. doi:10.3390/molecules29030559
4. He, G. S.; Tan, L.-S.; Zheng, Q.; Prasad, P. N. *Chem. Rev.* **2008,** *108,* 1245–1330. doi:10.1021/cr050054x
5. Allard, S.; Forster, M.; Souharce, B.; Thiem, H.; Scherf, U. *Angew. Chem., Int. Ed.* **2008,** *47,* 4070–4098. doi:10.1002/anie.200701920
6. Ohmori, Y. *Laser Photonics Rev.* **2010,** *4,* 300–310. doi:10.1002/lpor.200810059
7. Jaswal, S.; Kumar, J. *Mater. Today: Proc.* **2020,** *26,* 566–580. doi:10.1016/j.matpr.2019.12.161
8. Wang, L.; Zhu, W. *Adv. Sci.* **2024,** *11,* 2307227. doi:10.1002/advs.202307227
9. Wu, Y.; Zhu, W. *Chem. Soc. Rev.* **2013,** *42,* 2039–2058. doi:10.1039/c2cs35346f
10. Sil, A.; Ghosh, U.; Dolai, S.; Manna, S.; Maity, A.; Patra, S. K. *Mater. Adv.* **2022,** *3,* 5497–5509. doi:10.1039/d1ma01179k
11. Huang, T.; Jiang, W.; Duan, L. *J. Mater. Chem. C* **2018,** *6,* 5577–5596. doi:10.1039/c8tc01139g
12. Da Lama, A.; Sestelo, J. P.; Valencia, L.; Esteban-Gómez, D.; Sarandeses, L. A.; Martínez, M. M. *Dyes Pigm.* **2022,** *205,* 110539. doi:10.1016/j.dyepig.2022.110539
13. Stanitska, M.; Volyniuk, D.; Minaev, B.; Agren, H.; Grazulevicius, J. V. *J. Mater. Chem. C* **2024,** *12,* 2662–2698. doi:10.1039/d3tc04514e
14. Lipunova, G. N.; Nosova, E. V.; Trashakhova, T. V.; Charushin, V. N. *Russ. Chem. Rev.* **2011,** *80,* 1115–1133. doi:10.1070/rc2011v080n11abeh004234
15. Sorokin, S. P.; Ershov, O. V. *Chem. Heterocycl. Compd.* **2022,** *58,* 582–584. doi:10.1007/s10593-022-03132-4
16. Sorokin, S. P.; Ievlev, M. Y.; Ershov, O. V. *Dyes Pigm.* **2023,** *219,* 111581. doi:10.1016/j.dyepig.2023.111581
17. Ershova, A. I.; Fedoseev, S. V.; Blinov, S. A.; Ievlev, M. Y.; Lipin, K. V.; Ershov, O. V. *Org. Biomol. Chem.* **2023,** *21,* 7935–7943. doi:10.1039/d3ob01326j
18. Sorokin, S. P.; Ievlev, M. Y.; Ershov, O. V. *Org. Biomol. Chem.* **2024,** *22,* 3468–3476. doi:10.1039/d4ob00177j
19. Cao, C.; Zeng, Z.; Cao, C. *J. Phys. Org. Chem.* **2022,** *35,* e4319. doi:10.1002/poc.4319
20. Choi, H.-J.; Song, M.-G.; Sim, Y.-H.; Bae, H.-K.; Kim, J.-W.; Park, L. S. *Mol. Cryst. Liq. Cryst.* **2010,** *531,* 47/[347]–54/[354]. doi:10.1080/15421406.2010.499316
21. Risi, G.; Devereux, M.; Prescimone, A.; Housecroft, C. E.; Constable, E. C. *RSC Adv.* **2023,** *13,* 4122–4137. doi:10.1039/d3ra00437f
22. Poornima, L.; Babu, R. S.; Kalainathan, S. *J. Mol. Struct.* **2023,** *1280,* 134976. doi:10.1016/j.molstruc.2023.134976
23. Wang, T.; Ma, J.; Xu, K.; Chen, R.; Cao, L.; Teng, B. *Cryst. Growth Des.* **2022,** *22,* 5895–5903. doi:10.1021/acs.cgd.2c00523
24. Beuché, S.; Peyronneau, M.-A.; Jego, B.; Denis, C.; Bourbon, P.; Chauvière, C.; Santerre, C.; Truillet, C.; Kuhnast, B.; Caillé, F. *J. Med. Chem.* **2023,** *66,* 8030–8042. doi:10.1021/acs.jmedchem.3c00325
25. Xiong, Q.; Zhao, K.; Cheng, Y.; He, C.; Lai, Y.; Shi, M.; Ming, X.; Jin, F.; Tao, D.; Liao, R.; Liu, Y. *Spectrochim. Acta, Part A* **2023,** *286,* 122012. doi:10.1016/j.saa.2022.122012
26. Singh, D.; Shewale, D. J.; Sengupta, A.; Soppina, V.; Kanvah, S. *Org. Biomol. Chem.* **2022,** *20,* 7047–7055. doi:10.1039/d2ob00995a
27. Luo, Y.; Yu, Q.-Q.; Gao, J.-J.; Lang, X.-X.; Li, H.-Y.; Yu, X.-F.; Qi, X.-Y.; Wang, M.-Q. *Bioorg. Med. Chem. Lett.* **2021,** *53,* 128438. doi:10.1016/j.bmcl.2021.128438
28. Xie, L.; Wang, R.; Fan, C.; Tu, Y.; Liu, G.; Pu, S. *Food Chem.* **2023,** *410,* 135411. doi:10.1016/j.foodchem.2023.135411
29. Feng, X.; Li, Y.; He, X.; Liu, H.; Zhao, Z.; Kwok, R. T. K.; Elsegood, M. R. J.; Lam, J. W. Y.; Tang, B. Z. *Adv. Funct. Mater.* **2018,** *28,* 1802833. doi:10.1002/adfm.201802833
30. Zhou, H.; Sun, L.; Chen, W.; Tian, G.; Chen, Y.; Li, Y.; Su, J. *Tetrahedron* **2016,** *72,* 2300–2305. doi:10.1016/j.tet.2016.03.036
31. Liang, M.; Wang, K.; Guan, R.; Liu, Z.; Cao, D.; Wu, Q.; Shan, Y.; Xu, Y. *Spectrochim. Acta, Part A* **2016,** *160,* 34–38. doi:10.1016/j.saa.2016.02.008

32. Ma, C.; He, J.; Wu, Y.; Li, J.; Chen, J.; Zhang, Y.; Mo, J.; Xie, H.; Chi, Z.; Li, Y.; Jin, Y. *Luminescence* **2023,** *38,* 1720–1728. doi:10.1002/bio.4558
33. Senthil, K.; Kalainathan, S.; Kumar, A. R.; Aravindan, P. G. *RSC Adv.* **2014,** *4,* 56112–56127. doi:10.1039/c4ra09112d
34. Zhou, C.; Wang, M.; Guo, W.; Ye, G.; Wang, Y.; Yang, Y.; Xia, G.; Wang, H. *Dyes Pigm.* **2023,** *213,* 111198. doi:10.1016/j.dyepig.2023.111198
35. Xu, Z.; Liao, Q.; Shi, X.; Li, H.; Zhang, H.; Fu, H. *J. Mater. Chem. B* **2013,** *1,* 6035–6041. doi:10.1039/c3tb20841a
36. Kim, E.; Koh, M.; Ryu, J.; Park, S. B. *J. Am. Chem. Soc.* **2008,** *130,* 12206–12207. doi:10.1021/ja8020268
37. Radhakrishnan, R.; Sinu, B. B.; Anilkumar, V.; Sreejalekshmi, K. G. *Dyes Pigm.* **2020,** *181,* 108560. doi:10.1016/j.dyepig.2020.108560
38. Zhu, P.; Yang, Y.; Li, H.; Wang, J.; Li, S. *Chin. Chem. Lett.* **2024,** *35,* 109533. doi:10.1016/j.cclet.2024.109533
39. Zhu, Y.; Liao, K.; Li, Y.; Zhang, W.; Song, B.; Hao, X.-Q.; Zhu, X. *Dyes Pigm.* **2024,** *224,* 112004. doi:10.1016/j.dyepig.2024.112004
40. Zhang, X.; Wang, D.; Shen, H.; Wang, S.; Zhou, Y.; Lei, Y.; Gao, W.; Liu, M.; Huang, X.; Wu, H. *Org. Chem. Front.* **2021,** *8,* 856–867. doi:10.1039/d0qo01527j
41. Chen, S.-H.; Cao, X.-Y.; Hu, P.-T.; Jiang, K.; Liang, Y.-T.; Xu, B.-J.; Li, Z.-H.; Wang, Z.-Y. *Mater. Adv.* **2023,** *4,* 6612–6620. doi:10.1039/d3ma00876b
42. Chen, Z.; Qin, H.; Yin, Y.; Deng, D.-d.; Qin, S.-Y.; Li, N.; Wang, K.; Sun, Y. *Chem. – Eur. J.* **2023,** *29,* e202203797. doi:10.1002/chem.202203797
43. Wen, W.; Shi, Z.-F.; Cao, X.-P.; Xu, N.-S. *Dyes Pigm.* **2016,** *132,* 282–290. doi:10.1016/j.dyepig.2016.04.014
44. Ruan, B.; Kang, X.; Guo, B.; Deng, D.-d.; Tian, J.-j.; He, K.; Wang, X.-Y.; Pu, S.; Chen, Z. *J. Mol. Struct.* **2024,** *1309,* 138171. doi:10.1016/j.molstruc.2024.138171
45. Belmonte-Vázquez, J. L.; Amador-Sánchez, Y. A.; Rodríguez-Cortés, L. A.; Rodríguez-Molina, B. *Chem. Mater.* **2021,** *33,* 7160–7184. doi:10.1021/acs.chemmater.1c02460
46. Xia, G.; Si, L.; Wang, H. *Mater. Today Chem.* **2023,** *30,* 101596. doi:10.1016/j.mtchem.2023.101596
47. Stoerkler, T.; Pariat, T.; Laurent, A. D.; Jacquemin, D.; Ulrich, G.; Massue, J. *Molecules* **2022,** *27,* 2443. doi:10.3390/molecules27082443
48. Vachova, L.; Machacek, M.; Kučera, R.; Demuth, J.; Cermak, P.; Kopecky, K.; Miletin, M.; Jedlickova, A.; Simunek, T.; Novakova, V.; Zimcik, P. *Org. Biomol. Chem.* **2015,** *13,* 5608–5612. doi:10.1039/c5ob00651a
49. Ershova, A. I.; Ievlev, M. Y.; Maksimova, V. N.; Ershov, O. V. *Russ. J. Gen. Chem.* **2022,** *92,* 2690–2697. doi:10.1134/s1070363222120192
50. Fedoseev, S. V.; Belikov, M. Y.; Lipin, K. V.; Ershov, O. V.; Tafeenko, V. A. *Synth. Commun.* **2022,** *52,* 145–156. doi:10.1080/00397911.2021.2007403
51. Chunikhin, S. S.; Ershov, O. V.; Ievlev, M. Y.; Belikov, M. Y.; Tafeenko, V. A. *Dyes Pigm.* **2018,** *156,* 357–368. doi:10.1016/j.dyepig.2018.04.024
52. Arafa, W. A. A.; Hussein, M. F. *Chin. J. Chem.* **2020,** *38,* 501–508. doi:10.1002/cjoc.201900494
53. Ershov, O. V.; Shishlikova, M. A.; Ievlev, M. Y.; Belikov, M. Y.; Maksimova, V. N. *Tetrahedron* **2019,** *75,* 130465. doi:10.1016/j.tet.2019.130465
54. Maximova, V. N.; Naidenova, A. I.; Ershov, O. V.; Nasakin, O. E.; Tafeenko, V. A. *Russ. J. Org. Chem.* **2017,** *53,* 691–696. doi:10.1134/s1070428017050086
55. Chunikhin, S. S.; Ershov, O. V. *Russ. J. Org. Chem.* **2021,** *57,* 1103–1108. doi:10.1134/s1070428021070113
56. Lenci, E.; Trabocchi, A. *Eur. J. Org. Chem.* **2022,** e202200575. doi:10.1002/ejoc.202200575
57. Spring, D. R. *Org. Biomol. Chem.* **2003,** *1,* 3867–3870. doi:10.1039/b310752n
58. Ershov, O. V.; Maksimova, V. N.; Lipin, K. V.; Belikov, M. Y.; Ievlev, M. Y.; Tafeenko, V. A.; Nasakin, O. E. *Tetrahedron* **2015,** *71,* 7445–7450. doi:10.1016/j.tet.2015.06.031
59. Kawski, A. *Z. Naturforsch., A: Phys. Sci.* **2002,** *57,* 255–262. doi:10.1515/zna-2002-0509
60. Chamma, A.; Viallet, P. *C. R. Seances Acad. Sci., Ser. C* **1970,** *270,* 1901–1904.

License and Terms

BEILSTEIN JOURNAL OF ORGANIC CHEMISTRY

Synthesis, structure and π-expansion of tris(4,5-dehydro-2,3:6,7-dibenzotropone)

Yongming Xiong[1], Xue Lin Ma[1], Shilong Su[1] and Qian Miao*[1,2]

Full Research Paper

Open Access

Address:
[1]Department of Chemistry, The Chinese University of Hong Kong, Shatin, New Territories, Hong Kong, China and [2]State Key Laboratory of Synthetic Chemistry, The Chinese University of Hong Kong, Shatin, New Territories, Hong Kong, China

Email:
Qian Miao* - miaoqian@cuhk.edu.hk

* Corresponding author

Keywords:
carbon schwarzites; polycyclic arenes; Scholl reaction; seven-membered carbocycle; Yamamoto coupling

Beilstein J. Org. Chem. **2025,** *21,* 1–7.
https://doi.org/10.3762/bjoc.21.1

Received: 31 August 2024
Accepted: 11 December 2024
Published: 02 January 2025

This article is part of the thematic issue "π-Conjugated molecules and materials".

Guest Editor: A. Mateo-Alonso

Abstract

The polycyclic skeleton of tris(4,5-dehydro-2,3:6,7-dibenzotropone) is a key structural fragment in carbon schwarzites, a theoretical form of negatively curved carbon allotrope. This report presents a new synthesis of this compound using a Ni-mediated Yamamoto coupling reaction and structural analysis of it with X-ray crystallography. Interestingly, it is observed that tris(4,5-dehydro-2,3:6,7-dibenzotropone) crystallized from its solution in hexane resulting in colorless and yellow crystal polymorphs, where it adopts conformations of approximate C_s and C_2 symmetry, respectively. Furthermore, expanding its π-skeleton through the Barton–Kellogg and Scholl reactions led to the successful synthesis of a curved polycyclic arene containing three heptagons and two pentagons.

Introduction

The title compound (**1** in Figure 1), tris(4,5-dehydro-2,3:6,7-dibenzotropone), receives this name because it can formally result from cyclotrimerization of 4,5-dehydro-2,3:6,7-dibenzotropone (**2** in Figure 1). Similarly, compound **1** was called "a formal trimer of dibenzotropone" or "benzannulated tristropone" in literature [1,2], although it should be named as 9*H*,18*H*,27*H*-hexabenzo[*c*,*c*′,*c*″,*f*,*f*′,*f*″]benzo[1,2-*a*:3,4-*a*′:5,6-*a*″]triscycloheptene-9,18,27-trione according to the IUPAC nomenclature. We became interested in compound **1** because its polycyclic skeleton presents a key structural unit in carbon schwarzites, a theoretical form of negatively curved carbon allotrope, as shown in Figure 1.

Carbon allotropes composed solely of sp^2-hybridized carbon atoms can form surfaces that range from flat, like a carpet, to curved, resembling shapes such as bowls or saddles. The shape these surfaces take depends on the arrangement of the carbon atoms and is characterized by a geometric property known as curvature. When five-membered rings of carbon atoms are present, they induce a positive curvature, exemplified by fuller-

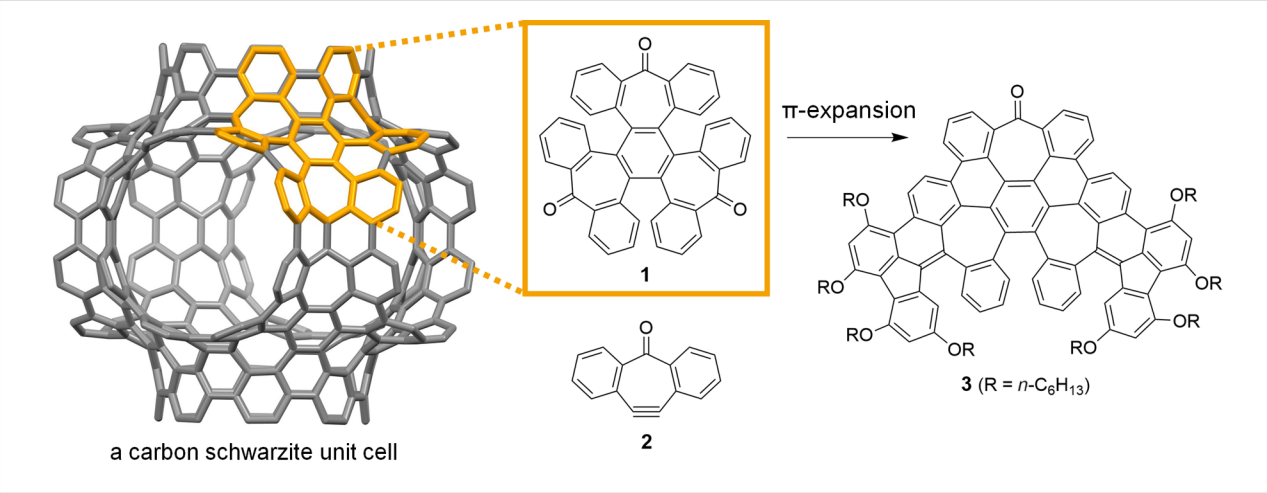

Figure 1: Structures of compounds **1**–**3** and the polycyclic skeleton of **1** as mapped on a carbon schwarzite unit cell.

enes. Conversely, seven- or eight-membered rings lead to negative curvature, as seen in theoretical carbon structures known as carbon schwarzites or Mackay crystals. These names honor A. L. Mackay and H. A. Schwarz for their pioneering contributions. In 1991, Mackay introduced the idea of negatively curved carbon allotropes by incorporating octagons into the graphitic lattice [3]. Earlier, in the 1880s, Schwarz described triply periodic minimal surfaces, which serve as the topological foundation for what are now known as Mackay crystals. Despite predictions that carbon schwarzites would have intriguing properties for various potential applications [4,5], they have not yet been definitively synthesized. The three-dimensional graphene-like carbons formed in a zeolite-template are the carbon forms that are the closest to carbon schwarzites so far [6,7]. Fragments of carbon schwarzites that retain their key structural characteristics are negatively curved polycyclic arenes [8,9]. These are three-dimensional molecular nanocarbons that include heptagons [10-14], octagons [15-18], or even larger carbocycles. In theory, these fragments can serve as building blocks in a bottom-up approach to constructing carbon schwarzites [19,20]. To validate this concept, we recently showed that polymerizing negatively curved polycyclic arenes produced an amorphous covalent network. This network was able to mimic the structure and function of carbon schwarzites, serving as an anode material in lithium-ion batteries with high capacity [21]. Further exploration of bottom-up approach to carbon schwarzites requires synthesizing of new negatively curved polycyclic arenes and expanding them to lager three-dimensional molecular nanocarbons.

Compound **1** was recently used as a starting material for the synthesis of nonplanar polycyclic arenes, in particular, molecular models of cubic graphite [22]. It was earlier prepared in Ar matrices [23] or via demetallation of a platinum complex of 4,5-dehydro-2,3:6,7-dibenzotropone [1]. More recently, compound **1** was prepared via Pd-catalyzed cyclotrimerization of 4-bromo-2,3:6,7-dibenzotropone (**4** in Scheme 1) [22]. Herein we report an alternative synthesis of **1** using a Ni-mediated Yamamoto coupling reaction and the simultaneous crystallization of its two different conformers from the same solution. Expanding the π-skeleton of **1** through a Barton–Kellogg reaction followed by a subsequent Scholl reaction resulted in a new polycyclic arene (**3** in Figure 1) featuring three heptagons and two pentagons, with its structure confirmed by X-ray crystallography. This π-expansion approach of compound **1** differs from the method reported by Müllen and co-workers, which involves Ramirez olefination and Suzuki coupling, resulting in the expansion of a seven-membered ring to an eight-membered ring [2].

Results and Discussion

As shown in Scheme 1a, the synthesis of trione **1** started from the bromination of 4-bromo-2,3:6,7-dibenzotropone (**4**) [24], giving tribromide **5** in a yield of 64%. The subsequent elimination reaction of **5** with KOH afforded dibromide **6** in a yield of 90%. Then, the Ni-mediated Yamamoto coupling reaction of **6** enabled cyclotrimerization to give trione **1** in a yield of 30%. It is worth mentioning that using 1,10-phenanthroline as the ligand in the Yamamoto coupling [25,26] led to a higher yield of compound **1** than using 2,2'-bipyridine. With trione **1** in hands, we explored the Scholl reaction and thionation reaction of it (Scheme 1b) because these reactions can potentially allow π-expansion of **1**. A variety of Scholl reaction conditions, such as $AlCl_3$/NaCl, $AlCl_3$/$CuCl_2$, $FeCl_3$, and DDQ/TfOH, were tested. However, these reactions either left the starting material unreacted or resulted in complex mixtures, from which cyclodehydrogenation products, such as compound **7** (Scheme 1b), could not be isolated in a pure form. This can be attributed to the electron-withdrawing carbonyl groups, which make com-

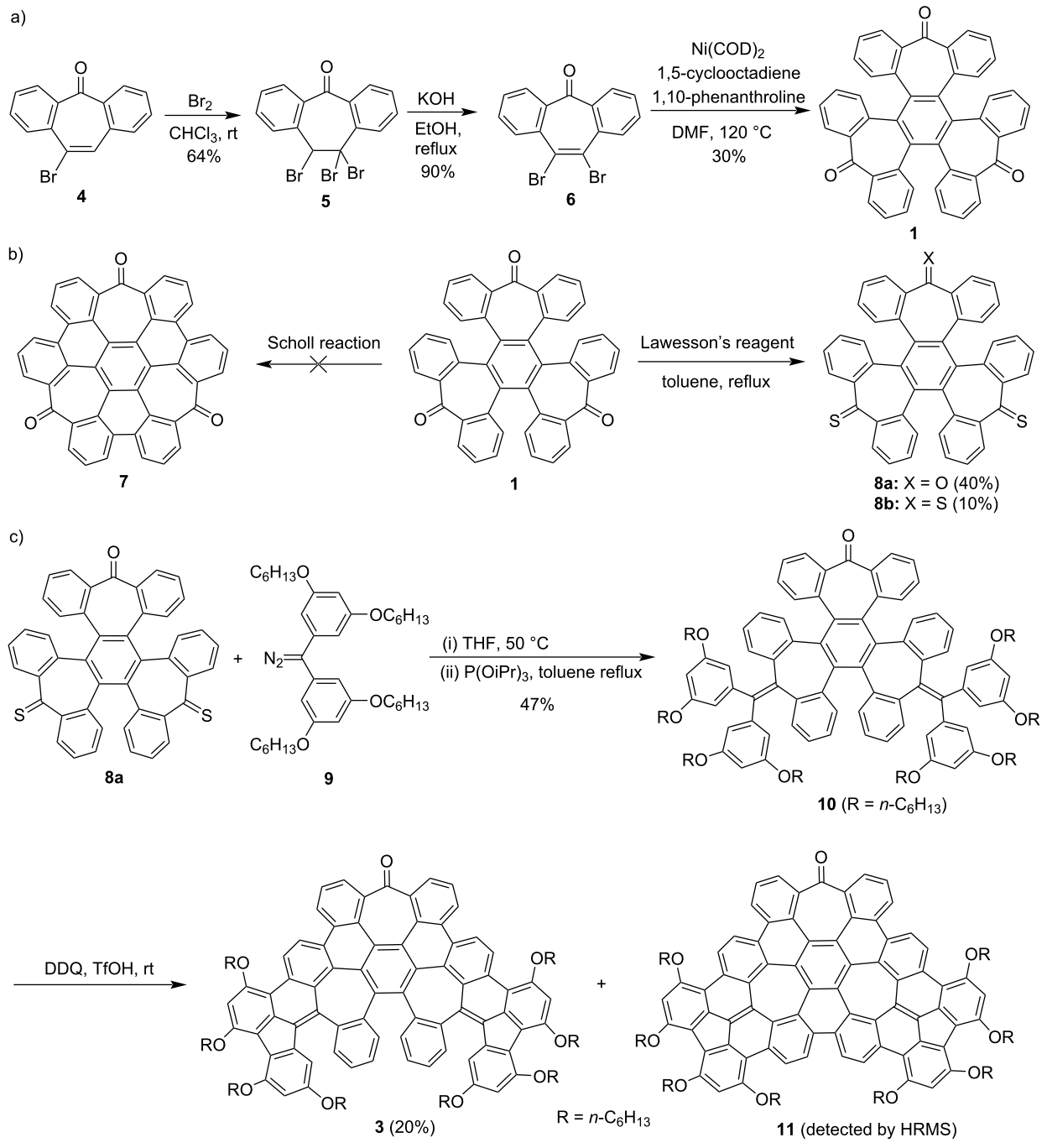

Scheme 1: a) Synthesis of **1**; b) reactions of **1**; c) synthesis of **3**.

pound **1** unreactive to oxidation. For thionation of the carbonyl groups in **1**, it was treated with three equivalents Lawesson's reagent, affording dithioketone **8a** in a 40% yield together with trithioketone **8b** in a yield of 10%.

To expand the π-skeleton of **1**, compound **8a** was subjected to the Barton–Kellogg reaction with diazo compound **9**, which was synthesized according to the procedures detailed in Supporting Information File 1. In this reaction, the first step of diazo–thioketone coupling occurred at 50 °C in THF, and the second step of desulfurization with triisopropyl phosphite occurred in refluxed toluene, giving diene **10** in a yield of 47%. The Barton–Kellogg reaction with **8b** under similar conditions gave the episulfide intermediate, which, however, could not be

desulfurized with triisopropyl phosphite, trimethyl phosphite or triphenylphosphine to give the corresponding triene. The subsequent Scholl reaction of **10** with DDQ and triflic acid at room temperature yielded partially fused nanographene **3** (20%), with formation of six C–C bonds giving four six-membered rings and two five-membered rings. Performing this reaction at a higher temperature led to a lower yield of compound **3** and the formation of byproducts with lower R_f values on thin-layer chromatography (TLC). When other typical conditions for Scholl reactions, such as $FeCl_3$ or DDQ/CH_3SO_3H, were employed to treat compound **10**, product **3** was not isolated. Instead, the starting material either remained unreacted or was converted to a complicated mixture of products. It is worth noting that the alkoxy groups in compound **10**, which are positioned *para* or *ortho* to the reacting site, play an important role in the Scholl reaction to form compound **3**. Similar substrates, where the alkoxy groups are replaced by hydrogen atoms or a 4-*tert*-butyl group, did not yield product **3** under similar Scholl reaction conditions. The structure of **3** was confirmed with single crystal X-ray crystallography, as detailed later. In addition, another product with a molecular ion peak of 1695.9115 in the high-resolution mass spectrum (Supporting Information File 1, Figure S6) was isolated in trace amounts. This corresponds to a molecular formula of $C_{119}H_{122}O_9$, which is in agreement with the fully fused product **11** in its protonated form. Unfortunately, clean ^1H and ^{13}C NMR spectra of this product could not be obtained to allow full characterization of this product. Efforts to increase the yield of **11**, such as increasing the amount of DDQ or elevating the reaction temperature in the Scholl reaction of **10**, only resulted in complex mixtures. Further attempts to subject **3** to the Scholl reaction conditions did not yield further cyclized products but led to the decomposition of the starting material. These findings suggest that the fully fused product **11** may have been formed through a different partially cyclized intermediate rather than directly from compound **3**.

Slow evaporation of solvent from a solution of **1** in hexane interestingly resulted in the simultaneous formation of both colorless and yellow crystals from the same solution. X-ray crystallography reveals that in the colorless crystal [27], compound **1** adopts a conformation with approximate C_s symmetry, with the plane of symmetry (σ) shown in the top view in Figure 2a. The structure of C_s-**1** in this crystal is essentially the same as that in the reported crystal structure of **1**·CH_2Cl_2 [22]. The side view of compound **1** indicates that two of its carbonyl groups are oriented upwards while the third one points downwards. Compound **1** comprises three [5]helicenoid moieties, each containing three benzene rings and two seven-membered rings. In the colorless crystal, two of these [5]helicenoid moieties display *P* and *M* helix structures respectively, whereas the third moiety (colored in light blue) adopts a structure with approximate plane symmetry, recognized as a transition state for the enantiomerization of helicenes. The central benzene ring of C_s-**1** is essentially flat, exhibiting the largest torsion angle of 8.15° (C4–C5–C6–C1).

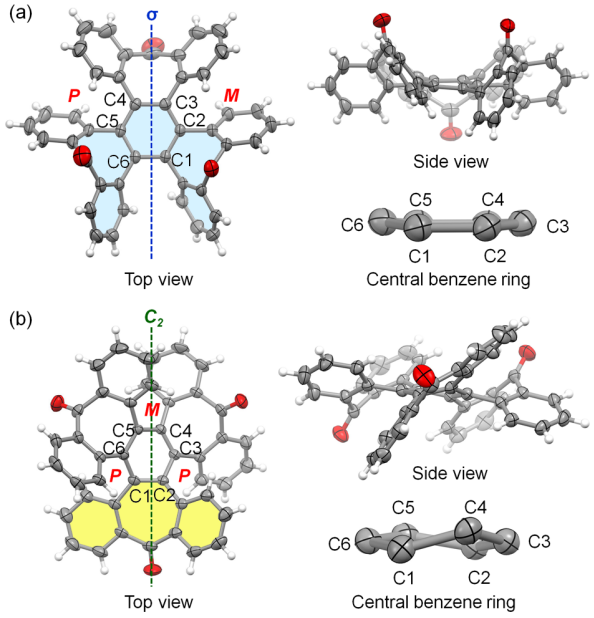

Figure 2: (a) Structures of **1** in the colorless crystal; (b) structures of (*P*,*M*,*P*)-**1** in the yellow crystal. (Carbon atoms are shown as ellipsoids at 50% probability level, in and H atoms are removed for clarification).

Unlike the colorless crystal, the yellow crystal consists of conformers of **1** with approximate C_2 symmetry [27]. They exist as a pair of enantiomers, namely, (*P*,*M*,*P*)-**1** and (*M*,*P*,*M*)-**1**, where *P* and *M* represent the helicity of the three [5]helicenoid moieties. This crystal structure is essentially the same as that reported by Jones earlier [1]. Figure 2b illustrates the structure of (*P*,*M*,*P*)-**1** with the C_2 axis, where one carbonyl group points upward, another downward, and the third one faces forwards. Compound **1** consists of three 2,3:6,7-dibenzotropone moieties. In the yellow crystal, one of these moieties (colored in yellow) is unique due to its less bent seven-membered ring, distinguishing it from the other two dibenzotropone moieties in C_2-**1** and those in C_s-**1**. As a result, C_2-1 in the yellow crystal presents an apparently twisted central benzene ring with large torsion angles: C1–C2–C3–C4 at 19.5°, C3–C4–C5–C6 at 21.8°, and C5–C6–C1–C2 at 21.5°. The crystallization of the two conformers of **1** in different polymorphs suggests the flexibility of its polycyclic skeleton, with both its [5]helicenoid and dibenzotropone moieties capable of flapping with small energy barriers. This is supported by the ^1H NMR spectrum of compound **1** (Supporting Information File 1, Figure

S11), which presents only four different signals due to rapid conformational shifts in solution. Additional evidence of the small energy barrier for conformational change is provided by the earlier report that the NMR spectrum of **1** at −80 °C did not display significant broadening [1].

To better understand the two conformers of **1** found in the crystals, density functional theory (DFT) calculations were carried out using the molecular geometries present in the crystal structures. The results showed that C_2-**1** is more stable than C_s-**1** by 3.85 kcal/mol at the B3LYP/6-311G(d,p) level of DFT. Additionally, C_2-**1** has a smaller gap (3.57 eV) between the highest occupied molecular orbital (HOMO) and the lowest unoccupied molecular orbital (LUMO) compared to C_s-**1** (4.37 eV) as calculated at the B3LYP/6-311++G(d,p) level of DFT. The reduced HOMO–LUMO gap of C_2-**1** can be attributed to the greater conjugation in the essentially flat dibenzotropone moiety. This finding aligns with the fact that the yellow crystal of C_2-**1** absorbs light of a longer wavelength than the colorless crystal of C_s-**1**.

Slow evaporation of solvent from a solution of **3** in CH_2Cl_2/CH_3OH resulted in the formation of single crystals suitable for X-ray crystallography [27]. Compound **3** consists of three [5]helicenoid moieties, with two of them containing three benzene rings, one five-membered ring, and one seven-membered ring, and the third one containing three benzene rings and two seven-membered rings. The crystal structure of **3**·CH_2Cl_2 reveals that each unit cell contains a pair of enantiomers, (*M*,*P*,*M*)-**3** and (*P*,*M*,*P*)-**3**, co-crystallized with two molecules of CH_2Cl_2. Here *P* and *M* represent the helicity of the three [5]helicenoid moieties. The geometry of **3** deviates from ideal C_2 symmetry, as the light blue moiety of **3** (top view in Figure 3) is shaped like a saddle. However, the ^{1}H NMR spectrum of **3** shows only 12 different signals in the aromatic region, indicating a two-fold symmetry in the polycyclic skeleton of **3**. This indicates that the polycyclic skeleton of **3** is flexible, similar to that of **1**. In the crystal, the neighbouring enantiomers of **3** show minimal π-overlap with each other and a large π to π distance of 3.68 Å between terminal benzene rings.

Compound **3** forms orange solution in common organic solvents, and its solution in cyclohexane exhibits very weak orange photoluminescence with a quantum yield as low as 3.9×10^{-4} upon excitation at 400 nm. Such a low photoluminescence quantum yield may be attributed to the conformational motions of the helicene moieties in **3**, which consume the energy of the excited state. Figure 4 shows the UV–vis absorption spectrum of **3** in cyclohexane with the absorption edge at 561 nm and its emission spectrum with a peak at 580 nm. In the test windows of cyclic voltammetry (Supporting Information File 1, Figure S1), **3** exhibits one reversible oxidation wave and one quasi-reversible oxidation wave with half-wave potentials of 0.40 V and 0.88 V, respectively, versus ferrocenium/ferrocene (Fc^+/Fc). The HOMO energy level is estimated from the first oxidation peak to be −5.5 eV [28], which is consistent with the DFT-calculated HOMO level (−5.47 eV).

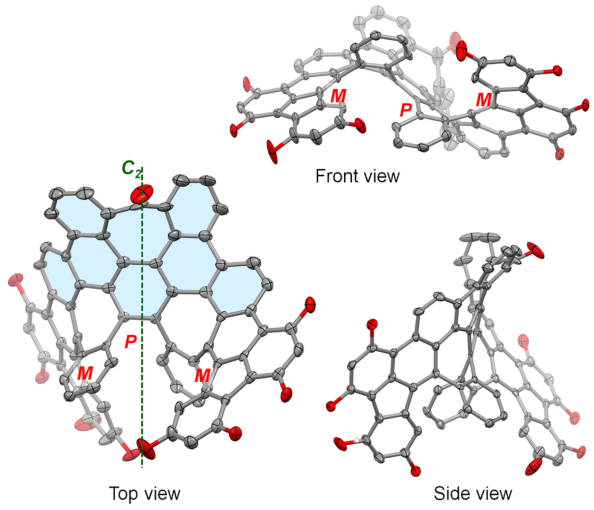

Figure 3: Structure of (*M*,*P*,*M*)-**3** in the crystal of **3**·CH_2Cl_2 (carbon and oxygen atoms are shown as grey and red ellipsoid at the level of 50% probability, and hexyl groups and hydrogen atoms are removed for clarity).

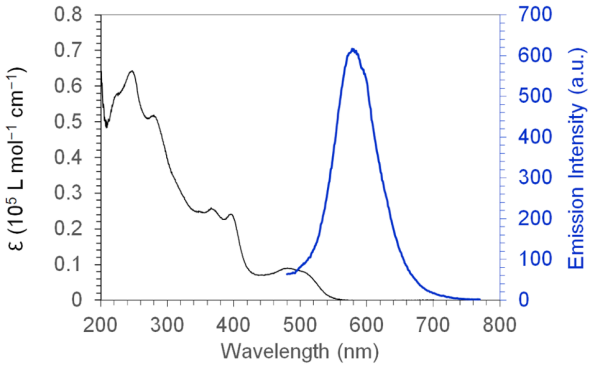

Figure 4: UV–vis absorption spectrum (black line) and emission spectrum (blue line, excited at 400 nm) of compound **3** in cyclohexane (1×10^{-5} mol/L).

Conclusion

In conclusion, we developed a new synthesis of tris(4,5-dehydro-2,3:6,7-dibenzotropone) (**1**) through a Ni-mediated Yamamoto coupling reaction. Upon crystallization from the same solution in hexane, this compound yielded colorless and yellow crystal polymorphs, adopting conformations of approximate C_s and C_2 symmetry, respectively. Furthermore, the

expansion of the π-skeleton of **1** through the Barton–Kellogg and Scholl reactions enabled the synthesis of compound **3**, whose curved polycyclic skeleton containing three heptagons and two pentagons was identified with X-ray crystallography.

Supporting Information

Supporting Information File 1

Experimental details, characterization data, and spectra.
[https://www.beilstein-journals.org/bjoc/content/supplementary/1860-5397-21-1-S1.pdf]

Supporting Information File 2

CIF-files of compounds **1** and **3**.
[https://www.beilstein-journals.org/bjoc/content/supplementary/1860-5397-21-1-S2.zip]

Acknowledgements

We are grateful to Ms. Hoi Shan Chan for the single-crystal crystallography.

Funding

We acknowledge the financial support provided by the Research Grants Council of Hong Kong (GRF 14300323) and the State Key Laboratory of Synthetic Chemistry.

ORCID® iDs

Xue Lin Ma - https://orcid.org/0009-0008-9996-6628
Shilong Su - https://orcid.org/0000-0002-4325-7565
Qian Miao - https://orcid.org/0000-0001-9933-6548

Data Availability Statement

All data that supports the findings of this study is available in the published article and/or the supporting information of this article.

References

1. Klosin, J.; Abboud, K. A.; Jones, W. M. *Organometallics* **1995,** *14,* 2892–2902. doi:10.1021/om00006a039
2. Ejlli, B.; Rominger, F.; Freudenberg, J.; Bunz, U. H. F.; Müllen, K. *Chem. – Eur. J.* **2023,** *29,* e202203735. doi:10.1002/chem.202203735
3. Mackay, A. L.; Terrones, H. *Nature* **1991,** *352,* 762. doi:10.1038/352762a0
4. Park, S.; Kittimanapun, K.; Ahn, J. S.; Kwon, Y.-K.; Tománek, D. *J. Phys.: Condens. Matter* **2010,** *22,* 334220. doi:10.1088/0953-8984/22/33/334220
5. Park, N.; Yoon, M.; Berber, S.; Ihm, J.; Osawa, E.; Tománek, D. *Phys. Rev. Lett.* **2003,** *91,* 237204. doi:10.1103/physrevlett.91.237204
6. Kim, K.; Lee, T.; Kwon, Y.; Seo, Y.; Song, J.; Park, J. K.; Lee, H.; Park, J. Y.; Ihee, H.; Cho, S. J.; Ryoo, R. *Nature* **2016,** *535,* 131–135. doi:10.1038/nature18284
7. Braun, E.; Lee, Y.; Moosavi, S. M.; Barthel, S.; Mercado, R.; Baburin, I. A.; Proserpio, D. M.; Smit, B. *Proc. Natl. Acad. Sci. U. S. A.* **2018,** *115,* E8116–E8124. doi:10.1073/pnas.1805062115
8. González Miera, G.; Matsubara, S.; Kono, H.; Murakami, K.; Itami, K. *Chem. Sci.* **2022,** *13,* 1848–1868. doi:10.1039/d1sc05586k
9. Chaolumen; Stepek, I. A.; Yamada, K. E.; Ito, H.; Itami, K. *Angew. Chem., Int. Ed.* **2021,** *60,* 23508–23532. doi:10.1002/anie.202100260
10. Kawasumi, K.; Zhang, Q.; Segawa, Y.; Scott, L. T.; Itami, K. *Nat. Chem.* **2013,** *5,* 739–744. doi:10.1038/nchem.1704
11. Cheung, K. Y.; Xu, X.; Miao, Q. *J. Am. Chem. Soc.* **2015,** *137,* 3910–3914. doi:10.1021/jacs.5b00403
12. Cruz, C. M.; Márquez, I. R.; Castro-Fernández, S.; Cuerva, J. M.; Maçôas, E.; Campaña, A. G. *Angew. Chem., Int. Ed.* **2019,** *58,* 8068–8072. doi:10.1002/anie.201902529
13. Elbert, S. M.; Paine, O. T. A.; Kirschbaum, T.; Schuldt, M. P.; Weber, L.; Rominger, F.; Mastalerz, M. *J. Am. Chem. Soc.* **2024,** *146,* 27324–27334. doi:10.1021/jacs.4c09185
14. Borrisov, B.; Beneventi, G. M.; Fu, Y.; Qiu, Z.-l.; Komber, H.; Deng, Q.-s.; Greißel, P. M.; Cadranel, A.; Guldi, D. M.; Ma, J.; Feng, X. *J. Am. Chem. Soc.* **2024,** *146,* 27335–27344. doi:10.1021/jacs.4c09224
15. Sakamoto, Y.; Suzuki, T. *J. Am. Chem. Soc.* **2013,** *135,* 14074–14077. doi:10.1021/ja407842z
16. Feng, C.-N.; Kuo, M.-Y.; Wu, Y.-T. *Angew. Chem., Int. Ed.* **2013,** *52,* 7791–7794. doi:10.1002/anie.201303875
17. Cheung, K. Y.; Chan, C. K.; Liu, Z.; Miao, Q. *Angew. Chem., Int. Ed.* **2017,** *56,* 9003–9007. doi:10.1002/anie.201703754
18. Pun, S. H.; Wang, Y.; Chu, M.; Chan, C. K.; Li, Y.; Liu, Z.; Miao, Q. *J. Am. Chem. Soc.* **2019,** *141,* 9680–9686. doi:10.1021/jacs.9b03910
19. Pun, S. H.; Miao, Q. *Acc. Chem. Res.* **2018,** *51,* 1630–1642. doi:10.1021/acs.accounts.8b00140
20. Kirschbaum, T.; Rominger, F.; Mastalerz, M. *Angew. Chem., Int. Ed.* **2020,** *59,* 270–274. doi:10.1002/anie.201912213
21. Zhang, Y.; Zhu, Y.; Lan, D.; Pun, S. H.; Zhou, Z.; Wei, Z.; Wang, Y.; Lee, H. K.; Lin, C.; Wang, J.; Petrukhina, M. A.; Li, Q.; Miao, Q. *J. Am. Chem. Soc.* **2021,** *143,* 5231–5238. doi:10.1021/jacs.1c01642
22. Ejlli, B.; Nußbaum, P.; Rominger, F.; Freudenberg, J.; Bunz, U. H. F.; Müllen, K. *Angew. Chem., Int. Ed.* **2021,** *60,* 20220–20224. doi:10.1002/anie.202106233
23. Krebs, A.; Cholcha, W.; Müller, M.; Eicher, T.; Pielartzik, H.; Schnöckel, H. *Tetrahedron Lett.* **1984,** *25,* 5027–5030. doi:10.1016/s0040-4039(01)91109-8
24. Rupard, J. H.; De Paulis, T.; Janowsky, A.; Smith, H. E. *J. Med. Chem.* **1989,** *32,* 2261–2268. doi:10.1021/jm00130a006
25. Ikemoto, K.; Yang, S.; Naito, H.; Kotani, M.; Sato, S.; Isobe, H. *Nat. Commun.* **2020,** *11,* 1807. doi:10.1038/s41467-020-15662-6
26. Ikemoto, K.; Akiyoshi, M.; Mio, T.; Nishioka, K.; Sato, S.; Isobe, H. *Angew. Chem., Int. Ed.* **2022,** *61,* e202204035. doi:10.1002/anie.202204035
27. CCDC 2381395–2381397 contain the supplementary crystallographic data for C_s-**1**, C_2-**1**, and **3**·CH_2Cl_2.
28. Cardona, C. M.; Li, W.; Kaifer, A. E.; Stockdale, D.; Bazan, G. C. *Adv. Mater. (Weinheim, Ger.)* **2011,** *23,* 2367–2371. doi:10.1002/adma.201004554

License and Terms

BEILSTEIN JOURNAL OF ORGANIC CHEMISTRY

Synthesis and characterizations of highly luminescent 5-isopropoxybenzo[*rst*]pentaphene

Islam S. Marae[1], Jingyun Tan[1], Rengo Yoshioka[2], Zakaria Ziadi[1], Eugene Khaskin[3], Serhii Vasylevskyi[4], Ryota Kabe[2], Xiushang Xu[*1] and Akimitsu Narita[*1]

Full Research Paper

Open Access

Address:
[1]Organic and Carbon Nanomaterials Unit, Okinawa Institute of Science and Technology Graduate University, 1919-1 Tancha, Onna-son, Kunigami-gun, Okinawa 904-0495, Japan, [2]Organic Optoelectronics Unit, Okinawa Institute of Science and Technology Graduate University, 1919-1 Tancha, Onna-son, Kunigami-gun, Okinawa 904-0495, Japan, [3]Science and Technology Group, Okinawa Institute of Science and Technology Graduate University, 1919-1 Tancha, Onna-son, Kunigami-gun, Okinawa 904-0495, Japan and [4]X-ray diffraction facility, Department of Chemistry, 100 E. 24th Street, The University of Texas at Austin, Austin, TX 78712, USA

Email:
Xiushang Xu[*] - xiushang.xu@oist.jp; Akimitsu Narita[*] - akimitsu.narita@oist.jp

* Corresponding author

Keywords:
benzo[*rst*]pentaphene; intramolecular charge transfer; nanocrystals; photoluminescence; polycyclic aromatic hydrocarbon

Beilstein J. Org. Chem. **2025,** *21,* 270–276.
https://doi.org/10.3762/bjoc.21.19

Received: 12 September 2024
Accepted: 16 January 2025
Published: 04 February 2025

This article is part of the thematic issue "π-Conjugated molecules and materials".

Guest Editor: A. Mateo-Alonso

Abstract

A benzo[*rst*]pentaphene (BPP) substituted by an isopropoxy group (BPP-OiPr) was synthesized in a facile manner. Its photophysical properties were investigated by UV–vis absorption and fluorescence spectroscopy in compassion to pristine BPP and its oxidation product, benzo[*rst*]pentaphene-5,8-dione (BPP-dione). BPP-OiPr exhibited a significantly enhanced photoluminescence quantum yield (PLQY), reaching 73% in comparison to pristine BPP (13%). BPP-dione, when compared to the parent BPP, also displayed improved absorption and emission from the first excited singlet (S_1) state with a PLQY of 62% and an intramolecular charge-transfer character. The rod-like nano- to microcrystals as well as longer wires of these BPPs were also revealed by scanning electron microscopy. The intriguing optical properties of BPP and its derivatives may lead to their application as fluorophores.

Introduction

Polycyclic aromatic hydrocarbons (PAHs) have attracted increasing attention in view of their fascinating optical and electronic properties, which strongly depend on their size, shape, and edge structures, e.g., armchair and zigzag [1-6]. Benzo[*rst*]pentaphene (BPP) is an intriguing PAH with a combination of zigzag and armchair edges, which may serve as a

key building block for obtaining multifunctional organic materials [7]. Since the initial synthesis of BPP by Scholl and Neumann [8], simplified synthetic methods for BPP have been reported over the past decades [9-14]. Recently, a facile access to BPP was reported by Amsharov and co-workers through the so-called "dehydrative π-extension (DPEX)" reaction [12]. However, functionalized derivatives of BPP have scarcely been explored in comparison to the extensive studies on the derivatives of other PAHs, such as pyrene [15-17], perylene [18,19], and coronene [20]. Besides their limited accessibility in the past, the lack of attention to BPP can presumably be ascribed to its low photoluminescence quantum yield (PLQY). We recently reported a PLQY of 13% for pristine BPP and revealed a symmetry-forbidden nature of its first excited singlet (S_1) state [21]. Notably, a dimer of BPP, 5,5'-bibenzo[*rst*]pentaphene (BBPP), exhibited an enhanced PLQY of 44% through intensity borrowing from its bright S_2 state as well as intriguing symmetry-breaking charge transfer between two BPP units. Moreover, the substitution of BPP with two electron-donating bis(methoxyphenyl)amino groups further improved the PLQY to 73%, displaying a mixed excitonic and charge-transfer character [22]. Additionally, the functionalization of BPP with two methyl benzoate groups enabled the development of hole-selective contact, which was applicable in significantly improving the stability of inverted perovskite solar cells [23]. On the other hand, benzo[*rst*]pentaphene-5,8-dione (BPP-dione) is known as an oxidation product of BPP [24,25], but to the best of our knowledge, the detailed optical properties of this BPP derivative have not been previously described in the literature.

During our attempt to scale up the preparation of BPP **2** through the "DPEX" reaction, we unexpectedly obtained a 5-isopropoxy-substituted derivative of BPP (BPP-OiPr **3**) (Scheme 1), whose structure was proven by NMR, mass spectrometry, and X-ray crystallography. In this work, we optimized the reaction conditions to selectively obtain BPP-OiPr **3** in 55% yield from dialdehyde **1**. Additionally, oxidation of BPP-OiPr **3** provided BPP-dione **4** in 70% yield. The photophysical properties of BPP-OiPr **3** and BPP-dione **4** were carefully studied, examining the solvent-polarity dependence of their optical spectra, in comparison with parent BPP **2**. Notably, both BPP-OiPr **3** and BPP-dione **4** displayed enhanced PLQYs while a significant solvent-polarity dependence of the emission was observed only for the latter, suggesting the photoinduced intramolecular charge-transfer character of **4**. Moreover, BPPs **2**–**4** formed intriguing rod-like nano- to microcrystals and/or longer wires, which were visualized by scanning electron microscopy (SEM).

Results and Discussion

BPP **2** could be prepared by the “DPEX” reaction [12] in 60% yield on a 0.1 g scale from dialdehyde **1** with a concentration of 0.60 mM (Table 1, entry 1). However, the yield of BPP decreased to 40% when the amount of **1** was increased to 1.0 g with a concentration of 2.6 mM (Table 1, entry 2). In our

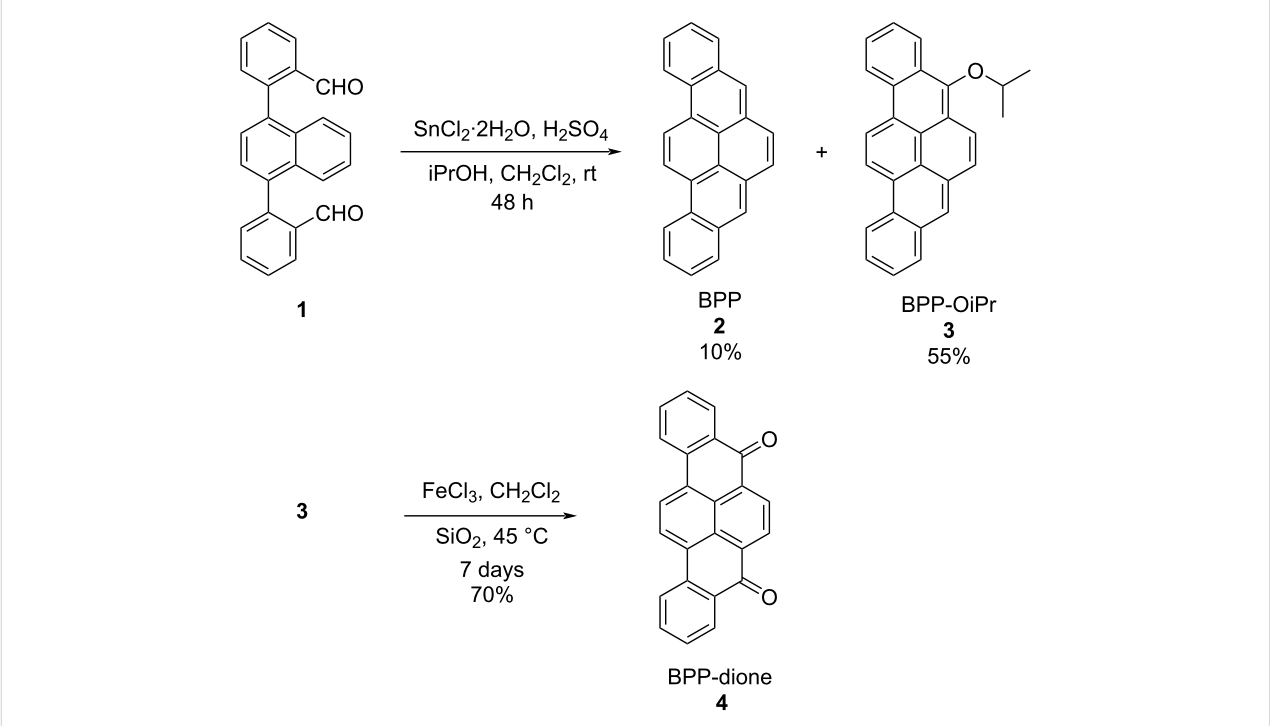

Scheme 1: Synthesis of BPP-OiPr **3** and BPP-dione **4**.

Table 1: Reaction conditions for the synthesis of BPP **2** and BPP-OiPr **3**.

Entry	Concentration of **1** (mM)	$SnCl_2·2H_2O$ (equiv)	iPrOH (vol %)	Concentrated H_2SO_4 (vol %)	Time (h)	Yields of **2**/**3** (%)[a]
1[b]	0.6	40	2.5	5.0	18	60/–
2[c]	2.6	40	2.5	5.0	24	40/–
3[c]	5.1	20	4.0	5.0	48	55/7
4[c]	6.0	20	10	5.0	72	29/37
5[c]	4.8	30	14	6.0	48	10/55

[a]Isolated yields. [b]Amount of **1**: 0.10 g. [c]Amount of **1**: 1.0 g.

attempt to improve the yield of BPP **2**, we decreased the equivalent of $SnCl_2·2H_2O$ and increased the volume ratio of iPrOH, which unexpectedly provided BPP-OiPr **3** as a byproduct in 7% yield along with BPP **2** in 55% yield (Table 1, entry 3). Further optimization of the reaction conditions by modifying the equivalent of $SnCl_2·2H_2O$ and volume ratios iPrOH and H_2SO_4 afforded BPP-OiPr **3** in 55% yield (Table 1, entries 4 and 5). Additionally, the oxidation of BPP-OiPr **3** using ferric chloride ($FeCl_3$) gave BPP-dione **4** in 70% yield. The chemical structures of BPP-OiPr **3** and BPP-dione **4** were characterized by ^1H and ^{13}C NMR spectroscopy as well as mass spectrometry (see Supporting Information File 1, Figures S8–S11).

A single crystal of BPP-OiPr **3** suitable for X-ray diffraction analysis was obtained by slow evaporation of a diethyl ether/*n*-hexane solution, enabling its unambiguous structural determination by single-crystal X-ray diffraction (Figure 1). The planar BPP core and the isopropyloxy group on the zigzag edge are clearly visualized (Figure 1a and b). In a unit cell consisting of four molecules, every two of them are stacked with the plane-to-plane distance of 3.45 Å (Figure 1c), displaying a lamellar π–π stacking motif in the overall packing structure (Figure S1 in Supporting Information File 1) [26-29]. The X-ray structure is well consistent with a model optimized by density functional theory (DFT) calculations (Figure S2 in Supporting Information File 1).

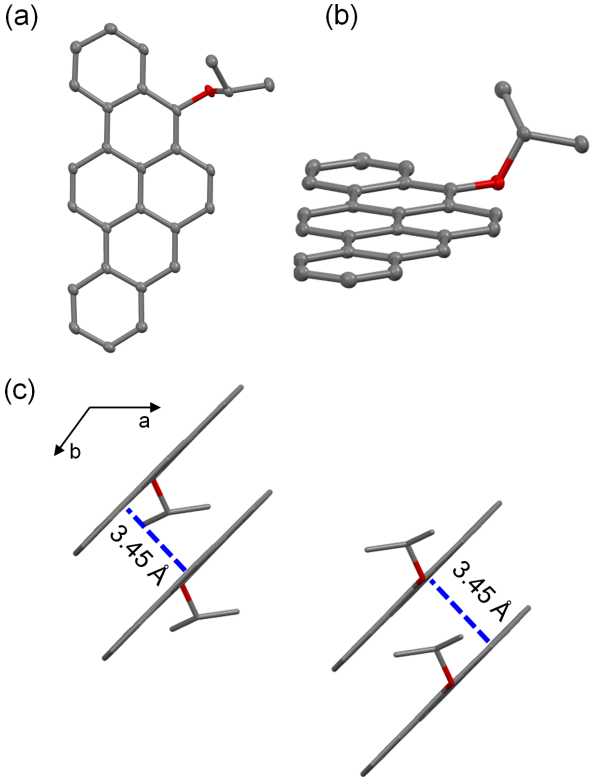

Figure 1: Single crystal structure of BPP-OiPr **3**: a) top view, b) side view (thermal ellipsoids shown at 50% probability), and c) molecular packing of **3** in a unit cell. All the hydrogen atoms are omitted for clarity.

The optoelectronic properties of BPP-OiPr **3** and BPP-dione **4** were initially investigated by UV–vis absorption spectroscopy in comparison with BPP **2** (Figure 2a). BPP **2** and BPP-OiPr **3** displayed similar and well-structured absorption peaks clearly showing the vibronic progressions. BPP-OiPr **3** also exhibited a small peak located at 442 nm with the molar extinction coefficient (ε) of 1800 M^{-1} cm^{-1}, which was similar to the previous observations of the dark S_1 states for BPP **2** and its mesityl- and *tert*-butyl-substituted derivatives [21,22]. In comparison to the absorption spectrum of BPP **2**, this lowest-energy absorption band of BPP-OiPr **3** was red-shifted by ≈26 nm, which marked the inductive and resonance effects of the electron-donating isopropyloxy group with lone pairs of electrons, raising the HOMO level (see Table S6 in Supporting Information File 1). BPP-dione **4** exhibited a broad absorption extending to 540 nm with a peak at 305 nm and featureless maxima at 469 and 497 nm, which were in line with the results of time-dependent DFT (TD-DFT) calculations at the M062X/6-311G(d,p) level of theory (Supporting Information File 1, Table S2). The longest-wavelength absorption maximum ($S_0 \rightarrow S_1$), attributed to the HOMO → LUMO transition, was calculated to be at 432 nm (f = 0.5674) for **4**. Compared to the S_1 states in BPP **2**

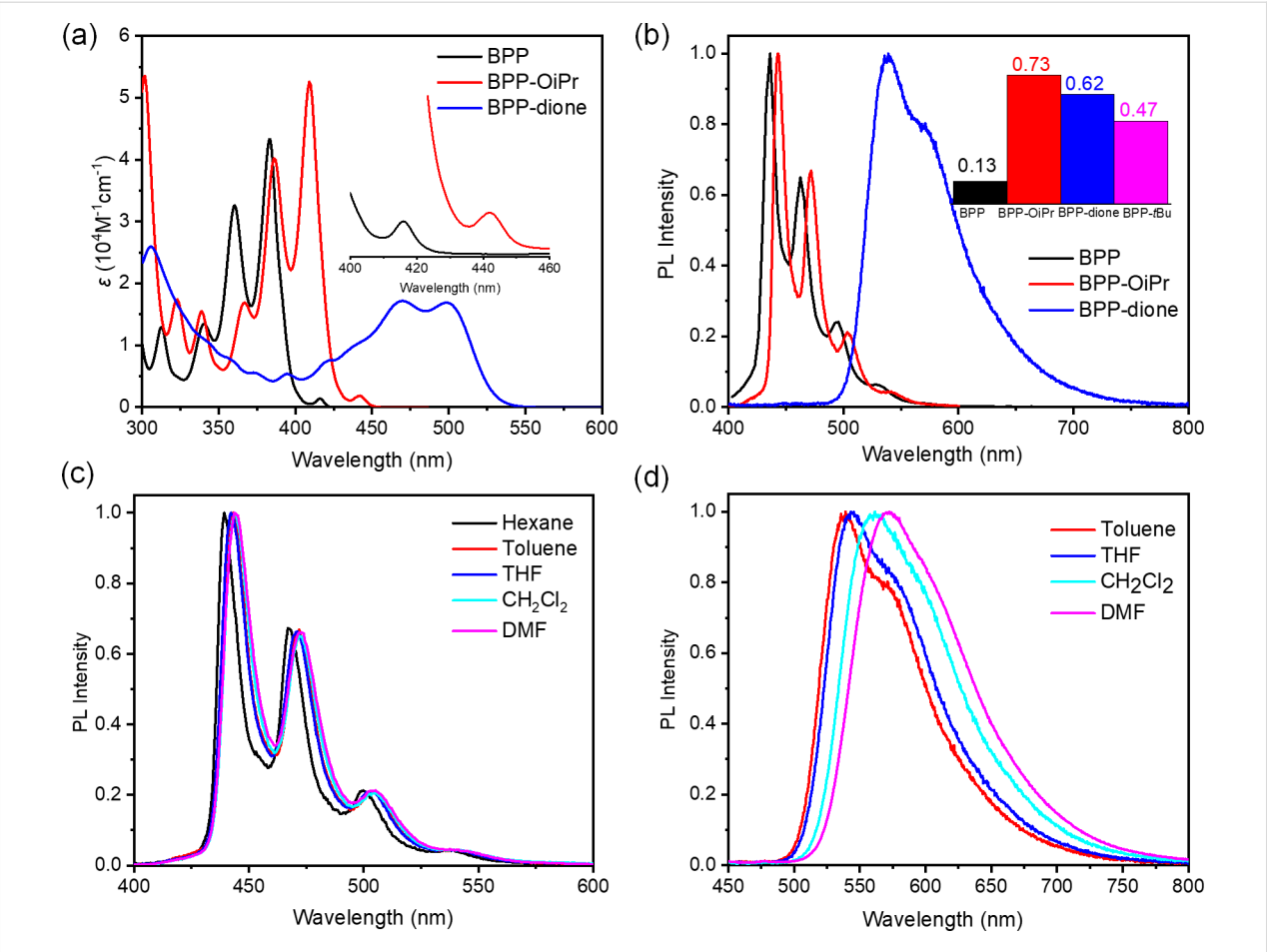

Figure 2: a) UV–vis absorption spectra of BPP **2**, BPP-OiPr **3**, and BPP-dione **4** measured in toluene. Inset: magnified spectra of **2** and **3** for the better visualization of the longest-wavelength peaks, b) normalized PL spectra of BPP **2**, BPP-OiPr **3**, and BPP-dione **4** measured in toluene with a 360 nm excitation. Inset: absolute PLQY of BPP **2** (excitation at 360 nm), BPP-OiPr **3** (excitation at 380 nm), BPP-dione **4** (excitation at 470 nm) in toluene, and BPP-*t*-Bu (excitation at 360 nm) [22], c) normalized PL spectra of BPP-OiPr **3** measured in hexane, toluene, tetrahydrofuran (THF), dichloromethane (CH_2Cl_2), and DMF, and d) normalized PL spectra of BPP-dione **4** measured in toluene, THF, CH_2Cl_2, and DMF.

(ε = 1200 M^{-1} cm^{-1}) and BPP-OiPr **3** (ε = 1800 M^{-1} cm^{-1}), corresponding to forbidden transitions as previously discussed for other BPP derivatives [21,22], the strikingly enhanced molar extinction coefficient observed for the lowest-energy band of BPP-dione **4** (ε = 17000 M^{-1} cm^{-1}) indicates that the optical transition to the S_1 state becomes allowed by this oxidation.

BPP **2** and BPP-OiPr **3** exhibited similar emission spectra in toluene with maxima at 436 and 443 nm, respectively, with well-defined vibronic structures (Figure 2b). Notably, the absolute PLQY of BPP-OiPr **3** was measured to be 0.73, demonstrating a remarkable enhancement of the photoluminescence from BPP **2** (PLQY: 0.13) and *tert*-butyl-substituted BPP (BPP-*t*-Bu, PLQY: 0.47) (Figure 2b) [21,22]. Considering that two *tert*-butyl groups should more effectively hinder the aggregation than one isopropyl group, we tentatively attribute the enhanced PLQY of **3** to the reduced molecular symmetry, which can relax the selection rule and allow more radiative transitions.

On the other hand, a broad and featureless PL spectrum with the maximum at 538 nm was observed for BPP-dione **4** in toluene with a high PLQY of 0.62, which is again significantly enhanced from that of BPP **2**. To gain further insight into the photophysical properties of BPP-OiPr **3** and BPP-dione **4**, their absorption and emission spectra were next measured in different solvents (Figure 2c and d and Supporting Information File 1, Figures S4 and S5). For BPP-OiPr **3** the well-defined vibronic structures were observed without showing any significant solvent-polarity dependence (Figure 2c). In contrast, BPP-dione **4** displayed a considerable redshift of the emission maximum from 538 nm in toluene to 572 nm in dimethylformamide (DMF) along with disappearance of the shoulder peak with increasing solvent polarity (Figure 2d). The UV–vis absorption spectra of **4** in different solvents also showed significant differences (Figure S5 in Supporting Information File 1), indicating an intramolecular charge-transfer character both in its ground and excited states [30,31].

DFT calculations were performed to understand the effects of the substituents on the frontier orbitals. As shown in Table S6 and Figure S1 in Supporting Information File 1, the highest occupied molecular orbital (HOMO) and the lowest unoccupied molecular orbital (LUMO) of BPP-OiPr **3** were calculated to be at −5.15 and −2.00 eV, respectively, with a slightly smaller HOMO–LUMO gap of 3.15 eV compared to that of BPP **2** (3.24 eV). BPP-dione **4** was revealed to have lower HOMO (−6.18 eV) and LUMO (−3.31 eV) and an even smaller HOMO–LUMO gap of 2.87 eV in agreement with the experimental optical spectra.

Nano- and microcrystals of organic semiconductors exhibit great potential in next-generation nanoscale optoelectronics and photonics [32-35]. However, precise preparation and shape control over organic crystals are still elusive targets [36]. We carried out SEM analysis of crystals of BPP-OiPr **3** obtained by slow evaporation of its solution in a mixture of dichloromethane and *n*-hexane (Figure 3). The formation of rod-shaped nano- and microcrystals and longer wires were revealed, with the widths from tens of nanometers to tens of micrometers and the lengths from hundreds of nanometers to hundreds of micrometers. For example, a nanocrystal (width: 143 nm, length: 661 nm; Figure 3b) and microcrystal (width: 12 µm, length: 318 µm; Figure 3c) of BPP-OiPr **3** were observed along with a long nanowire with the width of ≈50 nm and length over 1.8 µm (Figure 3d). Moreover, nano- and microcrystals of BPP **2** and BPP-dione **4** with similar shapes were also obtained and visualized by SEM (Figures S6 and S7 in Supporting Information File 1), suggesting that the BPP core can lead to such rod-shaped crystals and nanowires.

Conclusion

In summary, we achieved a facile synthesis of BPP-OiPr **3** and studied its optical properties in comparison to pristine BPP **2** and its oxidation product BPP-dione **4**. Both BPP-OiPr **3** and BPP-dione **4** displayed significantly enhanced PLQYs compared to BPP **2**, and only **4** displayed the intramolecular charge-transfer character. Additionally, these BPPs formed rod-shaped nano- and microcrystals as well as elongated nanowires with the lengths from hundreds of nanometers to hundreds of micrometers, as demonstrated by SEM. These results provide not only an easy access to highly emissive BPP derivatives with potential as organic fluorescent materials, but also an insight to design derivatives of other PAHs with enhanced fluorescence and charge transfer character.

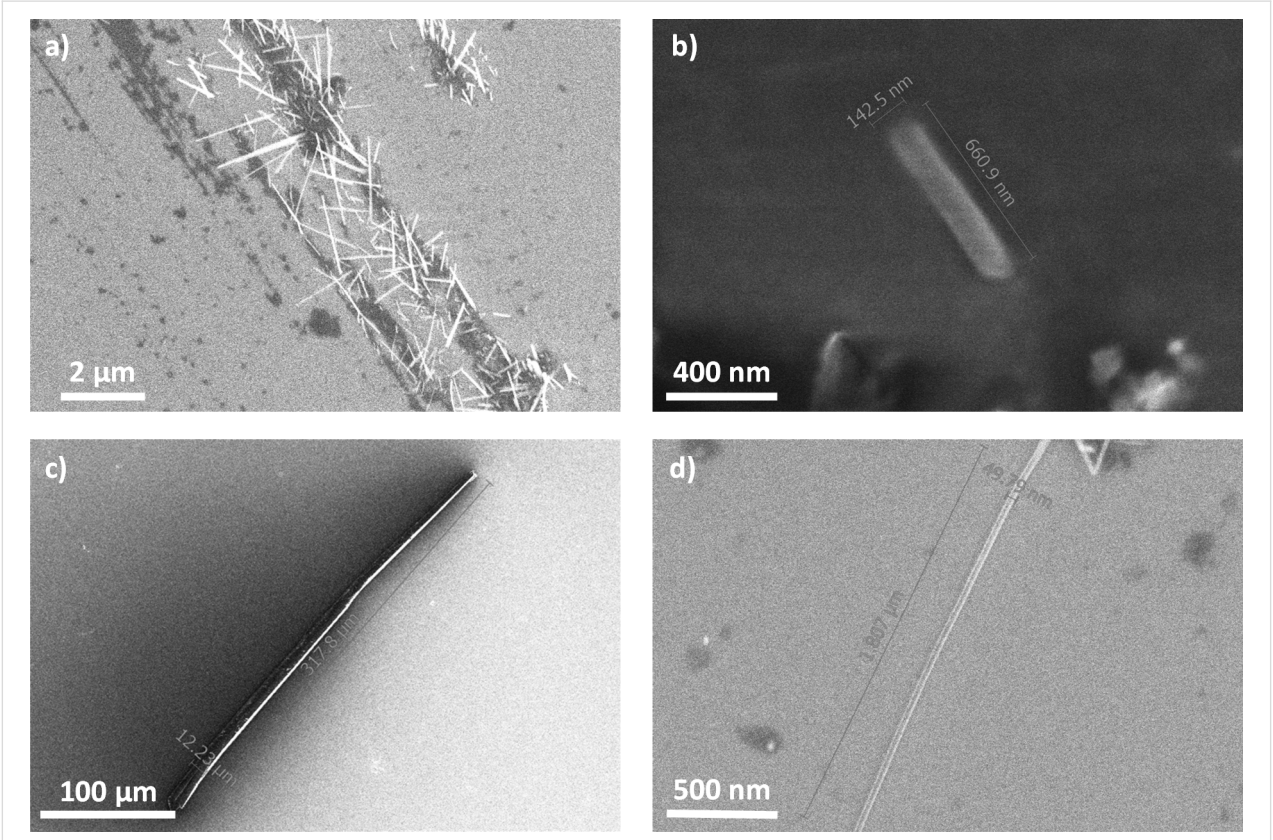

Figure 3: SEM images of BPP-OiPr showing: a) the variety in crystallization, including differences in shape, length, and width, b) rod-like crystals with lengths of hundreds of nanometers, c) rod-like crystals with lengths of hundreds of micrometers, and d) longer wire.

Supporting Information

Supporting Information File 1

Experimental and computational details, X-ray crystallography, synthesis and characterization of new compounds, additional PL, mass, and NMR spectra, and theoretical calculations.
[https://www.beilstein-journals.org/bjoc/content/supplementary/1860-5397-21-19-S1.pdf]

Acknowledgements

We appreciate the help and support provided by the Instrumental Analysis Section and the Scientific Computing and Data Analysis Section of Research Support Division at OIST. We thank Dr. Liliia Moshniaha from Organic Optoelectronics Unit at OIST for her support in optical measurements.

Funding

This work was financially supported by the Okinawa Institute of Science and Technology Graduate University (OIST), JSPS KAKENHI Grant No. JP21KK0091 and 23K04546, and JSPS International Joint Research Program (JRP-LEAD with DFG) No. JPJSJRP20221607.

ORCID® iDs

Islam S. Marae - https://orcid.org/0000-0002-9290-0174
Jingyun Tan - https://orcid.org/0000-0003-2957-7025
Rengo Yoshioka - https://orcid.org/0000-0002-6380-4140

Data Availability Statement

Data generated and analyzed during this study is available from the corresponding author upon reasonable request.

References

1. Wang, X.-Y.; Yao, X.; Müllen, K. *Sci. China: Chem.* **2019,** *62,* 1099–1144. doi:10.1007/s11426-019-9491-2
2. Xu, X.; Müllen, K.; Narita, A. *Bull. Chem. Soc. Jpn.* **2020,** *93,* 490–506. doi:10.1246/bcsj.20190368
3. Yang, K.; Li, Z.; Huang, Y.; Zeng, Z. *Acc. Chem. Res.* **2024,** *57,* 763–775. doi:10.1021/acs.accounts.3c00793
4. Paternò, G. M.; Goudappagouda; Chen, Q.; Lanzani, G.; Scotognella, F.; Narita, A. *Adv. Opt. Mater.* **2021,** *9,* 2100508. doi:10.1002/adom.202100508
5. Biagiotti, G.; Perini, I.; Richichi, B.; Cicchi, S. *Molecules* **2021,** *26,* 6306. doi:10.3390/molecules26206306
6. Majewski, M. A.; Stępień, M. *Angew. Chem., Int. Ed.* **2019,** *58,* 86–116. doi:10.1002/anie.201807004
7. Borissov, A.; Maurya, Y. K.; Moshniaha, L.; Wong, W.-S.; Żyła-Karwowska, M.; Stępień, M. *Chem. Rev.* **2022,** *122,* 565–788. doi:10.1021/acs.chemrev.1c00449
8. Scholl, R.; Neumann, H. *Ber. Dtsch. Chem. Ges. B* **1922,** *55,* 118–126. doi:10.1002/cber.19220550115
9. Clar, E. *Ber. Dtsch. Chem. Ges. B* **1939,** *72,* 1645–1649. doi:10.1002/cber.19390720903
10. Harvey, R. G.; Pataki, J.; Cortez, C.; Di Raddo, P.; Yang, C. X. *J. Org. Chem.* **1991,** *56,* 1210–1217. doi:10.1021/jo00003a050
11. Zhang, F.-J.; Cortez, C.; Harvey, R. G. *J. Org. Chem.* **2000,** *65,* 3952–3960. doi:10.1021/jo9918044
12. Lungerich, D.; Papaianina, O.; Feofanov, M.; Liu, J.; Devarajulu, M.; Troyanov, S. I.; Maier, S.; Amsharov, K. *Nat. Commun.* **2018,** *9,* 4756. doi:10.1038/s41467-018-07095-z
13. Xu, X.; Kinikar, A.; Di Giovannantonio, M.; Ruffieux, P.; Müllen, K.; Fasel, R.; Narita, A. *Bull. Chem. Soc. Jpn.* **2021,** *94,* 997–999. doi:10.1246/bcsj.20200382
14. Moriconi, E. J.; Salce, L. *J. Org. Chem.* **1967,** *32,* 2829–2837. doi:10.1021/jo01284a041
15. Figueira-Duarte, T. M.; Müllen, K. *Chem. Rev.* **2011,** *111,* 7260–7314. doi:10.1021/cr100428a
16. Feng, X.; Wang, X.; Redshaw, C.; Tang, B. Z. *Chem. Soc. Rev.* **2023,** *52,* 6715–6753. doi:10.1039/d3cs00251a
17. Feng, X.; Hu, J.-Y.; Redshaw, C.; Yamato, T. *Chem. – Eur. J.* **2016,** *22,* 11898–11916. doi:10.1002/chem.201600465
18. Kumari, A.; Sengupta, S. *ChemCatChem* **2024,** *16,* e202301033. doi:10.1002/cctc.202301033
19. Golshan, M.; Rostami-Tapeh-Esmail, E.; Salami-Kalajahi, M.; Roghani-Mamaqani, H. *Eur. Polym. J.* **2020,** *137,* 109933. doi:10.1016/j.eurpolymj.2020.109933
20. Kumar, S.; Tao, Y.-T. *Chem. – Asian J.* **2021,** *16,* 621–647. doi:10.1002/asia.202001465
21. Xu, X.; Gunasekaran, S.; Renken, S.; Ripani, L.; Schollmeyer, D.; Kim, W.; Marcaccio, M.; Musser, A.; Narita, A. *Adv. Sci.* **2022,** *9,* 2200004. doi:10.1002/advs.202200004
22. Xu, X.; Vonder Haar, A. L.; Yoshioka, R.; Zhang, Q.; Vasylevskyi, S.; Musser, A. J.; Narita, A. *Chem. Commun.* **2023,** *59,* 720–723. doi:10.1039/d2cc05369a
23. Wu, T.; Xu, X.; Ono, L. K.; Guo, T.; Mariotti, S.; Ding, C.; Yuan, S.; Zhang, C.; Zhang, J.; Mitrofanov, K.; Zhang, Q.; Raj, S.; Liu, X.; Segawa, H.; Ji, P.; Li, T.; Kabe, R.; Han, L.; Narita, A.; Qi, Y. *Adv. Mater. (Weinheim, Ger.)* **2023,** *35,* 2300169. doi:10.1002/adma.202300169
24. Cremonesi, P.; Hietbrink, B.; Rogan, E. G.; Cavalieri, E. L. *J. Org. Chem.* **1992,** *57,* 3309–3312. doi:10.1021/jo00038a015
25. Ünseren, E.; Fieser, L. F. *J. Org. Chem.* **1962,** *27,* 1386–1389. doi:10.1021/jo01051a063
26. Curtis, M. D.; Cao, J.; Kampf, J. W. *J. Am. Chem. Soc.* **2004,** *126,* 4318–4328. doi:10.1021/ja0397916
27. Wang, C.; Dong, H.; Hu, W.; Liu, Y.; Zhu, D. *Chem. Rev.* **2012,** *112,* 2208–2267. doi:10.1021/cr100380z
28. Hunter, C. A.; Sanders, J. K. M. *J. Am. Chem. Soc.* **1990,** *112,* 5525–5534. doi:10.1021/ja00170a016
29. Salini, P. S.; Rajagopal, S. K.; Hariharan, M. *Cryst. Growth Des.* **2016,** *16,* 5822–5830. doi:10.1021/acs.cgd.6b00919
30. Phan Huu, D. K. A.; Saseendran, S.; Dhali, R.; Franca, L. G.; Stavrou, K.; Monkman, A.; Painelli, A. *J. Am. Chem. Soc.* **2022,** *144,* 15211–15222. doi:10.1021/jacs.2c05537
31. Ishimatsu, R.; Matsunami, S.; Shizu, K.; Adachi, C.; Nakano, K.; Imato, T. *J. Phys. Chem. A* **2013,** *117,* 5607–5612. doi:10.1021/jp404120s
32. Zhao, Y. S.; Fu, H.; Peng, A.; Ma, Y.; Liao, Q.; Yao, J. *Acc. Chem. Res.* **2010,** *43,* 409–418. doi:10.1021/ar900219n

33. García de Arquer, F. P.; Armin, A.; Meredith, P.; Sargent, E. H. *Nat. Rev. Mater.* **2017,** *2,* 16100. doi:10.1038/natrevmats.2016.100
34. Jiang, H.; Hu, W. *Angew. Chem., Int. Ed.* **2020,** *59,* 1408–1428. doi:10.1002/anie.201814439
35. Lv, Q.; Zheng, M.; Wang, X.-D.; Liao, L.-S. *Small* **2022,** *18,* 2203961. doi:10.1002/smll.202203961
36. Shi, Y.-L.; Lv, Q.; Tao, Y.-C.; Ma, Y.-X.; Wang, X.-D. *Angew. Chem., Int. Ed.* **2022,** *61,* e202208768. doi:10.1002/anie.202208768

License and Terms

BEILSTEIN JOURNAL OF ORGANIC CHEMISTRY

Oxidation of [3]naphthylenes to cations and dications converts local paratropicity into global diatropicity

Abel Cárdenas[1], Zexin Jin[2], Yong Ni[3], Jishan Wu[2], Yan Xia[*3], Francisco Javier Ramírez[*1] and Juan Casado[*1]

Full Research Paper

Open Access

Address:
[1]Department of Physical Chemistry, University of Málaga, Andalucia-Tech, Campus de Teatinos s/n, 29071 Málaga, Spain, [2]Department of Chemistry, Stanford University, Stanford, CA 94305, USA and [3]Department of Chemistry, National University of Singapore, 3 Science Drive 3, Singapore, Singapore

Email:
Yan Xia[*] - yanx@stanford.edu; Francisco Javier Ramírez[*] - ramirez@uma.es; Juan Casado[*] - casado@uma.es

* Corresponding author

Keywords:
ACID; aromaticity; force constants; NICS; spectroscopy

Beilstein J. Org. Chem. **2025,** *21,* 277–285.
https://doi.org/10.3762/bjoc.21.20

Received: 22 August 2024
Accepted: 08 January 2025
Published: 05 February 2025

This article is part of the thematic issue "π-Conjugated molecules and materials".

Guest Editor: A. Mateo-Alonso

Abstract

Oxidized states of polycyclic aromatic hydrocarbons are of importance as they represent charged conductive species in organic semiconductor substrates. In this work, we investigated the properties of radical cations and dications of linear and angular [3]naphthylenes, consisting of fused aromatic naphthalenoid and antiaromatic cyclobutadienoid moieties and containing different degrees of paratropicity. Electronic absorption and vibrational Raman spectroscopies were used to describe the more relevant bonding changes. Stretching force constants were evaluated to monitor the aromatic–antiaromatic alternation pattern upon oxidation. They showed us that the dication of linear [3]naphthylene became an overall global π-electron delocalized molecule. This result was supported by nucleus independent chemical shift (NICS) calculations and anisotropy of the current induced density (ACID) plots, as they evidenced the presence of a perimetral diatropic global ring current upon oxidation.

Introduction

Since the discovery of conjugated polymers, it has been very insightful to study the molecular transformations associated with the generation of cationic species in conjugated aromatic oligomers displaying one-dimensional π-electron delocalization [1]. Oligothiophenes [2] and oligo(*para*-phenylene vinylenes) [3] have been used as models of systems in which charge defects are responsible for conductivity in their corresponding conducting polymers. Acenes are the archetypal structure of small polycyclic aromatic hydrocarbons with a π-electron structure expanded over a sequence of linearly fused benzenes [4]. Whereas acenes, up to substituted pentacenes, are relatively stable molecules under ambient conditions, longer acenes undergo spontaneous dimerization and react with oxygen [5,6], owing to the rising diradical character. This behavior was also

observed in the oxidized species of shorter acenes [7]. Surprisingly, Bettinger and Einholz [5] reported a stable heptacene dication in concentrated sulfuric acid, a stability attributed to the intermolecular Coulomb repulsion between the charged molecules, which prevents the dimerization of the acene. This exciting finding suggests possible modes of kinetic stabilization of oxidized species of π-conjugated compounds that are unstable in their neutral ground-electronic states.

According to the Hückel theory, antiaromatic molecules contain $4n$ π-electrons (n = 1, 2, 3…) and are highly unstable [8]. Though the antiaromatic molecules are much less common than their aromatic counterparts, they have attracted a growing interest in recent times, both from fundamental and technological reasons [9-11]. Antiaromaticity destabilizes the ground state of organic molecules by raising their highest energy occupied molecular orbitals, thus allowing for easy oxidation, doping, and electron-transfer reactions, all of which lead to conductive and photoactive species [9,12]. Given the inherent instability of neutral antiaromatic systems, including those systems containing fragments or moieties with local antiaromaticity, the detailed structural properties of the charged species formed from neutral antiaromatic precursors remain challenging to study. Haley and some of us reported the oxidization of partially antiaromatic diindenoanthracene, **DIAn**, Figure 1, forming charged molecules stabilized by the rearomatization of the central anthracene unit [13,14]. Porphyrinoid-based molecules [15-17] have also been reported as model systems to investigate redox charged species experiencing evolutions from neutral non-aromatic, to antiaromatic, and to aromatic structures.

Xia and co-workers recently reported a modular method to synthesize molecules containing cyclobutadienoid (CBD) groups [18-20], including [3]naphthylenes **1** and **2** in Figure 1 [18]. They are endowed by three aromatic naphthalenoid (NAP) moieties, fused by two antiaromatic CBD ones in two different topologies. Structurally, these polycyclic π-conjugated hydrocarbons consist of eight fused rings and thirty π-electrons. In this work, we report that compounds **1** and **2** can both be easily oxidized to form relatively stable radical cations ($\mathbf{1}^{\bullet+}$, $\mathbf{2}^{\bullet+}$) and dications ($\mathbf{1}^{2+}$, $\mathbf{2}^{2+}$). Interestingly, oxidation reverses local antiaromaticity to aromaticity, a transition that is particularly noticeable in $\mathbf{1} \rightarrow \mathbf{1}^{\bullet+} \rightarrow \mathbf{1}^{2+}$, where stabilization of the dication is associated to the appearance of a global diatropic ring current which stabilizes the whole molecule. On the contrary, $\mathbf{2}^{2+}$ can be better viewed as two segregated radical cations with slight, but high enough, local diatropic character in each. Here, we use electronic UV–vis–NIR absorption and vibrational Raman spectroscopies, normal mode and force field calculations, and magnetic-based analysis to gain comprehensive understanding of the electronic and molecular structures of the oxidized forms of these aromatic/antiaromatic molecular amalgams, aiming to discover the driving forces that govern the stabilization of such redox states.

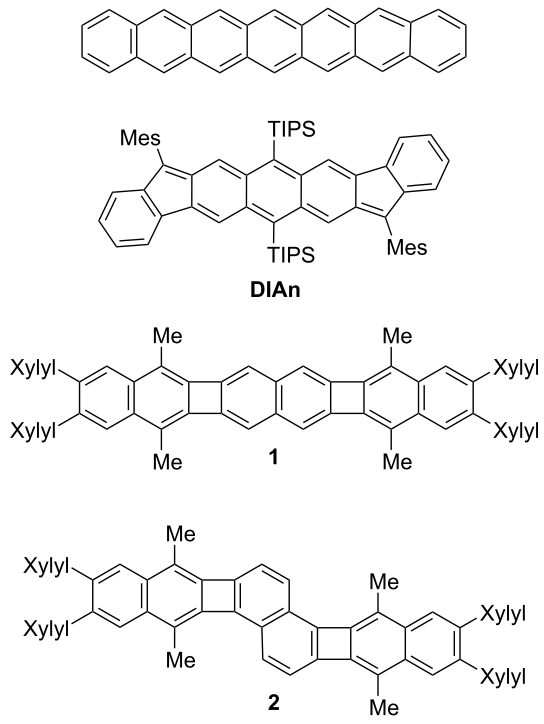

Figure 1: Chemical structures of heptacene, diindenoanthracene (**DIAn**), and the molecules of **1** and **2** studied in this work (TIPS: triisopropylsilyl, Mes: mesityl, Me: methyl).

Results and Discussion

Electrochemistry

Figure 2 shows the electrochemical cyclic voltammograms of **1** and **2**, in which two reversible oxidation processes can be observed. By considering the half-wave potential values obtained from the cyclic voltammograms, two one-electron peaks, at 0.67 and 1.16 V, were clearly resolved for the linear oligomer **1**. For the angular molecule **2**, two partially overlapped one-electron peaks appeared at noticeably lower voltages, 0.28 and 0.44 V. This result reflects the higher energy lying HOMO (and easy of oxidation) and stronger overall antiaromatic character of **2** compared to **1**. The decrease of the oxidation potentials with increasing antiaromaticity in the neutral states is opposite to the case of aromatic oligomers [21], where molecules with greater aromatic character have higher oxidation potentials. In addition, in $\mathbf{1}^{\bullet+}$ and $\mathbf{1}^{2+}$ the charge defects are extended over the whole molecule (vide infra). Thus, an extended π-electron delocalization effect in $\mathbf{1}^{\bullet+}$ stabilizes the cation and shifts anodically the second oxidation.

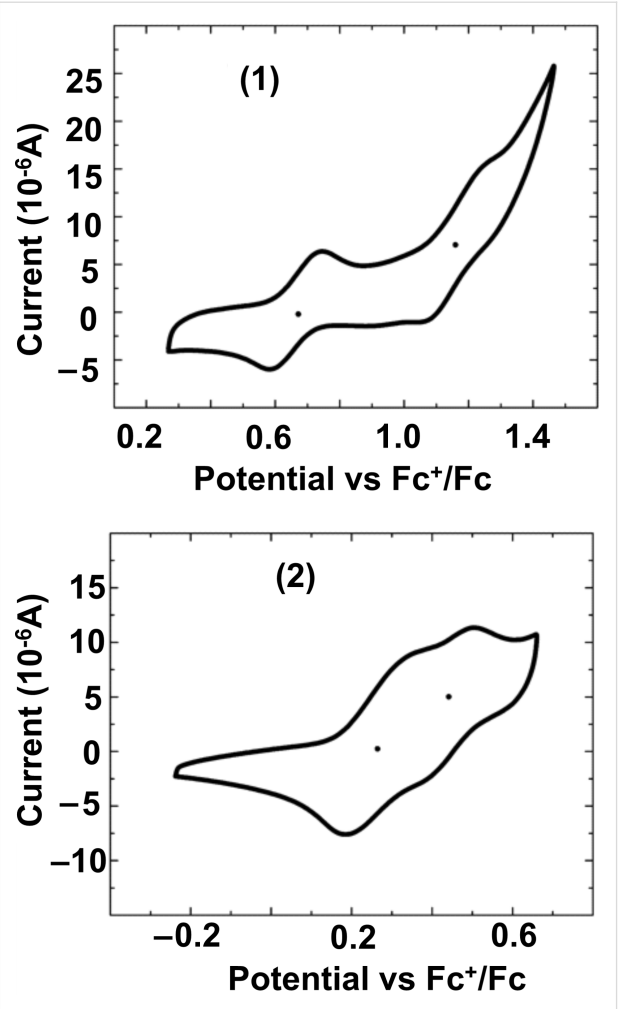

Figure 2: Cyclic voltammograms of **1** and **2**.

On the contrary, the charge in $\mathbf{2}^{\bullet+}$ is expected to be largely confined in the central NAP, and the second oxidation would give rise to two naphthylene-centered cations located at both sides of the molecule. The connection path would be partially interrupted by the angular topology, thus accounting for the more similar redox potentials.

Electronic spectroscopy

The UV–vis–NIR electronic absorption spectra of the neutral and oxidized species of compounds **1** and **2** are shown in Figure 3. Initial electrochemical oxidation of **1** resulted in the progressive replacement of its absorption bands by three new features, which were assigned to the $\mathbf{1}^{\bullet+}$ radical cation, namely at 352/369 nm, a multiplet in the 500–600 nm interval, and a broad peak centered at 1173 nm. Further oxidation resulted in a quite silent vis–NIR spectrum characterized by one main peak at 312 nm, which was assigned to the $\mathbf{1}^{2+}$ dication. The spectrum of the first oxidized species of **2**, the radical cation $\mathbf{2}^{\bullet+}$, shows a band at 363 nm, a shoulder at 439 nm, and a broad absorption at 1120 nm. Nonetheless, the spectra of the dications $\mathbf{1}^{2+}$ and $\mathbf{2}^{2+}$ display noticeably differences given that the features at 421 and at 1007 nm, present in the angular [3]naphthylene **2,** are apparently absent in the linear isomer **1**.

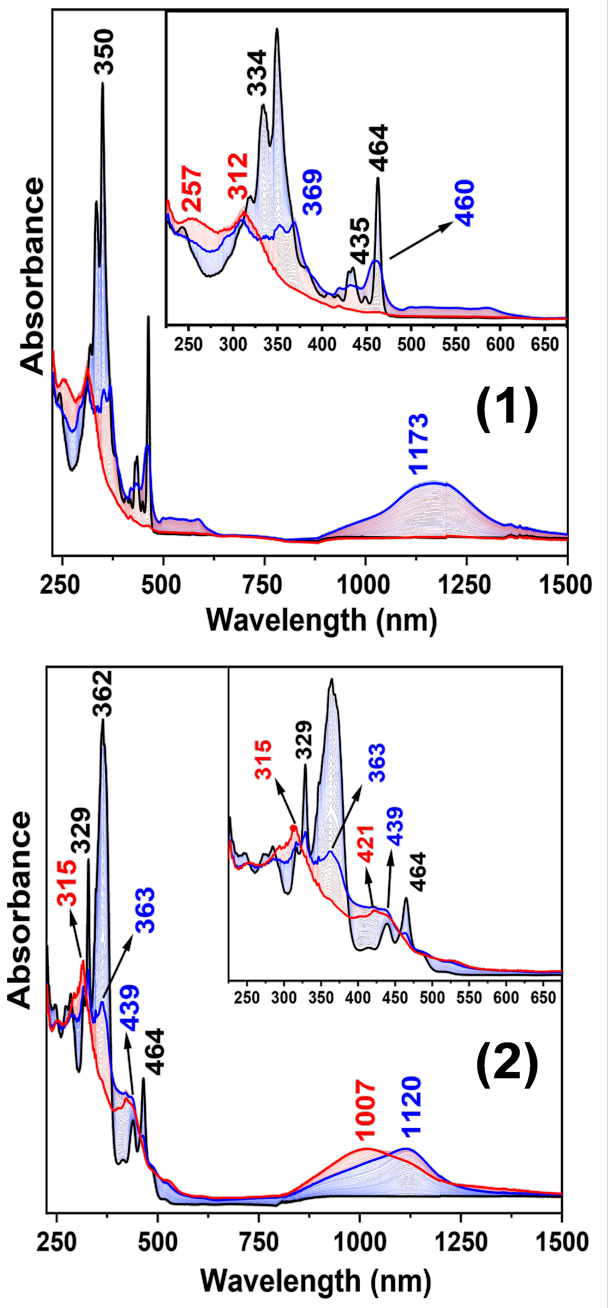

Figure 3: UV–vis–NIR electronic absorption spectra of **1** (top) and **2** (bottom) during the electrochemical oxidation in 0.1 M n-$Bu_4N{\cdot}PF_6$ in CH_2Cl_2 at room temperature. The traces are black lines for neutral, blue lines for radical cation, and red lines for dication species.

Raman spectroscopy

Figure 4 shows the experimental Raman spectrum of **1** in the neutral state and the theoretical Raman spectrum of a model

molecule, **m-1** (**1** without the xylyl and methyl substituents, Figure S1 in Supporting Information File 1), which can be closely correlated to the spectrum of **1**. In Tables S1–S6 of Supporting Information File 1, the theoretical characterization of all molecules is presented. A detailed assignment of the most relevant Raman bands obtained after vibrational analysis from the theoretical Raman spectrum obtained for the neutral state of **m-1** is included in Table S7 of Supporting Information File 1. The most significant Raman feature for the neutral species was measured at 1700 cm^{-1} and was predicted at 1730 cm^{-1} for **m-1**. This band was assigned to the symmetric CC stretching mode of the four bonds that are exocyclic to CBD, $\nu(CC)_{exo\text{-}CBD}$, or CBD breathing mode, as indicated by the atomic displacements shown in Figure 4. Other two strong Raman features were measured at 1448 and 1355 cm^{-1}. They were predicted at 1468 and 1354 cm^{-1}, respectively, for **m-1**, being assigned to CC stretching modes with slight contributions of aromatic CH bending vibrations. The complete eigenvector for these vibrations can be seen in Figure S2 in Supporting Information File 1. Given that former normal mode mainly involves the CBD moieties, the observed feature at 1700 cm^{-1} can be considered a suitable marker band of the structural and electronic changes of the antiaromatic CBD rings upon oxidation.

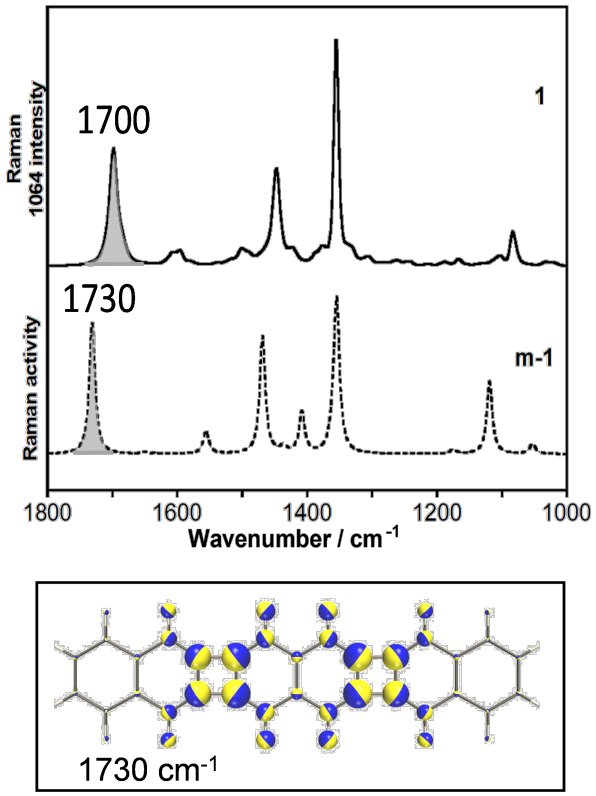

Figure 4: Top: B3LYP/6-311G(d,p) theoretical Raman spectrum of an unsubstituted model of **1** (denoted as **m-1** dotted lines which is **1** without methyl nor xylyl groups) compared with the experimental FT-Raman spectrum of **1**. Bottom: zoom in the CBO moiety of the vibrational normal mode associated with the theoretical Raman band at 1730 cm^{-1}.

The Raman spectra of **1**, $\mathbf{1}^{\bullet+}$, and $\mathbf{1}^{2+}$ are shown in Figure 5. Relative to **1**, the spectrum of $\mathbf{1}^{\bullet+}$ is characterized by a downshift by 11 cm^{-1} of the $\nu(CC)_{exo\text{-}CBD}$ vibration, together with the emergence of a new band at 1567 cm^{-1} which was assigned to a $\nu(CC)_{NAP}$ mode (CC stretching mode of the naphthalene moieties) on the basis of the normal mode calculation (Table S1 in Supporting Information File 1). Upon second oxidation, the former Raman vibrational band upshifts by 24 cm^{-1} for $\mathbf{1}^{2+}$, and the naphthalene $\nu(CC)_{NAP}$ stretching one disappears.

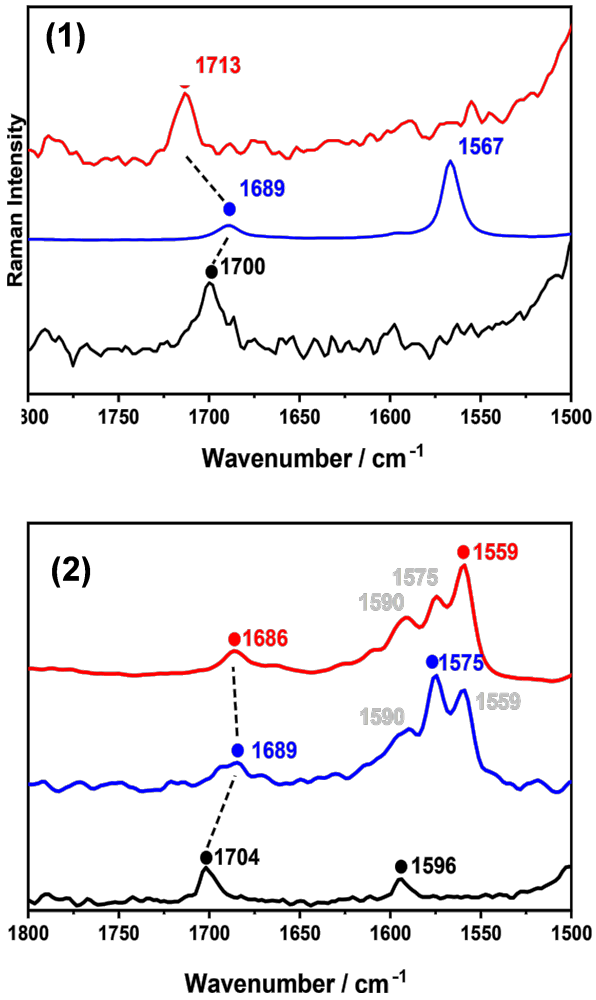

Figure 5: FT-Raman spectra in CH_2Cl_2 (approx. 10^{-2} to 10^{-3} M) of: top) **1** (black), $\mathbf{1}^{\bullet+}$ (blue), and $\mathbf{1}^{2+}$ (red). Bottom) **2** (black), $\mathbf{2}^{\bullet+}$ (blue), and $\mathbf{2}^{2+}$ (red). Oxidations are carried out by stepwise addition of $NOBF_4$ in CH_2Cl_2.

Overall, the evolution of the CBD breathing mode, throughout the series **1**→**1**$^{\bullet+}$→**1**$^{2+}$ is 1700 → 1689 → 1713 cm^{-1}.

Figure 5 shows the Raman spectra of neutral and oxidized species of **2** (the theoretical Raman spectrum of the model molecule **m-2** (depicted in Figure S1, Supporting Information File 1), which is **2** without the xylyl and methyl substituents can be seen in Figure S3 of Supporting Information File 1). The spectrum of the neutral form consists of a single band at 1704 cm^{-1}, assigned to the $\nu(CC)_{exo\text{-}CBD}$ vibration, which moved to 1689 cm^{-1} in **2**$^{\bullet+}$, and to 1686 cm^{-1} in **2**$^{2+}$. This continuous downshift upon oxidation is in contrast to the observed upshift in **1**$^{\bullet+}$ → **1**$^{2+}$, corroborating that the fusion topology of the two molecules determines the vibrational dynamics in connection with the fundamental role in the stabilization of the dications.

A second feature, measured at 1596 cm^{-1} in **2**, split into three peaks upon oxidation which are typically arising from $\nu(CC)_{NAP}$ modes. However, while the single peak of **1**$^{\bullet+}$ at 1567 cm^{-1} can be taken as an indicator of structural uniformity within the NAP rings, the three-folded band in **2**$^{\bullet+}$ suggests the presence of different CC bonds in the naphthalene groups. The Raman spectrum of the doubly oxidized form also showed a similar profile to that of **2**$^{\bullet+}$, with the only change of the relative intensities of the 1600–1550 cm^{-1} triplet. This result is fully compatible with the presence of the two rather overlapped (i.e., with similar energies) one-electron oxidations in the cyclic voltammetry of **2**. The spectral resemblances for **2**$^{\bullet+}$ and **2**$^{2+}$ might also indicate that the positive charge is mainly gathered by the central NAP for **2**$^{\bullet+}$, whereas in **2**$^{2+}$ the two charges would be localized towards the outermost NAPs. Nonetheless, **2**$^{\bullet+}$ and **2**$^{2+}$ both can be viewed as NAPs bearing positive charges.

Vibrational force field

A suitable tool to visualize the structural impact caused by the topological difference between **1** and **2** is using energetic parameters unequivocally associated to individual bonds. This is the case of the vibrational force constants [22]. They are defined as the second derivative of the molecular energy, in the minimum energy molecular structure, with respect to the nuclear displacement coordinates, which are usually the 3*N* Cartesian coordinates (*N* = number of atoms in the molecule). These Cartesian force constants are meaningless, so that they are transformed to a set of internal vibrational coordinates that account for single molecular motions, as stretchings, bendings or torsions. This procedure has been used here to calculate complete sets of stretching force constants associated to the individual CC bonds of **1** and **2**, hereafter designated as *k*[ν(CC)] (see Supporting Information File 1 for details of these calculations). They account for bond strengths, hence allowing a direct comparison between the bonds of parent molecules. In our case, they will reveal the transformation of the CC bond skeleton upon oxidation.

Figure 6 summarizes the set of *k*[ν(CC)] values calculated for neutral, radical cation, and dication of **m-1** and **m-2**, as well as those obtained at the same level for individual NAP and CBD. The reliability of the values is supported by the good fit between theoretical and experimental Raman spectra (see Figures S4 and S5 in Supporting Information File 1 for the calculated spectra of the oxidized species). As regarding the neutral species, fusion of these molecular groups provoked an increase of the *k*[ν(CC)] of the four exocyclic CBD bonds (i.e., d bonds in Figure 6) from 7.53 mdyn/Å in pristine NAP to 7.99–7.91 mdyn/Å in **m-1**, which accounts for the high wavenumber value of 1700 cm^{-1} (CBD breathing, or $\nu(CC)_{exo\text{-}CBD}$) of **1** in comparison with standard CC stretching wavenumbers of isolated NAP (usually lower than 1600 cm^{-1}) [23]. Force constants of the j and e CBD bonds in **m-1** are 5.61 and 4.45 mdyn/Å, respectively. Compared with pristine CBD, 9.63 and 3.91 mdyn/Å, this result involves a force constant equalization that clearly reveals the impact of mixing/fusing aromatic and antiaromatic cores. Conversely, the difference of the *k*[ν(CC)] for the adjacent CC bonds of NAP (i.e., d–c bonds), namely 7.99–5.47 mdyn/Å in **m-1** increase compared to

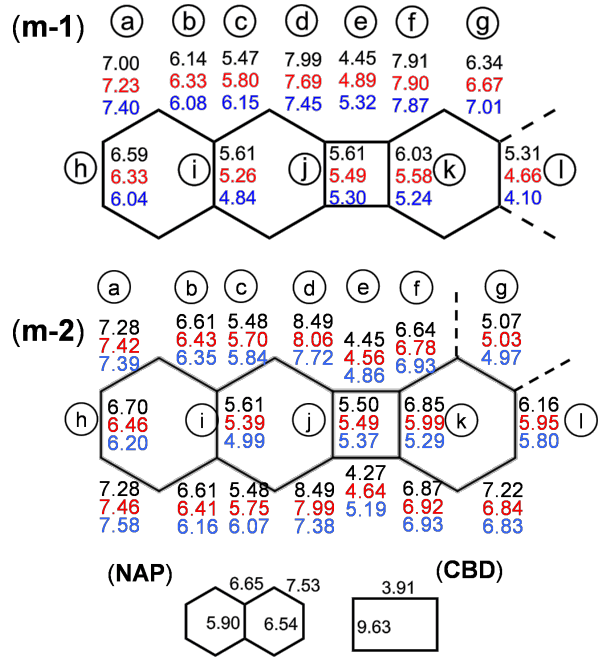

Figure 6: Force constants for the CC stretching vibrational coordinates of the neutral (black), radical cation (red) and dication (blue) of **m-1** and **m-2** compared with those obtained, under the same level or theory, for neutral naphthalene (NAP) and cyclobutadiene (CBD).

7.53–6.65 mdyn/Å for individual NAP which is compatible with an enhancement of the quinoid character of NAP.

The k[ν(CC)] values for exocyclic d bonds of CBD decreased from 7.99 to 7.69 mdyn/Å on going from **m-1** to **m-1**$^{\bullet+}$, which agrees with the observed 1700 → 1689 cm^{-1} downshift of the $\nu(CC)_{exo\text{-}CBD}$ Raman band. However, the further upshift observed in **m-1**$^{2+}$ cannot be justified by an increase of this CC stretching force constant, indeed, it decreases to 7.45 mdyn/Å in the dication. In such cases, the explanation must be sought by analyzing the complete set of CC bond force constants involved in the normal mode of Figure 4, which are those of d, e, f and j bonds. Oxidation decreases the d, f and j force constants while increases the e ones. The k[ν(CC)] values of the e bonds (which are the sole CBD bonds non shared with any naphthalene ring) evolves as 4.45 → 4.89 → 5.32 mdyn/Å throughout the series **m-1** → **m-1**$^{\bullet+}$ → **m-1**$^{2+}$, which involves differences of 0.44 mdyn/Å for the radical cation and 0.87 for the dication, both with respect to the neutral molecule. For the bonds whose force constants decrease upon oxidation, the greatest deviation is obtained for d (0.30 and 0.54 mdyn/Å, respectively). These values tell us that the second oxidation involves the enhancement on the k[ν(CC)] of the intrinsic CBD bond that is significantly higher than the reduction of force constant of the CC bonds shared with the adjacent NAP rings, which justifies the wavenumber upshift from 1689 to 1713 cm^{-1} on the $\nu(CC)_{exo\text{-}CBD}$ Raman band in the dication.

Despite the symmetry lowering with respect to **m-1**, D_{2h} → C_{2h}, the force field of neutral **m-2** (Figure 6) seems to preserve the punctual group of its linear analogue, especially concerning the outermost NAP moieties. Interestingly, this *quasi*-D_{2h} symmetry is broken upon oxidation, which is supported by the appearance of the triplet of Raman bands in the 1600–1550 cm^{-1} region. On the other hand, the k[ν(CC)] values of **m-2** and its cationic species follow all the same qualitative behavior exhibited for **m-1**, though with significant quantitative differences. The force constant of the e bond (intrinsic CBD) in the dication of **m-2** is only 0.41 mdyn/Å higher than in the neutral species, i.e., a reduction of 53% with respect to **m-1**. On the contrary, the decrease for the d bond (NAP adjacent) from **m-2** to **m-2**$^{2+}$ is 0.77 mdyn/Å, i.e., 30% higher than in **m-1**. In the case of the j bond, which is shared by CBD and NAP, both trends compensate each other, as its k[ν(CC)] decreases, upon double oxidation, 0.13 mdyn/Å for **m-2** and 0.31 mdyn/Å for **m-1**. These data evidence the sensitivity of the $\nu(CC)_{exo\text{-}CBD}$ Raman band to the fusion topology. In summary, the force constant analysis tells us that the structural changes upon oxidation are largely localized in CBD for **m-1** (marked by the zig-zag shift of the 1700 cm^{-1} Raman band) and in NAP for **m-2** (marked by the triplet in the 1500–1600 cm^{-1} region).

Nucleus-independent chemical shifts (NICS)

Among the different criteria to evaluate aromaticity, magnetic properties are the most confident, as they are directly connected with the ring currents associated to electronic delocalization. In order to figure out the driving force that leads the stabilization of the oxidized species of **1** and **2**, we calculated the NICS values of all fused rings in the neutral and cationic species of **m-1** and **m-2** (Figure 7), in order to obtain a precise and comparable measurement of the aromatic, antiaromatic, or non-aromaticity characters of each ring [24]. They were scanned along the main molecular axis, at a standard distance of 1.7 Å from the molecular plane to discard most of the contribution from the σ orbitals [25,26].

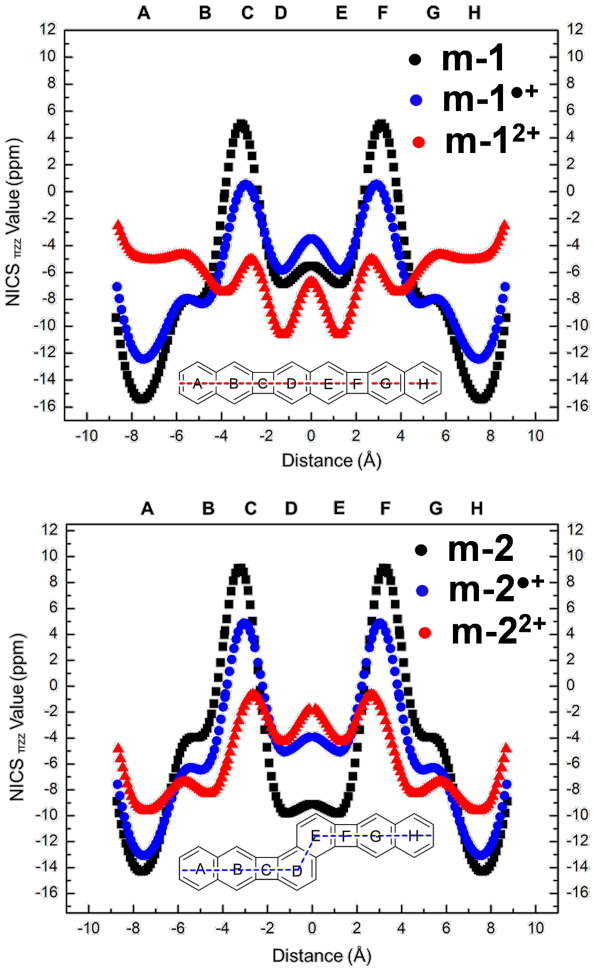

Figure 7: NICS-XY scans, at the (U)B3LYP/6-311G(d,p) level, for neutral **m-1** and **m-2** (black) and for their oxidized radical cations (blue) and dications (red).

In neutral **m-1**, NAP and CBD rings exhibited negative and positive NICS values, respectively, revealing their aromatic and antiaromatic characters. By oxidizing to **m-1**$^{\bullet+}$, this picture was

preserved, though the degrees of aromaticity and antiaromaticity in the constituent rings are reduced with respect to the neutral. Notably, the NICS values of CBD rings in **m-1**$^{\bullet+}$ were approaching zero, suggesting these units become non-aromatic. Removing a second electron turns all the rings aromatic, including the CBDs, as indicated by the negative NICS values across the entire molecule. Thus, on **m-1** → **m-1**$^{2+}$ transformation, the molecule converges towards a *quasi*-uniform sequence of fused rings, from the aromaticity viewpoint, in which we can stand out the following facts: i) the external/internal NAPs evolve from largely/slightly aromatic to slightly/more aromatic, and ii) the CBDs change from antiaromatic to slightly aromatic. This picture is quantitatively reflected by the difference between the largest (positive) and smallest (negative) NICS values, 8 ppm for **m-1**$^{2+}$ versus 23 ppm for **m-1**.

In **2**, the behavior is totally different, since the NICS patterns do not show sign inversion upon oxidation (Figure 7). The **m-2** → **m-2**$^{\bullet+}$ transformation localizes the largest changes on the central NAP, which accommodates the positive charges with the two CBD rings and acts as an antiaromatic barrier which prevents outermost charge delocalization. Conversely on **m-2**$^{\bullet+}$ → **m-2**$^{2+}$, NICS major changes are concentrated over the external NAP rings, on which the two charges mostly reside. In this case, the CBDs act as stoppers for whole innermost electron delocalization

Anisotropy of the current induced density (ACID)

The NICS analysis of the precedent paragraph is therefore consistent with the existence of an emergent global diatropic ring current in **m-1**$^{2+}$ along the entire molecular perimeter, whereas up to three independent ring currents are expected for the **m-2**$^{2+}$ structure. To visualize these results, we have analyzed the ACID plots for the neutral and cationic species of **m-1** and **m-2** [20,26]. Figure 8 shows these plots for the dications, while those of the neutral and radical cation species are included in Figures S6 and S7 of Supporting Information File 1. While the plot of **m-1** contains clockwise and counter-clockwise ring currents in the NAP and CBD units, respectively, **m-1**$^{2+}$ clearly showed a global diatropic peripheral ring current. This agrees with the negative NICS values across the entire molecule of **m-1**$^{2+}$. It also justifies the behavior of the Raman bands and the changes in the CC bond force constants. In further agreement with this description, we found that **m-1**$^{2+}$ discloses a singlet closed-shell ground electronic state without any trace of diradical character. Thus, the global current [27] provides a unique stabilizing effect for the dication of **m-1**. Such a stabilizing global current was not obvious in **m-2**$^{2+}$. Indeed, local ring currents are more evident in the outermost NAP rings, without showing a net circuit of diatropic current between them. This is consistent with the fact that the ground electronic state of **m-2**$^{2+}$ converges into an open-shell diradical structure (more stable than the closed-shell one by 1 kcal/mol at the DFT/(U)B3LYP/6-311G(d,p) level).

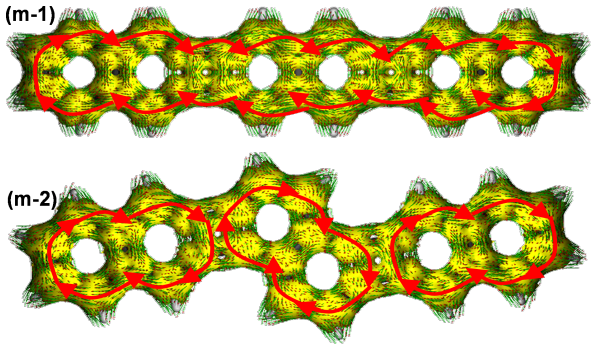

Figure 8: ACID plots at the CSGT-B3LYP/6-311G(d,p) level for dicationic species **m-1**$^{2+}$ (top) and **m-2**$^{2+}$ (bottom).

Both **1** and **2** are composed of a total of 30 π electrons, which correspond to the Hückel count of $4n + 2$, with $n = 7$. However, the two systems in their neutral states avoid this formulation and exhibit segmented structures, with attenuated aromatic character of the NAP rings due to the vicinal CBD ones, and mitigated antiaromaticity of the CBD as the result of the vicinal NAP rings. For the dications, the number of π electrons is $4n$ ($n = 7$), it is to say, an antiaromatic Hückel count which is clearly compensated in **m-1**$^{2+}$ by the formation of a well-defined diatropic global ring current. In the case of **m-2**$^{2+}$, antiaromaticity of CBD rings still remains because the electronic circulation is split in three independent ring currents.

Conclusion

Two [3]naphthylene isomers with different fusion topologies, linear (**1**) and angular (**2**), have been studied in their oxidized forms. The first oxidized states of both molecules attend to a concatenation of aromatic NAP and antiaromatic CBD units, in which the stability of the π-electronic structure arises from the dominance of local aromatic segments.

The generation of the linear dication, **1**$^{2+}$, erases this alternation pattern and conversely produces a global diatropic ring current which spreads over the whole molecule along the peripheral ribbons. On the contrary, the angular dication preserves the aromatic–antiaromatic confinement of the neutral and radical cation species. This is an unusual case scarcely described in 1D π-conjugated polycyclic molecules, where the stability of the linear dication is attributed to the formation of a global ring current.

Experimental

Electrochemistry

Cyclic voltammetry experiments were conducted with a three-electrode geometry operating with a glassy carbon as the working electrode. A Pt-coil counter electrode. and an Ag wire, as the pseudo-reference, were used. Potential values are given with respect to the ferrocene/ferrocenium (Fc/Fc^+) couple. Electrolyte solutions, at a concentration 0.1 M, were prepared from anhydrous, degassed HPLC grade CH_2Cl_2 and anhydrous Bu_4NPF_6. Voltammograms were recorded at a sweep rate of 100 mV s^{-1}. Sample concentrations were ca. 1–2 mM.

Electronic spectroscopy

UV–vis–NIR spectroelectrochemical studies were conducted on a Cary 5000 spectrophotometer. A C3 epsilon potentiostat from BASi was used for the electrolysis using a thin layer cell from a demountable Specac® Omni cell. In this cell, a three-electrode system was coupled to conduct in situ spectroelectrochemistry. A Pt gauze and a Pt wire were used as working and counter electrodes, respectively. A Ag wire was employed as the pseudo-reference electrode in a 0.1 M solution of Bu_4NPF_6 in freshly distilled CH_2Cl_2. Sample concentration was 1 mM. The spectra were collected by constant potential electrolysis, and the potentials were changed in intervals of 15 mV.

Raman spectroscopy

Raman spectra were obtained using a Bruker® RAMII Fourier transform Raman spectrometer, purged with dry nitrogen. Excitation radiation at 1064 nm was generated by a Nd-YAG laser working at 500 mW. Backscattering collection of the Raman radiation was performed. Typically, 2000 scans at a resolution better than 4 cm^{-1} were accumulated to optimize the signal-to-noise ratio.

Theoretical methods

Quantum chemistry was addressed with the Gaussian 09 suite of programs [28]. DFT calculations were performed at the (U)B3LYP[29,30] level, using the 6-311G* basis set [31]. This includes polarization functions on heavy atoms, being necessary for calculations on charged species. Geometry optimizations were achieved by allowing all the geometrical parameters to vary independently. The optimum energy structures were found to be a true minimum in the ground state potential energy surface. Analytical harmonic force constants, in Cartesian coordinates, and Raman intensities were evaluated at the ground-state-optimized geometry. The theoretical spectra were obtained by convoluting the calculated frequencies with Lorentzian functions. Bond stretching force constants were obtained using the given molecular symmetry for in-plane vibrations (see Supporting Information File 1).

Nucleus independent chemical shifts (NICS) were computed at the GIAO-B3LYP/6-311G* level. Calculations were carried out using the Aroma package [32], accordingly to published procedures [33]. The ACID plots were generated using the continuous set of gauge transformations (CSGT) method, as implemented in the Gaussian 09 suite, and the AICD 2.0.0 program [34].

Supporting Information

Supporting Information File 1

Chemical structures of **m-1** and **m-2**, vibrational assignment of **m-1**, the 1730 cm^{-1} normal mode, theoretical Raman spectrum of **m-1**, details of the force field calculations, theoretical Raman spectra of **m-1** and **m-2**, and ACID plots of **m-1** and **m-2**.
[https://www.beilstein-journals.org/bjoc/content/supplementary/1860-5397-21-20-S1.pdf]

Acknowledgements

We thank the Vibrational Spectroscopy Laboratory and the Computer Center of the Research Central Services of the University of Málaga.

Funding

Financial support was provided by the European Union and the *Ministerio de Ciencia e Innovación* of the Spanish Government (MINECO/FEDER program, project reference PID2021-127127NB-I00), the *Junta de Andalucía* (ProyExcel_00328), and the National Science Foundation (CHE-1855922).

Author Contributions

Abel Cárdenas: investigation. Zexin Jin: investigation. Yong Ni: investigation. Jishan Wu: conceptualization; formal analysis. Yan Xia: conceptualization; formal analysis; supervision. Francisco Javier Ramírez: conceptualization; data curation; supervision; validation. Juan Casado: conceptualization; formal analysis; funding acquisition; project administration; software; supervision; validation; writing – original draft; writing – review & editing.

ORCID® iDs

Abel Cárdenas - https://orcid.org/0000-0002-0631-0160
Juan Casado - https://orcid.org/0000-0003-0373-1303

Data Availability Statement

Additional research data generated and analyzed during this study is not shared.

References

1. Brédas, J. L.; Street, G. B. *Acc. Chem. Res.* **1985,** *18,* 309–315. doi:10.1021/ar00118a005
2. Perepichka, I. F.; Perepichka, D. F., Eds. *Handbook of Thiophene-Based Materials: Applications in Organic Electronics and Photonics;* John Wiley & Sons: New York, NY, USA, 2009. doi:10.1002/9780470745533
3. Furukawa, Y. *J. Phys. Chem.* **1996,** *100,* 15644–15653. doi:10.1021/jp960608n
4. Tönshoff, C.; Bettinger, H. F. *Chem. – Eur. J.* **2021,** *27,* 3193–3212. doi:10.1002/chem.202003112
5. Einholz, R.; Bettinger, H. F. *Angew. Chem., Int. Ed.* **2013,** *52,* 9818–9820. doi:10.1002/anie.201209722
6. Plasser, F.; Pašalić, H.; Gerzabek, M. H.; Libisch, F.; Reiter, R.; Burgdörfer, J.; Müller, T.; Shepard, R.; Lischka, H. *Angew. Chem.* **2013,** *125,* 2641–2644. doi:10.1002/ange.201207671
7. Zade, S. S.; Zamoshchik, N.; Reddy, A. R.; Fridman-Marueli, G.; Sheberla, D.; Bendikov, M. *J. Am. Chem. Soc.* **2011,** *133,* 10803–10816. doi:10.1021/ja106594v
8. Breslow, R. *Acc. Chem. Res.* **1973,** *6,* 393–398. doi:10.1021/ar50072a001
9. Fujii, S.; Marqués-González, S.; Shin, J.-Y.; Shinokubo, H.; Masuda, T.; Nishino, T.; Arasu, N. P.; Vázquez, H.; Kiguchi, M. *Nat. Commun.* **2017,** *8,* 15984. doi:10.1038/ncomms15984
10. Breslow, R.; Murayama, D. R.; Murahashi, S.-I.; Grubbs, R. *J. Am. Chem. Soc.* **1973,** *95,* 6688–6699. doi:10.1021/ja00801a027
11. Chen, W.; Li, H.; Widawsky, J. R.; Appayee, C.; Venkataraman, L.; Breslow, R. *J. Am. Chem. Soc.* **2014,** *136,* 918–920. doi:10.1021/ja411143s
12. Breslow, R.; Foss, F. W., Jr. *J. Phys.: Condens. Matter* **2008,** *20,* 374104. doi:10.1088/0953-8984/20/37/374104
13. Rudebusch, G. E.; Espejo, G. L.; Zafra, J. L.; Peña-Alvarez, M.; Spisak, S. N.; Fukuda, K.; Wei, Z.; Nakano, M.; Petrukhina, M. A.; Casado, J.; Haley, M. M. *J. Am. Chem. Soc.* **2016,** *138,* 12648–12654. doi:10.1021/jacs.6b07882
14. Barker, J. E.; Dressler, J. J.; Cárdenas Valdivia, A.; Kishi, R.; Strand, E. T.; Zakharov, L. N.; MacMillan, S. N.; Gómez-García, C. J.; Nakano, M.; Casado, J.; Haley, M. M. *J. Am. Chem. Soc.* **2020,** *142,* 1548–1555. doi:10.1021/jacs.9b11898
15. Peeks, M. D.; Jirasek, M.; Claridge, T. D. W.; Anderson, H. L. *Angew. Chem., Int. Ed.* **2019,** *58,* 15717–15720. doi:10.1002/anie.201909032
16. Jirásek, M.; Anderson, H. L.; Peeks, M. D. *Acc. Chem. Res.* **2021,** *54,* 3241–3251. doi:10.1021/acs.accounts.1c00323
17. Ren, L.; Gopalakrishna, T. Y.; Park, I.-H.; Han, Y.; Wu, J. *Angew. Chem., Int. Ed.* **2020,** *59,* 2230–2234. doi:10.1002/anie.201911269
18. Jin, Z.; Teo, Y. C.; Teat, S. J.; Xia, Y. *J. Am. Chem. Soc.* **2017,** *139,* 15933–15939. doi:10.1021/jacs.7b09222
19. Jin, Z.; Yao, Z.-F.; Barker, K. P.; Pei, J.; Xia, Y. *Angew. Chem., Int. Ed.* **2019,** *58,* 2034–2039. doi:10.1002/anie.201812581
20. Jin, Z.; Teo, Y. C.; Zulaybar, N. G.; Smith, M. D.; Xia, Y. *J. Am. Chem. Soc.* **2017,** *139,* 1806–1809. doi:10.1021/jacs.6b12888
21. Müllen, K.; Wegner, G., Eds. *Electronic Materials: The Oligomer Approach;* Wiley-VCH: Weinheim, Germany, 1998. doi:10.1002/9783527603220
22. Wilson, E. B., Jr.; Decius, J. C.; Cross, P. C. *Phys. Today* **1955,** *8* (11), 21–22. doi:10.1063/1.3061820
23. Martin, J. M. L.; El-Yazal, J.; François, J.-P. *J. Phys. Chem.* **1996,** *100,* 15358–15367. doi:10.1021/jp960598q
24. Chen, Z.; Wannere, C. S.; Corminboeuf, C.; Puchta, R.; Schleyer, P. v. R. *Chem. Rev.* **2005,** *105,* 3842–3888. doi:10.1021/cr030088+
25. Stanger, A. *J. Org. Chem.* **2006,** *71,* 883–893. doi:10.1021/jo051746o
26. Gershoni-Poranne, R.; Stanger, A. *Chem. – Eur. J.* **2014,** *20,* 5673–5688. doi:10.1002/chem.201304307
27. Herges, R.; Geuenich, D. *J. Phys. Chem. A* **2001,** *105,* 3214–3220. doi:10.1021/jp0034426
28. *Gaussian 09,* Revision C.01; Gaussian, Inc.: Wallingford, CT, 2010.
29. Becke, A. D. *J. Chem. Phys.* **1993,** *98,* 5648–5652. doi:10.1063/1.464913
30. Lee, C.; Yang, W.; Parr, R. G. *Phys. Rev. B* **1988,** *37,* 785–789. doi:10.1103/physrevb.37.785
31. Clark, T.; Chandrasekhar, J.; Spitznagel, G. W.; Schleyer, P. V. R. *J. Comput. Chem.* **1983,** *4,* 294–301. doi:10.1002/jcc.540040303
32. AROMA plugin; Rahalkar, A.; Stanger, A. This software may be downloaded free of charge from https://chemistry.technion.ac.il/en/team/amnon-stanger/
33. Gershoni-Poranne, R.; Stanger, A. *Chem. Soc. Rev.* **2015,** *44,* 6597–6615. doi:10.1039/c5cs00114e
34. Geuenich, D.; Hess, K.; Köhler, F.; Herges, R. *Chem. Rev.* **2005,** *105,* 3758–3772. doi:10.1021/cr0300901

License and Terms

BEILSTEIN JOURNAL OF ORGANIC CHEMISTRY

Unraveling aromaticity: the dual worlds of pyrazole, pyrazoline, and 3D carborane

Zahra Noori[1], Miquel Solà[2], Clara Viñas[3], Francesc Teixidor[*3] and Jordi Poater[*1,4]

Full Research Paper

Open Access

Address:
[1]Departament de Química Inorgànica i Orgànica & Institut de Química Teòrica i Computacional (IQTCUB), Universitat de Barcelona, Martí i Franquès 1-11, 08028 Barcelona, Spain, [2]Institut de Química Computacional i Catàlisi and Departament de Química, Universitat de Girona, Maria Aurèlia Capmany 69, 17003 Girona, Catalonia, Spain, [3]Institut de Ciència de Materials de Barcelona, Consejo Superior de Investigaciones Científicas, Campus Universitat Autònoma de Barcelona, 08193 Bellaterra, Spain and [4]ICREA, Pg. Lluís Companys 23, 08010 Barcelona, Spain

Email:
Francesc Teixidor[*] - teixidor@icmab.es; Jordi Poater[*] - jordi.poater@ub.edu

* Corresponding author

Keywords:
3D aromaticity; carborane; density functional theory; NICS ambiguity; pyrazole

Beilstein J. Org. Chem. **2025,** *21,* 412–420.
https://doi.org/10.3762/bjoc.21.29

Received: 27 September 2024
Accepted: 15 January 2025
Published: 21 February 2025

This article is part of the thematic issue "π-Conjugated molecules and materials".

Guest Editor: A. Mateo-Alonso

Abstract

A new series of *o*-carborane-fused pyrazoles has been recently successfully synthesized. This fusion was expected to create a hybrid 3D/2D aromatic system, combining the 3D aromaticity of *o*-carborane with the 2D aromaticity of pyrazole. However, while the boron cage retains its aromatic character, the pyrazole's aromaticity is lost. As a result, rather than forming *o*-carborane-fused pyrazoles, the synthesis yielded *o*-carborane-fused pyrazolines, which are non-aromatic. The limited overlap between the π molecular orbitals (MOs) of the planar heterocycle and the $n + 1$ MOs of the carborane prevents significant electronic delocalization between the two fused components. This contrasts with the fusion of pyrazole and benzene to form indazole, where both rings maintain their 2D aromaticity. Our findings demonstrate that the peripheral σ-aromaticity of carborane and the π-aromaticity of the heterocycle are orthogonal, making a true 3D/2D aromatic system unachievable. The carborane is highly aromatic, generating highly negative NICS values (−25 to −30 ppm). We have observed that these high NICS values extend to fused rings, leading to incorrect estimations of aromaticity. Therefore, relying solely on NICS can be misleading, and other computational indicators, along with experimental or structural data, should be used to accurately assess aromaticity.

Introduction

Pyrazoles and 1,2-diazoles are five-membered aromatic heterocyclic compounds that have garnered significant attention in recent years [1-3]. While these compounds are rarely found in nature, they exhibit a wide range of biological activities, making them highly useful in pharmaceutical chemistry [4-6]. Pyrazoles are also extensively employed in agrochemicals,

serving as key components in insecticides, herbicides, and fungicides [7]. Beyond their chemical uses, pyrazoles play an important role in the construction of supramolecular assemblies and molecular systems designed for photoinduced electron transfer [8,9]. Thanks to their notable photophysical properties, pyrazoles are applied in OLED technology [10]. Noticeably, in its ground state, pyrazole ($C_3H_4N_2$) is an aromatic molecule that follows Hückel's rule, with two formal double bonds and a lone pair on one nitrogen generating a π system with 6 π electrons [11]. When fused with a benzene ring, sharing a C–C bond, it remains aromatic, which is the case of indazole. Pyrazoline ($C_3H_6N_2$), similar to pyrazole, formally has only one double bond and a lone pair on the nitrogen, so it does not satisfy Hückel's rule and it is therefore non-aromatic. Even when fused with benzene via a C–C bond, pyrazoline remains non-aromatic, which is the case of indazoline.

Icosahedral carboranes are globular molecular clusters made of carbon and boron, displaying 3D aromaticity [12-15]. Their unique properties – such as aromaticity, exceptional thermal and chemical stability, and robust synthetic versatility [16,17] – make carborane derivatives essential components in various fields. These include pharmaceuticals [18-22], boron neutron capture therapy (BNCT) [23-26], organometallic ligands [27], and functional materials [28-30]. As a result, developing efficient methods for selectively introducing functional groups into carboranes has become a key area of research [29,31]. Moreover, replacing planar aryl rings in biologically active molecules with spherical carborane units has led to novel alternatives [32], offering enhanced properties and efficacy [28,30,33-35]. Therefore, the advancement of simple, efficient methodologies for synthesizing *o*-carborane-fused heterocycles is critically needed. However, the limited number of synthetic strategies for carborane functionalization [36] continues to constrain their broader use.

With this in mind, Lee and colleagues have recently developed an efficient synthetic method for producing *o*-carborane-fused pyrazoles as a novel scaffold, without using transition metals. Their approach involves reacting B(4)-acylmethyl and B(3,5)-diacylmethyl *o*-carborane with 2-azido-1,3-dimethylimidazolinium hexafluorophosphate (ADMP) in the presence of DBU in acetonitrile. This one-pot process enables sequential diazotization and cyclization, leading to the formation of two or three C–N bonds under extremely mild conditions, with excellent tolerance for various functional groups [37]. A priori, this fusion between 3D aromatic *o*-carborane and 2D aromatic pyrazole should give a 3D/2D aromatic *o*-carborane-fused pyrazole. However, we recently demonstrated that, unlike many 2D/2D and 3D/3D aromatic fusions that retain their aromaticity, a 3D/2D aromatic combination is not feasible due to the ineffective overlap between the π molecular orbitals of the planar species and the (n + 1) molecular orbitals of the aromatic cage. This lack of overlap prevents effective electronic delocalization between the two fused units [38]. Soon after, Kelemen and colleagues confirmed our findings also applied to *o*-carboranes fused with five-membered ring systems [39,40]. The positioning of the heteroatom in these exo rings governs bonding, leading to restricted conjugation and, consequently, no aromatic stabilization. Importantly, the magnetic field generated by the 3D cluster influences the conjugation and the computed magnetic properties of the fused exo ring [34,38,40], which can lead to the incorrect assignment of aromatic character to this ring.

This study aims to determine whether *o*-carborane-fused pyrazoles can be classified as aromatic 3D/2D systems. While previous research has not specifically examined pyrazoles in this context, we hypothesize that although the 3D *o*-carborane maintains its aromaticity, the 2D pyrazole may lose its aromatic character. If our hypothesis holds, these compounds should be termed *o*-carborane-fused pyrazolines rather than pyrazoles. Alternatively, the presence of the N–N bond in pyrazole might help preserve its aromaticity. To explore this, we performed quantum chemical analyses on a range of *o*-carborane-fused pyrazoles and pyrazolines and compared them with their fully planar indazole and indazoline analogues. Aromaticity or non-aromaticity can be assessed using indicators such as magnetic-based NICS, electronic-based MCI, or bond lengths, among others, given its multidimensional character [41-43].

Results and Discussion

We have first analyzed a series *o*-carborane-fused pyrazoles involving the fusion to either a C–C, C–B or B–B bond in the boron cluster, referred as pyrazole^{CC}, pyrazole^{CB}, and pyrazole^{BB}, respectively (Figure 1). Among these isomers, pyrazole^{BB} is the most stable, followed by pyrazole^{CB} and pyrazole^{CC} by 19.2 and 24.5 kcal mol^{-1}, respectively. This order of stability correlates with the length of the fusing bond between the carborane and the pyrazole, i.e., B–B, C–B and C–C decrease from 1.760, to 1.674 and to 1.605 Å, respectively (Figure 2). Thus, the longer the length of the fusing bond, the lower the tension of the formed five-membered ring and the more stable the complex. The stronger strength of the C–B bond compared to the C–C bond by 2.4 kcal/mol further supports the above statement [44].

Next, we have compared the above *o*-carborane-fused pyrazoles with a series of reference systems with the aim to better understand the electronic structure of the fused heterocycle and its aromaticity (Figure 3). First, the C–C bond length connecting the boron cage and pyrazole is 1.605 Å (pyrazole^{CC}), very similar to that of *closo*-$C_2B_{10}H_{12}$ [45,46]

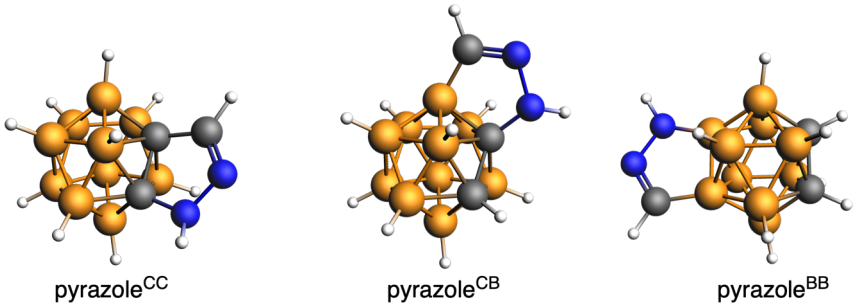

Figure 1: Series *o*-carborane-fused pyrazoles under analysis.

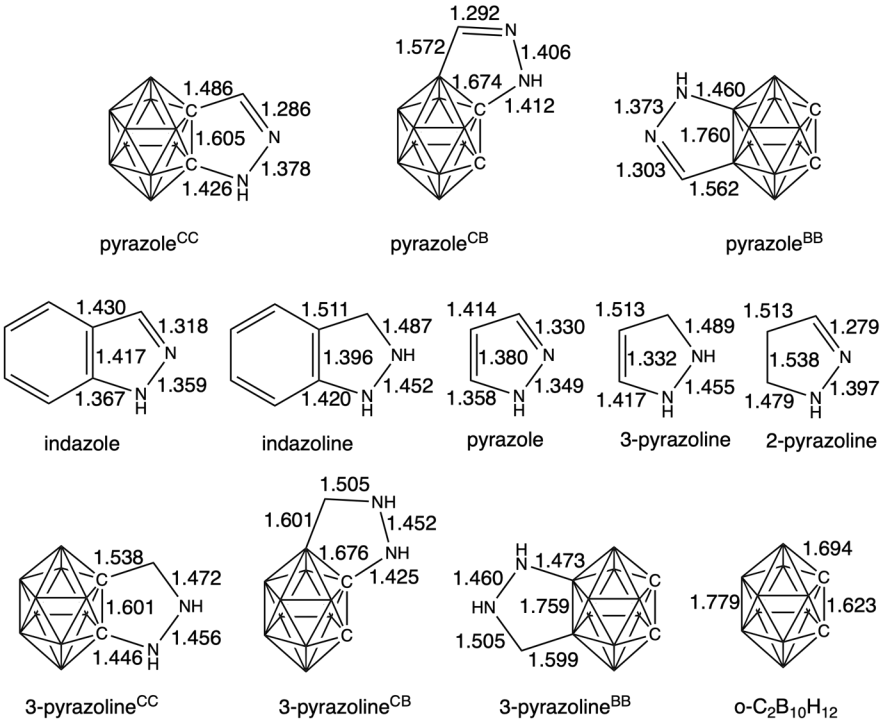

Figure 2: Bond lengths (in Å) of systems under analysis (top row) and reference systems (second and third rows) from the fusion of *o*-carborane and pyrazole/pyrazoline.

computed at the same level of theory (1.623 Å), a length that should be assigned to less than a single C–C bond as it shall be because the lines represent connections and not bonds (Figure 2). At difference, that of pyrazole is 1.380 Å, i.e., a bond length characteristic of a double C–C bond. Or even more, if instead of fusing the pyrazole to the *o*-carborane, we fuse it to benzene, and thus we have indazole, the fusing C–C bond length amounts to 1.417 Å, that can also be assigned to an aromatic C–C bond (that of benzene is 1.394 Å, computed at the same level of theory). Noticeably, highly diagnostic are also the NN bond lengths. In the aromatic indazole and pyrazole this NN distance is near 1.35 Å, whereas it is longer near 1.46 Å for the non-aromatic 3-pyrazoline, although 2-pyrazoline presents a shorter 1.40 Å distance (Figure 2). Thus, and based on the above geometrical data, compared to either pyrazole or indazole molecules, can the pyrazole fused to *o*-carborane be referred as pyrazole? Or otherwise, should we refer to this five-membered ring as pyrazoline due to the fact that the fusing C–C bond between *o*-carborane and the pyrazole is not a double bond? Finally, in agreement with the above discussion on the bond lengths, Pierrefixe and Bickelhaupt revealed the underlying electronic bonding mechanisms in the π-electron and σ-electron systems that cause the typical aromatic bond-length patterns in aromatic and heteroaromatic species. In particular,

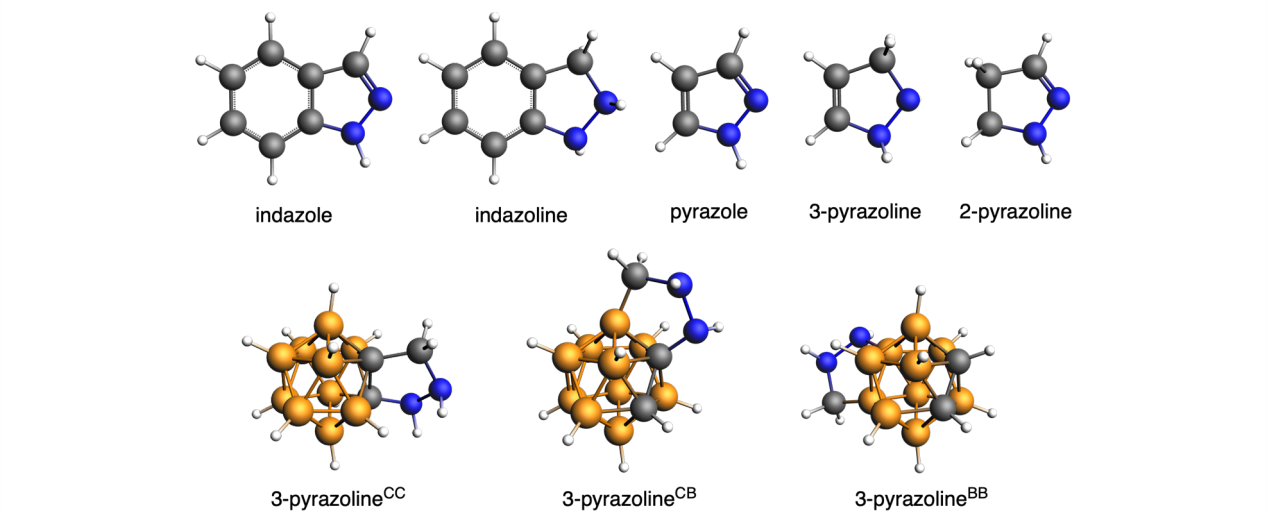

Figure 3: Series of reference systems for the *o*-carborane-fused pyrazoles under analysis.

the authors proved the propensity of the π electrons to localize double bonds against the delocalizing force of the σ electrons [47-49].

Let us focus now on the aromaticity of the *o*-carborane-fused pyrazoles under analysis (Figure 4). The aromaticity of the *o*-carborane is hardly affected by the fusion to the pyrazole, with NICS in the center of the cage that amount to −27.1, −27.4, and −27.4 ppm for pyrazole^{CC}, pyrazole^{CB}, and pyrazole^{BB}, respectively (compared to −27.3 ppm for *closo*-$C_2B_{10}H_{12}$). However, whereas the boron cage is aromatic, the heterocyclic ring is clearly non-aromatic, with MCI that amount to 0.002, 0.000 and 0.003 a.u., respectively (Figure 4). At difference, based on NICS, these heterocycles should be considered aromatic (−8.5, −7.1, and −8.3 ppm, respectively). However, we have previously proven that this abnormal NICS values

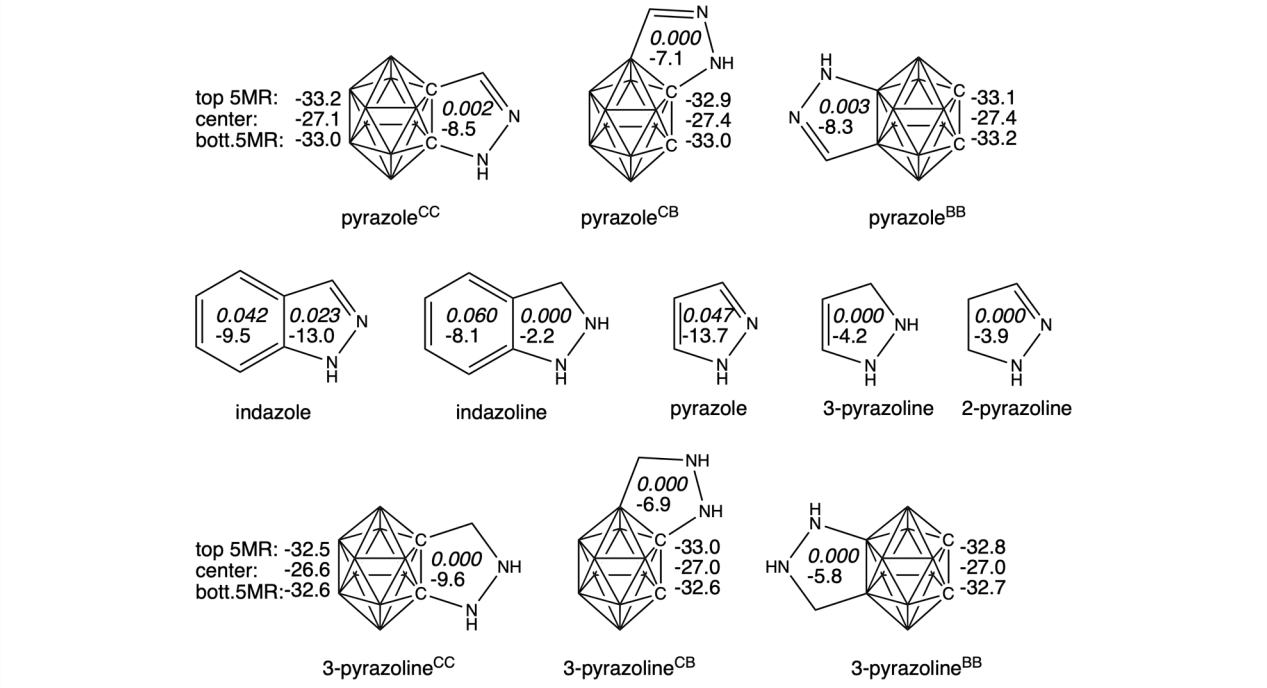

Figure 4: NICS (in ppm) of the boron cages (computed for the top 5-membered ring, center and bottom 5-membered ring) and the rings (center of the ring) of the systems under analysis from the fusion of *o*-carborane and pyrazole/pyrazoline and reference systems. MCI for indazole/pyrazole are also included (top value in italics).

are caused by the induced magnetic ring current of the *o*-carborane [15,34,39]. This suggests we should exercise caution when assessing the aromaticity of a ring based solely on magnetic criteria such as NICS [50-53], especially in cases where neighboring cycles exhibit high or very high NICS values. For a more reliable evaluation, it is important to also consider structural factors and additional indicators like the multicenter index (MCI) [54-57]. Thus, from now on, we will evaluate the aromaticity of heterocycles solely using the electron-based MCI criterion [58,59].

At difference to the *o*-carborane-fused pyrazoles, the pyrazole molecule is clearly aromatic with MCI = 0.047 a.u. (MCI for benzene is 0.072 a.u., computed at the same level of theory), whereas the aromaticity of the five-membered ring of indazole is reduced to 0.023 a.u. The aromaticity of both indazole and pyrazole molecules is further supported by the computed AICD plots (Figure 5), clearly showing a strong diatropic ring current around the five-membered rings. At difference, such current is interrupted in case of all *o*-carborane-fused pyrazoles between the cage and the heterocycle. This latter conclusion is further supported by the computed current density maps for the *o*-carborane-fused pyrazoles (Figure 6). It is observed a non-continuous diatropic ring current in the five-membered ring, interrupted by the fusing bond between the cage and the pyrazole with a paratropic current. Meanwhile, the cage is con-

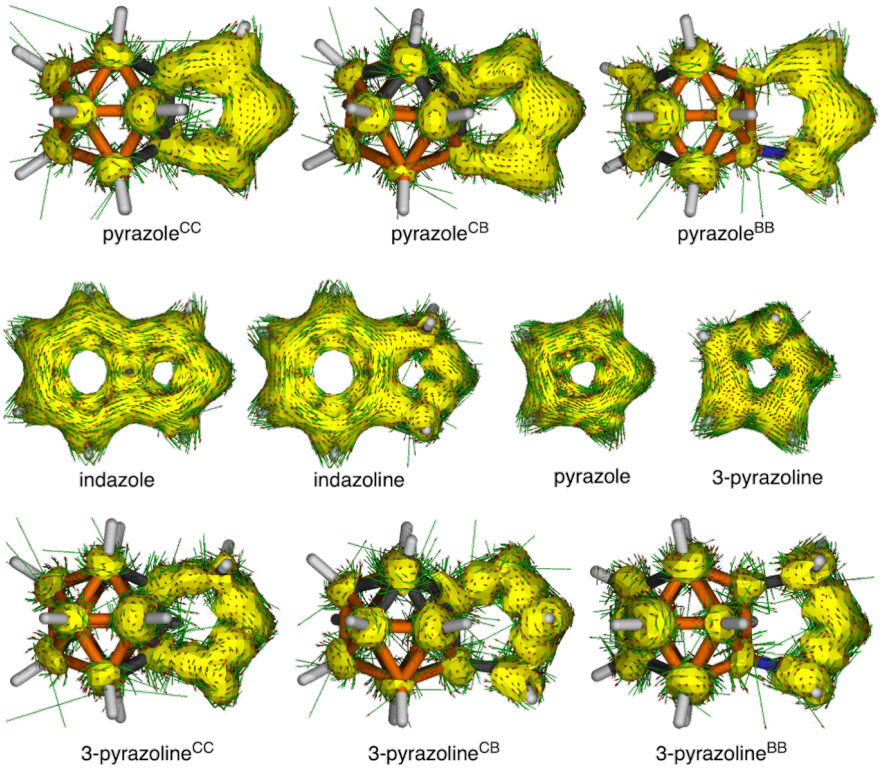

Figure 5: AICD plots of systems under analysis from the fusion of *o*-carborane and pyrazole/pyrazoline and reference systems (isosurface = 0.04).

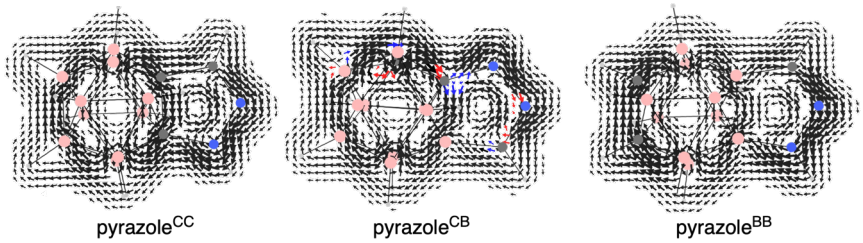

Figure 6: Current density maps (all-electron contributions) for a perpendicular magnetic field over a plane 1 a.u. above the molecular plane of the pyrazole ring of the *o*-carborane-fused pyrazoles. Red/blue arrows when the component parallel/antiparallel to **B** is greater than 30% of the vector modulus. Diatropic/paratropic circulations are clockwise/anticlockwise. Figure S3 in Supporting Information File 1 encloses the rest of the systems.

firmed to be 3D aromatic with diatropic ring currents that extent to the five-membered ring. Once again, if the pyrazole ring fused to *o*-carborane is confirmed to be non-aromatic, can we still refer to it as pyrazole?

At this stage, it is important to reference a recent study in which we sought to gain a deeper understanding of the C–C bond in *o*-carborane by comparing *o*-carboryne and *o*-benzyne [60]. Noticeably, we found out that although *o*-carboryne and *o*-benzyne share similarities, the nature of the C–C bond formed between two adjacent carbons following the loss of hydrogen atoms differs. In *o*-benzyne, the C–C bond behaves as a triple bond, while in *o*-carboryne, it is a double bond.

Thus, in the present case with pyrazole, once again the ineffective overlap between the π molecular orbitals of the planar pyrazole and the (n + 1) molecular orbitals of the aromatic cage causes the aromaticity of the former to be vanished. Such ineffective overlap has been proven by means of a model system derived from pyrazole^{CC} in which the C–N and C–C bonds linking the carborane to the pyrazole have been broken and its interaction has been analyzed by means of a Kohn–Sham molecular orbital analysis together with an energy decomposition analysis (Figure S1 in Supporting Information File 1). To form the broken bonds, both fragments have two unpaired electrons (at their triplet state). The interaction between both fragments amounts to −227.9 kcal mol^{-1}, mainly driven by the very attractive orbital interaction (ΔE_{oi} = −543.7 kcal mol^{-1}) due to the favorable interaction between the two single-occupied molecular orbitals (SOMO) of each fragment to form the two broken bonds. Such strong interaction is supported by large overlaps between these SOMO of each fragment (Table S1 in Supporting Information File 1). However, the interaction between the π molecular orbitals of the pyrazole fragment (HOMO−1 and HOMO−2, Figure S2 in Supporting Information File 1) and those of the carborane is very weak, as supported by the small overlaps between these orbitals.

On the other hand, the fact that the fusing C–C bond between the *o*-carborane and the pyrazole is not a double bond is the reason why we question referring to the five-membered ring as pyrazole. Instead, this ring should be referred as pyrazoline. For this reason, we have also analyzed the fusion between *o*-carborane and pyrazoline (Figure 3). In particular, if we assume that the fusing C–C linkage is single, the fused five-membered ring corresponds to 2-pyrazoline. This latter, as a molecule alone is clearly non-aromatic (MCI = 0.000). For comparison, we have also considered the fusion of *o*-carborane to 3-pyrazoline (13.0 kcal mol^{-1} higher in energy). Also in this case, the five-membered rings are clearly confirmed to be non-aromatic (Figure 4).

Conclusion

In this work, we have quantum chemically analyzed a series of *o*-carborane-fused pyrazoles that have been recently synthesized, and whose fusion was expected to create a hybrid 3D/2D aromatic system, combining the 3D aromaticity of *o*-carborane with the 2D aromaticity of pyrazole. Notably for the case of pyrazole or pyrazoline, the N–N bond length is diagnostic, being approximately 0.1 Å longer when the molecule lacks aromaticity. In contrast, *o*-carborane (1,2-$C_2B_{10}H_{12}$) is 3D aromatic and follows Wade–Mingos' rule [61-63]. When fused to a C_3N_2 five-membered ring, that could lead to a pyrazole or pyrazoline moiety, the cluster retains its aromaticity, but the C_3N_2 five-membered ring does not. Our interpretation, consistent with our previous results, suggests that this phenomenon arises because carborane exhibits peripheral σ-aromaticity, while pyrazole shows π-aromaticity, and these two types of bonding are orthogonal.

For pyrazole to maintain aromaticity, either the C–C, C–B, or B–B bond in the carborane/pyrazole-fusing linkage would need to exhibit double-bond character. However, these bonds are weaker than a typical single bond. Thus, it is difficult to preserve global aromaticity when combining a 3D aromatic system with a 2D one. The MCI indicator, along with the C–C, C–N, and N–N bond distances – particularly the latter – suggest that the fused pyrazole ring is more accurately described as pyrazoline.

It is important to note that NICS values might incorrectly indicate aromaticity, showing negative values in cases where other indicators and bond distances suggest non-aromaticity. This is particularly true for rings fused with highly aromatic systems with highly negative NICS values (−25 to −30 ppm), although it can also happen with lower values. Thus, relying solely on NICS can be misleading, and other computational indicators, as well as experimental or structural data, should be considered.

Computational Details

All calculations were performed with the Gaussian 16 package [64] by means of the B3LYP [65-67] hybrid density functional and the 6-311++G(d,p) basis set [68]. The geometry optimizations were carried out without symmetry constraints (Table S2 in Supporting Information File 1). Analytical Hessians were computed to characterize the optimized structures as minima (zero imaginary frequencies). Aromaticity was first evaluated by means of the nucleus-independent chemical shift (NICS) [12,69-71], proposed by Schleyer and co-workers as a magnetic descriptor of aromaticity. NICS is defined as the negative value of the absolute shielding computed at a ring center or at some other point of the system. Rings with large negative NICS values are considered aromatic. NICS values were computed

using the gauge-including atomic orbital method (GIAO) [72]. Multicenter indices (MCI) [54-56,73,74] were computed with the ESI-3D program using AIM partition of space [75,76]. The anisotropy of the induced current density (AICD) plots have been computed at the same level of theory [77]. Current density maps have been computed by means of the SYSMOIC package [78-80], at the same level of theory. Finally, the energy decomposition analysis has been performed at the ZORA-BLYP-D3(BJ)/TZ2P level of theory with AMS software [81-84].

Supporting Information

Supporting Information File 1

Energy decomposition analysis of pyrazole^{CC} (fragments used, molecular orbitals overlaps, and fragment molecular orbitals), cartesian coordinates and energies of all compounds under analysis, and whole set of ring current density maps.
[https://www.beilstein-journals.org/bjoc/content/supplementary/1860-5397-21-29-S1.pdf]

Funding

We thank the Spanish Ministerio de Ciencia, Innovación y Universidades (MCIN/AEI/10.13039/501100011033) for projects PID2019-106832RB-100, PID2023-147424NB-I00, PID2020-113711GB-I00, PID2021-127423NB-I00, PID2022-138861NB-I00, and CEX2021-001202-M, and the Generalitat de Catalunya for projects 2021SGR623 and 2021SGR442. We also acknowledge CSUC for HPC facilities.

ORCID® iDs

Zahra Noori - https://orcid.org/0000-0002-8624-6671
Miquel Solà - https://orcid.org/0000-0002-1917-7450
Clara Viñas - https://orcid.org/0000-0001-5000-0277
Francesc Teixidor - https://orcid.org/0000-0002-3010-2417
Jordi Poater - https://orcid.org/0000-0002-0814-5074

Data Availability Statement

All data that supports the findings of this study is available in the published article and/or the supporting information of this article.

References

1. Betcke, I.; Götzinger, A. C.; Kornet, M. M.; Müller, T. J. J. *Beilstein J. Org. Chem.* **2024,** *20,* 2024–2077. doi:10.3762/bjoc.20.178
2. Wu, J.; Shi, H.; Li, X.; He, J.; Zhang, C.; Sun, F.; Du, Y. *Beilstein J. Org. Chem.* **2024,** *20,* 1453–1461. doi:10.3762/bjoc.20.128
3. Curutchet, C.; Poater, J.; Solà, M.; Elguero, J. *J. Phys. Chem. A* **2011,** *115,* 8571–8577. doi:10.1021/jp204263p
4. Pérez-Fernández, R.; Goya, P.; Elguero, J. *ARKIVOC* **2014,** No. ii, 233–293. doi:10.3998/ark.5550190.p008.131
5. Bekhit, A. A.; Hymete, A.; Bekhit, A.E.-D. A.; Damtew, A.; Aboul-Enein, H. Y. *Mini-Rev. Med. Chem.* **2010,** *10,* 1014–1033. doi:10.2174/138955711009011014
6. Li, G.; Cheng, Y.; Han, C.; Song, C.; Huang, N.; Du, Y. *RSC Med. Chem.* **2022,** *13,* 1300–1321. doi:10.1039/d2md00206j
7. Motoba, K.; Nishizawa, H.; Suzuki, T.; Hamaguchi, H.; Uchida, M.; Funayama, S. *Pestic. Biochem. Physiol.* **2000,** *67,* 73–84. doi:10.1006/pest.2000.2477
8. Maeda, H.; Ito, Y.; Kusunose, Y.; Nakanishi, T. *Chem. Commun.* **2007,** 1136–1138. doi:10.1039/b615787d
9. Catalan, J.; Fabero, F.; Claramunt, R. M.; Santa Maria, M. D.; Foces-Foces, M. d. l. C.; Hernandez Cano, F.; Martinez-Ripoll, M.; Elguero, J.; Sastre, R. *J. Am. Chem. Soc.* **1992,** *114,* 5039–5048. doi:10.1021/ja00039a014
10. Chen, X.-L.; Yu, R.; Zhang, Q.-K.; Zhou, L.-J.; Wu, X.-Y.; Zhang, Q.; Lu, C.-Z. *Chem. Mater.* **2013,** *25,* 3910–3920. doi:10.1021/cm4024309
11. El-Hamdi, M.; Tiznado, W.; Poater, J.; Solà, M. *J. Org. Chem.* **2011,** *76,* 8913–8921. doi:10.1021/jo201639k
12. Poater, J.; Solà, M.; Viñas, C.; Teixidor, F. *Angew. Chem., Int. Ed.* **2014,** *53,* 12191–12195. doi:10.1002/anie.201407359
13. Chen, Z.; King, R. B. *Chem. Rev.* **2005,** *105,* 3613–3642. doi:10.1021/cr0300892
14. Poater, J.; Solà, M.; Viñas, C.; Teixidor, F. *Chem. – Eur. J.* **2013,** *19,* 4169–4175. doi:10.1002/chem.201204397
15. Poater, J.; Viñas, C.; Bennour, I.; Escayola, S.; Solà, M.; Teixidor, F. *J. Am. Chem. Soc.* **2020,** *142,* 9396–9407. doi:10.1021/jacs.0c02228
16. Núñez, R.; Romero, I.; Teixidor, F.; Viñas, C. *Chem. Soc. Rev.* **2016,** *45,* 5147–5173. doi:10.1039/c6cs00159a
17. Núñez, R.; Tarrés, M.; Ferrer-Ugalde, A.; de Biani, F. F.; Teixidor, F. *Chem. Rev.* **2016,** *116,* 14307–14378. doi:10.1021/acs.chemrev.6b00198
18. Grams, R. J.; Santos, W. L.; Scorei, I. R.; Abad-García, A.; Rosenblum, C. A.; Bita, A.; Cerecetto, H.; Viñas, C.; Soriano-Ursúa, M. A. *Chem. Rev.* **2024,** *124,* 2441–2511. doi:10.1021/acs.chemrev.3c00663
19. Valliant, J. F.; Guenther, K. J.; King, A. S.; Morel, P.; Schaffer, P.; Sogbein, O. O.; Stephenson, K. A. *Coord. Chem. Rev.* **2002,** *232,* 173–230. doi:10.1016/s0010-8545(02)00087-5
20. Sivaev, I. B.; Bregadze, V. V. *Eur. J. Inorg. Chem.* **2009,** 1433–1450. doi:10.1002/ejic.200900003
21. Stockmann, P.; Gozzi, M.; Kuhnert, R.; Sárosi, M. B.; Hey-Hawkins, E. *Chem. Soc. Rev.* **2019,** *48,* 3497–3512. doi:10.1039/c9cs00197b
22. Marfavi, A.; Kavianpour, P.; Rendina, L. M. *Nat. Rev. Chem.* **2022,** *6,* 486–504. doi:10.1038/s41570-022-00400-x
23. Hawthorne, M. F.; Maderna, A. *Chem. Rev.* **1999,** *99,* 3421–3434. doi:10.1021/cr980442h
24. Monti Hughes, A.; Hu, N. *Cancers* **2023,** *15,* 4091. doi:10.3390/cancers15164091
25. Barth, R. F.; Gupta, N.; Kawabata, S. *Cancer Commun.* **2024,** *44,* 893–909. doi:10.1002/cac2.12582
26. Das, B. C.; Nandwana, N. K.; Das, S.; Nandwana, V.; Shareef, M. A.; Das, Y.; Saito, M.; Weiss, L. M.; Almaguel, F.; Hosmane, N. S.; Evans, T. *Molecules* **2022,** *27,* 2615. doi:10.3390/molecules27092615
27. Xie, Z. *Acc. Chem. Res.* **2003,** *36,* 1–9. doi:10.1021/ar010146i
28. Saha, A.; Oleshkevich, E.; Viñas, C.; Teixidor, F. *Adv. Mater. (Weinheim, Ger.)* **2017,** *29,* 1704238. doi:10.1002/adma.201704238
29. Qiu, Z.; Xie, Z. *Acc. Chem. Res.* **2021,** *54,* 4065–4079. doi:10.1021/acs.accounts.1c00460

30. Cioran, A. M.; Musteti, A. D.; Teixidor, F.; Krpetić, Ž.; Prior, I. A.; He, Q.; Kiely, C. J.; Brust, M.; Viñas, C. *J. Am. Chem. Soc.* **2012,** *134,* 212–221. doi:10.1021/ja203367h
31. Olid, D.; Núñez, R.; Viñas, C.; Teixidor, F. *Chem. Soc. Rev.* **2013,** *42,* 3318–3336. doi:10.1039/c2cs35441a
32. Endo, Y.; Iijima, T.; Yamakoshi, Y.; Fukasawa, H.; Miyaura, C.; Inada, M.; Kubo, A.; Itai, A. *Chem. Biol.* **2001,** *8,* 341–355. doi:10.1016/s1074-5521(01)00016-3
33. Chan, T. L.; Xie, Z. *Chem. Sci.* **2018,** *9,* 2284–2289. doi:10.1039/c7sc04722c
34. Sun, F.; Tan, S.; Cao, H.-J.; Lu, C.-s.; Tu, D.; Poater, J.; Solà, M.; Yan, H. *J. Am. Chem. Soc.* **2023,** *145,* 3577–3587. doi:10.1021/jacs.2c12526
35. Ni, H.; Qiu, Z.; Xie, Z. *Angew. Chem., Int. Ed.* **2017,** *56,* 712–716. doi:10.1002/anie.201610810
36. Ren, H.; Zhou, N.; Ma, W.; Zhang, P.; Tu, D.; Lu, C.-S.; Yan, H. *J. Am. Chem. Soc.* **2024,** *146,* 26543–26555. doi:10.1021/jacs.4c10728
37. Maeng, C.; Ko, G. H.; Yang, H.; Han, S. H.; Han, G. U.; Chan Noh, H.; Lee, K.; Kim, D.; Lee, P. H. *Org. Lett.* **2022,** *24,* 3526–3531. doi:10.1021/acs.orglett.2c01232
38. Poater, J.; Viñas, C.; Solà, M.; Teixidor, F. *Nat. Commun.* **2022,** *13,* 3844. doi:10.1038/s41467-022-31267-7
39. Buzsáki, D.; Kovács, M. B.; Hümpfner, E.; Harcsa-Pintér, Z.; Kelemen, Z. *Chem. Sci.* **2022,** *13,* 11388–11393. doi:10.1039/d2sc03511a
40. Buzsáki, D.; Gál, D.; Harcsa-Pintér, Z.; Kalabay, L.; Kelemen, Z. *Chem. – Eur. J.* **2024,** *30,* e202402970. doi:10.1002/chem.202402970
41. Katritzky, A. R.; Barczynski, P.; Musumarra, G.; Pisano, D.; Szafran, M. *J. Am. Chem. Soc.* **1989,** *111,* 7–15. doi:10.1021/ja00183a002
42. Katritzky, A. R.; Karelson, M.; Sild, S.; Krygowski, T. M.; Jug, K. *J. Org. Chem.* **1998,** *63,* 5228–5231. doi:10.1021/jo970939b
43. Jug, K.; Köster, A. M. *J. Phys. Org. Chem.* **1991,** *4,* 163–169. doi:10.1002/poc.610040307
44. Benson, S. W. *J. Chem. Educ.* **1965,** *42,* 502. doi:10.1021/ed042p502
45. Jemmis, E. D.; Kiran, B. *J. Am. Chem. Soc.* **1997,** *119,* 4076–4077. doi:10.1021/ja964385q
46. Priyakumari, C. P.; Jemmis, E. D. Electron-Counting Rules in Cluster Bonding – Polyhedral Boranes, Elemental Boron, and Boron-Rich Solids. In *The Chemical Bond: Chemical Bonding Across the Periodic Table;* Frenking, G.; Shaik, S., Eds.; Wiley-VCH: Weinheim, Germany, 2014; pp 113–148. doi:10.1002/9783527664658.ch5
47. Pierrefixe, S. C. A. H.; Bickelhaupt, F. M. *Chem. – Eur. J.* **2007,** *13,* 6321–6328. doi:10.1002/chem.200700206
48. Pierrefixe, S. C. A. H.; Bickelhaupt, F. M. *J. Phys. Chem. A* **2008,** *112,* 12816–12822. doi:10.1021/jp800514n
49. Pierrefixe, S. C. A. H.; Bickelhaupt, F. M. *Aust. J. Chem.* **2008,** *61,* 209–215. doi:10.1071/ch08043
50. Foroutan-Nejad, C. *Theor. Chem. Acc.* **2015,** *134,* 8. doi:10.1007/s00214-015-1617-7
51. Foroutan-Nejad, C. *J. Org. Chem.* **2023,** *88,* 14831–14835. doi:10.1021/acs.joc.3c01807
52. Foroutan-Nejad, C.; Badri, Z.; Shahbazian, S.; Rashidi-Ranjbar, P. *J. Phys. Chem. A* **2011,** *115,* 12708–12714. doi:10.1021/jp203681x
53. Foroutan-Nejad, C.; Shahbazian, S.; Feixas, F.; Rashidi-Ranjbar, P.; Solà, M. *J. Comput. Chem.* **2011,** *32,* 2422–2431. doi:10.1002/jcc.21824
54. Bultinck, P.; Ponec, R.; Van Damme, S. *J. Phys. Org. Chem.* **2005,** *18,* 706–718. doi:10.1002/poc.922
55. Feixas, F.; Matito, E.; Poater, J.; Solà, M. *Chem. Soc. Rev.* **2015,** *44,* 6434–6451. doi:10.1039/c5cs00066a
56. Matito, E.; Duran, M.; Solà, M. *J. Chem. Phys.* **2005,** *122,* 014109. doi:10.1063/1.1824895
57. Feixas, F.; Matito, E.; Solà, M.; Poater, J. *Phys. Chem. Chem. Phys.* **2010,** *12,* 7126–7137. doi:10.1039/b924972a
58. Feixas, F.; Matito, E.; Poater, J.; Solà, M. *J. Comput. Chem.* **2008,** *29,* 1543–1554. doi:10.1002/jcc.20914
59. Feixas, F.; Matito, E.; Poater, J.; Solà, M. *J. Phys. Chem. A* **2007,** *111,* 4513–4521. doi:10.1021/jp0703206
60. Poater, J.; Viñas, C.; Escayola, S.; Solà, M.; Teixidor, F. *Chem. – Eur. J.* **2023,** *29,* e202302448. doi:10.1002/chem.202302448
61. Poater, J.; Solà, M.; Viñas, C.; Teixidor, F. *Chem. – Eur. J.* **2016,** *22,* 7437–7443. doi:10.1002/chem.201600510
62. Mingos, D. M. P. *Acc. Chem. Res.* **1984,** *17,* 311–319. doi:10.1021/ar00105a003
63. Wade, K. *Chem. Br.* **1975,** *11,* 177–183.
64. *Gaussian 16,* Revision B01; Gaussian, Inc.: Wallingford, CT, 2016.
65. Becke, A. D. *J. Chem. Phys.* **1993,** *98,* 5648–5652. doi:10.1063/1.464913
66. Lee, C.; Yang, W.; Parr, R. G. *Phys. Rev. B* **1988,** *37,* 785–789. doi:10.1103/physrevb.37.785
67. Stephens, P. J.; Devlin, F. J.; Chabalowski, C. F.; Frisch, M. J. *J. Phys. Chem.* **1994,** *98,* 11623–11627. doi:10.1021/j100096a001
68. Frisch, M. J.; Pople, J. A.; Binkley, J. S. *J. Chem. Phys.* **1984,** *80,* 3265–3269. doi:10.1063/1.447079
69. Chen, Z.; Wannere, C. S.; Corminboeuf, C.; Puchta, R.; Schleyer, P. v. R. *Chem. Rev.* **2005,** *105,* 3842–3888. doi:10.1021/cr030088+
70. Poater, J.; Escayola, S.; Poater, A.; Teixidor, F.; Ottosson, H.; Viñas, C.; Solà, M. *J. Am. Chem. Soc.* **2023,** *145,* 22527–22538. doi:10.1021/jacs.3c07335
71. Poater, J.; Viñas, C.; Olid, D.; Solà, M.; Teixidor, F. *Angew. Chem., Int. Ed.* **2022,** *61,* e202200672. doi:10.1002/anie.202200672
72. Wolinski, K.; Hinton, J. F.; Pulay, P. *J. Am. Chem. Soc.* **1990,** *112,* 8251–8260. doi:10.1021/ja00179a005
73. Tu, D.; Yan, H.; Poater, J.; Solà, M. *Angew. Chem., Int. Ed.* **2020,** *59,* 9018–9025. doi:10.1002/anie.201915290
74. Tu, D.; Li, J.; Sun, F.; Yan, H.; Poater, J.; Solà, M. *JACS Au* **2021,** *1,* 2047–2057. doi:10.1021/jacsau.1c00348
75. *ESI-3D: Electron Sharing Indices Program for 3D Molecular Space Partitioning;* Institute of Computational Chemistry and Catalysis (IQCC), University of Girona: Catalonia, Spain, 2006.
76. Matito, E.; Solà, M.; Salvador, P.; Duran, M. *Faraday Discuss.* **2007,** *135,* 325–345. doi:10.1039/b605086g
77. Geuenich, D.; Hess, K.; Köhler, F.; Herges, R. *Chem. Rev.* **2005,** *105,* 3758–3772. doi:10.1021/cr0300901
78. Monaco, G.; Summa, F. F.; Zanasi, R. *J. Chem. Inf. Model.* **2021,** *61,* 270–283. doi:10.1021/acs.jcim.0c01136
79. Monaco, G.; Summa, F. F.; Zanasi, R. *Chem. Phys. Lett.* **2020,** *745,* 137281. doi:10.1016/j.cplett.2020.137281
80. Berger, R. J. F.; Monaco, G.; Zanasi, R. *J. Chem. Phys.* **2020,** *152,* 194101. doi:10.1063/5.0006992
81. te Velde, G.; Bickelhaupt, F. M.; Baerends, E. J.; Fonseca Guerra, C.; van Gisbergen, S. J. A.; Snijders, J. G.; Ziegler, T. *J. Comput. Chem.* **2001,** *22,* 931–967. doi:10.1002/jcc.1056

82. Bickelhaupt, F. M.; Baerends, E. J. Kohn-Sham Density Functional Theory: Predicting and Understanding Chemistry. In *Reviews in Computational Chemistry;* Lipkowitz, K. B.; Boyd, D. B., Eds.; Wiley-VCH: New York, NY, USA, 2000; Vol. 15, pp 1–86. doi:10.1002/9780470125922.ch1
83. Vermeeren, P.; Hamlin, T. A.; Bickelhaupt, F. M. *Chem. Commun.* **2021,** *57,* 5880–5896. doi:10.1039/d1cc02042k
84. Vermeeren, P.; van der Lubbe, S. C. C.; Fonseca Guerra, C.; Bickelhaupt, F. M.; Hamlin, T. A. *Nat. Protoc.* **2020,** *15,* 649–667. doi:10.1038/s41596-019-0265-0

License and Terms

BEILSTEIN JOURNAL OF ORGANIC CHEMISTRY

Photochemically assisted synthesis of phenacenes fluorinated at the terminal benzene rings and their electronic spectra

Yuuki Ishii[1], Minoru Yamaji[2], Fumito Tani[3], Kenta Goto[3], Yoshihiro Kubozono[4] and Hideki Okamoto[*1,5]

Full Research Paper

Open Access

Address:
[1]Graduate School of Environmental, Life, Natural Science and Technology, Okayama University, Okayama 700-8530, Japan, [2]Division of Molecular Science, Graduate School of Science and Engineering, Gunma University, Ota, Gunma 373-0057, Japan, [3]Institute for Materials Chemistry and Engineering, Kyushu University, Fukuoka 819-0395, Japan, [4]Research Institute for Interdisciplinary Science, Okayama University, Okayama 700-8530, Japan and [5]Department of Chemistry, Faculty of Environmental, Life, Natural Science and Technology, Okayama University, Okayama 700-8530, Japan

Email:
Hideki Okamoto[*] - hokamoto@okayama-u.ac.jp

* Corresponding author

Keywords:
fluorescence; fluorinated aromatics; phenacene; photoreaction

Beilstein J. Org. Chem. **2025,** *21,* 670–679.
https://doi.org/10.3762/bjoc.21.53

Received: 22 December 2024
Accepted: 14 March 2025
Published: 24 March 2025

This article is part of the thematic issue "π-Conjugated molecules and materials".

Guest Editor: A. Mateo-Alonso

Abstract

[*n*]Phenacenes ([*n*] = 5–7), octafluorinated at the terminal benzene rings (F_8-phenacenes: **F_8PIC**, **F_8FUL**, and **$F_8$7PHEN**), were photochemically synthesized, and their electronic spectra were investigated to reveal the effects of the fluorination on the electronic features of phenacene molecules. F_8-Phenacenes were conveniently synthesized by the Mallory photoreaction of the corresponding fluorinated diarylethenes as the key step. Upon fluorination on the phenacene cores, the absorption and fluorescence bands of the F_8-phenacenes in $CHCl_3$ systematically red-shifted by ca. 3–5 nm compared to those of the corresponding parent phenacenes. The vibrational progressions of the absorption and fluorescence bands were little affected by the fluorination in the solution phase. In the solid state, the absorption band of F_8-phenacenes appeared in the similar wavelength region for the corresponding parent phenacenes whereas their fluorescence bands markedly red-shifted and broadened. These observations suggest that the intermolecular interactions of excited-state F_8-phenacene molecules are significantly different from those of the corresponding parent molecules, most likely due to different crystalline packing motifs.

Introduction

Polycyclic aromatic hydrocarbons (PAHs) have been subject of continuous interest not only from aspects of fundamental synthetic, structural, and physical chemistry, but also for their application in materials science, in particular, in organic electronics [1-4]. Among the structural classifications of PAHs, the representatives are acenes and phenacenes; the former

consisting of linearly fused benzene-ring arrays while the latter exhibit zigzag ones due to the angular annelation. These series are known as one-dimensional graphene ribbons. As has been commonly recognized, acene molecules have been intensively and extensively studied in the organic functional materials field [5-7]. By contrast, phenacenes had been hardly applied as functional molecules in spite of their long history; phenacenes were recognized as contents in petroleum-industry residues as early as in the 19th century [8,9]. In the last decade, phenacenes were demonstrated to serve as platform materials namely in organic electronics, such as chromophores for photovoltaics [10-12], luminophores in light-emitting devices [13-15], organic semiconductors [16-18], and even as aromatic superconductors [19]. Later, parent and chemically modified phenacenes were applied to active layers in high-performance organic field-effect transistors. Thus, the phenacene molecules displayed high hole mobility [20-26] and imide-fused phenacenes served as n-type organic semiconductors [27]. It was also disclosed that donor–acceptor-type phenacenes provided environment-dependent fluorophores showing solvatochromic fluorescence behavior [28,29]. Because phenacene molecules are quite robust against an oxidative environment even under photoillumination, they are considered to be promising platforms for constructing practical organic functional molecules.

Recently, fluorinated PAHs attracted considerable attention because the introduction of fluorine atoms significantly affects their electronic features as well as molecular and crystalline structures [30-32]. For example, the fluorination of oligoacene frameworks manipulates their electronic properties as well as their solid-state packing motifs [33-36]. The most pronounced example is that pentacene serves as a p-channel organic semiconductor [37], whereas perfluoropentacene can be used as an n-channel material [38]. It has been demonstrated that the molecular structure of [7]helicenes was modified by fluorination, thus, the helicenes' pitch was manipulated by terminal fluorination modes [39,40]. Also, the effects of fluorination on the chiroptical features of [*n*]helicenes were theoretically predicted [41].

In addition to the manipulation of electronic natures, partial fluorination of PAHs has been recognized to be significant for crystal design and engineering. Thus, molecular packing patterns of PAHs were altered depending on the positions and extent of fluorination on the molecules [42-44]. For phenacene molecules, mono- and difluorinated picenes were synthesized, and their molecular and crystal structures were systematically investigated [45]. Monofluorinated picenes, such as 6- and 13-fluoropicene, formed dimeric structures through intermolecular F···H contacts and behaved as p-channel semiconductors. By contrast, little information is available about the effects of polyfluorination on the physical properties and structures of phenacenes. It is expected that polyfluorination of phenacene cores could produce a functional aromatic material alternative to fluorinated acenes.

In this context, it would be of interest to construct highly fluorinated phenacene derivatives and reveal their structural and electronic natures in order to develop future organic functional molecules. In this study, octafluorinated phenacenes, F_8-phenacenes **F_8PIC**, **F_8FUL**, and **$F_8$7PHEN** (see Figure 1 for their chemical structures), were systematically synthesized via the Mallory

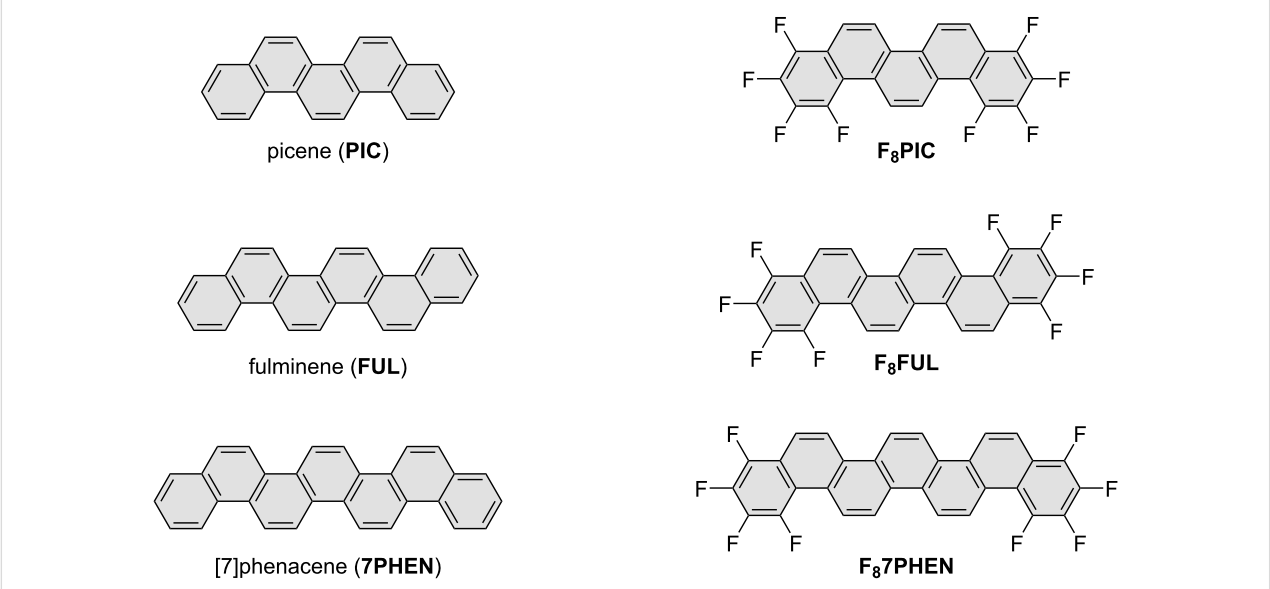

Figure 1: Chemical structures of phenacenes studied in this work.

photoreaction [46] as the key step, and their UV–vis and fluorescence spectra were investigated in comparison with those of the corresponding parent phenacenes **PIC**, **FUL**, and **7PHEN** to reveal the effects of the fluorination at the terminal rings.

Results and Discussion

Synthesis of F_8-phenacenes

The synthetic routes to building blocks **10**, **13**, and **15** and those to the desired **F_8PIC**, **F_8FUL**, and **$F_8$7PHEN** are respectively shown in Scheme 1 and Scheme 2. The newly synthesized com-

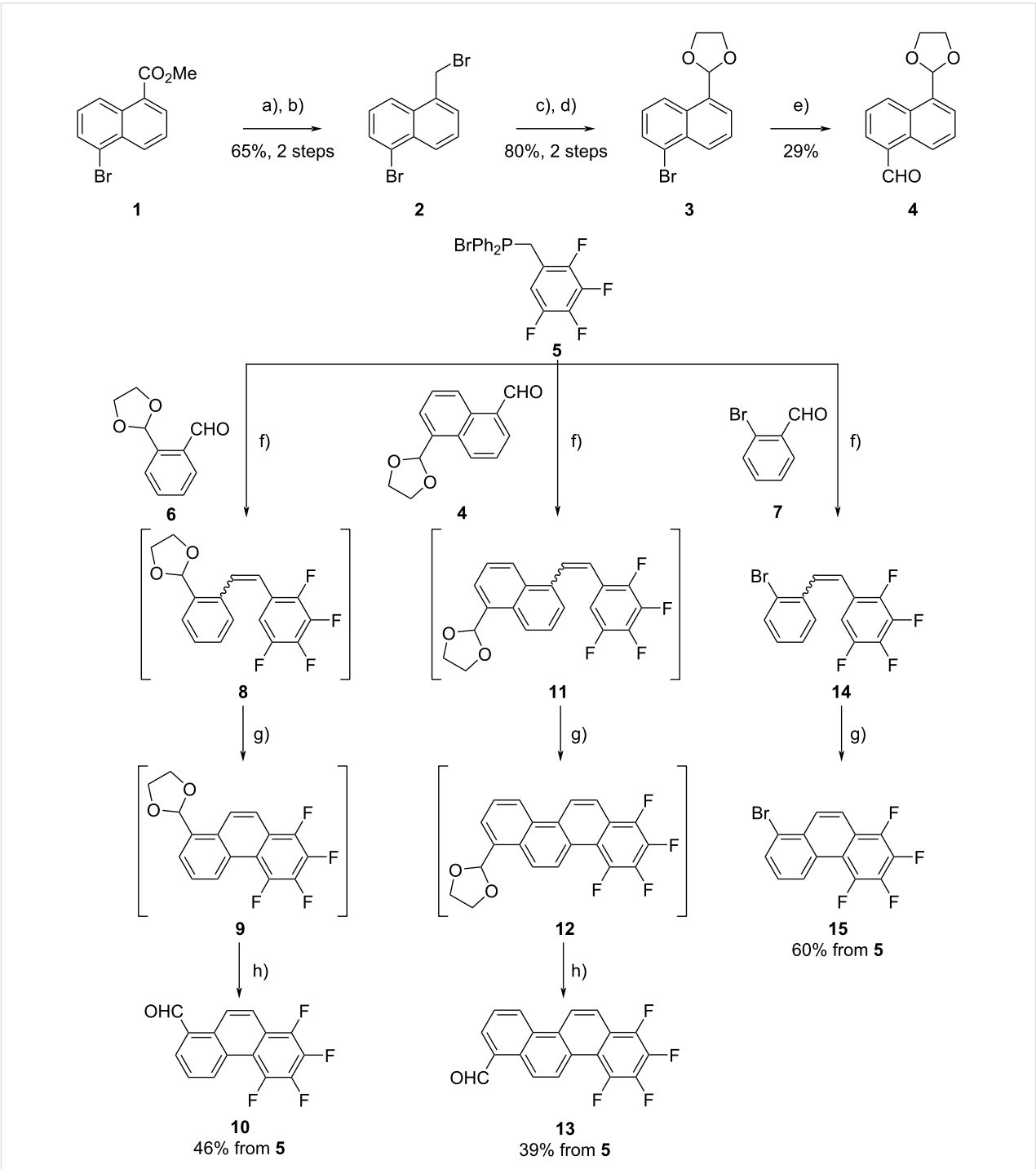

Scheme 1: Synthesis of building blocks **10**, **13**, and **15**. Reagents and conditions: a) $NaBH_4$, MeOH, THF, reflux; b) PBr_3, reflux; c) *N*-methylmorpholine-*N*-oxide, THF, reflux; d) ethylene glycol, *p*-TsOH, toluene, reflux; e) *tert*-BuLi, DMF, THF, −78 °C; f) KOH, 18-crown-6, CH_2Cl_2, reflux (rt for **8**); g) *hν*, I_2, cyclohexane (toluene/THF mixture for **11**); h) *p*-TsOH, acetone, reflux.

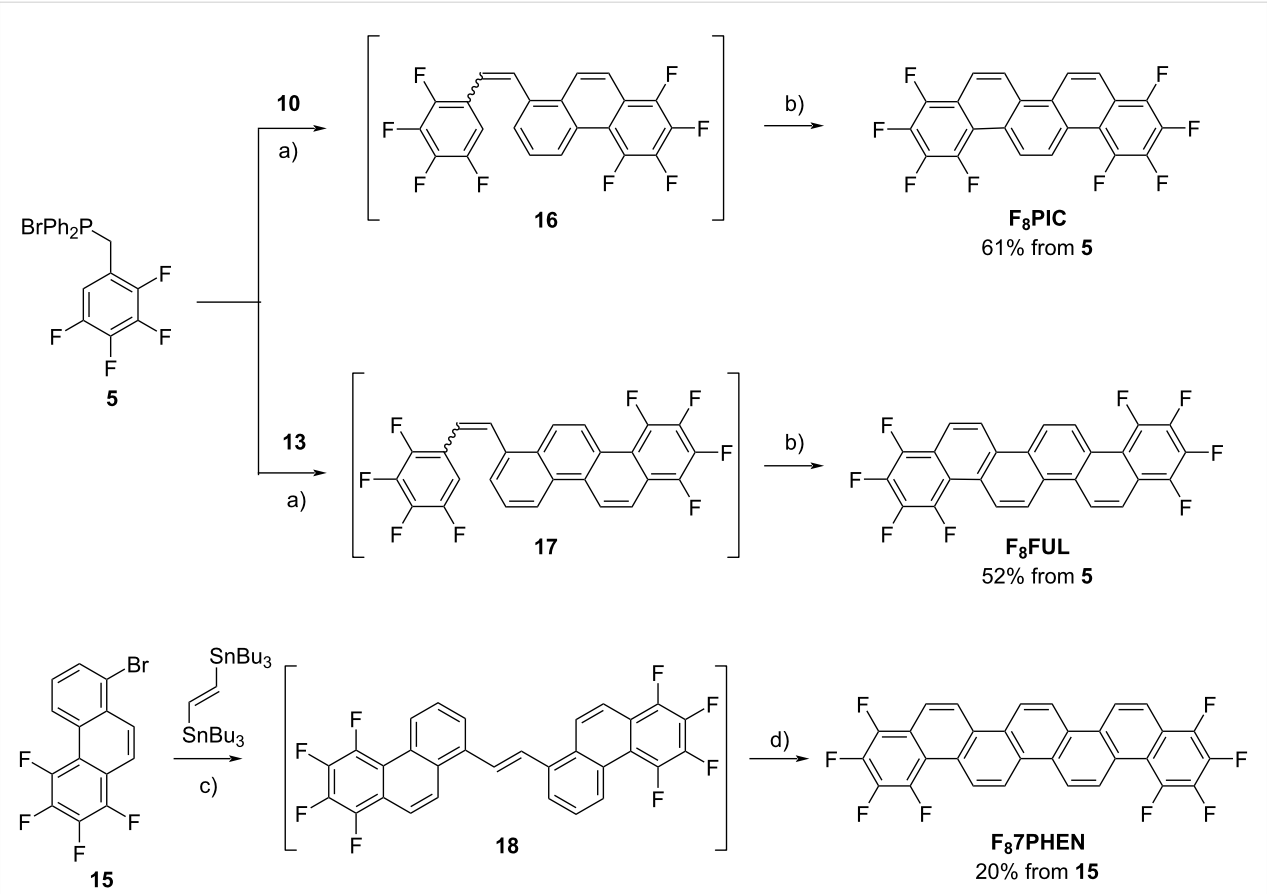

Scheme 2: Synthesis of **F_8PIC**, **F_8FUL**, and **$F_8$7PHEN**. Reagents and conditions: a) KOH, 18-crown-6, CH_2Cl_2, reflux; b) *hν*, I_2, toluene, rt (reflux for **F_8FUL**); c) $Pd(PPh_3)_4$, toluene, reflux; d) *hν*, I_2, toluene, reflux.

pounds were characterized by NMR spectroscopy as well as elemental analysis or high-resolution mass spectrometry. The experimental details and compound data are provided in Supporting Information File 1.

Aldehyde **4**, in which one of the formyl groups in napthalene-1,5-dicarboxaldehyde was protected as an acetal, was prepared through a 5-step reaction sequence. Phosphonium salt **5** [39] and the partly protected *o*-phthalaldehyde **6** [47] were obtained by previously reported procedures.

The reaction of phosphonium salt **5** with aldehyde **6** in the presence of KOH and 18-crown-6 produced fluorine-containing diarylethene **8** as a mixture of *E*- and *Z*-isomers. Subsequently, the *E*/*Z* mixture of **8** was subjected to the Mallory photoreaction without separation. Thus, compound **8** was irradiated with fluorescent black-light lamps (300 nm, 6 × 16 W) in the presence of a catalytic amount of I_2 under an aerated condition. After the photolysis, the acetal moiety was partly cleaved to produce a mixture of acetal **9** and aldehyde **10**. The obtained reaction mixture was treated with TsOH in acetone to afford desired fluorinated phenanthrenecarbaldehyde **10** in moderate yield (46% from **5**). The homologous chrysenecarbaldehyde **13** was obtained starting from aldehyde **4** via the same two-step procedure in a 39% yield from **5**. Bromophenanthrene derivative **15** was prepared by Wittig reaction between compounds **5** and **7** followed by Mallory photoreaction in a 60% yield from **5**.

The target compounds, **F_8PIC** and **F_8FUL**, were obtained through the Wittig-reaction and Mallory-photoreaction sequence (Scheme 2). Thus, reactions between phosphonium salt **5** and specific aldehydes, **10** and **13**, followed by photolysis in the presence of I_2 and O_2, respectively, afforded **F_8PIC** (57%) and **F_8FUL** (52%). **$F_8$7PHEN** was obtained by a Migita–Kosugi–Stille coupling between bromophenanthrene **15** and (*E*)-1,2-bis(tributylstannyl)ethene to afford diarylethene **18** followed by Mallory photoreaction. The obtained intermediate **18** contained residual palladium and isolation was not successful due to its poor solubility in common organic solvents. Therefore, the crude **18** was subjected to the Mallory photoreaction without purification. Photoirradiation of diarylethene **18** was performed in the presence of a catalytic amount of I_2 in

refluxing toluene to afford **F$_8$7PHEN** which was isolated by sublimation under vacuum.

Absorption and fluorescence spectra of F$_8$-phenacenes

In order to get insights into the electronic characteristics of **F$_8$PIC**, **F$_8$FUL**, and **F$_8$7PHEN**, their UV–vis and fluorescence spectra were measured in $CHCl_3$ (Figure 2). The electronic spectra of the corresponding parent phenacenes [48,49] are also illustrated as reference. The selected photophysical parameters are summarized in Table 1. The fluorescence excitation spectra were consistent with absorption spectra to unambiguously assign the fluorescence bands to the studied F$_8$-phenacenes (Figure S1 in Supporting Information File 1).

In the UV–vis spectra, a small-intensity band at 376–393 nm and a moderate-intensity one at 333–347 nm were observed for all compounds studied. The former and the latter absorption bands are, respectively, assigned to the α- and *p*-bands according to Clar's description [50]. The absorption bands only slightly red-shifted upon the π-extension ($\Delta\lambda_{ABS}$ = ca. 6 nm per increment of one benzene ring) and the spectral profiles resemble each other irrespective of the length of the phenacene π conjugation and the fluorine substitution. The results suggest that these factors could provide insignificant effects on the apparent electronic spectral nature of the phenacenes in solution. The fluorescence spectra of the phenacenes displayed well-resolved vibrational structures as characteristics of rigid aromatic molecules. Like the UV–vis spectral behavior, the fluorescence bands gradually red-shifted with increasing the

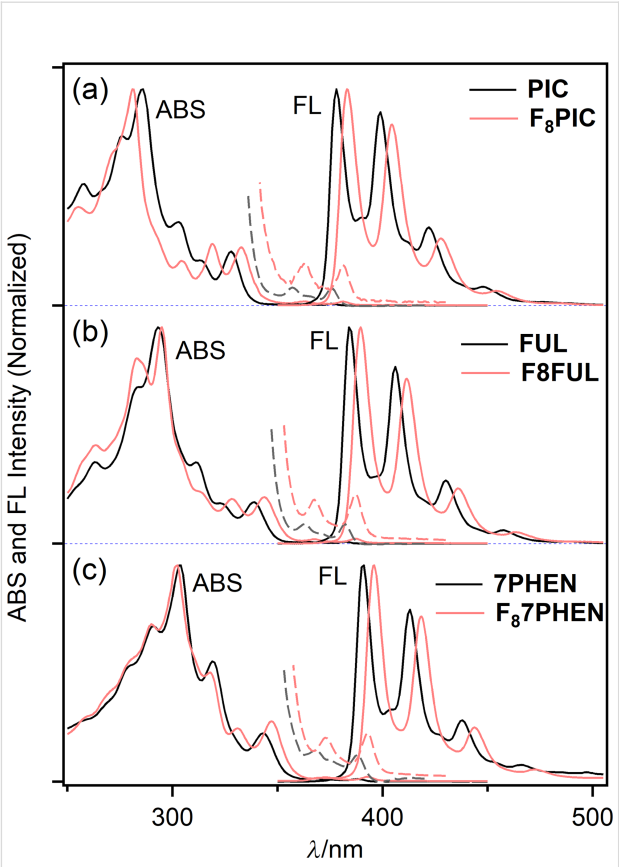

Figure 2: UV–vis and fluorescence spectra of **F$_8$PIC** (a), **F$_8$FUL** (b), and **F$_8$7PHEN** (c) (red lines) and the corresponding parent phenacenes (black lines) in $CHCl_3$. The broken lines show long-wavelength absorption bands at 10-times magnification of the intensity for clarity.

Table 1: Photophysical parameters for F$_8$-phenacenes and the parent phenacenes.

Compound	λ_{ABS}/nm		λ_{FL}/nm		$\Delta\lambda_{FL}$/nm ($\Delta\tilde{\nu}_{FL}$/cm^{-1})[b]
	(α band)[a]	(*p* band)[a]	in $CHCl_3$ (Φ_F)	in solid	
F$_8$PIC	381	333	383 (0.08)	458	75 (4280)
F$_8$FUL	387	344	390 (0.12)	467	77 (4230)
F$_8$7PHEN	393	347	396 (0.08)	489	93 (4800)
PIC	376[c]	328[c]	380 (0.09)[c]	391 sh, 408	28 (1810)
FUL	382[c]	339[c]	386 (0.12)[c]	398 sh, 416	30 (1870)
7PHEN	388[d]	343[d]	391 (0.12)[d]	407 sh, 424[d]	33 (1990)

[a]The Clar's descriptions for the absorption bands; [b]$\Delta\lambda_{FL} = \lambda_{FL}(solid) - \lambda_{FL}(CHCl_3)$, $\Delta\lambda_{FL} = \lambda_{FL}(solid) - \lambda_{FL}(CHCl_3)$, $\Delta\tilde{\nu}_{FL} = \tilde{\nu}_{FL}(CHCl_3) - \tilde{\nu}_{FL}(solid)$; [c]Ref. [48]; [d]Ref. [49].

benzene-ring numbers, by ca. 6 nm per increment of one benzene ring, for both F_8-phenacenes and the parent phenacenes.

As seen in Figure 2, it is characteristic that the α- and *p*-absorption bands and fluorescence bands systematically red-shifted by 5–6 nm compared to the parent molecules upon the fluorination. The effects of fluorination on UV–vis and fluorescence spectral behavior was similar to those reported for fluorinated [7]helicenes [38]. The fluorescence quantum yields, Φ_F of F_8-phenacenes were ca. 0.1 (0.08 for **F_8PIC**, 0.12 for **F_8FUL**, and 0.08 for **$F_8$7PHEN**) which were similar to those of the corresponding parent phenacenes [48,49]. Thus, in the solution phase, the introduction of fluorine substituents provided seemingly minimal effects on the electronic spectral features of phenacenes.

It has been demonstrated that parent phenacenes phosphoresce in a 500–620 nm wavelength region at 77 K showing the clear vibrational progression. The first phosphorescence vibrational peak was observed at 501 nm for **PIC** and 514 nm for **FUL** [48]. In the case of F_8-phenacenes, at 77 K, in addition to fluorescence bands, photoluminescence bands assignable to phosphorescence were detected (λ_{PHOS} = 518 nm for **F_8PIC**, 528 nm for **F_8PIC**, and 525 nm for **$F_8$7PHEN**, Figure 3). The red-shift for phosphorescence upon the octafluorination was slightly more pronounced compared to that for fluorescence. The fact that the phosphorescence bands were observed for F_8-phenacenes indicates that intersystem crossing is operative as one of the non-radiative processes contributing to the low fluorescence quantum yield of the F_8-phenacenes (cf. Table 1).

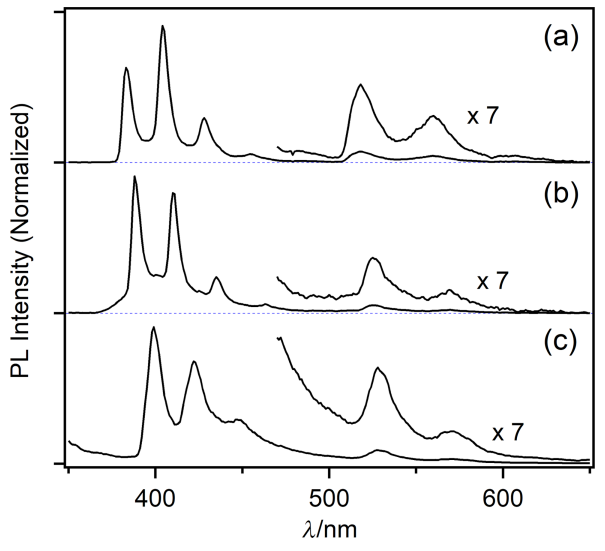

Figure 3: Photoluminescence spectra of **F_8PIC** (a), **F_8FUL** (b), and **$F_8$7PHEN** (c) in toluene at 77 K.

Because fluorescence behavior in the solid state reflects molecular alignment and intermolecular interactions in the crystals, solid-state fluorescence of the F_8-phenacenes was investigated. We observed fluorescence behavior significantly different from those observed in solution. Figure 4 compares absorption and fluorescence spectra between F_8-phenacenes and the parent phenacenes in the solid phase.

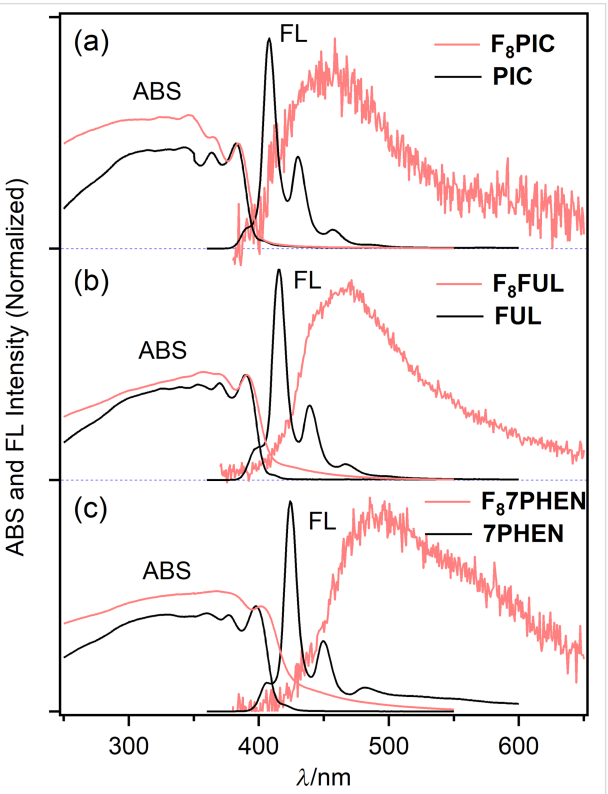

Figure 4: Electronic spectra of **F_8PIC** (a), **F_8FUL** (b), and **$F_8$7PHEN** (c) (red lines) and the corresponding parent phenacenes (black lines) in the solid state.

The parent phenacenes displayed sharp and vibrationally resolved fluorescence bands with maxima in the 380–390 nm region which were consistent with those observed in solution. By contrast, for the F_8-phenacenes, the solid-state fluorescence spectra significantly broadened and red-shifted compared to those observed in solution: **F_8PIC**, **F_8FUL**, and **$F_8$7PHEN**, respectively, displayed fluorescence maxima at 458, 467, and 489 nm. As shown in Table 1, the differences in the fluorescence maxima shifts between the solution and solid phases ($\Delta\lambda_{FL}$ and $\Delta\tilde{\nu}_{FL}$) are obviously larger for F_8-phenacenes than the parent phenacenes. These observations explicitly indicate that the alignment of the phenacene molecules in the solid phase changed upon the fluorination. It can be expected that the fluorinated phenacenes are aligned in a π–π interacting manner to display the excimeric fluorescence band in the solid state. Previously, excimer fluorescence of picene chromophores was ob-

served in a 450–650 nm wavelength region for a macrocyclic picenophadiene [51]. As the solid-state fluorescence bands of the F_8-phenacenes were observed in the similar wavelength region of the picenophadiene, the solid-state F_8-phenacene molecules have excimeric character in the fluorescing state.

It is critical to know the crystal packing of the F_8-phenacenes for clarifying the different solid-fluorescence behavior between the parent and fluorinated phenacenes. Although we have extensively examined crystallization of F_8-phenacenes, no single crystal suitable for an X-ray diffraction analysis was obtained. The crystalline structural analysis is still under examination.

Theoretical analyses

Quantum chemical studies were performed to understand the electronic spectral behavior of the F_8-phenacenes. The calculation level at B3LYP/6-31+G(d,p) [52] was chosen because the B3LYP functional qualitatively reproduced the experimental properties of some fused aromatics [53]. Figure 5 shows the molecular orbitals (MOs) around the frontier MO levels and the eigenvalues.

The shapes (symmetries) and the energy-level order of the MOs in the F_8-phenacenes are the same as those of the corresponding parent phenacenes. It is characteristic that, upon the fluorination, the MO levels systematically lowered by 0.7–0.8 eV compared to the parent phenacenes, and that the energy gaps and the symmetry of the MOs are little affected by the fluorination. Accordingly, the electronic spectral behavior of the F_8-phenacenes is essentially the same as that of the parent phenacenes. The theoretical calculation results were consistent with the experimentally observed electronic spectral features in solution, i.e., the absorption and fluorescence bands only slightly red-shifted (by 5–10 nm) and the spectral shapes were little affected by the fluorination. It can be concluded that, through the fluorination, one can tune the MO energy levels without changing the apparent electronic spectral features in solution, such as, electronic spectral shapes, wavelengths, and fluorescence quantum yields. Such fluorine-substitution effects on electronic spectra and MO levels were recognized for fluorinated oligoacene systems [30,34,36].

The theoretical calculations suggest that, in the ground state, the polarization of the phenacene molecules inverted upon the introduction of fluorine atoms. As seen from electrostatic potential (ESP) mapping (Figure 5b), the phenacene cores are negative (orange region) in the parent compounds, whereas the phenacene cores turned to be positive (blue) for the F_8-phenacenes. Therefore, one can manipulate the polarization of the phenacene cores through the introduction of fluorine atoms without altering the electronic spectral features.

The excited-state electronic characteristics were also calculated, and the electronic transitions for the first two vertical absorption bands are summarized in Table 2. Although the calculated $S_1 \leftarrow S_0$ and $S_2 \leftarrow S_0$ electronic transition energies were slightly

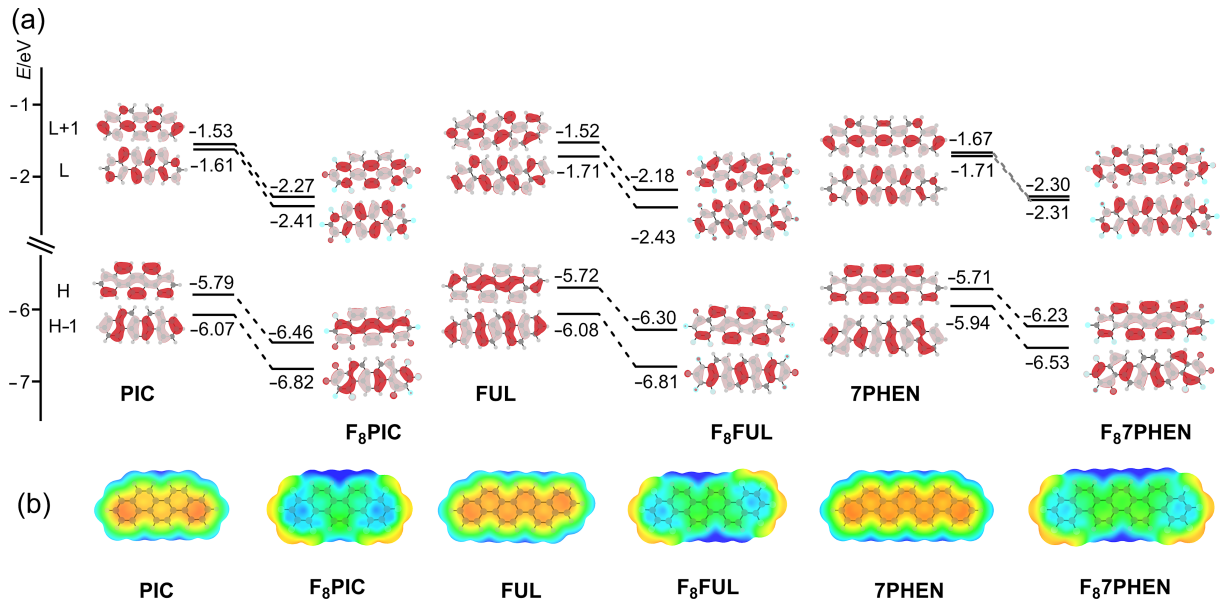

Figure 5: (a) The MO diagrams of the parent and fluorinated phenacenes (B3LYP/6-31+G(d,p)). H and L, respectively, denote HOMO and LUMO; (b) electrostatic potentials mapped on the total S_0 electron density surface in the ground state. The orange and blue sites, respectively, indicate negative and positive regions (−0.02 ≈ 0.02 hartree).

Table 2: Calculated vertical electronic transitions for F_8-phenacenes and the parent phenacenes.

Compound	$S_1 \leftarrow S_0$ (α band)			$S_2 \leftarrow S_0$ (*p* band)		
	λ_1/nm[a]	*f*[b]	configuration[c]	λ_2/nm[a]	*f*[b]	configuration[c]
F_8PIC	355	0.0109	H – 1→L (28%) H→L + 1 (68%)	344	0.2276	H – 1→L + 1 (10%) H→L (90%)
F_8FUL	365	0.0731	H – 1→L (12%) H→L (62%) H→L + 1 (19%)	356	0.1742	H – 1→L (18%) H→L (31%) H→L + 1 (51%)
$F_8$7PHEN	372	0.0160	H – 1→L (18%) H→L + 1 (73%)	361	0.3166	H→L (90%)
PIC	350	0.0053	H – 1→L (35%) H→L + 1 (65%)	336	0.1602	H – 1→L + 1 (14%) H→L (86%)
FUL	357	0.0162	H – 1→L (29%) H→L (22%) H→L + 1 (46%)	349	0.1768	H→L (68%) H→L + 1 (19%)
7PHEN	366	0.0085	H – 1→L (28%) H→L + 1 (65%)	355	0.2497	H – 1→L + 1 (11%) H→L (88%)

[a]Calculated wavelengths of vertical transitions for $S_1 \leftarrow S_0$ (λ_1) and $S_0 \leftarrow S_2$ (λ_2); [b]calculated oscillator strength; [c]configurations for the electronic transitions, with H and L, respectively, denote HOMO and LUMO. Electronic transitions with low contribution (<10%) are omitted.

overestimated to show a systematic difference between the experimental and calculated absorption wavelengths, $\Delta\lambda_1$ = 21–26 nm for the $S_1 \leftarrow S_0$ transition and $\Delta\lambda_2$ = 11–14 nm for the $S_2 \leftarrow S_0$ transition, the calculation results qualitatively explain the absorption spectral behavior of the fluorinated phenacenes (cf. Table S2 in Supporting Information File 1). Therefore, the S_0–S_1 transition band, experimentally observed in the 381–393 nm wavelength region for F_8-phenacenes, was assigned to a forbidden transition contributed from (H − 1)-to-L and H-to-(L + 1) electronic transitions (α band according to Clar's description with H and L, respectively, denote HOMO and LUMO). The $S_2 \leftarrow S_0$ transition is assignable to H–L one (*p*-band). The calculated results, in particular for **F_8PIC** and **$F_8$7Phen** possessing odd benzene-ring π conjugations, were well consistent with the electronic transition characteristics of phenacenes [54]. In the case of **F_8FUL** possessing an even-benzene-ring homologue structure, there was a significant contribution from the H–L transition in the α band, presumably because of the difference in the molecular symmetry.

Conclusion

Octafluorinated phenacenes, **F_8PIC**, **F_8FUL**, and **$F_8$7PHEN**, were conveniently synthesized through the Mallory photoreaction as the key step, and their electronic spectral features were investigated. They displayed UV–vis and fluorescence spectra which were seemingly the same as those of the parent phenacene molecules in the solution phase although theoretical calculations predicted the MO energy levels of F_8-phenacenes markedly lowered by the fluorination. By contrast, in the solid phase, **F_8PIC**, **F_8FUL**, and **$F_8$7PHEN** showed significantly broadened and red-shifted fluorescence bands indicating that the intermolecular interactions in the solid phase were modified by the fluorine substitution. The present results could provide a strategy for the manipulation of the solid-state optoelectronic nature of polycyclic aromatic molecules to develop future functional materials in organic electronics.

Supporting Information

Supporting Information File 1

Excitation spectra of the fluorescence, synthetic procedures and physical data for the new compounds, theoretical calculation results, copy of ^{1}H and ^{13}C NMR spectra of the prepared compounds.
[https://www.beilstein-journals.org/bjoc/content/supplementary/1860-5397-21-53-S1.pdf]

Acknowledgements

HO thanks Prof. Kan Wakamatsu (Okayama University of Science) for fruitful discussions and Prof. Takayoshi Suzuki (Okayama University) for solid-state absorption spectral measurements.

Funding

The present study was supported by Grants-in-Aid for Scientific Research, KAKENHI, from JSPS, Japan (JP18H02043, JP20K05648, JP23K04877), and by the Cooperative Research Program of the 'Network Joint Research Centre for Materials and Devices.

Author Contributions

Yuuki Ishii: data curation; investigation; validation. Minoru Yamaji: data curation; formal analysis; investigation; writing – review & editing. Fumito Tani: formal analysis; investigation; validation; writing – review & editing. Kenta Goto: formal analysis; investigation; validation. Yoshihiro Kubozono: data curation; formal analysis; investigation. Hideki Okamoto: conceptualization; data curation; formal analysis; funding acquisition; investigation; supervision; validation; visualization; writing – original draft.

ORCID® iDs

Minoru Yamaji - https://orcid.org/0000-0001-9963-2136
Fumito Tani - https://orcid.org/0000-0002-9166-2127
Kenta Goto - https://orcid.org/0000-0002-7369-5996
Yoshihiro Kubozono - https://orcid.org/0000-0002-7910-0308
Hideki Okamoto - https://orcid.org/0000-0002-8742-4089

Data Availability Statement

All data that supports the findings of this study is available in the published article and/or the supporting information of this article.

References

1. Bronstein, H.; Nielsen, C. B.; Schroeder, B. C.; McCulloch, I. *Nat. Rev. Chem.* **2020,** *4,* 66–77. doi:10.1038/s41570-019-0152-9
2. Xie, Z.; Liu, D.; Zhao, Z.; Gao, C.; Wang, P.; Jiang, C.; Liu, X.; Zhang, X.; Ren, Z.; Yan, S.; Hu, W.; Dong, H. *Angew. Chem., Int. Ed.* **2024,** *63,* e202319380. doi:10.1002/anie.202319380
3. Mei, J.; Diao, Y.; Appleton, A. L.; Fang, L.; Bao, Z. *J. Am. Chem. Soc.* **2013,** *135,* 6724–6746. doi:10.1021/ja400881n
4. Okamoto, T.; Yu, C. P.; Mitsui, C.; Yamagishi, M.; Ishii, H.; Takeya, J. *J. Am. Chem. Soc.* **2020,** *142,* 9083–9096. doi:10.1021/jacs.9b10450
5. Ye, Q.; Chi, C. *Chem. Mater.* **2014,** *26,* 4046–4056. doi:10.1021/cm501536p
6. Anthony, J. E. *Angew. Chem., Int. Ed.* **2008,** *47,* 452–483. doi:10.1002/anie.200604045
7. Tönshoff, C.; Bettinger, H. F. *Chem. – Eur. J.* **2021,** *27,* 3193–3212. doi:10.1002/chem.202003112
8. Lang, K. F. *Angew. Chem.* **1951,** *63,* 345–349. doi:10.1002/ange.19510631503
9. Burg, O. *Ber. Dtsch. Chem. Ges.* **1880,** *13,* 1834–1837. doi:10.1002/cber.188001302149
10. Liu, W.; Xu, X.; Yuan, J.; Leclerc, M.; Zou, Y.; Li, Y. *ACS Energy Lett.* **2021,** *6,* 598–608. doi:10.1021/acsenergylett.0c02384
11. Zhao, J.; Yao, C.; Zhu, Y.; Cai, J.; Ali, M. U.; Miao, J.; Meng, H. *Dyes Pigm.* **2020,** *174,* 108012. doi:10.1016/j.dyepig.2019.108012
12. Yao, Z.; Liao, X.; Gao, K.; Lin, F.; Xu, X.; Shi, X.; Zuo, L.; Liu, F.; Chen, Y.; Jen, A. K.-Y. *J. Am. Chem. Soc.* **2018,** *140,* 2054–2057. doi:10.1021/jacs.7b13239
13. Chawanpunyawat, T.; Chasing, P.; Nalaoh, P.; Maitarad, P.; Sudyodsuk, T.; Promarak, V. *Chem. – Asian J.* **2021,** *16,* 4145–4154. doi:10.1002/asia.202101154
14. Nathusius, M.; Ejlli, B.; Rominger, F.; Freudenberg, J.; Bunz, U. H. F.; Müllen, K. *Chem. – Eur. J.* **2020,** *26,* 15089–15093. doi:10.1002/chem.202001808
15. Watanabe, T.; Sasabe, H.; Owada, T.; Maruyama, T.; Watanabe, Y.; Katagiri, H.; Kido, J. *Chem. Lett.* **2019,** *48,* 457–460. doi:10.1246/cl.180992
16. Kubozono, Y.; He, X.; Hamao, S.; Teranishi, K.; Goto, H.; Eguchi, R.; Kambe, T.; Gohda, S.; Nishihara, Y. *Eur. J. Inorg. Chem.* **2014,** 3806–3819. doi:10.1002/ejic.201402168
17. Zhang, L.; Cao, Y.; Colella, N. S.; Liang, Y.; Brédas, J.-L.; Houk, K. N.; Briseno, A. L. *Acc. Chem. Res.* **2015,** *48,* 500–509. doi:10.1021/ar500278w
18. Kubozono, Y.; Hamao, S.; Mikami, T.; Shimo, Y.; Hayashi, Y.; Okamoto, H. Transistor Application and Intercalation Chemistry of π-Conjugated Hydrocarbon Molecules. In *Physics and Chemistry of Carbon-Based Materials;* Kubozono, Y., Ed.; Springer: Singapore, 2019; pp 229–252. doi:10.1007/978-981-13-3417-7_8
19. Mitsuhashi, R.; Suzuki, Y.; Yamanari, Y.; Mitamura, H.; Kambe, T.; Ikeda, N.; Okamoto, H.; Fujiwara, A.; Yamaji, M.; Kawasaki, N.; Maniwa, Y.; Kubozono, Y. *Nature* **2010,** *464,* 76–79. doi:10.1038/nature08859
20. Okamoto, H.; Kawasaki, N.; Kaji, Y.; Kubozono, Y.; Fujiwara, A.; Yamaji, M. *J. Am. Chem. Soc.* **2008,** *130,* 10470–10471. doi:10.1021/ja803291a
21. Eguchi, R.; He, X.; Hamao, S.; Goto, H.; Okamoto, H.; Gohda, S.; Sato, K.; Kubozono, Y. *Phys. Chem. Chem. Phys.* **2013,** *15,* 20611–20617. doi:10.1039/c3cp53598c
22. Okamoto, H.; Eguchi, R.; Hamao, S.; Goto, H.; Gotoh, K.; Sakai, Y.; Izumi, M.; Takaguchi, Y.; Gohda, S.; Kubozono, Y. *Sci. Rep.* **2014,** *4,* 5330. doi:10.1038/srep05330
23. Shimo, Y.; Mikami, T.; Hamao, S.; Goto, H.; Okamoto, H.; Eguchi, R.; Gohda, S.; Hayashi, Y.; Kubozono, Y. *Sci. Rep.* **2016,** *6,* 21008. doi:10.1038/srep21008
24. Okamoto, H.; Hamao, S.; Eguchi, R.; Goto, H.; Takabayashi, Y.; Yen, P. Y.-H.; Liang, L. U.; Chou, C.-W.; Hoffmann, G.; Gohda, S.; Sugino, H.; Liao, Y.-F.; Ishii, H.; Kubozono, Y. *Sci. Rep.* **2019,** *9,* 4009. doi:10.1038/s41598-019-39899-4
25. Okamoto, H.; Hamao, S.; Goto, H.; Sakai, Y.; Izumi, M.; Gohda, S.; Kubozono, Y.; Eguchi, R. *Sci. Rep.* **2014,** *4,* 5048. doi:10.1038/srep05048
26. Zhang, Y.; Eguchi, R.; Okamoto, H.; Goto, K.; Tani, F.; Yamaji, M.; Goto, H.; Kubozono, Y. *J. Mater. Chem. C* **2022,** *10,* 16309–16320. doi:10.1039/d2tc03383f
27. Guo, Y.; Yoshioka, K.; Hamao, S.; Kubozono, Y.; Tani, F.; Goto, K.; Okamoto, H. *RSC Adv.* **2020,** *10,* 31547–31552. doi:10.1039/d0ra06629j
28. Nose, K.; Yamaji, M.; Tani, F.; Goto, K.; Okamoto, H. *J. Photochem. Photobiol., A* **2024,** *452,* 115613. doi:10.1016/j.jphotochem.2024.115613
29. Nose, K.; Yoshioka, K.; Yamaji, M.; Tani, F.; Goto, K.; Okamoto, H. *RSC Adv.* **2023,** *13,* 4096–4101. doi:10.1039/d2ra07771j

30. Delgado, M. C. R.; Pigg, K. R.; da Silva Filho, D. A.; Gruhn, N. E.; Sakamoto, Y.; Suzuki, T.; Osuna, R. M.; Casado, J.; Hernández, V.; Navarrete, J. T. L.; Martinelli, N. G.; Cornil, J.; Sánchez-Carrera, R. S.; Coropceanu, V.; Brédas, J.-L. *J. Am. Chem. Soc.* **2009,** *131,* 1502–1512. doi:10.1021/ja807528w
31. Geiger, T.; Schundelmeier, S.; Hummel, T.; Ströbele, M.; Leis, W.; Seitz, M.; Zeiser, C.; Moretti, L.; Maiuri, M.; Cerullo, G.; Broch, K.; Vahland, J.; Leo, K.; Maichle-Mössmer, C.; Speiser, B.; Bettinger, H. F. *Chem. – Eur. J.* **2020,** *26,* 3420–3434. doi:10.1002/chem.201905843
32. Babudri, F.; Farinola, G. M.; Naso, F.; Ragni, R. *Chem. Commun.* **2007,** 1003–1022. doi:10.1039/b611336b
33. Tang, M. L.; Bao, Z. *Chem. Mater.* **2011,** *23,* 446–455. doi:10.1021/cm102182x
34. Bischof, D.; Zeplichal, M.; Anhäuser, S.; Kumar, A.; Kind, M.; Kramer, F.; Bolte, M.; Ivlev, S. I.; Terfort, A.; Witte, G. *J. Phys. Chem. C* **2021,** *125,* 19000–19012. doi:10.1021/acs.jpcc.1c05985
35. Sakamoto, Y.; Suzuki, T. *J. Org. Chem.* **2017,** *82,* 8111–8116. doi:10.1021/acs.joc.7b01383
36. Shen, B.; Geiger, T.; Einholz, R.; Reicherter, F.; Schundelmeier, S.; Maichle-Mössmer, C.; Speiser, B.; Bettinger, H. F. *J. Org. Chem.* **2018,** *83,* 3149–3158. doi:10.1021/acs.joc.7b03241
37. Watanabe, M.; Chen, K.-Y.; Chang, Y. J.; Chow, T. J. *Acc. Chem. Res.* **2013,** *46,* 1606–1615. doi:10.1021/ar400002y
38. Sakamoto, Y.; Suzuki, T.; Kobayashi, M.; Gao, Y.; Fukai, Y.; Inoue, Y.; Sato, F.; Tokito, S. *J. Am. Chem. Soc.* **2004,** *126,* 8138–8140. doi:10.1021/ja0476258
39. Církva, V.; Jakubík, P.; Strašák, T.; Hrbáč, J.; Sýkora, J.; Císařová, I.; Vacek, J.; Žádný, J.; Storch, J. *J. Org. Chem.* **2019,** *84,* 1980–1993. doi:10.1021/acs.joc.8b02870
40. Matsuda, C.; Suzuki, Y.; Katagiri, H.; Murase, T. *Chem. – Asian J.* **2021,** *16,* 538–547. doi:10.1002/asia.202001295
41. Mahato, B.; Panda, A. N. *J. Phys. Chem. A* **2023,** *127,* 2284–2294. doi:10.1021/acs.jpca.2c08474
42. Suzuki, R.; Uziie, Y.; Fujiwara, W.; Katagiri, H.; Murase, T. *Chem. – Asian J.* **2020,** *15,* 1330–1338. doi:10.1002/asia.202000037
43. Cozzi, F.; Bacchi, S.; Filippini, G.; Pilati, T.; Gavezzotti, A. *Chem. – Eur. J.* **2007,** *13,* 7177–7184. doi:10.1002/chem.200700267
44. Fuchibe, K.; Morikawa, T.; Shigeno, K.; Fujita, T.; Ichikawa, J. *Org. Lett.* **2015,** *17,* 1126–1129. doi:10.1021/ol503759d
45. Fuchibe, K.; Fujita, T.; Ichikawa, J. *Bull. Chem. Soc. Jpn.* **2024,** *97,* No. uoad024. doi:10.1093/bulcsj/uoad024
46. Mallory, F. B.; Mallory, C. W. *Org. React.* **1984,** *30,* 1–456. doi:10.1002/0471264180.or030.01
47. Raveendra, B.; Das, B. G.; Ghorai, P. *Org. Lett.* **2014,** *16,* 5580–5583. doi:10.1021/ol502614n
48. Okamoto, H.; Yamaji, M.; Gohda, S.; Sato, K.; Sugino, H.; Satake, K. *Res. Chem. Intermed.* **2013,** *39,* 147–159. doi:10.1007/s11164-012-0639-1
49. Fujino, S.; Yamaji, M.; Okamoto, H.; Mutai, T.; Yoshikawa, I.; Houjou, H.; Tani, F. *Photochem. Photobiol. Sci.* **2017,** *16,* 925–934. doi:10.1039/c7pp00040e
50. Clar, E. *Polycyclic Hydrocarbons;* Springer-Verlag: Berlin, Heidelberg, Germany, 1964; Vol. 1. doi:10.1007/978-3-662-01665-7
51. Tang, M.-C.; Wei, Y.-C.; Chu, Y.-C.; Jiang, C.-X.; Huang, Z.-X.; Wu, C.-C.; Chao, T.-H.; Hong, P.-H.; Cheng, M.-J.; Chou, P.-T.; Wu, Y.-T. *J. Am. Chem. Soc.* **2020,** *142,* 20351–20358. doi:10.1021/jacs.0c08115
52. Becke, A. D. *J. Chem. Phys.* **1993,** *98,* 5648–5652. doi:10.1063/1.464913
53. Jones, L.; Lin, L. *J. Phys. Chem. A* **2017,** *121,* 2804–2813. doi:10.1021/acs.jpca.6b11770
54. Klessinger, M.; Michl, J. *Excited states and Photochemistry of Organic Molecules;* Wiley VCH: Weinheim, Germany, 1995.

License and Terms

BEILSTEIN JOURNAL OF ORGANIC CHEMISTRY

Recent advances and future challenges in the bottom-up synthesis of azulene-embedded nanographenes

Bartłomiej Pigulski

Review

Open Access

Address:
Faculty of Chemistry, University of Wrocław, 14 F. Joliot-Curie, 50-383 Wrocław, Poland

Email:
Bartłomiej Pigulski - bartlomiej.pigulski@uwr.edu.pl

Keywords:
azulene; nanographenes; non-alternant; non-benzenoid; polycyclic aromatic hydrocarbons

Beilstein J. Org. Chem. **2025,** *21,* 1272–1305.
https://doi.org/10.3762/bjoc.21.99

Received: 26 February 2025
Accepted: 06 June 2025
Published: 26 June 2025

This article is part of the thematic issue "π-Conjugated molecules and materials".

Guest Editor: A. Mateo-Alonso

Abstract

In recent years, significant progress has been made in the synthesis of various nanographenes incorporating non-benzenoid rings, expanding the scope of molecular design beyond all-hexagon polycyclic aromatic hydrocarbons (PAHs). Among these, π-conjugated scaffolds featuring embedded azulene units have gained considerable attention due to their unique optical and electronic properties. This review provides an overview of representative azulene-embedded nanographenes, with a particular focus on the synthetic strategies. Additionally, it explores selected aspects of aromaticity and spectroscopic properties.

Introduction

The discovery of graphene and fullerenes has sparked a continuously growing interest in synthesis of new carbon-rich unsaturated molecules and materials [1]. Graphene is a revolutionary material with exceptional properties, driving advancements across various scientific, industrial, and technological fields like organic electronics [2], medicine [3], sensing [4] and energy storage [5]. Typically, bulk graphene is obtained using a top-down approach, where graphite is exfoliated using chemical or mechanical methods [6,7]. However, this method does not provide precise control over the structure of graphene and graphenoid materials, which is crucial for fine-tuning their properties. An alternative is the bottom-up approach where various nanographenes are synthesized form smaller building blocks via classical organic synthesis. This strategy enables precise control over the structure and topology, leading to the development of a vast array of benzenoid nanographenes, also known as polycyclic aromatic hydrocarbons (PAHs) [8,9]. PAHs can be considered molecular models of bulk graphene, offering invaluable insights into structure–property relationships in graphene and graphene-based materials.

Structural defects appear to be inevitable in real graphene and graphenoid structures. The presence of heteroatoms, dislocations and grain boundaries [10] has a significant impact on the

properties of graphene [11]. From both fundamental and applied perspectives, a thorough understanding of these topological defects is of great importance. Consequently, the investigation of well-defined defects in atomically precise and monodisperse nanographenes plays a unique role in engineering defects in graphene, helping to elucidate the structure–property relationships.

Non-benzenoid rings are among the most important types of defects found in graphene [12,13] with Stone–Wales [14] and azulene [10] defects being the most representative examples (Figure 1a). Modelling and understanding these defects is a key motivation behind the growing interest in non-alternant, non-benzenoid PAHs [15]. In particular, the incorporation of azulene moieties into various PAHs is highly valuable, as such molecules provide deeper insights into structure–property relationships [16,17].

Azulene, an isomer of naphthalene, is the smallest non-alternant, non-benzenoid aromatic compound (Figure 1b). It consists of an electron-rich pentagon and an electron-deficient heptagon, resulting in a significant dipole moment of 1.08 D [18]. Due to its unique non-alternant topology, azulene exhibits a smaller energy gap compared to that of isomeric naphthalene and unusual emission from the S_2 state (*anti*-Kasha's emission), as a consequence of its non-mirror related highest occupied molecular orbital (HOMO) and lowest unoccupied molecular orbital (LUMO) [19]. This distinctive behaviour gives rise to intriguing optoelectronic properties, making azulene an attractive candidate for practical applications. For example, graphene nanoribbons with azulene defects are promising materials for nonlinear optics (NLO) [20]. Furthermore, azulene subunits are present in many hypothetical allotropic two-dimensional carbon allotropes. In recent years many 2D graphenoid allotropic forms of carbon were theoretically predicted like a family based on the azulenoid kekulene [21], phagraphene (Figure 2a) [22], TPH-graphene (Figure 2b) [23], PHH-graphene [24] and ψ-graphene [25]. Notably, fragments phagraphene and TPH-graphene have already been synthesized via on-surface chemistry and characterized using low-temperature scanning probe microscopy with CO-functionalized tips [23]. These non-alternant carbon allotropes represent promising candidates for novel carbon-based materials with exotic properties.

Given the points discussed above, it is evident that exploring of synthetic pathways for azulene-embedded nanographenes is a highly relevant and important topic in contemporary synthetic organic chemistry. These well-defined molecules are not only valuable as fundamental models of defective graphene but also hold significant potential in organic electronics [26,27] despite the considerable challenges in their synthesis [28,29].

One important factor should be considered regarding azulene-embedded nanographenes. In the literature terms such as "azulene-embedded nanographenes" or "azulene-embedded PAHs" generally refer to any conjugated carbon scaffold composed of

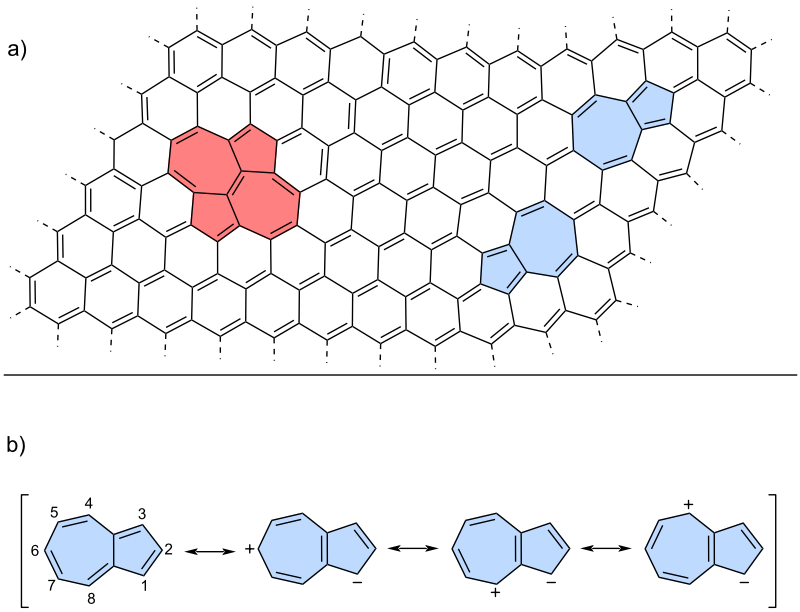

Figure 1: a) Stone–Wales (red) and azulene (blue) defects in graphene; b) azulene and its selected resonance forms.

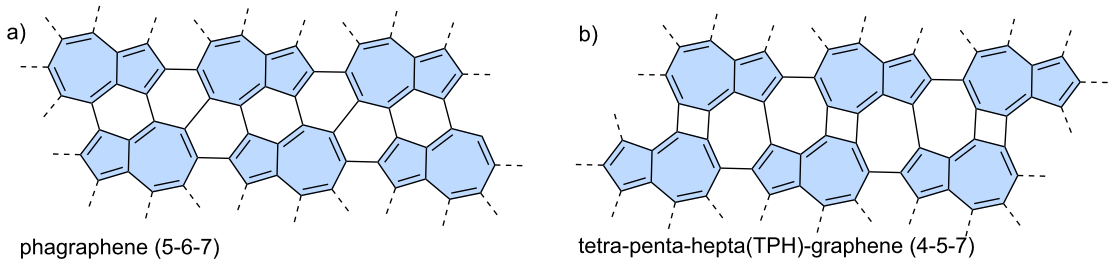

Figure 2: Examples of azulene-embedded 2D allotropic forms of carbon: a) phagraphene and b) TPH-graphene.

sp^2 carbons with adjacent pentagonal and heptagonal rings. However, in many cases, the distinctive electronic structure of azulene is absent due to the dominance of surrounding benzenoid rings or the presence of biradical character. As a result, these PAHs despite, possessing formal azulene may exhibit properties typical of benzenoid molecules rather than the characteristic azulene features such as red-shifted absorption, a small HOMO–LUMO gap, aromaticity of azulene subunit and *anti*-Kasha's emission from higher excited states. In such cases, the azulene unit merely acts as a linker within a more complex benzenoid framework.

This review covers all types of azulene-embedded molecular scaffolds, regardless of whether they contain a "formal" or "true" azulene subunits. However, one of the key objectives here is to highlight the differences between these structural types and provide a clear distinction between benzenoid structures with azulene-like linkers and molecules that can be considered "true" aromatic π-extended azulenes. This is why, in many cases, the aromaticity of the azulene moiety is discussed, particularly through the analysis of the most used variations of NICS (nucleus-independent chemical shifts) parameters [30]. Additionally, whenever possible, information on the wavelength of the lowest-energy optical transition is included, as it serves as an important indicator of the electronic structure.

This review provides an up-to-date summary of known synthetic strategies for azulene-embedded polycyclic aromatic hydrocarbons (PAHs) as models of defective graphene, offering guidelines for designing new carbon scaffolds of this type. Given the rapid progress in this field, with nearly half of the cited works published since 2020, this review focuses primarily on purely hydrocarbon structures, with less emphasis on heteroatom-containing molecules. Typically, only the final synthetic steps leading to the fused structures are discussed. However, in cases where it provides valuable context, key reactions leading to direct precursors are also described.

Review

Early approaches to azulene-embedded nanographenes

The following section provides a short historical overview of synthetic approaches leading to smaller purely hydrocarbon-based azulene-embedded nanographenes. The synthesis of smaller non-alternant PAHs containing azulene moiety dates to the 1950s. The most common strategy involved synthesizing a partially saturated scaffold, which was then dehydrogenated in the final step. One of the earliest examples of the synthesis of π-extended azulene was the non-benzenoid isomer of pyrene published by Ward and co-workers (Scheme 1) [31].

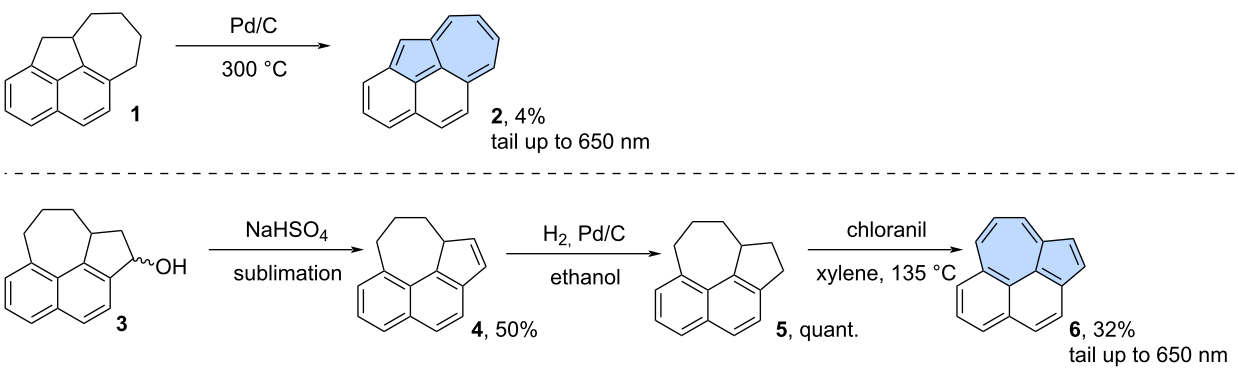

Scheme 1: Synthesis of non-alternant isomers of pyrene (**2** and **6**) using dehydrogenation.

Cyclohept[*bc*]acenaphthylene (**2**) was obtained from a partially saturated precursor **1** via dehydrogenation using palladium on carbon. However, the reaction carried out at 300 °C gave **2** as a red solid in only 4% yield. A similar strategy was used by Osborn for the synthesis of isomeric compound **6** (Scheme 1) [32]. In this case, compound **3** was dehydrogenated giving compound **4** which was then reduced to the direct precursor **5**. Subsequent oxidation using chloranil yielded cyclohepta[*klm*]benz[*e*]indene (**6**) as black plates in a 32% yield. The azulene-containing isomers of pyrene exhibit azulene-like absorption tailing up to around 650 nm. Interestingly, despite their initial synthesis in the 1950s, no further attempts have been made to synthesize compounds **2** and **6** using more modern methods.

Dehydrogenation played a pivotal role as a key step also in the synthesis of larger π-scaffolds. For example, Murata and co-workers reported the synthesis of an azulene containing isomer of benzo[*a*]pyrene **9** (Scheme 2) [33]. Reduction of ketone **7** using $LiAlH_4$ resulted in alcohol **8** which was subsequently dehydrogenated using sulfur in trichlorobenzene at 220 °C to yield the azulene-containing isomer of benzo[*a*]pyrene **9** in 18% isolated yield. Bestmann and Ruppert reported the synthesis of a dinaphthoazulene **14**, a non-alternant isomer of benzo[*a*]perylene (Scheme 2) [34]. In their method, bisylide **10** was reacted with dibromide **11** to form cyclic bisphosphonium salt **12,** which was then subjected to alkaline hydrolysis. The direct precursor **13** was isolated in 10% yield after two steps and, finally, oxidized to PAH **14** using DDQ (2,3-dichloro-5,6-dicyano-1,4-benzoquinone).

The second approach was inspired by well-known Ziegler–Hafner azulene synthesis [35]. The key step in this method involves the synthesis of the intermediate pentafulvene, which is subsequently cyclized to yield the target azulene. An example of this strategy is the synthesis of the azulene-embedded isomer of benzo[*a*]pyrene which was reported by Jutz and Kirchlechner in 1966 (Scheme 3) [36]. Condensation between phenalene **15** and pentafulvene **16** gave pentafulvene **17**. Pentafulvene **17** was finally subjected to Ziegler–Hafner reaction in quinoline at 180 °C, resulting in the π-extended azulene **18** in 60% yield. A similar synthetic strategy was employed by Hara and co-workers in 1975 (Scheme 3) [37]. Compound **19** reacted with cyanine **20** to give pentafulvene **21**. Compound **21** was later cyclized in quinoline at 180 °C giving non-alternant isomer of benzo[*a*]pyrene **22** in 62% isolated yield. PAH **22** has remarkable re-shifted optical absorption with λ_{max} = 1010 nm, which is a strong indicator of its dominant non-alternant character.

Traditional methods for synthesizing azulene-embedded PAHs often require harsh conditions, making them challenging to apply to larger π-scaffolds. Furthermore, these methods frequently suffer from low yields and are not easily adapted to more modular approaches, limiting the variety of possible substitution patterns. This is why more modern approaches continue to be developed.

Modern approaches to azulene-embedded nanographenes

Modern synthetic approaches have greatly benefited from the discovery of palladium-catalysed cross-coupling reactions, such as the Suzuki sp^2–sp^2 coupling or Sonogashira sp^2–sp coupling. These reactions enable the modular construction of complex precursors, which can then be transformed into azulene-embedded PAHs in the final step. Two main synthetic strategies are

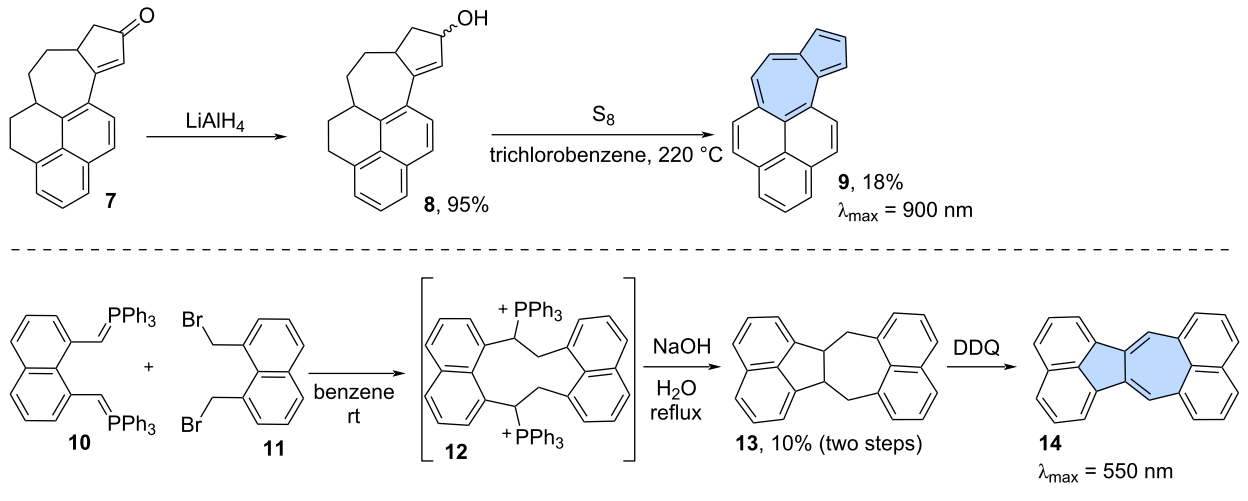

Scheme 2: Synthesis of non-alternant isomer **9** of benzo[*a*]pyrene and **14** of benzo[*a*]perylene using dehydrogenation.

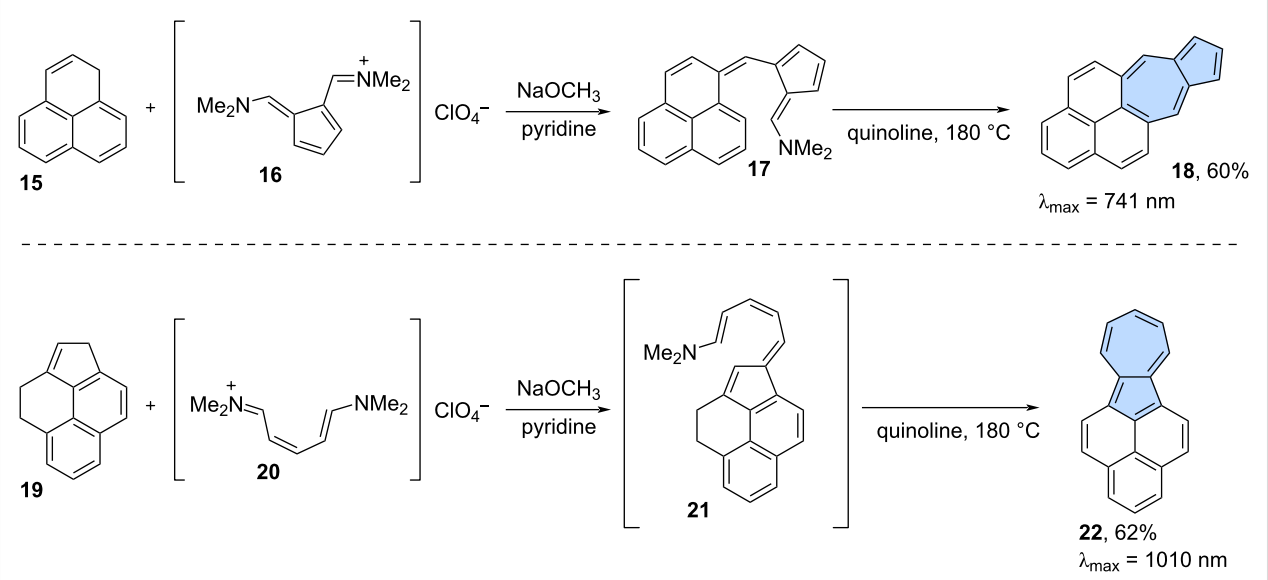

Scheme 3: Synthesis of azulene-embedded isomers of benzo[*a*]pyrene (**18** and **22**) inspired by Ziegler–Hafner azulene synthesis.

commonly employed: 1) The construction of the azulene moiety in the final step by creation of new C–C bond(s) or oxidation of a partially saturated precursor (Figure 3a); 2) The use of precursors that already contain the azulene moiety or moieties, which are then annulated into fully fused PAHs in the final step (Figure 3b). Obviously, the synthesis of more complex molecules may require elements of both strategies.

Construction of the azulene moiety in the final step

Oxidation of partially saturated precursors: With modern cross-coupling reactions providing access to larger precursors, a synthetic strategy involving the dehydrogenation of partially unsaturated precursors in the final stage can be applied to larger molecules as well. In this approach, the final PAHs with embedded formal azulene moieties are formed from substrates that

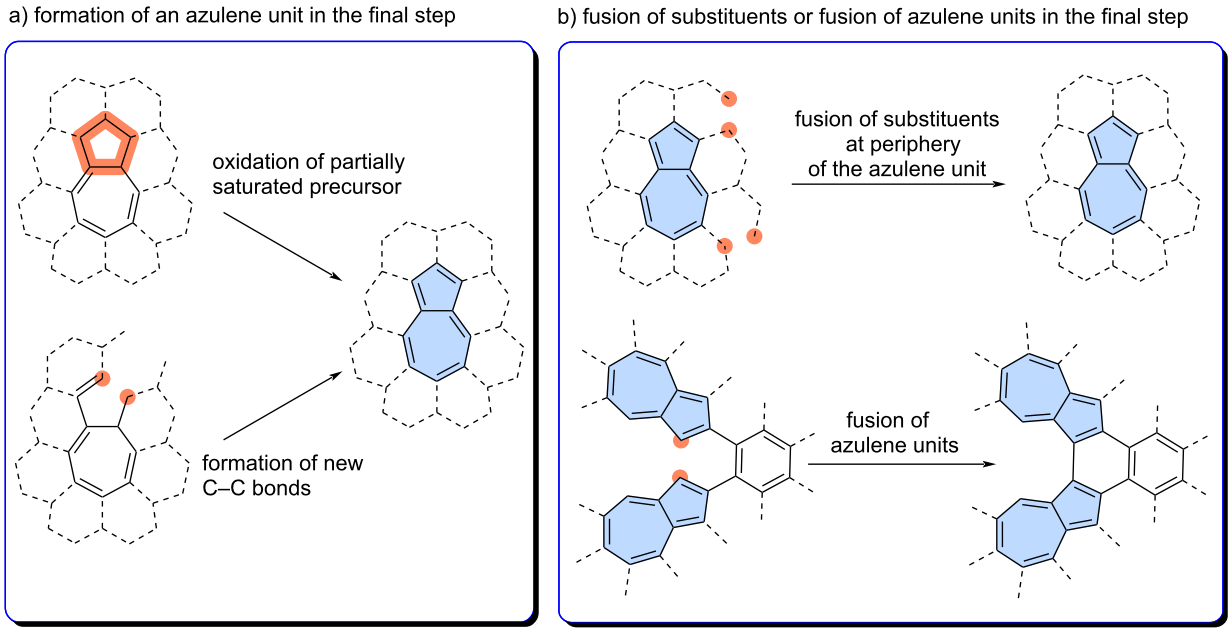

Figure 3: General strategies leading to azulene-embedded nanographenes: a) construction of azulene moiety in the final step: b) fusion of substituents at the periphery of fusion of azulene units.

already possess adjacent heptagons and pentagons but are partially saturated [38].

Ie, Aso and co-workers reported the oxidation of partially saturated precursor **23** using DDQ, which led to the isolation of PAH **24** in 50% yield which contains two formal azulene units (Scheme 4) [39]. However, compound **24** was found to possess a biradical structure (biradical character index, y_0 = 0.49) with antiaromatic character of the pentagon, in contrast to pristine azulene. This results in a significantly red-shifted optical absorption at 997 nm. Therefore, compound **24** should be considered a formally antiaromatic extended indeno[1,2-*b*]fluorene, rather than a 'true' extended azulene.

Similarly, Müllen and co-workers reported the synthesis of non-benzenoid open-shell nanographene **26** from partially saturated precursor **25** in 25% yield after oxidation using DDQ (Scheme 4) [40]. Extensive characterization of the resulting nanographene in solution revealed a low optical gap, and an open-shell singlet ground state with a low singlet−triplet gap. Nanographene **26**, which also contains the indeno[1,2-*b*]fluorene structural motif, displays an extremely narrow energy gap of 0.27 eV and exhibits a pronounced open-shell biradical character, with biradical character index close to 1 (y_0 = 0.92). Very recently, a similar synthetic strategy was used by Jiang and co-workers for the synthesis of very stable non-alternant nanographene with a triplet ground state [41].

Zhang and co-workers reported the synthesis of diazulenorubicene **29**, a non-benzenoid isomer of *peri*-tetracene (Scheme 5) [42]. The stepwise oxidation of compound **27** [43] which first yields the partially saturated product of the Scholl reaction (**28**) when $FeCl_3$ in CH_2Cl_2/$MeNO_2$ was used as an oxidant. Further oxidation was possible using DDQ in 1,4-dioxane and finally fully unsaturated PAH **29** was isolated in 87% yield. Compound **29** is a substructure of PAH **26** but does not exhibit biradical character. Instead, heptagons and pentagons are primarily non-aromatic, with a localized double C=C bond in the seven-membered ring, giving compound **29** predominantly benzenoid properties. Interestingly, PAH **29** undergoes single or double bromination with NBS in a mixture of $CHCl_3$, AcOH and *o*-DCB [44]. The resulting mixture of brominated PAHs **30** and **31** was then subjected to single or double [3 + 2] annulation with various alkynes, leading to the extended structures **32** and **33**. Notably, compound **33d** can undergo Pd-catalysed dimerization, resulting in the formation of a chiral non-benzenoid nanographene **34** [45]. Single crystals of **34** surprisingly exhibit SHG-CD (second harmonic generation–circular dichroism) properties due to the unusual self-sorting of *R* and *S* enantiomers in the crystalline state.

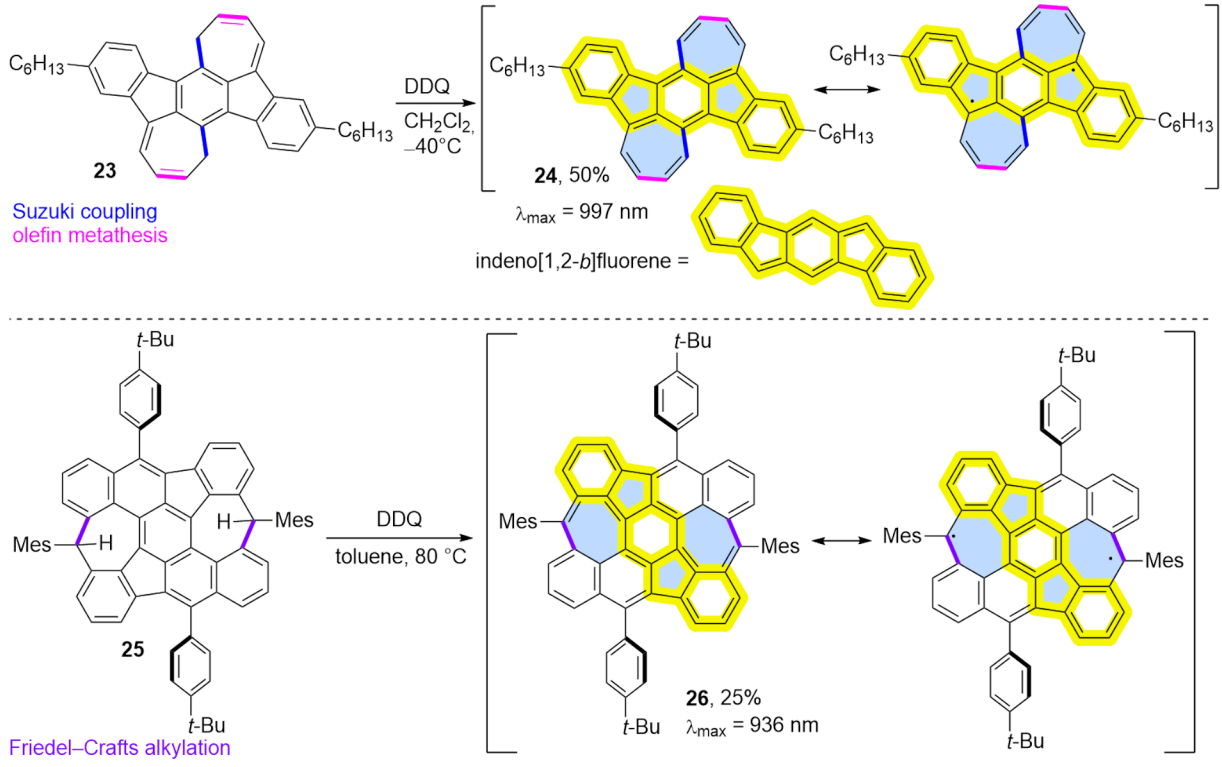

Scheme 4: Synthesis of biradical PAHs possessing significant biradical character using oxidation of partially unsaturated precursors.

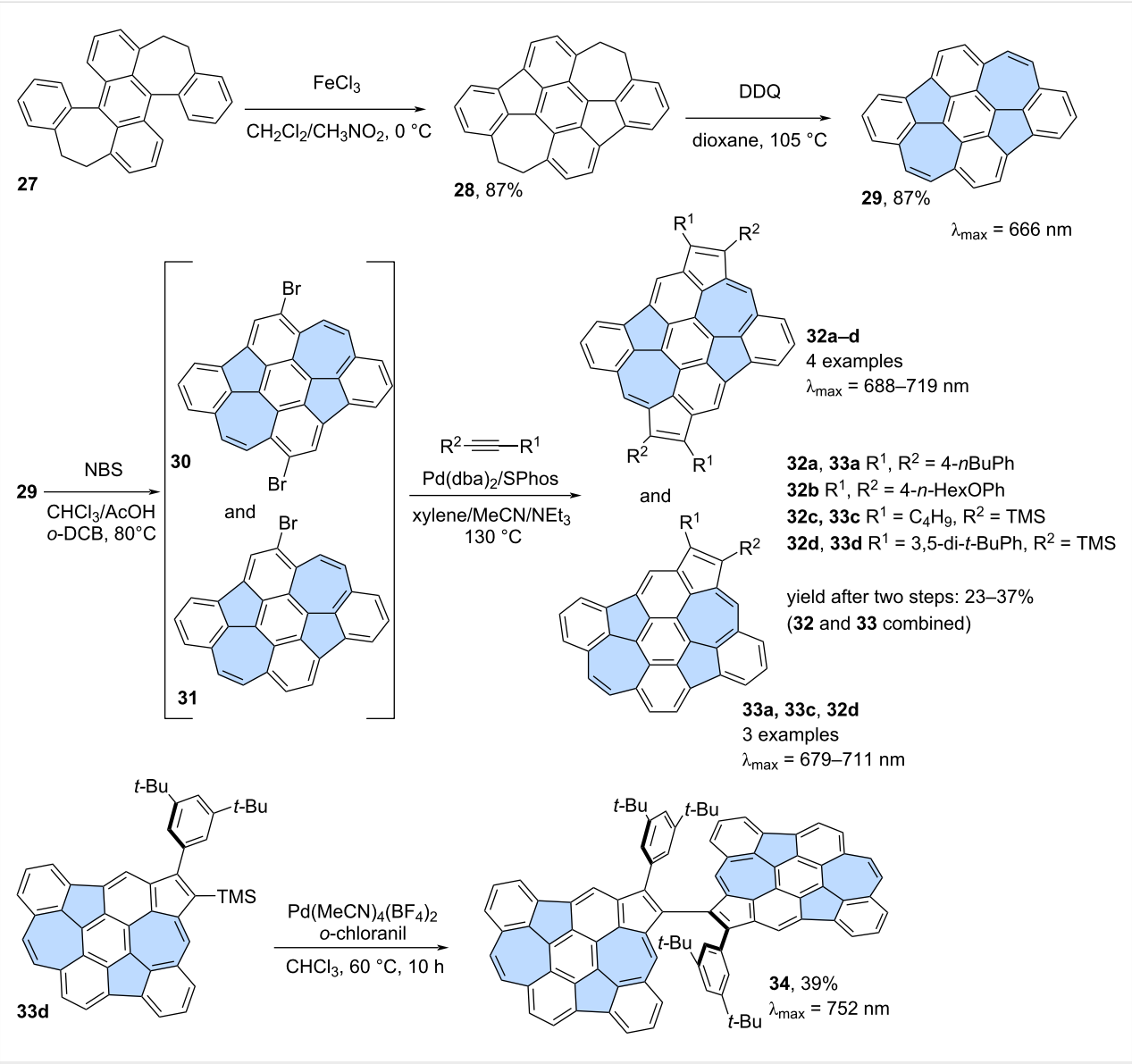

Scheme 5: Synthesis of dicyclohepta[*ijkl*,*uvwx*]rubicene (**29**) and its further modifications.

Scholl-type oxidation: The Scholl oxidation is a highly useful tool for constructing various benzenoid polycyclic aromatic hydrocarbons (PAHs) [9]. So it is not a surprise that such fusion reactions were used in construction of azulene embedded in various nanographenes. However, when applied to complex and sterically crowded precursors, the reaction often involves a degree of unpredictability. Additional rearrangements and substitutions might occur making the exact outcome of the reaction difficult to predict.

For example, Chi and co-workers unexpectedly obtained azulene-embedded nanographene **36** and its triflyloxylated derivative **37** from precursor **35** during the an attempted synthesis of a naphthalene-bridged double [6]helicene (Scheme 6) [46]. Depending on the amount of DDQ used for oxidation, the yield of **36** reached up to 22%, while **37** was obtained in up to 27% yield. The proposed mechanism for the formation of **36** and **37** involves an arenium ion-mediated 1,2-phenyl shift followed by a naphthalene-to-azulene rearrangement. The alternative radical cation mechanism has a higher energy barrier than the arenium cation-mediated reaction. Notably, only one of the pentagon–heptagon pairs exhibits an azulene-like electronic structure and aromaticity, as confirmed by the analysis of calculated NICS values. Similarly, Liu and co-workers reported the synthesis of two related nanographenes from precursor **38** (Scheme 6) [47]. Oxidation using DDQ/TfOH yielded two PAHs **39** and **40** in 34% and 22% yield, respectively. The authors postulated here formation of azulene moiety through

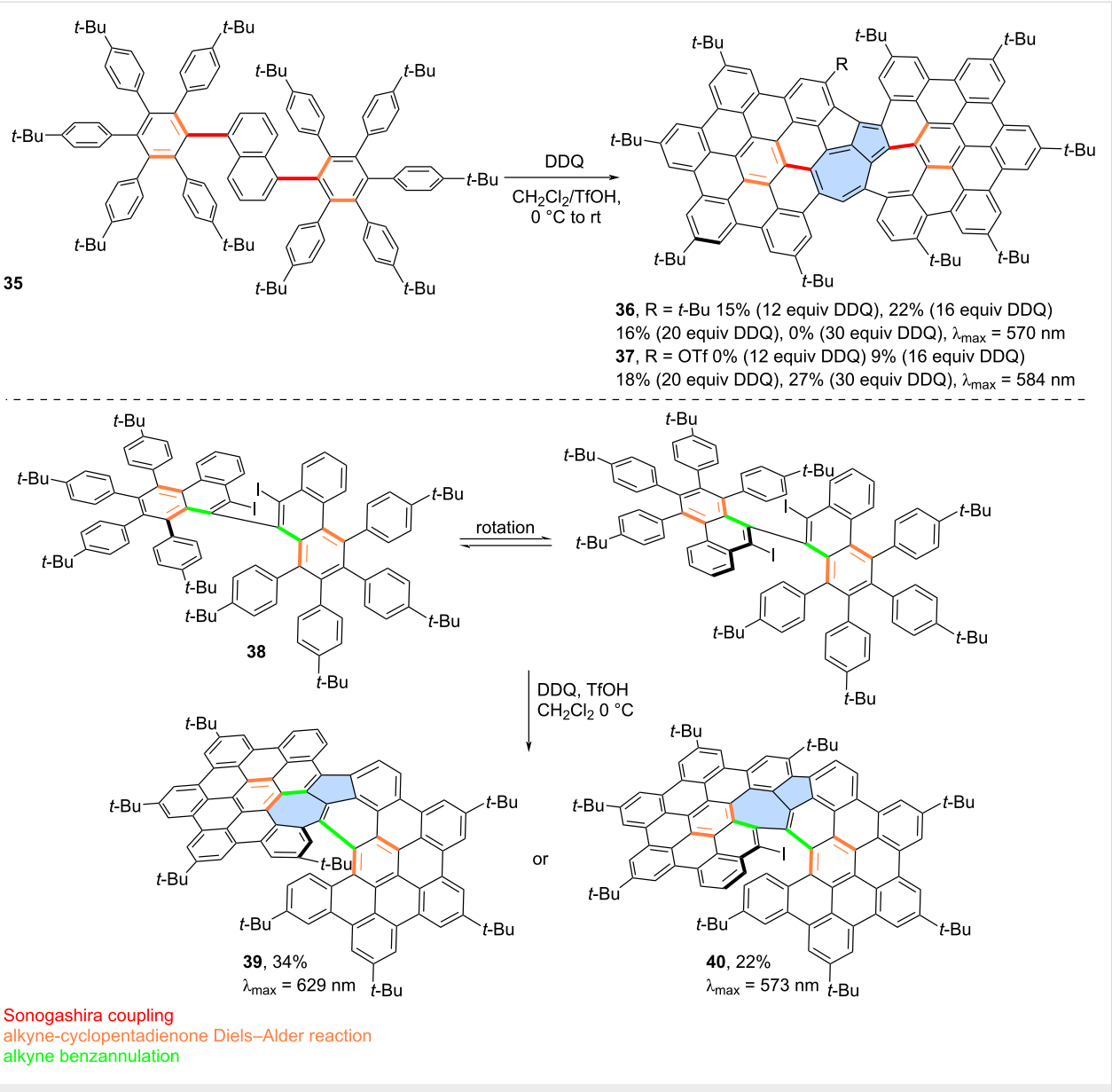

Scheme 6: Synthesis of warped PAHs with one embedded azulene subunit using Scholl-type oxidation.

radical cation mechanism and 1,2-phenyl shift. However, in this case, analysis of NICS values indicated that the azulene moiety does not exhibit aromatic character, and the electronic properties of the final molecules are primarily determined by the surrounding benzenoid rings.

Mastalerz and co-workers reported the oxidation of precursor **41** using DDQ which led to a mixture of azulene-embedded PAHs **42**–**44** (Scheme 7) [48]. Contorted PAHs **42**–**44** containing two azulene subunits, were formed through a single-step cyclopentannulation and cycloheptannulation process. The cyclodehydrogenation reaction was accompanied by further regioselective functionalization at the periphery of the PAHs. Besides triflyloxylation (**42**, **43**), the introduction of one or two dichlorovinylene groups (**43**, **44**) was observed. As in previous cases, the exact ratio of the products depended on the amount of DDQ and concentration of the precursor. Analysis of NICS values of **42**–**44** revealed that the "formal azulene" units do not exhibit aromatic character, and the electronic properties of the molecules are primarily determined by the surrounding benzenoid rings.

Takasu and co-workers reported a more complex application of Scholl-like oxidation for the construction of an azulene-embedded nanographene **49**, featuring embedded contiguous azulene units and a narrowed cove-type edge (Scheme 7) [49]. Com-

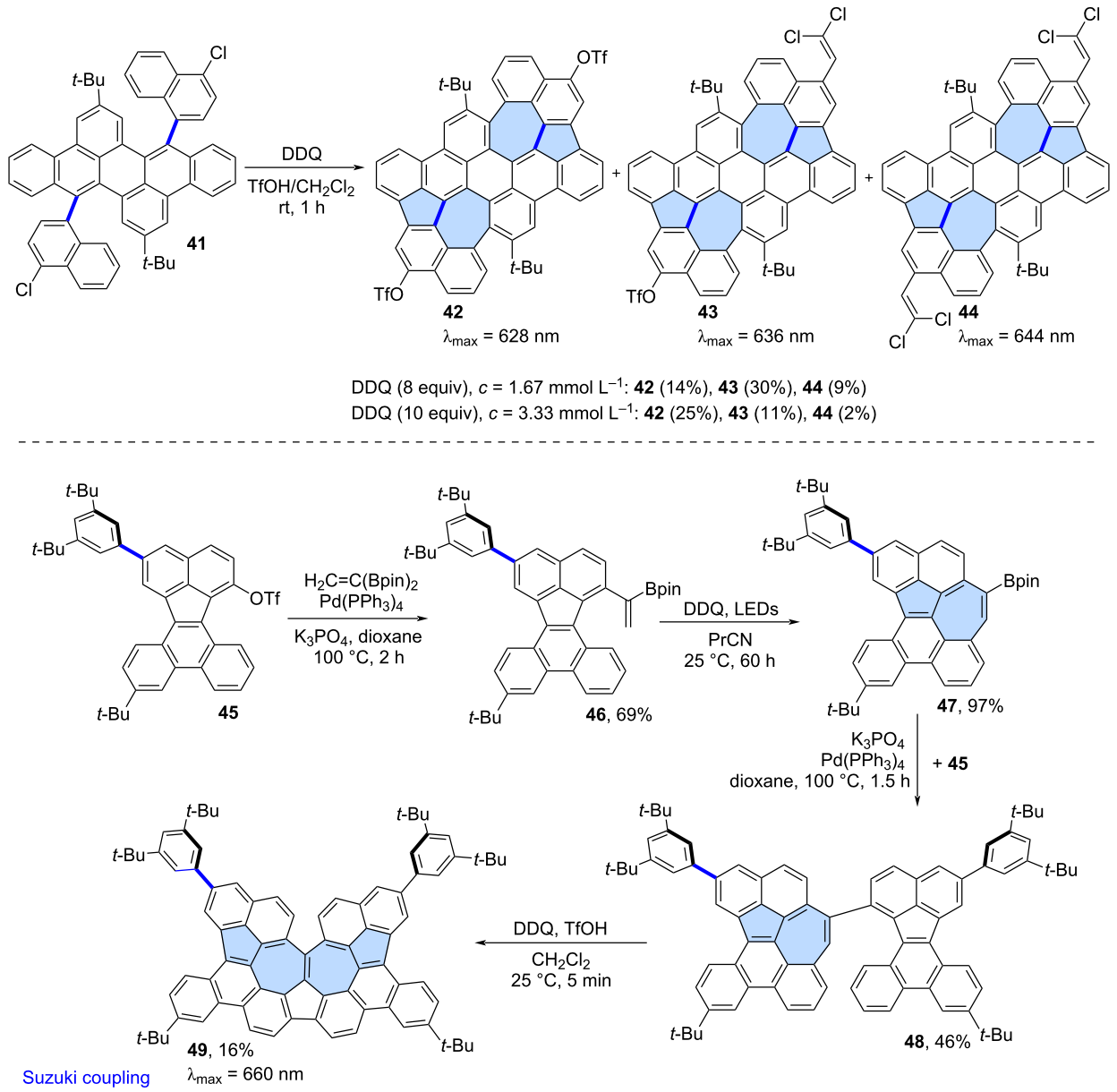

Scheme 7: Synthesis of warped PAHs with two embedded azulene subunits using Scholl oxidation.

pound **46** was first subjected to intramolecular oxidation using light-promoted DDQ and as the result the first azulene subunit was introduced giving PAH **47** in an exceptionally high yield (97%). A Suzuki cross-coupling reaction between **47** and **45** gave compound **48** which was subjected to a final Scholl oxidation using DDQ. The target compound **49**, containing two azulene subunits, was obtained in a relatively low yield (16%). Analysis of NICS values for **49** revealed similar characteristics to most azulene-embedded PAHs obtained via Scholl oxidation – specifically, the azulene subunit does not exhibit aromaticity, and the surrounding benzenoid rings predominantly determine the electronic structure of **49**.

[3 + 2] Annulation of alkynes accompanied by a phenyl ring expansion: The dimerization of alkynes, followed by the expansion of a phenyl ring leading to the formation of an azulene moiety, was first reported over half a century ago. These reactions can be carried out using various catalytic systems, including sulfenyl chloride/$AlCl_3$ [50], palladium catalysts [51] or gold catalysts [52]. With the appropriate choice of substrates, this approach can also be used for the synthesis of π-extended azulenes. For example, Tobe and co-workers conducted the intramolecular cyclization of 1,4,5,8-tetrakis(mesitylethynyl)naphthalene **50** using I_2 in CH_2Cl_2 (Scheme 8) [53]. In the reaction resulted in the mixture of isomeric π-extended azul-

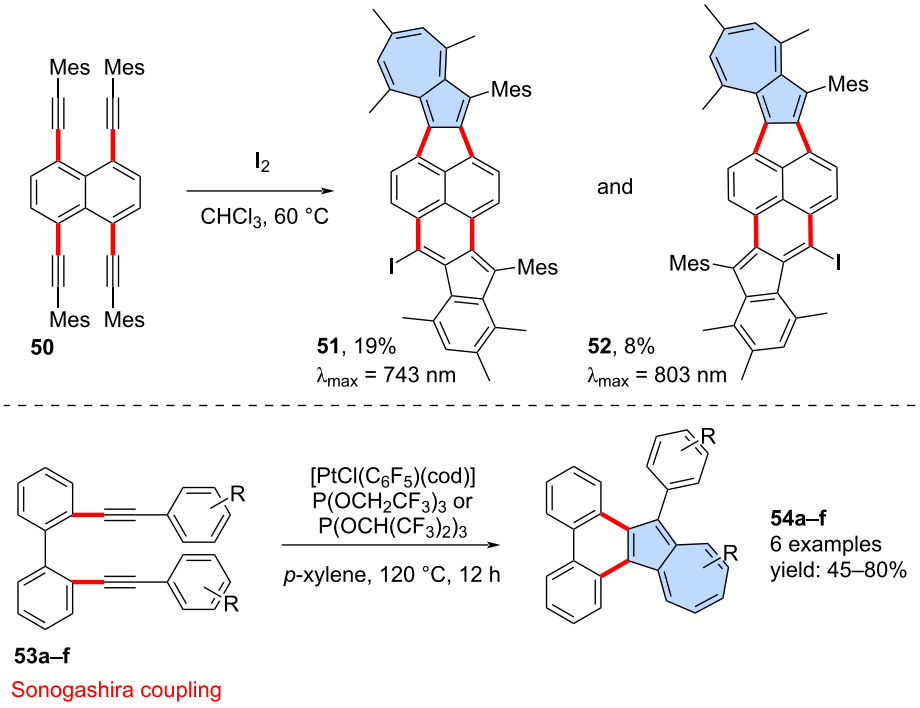

Scheme 8: Synthesis of azulene-embedded PAHs using [3 + 2] annulation accompanied by ring expansion.

enes **51** and **52** in rather moderate yields of 8% and 8%, respectively. Both PAHs **51** and **52** contain also embedded non-alternant indenophenalene subunits. Similarly, Murakami and co-workers reported intramolecular dimerization of alkynes followed by a phenyl ring expansion for 2,2'-di(arylethynyl)biphenyls **53a–f** [54]. The platinum-catalysed reaction led to a series of azulenophenanthrens **54a–f** in yields ranging from 40% to 80%.

A similar strategy was employed very recently in the synthesis of azulene-embedded isomers of linear acenes (Scheme 9) by Zhang and co-workers [55]. A palladium-catalysed variation of

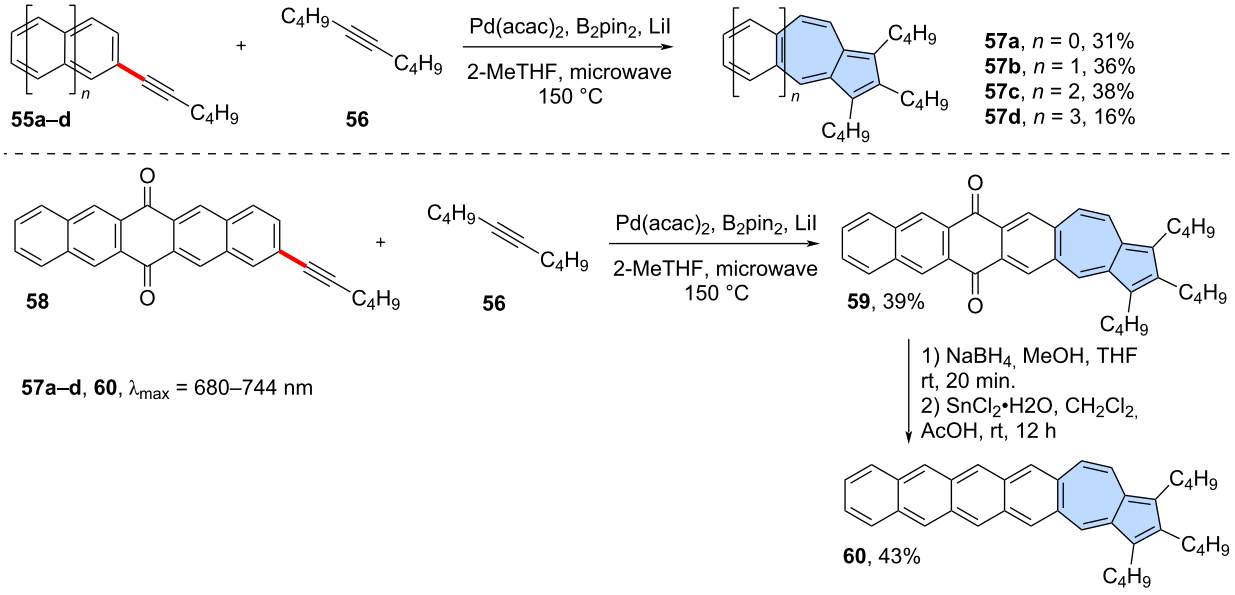

Scheme 9: Synthesis of azulene-embedded isomers of linear acenes using [3 + 2] annulation accompanied by ring expansion.

[3 + 2] annulation, accompanied by ring expansion [56], was used for the intermolecular reaction between acenes bearing alkyne substituents **55a**–**d** and di-*n*-butylacetylene (**56**). The reaction gave a series of azulene-embedded isomers of linear acenes from anthracene to pentacene (**57a**–**d**) in rather low yields (16–38%). The synthetic pathway leading to the hexacene isomer **60** was more complex due to the high reactivity of intermediate pentacenes. Instead, pentacene-6,13-dione **58** was subjected to the reaction with di-*n*-butylacetylene (**56**) giving azulene-embedded dione **59** in 39% yield. Finally, $NaBH_4$ reduction followed by $SnCl_2$/AcOH dehydration gave target non-alternant isomer of hexacene **60** in 43% yield. Interestingly, for the same number of rings, azulene-embedded acene isomers isomers exhibit greater stability than their fully benzenoid acene counterparts. Moreover, the azulene-like electronic structure is preserved, leading PAHs **57a**–**d** and **60** to display characteristic low-energy azulene absorption and *anti*-Kasha emission.

Intramolecular C–H arylation: Various C–H arylation strategies have proven to be effective as the final step in the synthesis of azulene-embedded PAHs. This approach requires a halogen-functionalized precursor and typically employs a palladium catalyst. Dou and co-workers reported a last-stage intramolecular C–H arylation of substituted indenofluorenes **61** and **62** (Scheme 10) [57]. The palladium-catalysed reaction yielded fused products containing either two (**63**) or four azulene subunits (**64**). Analysis of NICS values revealed that the formally antiaromatic character indeno[1,2-*b*]fluorene units remain dominant in fused PAHs **63** and **64** resulting also in a biradical character. Considering these factors, PAHs **63** and **64** should be

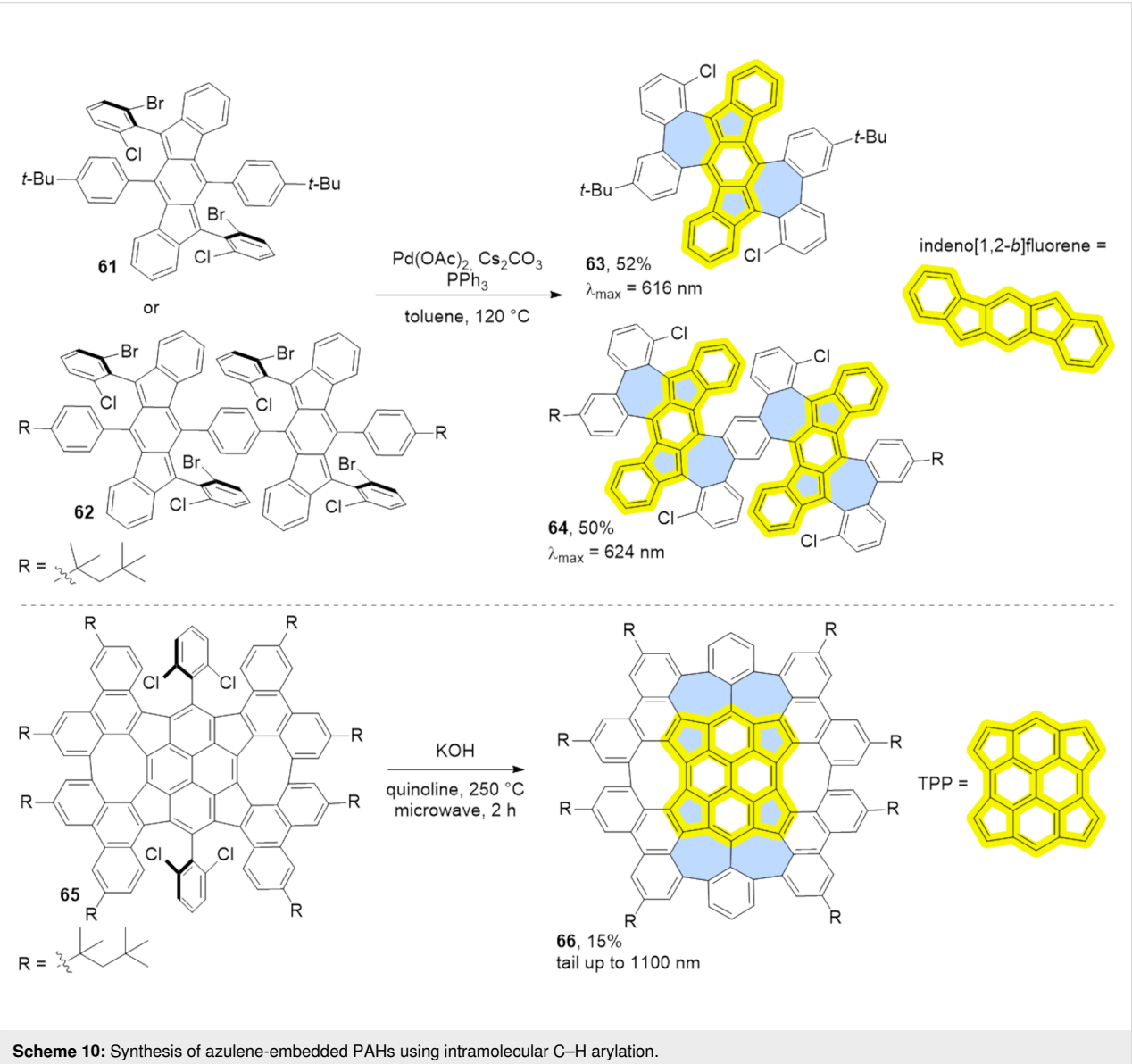

Scheme 10: Synthesis of azulene-embedded PAHs using intramolecular C–H arylation.

regarded as extended indenofluorenes that contain only "formal azulene" subunits rather than exhibiting true azulene-like electronic properties.

Zhang and co-workers reported the synthesis C_{84} molecular carbon **66**, which contains 10 non-benzenoid rings including four "formal azulene" units (Scheme 10) [58]. Interestingly, initial attempts to convert **65** into **66** using various procedures for the palladium-catalysed C–H activation were unsuccessful, even when conducted at elevated temperatures. However, treatment of **65** with KOH in refluxing quinoline successfully yielded the desired PAH **66**, albeit in a modest 15% yield. Despite the presence of four "formal azulene" units, the TPP (tetracyclopenta[*cd*,*fg*,*jk*,*mn*]pyrene) core of compound **66** exhibits antiaromatic properties. As a result, the pentagons within the structure remain antiaromatic, while the heptagons are non-aromatic, indicating the absence of an azulene-like electronic structure.

Liu and co-workers developed a modular approach to for synthesizing azulene-embedded isomers of linear acenes (Scheme 11) [59]. Precursors **67**–**70** were obtained from aldehydes and substituted cyclopentadienes using Knoevenagel-type condensation. Finally, intramolecular palladium-catalyzed C–H arylation afforded the fused azulene-embedded PAHs **71**–**74** in good yields (40–70%). All non-alternant isomers of linear acenes exhibit azulene-like lowest energy optical absorption, attributed to the azulene-like $S_0 \rightarrow S_1$ transition.

Condensation reactions: Various condensation reactions can also serve as valuable synthetic tools for constructing azulene subunits in the final step. For example, Ma and co-workers reported a modular synthetic strategy for the synthesis of diverse azulene-embedded PAHs via a tandem Suzuki coupling and base-promoted Knoevenagel-type condensation, achieving good yields and high structural versatility (Scheme 12) [60]. In this approach, precursors **75a**–**m** were first obtained using a Suzuki cross-coupling and subsequently subjected to the Knoevenagel-type condensation using *t*-BuOK. As a result, 13 PAHs **76a**–**m** containing an azulene subunit were synthesized in very good yields (82–96%). This strategy was later extended to larger molecules incorporating two azulene subunits. Precursors **77a**,**b**, **78a**,**b** and **79** underwent a similar intramolecular condensation, yielding PAHs with two azulene subunits (**80a**,**b**, **81a**, **81b** and **82**) in yields ranging from 33% to 63%. Analysis of NICS values for the resulting PAHs revealed that the azulene subunits did not exhibit typical azulene-like aromaticity. Notably, this represents one of the few modular approaches to azulene-embedded nanographenes that enables the synthesis of a larger family of molecules using a unified synthetic strategy.

The tandem Suzuki coupling/Knoevenagel condensation strategy leading to PAH **85** was independently reported by Liu [61] and Mastalerz (Scheme 12) [62]. The first group reported a cascade formal [3 + 4] annulation between triple boronic ester **83** and naphthalene **84** which combines a Suzuki cross-coupling and Knoevenagel-type condensation in a single synthetic

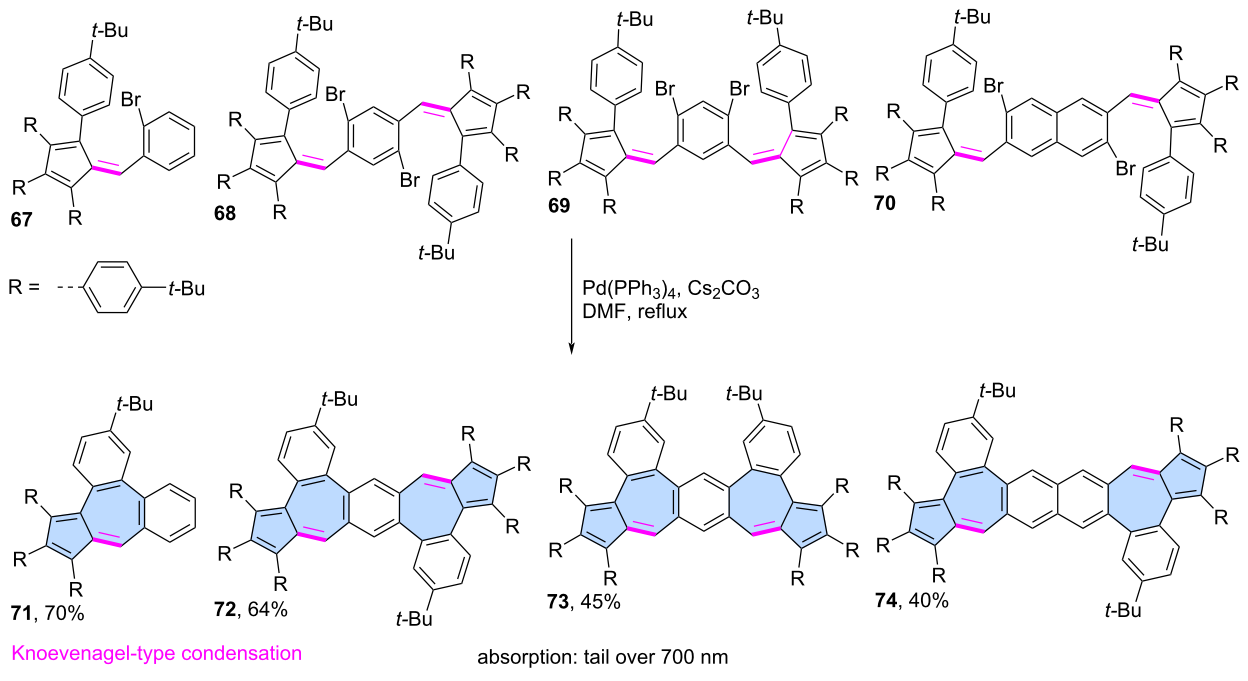

Scheme 11: Synthesis of azulene-embedded isomers of acenes using intramolecular C–H arylation.

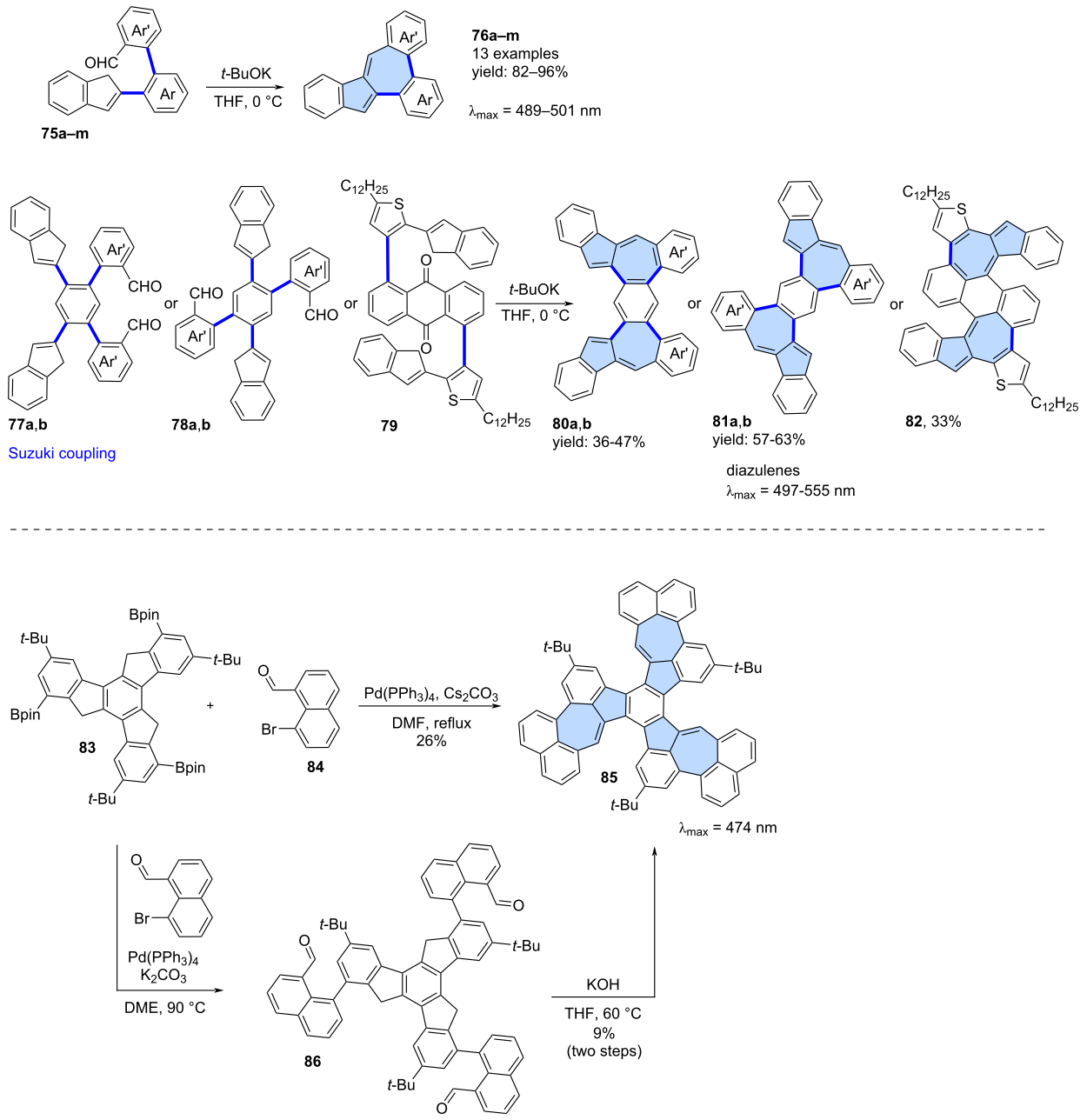

Scheme 12: Synthesis of azulene-embedded PAHs using intramolecular condensations.

step. This transformation was facilitated by Cs_2CO_3, which acted as a base for both the coupling and condensation reactions, ultimately yielding nanographene **85** in 26%. In contrast, Mastalerz and co-workers used a two-step strategy where the product of the Suzuki coupling **86** was first isolated. Compound **86** was then subjected to condensation with KOH in THF, affording **85** in an overall 9% yield over two steps. Additionally, the group reported an alternative synthetic route via trioxobenzotrisazulene, achieving a 25% total yield of **85** over three steps. It is worth noting that an alternative synthetic route via trioxobenzotrisazulene was also developed, achieving a 25% total yield of **85** over three steps [61,62].

Miscellaneous reactions: Less conventional reactions can also serve as valuable synthetic tools for constructing "formal azulene" subunits in the final step. Würthner and co-workers utilized a palladium-catalysed [5 + 2] annulation reaction which was developed in the group [63]. This strategy has been demonstrated previously as an efficient approach for constructing sp^2-hybridized heptagons. In their study, a two-fold palladium-cata-

lyzed [5 + 2] annulation was performed using 3,9-diboraperylene [64] **87** and 1,2-dibromoacenaphthylene **88**, yielding the azulene-embedded PAH **89** with an isolated yield of 15% (Scheme 13) [65]. While the azulene subunits in **89** were shown to be antiaromatic in the neutral PAH, oxidation to the dication induced an aromaticity switch, resulting in the pentagon–heptagon pair adopting an aromatic character. The group later extended this strategy to scaffold **91** decorated with two imide substituents, which was isolated in 4% yield [66].

Annulation of substituted azulenes

Scholl-type oxidation: The Scholl-type oxidation has also been employed also for azulene-embedded PAHs. where it was used to fuse substituents around the already existing azulene moiety in the direct precursor. However, such reactions often lead to suboptimal results in terms of yield and selectivity. Positions 1 and 3 of the azulene moiety are the most electron-rich, and pristine azulene is known to form 1,3-polyazulene upon oxidation [67], which may hinder the formation of the desired fused products. For instance, Itami and co-workers [68] reported that the oxidation of compound **92** resulted in the expected fully fused product **93**, but only in 8% yield after oxidation with $FeCl_3$, while the major product was 1,1′-biazulene **94**, obtained in 88% yield (Scheme 14). Compound **94** could further be oxidized using $FeCl_3$ to yield the partially fused chiral compound **95**. More recently, Morin and co-workers explored various strategies to achieve π-extended azulenes [69]. Amon other approaches, the group tested the Scholl-type oxidation of precursors **96** and **97**. However, the reaction yield was low for **96** when position 1 of azulene was involved in oxidation and fused azulene **98** was isolated only in 30% yield. The attempts to fuse position 5 in case of **97** resulted exclusively in oligomeric products and no **99** was observed.

One way to address the problem of the reactive positions (1 and 3) of the azulene unit is by blocking them in the precursor. Pigulski and co-workers explored Scholl-type oxidation of 1,2,3-triarylazulenes **100a**–**f** using $FeCl_3$ as the oxidant (Scheme 14) [70]. The use of K_2CO_3 as an additional base was necessary because residual moisture, in the presence of $FeCl_3$, led to the protonation of the starting azulenes. Interestingly, when azulenes were substituted exclusively with phenyl groups, no desired product was formed, instead surprisingly a 1,2-phenyl shift occurred, yielding azulen-1(8a*H*)-ones **101a**–**c**. However, when one or more of the substituents were replaced with a 2-pyrenyl group, partially fused (**102**, **103**) or fully fused (**104**, **105**) π-extended azulenes were obtained. This synthetic approach enabled the synthesis of a series of 'true' aromatic π-extended azulenes, which exhibited red-shifted azulene-like optical absorption, reaching into the NIR region.

The facile oxidation of positions 1 and 3 of the azulene moiety might be used as an advantage in the synthesis of azulene-embedded PAHs. The intramolecular oxidation of azulene units is particularly efficient when performed in an electron-deficient system, as demonstrated by Tani and co-workers [71] in their synthesis of azulene-fused tetracene diimide **107** from precursor **106** (Scheme 15). Oxidation with DDQ gave the target product in very high yield (95%). Interestingly, compound **107** contains four azulene subunits and exhibits strongly red-shifted

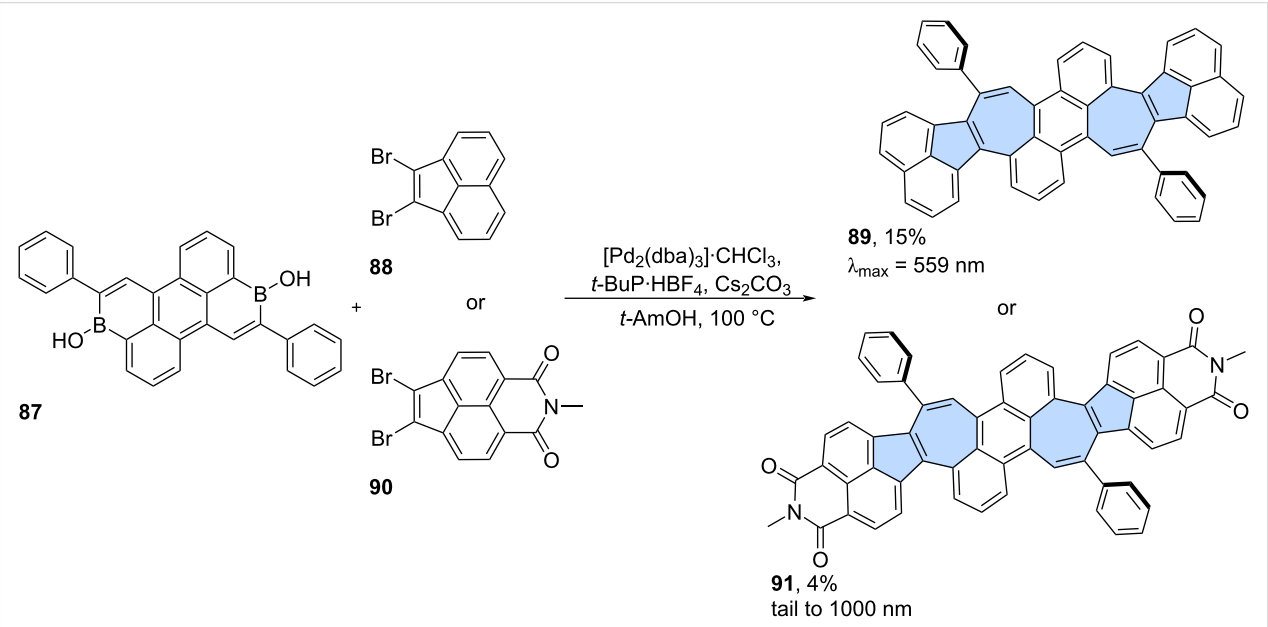

Scheme 13: Synthesis of azulene-embedded PAH **89** using palladium-catalysed [5 + 2] annulation.

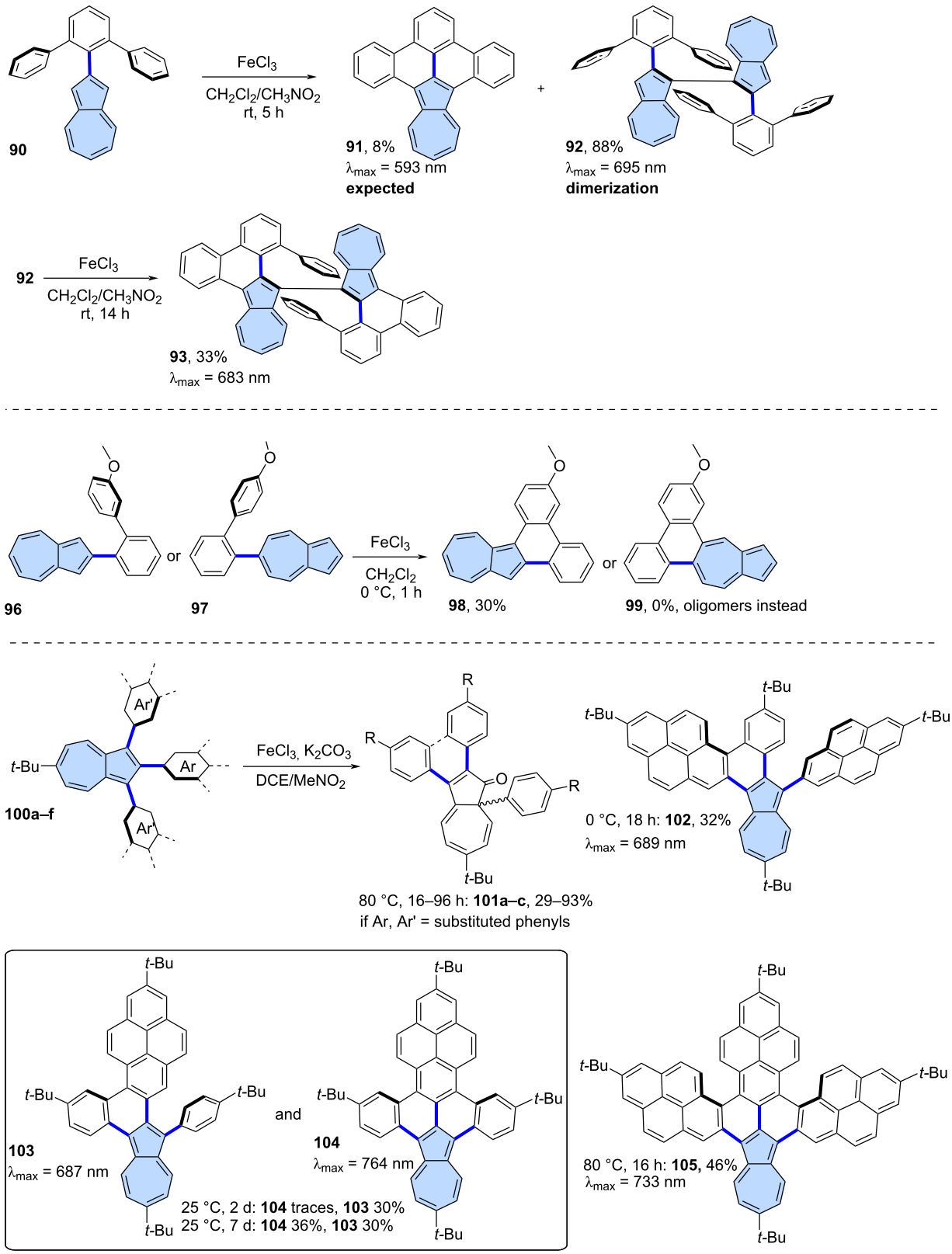

Scheme 14: Synthesis of azulene-embedded PAHs using oxidation of substituents around the azulene core.

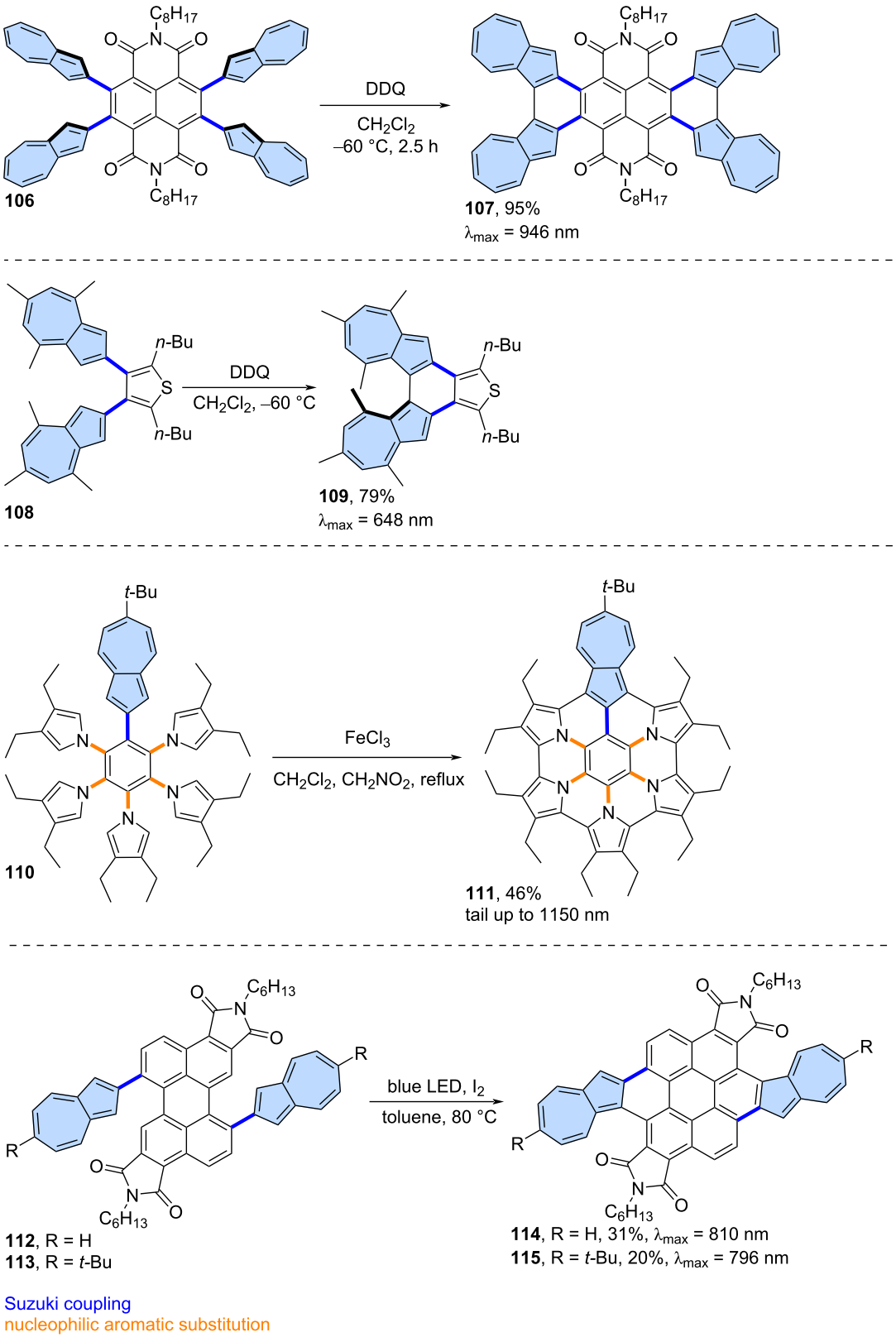

Scheme 15: Synthesis of azulene-embedded PAHs using the oxidation of reactive positions 1 and 3 of azulene subunits.

azulene like optical absorption, with a maximum at 946 nm. A similar approach was demonstrated by the same group in the synthesis of azulene-based helicene **109**, achieved by oxidizing precursor **108** using DDQ [72]. Notably, PAH **109** forms an air-stable radical cation after oxidation. A similar intramolecular oxidation of two adjacent azulene units was also reported with the use of $FeCl_3$ as an oxidant [73] or in one step during Suzuki coupling between 1,8-dibromonaphthalene and borylated azulene [74].

The ease of oxidation at positions 1 and 3 of azulene was utilized by Uno and co-workers in the synthesis of azulene-fused azacoronene **111** [75]. Oxidation of **110** using $FeCl_3$ gave the nanographene **111** in 46% yield. Compound **111** exhibits red-shifted azulene-like NIR absorption with tail up to 1150 nm in CS_2 and contains an aromatic azulene subunit. A similar oxidation can also be carried out under photochemical conditions, as demonstrated by Zhang and co-workers [76]. Precursors **112** and **113** were oxidized using I_2 under blue LED irradiation, yielding bisimides **114** and **115** in 31% and 20% yield, respectively. Both PAHs **114** and **115** exhibit NIR optical absorption, with azulene subunits that retain their aromatic properties.

Intramolecular C–H arylation: The intramolecular, palladium-catalysed C–H arylation can also serve as an effective tool for the fusion of azulene-embedded nanographenes. Liu and co-workers reported the synthesis of azulene-embedded nanographenes **117** and **118** using this method (Scheme 16) [77]. Precursor **116** was designed to undergo a four-fold intramolecular C–H arylation, but due to dehalogenation, only the

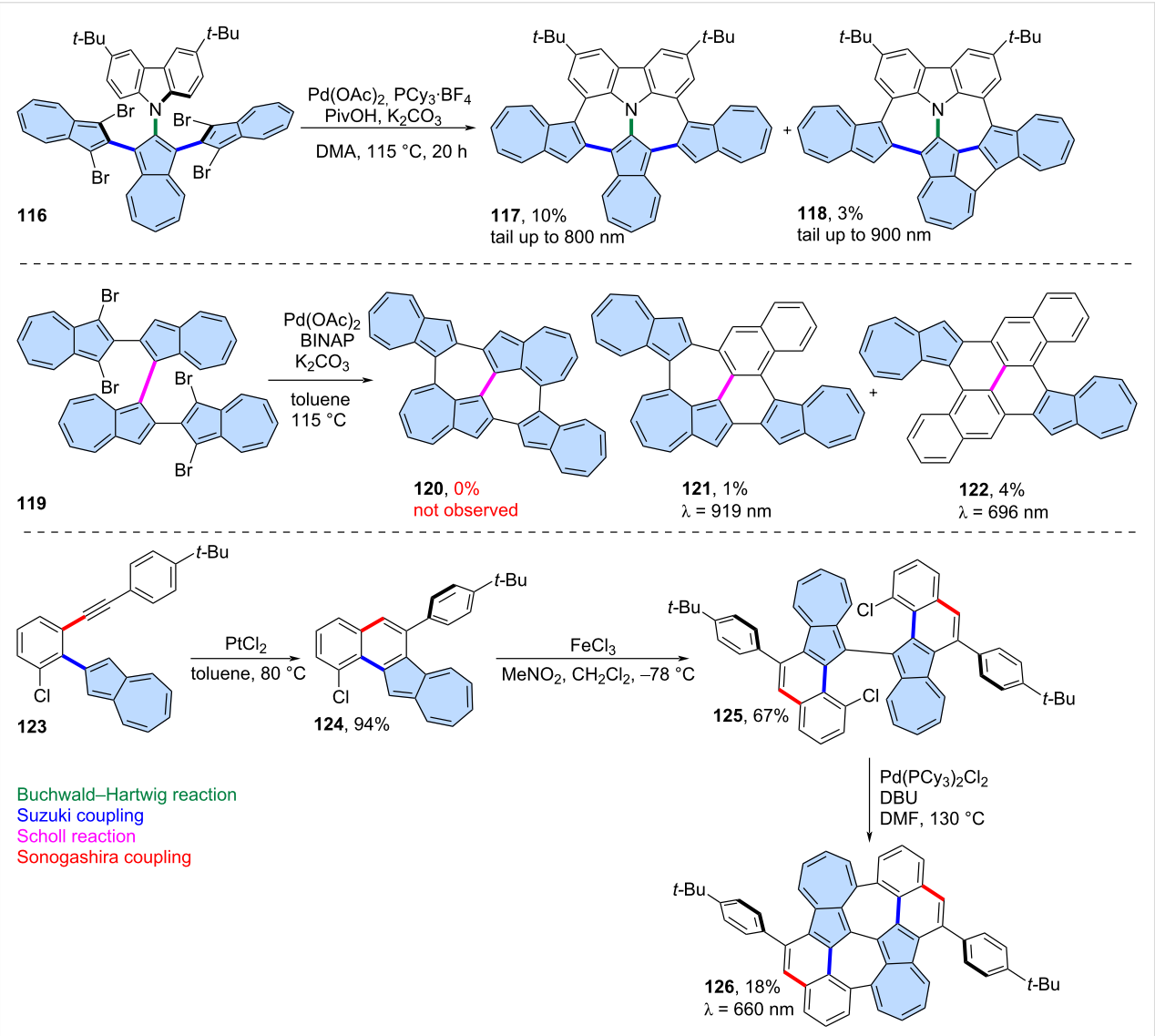

Scheme 16: Synthesis of azulene-embedded PAHs using intramolecular C–H arylation.

products of double (**117**) and triple C–H arylation were isolated in 10% and 3% yields, respectively. The optical absorption of **117** and **118** reaches the desired NIR region, owing to the retention of the azulene-like electronic structure within the azulene subunits. The same group applied this strategy to precursor **119**, however, the target PAH **120** was not observed after the reaction (Scheme 16) [78]. Instead, products of a skeletal arrangement of one azulene moiety **121** and two azulene moieties **122** were isolated in low yields (1% and 4%, respectively). Plausible mechanisms of such a cyclopenta[*ef*]heptalene to phenanthrene rearrangement were proposed by the authors and involve the arenium ion pathway or Pd catalyst pathway. Both **121** and **122** exhibit typical azulene-like red-shifted absorption due to almost forbidden $S_0 \rightarrow S_1$ transition.

Liu and co-workers reported also an isomer of bischrysene containing two azulene subunits (Scheme 16) [79]. Precursor **125** was obtained through $PtCl_2$-catalysed intramolecular annulation of alkyne **123**, followed by a Scholl-type oxidation of **124**. Finally, double intramolecular C–H arylation catalysed by $Pd(PCy_3)_2Cl_2$ gave non-alternant PAH **126** in an 18% yield. Interestingly, according to the calculated NICS values, all heptagons of **126** lost their aromatic character. Later, it was reported that PAH **126** exhibits *anti*-Kasha fluorescence [80] from the S_3 state in the range of 410–470 nm upon excitation at 370 nm. This was well verified by femtosecond time-resolved absorption spectroscopy (fs-TAS), with corresponding high-energy excited state absorption bands observed at 660 nm.

Würthner and co-workers developed a cascade [3 + 3] annulation strategy, where Suzuki cross-coupling is followed by C–H arylation, and applied it to various electron-deficient nanographenes [81-84]. This strategy can also be applied to non-alternant PAHs. For example, azulene **127** reacts effectively with imide to yield the non-alternant PAH **129** in 47% yield (Scheme 17) [85]. The resulting non-alternant isomer of perylenebisimide **129** exhibits strongly red-shifted absorption (λ_{max} = 1041 nm) and an azulene-like electronic structure. The optical absorption of PAH **129** is strongly bathochromically shifted compared to isomeric terrylenebisimide (λ_{max} = 650 nm) [86] and even larger rylene bisimides like hexarylenebisimide (λ_{max} = 953 nm) [87]. Bisimide **129** might be regioselectivily brominated using NBS, yielding PAH **130** in 80%. The bromide **130** undergoes nucleophilic substitution with methoxide or morpholine, giving the corresponding substitution products **131** and **132** in 60% and 74%, respectively. Very recently, during revision of this work, Aratani and co-workers reported the use of this strategy in the synthesis of two azulene-embedded isomers of perylene monoimide [88].

Cyclization of alkenes: A bismuth-catalysed cyclization of alkenes has been demonstrated as an efficient synthetic tool for the creation of benzenoid PAHs [89]. Murai and co-workers applied this approach to the synthesis of azulene-embedded nanographenes (Scheme 18) [90]. Vinyl ethers **133a–d** were cyclized using $Bi(OTf)_3$ in 1,2-dichloroethane giving PAHs **134–137** in high yields (71–85%). All the new PAHs exhibit

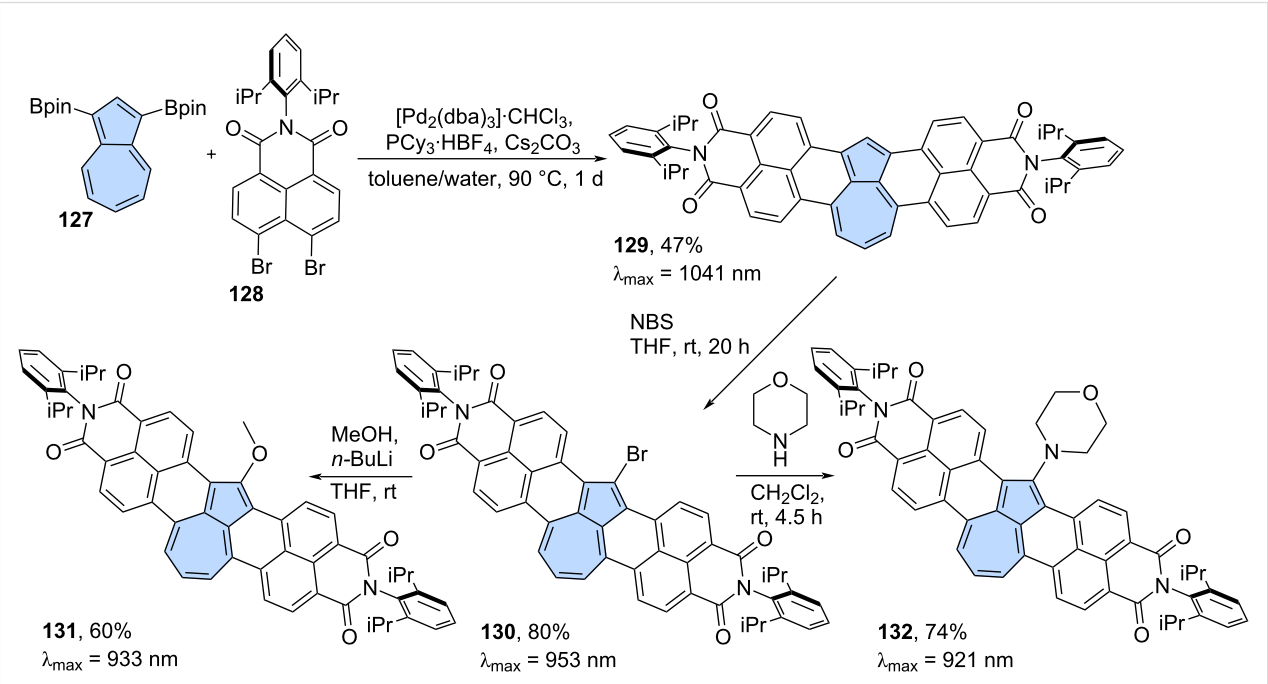

Scheme 17: Synthesis of an azulene-embedded isomer of terylenebisimide using tandem Suzuki coupling and C–H arylation.

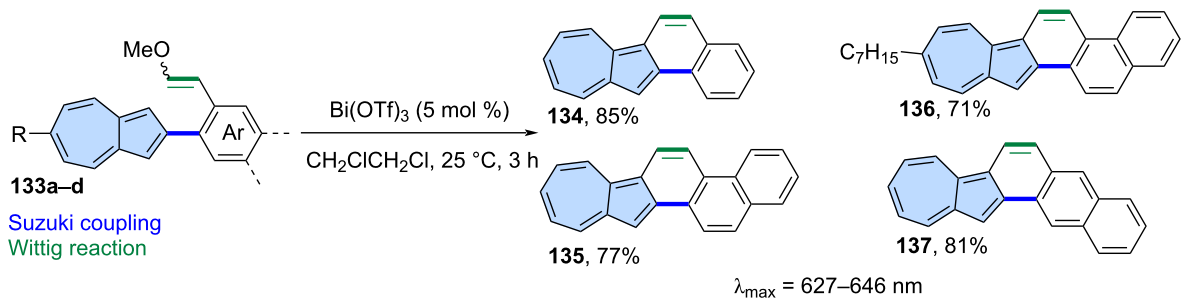

Scheme 18: Synthesis of azulene embedded PAHs using a bismuth-catalyzed cyclization of alkenes.

characteristics typical for "true" π-extended azulenes, such as azulene-like optical absorption and narrow HOMO–LUMO gaps. In addition, compounds **134**–**137** show reversible stimuli-responsiveness against the acid–base reaction.

Cyclization of alkynes: The extension of π-conjugation in polycyclic aromatic hydrocarbons (PAHs) through alkyne-benzannulation reactions has become an increasingly popular method in recent years [91]. Such benzannulations can be mediated by Brønsted acids, Lewis acids or transition metals, and have been applied to a wide range of PAHs [92] and graphene nanoribbons [93]. More recently, this synthetic strategy has been independently employed by several research groups for the synthesis of non-alternant azulene-embedded PAHs. Typically, modular synthesis of direct precursors can be achieved using Suzuki and Sonogashira cross-coupling reactions.

One of the first examples was the synthesis of diazuleno[1,2,3-*cd*:10,20,30-*fg*]pyrene, which was later subjected to on-surface transformations [94]. More recently, a more general approach was reported by Langer and co-workers, who described the simple single benzannulation of a series of precursors **138a**–**k** (Scheme 19) [95]. The reaction was mediated by MsOH and carried out in hexafluoroisopropanol (HFIP), yielding the final products (**139a**–**k**) in 53–93% yield. In general, the absorption spectra of the products show a typical "azulene-like" fine-structured low-energy absorption profile. Similarly, Morin and co-workers reported a similar approach to synthesize PAHs with two embedded azulene subunits (Scheme 19) [69]. Three precursors **140a**–**c** were annulated using $InCl_3/AgNTf_2$ or $PtCl_2$ yielding azulene-embedded nanographenes **141**–**143**.

A similar approach was employed by Xin and co-workers in the synthesis of isomeric π-scaffolds (Scheme 19) [96]. Precursors **144a**–**c** were annulated using $PtCl_2$, yielding target PAHs **145**–**147** in yields ranging from 26% to 46%. Compounds **141**–**143** and **145**–**147** can undergo a two-fold protonation process, resulting in the formation of two tropylium fragments within a single molecule. Additionally, they exhibit typical azulene-like optical absorption and the aromatic properties characteristic of azulene subunits.

Liu and co-workers extended this chemistry to substituted naphthalene derivatives which led to chrysene fused with two azulene moieties (Scheme 19) [97]. Precursors **148** and **149** were annulated using DBU (1,8-diazabicyclo(5.4.0)undec-7-ene) in NMP (*N*-methyl-2-pyrrolidone) at 180 °C. The resulting PAHs **150** and **151** were isolated in relatively good yields (40% and 48%, respectively) and exhibited typical azulene-like optical absorption. The UV–vis absorption spectra, fluorescence properties and ^{1}H NMR spectroscopy, indicate that **150** and **151** can be protonated to form the corresponding tropylium cation and consecutive dication under acidic conditions, with reversible protonation−deprotonation capabilities. Additionally, new OFET-based acid vapor sensors were developed from **150** by synergistically utilizing its charge transport and protonation−deprotonation properties.

The solution-phase synthesis of a non-benzenoid nanoribbon from an azulene-containing polymer via alkyne benzannulation was reported by Morin and co-workers (Scheme 20) [98]. The starting polymer **152** was synthesized using Suzuki cross coupling and is regiorandom, meaning the orientation of the azulene units within the main chain is not defined. Polymer **152** was annulated using MsOH (methanesulfonic acid) yielding the non-alternant graphene nanoribbon **153**. The nanoribbon is soluble in common organic solvents and exhibits conductivity values up to $1.5{\cdot}10^{-3}$ S·cm^{-1} when doped by TFA in the thin film state.

The serendipitous synthesis of azulene-embedded [5]helicenes was reported by Usui, Suemune, and co-workers [99]. The unexpected formation of an azulene skeleton from a benzenoid alkyne derivative occurred when a catalytic amount of $PtCl_2$ was used. A more systematic approach to [5]-, [6]-, and [7]helicenes with embedded azulene units was reported recently

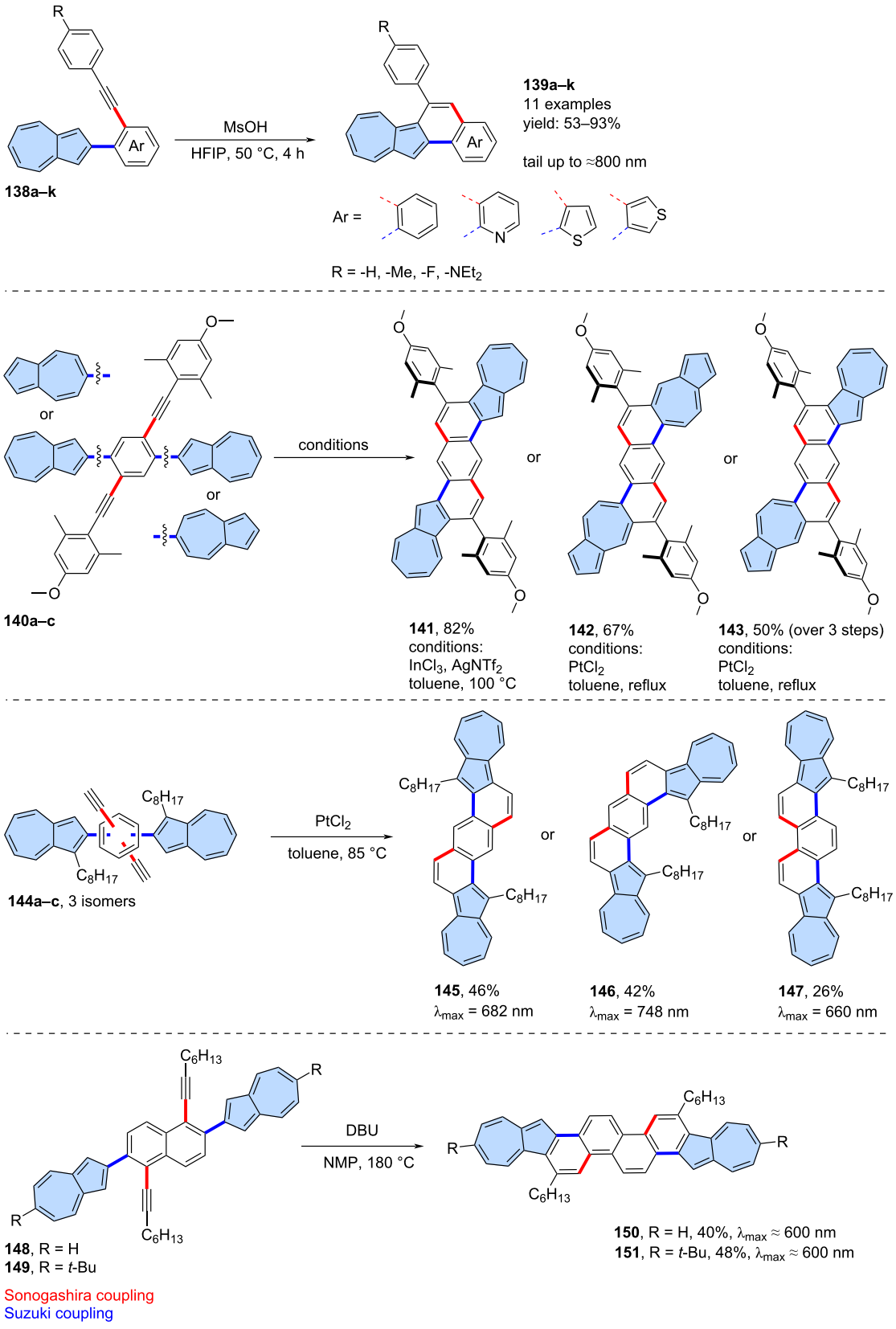

Scheme 19: Synthesis of azulene-embedded nanographenes using intramolecular cyclization of alkynes.

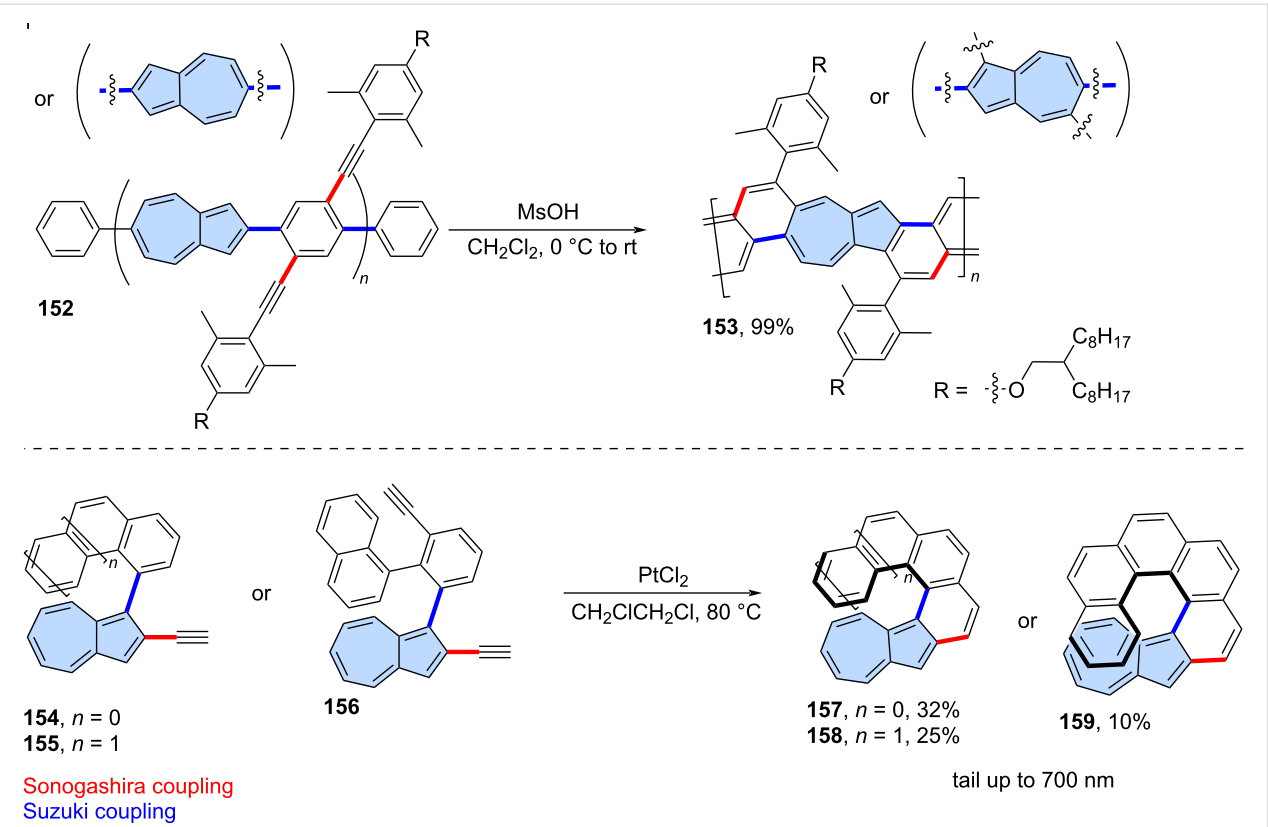

Scheme 20: Synthesis of azulene-embedded graphene nanoribbons and azulene-embedded helicenes using annulation of alkynes.

by Gao, Yang, and co-workers (Scheme 20) [100]. Alkyne precursors **154**–**156** were annulated using $PtCl_2$, yielding a series of [*n*]helicenes (*n* = 5–7) with embedded azulene units (**157**–**159**), which were isolated in relatively low yields (10–32%). The incorporation of the azulene subunit into helicenes causes significant perturbation in the molecular electronic structure, resulting in the dark cyan or green colours of **157**–**159** and azulene-like weak absorption due to $S_0 \rightarrow S_1$ transition. Strong chiroptical responses were revealed by ECD spectra, with the maximum $|g_{abs}|$ values reaching 0.022 (at 421 nm) and 0.021 (at 427 nm) for **158**, and **159**, respectively. These values are among the highest $|g_{abs}|$ values of helicenes in the visible range.

Miscellaneous reactions: The scope of reactions that can be used as the final fusion step when azulene-containing precursors are employed is not limited to those described above. A synthetic strategy involving condensation followed by the reaction of the resulting 1,4-dienone with metal acetylides and dehydration is a commonly used tool for the synthesis of (hetero)acenes [101]. Jiang and co-workers applied this approach to azulene-embedded isomers of pentacene, hexacene and heptacene (Scheme 21) [102]. First, the carbon scaffolds of the target acenes were constructed by condensation of dialdehyde **160** with compounds **161**–**163** yielding diketones **164**–**166**. Next, diketones **164**–**166** were subjected to nucleophilic addition reaction by lithiated triisopropylsilyl (TIPS) acetylene, followed by $SnCl_2$-mediated reduction of the intermediate diols. Finally, azulene-embedded isomers of pentacene (**167**), hexacene (**168**) and heptacene (**169**) were isolated in very good yields. Compounds **167**–**169** exhibit excellent photostability under ambient air and light conditions, as compared to their isoelectronic acene counterparts, and red-shifted azulene like optical absorption with tail up to 900 nm.

The Yamamoto homocoupling reaction catalysed by low-valent nickel compounds [103] may be used instead of Scholl-type oxidation in the synthesis of azulene-embedded PAHs. Yamada and co-workers very recently reported the synthesis of azulene dimer **172** (Scheme 22) [104]. Initially, the authors attempted to directly oxidize **170** to **172** using Scholl reaction. However, compound **172** was isolated in only 1% yield. As an alternative, they brominated **170** to form **171**, followed by Yamamoto-type coupling using $Ni(COD)_2$ and 2,2'bipirydyl (COD = 1,5-cyclooctadiene), which produced **172** in high yield (89%). Interestingly, the fusion of two azulene units at *peri*-position induces the significant orbital interaction, resulting in a very narrow HOMO–LUMO gap in **172**. Consequently, **172** exhibits

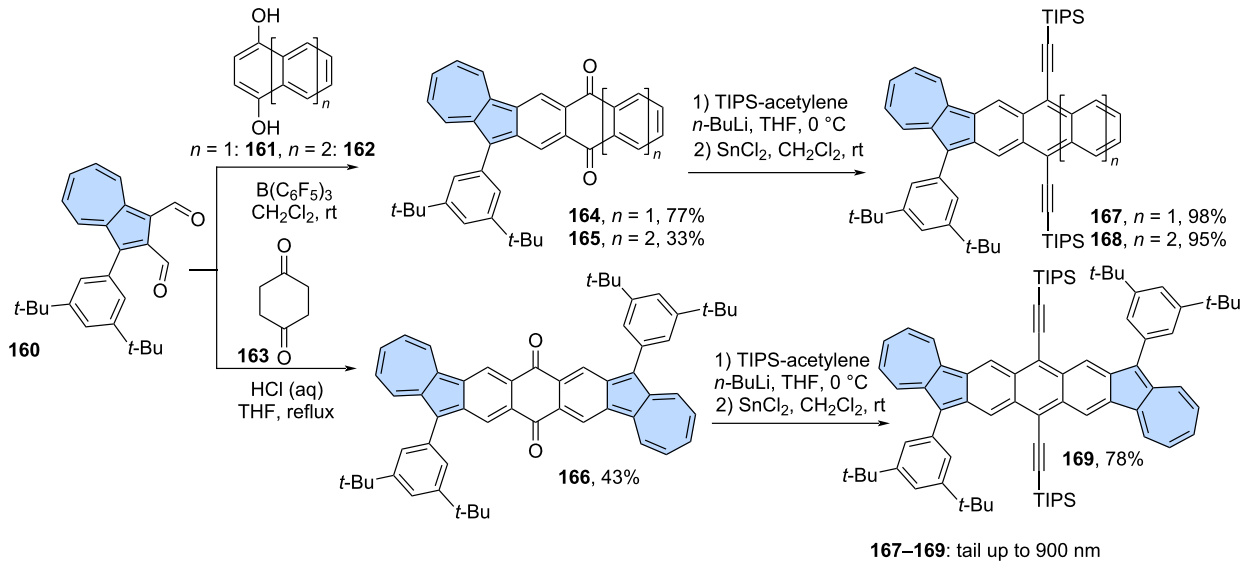

Scheme 21: Synthesis of azulene-fused acenes.

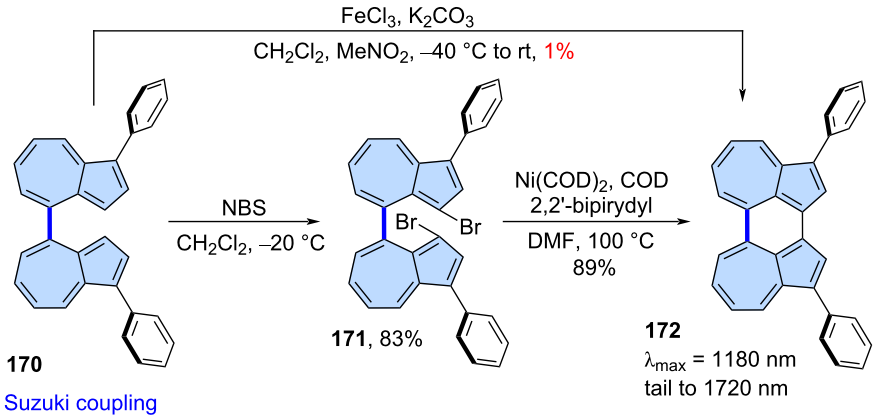

Scheme 22: Synthesis of non-alternant isomer of perylene **172** using Yamamoto-type homocoupling.

NIR absorption properties (λ_{max} = 1180 nm, tail to 1720 nm) and reversible redox behaviours (electrochemical gap 1.07 eV) which is impressive for such small π-scaffold.

Formation of carbon–heteroatom bonds: Although the primary focus of this review is the synthesis of all-carbon azulene-embedded nanographenes, some carbon–heteroatom fusion reactions are also worth mentioning. In general, azulene-fused heteroaromatics are rare due to the limited synthetic methods available, although some N- or BN-nanographenes are known.

An efficient synthesis of azulene−pyridine-fused heteroaromatics was reported by Swager and co-workers (Scheme 23) [105]. A series of monoazulene PAHs **174a–e** was obtained from 1-nitroazulene precursors **173a–e** using triphenylphosphine, instead of the expected Cadogan reaction products. This synthetic approach also works for precursors containing two azulene subunits, ultimately yielding PAH **176** in 34% yield. The results showed that these hetero-aromatics display strong aromaticity with rigid planar π-structures and exhibit weak azulene-like $S_0 \rightarrow S_1$ transition absorptions in the visible regions. Single-crystal ribbons of **176** exhibit p-type semiconducting behaviour with hole mobilities of up to 0.29 $m^2 V^{-1}s^{-1}$. Typical Cadogan products can be obtained when the NO_2 group is localized in the benzenoid part of the precursor (Scheme 23) [106]. As a result, the reaction of precursor **177** with $P(OEt)_3$ gave fused π-scaffold **178** in 40% yield. Compound **178** features a

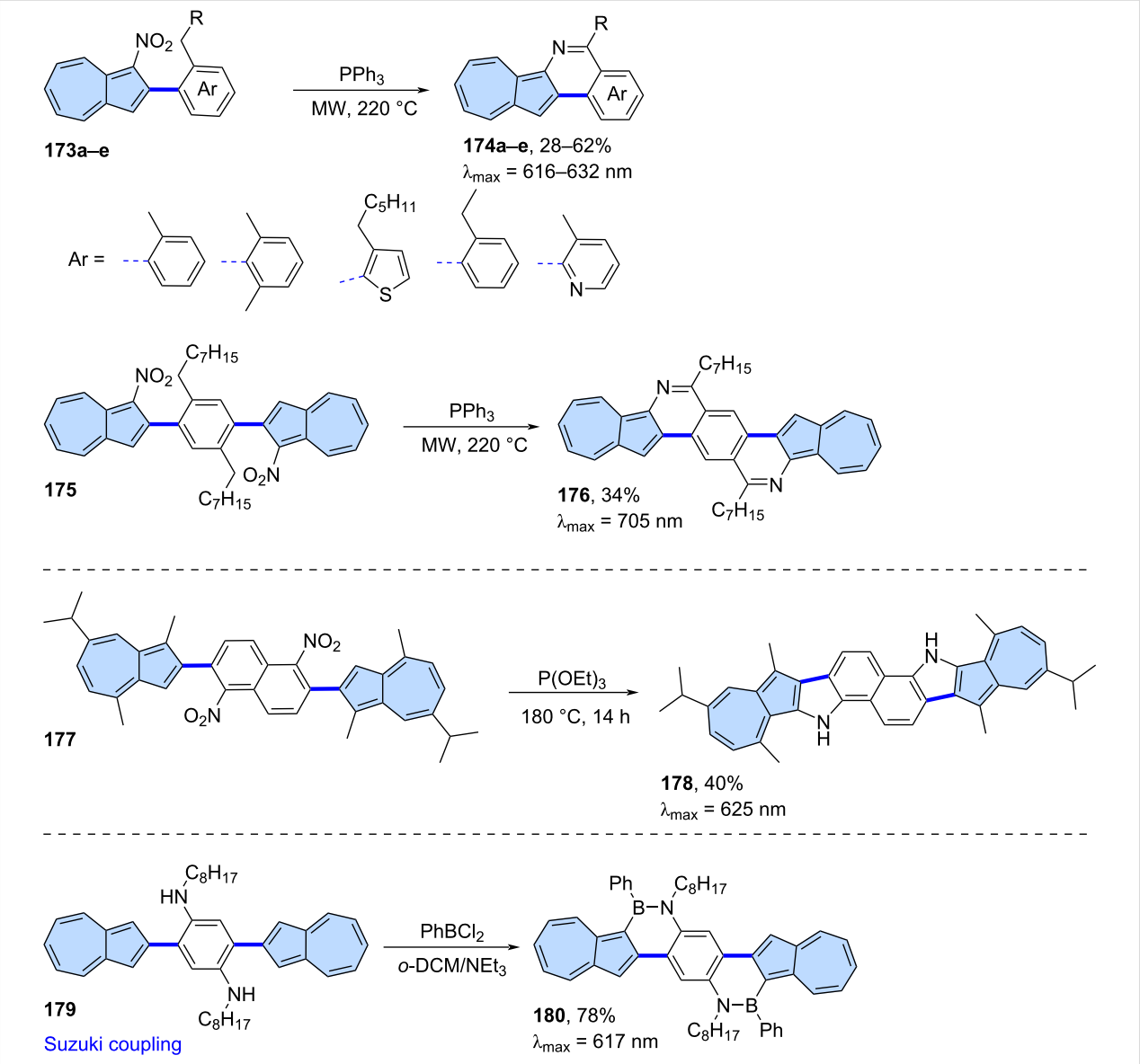

Scheme 23: Synthesis of N- and BN-nanographenes with embedded azulene unit(s).

highly planar geometry, narrow optical band gaps, *anti*-Kasha fluorescence, and reversible stimuli-responsiveness to acid and base. Gao and co-workers demonstrated that also BN heterocycles can be obtained using similar types of precursors (Scheme 23) [107]. Compound **179** was reacted with $PhBCl_2$ to yield BN heterocycle **180** in 78% yield. Compound **180** exhibits high sensitivity for the visual detection of fluoride ions and undergoes an unexpected deboronization reaction upon the addition of TFA.

On-surface synthesis

Recently, the field of on-surface chemistry has made significant progress, with the successful development of complex metal-catalyzed on-surface reactions that are not accessible through classical solution-based organic chemistry [108,109]. Ultra-high vacuum (UHV) conditions on metallic surface allow to observe chemical species which are very reactive and impossible to isolate using classical chemical synthesis. Therefore, it is not surprising that such synthetic techniques have been applied to the synthesis of azulene-embedded nanographenes. One of the main challenges in this area is that the outcome of reactions is often difficult to predict, and various skeletal rearrangements can occur under typical on-surface reaction conditions.

The synthesis of most of the reported azulene-embedded PAHs involves the generation of azulene moieties on-surface. This means that the precursors obtained through traditional solution

chemistry are typically benzenoid hydrocarbons. These precursors are usually dehydrogenated on the surface, leading to the formation of formal azulene subunits. A good example of this strategy is the reaction reported by Feng and co-workers (Scheme 24) [110]. Precursor **181** was annealed on an Au(111) surface at 300 °C, resulting in PAH **182** with two embedded azulene subunits. Spin-polarized density functional theory calculations predicted that PAH **182** would exhibit an open-shell singlet ground state, as it contains five Clar sextets, compared to only two in the closed-shell structure. The same group later proposed an extension of this strategy [111]. Precursor **183**, which contains subunit **181**, was first annealed at 300 °C giving two rotamers **184** and **185** which are products of an Ullmann-type dimerization (Scheme 24). Further heating on the Au(111) surface led to products with partial skeletal rearrangement, driven by intramolecular structural strain. Both nanographenes, **186** and **187**, contain six formal azulene subunits and exhibit nearly planar geometry. However, theoretical analysis of NICS values revealed that none of the azulene subunits exhibits the characteristic azulene-like aromaticity. Additionally, both **186** and **187** show moderate open-shell biradical character, according to theoretical calculations.

A similar strategy, leading to different types of skeletal rearrangements, was reported by Ma and co-workers (Scheme 24) [112]. The reaction of precursor **188** at 290 °C on Au(111) surface produced a series of isomeric products **189**–**194**, which contains azulene and/or Stone–Wales type of defects. The main product, nanographene **189**, is formed via oxidative ring-closure of the four methyl substituents of precursor **188** after annealing. In contrast, all the other observed PAHs **189**–**194** result from oxidative ring-closure and skeletal ring-rearrangement reactions. Theoretical calculations revealed that nanographene **188** possesses an antiferromagnetic open-shell singlet ground state, whereas the other products do not.

Peña and co-workers reported a two-step on-surface synthesis of impressive propeller-shaped nanographenes **196** and **197** (Scheme 25) [113]. First, benzenoid precursor **195** underwent Ullmann-type cyclotrimerization on an Au(111) surface at 200 °C, resulting in compound **196**. PAH **196** was then further heated to 375 °C, which triggered dehydrogenation and the formation of two isomeric compounds **197** and **198**. Both **197** and **198** possess six azulene subunits and an [18]annulene core. The creation of azulene moieties follows a novel cyclodehydrogenation pattern in conjoined cove regions, leading to the formation of two new C–C bonds and the relaxation of the twisted regions into a flat-lying molecule on the surface.

Ruffieux and co-workers recently reported a synthetic approach toward tetrabenzo-fused circumazulene starting from precursor **199** (Scheme 25) [114]. However, the desired circumazulene was not detected, and instead, products of some additional annulations were observed (**200**–**202**). The more planar structure of nanographenes **200**–**202** likely drives the process toward more annulated configurations. Theoretical calculations of the studied azulene-embedded PAHs indicated a strong antiaromatic character of the inner nonbenzenoid rings, particularly heptagonal rings, in contrast to pristine azulene.

Dihalogenated precursors offer the potential to obtain polymeric structures through on-surface chemistry. A notable example was reported by Ebeling and co-workers (Scheme 26) [23]. First, simple 2,6-dibromoazulene (**203**) was annealed on an Au(111) surface, leading to the formation of 2,6-polyazulene chains **204**. Upon heating these chains to 730 K, laterally fused chains were observed. The distinctive phagraphene nanoribbon **205** and the THP-graphene nanoribbon **206** were formed. This transformation provides solid evidence that large fragments of non-alternant analogues of graphene can be synthesized from simple precursors. Similarly, Müllen and co-workers applied an analogous strategy for 3,3'-dibromo-1,1'-biazulene **207** (Scheme 26) [115]. First, biazulene **207** was polymerized to yield oligoazulene **208**. However, further annealing at 250 °C did not result in the expected products of simple fusion, but rather a mixture of various non-benzenoid PAHs due to skeletal rearrangements. Initially, polymeric structures where fused fragments were linked by single C–C bonds were observed (**209**). Additionally, fully fused PAH **210** was identified using STM. Theoretical calculations revealed that the hexagons and most of the heptagons in **210** are nonaromatic, while the pentagons, especially those in the aceheptalene subunit, are highly aromatic.

Optical and electronic properties

Analyzing the optical and electronic properties of the diverse range of azulene-embedded nanographenes discussed in this review presents a significant challenge, as many of the original studies lack comprehensive data. In numerous cases, fluorescence characteristics were not thoroughly examined, and time-dependent density functional theory (TD-DFT) calculations – essential for accurately identifying the $S_0 \rightarrow S_1$ electronic transitions – were not reported. Nevertheless, certain general structure–property relationships can still be proposed for these systems. Representative examples of polycyclic aromatic hydrocarbons (PAHs) featured in this review are summarized in Table 1, which provides key data on their lowest-energy electronic transitions ($S_0 \rightarrow S_1$), fluorescence behavior, and first reduction/oxidation potentials. Several structural factors are particularly influential in determining properties such as near-infrared (NIR) absorption and narrow electrochemical gaps. These include: (1) the presence or absence of an

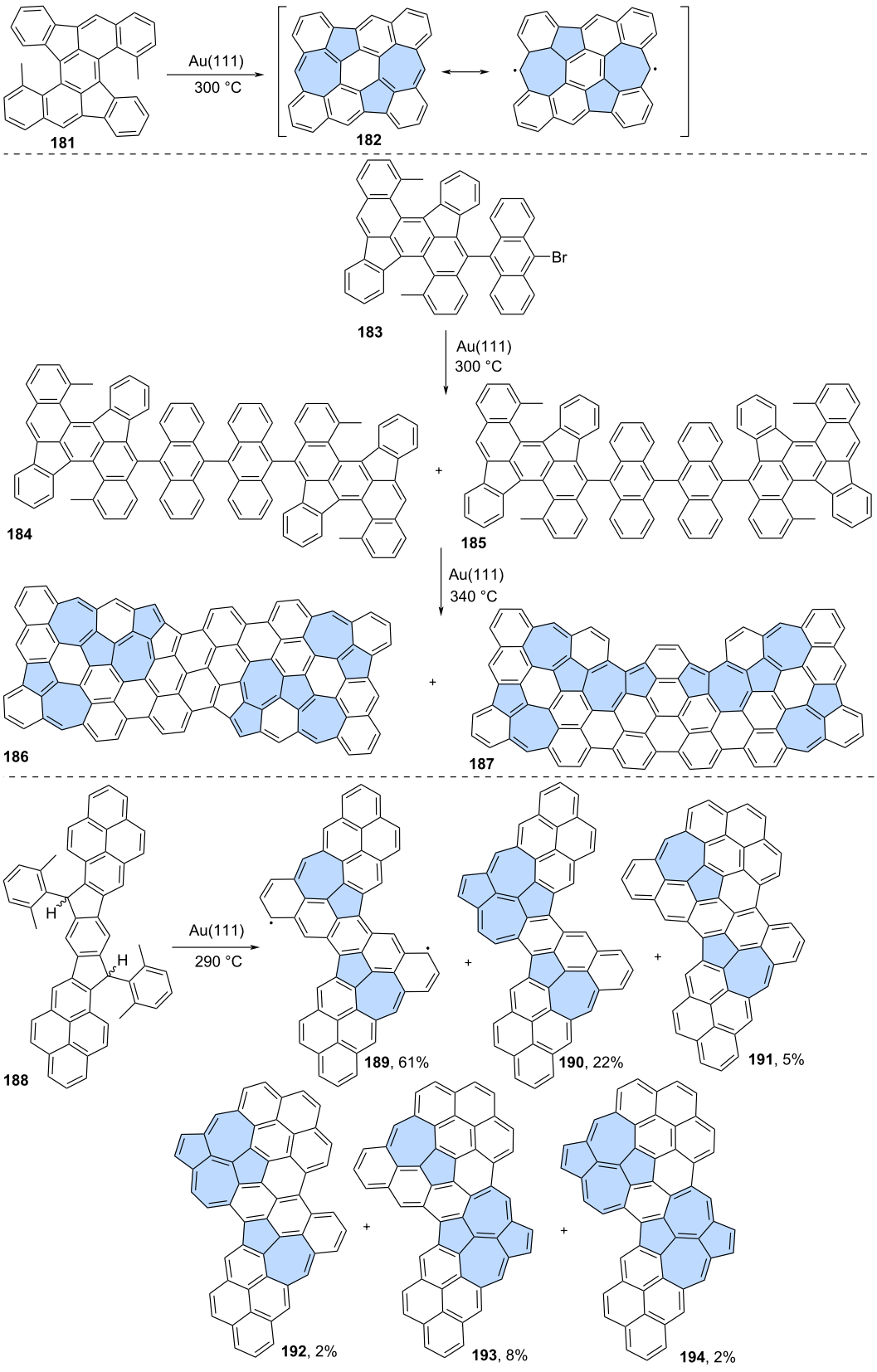

Scheme 24: On-surface synthesis of azulene-embedded nanographenes from benzenoid precursors via dehydrogenation of methyl groups.

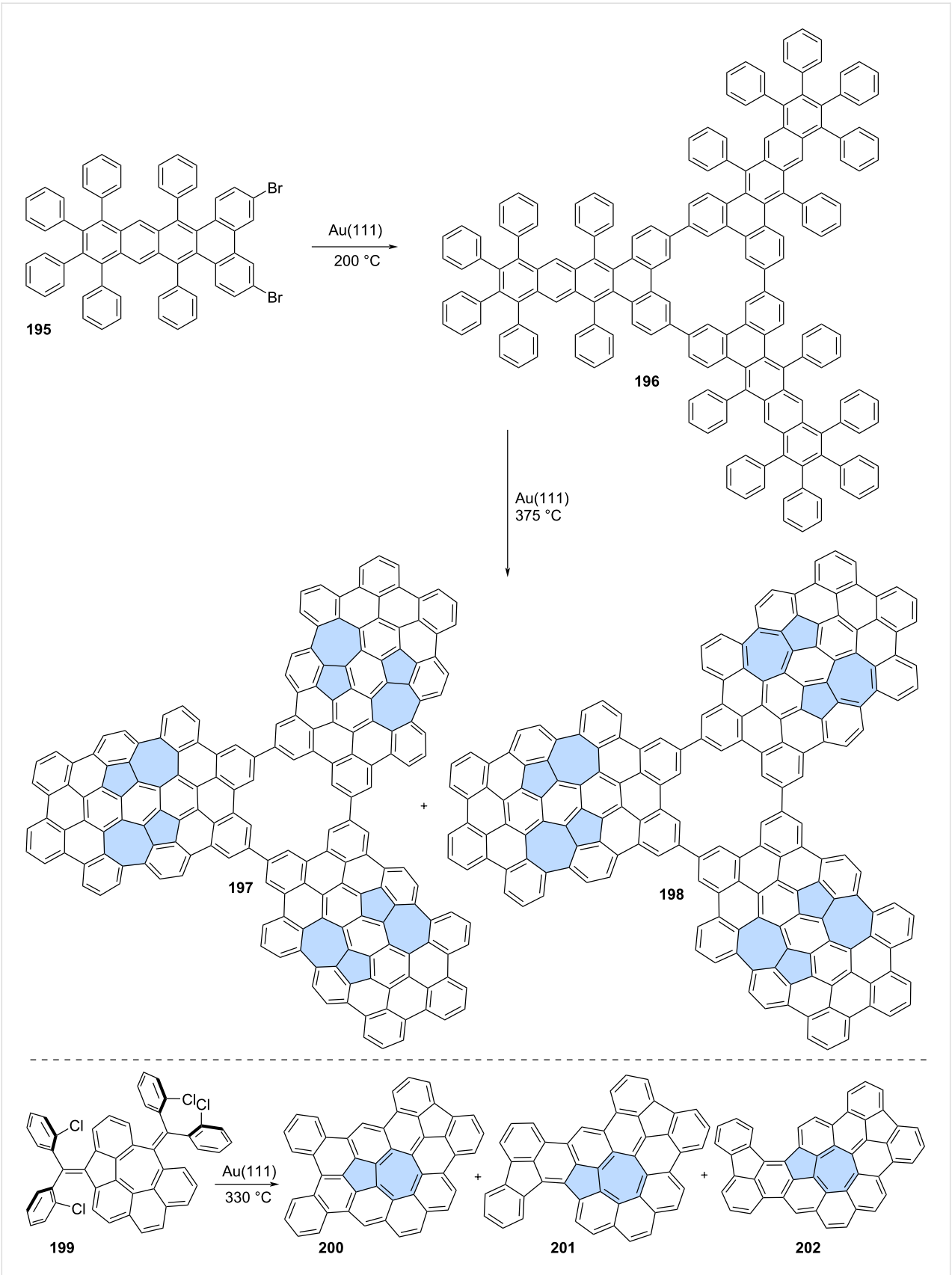

Scheme 25: On-surface synthesis of azulene-embedded nanographenes from benzenoid precursors.

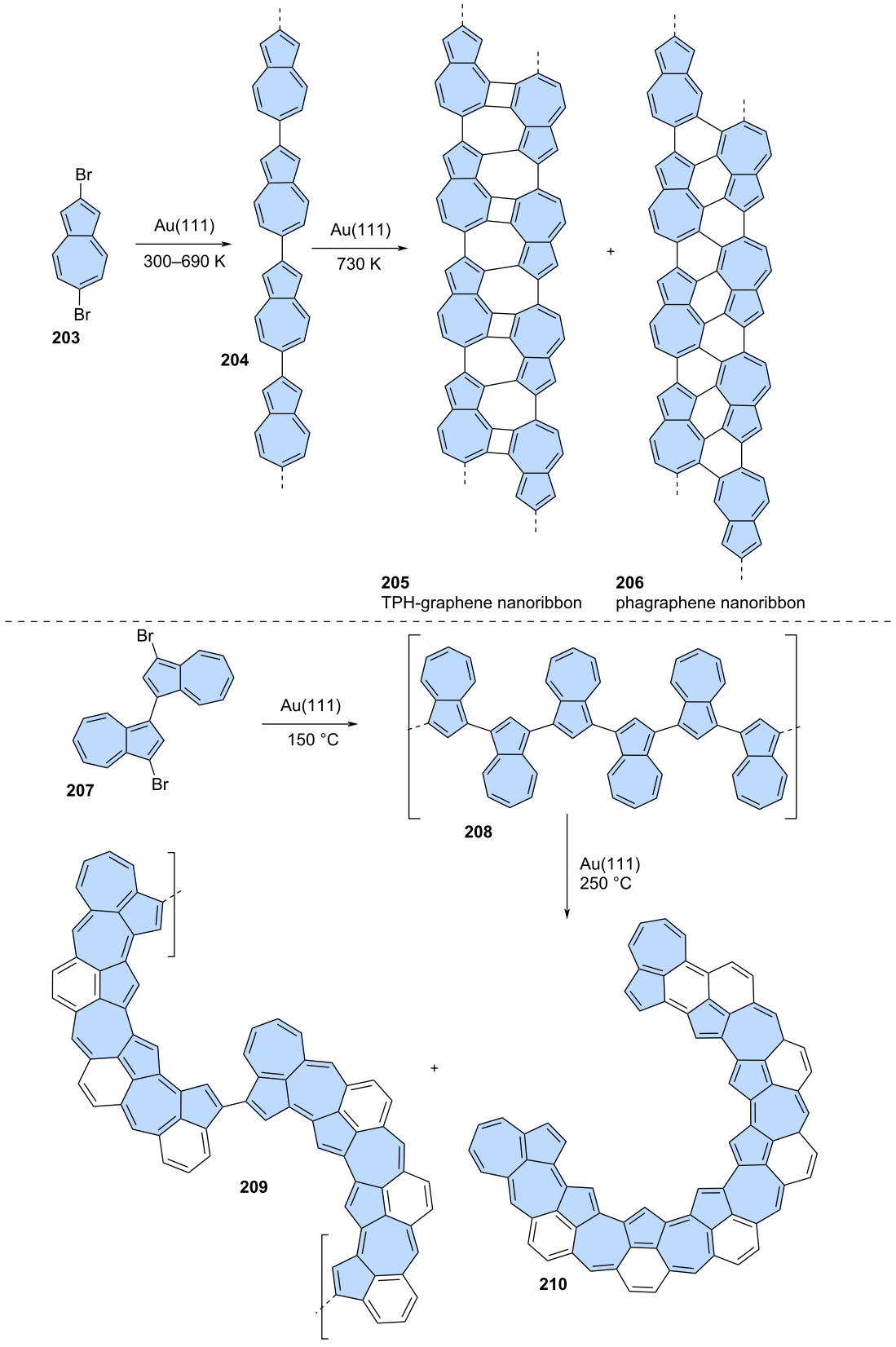

Scheme 26: On-surface synthesis of azulene-embedded nanoribbons.

Table 1: Optical and electronic properties of selected azulene-embedded nanographenes.

Structure	λ_{max}^{Abs} (ε)[a] [nm]/[$cm^{-1}M^{-1}$]	λ_{max}^{Em} [nm]	$E_{1/2}^{ox}/E_{1/2}^{red}$ [b] [V]	E_g[c] [V]	Ref.
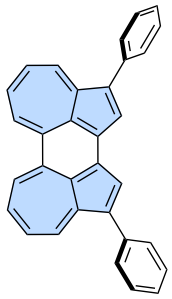 **172**	1180 (521) tail to 1720 nm (CCl_4)	–	–0.10/–1.17 (PhCN)	1.07	[104]
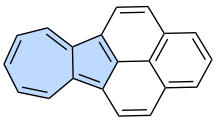 **22**	1010 (98)	–	–	–	[37]
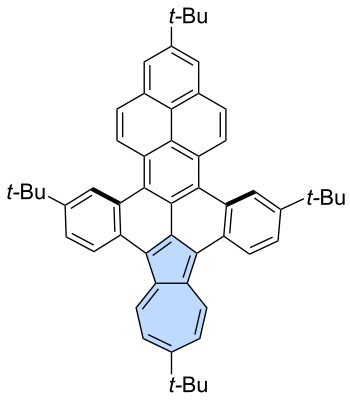 **104**	764 (450) (CH_2Cl_2)	–	0.10/–1.34	1.81	[70]
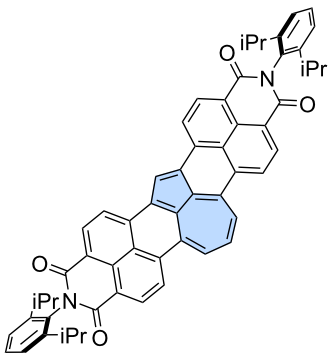 **129**	1041 (4500) (CH_2Cl_2)	–	0.59/–1.03 (CH_2Cl_2)	1.62	[85]
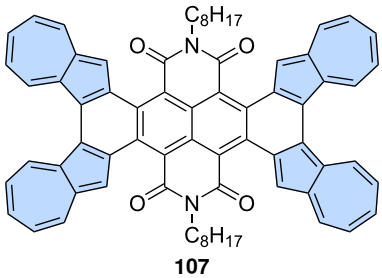 **107**	946 (2500) (THF)	–	0.19/–0.77 (PhCN)	0.96	[71]

Table 1: Optical and electronic properties of selected azulene-embedded nanographenes. (continued)

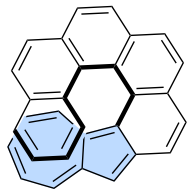 **159**	tail up to 700 nm (CH_2Cl_2)	463[d] (Φ_{FL} < 0.1%) (CH_2Cl_2)	0.09/–1.84 (onsets, CH_2Cl_2)	1.93	[100]
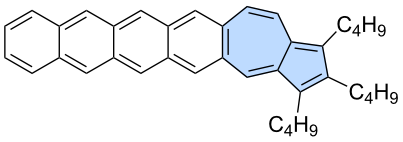 **60**	680 (weak) (CH_2Cl_2)	529[d] (CH_2Cl_2)	0.06/–1.69 (CH_2Cl_2)	1.75	[55]
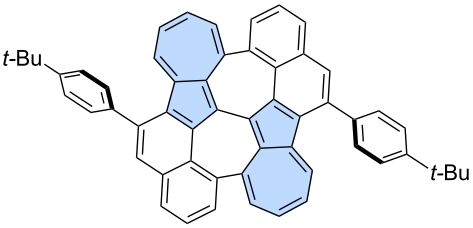 **126**	≈660 (weak) (THF)	410[d] (THF)	0.12/–1.45 (THF)	1.55	[79,80]
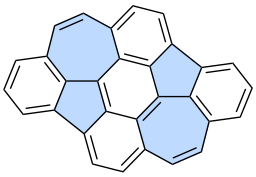 **29**	666 (15800) (THF)	400[d], 670 (THF)	0.22/–1.74 (*o*-DCB/CH_2Cl_2)	1.96	[42]
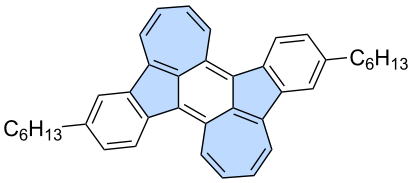 **24**	997 (weak) (CH_2Cl_2)	–	–0.11/–1.34 (CH_2Cl_2)	1.45	[39]
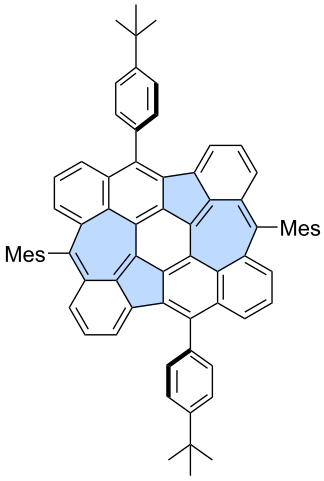 **26**	936 (weak) (CH_2Cl_2)	–	0.11/– (CH_2Cl_2)	–	[40]

Table 1: Optical and electronic properties of selected azulene-embedded nanographenes. (continued)

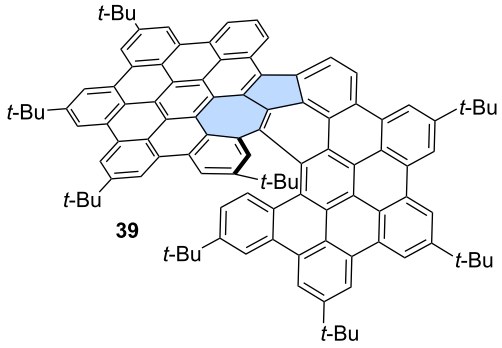 **39**	629 (CH_2Cl_2)	–	0.31/–1.69 (CH_2Cl_2)	2.00	[47]
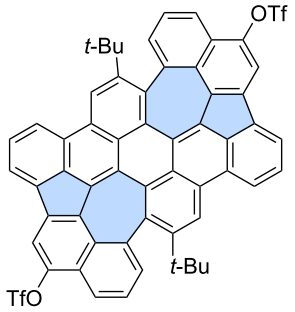 **42**	628 (CH_2Cl_2)	648 (Φ_{FL} = 20%) (CH_2Cl_2)	0.42/–1.67 (CH_2Cl_2)	2.09	[48]

[a]λ_{max} – maximum of the lowest energy electron transition, ε – extinction coefficient; [b]First oxidation and reduction potentials versus Fc/Fc^+ couple; [c]$E_g = E_{1/2}^{ox} - E_{1/2}^{red}$; [d]*anti*-Kasha emission.

azulene-like electronic structure; (2) the degree of aromaticity within the azulene subunit; and (3) the biradical character of molecule.

Purely hydrocarbon PAHs containing 'true' aromatic azulene subunits (e.g., compounds **172**, **22**, and **104**) can exhibit remarkably red-shifted absorption, even when incorporated into relatively small π-conjugated frameworks. Through careful molecular design – retaining the azulene-like electronic structure and promoting spatial separation of the HOMO and LUMO orbitals – it is possible to achieve exceptionally narrow optical gaps. A striking example is the perylene isomer **172**, which displays absorption extending to 1720 nm and an electrochemical gap of just 1.07 V [104]. The presence of two parallel azulene moieties in this structure results in an enhanced dipole moment (1.97 D) compared to pristine azulene (1.28 D). This parallel alignment appears to be critical for achieving a narrow optical gap: in contrast, a recently reported azulene dimer with antiparallel azulene units exhibits a lowest-energy transition at 680 nm [116], comparable to that of pristine azulene. However, the molar extinction coefficients (ε) of compounds **172**, **22**, and **104** are relatively low (below 1000 M^{-1} cm^{-1}), reflecting the partially forbidden nature of the $S_0 \rightarrow S_1$ transitions. Incorporating strongly electron-withdrawing imide groups can enhance the intensity of these transitions, as demonstrated in the cases of the terylene bisimide isomer **129** (λ_{max} = 1041 nm, ε = 4500 M^{-1} cm^{-1}) [85] and bisimide **107** (λ_{max} = 946 nm, ε = 2500 M^{-1} cm^{-1}) [71]. Notably, none of the aforementioned compounds exhibit Kasha-type or *anti*-Kasha fluorescence.

Some azulene-embedded PAHs exhibit *anti*-Kasha fluorescence, akin to that observed in pristine azulene [117]. Notable examples include two series of compounds that feature aromatic azulene subunits: isomers of [*n*]helicenes (*n* = 5, 6, 7) [100] and [*n*]acenes (*n* = 2–6) [55], all of which display *anti*-Kasha fluorescence. Selected representatives from both series are listed in Table 1; for instance, [7]helicene **159** emits at 463 nm, while [6]acene **60** emits at 529 nm. Azulene-embedded nanographenes containing only 'formal' (structurally defined but not truly aromatic) azulene subunits can also exhibit *anti*-Kasha emission. PAH **126** shows *anti*-Kasha emission at 410 nm, whereas compound **29** displays dual emission behavior – both *anti*-Kasha (400 nm) and Kasha-type (670 nm) fluorescence. Nanographenes with formal azulene subunits and significant biradical character (e.g., compounds **24** and **26**) typically show strongly red-shifted optical absorption but no fluorescence.

Interestingly, when the benzenoid framework dominates and the formal azulene unit acts primarily as a structural linker, even large nanographenes may not exhibit red-shifted absorption. PAHs **39** and **42** exemplify this behavior: despite their extended π-conjugation, both show optical absorption and electrochemical gaps characteristic of benzenoid PAHs, with either no fluorescence (compound **39**) or weak Kasha-type fluorescence (compound **42**). Lack or weak fluorescence is a typical behavior of warped, distorted benzenoid PAHs due to the fact that they can suffer from enhanced intersystem crossing [118].

Conclusion

All modern synthetic approaches to azulene-embedded nanographenes have been summarized. These molecules demonstrate a diverse range of electronic properties depending on their specific π-conjugated scaffold. While some PAHs contain aromatic „true" azulene subunits, while the others exhibit biradical properties or benzenoid part of molecules has dominant impact on the properties. Moreover, the incorporation of azulene units into PAHs results in unique and exciting properties, including biradical character, near-infrared (NIR) absorption, stimuli responsiveness, and *anti*-Kasha emission. These characteristics make azulene-embedded nanographenes promising candidates for applications in organic electronics, optoelectronics, and molecular materials.

Despite recent progress, several challenges remain to be addressed. The number of modular synthetic strategies for azulene-embedded nanographenes is still limited, necessitating the development of more efficient and scalable approaches. Additionally, the role of serendipity, particularly in reactions such as the Scholl oxidation, continues to hinder precise control over molecular structures. A deeper mechanistic understanding of these transformations is essential for achieving predictable and reproducible outcomes. Finally, the design and synthesis of substructures related to hypothetical non-benzenoid carbon allotropes represent an exciting avenue for future research, potentially leading to the discovery of novel materials with unprecedented electronic and structural properties.

Funding

The author thanks the National Science Centre Poland (Grant UMO-2022/47/D/ST4/03312) for support of this research.

Author Contributions

Bartłomiej Pigulski: conceptualization; funding acquisition; investigation; project administration; visualization; writing – original draft; writing – review & editing.

ORCID® iDs

Bartłomiej Pigulski - https://orcid.org/0000-0002-9925-2878

Data Availability Statement

Data sharing is not applicable as no new data was generated or analyzed in this study.

References

1. Hirsch, A. *Nat. Mater.* **2010,** *9,* 868–871. doi:10.1038/nmat2885
2. Wu, J.; Pisula, W.; Müllen, K. *Chem. Rev.* **2007,** *107,* 718–747. doi:10.1021/cr068010r
3. Zhang, Y.; Nayak, T. R.; Hong, H.; Cai, W. *Nanoscale* **2012,** *4,* 3833–3842. doi:10.1039/c2nr31040f
4. Shahdeo, D.; Roberts, A.; Abbineni, N.; Gandhi, S. Graphene Based Sensors. *Comprehensive Analytical Chemistry;* Elsevier: Amsterdam, Netherlands, 2020; Vol. 91, pp 175–199. doi:10.1016/bs.coac.2020.08.007
5. Olabi, A. G.; Abdelkareem, M. A.; Wilberforce, T.; Sayed, E. T. *Renewable Sustainable Energy Rev.* **2021,** *135,* 110026. doi:10.1016/j.rser.2020.110026
6. Olatomiwa, A. L.; Adam, T.; Gopinath, S. C. B.; Kolawole, S. Y.; Olayinka, O. H.; Hashim, U. *J. Semicond.* **2022,** *43,* 061101. doi:10.1088/1674-4926/43/6/061101
7. Tour, J. M. *Chem. Mater.* **2014,** *26,* 163–171. doi:10.1021/cm402179h
8. Gu, Y.; Qiu, Z.; Müllen, K. *J. Am. Chem. Soc.* **2022,** *144,* 11499–11524. doi:10.1021/jacs.2c02491
9. Narita, A.; Wang, X.-Y.; Feng, X.; Müllen, K. *Chem. Soc. Rev.* **2015,** *44,* 6616–6643. doi:10.1039/c5cs00183h
10. Yazyev, O. V.; Louie, S. G. *Phys. Rev. B: Condens. Matter Mater. Phys.* **2010,** *81,* 195420. doi:10.1103/physrevb.81.195420
11. Luo, H.; Liu, J. *Angew. Chem., Int. Ed.* **2024,** *63,* e202410759. doi:10.1002/anie.202410759
12. Bhatt, M. D.; Kim, H.; Kim, G. *RSC Adv.* **2022,** *12,* 21520–21547. doi:10.1039/d2ra01436j
13. Ihara, S.; Itoh, S.; Akagi, K.; Tamura, R.; Tsukada, M. *Phys. Rev. B* **1996,** *54,* 14713–14719. doi:10.1103/physrevb.54.14713
14. Meyer, J. C.; Kisielowski, C.; Erni, R.; Rossell, M. D.; Crommie, M. F.; Zettl, A. *Nano Lett.* **2008,** *8,* 3582–3586. doi:10.1021/nl801386m
15. Konishi, A.; Yasuda, M. *Chem. Lett.* **2021,** *50,* 195–212. doi:10.1246/cl.200650
16. Chaolumen; Stepek, I. A.; Yamada, K. E.; Ito, H.; Itami, K. *Angew. Chem., Int. Ed.* **2021,** *60,* 23508–23532. doi:10.1002/anie.202100260
17. Fei, Y.; Liu, J. *Adv. Sci.* **2022,** *9,* 2201000. doi:10.1002/advs.202201000
18. Anderson, A. G., Jr.; Steckler, B. M. *J. Am. Chem. Soc.* **1959,** *81,* 4941–4946. doi:10.1021/ja01527a046
19. Michl, J.; Thulstrup, E. W. *Tetrahedron* **1976,** *32,* 205–209. doi:10.1016/0040-4020(76)87002-0
20. He, Y.-Y.; Chen, J.; Zheng, X.-L.; Xu, X.; Li, W.-Q.; Yang, L.; Tian, W. Q. *ACS Appl. Nano Mater.* **2019,** *2,* 1648–1654. doi:10.1021/acsanm.9b00089
21. Zhang, Z.; Pham, H. D. M.; Perepichka, D. F.; Khaliullin, R. Z. *Nat. Commun.* **2024,** *15,* 1953. doi:10.1038/s41467-024-46279-8
22. Wang, Z.; Zhou, X.-F.; Zhang, X.; Zhu, Q.; Dong, H.; Zhao, M.; Oganov, A. R. *Nano Lett.* **2015,** *15,* 6182–6186. doi:10.1021/acs.nanolett.5b02512

23. Fan, Q.; Martin-Jimenez, D.; Ebeling, D.; Krug, C. K.; Brechmann, L.; Kohlmeyer, C.; Hilt, G.; Hieringer, W.; Schirmeisen, A.; Gottfried, J. M. *J. Am. Chem. Soc.* **2019,** *141,* 17713–17720. doi:10.1021/jacs.9b08060
24. Li, J.; Li, S.; Ouyang, T.; Zhang, C.; Tang, C.; He, C.; Zhong, J. *J. Phys. Chem. Lett.* **2021,** *12,* 732–738. doi:10.1021/acs.jpclett.0c03518
25. Li, X.; Wang, Q.; Jena, P. *J. Phys. Chem. Lett.* **2017,** *8,* 3234–3241. doi:10.1021/acs.jpclett.7b01364
26. Xin, H.; Gao, X. *ChemPlusChem* **2017,** *82,* 945–956. doi:10.1002/cplu.201700039
27. Xin, H.; Hou, B.; Gao, X. *Acc. Chem. Res.* **2021,** *54,* 1737–1753. doi:10.1021/acs.accounts.0c00893
28. Konishi, A.; Horii, K.; Yasuda, M. *J. Phys. Org. Chem.* **2023,** *36,* e4495. doi:10.1002/poc.4495
29. Horii, K.; Kishi, R.; Nakano, M.; Shiomi, D.; Sato, K.; Takui, T.; Konishi, A.; Yasuda, M. *J. Am. Chem. Soc.* **2022,** *144,* 3370–3375. doi:10.1021/jacs.2c00476
30. Chen, Z.; Wannere, C. S.; Corminboeuf, C.; Puchta, R.; Schleyer, P. v. R. *Chem. Rev.* **2005,** *105,* 3842–3888. doi:10.1021/cr030088+
31. Reid, D. H.; Stafford, W. H.; Ward, J. P. *J. Chem. Soc.* **1955,** 1193–1201. doi:10.1039/jr9550001193
32. Gardner, P. D.; Wulfman, C. E.; Osborn, C. L. *J. Am. Chem. Soc.* **1958,** *80,* 143–148. doi:10.1021/ja01534a039
33. Nakasuji, K.; Todo, E.; Murata, I. *Angew. Chem., Int. Ed. Engl.* **1977,** *16,* 784–785. doi:10.1002/anie.197707841
34. Bestmann, H. J.; Ruppert, D. *Angew. Chem., Int. Ed. Engl.* **1968,** *7,* 637. doi:10.1002/anie.196806371
35. Ziegler, K.; Hafner, K. *Angew. Chem.* **1955,** *67,* 301. doi:10.1002/ange.19550671103
36. Jutz, C.; Kirchlechner, R. *Angew. Chem., Int. Ed. Engl.* **1966,** *5,* 516. doi:10.1002/anie.196605161
37. Murata, I.; Nakasuji, K.; Yamamoto, K.; Nakazawa, T.; Kayane, Y.; Kimura, A.; Hara, O. *Angew. Chem., Int. Ed. Engl.* **1975,** *14,* 170–171. doi:10.1002/anie.197501702
38. Fei, Y.; Fu, Y.; Bai, X.; Du, L.; Li, Z.; Komber, H.; Low, K.-H.; Zhou, S.; Phillips, D. L.; Feng, X.; Liu, J. *J. Am. Chem. Soc.* **2021,** *143,* 2353–2360. doi:10.1021/jacs.0c12116
39. Yamamoto, K.; Ie, Y.; Tohnai, N.; Kakiuchi, F.; Aso, Y. *Sci. Rep.* **2018,** *8,* 17663. doi:10.1038/s41598-018-35839-w
40. Liu, J.; Mishra, S.; Pignedoli, C. A.; Passerone, D.; Urgel, J. I.; Fabrizio, A.; Lohr, T. G.; Ma, J.; Komber, H.; Baumgarten, M.; Corminboeuf, C.; Berger, R.; Ruffieux, P.; Müllen, K.; Fasel, R.; Feng, X. *J. Am. Chem. Soc.* **2019,** *141,* 12011–12020. doi:10.1021/jacs.9b04718
41. Zhou, W.; Fei, Y.; Zhang, Y.-S.; Miao, X.; Jiang, S.-D.; Liu, J. *Nat. Commun.* **2025,** *16,* 1006. doi:10.1038/s41467-024-54276-0
42. Zhang, X.-S.; Huang, Y.-Y.; Zhang, J.; Meng, W.; Peng, Q.; Kong, R.; Xiao, Z.; Liu, J.; Huang, M.; Yi, Y.; Chen, L.; Fan, Q.; Lin, G.; Liu, Z.; Zhang, G.; Jiang, L.; Zhang, D. *Angew. Chem., Int. Ed.* **2020,** *59,* 3529–3533. doi:10.1002/anie.201914416
43. Agranat, I.; Cohen, S.; Isaksson, R.; Sandström, J.; Suissa, M. R. *J. Org. Chem.* **1990,** *55,* 4943–4950. doi:10.1021/jo00303a035
44. Qin, L.; Huang, Y.-Y.; Wu, B.; Pan, J.; Yang, J.; Zhang, J.; Han, G.; Yang, S.; Chen, L.; Yin, Z.; Shu, Y.; Jiang, L.; Yi, Y.; Peng, Q.; Zhou, X.; Li, C.; Zhang, G.; Zhang, X.-S.; Wu, K.; Zhang, D. *Angew. Chem., Int. Ed.* **2023,** *62,* e202304632. doi:10.1002/anie.202304632
45. Qin, L.; Xie, J.; Wu, B.; Hong, H.; Yang, S.; Ma, Z.; Li, C.; Zhang, G.; Zhang, X.-S.; Liu, K.; Zhang, D. *J. Am. Chem. Soc.* **2024,** *146,* 12206–12214. doi:10.1021/jacs.4c03007
46. Han, Y.; Xue, Z.; Li, G.; Gu, Y.; Ni, Y.; Dong, S.; Chi, C. *Angew. Chem., Int. Ed.* **2020,** *59,* 9026–9031. doi:10.1002/anie.201915327
47. Ma, J.; Fu, Y.; Dmitrieva, E.; Liu, F.; Komber, H.; Hennersdorf, F.; Popov, A. A.; Weigand, J. J.; Liu, J.; Feng, X. *Angew. Chem., Int. Ed.* **2020,** *59,* 5637–5642. doi:10.1002/anie.201914716
48. Yang, X.; Rominger, F.; Mastalerz, M. *Angew. Chem., Int. Ed.* **2019,** *58,* 17577–17582. doi:10.1002/anie.201908643
49. Ogawa, N.; Yamaoka, Y.; Takikawa, H.; Yamada, K.-i.; Takasu, K. *J. Am. Chem. Soc.* **2020,** *142,* 13322–13327. doi:10.1021/jacs.0c06156
50. Assony, S. J.; Kharasch, N. *J. Am. Chem. Soc.* **1958,** *80,* 5978–5982. doi:10.1021/ja01555a023
51. Lambert, C.; Nöll, G.; Zabel, M.; Hampel, F.; Schmälzlin, E.; Bräuchle, C.; Meerholz, K. *Chem. – Eur. J.* **2003,** *9,* 4232–4239. doi:10.1002/chem.200304923
52. Claus, V.; Schukin, M.; Harrer, S.; Rudolph, M.; Rominger, F.; Asiri, A. M.; Xie, J.; Hashmi, A. S. K. *Angew. Chem., Int. Ed.* **2018,** *57,* 12966–12970. doi:10.1002/anie.201805918
53. Hibi, D.; Kitabayashi, K.; Fujita, K.; Takeda, T.; Tobe, Y. *J. Org. Chem.* **2016,** *81,* 3735–3743. doi:10.1021/acs.joc.6b00389
54. Matsuda, T.; Goya, T.; Liu, L.; Sakurai, Y.; Watanuki, S.; Ishida, N.; Murakami, M. *Angew. Chem., Int. Ed.* **2013,** *52,* 6492–6495. doi:10.1002/anie.201300570
55. Huang, F.; Díaz-Fernández, M.; Marín-Beloqui, J. M.; Sun, L.; Chen, Y.; Liu, S.; Wang, Y.; Zheng, H.; Li, S.; Zhang, C.; You, J.; Casado, J. *J. Am. Chem. Soc.* **2025,** *147,* 1574–1583. doi:10.1021/jacs.4c11186
56. Zhou, F.; Shi, W.; Liao, X.; Yang, Y.; Yu, Z.-X.; You, J. *ACS Catal.* **2022,** *12,* 676–686. doi:10.1021/acscatal.1c04549
57. Li, Z.; Zhao, H.; Liu, Y.; Zhang, T.; Sun, W.; Wang, Y.; Dou, C. *Org. Lett.* **2024,** *26,* 10345–10350. doi:10.1021/acs.orglett.4c03969
58. Liu, B.; Chen, M.; Liu, X.; Fu, R.; Zhao, Y.; Duan, Y.; Zhang, L. *J. Am. Chem. Soc.* **2023,** *145,* 28137–28145. doi:10.1021/jacs.3c10303
59. Wang, S.; Tang, M.; Wu, L.; Bian, L.; Jiang, L.; Liu, J.; Tang, Z.-B.; Liang, Y.; Liu, Z. *Angew. Chem., Int. Ed.* **2022,** *61,* e202205658. doi:10.1002/anie.202205658
60. Liu, R.; Fu, Y.; Wu, F.; Liu, F.; Zhang, J.-J.; Yang, L.; Popov, A. A.; Ma, J.; Feng, X. *Angew. Chem., Int. Ed.* **2023,** *62,* e202219091. doi:10.1002/anie.202219091
61. Liang, Y.; Wang, S.; Tang, M.; Wu, L.; Bian, L.; Jiang, L.; Tang, Z.-B.; Liu, J.; Guan, A.; Liu, Z. *Angew. Chem., Int. Ed.* **2023,** *62,* e202218839. doi:10.1002/anie.202218839
62. Kirschbaum, T.; Rominger, F.; Mastalerz, M. *Chem. – Eur. J.* **2023,** *29,* e202301470. doi:10.1002/chem.202301470
63. Farrell, J. M.; Grande, V.; Schmidt, D.; Würthner, F. *Angew. Chem., Int. Ed.* **2019,** *58,* 16504–16507. doi:10.1002/anie.201909975
64. Farrell, J. M.; Schmidt, D.; Grande, V.; Würthner, F. *Angew. Chem., Int. Ed.* **2017,** *56,* 11846–11850. doi:10.1002/anie.201706346
65. Zhu, C.; Shoyama, K.; Würthner, F. *Angew. Chem., Int. Ed.* **2020,** *59,* 21505–21509. doi:10.1002/anie.202010077
66. Spengler, J.; Zhu, C.; Shoyama, K.; Würthner, F. *Chem. Sci.* **2023,** *14,* 10861–10866. doi:10.1039/d3sc04015a

67. Zeng, H. N.; Png, Z. M.; Xu, J. *Chem. – Asian J.* **2020,** *15,* 1904–1915. doi:10.1002/asia.202000444
68. Chaolumen; Ito, H.; Itami, K. *Chem. Commun.* **2019,** *55,* 9606–9609. doi:10.1039/c9cc03510a
69. Mathey, P.; Fernández, I.; Morin, J.-F. *New J. Chem.* **2024,** *48,* 4801–4809. doi:10.1039/d4nj00729h
70. Biesaga, J.; Szafert, S.; Pigulski, B. *Org. Chem. Front.* **2024,** *11,* 6026–6035. doi:10.1039/d4qo01459f
71. Koide, T.; Takesue, M.; Murafuji, T.; Satomi, K.; Suzuki, Y.; Kawamata, J.; Terai, K.; Suzuki, M.; Yamada, H.; Shiota, Y.; Yoshizawa, K.; Tani, F. *ChemPlusChem* **2017,** *82,* 1010–1014. doi:10.1002/cplu.201600356
72. Narita, M.; Teraoka, T.; Murafuji, T.; Shiota, Y.; Yoshizawa, K.; Mori, S.; Uno, H.; Kanegawa, S.; Sato, O.; Goto, K.; Tani, F. *Bull. Chem. Soc. Jpn.* **2019,** *92,* 1867–1873. doi:10.1246/bcsj.20190219
73. Ito, S.; Nomura, A.; Morita, N.; Kabuto, C.; Kobayashi, H.; Maejima, S.; Fujimori, K.; Yasunami, M. *J. Org. Chem.* **2002,** *67,* 7295–7302. doi:10.1021/jo020381u
74. Uehara, K.; Mei, P.; Murayama, T.; Tani, F.; Hayashi, H.; Suzuki, M.; Aratani, N.; Yamada, H. *Eur. J. Org. Chem.* **2018,** 4508–4511. doi:10.1002/ejoc.201800769
75. Sasaki, Y.; Takase, M.; Okujima, T.; Mori, S.; Uno, H. *Org. Lett.* **2019,** *21,* 1900–1903. doi:10.1021/acs.orglett.9b00515
76. Chen, L.; Wu, B.; Qin, L.; Huang, Y.-Y.; Meng, W.; Kong, R.; Yu, X.; ChenChai, K.; Li, C.; Zhang, G.; Zhang, X.-S.; Zhang, D. *Chem. Commun.* **2022,** *58,* 5100–5103. doi:10.1039/d2cc01061e
77. Wang, C.; Deng, Z.; Phillips, D. L.; Liu, J. *Angew. Chem., Int. Ed.* **2023,** *62,* e202306890. doi:10.1002/anie.202306890
78. Wang, C.; Hu, C.; Wang, W.; Yang, J.; Liu, J. *CCS Chem.* **2025,** in press. doi:10.31635/ccschem.024.202404765
79. Wang, J.; Gámez, F. G.; Marín-Beloqui, J.; Diaz-Andres, A.; Miao, X.; Casanova, D.; Casado, J.; Liu, J. *Angew. Chem., Int. Ed.* **2023,** *62,* e202217124. doi:10.1002/anie.202217124
80. Diaz-Andres, A.; Marín-Beloqui, J.; Wang, J.; Liu, J.; Casado, J.; Casanova, D. *Chem. Sci.* **2023,** *14,* 6420–6429. doi:10.1039/d3sc00405h
81. Shoyama, K.; Würthner, F. *J. Am. Chem. Soc.* **2019,** *141,* 13008–13012. doi:10.1021/jacs.9b06617
82. Seifert, S.; Shoyama, K.; Schmidt, D.; Würthner, F. *Angew. Chem., Int. Ed.* **2016,** *55,* 6390–6395. doi:10.1002/anie.201601433
83. Pigulski, B.; Shoyama, K.; Sun, M.-J.; Würthner, F. *J. Am. Chem. Soc.* **2022,** *144,* 5718–5722. doi:10.1021/jacs.2c00142
84. Pigulski, B.; Ximenis, M.; Shoyama, K.; Würthner, F. *Org. Chem. Front.* **2020,** *7,* 2925–2930. doi:10.1039/d0qo00968g
85. Pigulski, B.; Shoyama, K.; Würthner, F. *Angew. Chem., Int. Ed.* **2020,** *59,* 15908–15912. doi:10.1002/anie.202005376
86. Holtrup, F. O.; Müller, G. R. J.; Quante, H.; De Feyter, S.; De Schryver, F. C.; Müllen, K. *Chem. – Eur. J.* **1997,** *3,* 219–225. doi:10.1002/chem.19970030209
87. Pschirer, N. G.; Kohl, C.; Nolde, F.; Qu, J.; Müllen, K. *Angew. Chem., Int. Ed.* **2006,** *45,* 1401–1404. doi:10.1002/anie.200502998
88. Hirakawa, M.; Uehara, K.; Oyama, R.; Aratani, N. *Asian J. Org. Chem.* **2025,** e202500373. doi:10.1002/ajoc.202500373
89. Murai, M.; Hosokawa, N.; Roy, D.; Takai, K. *Org. Lett.* **2014,** *16,* 4134–4137. doi:10.1021/ol5018273
90. Murai, M.; Iba, S.; Ota, H.; Takai, K. *Org. Lett.* **2017,** *19,* 5585–5588. doi:10.1021/acs.orglett.7b02729
91. Senese, A. D.; Chalifoux, W. A. *Molecules* **2019,** *24,* 118. doi:10.3390/molecules24010118
92. Yang, W.; Monteiro, J. H. S. K.; de Bettencourt-Dias, A.; Catalano, V. J.; Chalifoux, W. A. *Angew. Chem., Int. Ed.* **2016,** *55,* 10427–10430. doi:10.1002/anie.201604741
93. Yang, W.; Lucotti, A.; Tommasini, M.; Chalifoux, W. A. *J. Am. Chem. Soc.* **2016,** *138,* 9137–9144. doi:10.1021/jacs.6b03014
94. Shiotari, A.; Nakae, T.; Iwata, K.; Mori, S.; Okujima, T.; Uno, H.; Sakaguchi, H.; Sugimoto, Y. *Nat. Commun.* **2017,** *8,* 16089. doi:10.1038/ncomms16089
95. Vardanyan, A.; Villinger, A.; Ehlers, P.; Langer, P. *J. Org. Chem.* **2023,** *88,* 11411–11423. doi:10.1021/acs.joc.2c02997
96. Guo, J.; Du, F.; Yu, B.; Du, P.; Li, H.; Zhang, J.; Xin, H. *Chem. Sci.* **2024,** *15,* 12589–12597. doi:10.1039/d4sc02566k
97. Ren, P.; Chen, L.; Sun, C.; Hua, X.; Luo, N.; Fan, B.; Chen, P.; Shao, X.; Zhang, H.-L.; Liu, Z. *J. Phys. Chem. Lett.* **2024,** *15,* 8410–8419. doi:10.1021/acs.jpclett.4c01917
98. Mathey, P.; Sobczak, Q.; Darvish, A.; Morin, J.-F. *Chem. Commun.* **2024,** *60,* 4854–4857. doi:10.1039/d4cc00968a
99. Yamamoto, K.; Okazumi, M.; Suemune, H.; Usui, K. *Org. Lett.* **2013,** *15,* 1806–1809. doi:10.1021/ol400332j
100. Duan, C.; Zhang, J.; Xiang, J.; Yang, X.; Gao, X. *Angew. Chem., Int. Ed.* **2022,** *61,* e202201494. doi:10.1002/anie.202201494
101. Jiang, J.; Kaafarani, B. R.; Neckers, D. C. *J. Org. Chem.* **2006,** *71,* 2155–2158. doi:10.1021/jo0522198
102. Ong, A.; Tao, T.; Jiang, Q.; Han, Y.; Ou, Y.; Huang, K.-W.; Chi, C. *Angew. Chem., Int. Ed.* **2022,** *61,* e202209286. doi:10.1002/anie.202209286
103. Zhou, Z.-h.; Yamamoto, T. *J. Organomet. Chem.* **1991,** *414,* 119–127. doi:10.1016/0022-328x(91)83247-2
104. Hatakenaka, R.; Urabe, K.; Ueno, S.; Yamauchi, M.; Mizuhata, Y.; Yamada, H.; Mikata, Y.; Kamijo, S.; Tani, F.; Murafuji, T. *Chem. – Eur. J.* **2025,** *31,* e202404679. doi:10.1002/chem.202404679
105. Xin, H.; Li, J.; Lu, R.-Q.; Gao, X.; Swager, T. M. *J. Am. Chem. Soc.* **2020,** *142,* 13598–13605. doi:10.1021/jacs.0c06299
106. Duan, C.; Zhang, J.; Cai, S.; Xiang, J.; Yang, X.; Gao, X. *Eur. J. Org. Chem.* **2023,** *26,* e202201347. doi:10.1002/ejoc.202201347
107. Xin, H.; Li, J.; Yang, X.; Gao, X. *J. Org. Chem.* **2020,** *85,* 70–78. doi:10.1021/acs.joc.9b01724
108. Qin, T.; Wang, T.; Zhu, J. *Commun. Chem.* **2024,** *7,* 154. doi:10.1038/s42004-024-01222-2
109. Méndez, J.; López, M. F.; Martín-Gago, J. A. *Chem. Soc. Rev.* **2011,** *40,* 4578–4590. doi:10.1039/c0cs00161a
110. Mishra, S.; Lohr, T. G.; Pignedoli, C. A.; Liu, J.; Berger, R.; Urgel, J. I.; Müllen, K.; Feng, X.; Ruffieux, P.; Fasel, R. *ACS Nano* **2018,** *12,* 11917–11927. doi:10.1021/acsnano.8b07225
111. Lohr, T. G.; Urgel, J. I.; Eimre, K.; Liu, J.; Di Giovannantonio, M.; Mishra, S.; Berger, R.; Ruffieux, P.; Pignedoli, C. A.; Fasel, R.; Feng, X. *J. Am. Chem. Soc.* **2020,** *142,* 13565–13572. doi:10.1021/jacs.0c05668
112. Biswas, K.; Chen, Q.; Obermann, S.; Ma, J.; Soler-Polo, D.; Melidonie, J.; Barragán, A.; Sánchez-Grande, A.; Lauwaet, K.; Gallego, J. M.; Miranda, R.; Écija, D.; Jelínek, P.; Feng, X.; Urgel, J. I. *Angew. Chem., Int. Ed.* **2024,** *63,* e202318185. doi:10.1002/anie.202318185
113. Hieulle, J.; Carbonell-Sanromà, E.; Vilas-Varela, M.; Garcia-Lekue, A.; Guitián, E.; Peña, D.; Pascual, J. I. *Nano Lett.* **2018,** *18,* 418–423. doi:10.1021/acs.nanolett.7b04309

114. Wu, F.; Xu, W.; Fu, Y.; Liu, R.; Yang, L.; Ruffieux, P.; Fasel, R.; Ma, J.; Feng, X. *Org. Mater.* **2024,** *6,* 71–77. doi:10.1055/a-2333-9789
115. Hou, I. C.-Y.; Sun, Q.; Eimre, K.; Di Giovannantonio, M.; Urgel, J. I.; Ruffieux, P.; Narita, A.; Fasel, R.; Müllen, K. *J. Am. Chem. Soc.* **2020,** *142,* 10291–10296. doi:10.1021/jacs.0c03635
116. Liu, S.; Díaz-Fernández, M.; Zhang, M.; Huang, F.; Chen, Y.; Yang, Y.; Marín-Beloqui, J. M.; Lan, J.; You, J.; Casado, J.; Zhang, C. *Angew. Chem., Int. Ed.* **2025,** e202505897. doi:10.1002/anie.202505897
117. Beer, M.; Longuet-Higgins, H. C. *J. Chem. Phys.* **1955,** *23,* 1390–1391. doi:10.1063/1.1742314
118. Nagarajan, K.; Mallia, A. R.; Muraleedharan, K.; Hariharan, M. *Chem. Sci.* **2017,** *8,* 1776–1782. doi:10.1039/c6sc05126j

License and Terms

BEILSTEIN JOURNAL OF ORGANIC CHEMISTRY

On the aromaticity and photophysics of 1-arylbenzo[*a*]imidazo[5,1,2-*cd*]indolizines as bicolor fluorescent molecules for barium tagging in the study of double-beta decay of ^{136}Xe

Eric Iván Velazco-Cabral[1,2], Fernando Auria-Luna[1], Juan Molina-Canteras[1], Miguel A. Vázquez[2], Iván Rivilla[*3,4] and Fernando P. Cossío[*1,3]

Full Research Paper

Open Access

Address:
[1]Departamento de Química Orgánica I and Centro de Innovación y Química Avanzada (ORFEO-CINQA), Facultad de Química/Kimika Fakultatea, Universidad del País Vasco/Euskal Herriko Unibertsitatea (UPV/EHU), 20018 Donostia/San Sebastián, Spain, [2]Departmento de Química, Universidad de Guanajuato, 36050 Guanajuato, Gto, Mexico, [3]Donostia International Physics Center (DIPC), 20018 Donostia/San Sebastián, Spain and [4]Ikerbasque, Basque Foundation for Science, 48009 Bilbao, Spain

Email:
Iván Rivilla[*] - ivan.rivilla@ehu.es; Fernando P. Cossío[*] - fp.cossio@ehu.es

* Corresponding author

Keywords:
aromaticity; DFT-TDDFT calculations; double-beta decay; fluorescent sensors; polycyclic arenes

Beilstein J. Org. Chem. **2025,** *21,* 1627–1638.
https://doi.org/10.3762/bjoc.21.126

Received: 23 April 2025
Accepted: 02 July 2025
Published: 13 August 2025

This article is part of the thematic issue "π-Conjugated molecules and materials".

Guest Editor: A. Mateo-Alonso

Abstract

In this paper, the behavior of a bicolor fluorescent indicator for the detection of barium cations formed by double-beta decay of ^{136}Xe is analyzed by means of computational tools. Both DFT and TDDFT permit to understand the origin of the bicolor fluorescent signal emitted by 1-arylbenzo[*a*]imidazo[5,1,2-*cd*]indolizines in the free and Ba^{2+}-bound states. The aromatic character of the fluorophore is analyzed by means of energetic (hyperhomodesmotic equations), structural (harmonic oscillator model of aromaticity, HOMA) and magnetic (nucleus independent chemical shifts, NICS) criteria. It is concluded that the aromatic character of the fluorophore is better described as the combination of two aromatic subunits integrated in the polycyclic system. Different DFT functional are used to analyze the photochemical behavior of this family of sensors. It is concluded that PBE0 and M06 functionals describe better the excitation process in the free state, whereas interaction of the sensor with Ba^{2+} requires the M06L functional. TDDFT analysis of the emission spectra shows larger errors, which have been corrected by means of a structural model. The bicolor behavior is rationalized based on the decoupling between the *para*-phenylene and benzo[*a*]imidazo[5,1,2-*cd*]indolizine components that results in a blue shift upon Ba^{2+} coordination.

Introduction

Double beta-decay [1] is a radioactive decay in which two neutrons are converted into two protons by means of the transformation of two quarks *down* into two quarks *up* (Figure 1). This process involves the emission of two W^- bosons that in turn evolve towards the emission of two electrons. In the two-neutrino double-beta decay (ββ2ν), two electronic antineutrinos are also produced. Another possibility corresponds to the neutrinoless double-beta decay [2] (ββ0ν). This latter process could take place if the electronic neutrino is a Majorana particle [3], namely, it coincides with its own antiparticle ($\nu_e = \overline{\nu}_e$). This would result in a mutual annihilation, according to which the two emitted electrons would take more energy than in the ββ2ν process. In both processes, the initial nuclide must advance two steps beyond the periodic table. Among the possible candidates for double-beta decay, ^{136}Xe is a suitable isotope. In the ββ2ν radioactive decay, the reaction is $^{136}Xe \rightarrow {}^{136}Ba^{2+} + 2e^- + 2\overline{\nu}_e$. The ββ0ν analog would consist of simply $^{136}Xe \rightarrow {}^{136}Ba^{2+} + 2e^-$. Both transformations are extraordinarily rare events. For instance, the estimated half-life for the ββ0ν decay is at least higher than $2.3 \cdot 10^{26}$ years, whereas the current best estimate of the age of the universe [4] is $13.8 \cdot 10^9$ years. However, characterization of the neutrino as a Majorana particle constitutes a formidable challenge that would have an extraordinary impact in cosmology since this would contribute decisively to explain why our universe is formed by matter and not antimatter [5].

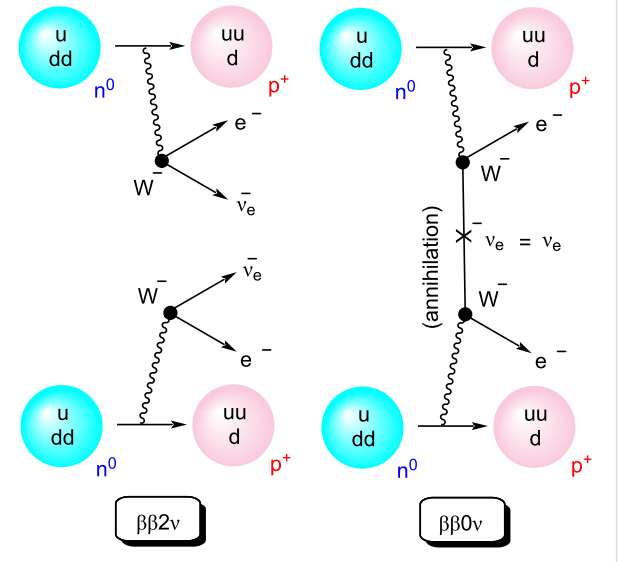

Figure 1: Two possible double beta decay modes. Left: with emission of two electronic antineutrinos (ββ2ν). Right: neutrinoless double beta decay (ββ0ν).

Within this context, from a chemical point of view, detection of ββ0ν radioactive decay of ^{136}Xe requires an extremely sensitive detection of $^{136}Ba^{2+}$. One promising candidate [6] would be a radiometric fluorescent sensor. With this idea in mind, we started a project aiming at designing, synthetizing and validating a fluorescent indicator that would fulfill the following conditions: (i) high discrimination between the free and Ba^{2+}-bound states; (ii) high binding affinity for Ba^{2+}, and low background signal for the chelated state. We reasoned that a bicolor fluorescent indicator [7] (FBI), namely, a radiometric sensor that emit the fluorescent signal at different wavelengths in the free and bound states, would be the best option given the extremely rare character of the ββ0ν event.

After analyzing different possibilities, we finally observed that FBIs based on benzo[*a*]imidazo[5,1,2-*cd*]indolizines as fluorescent moieties constitute promising candidates to detect Ba^{2+} cations [8,9] (Figure 2). Another essential component is an aza-crown ether of appropriate dimensions to capture the barium cation. In addition, one *para*-disubstituted phenyl (or aryl) group is installed to generate selective cation–π interactions. Finally, a spacer (denoted as X and Y in Figure 2) and a linker (denoted as Z) to anchor the sensor to a suitable surface via a covalent interaction are required. Ideally, different configurations and conformations of the fluorophore in the free and chelated states would result in a bicolor behavior in the emission spectra. Indeed, initial experiments were successful. However, we observed that translation of the behavior of these FBIs from supramolecular chemistry to solid–gas interfaces raises

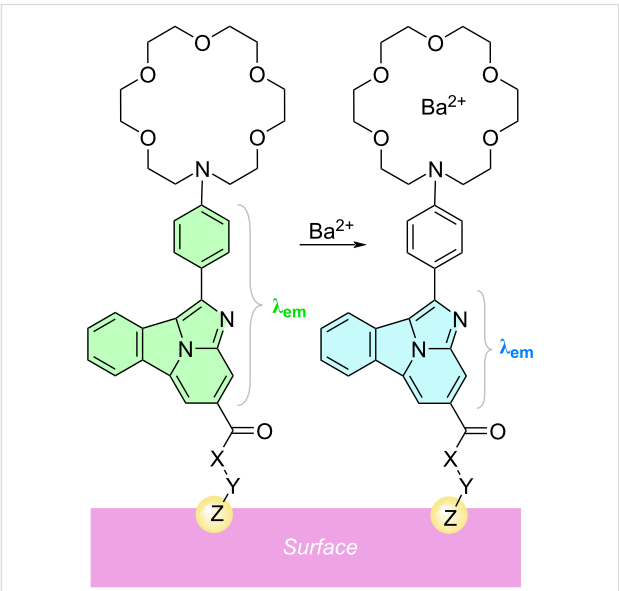

Figure 2: General structure of first-generation bicolor fluorescent indicators based on 1-aryl benzo[*a*]imidazo[5,1,2-*cd*]indolizines. X and Y represent the spacer and Z stands for the linker to the surface, respectively. The different emission wavelengths in the free and bound states are highlighted.

important issues in terms of both discrimination between free and chelated states and photophysical properties [10].

Therefore, in this paper, we reexamine the electronic features of these 1-arylbenzo[*a*]imidazo[5,1,2-*cd*]indolizine-based FBIs in terms of aromaticity (a relevant feature to analyze the nature of the excited states) and emission properties. The final goal of this research has been to contribute to the design of a second generation of bicolor fluorescent indicators for barium tagging in neutrinoless double-beta decay.

Results and Discussion

First, we analyzed the aromaticity of parent benzo[*a*]imidazo[5,1,2-*cd*]indolizine **1** (Scheme 1) in order to get a better understanding of the properties of this tetracyclic system [11]. Since ground state aromaticity can be assessed by energetic [12], geometric [13] and magnetic [14,15] criteria, among others [16-18], we analyzed first the resonance energy of **1** with respect to the aromatic resonance energies of the *ortho*-phenyl and the bicyclic imidazo[1,2-*a*]pyridine components. In reaction A, an hyperhomodesmotic equation [19] **2** + **3** → **4** + **1** was defined, in which the conjugation of the bicyclic imidazo[1,2-*a*]pyridine unit was removed, while preserving the *ortho*-disubstituted phenyl ring, highlighted in yellow in Scheme 1A. This reaction yielded a stabilization energy of ca. 17 kcal/mol. In the alternative hyperhomodesmotic reaction B, defined as **5** + **6** → **7** + **1**, the formal ten-electron Hückel aromaticity of the imidazo[1,2-*a*]pyridine moiety (in blue) was preserved while the phenyl component was decomposed. The computed stabilization energy of this second reaction was calculated to be of 28 kcal/mol, slightly lower than the aromatic stabilization energy (ASE) and isomerization stabilization energy (ISE) calculated for benzene [20] (see reaction D in Scheme 1). Most likely this lowering stems from the strain imposed to the *ortho*-phenylene moiety in the tetracyclic structure. Combination of reactions A and B in the form

$$\tfrac{1}{2}(\mathbf{2}+\mathbf{3}+\mathbf{5}+\mathbf{6}) \rightarrow \tfrac{1}{2}(\mathbf{4}+\mathbf{7})+\mathbf{1}$$

yields an average value of $\langle \Delta E_{AB} \rangle$ = −22.6 kcal/mol. A similar treatment of the separate components as outlined in reactions C and D shows a much lower stabilization energy for imidazo[1,2-

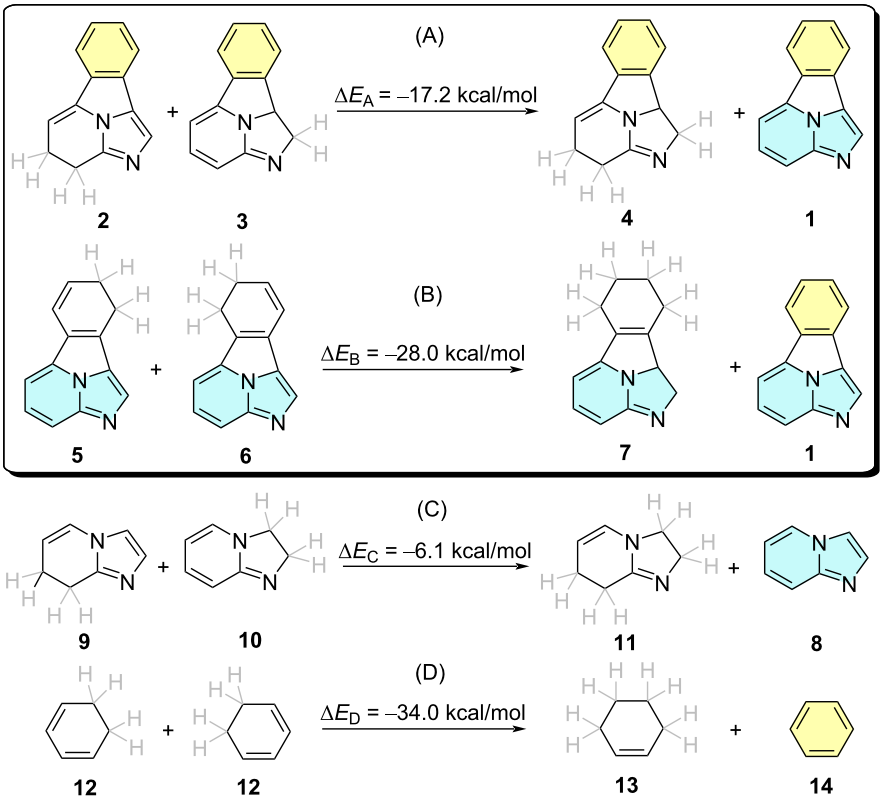

Scheme 1: Hyperhomodesmotic equations used to analyze the resonance energy of benzo[*a*]imidazo[5,1,2-*cd*]indolizine **1** with respect to the imidazo[1,2-*a*]pyridine unit (A) and the *ortho*-disubstituted phenyl ring (B). Similar reactions for the separate components of **1** are shown in (C) and (D). All the relative energies have been calculated at the B3LYP-D3BJ/6-311+G** level of theory. Explicit hydrogens on the saturated C_{sp^3} atoms are highlighted in gray.

a]pyridine **8** and a higher stabilization energy of benzene (**15**). Combination of these latter equations yields

$$\mathbf{9}+\mathbf{10}+2\cdot\mathbf{12}\rightarrow\mathbf{11}+\mathbf{8}+\mathbf{13}+\mathbf{14}.$$

This second averaged equation results in a computed stabilization energy of $\langle\Delta E_{CD}\rangle$ = −20.5 kcal/mol, 2.1 kcal/mol lower than that calculated for $\langle\Delta E_{AB}\rangle$. These results indicate that there is a noticeable interplay between the phenyl (yellow) and imidazo[1,2-*a*]pyridine (blue) components of **1** and that these aromatic units preserve their respective aromatic characters.

We next examined the aromatic character of benzo[*a*]imidazo[5,1,2-*cd*]indolizine **1** by analyzing its geometry in terms of bond equalization. Three possibilities were considered: a total delocalized geometry denoted as **1a** in Figure 3A, a peripheric conjugation **1b** that excludes the participation of the lone pair of the central N atom and, finally, a two-component delocalization scheme denoted as **1c**. The chief features of fully optimized structures of **1** at the ground state (S_0) and first singlet excited state (S_1) are reported in Figure 3B. Using geometric criteria, we computed the HOMA [21,22] for **1** at the ground state, according to the following expression:

$$\mathrm{HOMA}=1-\frac{1}{n}\sum_{i=1}^{n}\alpha_k(R_k^{\mathrm{opt}}-R_k^{\mathrm{i}})^2. \qquad (1)$$

In this equation, n is the number of covalent bonds, k describes the type of bond (CC or CN), R_k^{opt} stands for the optimal CC or CN distances associated with aromatic structures, R_k^{i} represents the corresponding bond distance gathered in Figure 3B, and α_k is a parametric term defined as

$$\alpha_k=\frac{2}{(R_k^{\mathrm{s}}-R_k^{\mathrm{d}})^2+(R_k^{\mathrm{d}}-R_k^{\mathrm{opt}})^2}, \qquad (2)$$

where R_k^{s} is the standard single bond distance of the k-pair of atoms (C–C, C–N) and R_k^{d} is the same paremeter but referred to the corresponding double bonds (C=C, C=N).

We computed the HOMA values associated with the total, peripheral and modular patterns using the standard parameters and a more recent set based on computational parameters that take into account antiaromaticity, denoted as HOMAc [23]. According to our results, formal structure **1a** is the less aromatic one, a result compatible with the formal anti-Hückel character of this structure, with 16 π-electrons if the central nitrogen atom is included in the electron counting. Peripheral structure **1b** is formally Hückel aromatic since the lone pair of this atom is not considered, thus resulting in 14 π-electrons and a higher HOMA value. Finally, modular structure **1c** includes formally separated components with six and ten π-electrons, both units being Hückel aromatic. This structure shows the highest HOMA and HOMAc values, which is in agreement with our conclusion from the analysis in terms of stabilization energy. In addition, an analysis of the Anisotropy of the induced current density (ACID) plot [24] calculated for **1** (Figure 3B) shows a significant diatropic ring current formally associated with the peripheral model **1b**. Another diatropic contribution can be assigned to the modular model **1c**, with a vortex in the bond connecting

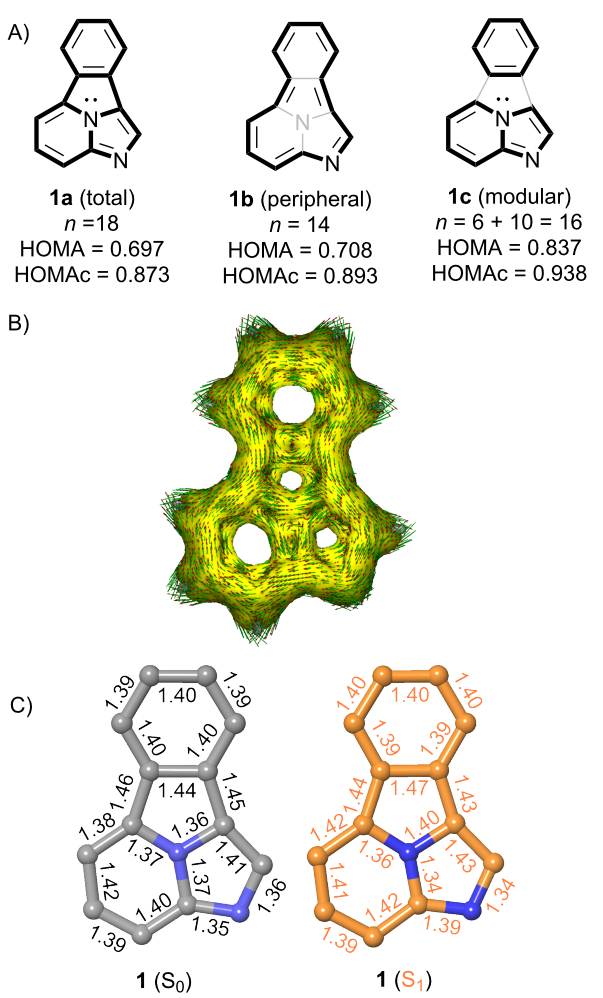

Figure 3: (A) Total, peripheral and modular delocalization patterns for fluorophore **1**. The ground state (S_o) Harmonic oscillator models of aromaticity, both standard (HOMA) and computational antiaromaticity-including (HOMAc) descriptors are gathered for each pattern. Descriptor *n* stands for the number of covalent bonds, of each pattern, according to Equation 1. (B) Anisotropy of the current induced density (ACID) diagram of compound **1**. (isosurface value: 0.035 a.u.) (C) Bond distances (in Å) for fully optimized structure of **1**, computed at the ground state (S_0) and at the first singlet excited state (S_1, in orange). Results obtained at the B3LYP-D3BJ/6-311+G** (S_0) and using TDDFT (S_1). Hydrogen atoms have been omitted for clarity.

the phenyl group with the pyrrole ring. Interestingly, paratropic ring currents are observed close to the molecular plane.

This conclusion is reinforced by the NICS computed for the four rings of **1**. As shown in Table 1, the isotropic NICS values at the molecular plane are always negative, but the pyrrole ring shows the lowest value. Indeed, if the NICSzz(0) values are considered, a paratropic character is observed at the center of the pyrrole and imidazole rings. The situation is more consistent when the NICS values are computed 1 Å above the molecular plane [25,26] since diatropic ring currents are observed over the centers of the four ring points of electron density. However, the issues associated with magnetic criteria to describe the aromaticity of polycyclic systems must be taken into account. Thus, a recent study [27] emphasizes the relative (and competitive) contributions of global, semi-local and local ring currents associated with Kekulé resonance and Clar's disjoint aromatic π–sextets, which reveals different coexisting ring current circuits in this kind of systems. Therefore, the assessment of the aromaticity of system **1** relies on the combined agreement among conceptually different criteria. In summary, thermochemical, structural and magnetic analysis permit to conclude that the aromaticity of the fluorophore defined by **1** has modular and peripheral character, which results in a moderate total aromaticity for this parent compound in the ground state. Since it is known that the aromaticity rules are reversed in $^1\pi\pi^*$ excited states [28], the high fluorescent response of **1** is connected with its higher aromaticity at the excited S_1 state. Actually, the two peripheric C–C bonds of the central pyrrole ring are slightly shorter in the optimized S_1 state, thus suggesting a less modular aromatic character. Unfortunately, since the HOMA parameters for excited states [29] are available for triplet $^3\pi\pi^*$ states only and we are interested in fluorescence emission spectra, this kind of quantitative assessment of aromaticity was not possible.

The role of the crown ether and the *para*-phenylene moieties was also analyzed. The interactions of different sized crown ethers with Ba^{2+} and coordination with the aromatic ring modeled by means of benzene (**14**, highlighted in yellow in Scheme 2) were studied computationally. Although the efficiency of crown ethers as components in cation-selective fluorescent probes has been extensively explored [7,30], to the best of our knowledge no previous computational DFT studies on the selectivity of crown ethers of different sizes with Ba^{2+} have been reported. Therefore, we explored (Scheme 2A) the binding between this cation and 12-crown-4 (**16a**, n = 1), 15-crown-5 (**16b**, n = 2), 18-crown-6 (**16c**, n = 3) and 21-crown-7 (**16d**, n = 4), to form Ba^{2+}·crown ethers **15a–d**. We compared the corresponding binding energies by means of the following isodesmic equation:

Table 1: NICS(iso) and NICSzz values at the molecular plane (z = 0) and 1 Å (z = 1) above this plane in a perpendicular direction. Points *a–c* correspond to the respective ring points, in light red. Perpendicular points at z = 1 are shown in light green.

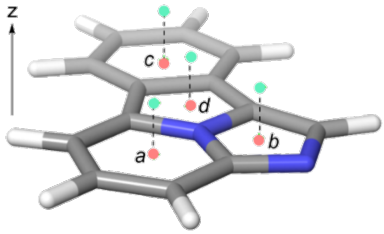

Point	NICS(iso)[a]		NICSzz[a]	
	z = 0	z = 1	z = 0	z = 1
a	−11.729	−16.728	−11.798	−32.255
b	−12.486	−11.486	+8.812	−31.343
c	−8.740	−10.298	−12.648	−27.974
d	−7.287	−7.705	+8.730	−17.884

[a]Values computed using the B3LYP/6-311+G** hybrid functional and the GIAO method.

$$\Delta G_{iso}(\mathbf{a-d}) = \Delta G_{298}(\mathbf{15a-d}) + \Delta G_{298}(\mathbf{16a}) - [\Delta G_{298}(\mathbf{16a-d}) + \Delta G_{298}(\mathbf{15a})]. \quad (3)$$

Where the different terms correspond to Gibbs energies computed at 298.17 K. We also extended this study to the interaction between complexes **15a–d** and benzene (**14**) and computed the corresponding complexation energies as

$$\Delta G_{rxn}(\mathbf{a-d}) = \Delta G_{298}(\mathbf{17a-d}) - [\Delta G_{298}(\mathbf{14}) + \Delta G_{298}(\mathbf{15a-d})]. \quad (4)$$

In addition, Figure 4 includes the chief geometric parameters of the different complexes, as well as the corresponding free energy values.

Our calculations show that, as expected, 12-crown-4 **16a** and 15-crown-5 **16b** are too small and consequently the barium cation lies outside the average molecular plane determined by the macrocycle. In the case of 18-crown-6 **16c**, the cyclic ligand accommodates very well the cation, which is now within the average molecular plane. In addition, the corresponding ΔG_{iso} values increase with the n-values (Figure 4A). Ligand 21-crown-7 **15d** suggests that this size of the cyclic ligand is less than optimal, since the calculated structure shown a concave-convex topology, in which one oxygen atom, highlighted by an asterisk, lies out from the direct coordination perimeter, thus suggesting that this ligand is too big. The rela-

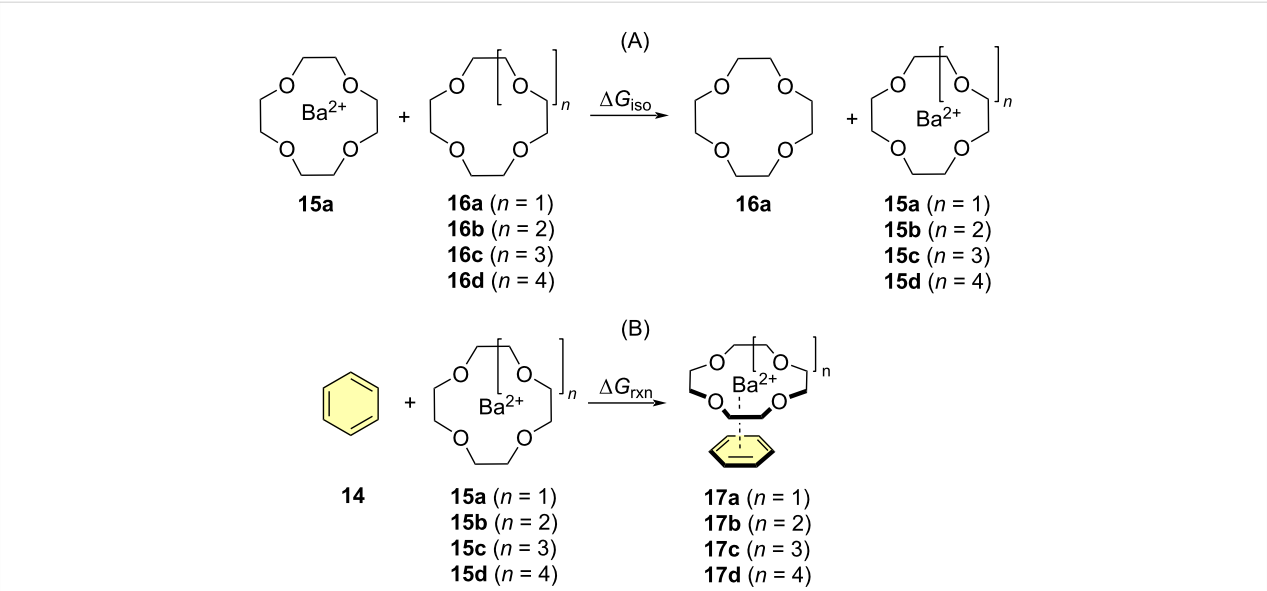

Scheme 2: Isodesmic (A) and reaction profiles (B) for the analysis of the interaction of Ba^{2+} with different crown ethers and a benzene ring as a computational model of *para*-phenylene ring shown in Figure 2.

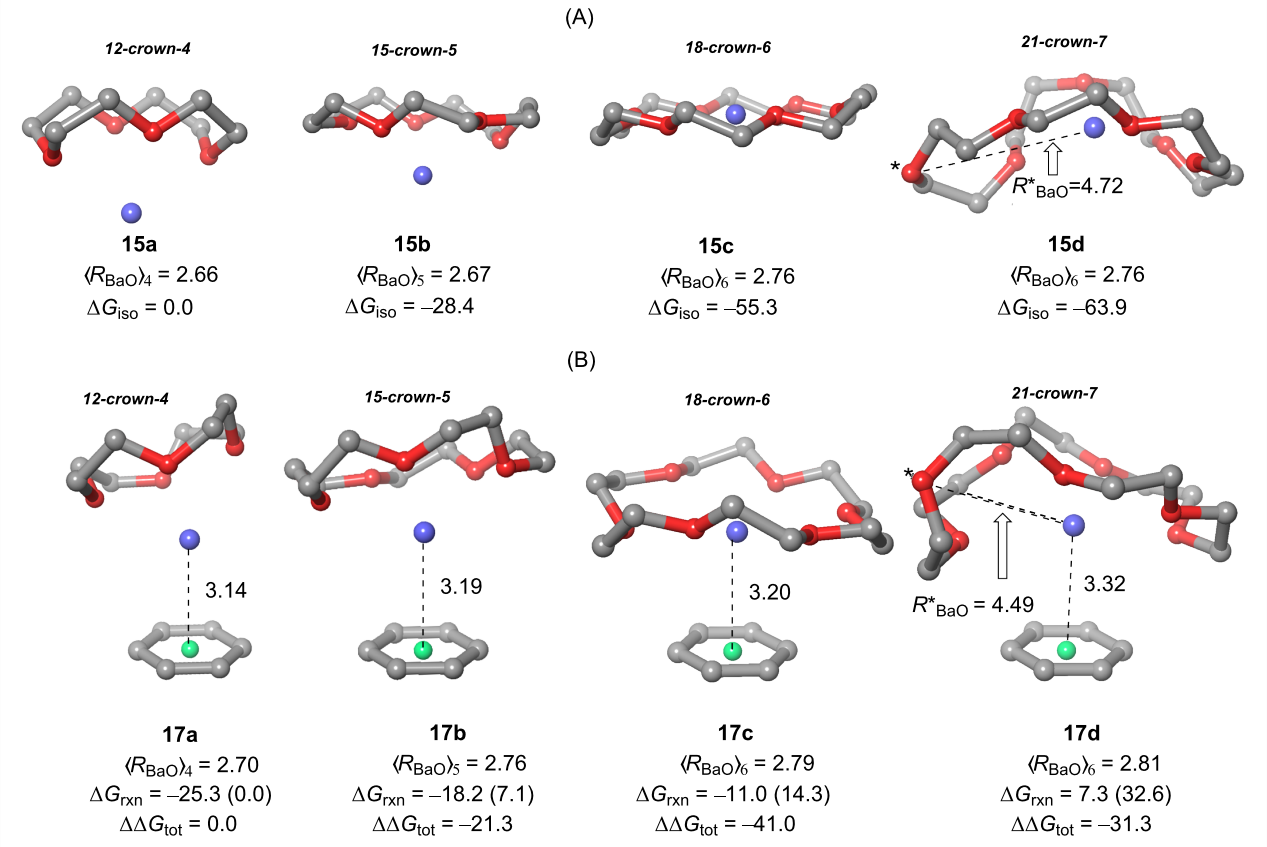

Figure 4: Fully optimized geometries (B3LYP-D3BJ/6ccrow-311++G**&DefTZVPP(Ba) level of theory) of Ba^{2+}·crown ethers **15a–d** (A) and phenyl·Ba^{2+}·crown ether complexes **17a–d** (B). Barium cations are represented in dark blue. Descriptors $(\langle R_{Ba0}\rangle)_n$ denote the average Ba–O bond distances (in Å) for the different crown ethers. Distances between Ba^{2+} and the ring points of electron density of benzene (in green) are also gathered in (B). ΔG_{iso} and ΔG_{rxn} terms stand for the Gibbs energies (in kcal/mol) described in Scheme 2 and have been calculated according to Equation 3 and Equation 4. Numbers in parentheses are the relative ΔG_{rxn} energies with respect to complex **17a**. $\Delta\Delta G_{tot}$ energies have been calculated according to Equation 5. Hydrogen atoms have been omitted for clarity.

tively lower increase of the ΔG_{iso}(**d**) with respect to its ΔG_{iso}(**c**) congener also indicate that the stabilization induced by the additional oxygen atom is lower in magnitude.

An analysis of the effect of the aromatic ring represented by the benzene ring shown in Scheme 2 and in Figure 4B was also performed. We observed that for complexes **17a** (n = 1) and **17b** (n = 2) the low size of the crown ethers generates a poor coordination to Ba^{2+}, which results in more charge available for further coordination thus giving rise to a relatively strong π–cation interaction with the phenyl group. In the case of complex **17c** (n = 3) stemming from 18-crown-6, the barium cation remains within the average molecular plane determined by the macrocyclic moiety. The larger ΔG_{iso} value for **15c** results in a relatively lower ΔG_{rxn} free energy for **17c**, given the lower charge available for further interaction with the phenyl group. The geometry of complex **17d** (n = 4) resembles that found for parent **15d**, since the 21-crown-7 moiety adopts a concave–convex shape, in which the barium cation occupies a central position within the concave face. Also in this case, one oxygen atom of the oversized macrocycle does not interact directly with Ba^{2+}, thus resulting in a non-optimal coordination pattern. Therefore, the shape of the ligand and the low positive charge available for the cation result in the largest Ba^{2+}-ring point distance and in a positive value of ΔG_{rxn}(**d**) although the corresponding energy is slightly negative (ca. −4 kcal/mol). If we combine both relative magnitudes in the form

$$\Delta\Delta G_{tot}(\mathbf{a}-\mathbf{d}) = \Delta G_{iso}(\mathbf{a}-\mathbf{d}) - [\Delta G_{rxn}(\mathbf{a}-\mathbf{d}) - \Delta G_{rxn}(\mathbf{a})] \quad (5)$$

in which the second term of the right hand (in brackets) correspond to the relative Gibbs reaction energy with respect to **17a**, gathered in parentheses in Figure 4. These combined $\Delta\Delta G_{tot}$ values permit to conclude that 18-crown-6 (n = 3) is the best tradeoff between coordination to the cation and subsequent interaction with the phenyl group. This is the reason why in our design we introduced and aza-equivalent of 18-crown-6, namely the 1,4,7,10,13-pentaoxa-16-azacyclooctadecane moiety.

We next investigated the coupling between the two components of the sensor gathered in Figure 2 at the free and Ba^{2+}-bound states, namely the aza-crown ether-Ba^{2+}-*para*-phenylene and the benzo[*a*]imidazo[5,1,2-*cd*]indolizine components. We chose compound **18** (Figure 5) as a convenient computational model. We calculated the energy profile associated with the rotation between the 1,4-phenylene and benzo[*a*]imidazo[5,1,2-*cd*]indolizine **1** components, defined as variation of the ω = *a*–*d*–*c*–*d* dihedral angle shown in Figure 5. Our calculations show that, in the absence of barium, compound **18** exhibits almost coplanar components, so both systems form a combined fluorophore highlighted in green in Figure 5. The correlation between energy and this dihedral angle by means of a Karplus-like [31] equation up to the fourth degree in the form

$$E(\omega) - E(0) = 13.89\cos^4\omega - 10.61\cos^3\omega - 9.73\cos^2\omega - 0.20\cos\omega + 6.55 \quad (6)$$

shows an excellent correlation (R^2 = 0.9987). The situation is completely different in the presence of a naked barium cation (Figure 5B). Thus, the $E(\omega) - E(0)$ vs ω curve shows a wide minimum in the region of 90 deg. Also in this case, the correlation for a fourth-degree polynomial expansion in terms of $\cos^n\omega$ in the form

$$E(\omega) - E(0) = 84.56\cos^4\omega - 113.49\cos^3\omega - 40.10\cos^2\omega - 2.32\cos\omega - 14.12 \quad (7)$$

with a correlation factor of R^2 = 0.9829. This minimum involves the simultaneous coordination of the cation to one nitrogen atom of the fluorophore **1**, to the *para*-phenylene group and the crown ether, a result in line with our experimental results [8].

Next, we analyzed the geometry and electronic features of synthetic compounds **18** and **18·Ba^{2+}** as a model case study of the general design shown in Figure 2. Instead of the isolated cation generated by the ββ0ν process, we included barium perchlorate since this salt was used in experimental studies, as it can be observed in Scheme 3. DFT and TDDFT calculations show that the geometries of **18** at the ground first excited states are quite similar (Figure 6), the aza-crown ether component being more flexible, in good agreement with our experimental observations [9], with very low values of the dihedral angle formed by the benzo[*a*]imidazo[5,1,2-*cd*]indolizine and the *para*-phenylene groups, especially in the S_1 state, thus indicating that both aromatic units are coupled under excitation–relaxation to produce the corresponding absorption–emission spectra (vide infra). The calculated structures of **18** complexed with barium perchlorate are more rigid, with only small modifications on going from the ground state to the first single excited state (Figure 6). However, the presence of the two perchlorate anions results in additional coordination with Ba^{2+}, thus resulting in larger values of the Ba–N distances, as well as of the average Ba–O and Ba–phenylene distances. In addition, the ω = *a*–*b*–*c*–*d* dihedral angle between fluorophore **1** and the 1,4-phenylene ring is smaller than that calculated for the naked barium cation, but still shows a noticeable departure from coplanarity.

The peculiar behavior of barium perchlorate with respect to naked Ba^{2+} prompted us to compare the photophysical proper-

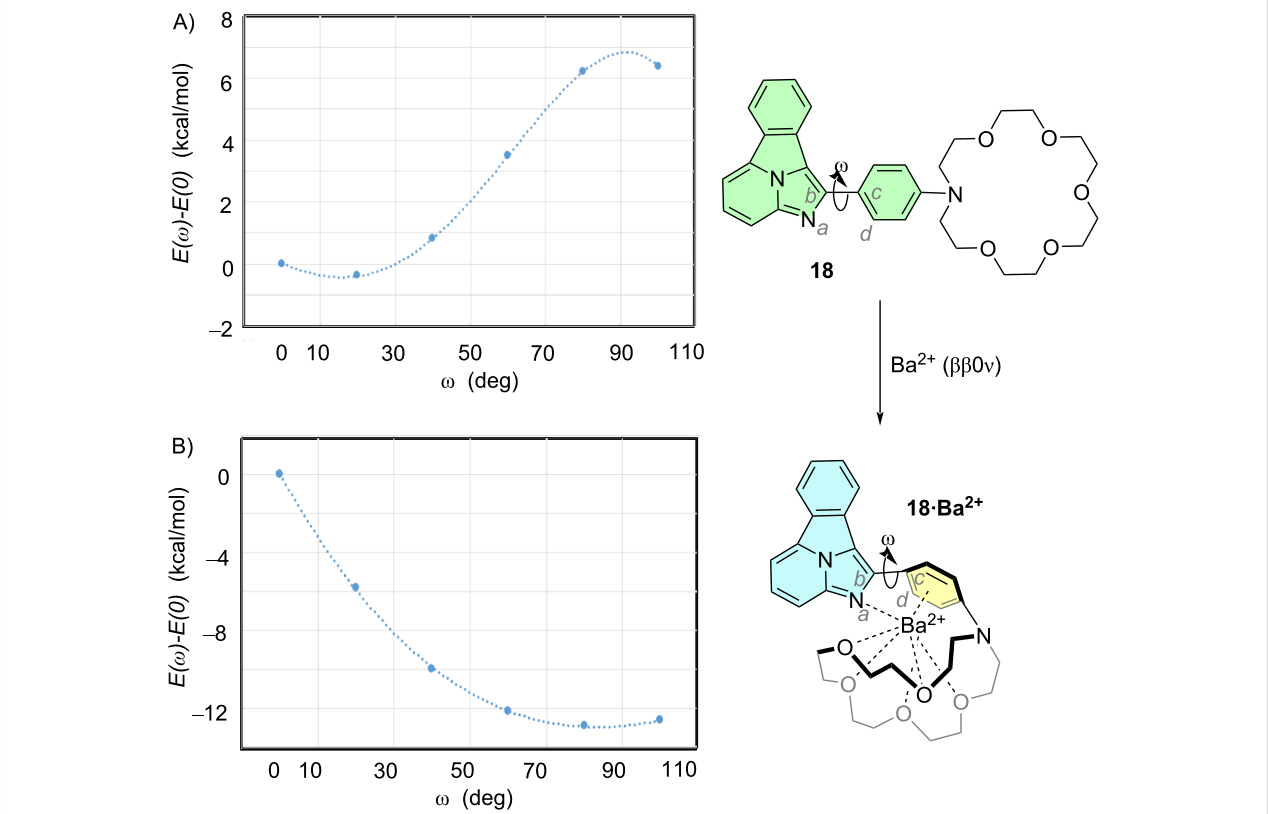

Figure 5: Relaxed scan of the relative conformational energies of sensor **18** at the free state (A) and bound to barium cation **18·Ba^{2+}** (B), calculated at the B3LYP-D3BJ/6-31G*&DefTZVPP(Ba) level of theory. Capture of one naked barium cation generated after a neutrinoless double-beta decay (ββ0ν) is assumed. The dihedral angle ω = *a*–*b*–*c*–*d* formed by the two components of the fluorophore are graphically defined.

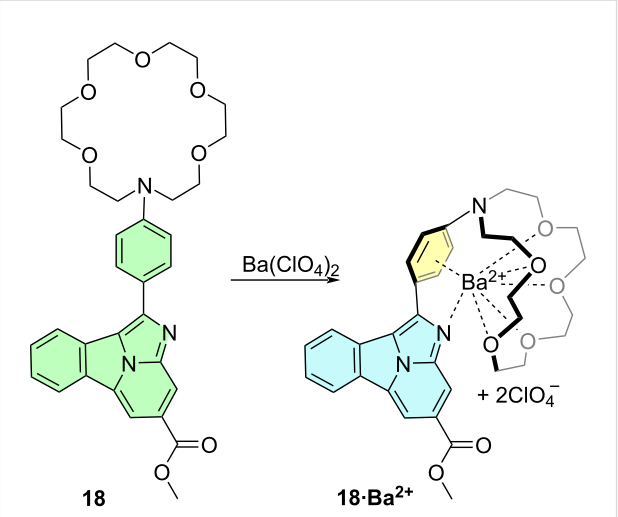

Scheme 3: Reaction of fluorescent probe **18** with barium perchlorate, as indicated in Figure 2 (X = O, Y, Z = Me). The possible coordination patterns are shown.

ties of unbound compound **18** in the presence of $Ba(ClO_4)_2$. The values corresponding to the adiabatic absorption (S_0(optimized) → S_1*, adiabatic absorption) and emission (S_1(optimized) → S_0, fluorescence) are reported in Table 2, together with the differences between the free and bound states. The corresponding signed errors are gathered in Figure 7.

The behavior of the different functionals resulted to be very variable, although the ground state and excited state geometries were very similar. In the case of absorption wavelengths, wB97XD, BHandHHLYP and CAM-B3LYP were the most convenient functionals to describe the blue shift on going from the free to the Ba-chelated state. If errors for the free and chelated states are considered, B3LYP and ωB97XD are the functionals that introduce the lowest error values, although these data are less relevant than $\Delta\lambda_{abs}$.

Calculated emission wavelengths and the differences between the calculated fluorescent emissions in the free and bound states showed in some cases noticeable differences. Thus, M06-L and wB97XD functionals described better the emission of **18** at the unbound state, whereas M06 and M06-L gave the lower errors for the λ_{em} values of **18·Ba(ClO$_4$)$_2$**. However, the situation was found to be different when the $\Delta\lambda_{em}$ values were calculated. In this case, M06 (which even predicted a red shift) and PBE were the less accurate functionals, whereas M06-2X was the most

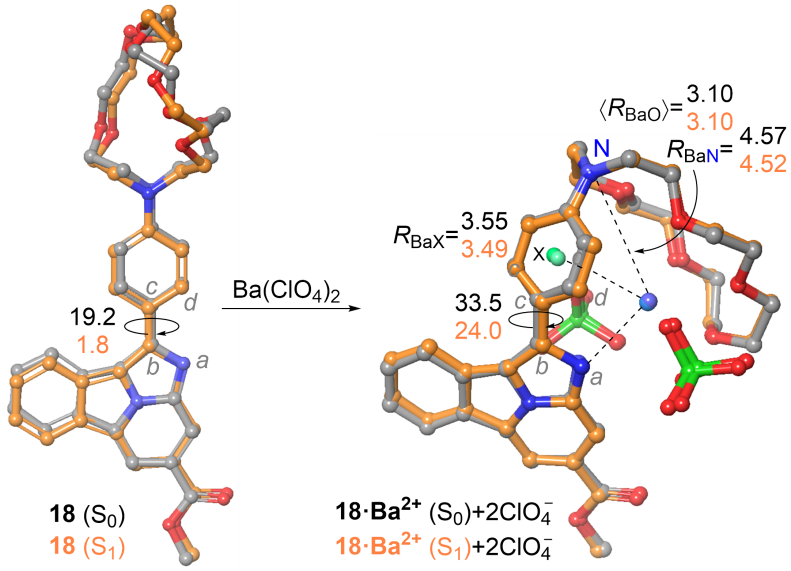

Figure 6: Fully optimized structures (B3LYP-D3BJ/6-311++G(d,p)&DefTZVPP(Ba) level of theory) of compounds **18** and **18·Ba^{2+}** at the ground (S_0, carbon atoms in gray) and first excited (S_1, carbons in orange) sates. Bond distances are given in Å. The dihedral angles ω = *a–b–c–d*, in absolute value, are reported in deg.

Table 2: Calculated[a] absorption (λ_{abs}, in nm) and emission (λ_{em}, in nm) wavelengths of compound **19** at the free and barium perchlorate bound states, using different DFT functionals.

Functional	λ_{abs}			λ_{em}		
	18	**18·Ba(ClO$_4$)$_2$**	$\Delta\lambda_{abs}$[b]	**18**	**18·Ba(ClO$_4$)$_2$**	$\Delta\lambda_{em}$[b]
experimental[c]	434	420	−14	508	434	−74
BHandH	377	335	−42	425	364	−61
BHandHLYP	376	335	−41	427	376	−51
B3LYP	462	397	−36	462	426	−36
CAM-B3LYP	382	342	−40	435	375	−60
M06	431	382	−49	478	420	−58
M06-L	384	341	−43	621	645	+24
M06-2X	518	432	−86	445	379	−66
PBE	433	369	−64	473	457	−16
ωB97XD	377	340	−37	434	372	−62

[a]Calculations performed with the 6-311++G(d,p)& DefTZVPP (Ba) basis sets and effective-core potential. [b]Difference between the free and chelated values: Δλ = λ(**19·Ba(ClO$_4$)$_2$**) − λ(**19**). [c]Data taken from ref. [8].

precise functional, followed by wB97XD, the other functionals being quite similar among them. Therefore, we concluded that M06-2X, whose calculated geometry is almost coincident with that computed with B3LYP-D3BJ, is the most precise functional to predict the two-color behavior of these fluorescent sensors.

Computational Methods

All the DFT [32] and TDDFT [33] calculations were performed using the B3LYP[34-36], B3LYP-D3BJ [37,38], CAM-B3LYP [39], M06 [40,41], M06-2X [42], M06-L [43-45], PBE0 [46] and ωB97XD [47] functionals. The 6-311+G* and 6-31++G** bases sets [48,49] were used for C, N, O, and H. The DefTZVPP [50] effective-core potential and basis set were used for Na and Ba. NICS calculations were carried out by using the GIAO [51] method. Wiberg bond orders [52] were computed within the NBO bicentric localized orbitals [53,54]. All structures were fully optimized [55] and characterized by harmonic analysis. All the calculations were performed by using the Gaussian 16 suite of programs [56].

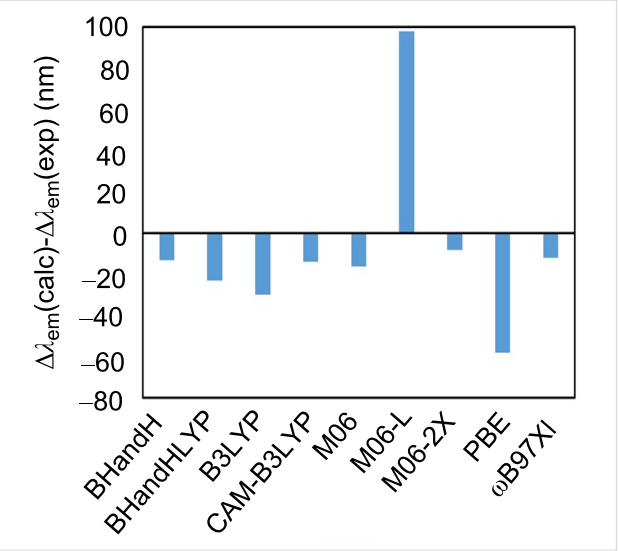

Figure 7: Comparison between the calculated and experimental differences between the emission wavelength of **18** and **18**·$Ba(ClO_4)_2$, with different functionals within DFT and TDDFT frameworks.

Conclusion

From the computational study reported in this paper, we conclude that the benzo[*a*]imidazo[5,1,2-*cd*]indolizine scaffold is a convenient fluorophore for barium tagging in neutrinoless double-beta decay. This fluorophore exhibits modular aromaticity in which the central pyrrole ring is less aromatic that the other three rings, as proved by energetic, geometric and magnetic criteria of aromaticity. The lower ground state aromaticity of the tetracyclic system, as a whole, results in a highly fluorescent signal in the first singlet excited state. Analysis of the crown-ether component permits to conclude that the aza-analog equivalent to 18-crown-6 represents the best compromise between coordinating oxygen atoms and ability to form a π–Ba^{2+} complex with the *para*-phenylene component of the sensor. Rotation about the dihedral angle defined by the two aromatic components of the sensor result in an essentially planar conformation at the free state, whereas binding to a naked barium cation results in a perpendicular arrangement between the benzo[*a*]imidazo[5,1,2-*cd*]indolizine and the 1,4-phenylene components, thus promoting a blue shift responsible for the bicolor behavior of the sensor. Interaction with barium perchlorate results in a slightly different coordination pattern, although the bicolor behavior observed in the experimental fluorescence spectra is preserved. These photophysical properties were observed in DFT and TDDFT calculations. Although the calculated geometries were found to be very similar, the emission wavelengths varied significantly depending upon the functional used.

These conclusions have permitted us to design a second generation of fluorescent bicolor sensors with modifications at the benzo[*a*]imidazo[5,1,2-*cd*]indolizine scaffold. The chemical synthesis, photophysical properties and suitability for barium tagging will be published in due course.

Supporting Information

Supporting Information File 1

Energies, calculated absorption and emission wavelengths.
[https://www.beilstein-journals.org/bjoc/content/supplementary/1860-5397-21-126-S1.pdf]

Supporting Information File 2

Cartesian coordinates of the optimized structures.
[https://www.beilstein-journals.org/bjoc/content/supplementary/1860-5397-21-126-S2.pdf]

Acknowledgements

The authors thank the SGI/IZO-SGIker of the UPV/EHU and the DIPC for the generous allocation of analytical and computational resources.

Funding

Financial support for this work was provided by the European Research Council (ERC) under the European's Union Horizon 2020 research and innovation programme (H2020 ERC-SyG 951281), by the Spanish Ministerio de Ciencia, Innovación y Universidades (Grant PID2023-151549NB-I00, funded by MICIU/AEI/10.13039/501100011033 and by FEDER, EU) and by the Gobierno Vasco/Eusko Jaurlaritza (GV/EJ, Grant IT-1553-22).

Author Contributions

Eric Iván Velazco-Cabral: investigation; validation. Fernando Auria-Luna: data curation; investigation; project administration; writing – review & editing. Juan Molina-Canteras: investigation; validation. Miguel A. Vázquez: supervision. Iván Rivilla: data curation; formal analysis; investigation; methodology; supervision; validation; writing – review & editing. Fernando P. Cossío: conceptualization; formal analysis; funding acquisition; investigation; project administration; resources; supervision; validation; writing – original draft.

ORCID® iDs

Eric Iván Velazco-Cabral - https://orcid.org/0000-0002-1487-1857
Fernando Auria-Luna - https://orcid.org/0000-0002-3726-0493
Juan Molina-Canteras - https://orcid.org/0000-0001-9953-1132
Miguel A. Vázquez - https://orcid.org/0000-0002-2240-4669
Iván Rivilla - https://orcid.org/0000-0003-1984-7183
Fernando P. Cossío - https://orcid.org/0000-0002-4526-2122

Data Availability Statement

All data that supports the findings of this study is available in the published article and/or the supporting information of this article.

Preprint

A non-peer-reviewed version of this article has been previously published as a preprint: https://doi.org/10.3762/bxiv.2025.27.v1

References

1. Goeppert-Mayer, M. *Phys. Rev.* **1935,** *48,* 512–516. doi:10.1103/physrev.48.512
2. Giuliani, A.; Poves, A. *Adv. High Energy Phys. (Hoboken, NJ, U. S.)* **2012,** 857016. doi:10.1155/2012/857016
3. Majorana, E. *Il Nuovo Cim.* **1937,** *14,* 171–184. doi:10.1007/bf02961314
4. Planck Collaboration; Aghanim, N.; Akrami, Y.; Ashdown, M.; Aumont, J.; Baccigalupi, C.; Ballardini, M.; Banday, A. J.; Barreiro, R. B.; Bartolo, N.; Basak, S.; Battye, R.; Benabed, K.; Bernard, J.-P.; Bersanelli, M.; Bielewicz, P.; Bock, J. J.; Bond, J. R.; Borrill, J.; Bouchet, F. R.; Boulanger, F.; Bucher, M.; Burigana, C.; Butler, R. C.; Calabrese, E.; Cardoso, J.-F.; Carron, J.; Challinor, A.; Chiang, H. C.; Chluba, J.; Colombo, L. P. L.; Combet, C.; Contreras, D.; Crill, B. P.; Cuttaia, F.; de Bernardis, P.; de Zotti, G.; Delabrouille, J.; Delouis, J.-M.; Di Valentino, E.; Diego, J. M.; Doré, O.; Douspis, M.; Ducout, A.; Dupac, X.; Dusini, S.; Efstathiou, G.; Elsner, F.; Enßlin, T. A.; Eriksen, H. K.; Fantaye, Y.; Farhang, M.; Fergusson, J.; Fernandez-Cobos, R.; Finelli, F.; Forastieri, F.; Frailis, M.; Fraisse, A. A.; Franceschi, E.; Frolov, A.; Galeotta, S.; Galli, S.; Ganga, K.; Génova-Santos, R. T.; Gerbino, M.; Ghosh, T.; González-Nuevo, J.; Górski, K. M.; Gratton, S.; Gruppuso, A.; Gudmundsson, J. E.; Hamann, J.; Handley, W.; Hansen, F. K.; Herranz, D.; Hildebrandt, S. R.; Hivon, E.; Huang, Z.; Jaffe, A. H.; Jones, W. C.; Karakci, A.; Keihänen, E.; Keskitalo, R.; Kiiveri, K.; Kim, J.; Kisner, T. S.; Knox, L.; Krachmalnicoff, N.; Kunz, M.; Kurki-Suonio, H.; Lagache, G.; Lamarre, J.-M.; Lasenby, A.; Lattanzi, M.; Lawrence, C. R.; Le Jeune, M.; Lemos, P.; Lesgourgues, J.; Levrier, F.; Lewis, A.; Liguori, M.; Lilje, P. B.; Lilley, M.; Lindholm, V.; López-Caniego, M.; Lubin, P. M.; Ma, Y.-Z.; Macías-Pérez, J. F.; Maggio, G.; Maino, D.; Mandolesi, N.; Mangilli, A.; Marcos-Caballero, A.; Maris, M.; Martin, P. G.; Martinelli, M.; Martínez-González, E.; Matarrese, S.; Mauri, N.; McEwen, J. D.; Meinhold, P. R.; Melchiorri, A.; Mennella, A.; Migliaccio, M.; Millea, M.; Mitra, S.; Miville-Deschênes, M.-A.; Molinari, D.; Montier, L.; Morgante, G.; Moss, A.; Natoli, P.; Nørgaard-Nielsen, H. U.; Pagano, L.; Paoletti, D.; Partridge, B.; Patanchon, G.; Peiris, H. V.; Perrotta, F.; Pettorino, V.; Piacentini, F.; Polastri, L.; Polenta, G.; Puget, J.-L.; Rachen, J. P.; Reinecke, M.; Remazeilles, M.; Renzi, A.; Rocha, G.; Rosset, C.; Roudier, G.; Rubiño-Martín, J. A.; Ruiz-Granados, B.; Salvati, L.; Sandri, M.; Savelainen, M.; Scott, D.; Shellard, E. P. S.; Sirignano, C.; Sirri, G.; Spencer, L. D.; Sunyaev, R.; Suur-Uski, A.-S.; Tauber, J. A.; Tavagnacco, D.; Tenti, M.; Toffolatti, L.; Tomasi, M.; Trombetti, T.; Valenziano, L.; Valiviita, J.; Van Tent, B.; Vibert, L.; Vielva, P.; Villa, F.; Vittorio, N.; Wandelt, B. D.; Wehus, I. K.; White, M.; White, S. D. M.; Zacchei, A.; Zonca, A. *Astronom. Astrophys.* **2020,** *641,* A6. doi:10.1051/0004-6361/201833910
5. Fukugita, M.; Yanagida, T. *Phys. Lett. B* **1986,** *174,* 45–47. doi:10.1016/0370-2693(86)91126-3
6. Nygren, D. R. *J. Phys.: Conf. Ser.* **2015,** *650,* 012002. doi:10.1088/1742-6596/650/1/012002
7. Freixa, Z.; Rivilla, I.; Monrabal, F.; Gómez-Cadenas, J. J.; Cossío, F. P. *Phys. Chem. Chem. Phys.* **2021,** *23,* 15440–15457. doi:10.1039/d1cp01203g
8. Rivilla, I.; Aparicio, B.; Bueno, J. M.; Casanova, D.; Tonnelé, C.; Freixa, Z.; Herrero, P.; Rogero, C.; Miranda, J. I.; Martínez-Ojeda, R. M.; Monrabal, F.; Olave, B.; Schäfer, T.; Artal, P.; Nygren, D.; Cossío, F. P.; Gómez-Cadenas, J. J. *Nature* **2020,** *583,* 48–54. doi:10.1038/s41586-020-2431-5
9. Herrero-Gómez, P.; Calupitan, J. P.; Ilyn, M.; Berdonces-Layunta, A.; Wang, T.; de Oteyza, D. G.; Corso, M.; González-Moreno, R.; Rivilla, I.; Aparicio, B.; Aranburu, A. I.; Freixa, Z.; Monrabal, F.; Cossío, F. P.; Gómez-Cadenas, J. J.; Rogero, C.; Adams, C.; Almazán, H.; Álvarez, V.; Arazi, L.; Arnquist, I. J.; Ayet, S.; Azevedo, C. D. R.; Bailey, K.; Ballester, F.; Benlloch-Rodríguez, J. M.; Borges, F. I. G. M.; Bounasser, S.; Byrnes, N.; Cárcel, S.; Carrión, J. V.; Cebrián, S.; Church, E.; Conde, C. A. N.; Contreras, T.; Denisenko, A. A.; Dey, E.; Díaz, G.; Dickel, T.; Escada, J.; Esteve, R.; Fahs, A.; Felkai, R.; Fernandes, L. M. P.; Ferrario, P.; Ferreira, A. L.; Foss, F. W.; Freitas, E. D. C.; Freixa, Z.; Generowicz, J.; Goldschmidt, A.; González-Moreno, R.; Guenette, R.; Haefner, J.; Hafidi, K.; Hauptman, J.; Henriques, C. A. O.; Morata, J. A. H.; Herrero, V.; Ho, J.; Ho, P.; Ifergan, Y.; Jones, B. J. P.; Kekic, M.; Labarga, L.; Larizgoitia, L.; Lebrun, P.; Gutierrez, D. L.; López-March, N.; Madigan, R.; Mano, R. D. P.; Martín-Albo, J.; Martínez-Lema, G.; Martínez-Vara, M.; Meziani, Z. E.; Miller, R.; Mistry, K.; Monteiro, C. M. B.; Mora, F. J.; Vidal, J. M.; Navarro, K.; Novella, P.; Nuñez, A.; Nygren, D. R.; Oblak, E.; Odriozola-Gimeno, M.; Palmeiro, B.; Para, A.; Querol, M.; Redwine, A. B.; Renner, J.; Ripoll, L.; Rodríguez, J.; Rogers, L.; Romeo, B.; Romo-Luque, C.; Santos, F. P.; dos Santos, J. M. F.; Simón, A.; Sorel, M.; Stanford, C.; Teixeira, J. M. R.; Toledo, J. F.; Torrent, J.; Usón, A.; Veloso, J. F. C. A.; Vuong, T. T.; Waiton, J.; White, J. T. *Nat. Commun.* **2022,** *13,* 7741. doi:10.1038/s41467-022-35153-0
10. Auria-Luna, F.; Foss, F. W.; Molina-Canteras, J.; Velazco-Cabral, I.; Marauri, A.; Larumbe, A.; Aparicio, B.; Vázquez, J. L.; Alberro, N.; Arrastia, I.; Nacianceno, V. S.; Colom, A.; Marcuello, C.; Jones, B. J. P.; Nygren, D.; Gómez-Cadenas, J. J.; Rogero, C.; Rivilla, I.; Cossío, F. P.; the NEXT collaboration. *RSC Appl. Interfaces* **2025,** *2,* 185–199. doi:10.1039/d4lf00227j
11. Balaban, A. T.; Oniciu, D. C.; Katritzky, A. R. *Chem. Rev.* **2004,** *104,* 2777–2812. doi:10.1021/cr0306790
12. Glukhovtsev, M. *J. Chem. Educ.* **1997,** *74,* 132. doi:10.1021/ed074p132
13. Krygowski, T. M.; Cyrański, M. K. *Chem. Rev.* **2001,** *101,* 1385–1420. doi:10.1021/cr990326u
14. Chen, Z.; Wannere, C. S.; Corminboeuf, C.; Puchta, R.; Schleyer, P. v. R. *Chem. Rev.* **2005,** *105,* 3842–3888. doi:10.1021/cr030088+
15. Gershoni-Poranne, R.; Stanger, A. *Chem. Soc. Rev.* **2015,** *44,* 6597–6615. doi:10.1039/c5cs00114e
16. Solà, M. *Front. Chem. (Lausanne, Switz.)* **2017,** *5,* 22. doi:10.3389/fchem.2017.00022
17. Poater, J.; Duran, M.; Solà, M.; Silvi, B. *Chem. Rev.* **2005,** *105,* 3911–3947. doi:10.1021/cr030085x
18. Merino, G.; Solà, M.; Fernández, I.; Foroutan-Nejad, C.; Lazzeretti, P.; Frenking, G.; Anderson, H. L.; Sundholm, D.; Cossío, F. P.; Petrukhina, M. A.; Wu, J.; Wu, J. I.; Restrepo, A. *Chem. Sci.* **2023,** *14,* 5569–5576. doi:10.1039/d2sc04998h

19. Wheeler, S. E.; Houk, K. N.; Schleyer, P. v. R.; Allen, W. D. *J. Am. Chem. Soc.* **2009,** *131,* 2547–2560. doi:10.1021/ja805843n
20. Schleyer, P. v. R.; Pühlhofer, F. *Org. Lett.* **2002,** *4,* 2873–2876. doi:10.1021/ol0261332
21. Krygowski, T. M. *J. Chem. Inf. Comput. Sci.* **1993,** *33,* 70–78. doi:10.1021/ci00011a011
22. Craig, N. C.; Groner, P.; McKean, D. C. *J. Phys. Chem. A* **2006,** *110,* 7461–7469. doi:10.1021/jp060695b
23. Arpa, E. M.; Stafström, S.; Durbeej, B. *J. Org. Chem.* **2025,** *90,* 1297–1308. doi:10.1021/acs.joc.4c02475
24. Geuenich, D.; Hess, K.; Köhler, F.; Herges, R. *Chem. Rev.* **2005,** *105,* 3758–3772. doi:10.1021/cr0300901
25. Morao, I.; Cossío, F. P. *J. Org. Chem.* **1999,** *64,* 1868–1874. doi:10.1021/jo981862+
26. Cossío, F. P.; Morao, I.; Jiao, H.; Schleyer, P. v. R. *J. Am. Chem. Soc.* **1999,** *121,* 6737–6746. doi:10.1021/ja9831397
27. Leyva-Parra, L.; Pino-Rios, R.; Inostroza, D.; Solà, M.; Alonso, M.; Tiznado, W. *Chem. – Eur. J.* **2024,** *30,* e202302415. doi:10.1002/chem.202302415
28. Rosenberg, M.; Dahlstrand, C.; Kilså, K.; Ottosson, H. *Chem. Rev.* **2014,** *114,* 5379–5425. doi:10.1021/cr300471v
29. Arpa, E. M.; Durbeej, B. *Phys. Chem. Chem. Phys.* **2023,** *25,* 16763–16771. doi:10.1039/d3cp00842h
30. Li, J.; Yim, D.; Jang, W.-D.; Yoon, J. *Chem. Soc. Rev.* **2017,** *46,* 2437–2458. doi:10.1039/c6cs00619a
31. Karplus, M. *J. Chem. Phys.* **1959,** *30,* 11–15. doi:10.1063/1.1729860
32. Cohen, A. J.; Mori-Sánchez, P.; Yang, W. *Chem. Rev.* **2012,** *112,* 289–320. doi:10.1021/cr200107z
33. Schirmer, J. *Phys. Chem. Chem. Phys.* **2025,** *27,* 4992–5005. doi:10.1039/d4cp04551c
34. Becke, A. D. *J. Chem. Phys.* **1993,** *98,* 5648–5652. doi:10.1063/1.464913
35. Lee, C.; Yang, W.; Parr, R. G. *Phys. Rev. B* **1988,** *37,* 785–789. doi:10.1103/physrevb.37.785
36. Vosko, S. H.; Wilk, L.; Nusair, M. *Can. J. Phys.* **1980,** *58,* 1200–1211. doi:10.1139/p80-159
37. Grimme, S.; Antony, J.; Ehrlich, S.; Krieg, H. *J. Chem. Phys.* **2010,** *132,* 154104. doi:10.1063/1.3382344
38. Grimme, S.; Ehrlich, S.; Goerigk, L. *J. Comput. Chem.* **2011,** *32,* 1456–1465. doi:10.1002/jcc.21759
39. Yanai, T.; Tew, D. P.; Handy, N. C. *Chem. Phys. Lett.* **2004,** *393,* 51–57. doi:10.1016/j.cplett.2004.06.011
40. Zhao, Y.; Truhlar, D. G. *J. Phys. Chem. A* **2006,** *110,* 5121–5129. doi:10.1021/jp060231d
41. Zhao, Y.; Truhlar, D. G. *J. Phys. Chem. A* **2006,** *110,* 13126–13130. doi:10.1021/jp066479k
42. Zhao, Y.; Truhlar, D. G. *Theor. Chem. Acc.* **2008,** *120,* 215–241. doi:10.1007/s00214-007-0310-x
43. Jacquemin, D.; Perpète, E. A.; Ciofini, I.; Adamo, C.; Valero, R.; Zhao, Y.; Truhlar, D. G. *J. Chem. Theory Comput.* **2010,** *6,* 2071–2085. doi:10.1021/ct100119e
44. Zhao, Y.; Truhlar, D. G. *Acc. Chem. Res.* **2008,** *41,* 157–167. doi:10.1021/ar700111a
45. Wang, Y.; Verma, P.; Jin, X.; Truhlar, D. G.; He, X. *Proc. Natl. Acad. Sci. U. S. A.* **2018,** *115,* 10257–10262. doi:10.1073/pnas.1810421115
46. Adamo, C.; Cossi, M.; Barone, V. *J. Mol. Struct.: THEOCHEM* **1999,** *493,* 145–157. doi:10.1016/s0166-1280(99)00235-3
47. Chai, J.-D.; Head-Gordon, M. *Phys. Chem. Chem. Phys.* **2008,** *10,* 6615–6620. doi:10.1039/b810189b
48. McLean, A. D.; Chandler, G. S. *J. Chem. Phys.* **1980,** *72,* 5639–5648. doi:10.1063/1.438980
49. Krishnan, R.; Binkley, J. S.; Seeger, R.; Pople, J. A. *J. Chem. Phys.* **1980,** *72,* 650–654. doi:10.1063/1.438955
50. Wadt, W. R.; Hay, P. J. *J. Chem. Phys.* **1985,** *82,* 284–298. doi:10.1063/1.448800
51. Ditchfield, R. *Mol. Phys.* **1974,** *27,* 789–807. doi:10.1080/00268977400100711
52. Wiberg, K. B. *Tetrahedron* **1968,** *24,* 1083–1096. doi:10.1016/0040-4020(68)88057-3
53. Foster, J. P.; Weinhold, F. *J. Am. Chem. Soc.* **1980,** *102,* 7211–7218. doi:10.1021/ja00544a007
54. Reed, A. E.; Weinhold, F. *J. Chem. Phys.* **1985,** *83,* 1736–1740. doi:10.1063/1.449360
55. Schlegel, H. B. *J. Comput. Chem.* **1982,** *3,* 214–218. doi:10.1002/jcc.540030212
56. *Gaussian 16,* Revision B.01; Gaussian, Inc.: Wallingford, CT, 2016.

License and Terms

BEILSTEIN JOURNAL OF ORGANIC CHEMISTRY

Symmetrical D–π–A–π–D indanone dyes: a new design for nonlinear optics and cyanide detection

Ergin Keleş[1,2], Alberto Barsella[3], Nurgül Seferoğlu[4], Zeynel Seferoğlu[2] and Burcu Aydıner[*2]

Full Research Paper

Open Access

Address:
[1]Department of Chemistry, Graduate School of Natural and Applied Sciences, Gazi University, Yenimahalle, Ankara 06560, Türkiye, [2]Department of Chemistry, Faculty of Science, Gazi University, Yenimahalle, Ankara 06560, Türkiye, [3]Département d'Optique ultrarapide et Nanophotonique, IPCMS, UMR CNRS 7504, Université de Strasbourg, 23 rue du Loess, BP 43, 67034 Strasbourg Cedex 2, France and [4]Department of Advanced Technology, Graduate School of Natural and Applied Sciences, Gazi University, Yenimahalle, Ankara 06560, Türkiye

Email:
Burcu Aydıner[*] - baydiner@gazi.edu.tr

* Corresponding author

Keywords:
chemosensor; DFT calculations; donor–π–acceptor–π–donor based organic dyes; indan-2-one; NLO

Beilstein J. Org. Chem. **2026,** *22,* 131–142.
https://doi.org/10.3762/bjoc.22.6

Received: 24 September 2025
Accepted: 29 December 2025
Published: 14 January 2026

This article is part of the thematic issue "π-Conjugated molecules and materials".

Guest Editor: A. Mateo-Alonso

Abstract

Three indan-2-one-based donor–π–acceptor–π–donor type dyes with symmetric donor groups were synthesized and characterized to study their nonlinear optical (NLO) properties and their potential use in the rapid and selective determination of cyanide. The designed structures feature symmetrical alkylaminophenyl donor groups and a strong electron-withdrawing dicyanovinylene as an acceptor connected through vinyl groups as a π-bridge. These strongly π-conjugated organic dyes can absorb in the NIR region, and they showed sensitivity towards the polarity of solvents with colorimetric and optical changes. Because of the strong donor–acceptor structure, second-order NLO properties were studied by measuring electric field-induced second harmonic (EFISH) values, which showed significant second-order NLO responses. The experimental results were explained using density functional theory (DFT) methods. The dyes also exhibit chemosensor properties, showing selectivity for cyanide via a Michael addition mechanism that causes the disappearance of the ICT band, and a significant color change was observed in both organic and aqueous media. In addition, the interaction mechanism between cyanide and the chemosensor is determined by a ^{1}H NMR study and explained by DFT calculations.

Introduction

Over the past decades, the functional heterocyclic push–pull dyes have attracted significant attention due to their widespread use in materials chemistry. This type of dye is of particular interest in the fields of organic electronics, photonics, and optoelectronics etc., used in areas such as dye-sensitized solar cells (DSSC), organic light-emitting diodes (OLED), nonlinear optics

(NLO), and organic semiconductors and are also broadly used in diagnostic kits for diseases, fluorescence sensors, and various biotechnological fields [1-7]. Especially, organic materials showing nonlinear optical (NLO) properties have considerable advantages, such as low-cost production and larger NLO responses over inorganic counterparts [8-10]. Conjugated organic molecules containing electron-donating and accepting groups exhibit higher second-order nonlinearity due to having planar structures, long π-conjugations, and thermal stability [11]. Organic dyes that display efficient second-order NLO have high hyperpolarizability (β) values through electron-donor (D) and -withdrawing (A) groups linked by π-bridges in their structures [12,13]. Thus, NLO responses can be tunable by adjusting the strength of the donor and acceptor groups based on the intramolecular charge transfer (ICT) efficiency [14-16]. Indanones are highly conjugated with a planar structure, which favors overlap between the molecules. They are building blocks for many compounds, such as organic materials for optoelectronic and NLO applications [17,18]. Research shows that the absorption wavelength of the region can be shifted in the deep red/NIR region by changing the donor group with increased conjugated systems [19-22]. Gupta et al. studied optical properties of D–π–A system-based indan-2-one derivatives, and symmetric derivatives showed a significant bathochromic shift (≈300 nm) compared to asymmetric ones [23].

Organic dyes are also used as chemosensors, which provide economical, fast, and equipment-free analysis for the detection of environmental pollutants affecting the environment and human health [24,25]. Colorimetric detection of specific ions like cyanide, which is considered a highly toxic anion and dangerous to human health, by dyes gives advantages such as high sensitivity, fast response, low cost, and ease of operation [26-28].

In this study, symmetric novel indan-2-one derivatives with a D–π–A–π–D system were synthesized, and their structures were characterized using ^{1}H NMR, ^{13}C NMR, and mass spectrometry methods. Dye structures were designed with alkylaminophenyl groups, known for their various electron-donating properties, as donors, and the dicyanovinyl group, with its strong electron-withdrawing properties, as acceptors, conjugated with an indan-2-one core (Figure 1). The vinyl bridges were added to the design, which have the potential to open nucleophilic addition reactions (Michael type) due to their electron deficiencies, in addition to acting as π-bridges for the D–A conjugation. Furthermore, a symmetric design with increased π-conjugation was planned to shift the absorption bands towards the NIR region. Syntheses of dyes were carried out using the conventional method and the microwave irradiation (MWI) method, and the results were compared with yields and reaction times. Absorption spectra in solvents of different polarities were examined to determine the photophysical properties of the dyes. The sensitivity/selectivity properties of the dyes to anions were investigated in DMSO and aqueous media, revealing that the dyes were selectively responsive only to cyanide anions. Changes after interactions were determined through absorption spectra and color changes under ambient light. In addition, interaction mechanisms of dyes with cyanide were studied using the ^{1}H NMR titration method, and it was determined that they interacted through an addition mechanism. Photophysical properties and interaction mechanisms of the compounds were also supported through density functional theory (DFT) and time-dependent DFT (TD-DFT) calculations, which were consistent

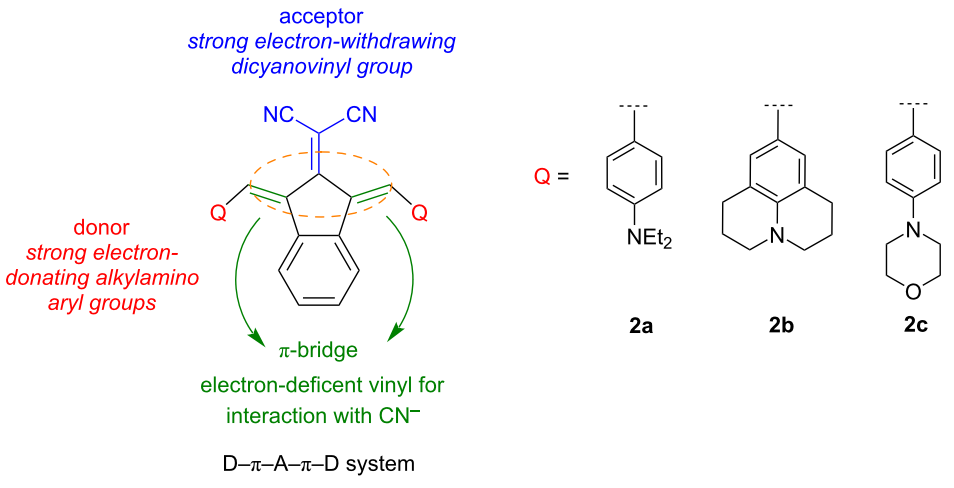

Figure 1: Design of the functional dyes.

with experimental results. NLO properties of the compounds were experimentally determined using the EFISH method and calculated using theoretical methods. Additionally, the thermal decomposition temperatures, an important parameter for compounds used in electro-optic (EO) application, were determined by thermogravimetric analysis (TGA).

Results and Discussion

Syntheses

In the first step, 2-(1,3-dihydro-2*H*-inden-2-ylidene)malononitrile (**1**) was synthesized by indan-2-one and malononitrile in DCM with ammonium acetate/acetic acid buffers with a good yield (84%). Target compounds were synthesized by a coupling reaction between 2-(1,3-dihydro-2*H*-inden-2-ylidene)malononitrile (**1**) and appropriate alkylaminobenzaldehyde derivatives in acetic anhydride. Compounds were obtained with low to good yields (25–75%, conventional method (CM)) (Scheme 1, Table 1). All syntheses were also carried out with microwave irradiation (MWI), which had a short reaction time; however, no improvement in yield was achieved (see Supporting Information File 1). The structural analyses of the compounds were performed using $^{1}H/^{13}C$ NMR and mass spectrometry methods (Figures S1–S10 in Supporting Information File 1).

Table 1: Summary of reaction conditions, yields, and solid state color of dyes **2a–c**.

	CM	MWI	
Dyes	Yield (Time)	Yield (Time)	Color
2a	75% (45 min)	62% (4.5 min)	dark purple
2b	46% (30 min)	45% (4.5 min)	dark green
2c	22% (2 h)	25% (4.5 min)	black

Optical properties of dyes

Photophysical properties of dyes **2a–c** were assessed in four different organic solvents with various polarities (DMSO, acetone, chloroform, and THF) via absorption spectra and DFT calculations (Table 2). Figure 2a–c displays the absorption spectra of the dyes and photographs under daylight in organic solvents (Figure S11 in Supporting Information File 1). The dyes exhibited two distinct absorption maxima in the range of 358–446 nm and 493–648 nm. The shorter wavelength absorption maxima are assigned the n–π* transition from the donor group to the dicyanovinyl, and longer wavelength absorption maxima are the n–π* transition of the conjugated structure [2].

Alkylamino groups (diethylamino, julolidine, and morpholine) as donor groups in chromophores have different electron-donor properties, causing a shift in the absorption wavelengths due to ICT transition to the dicyanovinylene acceptor [29-31]. The dyes show a bathochromic shift in absorption maxima, with the increased electron-donating tendency (Figure 2 and Table 2). Dyes **2a** and **2c** have free rotating alkylamino groups as diethylamino and morpholine, respectively, while **2b** have julolidine groups with restricted rotation, which makes the structure more planar. The absorption maxima are observed in order as **2b** > **2a** > **2c**. Therefore, these structural differences in donor groups showed that shifts towards longer wavelength absorption are attributed to the rigid planar structure, causing more delocalization of the π-electrons between donors and the acceptor (dicyanovinylene) group.

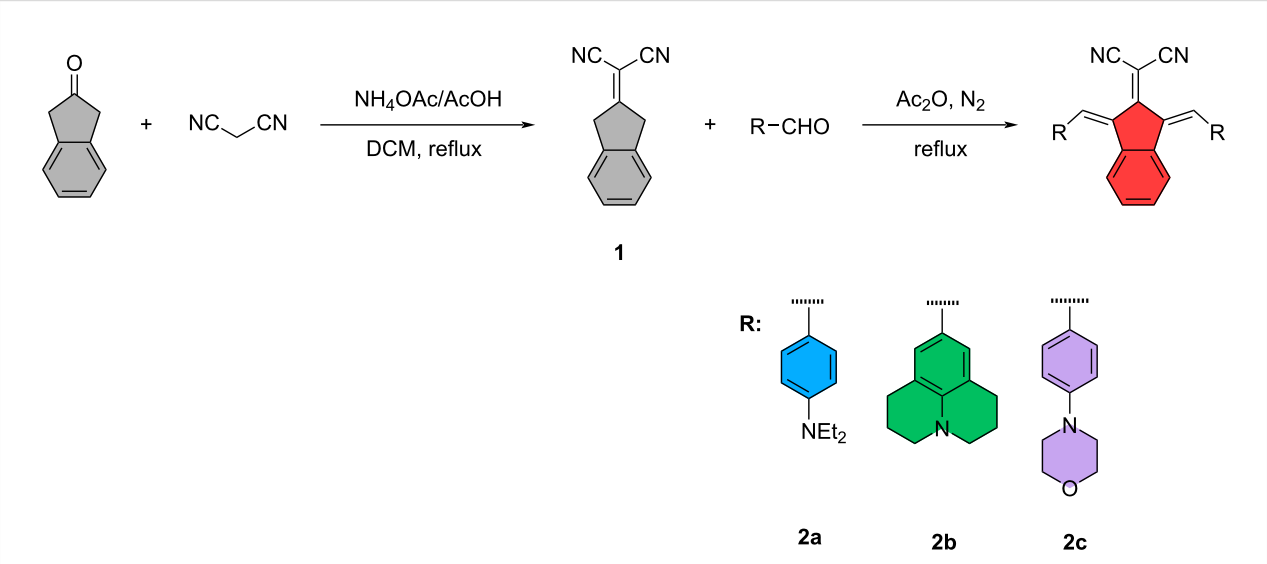

Scheme 1: Synthetic pathway of compounds.

Table 2: Photophysical properties of dyes **2a–c** in various solvents with different polarity and the calculated absorption spectra data[a].

		Experimental		DFT calculations		
	Solvent	λ_{Abs} (nm)	ε ($M^{-1}\cdot cm^{-1}$)	λ_{Abs} (nm)	*f*	Transitions, *w* (%)[b]
2a	DMSO	<u>591</u>	18413	607	0.8465	HOMO–1→LUMO, 99%
		410		422	0.7386	HOMO→LUMO+1, 99%
	acetone	<u>560</u>	16474	602	0.8231	HOMO–1→LUMO, 99%
		402		421	0.7418	HOMO→LUMO+1, 99%
	chloroform	<u>583</u>	14978	589	0.8191	HOMO–1→LUMO, 99%
		413		421	0.7639	HOMO→LUMO+1, 99%
	THF	<u>550</u>	19031	595	0.8209	HOMO–1→LUMO, 99%
		399		421	0.7540	HOMO→LUMO+1, 98%
2b	DMSO	<u>648</u>	19698	617	0.8785	HOMO–1→LUMO, 99%
		446		427	0.7331	HOMO→LUMO+1, 98%
	acetone	<u>608</u>	10470	612	0.8526	HOMO–1→LUMO, 99%
		430		426	0.7369	HOMO→LUMO+1, 98%
	chloroform	<u>604</u>	12566	598	0.8477	HOMO–1→LUMO, 99%
		423		425	0.7607	HOMO→LUMO+1, 98%
	THF	<u>589</u>	12650	604	0.8498	HOMO–1→LUMO, 99%
		424		426	0.7500	HOMO→LUMO+1, 99%
2c	DMSO	<u>523</u>	8103	572	0.5901	HOMO–1→LUMO, 3% HOMO→LUMO, 96%
		358		412	0.7351	HOMO–1→LUMO+1, 3% HOMO→LUMO+1, 96%
	acetone	<u>494</u>	7649	569	0.5829	HOMO–1→LUMO, 96% HOMO→LUMO, 3%
		377		411	0.5829	HOMO–1→LUMO+1, 3%
		<u>491</u>	8194	560	0.6331	HOMO→LUMO+1, 96%
	chloroform	<u>491</u>	8194	560	0.6331	HOMO–1→LUMO, 97% HOMO→LUMO, 2%
		372		411	0.7689	HOMO→LUMO+1, 97%
	THF	<u>493</u>	8784	564	0.6114	HOMO–1→LUMO, 97% HOMO→LUMO, 2%
		376		411	0.7561	HOMO–1→LUMO+1, 2% HOMO→LUMO+1, 97%

[a]ε was calculated according to the underlined band. [b]HOMO: highest occupied molecular orbital, LUMO: lowest unoccupied molecular orbital.

The effect of solvent media was investigated with solvents of varying polarities, which showed a bathochromic shift in the absorption maxima with increasing solvent polarity.

Dyes also showed significant color changes with increasing polarity. Color changes of **2a**; from purple to blue, **2b**; blue to green, and **2c**; pale orange to pale pink (Figure 2d). Dyes do not show any significant emission.

Chemosensor properties

Cyanide selectivity study

The dyes **2a–c** could have the ability to detect cyanide anions due to the presence of vinyl groups, where cyanide can be attacked via nucleophilic addition reaction. Therefore, the sensitivity and selectivity of dyes towards cyanide were investigated by the addition of cyanide (CN^-) and competing anions (F^-, Cl^-, Br^-, I^-, AcO^-, ClO_4^-, $H_2PO_4^-$, HSO_4^-, and NO_3^-) in the

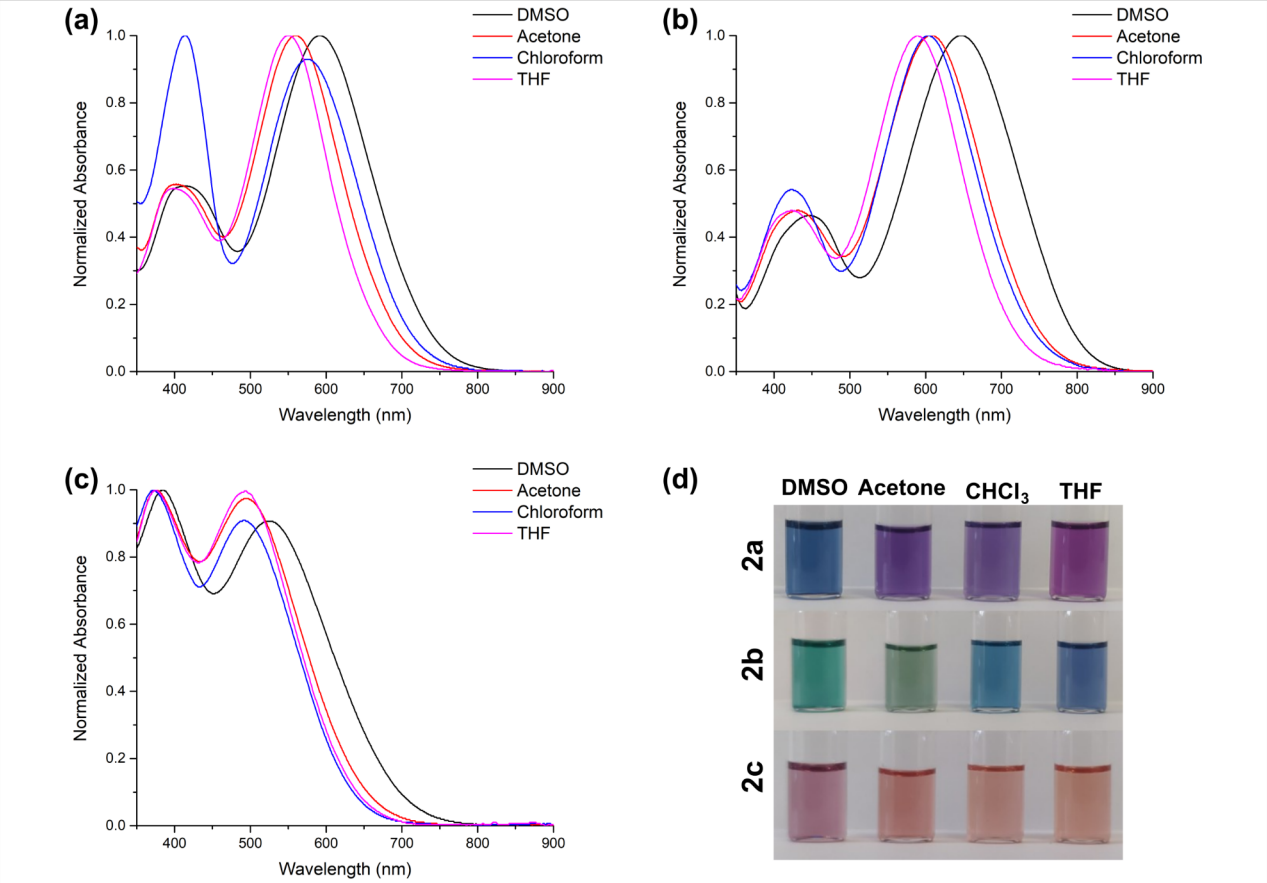

Figure 2: Normalized absorption spectra of dyes **2a** (a), **2b** (b), and **2c** (c); Photographs of dyes in the given solvents of different polarities under ambient light (d) c = 10 μM.

form of the corresponding tetrabutylammonium (TBA) salt. Firstly, a titration study was conducted by the addition of 20 equiv of anions to dyes in organic solvent as DMSO (Figure 3). A significant response was only observed during the addition of cyanide. Upon addition of cyanide to dyes, the absorption bands at longer wavelength, 550–700 nm, disappeared while shorter wavelength absorption maxima, 350-450 nm, showed a slight increment in absorbance. The disappearance of the ICT band indicates that the conjugation through the structure of dyes between the donor and acceptor groups is disrupted. These results strongly suggest the addition of cyanide to the vinyl bridge. Furthermore, the color of dyes **2a**–**c**, blue, green, and pink, respectively, under ambient light changed to yellow when interacting with cyanide. The interaction mechanism was determined by ^{1}H NMR, and the proposed mechanism was investigated in more detail by DFT studies. It is given in the next section.

In order to examine the sensitivity of the dyes to anions in aqueous media, firstly, the best ratio with DMSO as a co-solvent for aqueous medium was determined. For this purpose, absorption spectra were obtained by adding 50 equiv of CN^- to the DMSO/H_2O (v/v) solution mixtures at certain ratios (c = 30 μM) (Figures S12–S14 in Supporting Information File 1). This study was applied separately for all dyes, and the appropriate ratio was determined for each as **2a**; 6:4, **2b**; 7:3, and **2c**; 4:6, DMSO/H_2O, v/v. When the dyes were titrated with CN^- anions, the longer wavelength band decreased and disappeared, similar to the DMSO media (Figure 4). This result indicates that the interaction mechanism is similar in the aqueous environment. In addition, when the photographs taken with different solvents of the dyes were examined, similar changes in their colors were observed under daylight like those in DMSO (Figure 4, insets).

Additionally, the limit of detection (LOD) values of the compounds were calculated as 4.41 μM for **2a**, 9.49 μM for **2b** and 1.33 μM for **2c** in DMSO/H_2O binary solvent medium (Figure S15 in Supporting Information File 1).

Interaction mechanism

^{1}H NMR titration was performed to determine the interaction mechanism of the dyes (Figure 5). Upon the addition of 0.5 equiv of CN^-, the intensity of the signals of **2b** decreased

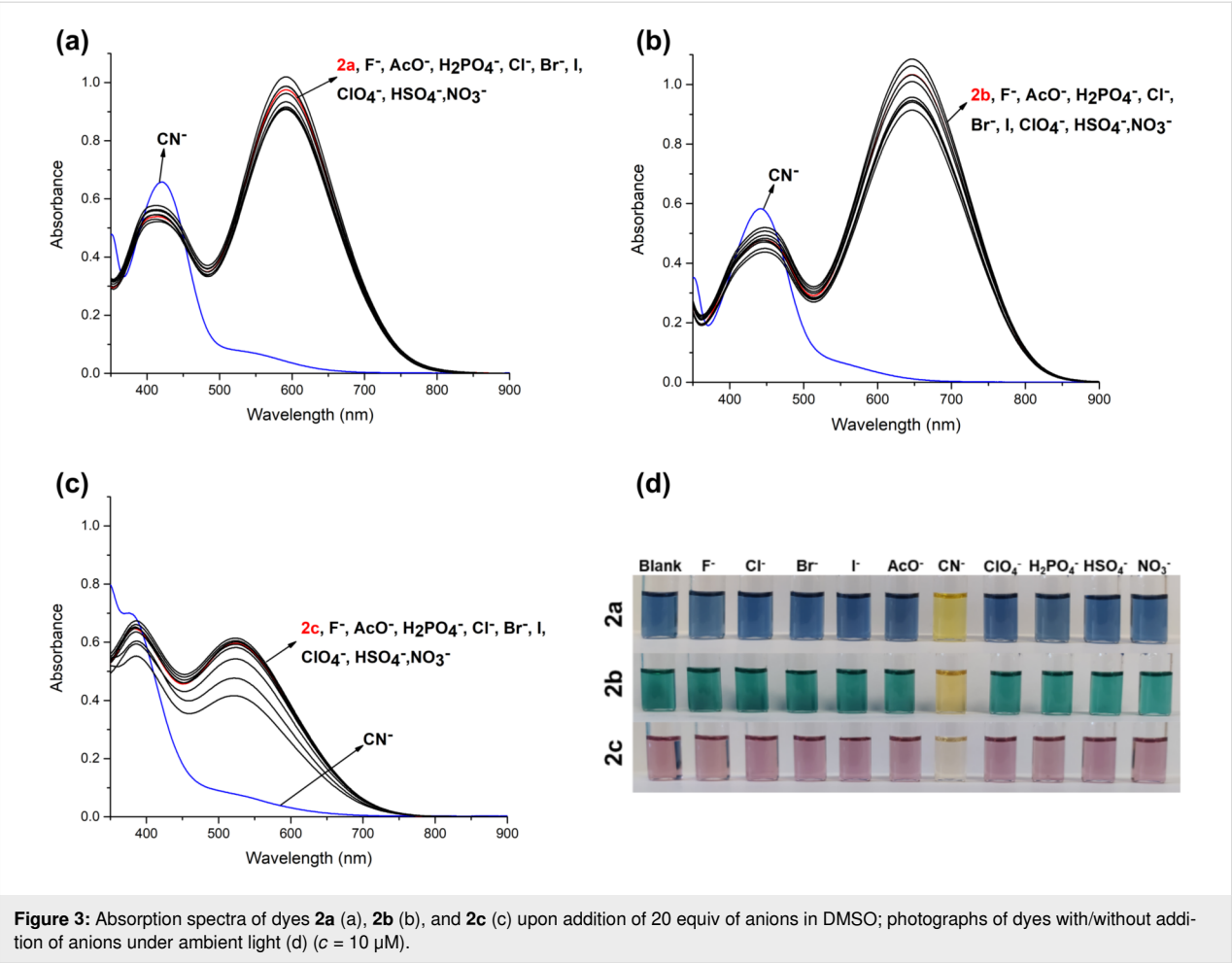

Figure 3: Absorption spectra of dyes **2a** (a), **2b** (b), and **2c** (c) upon addition of 20 equiv of anions in DMSO; photographs of dyes with/without addition of anions under ambient light (d) (c = 10 μM).

(green) while new signals appeared at the upfield, indicating the formation of another structure with increased electron density in conjugated system. Especially, the signal at 5.9 ppm (Hb, green to cyan) can be attributed to a change in aromatic hydrogen to aliphatic. The addition of cyanide to vinyl carbon can explain this change. Upon the addition of 1 equiv of CN^-, signals of **2b** protons have completely disappeared, and the protons of the new species become apparent. An increase in cyanide concentration did not cause any further changes in spectra. This result indicates that cyanide gives a mono-addition to the vinyl group (Scheme 2).

DFT results

To further confirm the proposed interaction mechanism involved between **2a–c** with CN^-, DFT calculations were performed at B3LYP/6-31+G(d,p) level of theory. The optimized geometries **2a–c** and **2a–c+CN⁻** were represented in Figure 6.

The optimized geometries of the study's molecules showed that π-conjugted linkers between the cyano fragments and indanone group are almost planar, with the dihedral angles with the atom-numbering in Supporting Information File 1, Figure S16, (C16–C14–C12–C13 and C15–C14–C12–C11): (0.57, −0.57) for **2a**; (0.79, −0.79) for **2b**; (0.07, −0.20) for **2c**. In addition, the dihedrals between indanone and phenyl rings (C13–C21–C23–C24 and C11–C19–C33–C34) are (157.30, −157.30); (159.29, −159.29); 154.46, −156.48) for **2a–c**, respectively, which is an indicator of large degrees of conjugation and good ICT. When CN^- interacts with the **2a–c** via the proposed addition mechanism (Scheme 2), the planarity between the cyano fragments and indanone group is partially reduced with the dihedrals (−26.19, −28.29) for **2a+CN⁻**, (−26.89, −28.94) for **2b+CN⁻**, (−24.77, −26.23) for **2c+CN⁻**. Furthermore, the planarity between the indanone and phenyl rings is disrupted where CN^- is attached, while remaining more planar on the other side, with the dihedral values (−52.13, 144.39); (−51.21, 144.32); (−51.84, 142.39) for **2a+CN⁻**, **2b+CN⁻** and **2c+CN⁻**, respectively. As a result, conjugation is disrupted on the side where planarity is disrupted and a decrease in ICT occurs, which causes shifts in the absorption spectra.

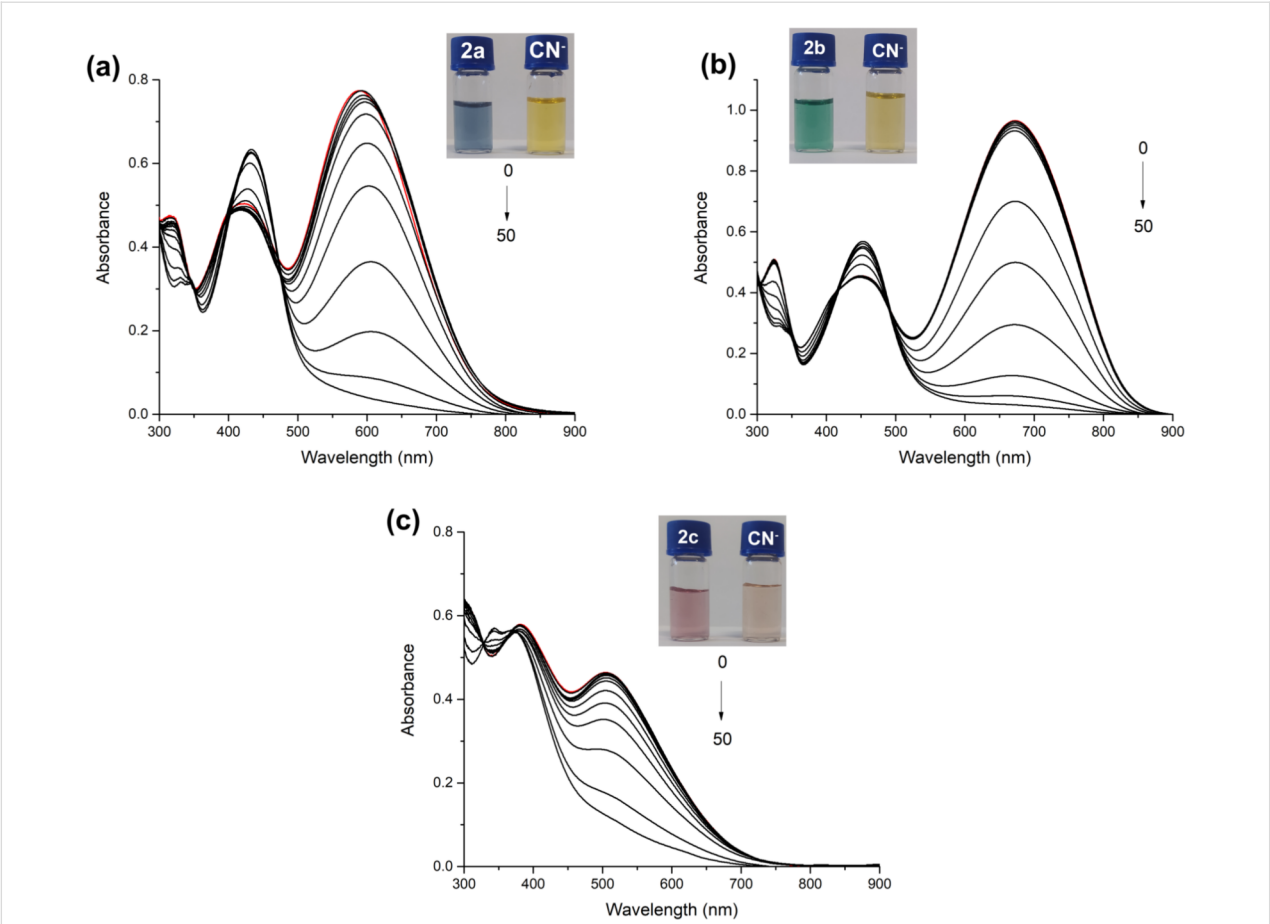

Figure 4: Absorption spectra of titrated dyes (**2a–c**) with up to 50 equiv of CN^- (a) 6:4, (b) 7:3, and (c) 4:6 in DMSO/H_2O (v/v) (*c* = 30 μM).

To get further information about the electronic structures of **2a**–**c** and **2a**–**c+CN**$^-$ adducts, TD-DFT calculations were performed with B3LYP/6-31+G(d,p) in DMSO. The calculated absorption maxima (λ_{abs}), oscillator strengths (*f*) and corresponding transitions are given in Table 3.

As given in Table 2, the obtained absorption wavelengths at 422 nm (427 nm) and 607 nm (617 nm) for **2a** (**2b**) had significant contributions (99%) from HOMO−1→LUMO and HOMO→LUMO+1, respectively. For **2c**, the major contributions come from HOMO→LUMO+1 (96%) and HOMO→LUMO (96%) for the transitions at 412 nm and 572 nm, respectively. The electron distribution is located at the donor groups and slightly at the dicyanovinylene unit in the HOMO. The distribution in the HOMO−1 mainly is over the donor groups (Figure 7 and Figure S17, Supporting Information File 1). The LUMO is delocalized over the dicyanovinylene unit and slightly over the indanone group, while the LUMO+1 is over the indanone group. From this, it is predicted that there is an ICT from donor groups to acceptor groups, resulting in absorption maxima in the spectrum.

In case of **2a**–**c+CN**$^-$ adducts formed after the interaction with CN^- anion with the studied molecules, a single peak appears at 436 nm, 461 nm and 403 nm, respectively, and the peak at the longer wavelength seen before interaction with CN^- disappeared. The peaks for **2a**–**b+CN**$^-$ arise from the HOMO−1→LUMO transitions, while for **2c+CN**$^-$ are contributed from the HOMO−2→LUMO transitions, with the contributions ≈94–99%.

Considering the molecular orbitals reveal that there are no contributions from the side where the planarity is disrupted after the addition of the CN^- anion and the electron distributions shift towards the other side where conjugation exists (Figure 7 and Figure S17, Supporting Information File 1).

NLO properties

The EFISH method and DFT calculation were used to examine the NLO responses of **2a**–**c**. Measurements were made using the EFISH method in a $CHCl_3$ solution at a non-resonant incident wavelength of 1907 nm. Experimental details for the EFISH measurements and results are presented in Table 4 [32]. The

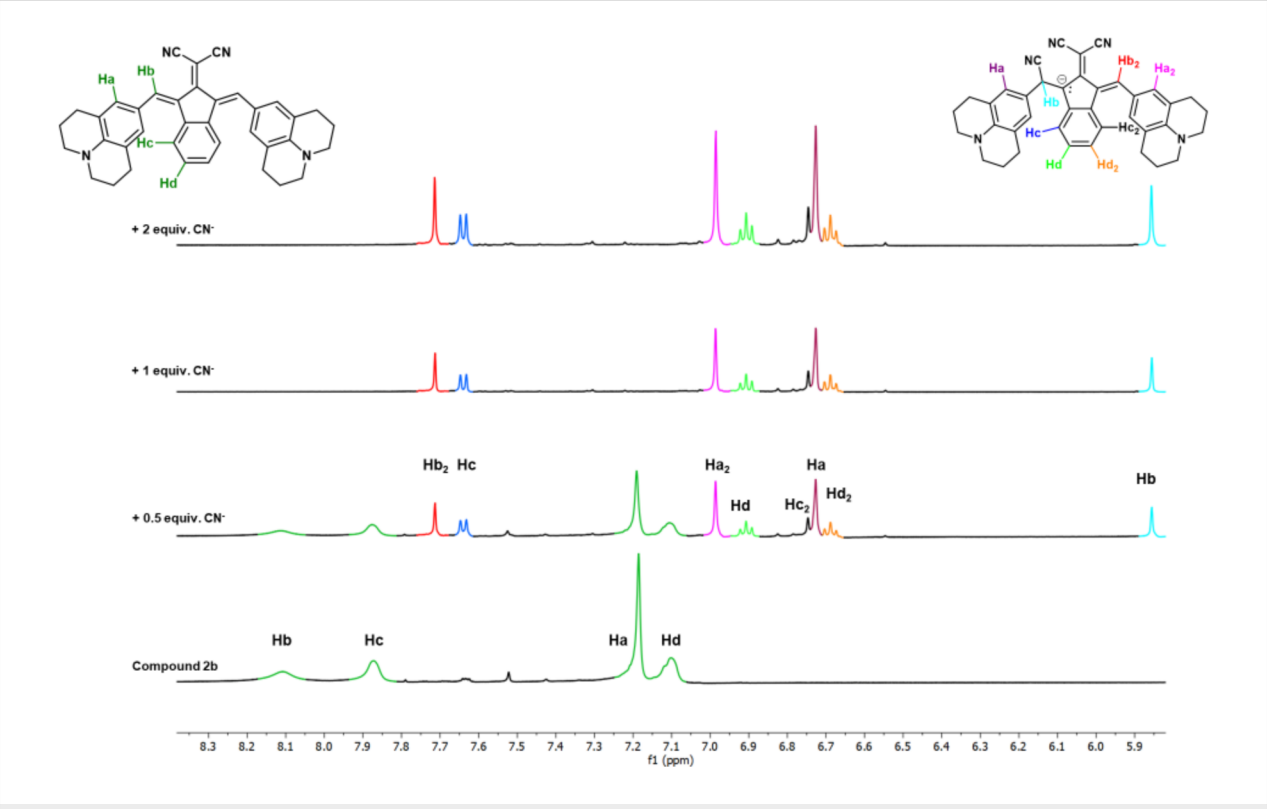

Figure 5: Partial ^{1}H NMR spectral change of **2b** (c = 10 mM) after up to 2 equiv of TBACN (c = 1 M) in DMSO-d_6.

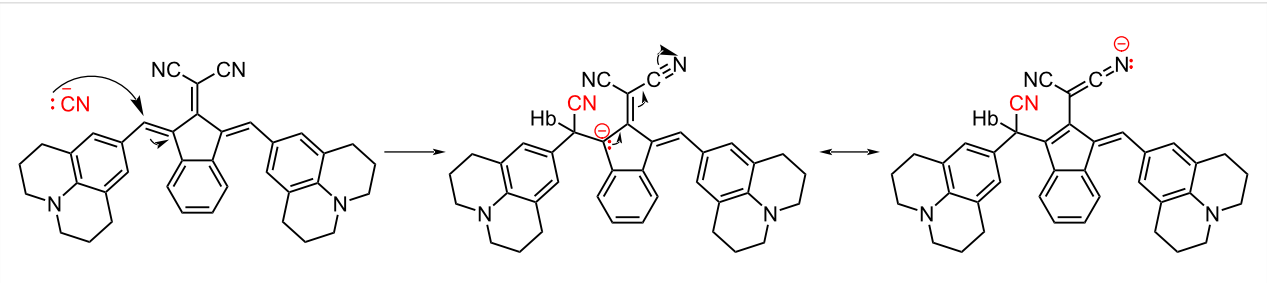

Scheme 2: Proposed interaction mechanism with CN^-.

excited states were more polarized than the ground states, as shown by the positive observed μβ values. Moreover, both the ground and excited states were polarized in the same direction for all studied compounds. The standard reference is Disperse Red 1 (μβ = 450 × 10^{-48} esu) [33]. Comparing the μβ values of Disperse Red 1 with the measured values of **2a**–**c** shows that the molecules exhibited a higher NLO response than Disperse Red 1, except for **2c**.

The dipole moment (μ), polarizability (α), first-order hyperpolarizability (β), and its components, which were calculated at the B3LYP/6-31+G(d,p) level of theory in $CHCl_3$, are also included in Table 4 and Table S1, Supporting Information File 1. According to the calculations, there is more charge delocalization in the xxy direction because the βxxy component is larger (Table S1, Supporting Information File 1). A significant first-order hyperpolarizability value (β) is indicative of a high NLO response in a typical organic NLO chromophore. Apart from the existence of donor (D) and acceptor (A) groups linked by a π-conjugation path, the NLO response is also influenced by the strength of the D and A groups in the structure. For high NLO responses, a small energy gap between the HOMO and the LUMO (ΔE), resulting from the presence of the strong D/A groups, is an important indicator. Based on the EFISH results, the calculations show that **2a** and **2b** have a small energy gap and a high β value because they have a stronger electron-donor group than **2c**. Additionally, **2a** and **2b** have higher polarizability values and dipole moments (μ) than **2c**.

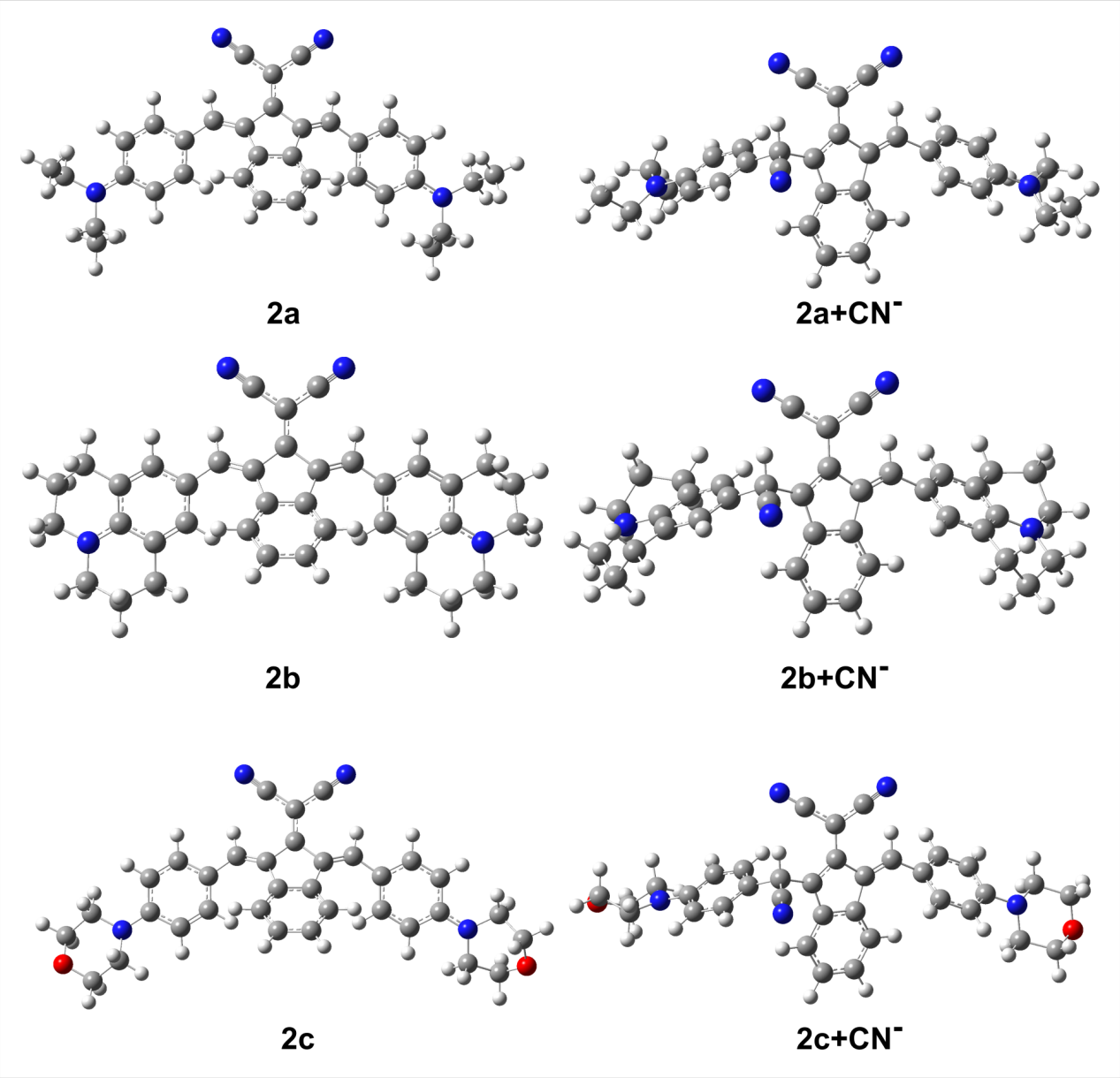

Figure 6: Optimized geometries of **2a–c** and **2a–c+CN⁻** obtained at the B3LYP/6-31+G(d,p) level.

TGA analysis

Thermogravimetric analyses (TGA) were performed to determine the thermal stability of the dyes. The TGA method allows the determination of thermal and gravimetric changes in the material following temperature increases. Dyes, especially those with potential for use in optical systems, must be stable up to certain temperatures depending on the systems [34-36].

The percentage mass loss versus temperature graph is shown in Figure 8. The decomposition temperatures (T_d) of the dyes are given in Table 5. Results show that the dyes are in the range of 254–339 °C.

The mass loss between 0 and 150 °C indicates the presence of water or an organic solvent in the structure of compound **2b**. The T_d values of the dyes are generally resistant to moderate to high temperatures. This result supports their potential use as optical dyes.

Conclusion

In summary, we have determined optical and chemosensor properties of symmetrical D−A dyes **2a**, **2b**, and **2c**. We found that strong electron-donating properties and increased planar structure of julolidine (**2b**) as a donor induced a significant bathochromic shift to the NIR region and the greatest extinction coefficient Also, dyes exhibit positive solvatochromism,

Table 3: The absorption maxima (λ_{abs}), oscillator strength (*f*) and transitions for **2a–c** and **2a–c+CN⁻**.

λ_{abs} (nm)	*f*	Transitions[a]	λ_{abs} (nm)	*f*	Transitions[a]
2a			**2a+CN⁻**		
607 422	0.8465 0.7386	HOMO–1→LUMO HOMO→LUMO+1	436	0.7139	HOMO–1→LUMO
2b			**2b+CN⁻**		
617 427	0.8785 0.7331	HOMO–1→LUMO HOMO→LUMO+1	461	0.5077	HOMO–1→LUMO
2c			**2c+CN⁻**		
572 412	0.5901 0.7351	HOMO→LUMO HOMO→LUMO+1	403	0.6076	HOMO–2→LUMO

[a]HOMO: highest occupied molecular orbital, LUMO: lowest unoccupied molecular orbital.

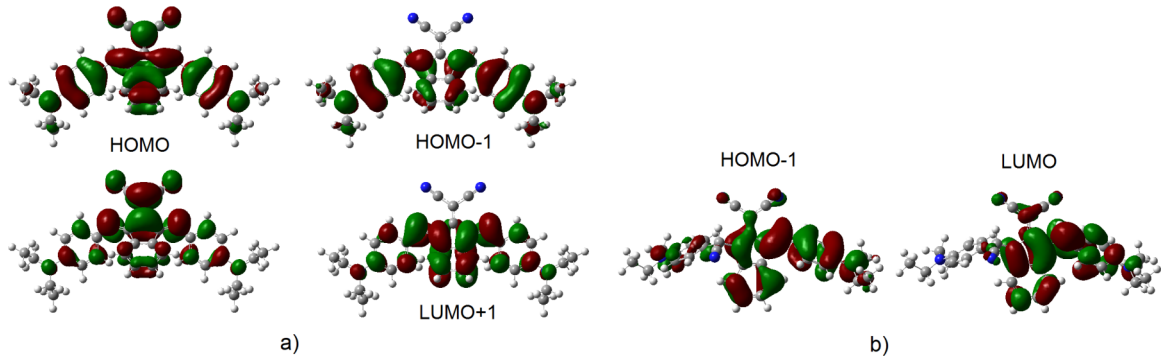

Figure 7: Frontier molecular orbitals of a) **2a,** b) **2a+CN⁻**.

Table 4: Experimental and calculated NLO properties and energy gap (Δ*E*) values for **2a–c**.

Dyes	$\mu\beta^{a}(\times10^{-48})$ (esu)	ΔE^{b} (eV)	μ^{b} (D)	$\alpha^{b}(\times10^{-24})$ (esu)	$\beta^{b}(\times10^{-30})$ (esu)
2a	1170	2.36	15	117	404
2b	1740	2.32	15	116	389
2c	300	2.42	12	113	362

[a]EFISH: μβ (2ω) at 1907 nm in $CHCl_3$, molecular concentrations used for the measurements were in the range of 10^{-3} to 10^{-2} M. μβ ± 10%. [b]DFT results at the B3LYP/6-31+G(d,p) level of theory in $CHCl_3$.; esu: electrostatic unit.

consistent with their ICT characteristics. Moreover, synthesized symmetric dyes containing D–π–A–π–D systems were analyzed using experimental and computational methods for second-order nonlinear optical properties. NLO measurements conducted using the EFISH method, where μβ values were found between 300×10^{-48} esu and 1740×10^{-48} esu and the highest value observed was with **2b**. Dyes also showed chemosensor properties for the selective detection of cyanide with colorimetric and optical responses in both organic and aqueous media. The interaction mechanism is determined as mono-cyanide addition to the vinyl group via Michael reaction. These results show that symmetrical indanone-based

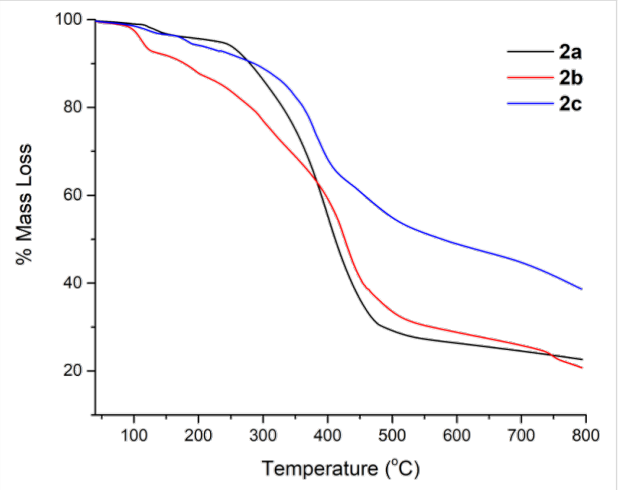

Figure 8: TGA curves of dyes.

Table 5: T_d values of the dyes.

Dyes	T_d (°C) (%85)
2a	263
2b	254
2c	339

D–π–A–π–D dyes can be used in future optoelectronic devices and environmental monitoring.

Supporting Information

Supporting Information File 1

Synthesis of compounds, copies of NMR, HRMS and UV–vis spectra and DFT results.
[https://www.beilstein-journals.org/bjoc/content/supplementary/1860-5397-22-6-S1.pdf]

Acknowledgements

The numerical calculations reported in this paper were fully performed at TUBITAK ULAKBIM, High Performance and Grid Computing Center (TRUBA resources). This study constitutes part of Ergin Keleş's Ph.D. thesis.

Funding

This research was supported by TUBITAK (Grant no: 122Z692).

Author Contributions

Ergin Keleş: investigation; visualization. Alberto Barsella: investigation. Nurgül Seferoğlu: formal analysis; visualization; writing – original draft; writing – review & editing. Zeynel Seferoğlu: conceptualization; supervision; writing – review & editing. Burcu Aydıner: conceptualization; funding acquisition; project administration; supervision; writing – original draft; writing – review & editing.

ORCID® iDs

Ergin Keleş - https://orcid.org/0000-0001-6456-4807
Alberto Barsella - https://orcid.org/0000-0002-3707-9221
Nurgül Seferoğlu - https://orcid.org/0000-0001-9368-3354
Burcu Aydıner - https://orcid.org/0000-0003-1823-6217

Data Availability Statement

All data that supports the findings of this study is available in the published article and/or the supporting information of this article.

References

1. Giordano, M.; Cardano, F.; Barolo, C.; Viscardi, G.; Fin, A. *Adv. Funct. Mater.* **2025,** *35,* 2411230. doi:10.1002/adfm.202411230
2. Stavrou, M.; Zyla, G.; Ladika, D.; Dumur, F.; Farsari, M.; Gray, D. *ACS Appl. Opt. Mater.* **2024,** *2,* 1653–1666. doi:10.1021/acsaom.4c00241
3. Barros, M.; Arroyo, P.; Sáez, J. A.; Gil, S.; Parra, M.; Costa, S. P. G.; Raposo, M. M. M.; Gaviña, P. *R. Soc. Open Sci.* **2025,** *12,* 241816. doi:10.1098/rsos.241816
4. Bui, T.-T.; Péralta, S.; Dumur, F. *Molecules* **2023,** *28,* 1489. doi:10.3390/molecules28031489
5. Persson, S.; Benesperi, I.; Goriya, Y.; Kand, D.; Rayavarapu, S.; Keller, T.; Freitag, M.; Wärnmark, K. *Sustainable Energy Fuels* **2025,** *9,* 2389–2395. doi:10.1039/d4se01772b
6. Seferoğlu, Z. *Org. Prep. Proced. Int.* **2017,** *49,* 293–337. doi:10.1080/00304948.2017.1336052
7. Islam, M. M.; Priya, S.; Kasana, S.; Kurmi, B. D.; Patel, P. *J. Mol. Struct.* **2025,** *1326,* 141146. doi:10.1016/j.molstruc.2024.141146
8. Mammadova, F.; Inyurt, F. C.; Barsella, A.; Dengiz, C. *Dyes Pigm.* **2023,** *209,* 110894. doi:10.1016/j.dyepig.2022.110894
9. Yahya, M.; Keleş, E.; Metin, R.; Aydıner, B.; Seferoğlu, N.; Barsella, A.; Şahin, E.; Sakalli, Y.; Seferoğlu, Z. *J. Photochem. Photobiol., A* **2025,** *462,* 116176. doi:10.1016/j.jphotochem.2024.116176
10. Erden, K.; Soyler, D.; Barsella, A.; Şahin, O.; Soylemez, S.; Dengiz, C. *J. Org. Chem.* **2024,** *89,* 13192–13207. doi:10.1021/acs.joc.4c01328
11. Lanke, S. K.; Sekar, N. *Dyes Pigm.* **2016,** *126,* 62–75. doi:10.1016/j.dyepig.2015.11.014
12. Khalid, M.; Wu, G.; Umber, A.; Khan, M.; Braga, A. A. C.; Alhokbany, N.; Ojha, S. C. *J. Mol. Liq.* **2024,** *401,* 124608. doi:10.1016/j.molliq.2024.124608
13. Shafiq, I.; Raza, N.; Dildar, S.; Bullo, S. *Sci. Rep.* **2025,** *15,* 23236. doi:10.1038/s41598-025-04911-7
14. Dalton, L. R.; Sullivan, P. A.; Bale, D. H. *Chem. Rev.* **2010,** *110,* 25–55. doi:10.1021/cr9000429
15. Pant, D.; Sitha, S. *J. Mol. Model.* **2024,** *30,* 284. doi:10.1007/s00894-024-06055-3
16. Hood, B. R.; de Coene, Y.; Jones, C. F.; Lopez Poves, I.; Deveaux, N.; Halcovitch, N. R.; Champagne, B.; Clays, K.; Fielden, J. *Inorg. Chem.* **2024,** *63,* 24250–24261. doi:10.1021/acs.inorgchem.4c04179

17. González, M. L.; Sánchez-Vergara, M. E.; Álvarez-Bada, J. R.; Chávez-Uribe, M. I.; Toscano, R. A.; Álvarez-Toledano, C. *J. Mater. Chem. C* **2014,** *2,* 5607–5614. doi:10.1039/c4tc00599f
18. Monzón-González, C. R.; Sánchez-Vergara, M. E.; Vallejo Narváez, W. E.; Rocha-Rinza, T.; Hernández, M.; Gómez, E.; Jiménez-Sandoval, O.; Álvarez-Toledano, C. *J. Phys. Chem. Solids* **2021,** *150,* 109840. doi:10.1016/j.jpcs.2020.109840
19. Ersoy, G.; Henary, M. *Biomolecules* **2025,** *15,* 119. doi:10.3390/biom15010119
20. Sparks, N. E.; Smith, C.; Stahl, T.; Amarasekara, D. L.; Hamadani, C.; Lambert, E.; Tang, S. W.; Kulkarni, A.; Derbigny, B. M.; Dasanayake, G. S.; Taylor, G.; Ghazala, M.; Hammer, N. I.; Sokolov, A. Y.; Fitzkee, N. C.; Tanner, E. E. L.; Watkins, D. L. *J. Mater. Chem. C* **2024,** *12,* 4369–4383. doi:10.1039/d3tc04747d
21. Gupta, A. K.; Cordes, D. B.; De, J.; Slawin, A. M. Z.; Warriner, S.; Samuel, I. D. W.; Zysman-Colman, E. *J. Mater. Chem. C* **2025,** *13,* 6123–6135. doi:10.1039/d4tc05238b
22. Yan, K.; Hu, Z.; Yu, P.; He, Z.; Chen, Y.; Chen, J.; Sun, H.; Wang, S.; Zhang, F. *Nat. Commun.* **2024,** *15,* 2593. doi:10.1038/s41467-024-46853-0
23. Gupta, A.; Ali, A.; Bilic, A.; Singh, T. B.; Evans, R. A. *Dyes Pigm.* **2014,** *108,* 15–23. doi:10.1016/j.dyepig.2014.04.008
24. Udhayakumari, D.; A, N. *J. Mol. Struct.* **2025,** *1321,* 140249. doi:10.1016/j.molstruc.2024.140249
25. Poovadichalil, N. M.; Ullah, A.; Maurya, M. R.; Hasan, A.; Sadasivuni, K. K. *Int. J. Environ. Sci. Technol.* **2025,** *22,* 15467–15478. doi:10.1007/s13762-025-06636-6
26. Tamizhselvi, R.; Bhaskar, R.; Ashok Kumar, S. K.; Mohandoss, S.; Lee, Y. R.; Napoleon, A. A. *ACS Omega* **2024,** *9,* 11223–11231. doi:10.1021/acsomega.3c06057
27. Kiran; Ranolia, A.; Priyanka; Duhan, A.; Dhaka, R. K.; Singh, S.; Joshi, G.; Kumar, P.; Singh, D.; Wahajuddin, M.; Sindhu, J. *RSC Adv.* **2025,** *15,* 9129–9140. doi:10.1039/d5ra00576k
28. Keleş, E.; Aydıner, B.; Seferoğlu, Z. *Curr. Org. Synth.* **2023,** *20,* 61–76. doi:10.2174/1570179419666211221163435
29. Abu Alrub, S.; Ali, A. I.; Hussein, R. K.; Alghamdi, S. K.; Eladly, S. A. *Int. J. Mol. Sci.* **2024,** *25,* 5586. doi:10.3390/ijms25115586
30. Wang, Z.; Jiang, J.; Huang, Y.; Liu, W. *Chin. J. Chem. Phys.* **2023,** *36,* 397–403. doi:10.1063/1674-0068/cjcp2203046
31. Bureš, F. *RSC Adv.* **2014,** *4,* 58826–58851. doi:10.1039/c4ra11264d
32. Ulrich, G.; Barsella, A.; Boeglin, A.; Niu, S.; Ziessel, R. *ChemPhysChem* **2014,** *15,* 2693–2700. doi:10.1002/cphc.201402123
33. Guerchais, V.; Le Bozec, H. *Top. Organomet. Chem.* **2010,** *28,* 171–225. doi:10.1007/978-3-642-01866-4_6
34. Deng, G.; Xu, H.; Huang, H.; Jiang, J.; Kun, J.; Zhang, X.; Li, Z.; Liu, J. *J. Mol. Struct.* **2019,** *1196,* 439–443. doi:10.1016/j.molstruc.2019.06.106
35. Hu, C.; Liu, F.; Zhang, H.; Huo, F.; Yang, Y.; Wang, H.; Xiao, H.; Chen, Z.; Liu, J.; Qiu, L.; Zhen, Z.; Liu, X.; Bo, S. *J. Mater. Chem. C* **2015,** *3,* 11595–11604. doi:10.1039/c5tc02702k
36. Liu, F.; Zhang, M.; Xiao, H.; Yang, Y.; Wang, H.; Liu, J.; Bo, S.; Zhen, Z.; Liu, X.; Qiu, L. *J. Mater. Chem. C* **2015,** *3,* 9283–9291. doi:10.1039/c5tc01610j

License and Terms